S. Morita
F.J. Giessibl
R. Wiesendanger
Editors

NANOSCIENCE AND TECHNOLOGY

Noncontact Atomic Force Microscopy

Volume 2

NanoScience and Technology

NanoScience and Technology

Series Editors:
P. Avouris   B. Bhushan   D. Bimberg   K. von Klitzing   H. Sakaki   R. Wiesendanger

The series NanoScience and Technology is focused on the fascinating nano-world, mesoscopic physics, analysis with atomic resolution, nano and quantum-effect devices, nanomechanics and atomic-scale processes. All the basic aspects and technology-oriented developments in this emerging discipline are covered by comprehensive and timely books. The series constitutes a survey of the relevant special topics, which are presented by leading experts in the field. These books will appeal to researchers, engineers, and advanced students.

Please view available titles in *NanoScience and Technology* on series homepage
http://www.springer.com/series/3705/

Seizo Morita
Franz J. Giessibl
Roland Wiesendanger
Editor

Noncontact Atomic Force Microscopy

Volume 2

With 196 Figures

Professor Dr. Seizo Morita
Osaka University
Graduate School of Engineering
Department of Electrical, Electronic
and Information Engineering
Yamada-Oka 2-1, Suita 565-0871, Japan
E-mail: smorita@eei.eng.osaka-u.ac.jp

Professor Dr. Roland Wiesendanger
Institut für Angewandte Physik
Universität Hamburg
Jungiusstr. 11, 20355 Hamburg, Germany
E-mail: rwiesendanger
@physnet.uni-hamburg.de

Professor Dr. Franz J. Giessibl
Universität Regensburg, Institut für Experimentelle und Angewandte Physik
Universitätsstr. 31, 93053 Regesnburg, Germany
E-mail: franz.giessibl@physik.uni-regensburg.de

Series Editors:
Professor Dr. Phaedon Avouris
IBM Research Division
Nanometer Scale Science & Technology
Thomas J. Watson Research Center
P.O. Box 218
Yorktown Heights, NY 10598, USA

Professor Dr. Bharat Bhushan
Ohio State University
Nanotribology Laboratory
for Information Storage
and MEMS/NEMS (NLIM)
Suite 255, Ackerman Road 650
Columbus, Ohio 43210, USA

Professor Dr. Dieter Bimberg
TU Berlin, Fakutät Mathematik/
Naturwissenschaften
Institut für Festkörperphyisk
Hardenbergstr. 36
10623 Berlin, Germany

Professor Dr., Dres. h.c. Klaus von Klitzing
Max-Planck-Institut
für Festkörperforschung
Heisenbergstr. 1
70569 Stuttgart, Germany

Professor Hiroyuki Sakaki
University of Tokyo
Institute of Industrial Science
4-6-1 Komaba, Meguro-ku
Tokyo 153-8505, Japan

Professor Dr. Roland Wiesendanger
Institut für Angewandte Physik
Universität Hamburg
Jungiusstr. 11
20355 Hamburg, Germany

NanoScience and Technology ISSN 1434-4904
ISBN 978-3-642-01494-9 e-ISBN 978-3-642-01495-6
DOI 10.1007/978-3-642-01495-6
Library of Congress Control Number: 2009930388

© Springer-Verlag Berlin Heidelberg 2009
This work is subject to copyright. All rights are reserved, whether the whole or part of the material is concerned, specifically the rights of translation, reprinting, reuse of illustrations, recitation, broadcasting, reproduction on microfilm or in any other way, and storage in data banks. Duplication of this publication or parts thereof is permitted only under the provisions of the German Copyright Law of September 9, 1965, in its current version, and permission for use must always be obtained from Springer. Violations are liable to prosecution under the German Copyright Law.
The use of general descriptive names, registered names, trademarks, etc. in this publication does not imply, even in the absence of a specific statement, that such names are exempt from the relevant protective laws and regulations and therefore free for general use.

Typesetting: Data prepared by SPi using a Springer TEX macro package
Cover concept: eStudio Calamar Steinen
SPIN: 12279104 57/3180/SPi Printed on acid-free paper 9 8 7 6 5 4 3 2 1
springer.com

Preface

Atomic force microscopy (AFM) was invented in 1985 by G. Binnig, C.F. Quate and Ch. Gerber. Since then it has successfully achieved many outstanding results on micro- and nanoscales and even on atomic and molecular scales by simple contact measurements, although contact AFM cannot achieve atomic resolution in a stable manner.

In 1994 F.J. Giessibl succeeded in obtaining an atomically resolved AFM (noncontact [NC]-AFM) image of the Si(111)-(7×7) surface under a weak attractive tip–sample interaction in UHV at room temperature (RT) by utilizing a frequency modulation (FM) detection method combined with a large oscillation amplitude of the cantilever. Soon the NC-AFM successfully accomplished atomically resolved imaging on various surfaces such as compound semiconductor [InP(110) (1995)], insulating [NaCl(001) (1997)] and metal oxide [TiO_2(110) (1997)]. Then in 1998 the first NC-AFM workshop that developed into the annual NC-AFM conference was held, where atomic and molecular resolution imaging of metal [Ag(111) and Cu(111)], molecule [C_{60}/Si(111)], layer material [Graphite(0001) at 22 K] and ferroelectric material [TGS] surfaces was reported. Moreover there were several remarkable achievements in this workshop such as force spectroscopy [tip–sample distance dependence of frequency shift and NC-AFM image], Kelvin probe force imaging on an atomic scale and electrostatic force imaging with atomic resolution.

In 2002 "Noncontact Atomic Force Microscopy" edited by S. Morita, R. Wiesendanger and E. Meyer was published from Springer, which introduced the principles of NC-AFM and remarkable progress achieved by NC-AFM. Since then the NC-AFM has developed further. This book deals with the outstanding results obtained with atomic resolution after the publication of the previous book.

At first, in Chap. 1, S. Morita introduces the history, present status and future prospects. Then, in Chap. 2, M. Abe and K. Morita introduce the method for precise force measurement even at room temperature by compensating the thermal drift. In Chap. 3 by O. Custance et al. and Chap. 4 by R. Hoffmann, applications of force spectroscopy to semiconductor surfaces

such as single atom chemical identification, and to insulating surfaces such as KBr(001) are explained.

In Chap. 5 by A. Schirmeisen et al., force field spectroscopy in three dimensions including energy dissipation is explained. In Chap. 6, F.J. Giessibl explains the principles and applications of the qPlus sensor based on a quartz tuning fork, which is becoming more and more important in this field. In Chap. 7 by M. Heyde et al., applications of NC-AFM/STM based on a quartz tuning fork at 5K to thin oxide films are explained.

In Chap. 8, Y. Sugimoto explains various modes of mechanical atom manipulation such as atom interchange manipulation, and applications to semiconductor surfaces such as the construction of "atom inlay" at RT. In Chap. 9 by M. Ternes et al., atomic manipulation based on a quartz tuning fork at 5 K, and applications to metal surfaces such as force measurements during adsorbate manipulating and mapping of the energy landscape are explained. In Chap. 10 by S. Hirth et al., atomic manipulation of atomic defects on an insulator surface is introduced. In Chap. 11 by P. Pou et al. and Chap. 12 by T. Trevethan et al., modeling, theoretical simulation and mechanism of mechanical atom manipulation in semiconductor and insulating surfaces are explained, respectively.

In Chap. 13, A. Schwarz et al. explain in detail the magnetic exchange force microscopy experiments such as tip preparation, and applications to NiO(001) and Fe/W(001). In Chap. 14 by C. Lazo et al., the contrast mechanism and first-principles simulation of magnetic exchange force microscopy on Fe/W(001) are explained.

In Chap. 15 by K. Kobayashi and H. Yamada, the principles of atomically resolved NC-AFM imaging in liquid, and then applications are explained. In Chap. 16 by T. Fukuma and S. P. Jarvis, biological applications in liquid environment such as lipid-ion network are explained. In Chap. 17 by H. Kawakatsu et al., high frequency more than 1–200 MHz and low amplitude of a few 10 pm to a few 100 pm based on heterodyne laser Doppler interferometry and photothermal vibration excitation both in the deflection and tortional modes, and application to imaging of structured water molecules are explained. In Chap. 18 by A. Raman et al., cantilever dynamics and nonlinear effects and their operation in liquids are discussed.

I thank all the authors for their contributions to this book on NC-AFM Vol. 2. I also thank Springer-Verlag for their fruitful collaborations. Finally I thank Yukako Miyatake, Masayuki Abe and Junko Abe for editing this book. It is hoped that this book will accelerate the NC-AFM field toward rapid and continuing growth and that it will stimulate further efforts to develop atomic and molecular tools based on mechanical methods.

Osaka, Japan, *Seizo Morita*
Regensburg, Germany *Franz J. Giessibl*
Hamburg, Germany *Roland Wiesendanger*
May 2009

Contents

1 Introduction
Seizo Morita 1
1.1 Rapidly Developing High Performance AFM 1
1.1.1 Present Status of High Performance AFM 4
1.2 Future Prospects for High Performance AFM 8
1.2.1 Atomic and Molecular Imaging in Liquids 8
1.2.2 Magnetic Exchange Force Microscopy 8
1.2.3 Rapid Growth of Tuning Fork/qPlus Sensor 11
1.2.4 Differentiation of Atomic Force 11
1.2.5 Atom-by-Atom Assembly of Complex Nanostructure at RT 12
References 13

2 Method for Precise Force Measurements
Masayuki Abe and Ken-ichi Morita 15
2.1 Quantitative Force Calculation 15
2.2 Thermal Drift 16
2.3 Three-Fold Feedback for Precise Tip–Sample Positioning 16
2.3.1 Principle of Atom-Tracking 17
2.3.2 Experimental Setup 18
2.3.3 Site-Specific Force Spectroscopy at Room Temperature 20
2.4 Thermal Drift Compensation
for Force Field Mapping 23
2.4.1 Concept of Feedforward 23
2.4.2 Force Mapping at Room Temperature with Feedforward . . . 24
2.4.3 Force Mapping with Feedforward 26
2.5 Summary 29
References 29

3 Force Spectroscopy on Semiconductor Surfaces
Oscar Custance, Noriaki Oyabu, and Yoshiaki Sugimoto 31
3.1 Introduction 31

3.2 Experimental Considerations ... 33
3.2.1 Extraction of the Short-Range Force from the Frequency Shift ... 34
3.2.2 Determination of Relevant Acquisition Parameters ... 36
3.3 Energy Dissipation and Force Spectroscopy ... 38
3.3.1 Tip-Apex Characterization Combining Force Spectroscopy and First-Principles Calculations ... 38
3.3.2 Identification of an Energy Dissipation Channel ... 42
3.3.3 Surface Adhesion Maps at Atomic Scale ... 45
3.3.4 Signatures of Energy Dissipation in Frequency Shift and Force Curves ... 46
3.4 Force Spectroscopy and Atomic Relaxations ... 48
3.5 Single Atom Chemical Identification ... 53
3.6 Force Spectroscopy with Higher Flexural Modes ... 61
3.7 Summary ... 65
References ... 66

4 Tip–Sample Interactions as a Function of Distance on Insulating Surfaces
Regina Hoffmann ... 69
4.1 Experimental Evaluation of Short-range Forces ... 70
4.1.1 Measurement Techniques ... 70
4.1.2 Conversion of Frequency Shift to Force ... 72
4.1.3 Separation of Short-range and Long-range Forces ... 73
4.2 Short-range Forces on Insulating Surfaces ... 76
4.2.1 Simple Model for Electrostatic Forces ... 76
4.2.2 Relaxation and Realistic Electrostatic Interactions ... 78
4.2.3 Interaction of a Tip with a Well-known Surface ... 80
4.2.4 Sublattice Identification on Alkali Halide Surfaces ... 82
4.2.5 Full Three-Dimensional Force Field ... 83
4.2.6 Atomic Jumps and Energy Dissipation ... 86
References ... 92

5 Force Field Spectroscopy in Three Dimensions
André Schirmeisen, Hendrik Hölscher, and Udo D. Schwarz ... 95
5.1 Introduction ... 95
5.2 Three-Dimensional Force Field Spectroscopy: The Technique ... 97
5.2.1 Experimental Set-up ... 97
5.2.2 The Interrelation Between Frequency Shift and Tip–Sample Forces ... 100
5.2.3 Extending Dynamic Force Spectroscopy to Three Dimensions ... 102
5.3 Force Field Spectroscopy on Ionic Crystals ... 104
5.3.1 Force Fields and Energy Dissipation on NaCl ... 104

5.3.2 Force Vector Fields on KBr 110
5.4 True 3D Force Field Spectroscopy on Graphite 113
References 117

6 Principles and Applications of the qPlus Sensor
Franz J. Giessibl 121
6.1 Motivation: qPlus Versus Si Cantilever 121
6.1.1 Specifications of an Atomic Force Probe 122
6.1.2 Cantilevers in Dynamic Force Microscopy 124
6.1.3 Advantages of Small Amplitude Operation 125
6.1.4 Ideal Physical Properties of Cantilevers 128
6.2 Theory of qPlus Versus Tuning Fork Sensors 128
6.2.1 Quartz Tuning Forks 128
6.2.2 qPlus Sensor 131
6.2.3 Manufacturing High Quality qPlus Sensors 132
6.2.4 Preamplifiers for qPlus Sensors 134
6.3 Applications 137
6.3.1 Own Results 137
6.3.2 External Groups 138
6.4 Outlook 138
References 140

7 Study of Thin Oxide Films with NC-AFM: Atomically Resolved Imaging and Beyond
M. Heyde, G.H. Simon, and T. König 143
7.1 Introduction 143
7.2 Methods and Experimental Setup 145
7.2.1 Quartz Tuning Fork-based Sensor for Dual-Mode NC-AFM/STM 145
7.2.2 Concepts for Force and Energy Extraction and Sensor Characterization 148
7.3 Atomic Resolution Imaging 150
7.4 Beyond Imaging: Spectroscopy 156
7.4.1 z-Spectroscopy on Specific Atomic Sites 157
7.4.2 Work Function Shift Measurements 160
7.5 Conclusion 165
References 165

8 Atom Manipulation on Semiconductor Surfaces
Yoshiaki Sugimoto 169
8.1 Introduction 169
8.2 Experimental 171
8.3 Vertical Atom Manipulation 172
8.4 Lateral Atom Manipulation at Low Temperature 173
8.5 Interchange Lateral Atom Manipulation 175
8.6 Lateral Atom Manipulation at Room Temperature 179

8.7 Interchange Vertical Atom Manipulation 184
8.8 Summary 188
References 189

9 Atomic Manipulation on Metal Surfaces
Markus Ternes, Christopher P. Lutz, and Andreas J. Heinrich 191
9.1 Introduction 192
9.2 Modes of Manipulation 193
9.3 Instrumentation 195
9.3.1 Detected Signals 197
9.4 Forces During Adsorbate Manipulating 199
9.4.1 Manipulating a Small Molecule: CO on Cu(111) 206
9.5 Modeling Forces and Conductance 207
9.6 Mapping the Energy Landscape 209
9.7 Summary 213
References 213

10 Atomic Manipulation on an Insulator Surface
Sabine Hirth, Frank Ostendorf, and Michael Reichling 217
10.1 Introduction 218
10.2 Basic Principles 218
10.2.1 Experimental Procedures 218
10.2.2 Surface Characterization 219
10.3 Experimental Results 221
10.3.1 Defect Preparation and Contrast Formation 221
10.3.2 Manipulation of Mobile Defects 223
10.3.3 Velocity Dependence of Manipulation 225
10.4 Conclusions 225
References 226

11 Basic Mechanisms for Single Atom Manipulation in Semiconductor Systems with the FM-AFM
Pablo Pou, Pavel Jelínek, and Rubén Pérez 227
11.1 Introduction 227
11.2 Theoretical Approach: First-Principles Simulations 229
11.3 The Short Range Chemical Interaction Between Tip and Sample 230
11.4 Manipulation in the Attractive Regime: Vacancies in the Si(111)-(7×7) Reconstruction 232
11.5 Manipulation in the Repulsive Tip–Surface Interaction Regime 237
11.5.1 A Complex Phase Space Under Strong Tip–Surface Interactions 237
11.5.2 Dip-Pen Atomic Lithography: Vertical Atom Interchange Between the Tip and the Surface in the α-Sn/Si(111)-$(\sqrt{3} \times \sqrt{3})$ Surface 240
11.6 Conclusion 247
References 248

12 Multi-Scale Modelling of NC-AFM Imaging and Manipulation at Insulating Surfaces
T. Trevethan, N. Martsinovich, L. Kantorovich, and A.L. Shluger 251
12.1 Introduction 251
12.2 Methods 253
12.2.1 Modelling the Instrument 253
12.2.2 Modelling the Tip–Surface Junction 254
12.2.3 Kinetic Monte Carlo 256
12.3 Applications 258
12.3.1 Pd Adatom on MgO (001) 258
12.3.2 H_2O Adsorbate on CeO_2 (111) 263
12.3.3 C_{60} on Si (001) 265
12.4 Discussion 270
References 272

13 Magnetic Exchange Force Microscopy
Alexander Schwarz, Uwe Kaiser, Rene Schmidt, and Roland Wiesendanger 275
13.1 Introduction 275
13.2 Tip Preparation 277
13.3 NiO(001) 278
13.4 Fe/W(001) 282
13.5 Future Perspectives 285
References 285

14 First-Principles Simulation of Magnetic Exchange Force Microscopy on Fe/W(001)
Cesar Lazo, Hendrik Hölscher, Vasile Caciuc, and Stefan Heinze 287
14.1 Introduction 287
14.2 Computational Method 289
14.3 Analysis of the Magnetic Exchange Forces 291
14.3.1 Unrelaxed Tip and Sample 291
14.3.2 Influence of Structural Relaxations 293
14.3.3 Electronic and Magnetic Structure Changes due to Tip–Sample Interaction 294
14.3.4 Influence of Tip Size 295
14.4 Simulation of MExFM Images 297
14.5 Summary 299
References 300

15 Frequency Modulation Atomic Force Microscopy in Liquids
Kei Kobayashi and Hirofumi Yamada 303
15.1 Brief Overview 303
15.2 Problems of Frequency Modulation AFM in Liquids 304

15.2.1 Viscous Damping of Cantilever in Fluid ... 304
15.2.2 Electric Double Layer Force [11] ... 307
15.3 Frequency Noise in Frequency Modulation Atomic Force Microscopy [12] ... 308
15.3.1 Basics of Frequency Modulation ... 308
15.3.2 Frequency Noise Analysis in High-Q Environment ... 310
15.3.3 Frequency Noise Analysis in Low-Q Environment ... 314
15.4 Improvement of FM-AFM for Liquid Environment ... 316
15.4.1 Optimization of Optical Beam Deflection Sensor ... 316
15.4.2 Reduction of Coherence Length of Laser ... 318
15.4.3 Reduction of Oscillation Amplitude ... 320
15.5 High-Resolution Imaging by FM-AFM in Liquid ... 321
15.5.1 Muscovite Mica [22] ... 321
15.5.2 Purple Membrane Proteins [23] ... 323
15.5.3 Isolated Protein Molecules [23] ... 323
15.5.4 Measurement of Local Hydration Strcutres ... 325
15.6 Summary and Outlook ... 326
References ... 327

16 Biological Applications of FM-AFM in Liquid Environment
Takeshi Fukuma and Suzanne P. Jarvis ... 329
16.1 Quantitative Force Measurements ... 329
16.1.1 Calculating Force from Frequency Shift ... 329
16.1.2 Cantilever Excitation in Liquid ... 330
16.1.3 Single Molecule Spectroscopy ... 332
16.2 Subnanometer-Resolution Imaging ... 333
16.2.1 Overview ... 333
16.2.2 Technical Progresses ... 336
16.2.3 Biological Applications ... 338
16.3 Future Prospects ... 343
References ... 344

17 High-Frequency Low Amplitude Atomic Force Microscopy
Hideki Kawakatsu, Shuhei Nishida, Dai Kobayashi, Kazuhisa Nakagawa, and Shigeki Kawai ... 347
17.1 Cantilever ... 347
17.2 Cantilever Vibration Excitation ... 348
17.3 Cantilever Vibration Detection ... 351
17.4 AFM Head ... 352
17.5 Control Scheme ... 354
17.6 Imaging with Small Amplitude of Drive ... 355
17.7 Lateral Dynamic Force Microscopy ... 356
17.8 Summary ... 358
References ... 359

18 Cantilever Dynamics and Nonlinear Effects in Atomic Force Microscopy
A. Raman, R. Reifenberger, J. Melcher, and R. Tung . . . 361
18.1 Introduction . . . 361
18.2 Eigenmodes of AFM Cantilevers . . . 363
18.2.1 Eigenmodes of Tipless Microcantilevers . . . 363
18.2.2 Influence of Tip Mass on AFM Cantilever Eigenmodes . . . 365
18.2.3 Eigenmodes of Triangular AFM Microcantilevers . . . 366
18.3 Cantilever Dynamics in AM-AFM . . . 368
18.3.1 Mathematical Simulations of Cantilever Dynamics . . . 368
18.3.2 Single Mode Nonlinear Phenomena in dAFM: Bifurcations, Higher Harmonics, and Chaos . . . 370
18.3.3 Multimode Nonlinear Dynamics in dAFM . . . 375
18.3.4 Cantilever Dynamics in Liquids . . . 376
18.4 Cantilever Dynamics in FM-AFM . . . 379
18.4.1 Origins of Frequency Shift and Its Measurement . . . 380
18.4.2 Selecting Probes for FM-AFM . . . 383
18.4.3 Dynamic Characteristics of High Frequency Cantilevers and Tuning Forks . . . 385
18.4.4 Higher Harmonics in FM-AFM . . . 388
18.4.5 FM-AFM Under Liquids . . . 389
18.5 Outlook . . . 389
References . . . 391

Index . . . 397

List of Contributors

Masayuki Abe
Osaka University/Graduate School of Engineering
2-1, Yamada-Oka,
Suita, Osaka 565-0871, Japan
(Also PRESTO-JST)
abe@eei.eng.osaka-u.ac.jp

Vasile Caciuc
Institut für Festkörperforschung (IFF),
Foschungszentrum Jülich, 52425 Jülich, Germany
v.caciuc@fz-juelich.de

Oscar Custance
National Institute For Materials Science (NIMS),
Sengen 1-2-1,
Tsukuba 305-0047, Japan
CUSTANCE.Oscar@nims.go.jp

Takeshi Fukuma
Kanazawa University/Frontier Science Organization,
Kakuma-machi, Kanazawa 920-1192, Japan
fukuma@kanazawa-u.ac.jp

Franz J. Giessibl
University of Regensburg/Institute of Experimental and Applied Physics,
93053 Regensburg,
Germany
franz.giessibl@physik.uniregensburg.de

Andreas J. Heinrich
IBM Almaden Research Center,
650 Harry Road, San Jose, California 95120, USA
heinrich@almaden.ibm.com

Stefan Heinze
University of Hamburg/Institute of Applied Physics,
Jungiusstrasse 11, 20355 Hamburg,
Germany
heinze@physnet.uni-hamburg.de

Markus Heyde
Fritz-Haber-Institute of the Max-Planck-Society,
Faradayweg 4-6, D-14195 Berlin,
Germany
heyde@fhi-berlin.mpg.de

Sabine Hirth
Universität Osnabrück/Fachbereich Physik,
Barbarastr. 7, 49076 Osnabruck,
Germany
hirth@uos.de

Regina Hoffmann
University of Karlsruhe/
Physikalisches Institut and
DFG-Center for Functional
Nanostructures,
D-76128,Karlsruhe, Germany
r.hoffmann@physik.
unikarlsruhe.de

Hendrik Hölscher
Institut für Mikrostrukturtechnik,
Forschungszentrum Karlsruhe
76061, Karlsruhe, Germany
hendrik.hoelscher@imt.fzk.de

Suzanne P. Jarvis
University College Dublin/
Conway Institute of
Biomolecular and
Biomedical Research,
Belfield, Dublin 4, Republic
of Ireland
Suzi.Jarvis@ucd.ie

Pavel Jelínek
Institute of Physics of the Academy
of Sciences of the Czech
Republic, Cukrovarnická 10, 1862
53, Prague, Czech Republic
jelinekp@fzu.cz

Uwe Kaiser
University of Hamburg/Institute of
Applied Physics,
Jungiusstrasse 11, 20355 Hamburg,
Germany
ukaiser@physnet.uni-hamburg.de

Lev N. Kantorovich
King's College London/Department
of Physics,
Strand, London WC2R 2LS, UK
lev.kantorovitch@kcl.ac.uk

Shigeki Kawai
University of Basel/Institute for
Physics,
82 Klingelbergstrasse, Basel,
Switzerland
shigeki.kawai@unibas.ch

Hideki Kawakatsu
The University of Tokyo/Institute
of Industrial Science,
4-6-1 Komaba, Meguro-ku, Tokyo
153-8505, Japan
kawakatu@iis.u-tokyo.ac.jp

Dai Kobayashi
The University of Tokyo/Institute
of Industrial Science,
4-6-1 Komaba, Meguro-ku, Tokyo
153-8505, Japan
dai@iis.u-tokyo.ac.jp

Kei Kobayashi
Kyoto University/Innovative
Collaboration Center,
Katsura, Nishikyo, Kyoto 615-8520,
Japan
keicoba@iic.kyoto-u.ac.jp

Thomas König
Fritz-Haber-Institute of the
Max-Planck-Society,
Faradayweg 4-6, D-14195 Berlin,
Germany
koenig@fhi-berlin.mpg.de

Cesar Lazo
University of Hamburg/Institute
of Applied Physics,
Jungiusstrasse 11, 20355 Hamburg,
Germany
clazo@physnet.uni-hamburg.de

Christopher P. Lutz
IBM Almaden Research Center,
650 Harry Road, San Jose, California
95120, USA
lutz@almaden.ibm.com

Natalia Martsinovich
King's College London/Department of Physics,
Strand, London WC2R 2LS, UK
natalia.martsinovich@kcl.ac.uk

John T. Melcher
Purdue University/School of Mechanical Engineering and the Birck Nanotechnology Center,
West Lafayette, Indiana 47907 USA
jmelcher@purdue.edu

Seizo Morita
Osaka University/Graduate School of Engineering
2-1, Yamada-Oka,
Suita, Osaka 565-0871, Japan
smorita@eei.eng.osaka-u.ac.jp

Ken-ichi Morita
Osaka University/Graduate School of Engineering
2-1, Yamada-Oka,
Suita, Osaka 565-0871, Japan
mrt@afm.eei.eng.osaka-u.ac.jp

Kazuhisa Nakagawa
The University of Tokyo/Institute of Industrial Science,
4-6-1 Komaba, Meguro-ku, Tokyo 153-8505, Japan
nakagawa@iis.u-tokyo.ac.jp

Shuhei Nishida
The University of Tokyo/Institute of Industrial Science,
4-6-1 Komaba, Meguro-ku, Tokyo 153-8505, Japan
snishida@iis.u-tokyo.ac.jp

Frank Ostendorf
Universität Osnabrück/Fachbereich Physik,
Barbarastr. 7, 49076 Osnabruck, Germany
fostendo@uos.de

Noriaki Oyabu
Kyoto University/Department of Electronic Science and Engineering,
Kyoto 606-8501, Japan
oyabu@piezo.kuee.kyoto-u.ac.jp

Rubén Pérez
Universidad Autónoma de Madrid/Departamento de Física Teórica de la Materia Condensada,
28049 Madrid, Spain
ruben.perez@uam.es

Pablo Pou
Universidad Autónoma de Madrid/Departamento de Física Teórica de la Materia Condensada,
28049 Madrid, Spain
pablo.pou@uam.es

Arvind Raman
Purdue University/School of Mechanical Engineering and the Birck Nanotechnology Center,
West Lafayette, Indiana 47907 USA
raman@purdue.edu

Michael Reichling
Universität Osnabrück/Fachbereich Physik,
Barbarastr. 7, 49076 Osnabruck, Germany
reichling@uos.de

Ronald G. Reifenberger
Purdue University/Department of Physics and the Birck Nanotechnology Center,
West Lafayette, Indiana 47907 USA
rr@physics.purdue.edu

André Schirmeisen
University of Münster/Institute of Physics and Center for NanoTechnology (CeNTech),
Germany
schirmeisen@uni-muenster.de

Rene Schmidt
University of Hamburg/Institute
of Applied Physics,
Jungiusstrasse 11, 20355 Hamburg,
Germany
rschmidt@physnet.uni-hamburg.de

Alexander Schwarz
University of Hamburg/Institute
of Applied Physics,
Jungiusstrasse 11, 20355 Hamburg,
Germany
aschwarz@physnet.uni-hamburg.de

Udo D. Schwarz
Yale University/Department of
Mechanical Engineering,
New Haven, Connecticut, USA
udo.schwarz@yale.edu

Alexander L. Shluger
University Col-
lege London/Department of
Physics and Astronomy,
Gower Street, London WC1E 6BT,
UK
a.shluger@ucl.ac.uk

Georg Hermann Simon
Fritz-Haber-Institute of the
Max-Planck-Society,
Faradayweg 4-6, D-14195 Berlin,
Germany
simon@fhi-berlin.mpg.de

Yoshiaki Sugimoto
Division Graduate School
of Engineering
Organization Osaka University
Address 2-1, Yamada-Oka,
565-0871, Suita, Osaka

Markus Ternes
IBM Almaden Research
Center,
650 Harry Road,
San Jose, California
95120, USA
m.ternes@fkf.mpg.de

Thomas Trevethan
University College
London/Department of
Physics and Astronomy,
Gower Street, London
WC1E 6BT, UK
t.trevethan@ucl.ac.uk

Ryan C. Tung
Purdue University/School
of Mechanical Engineering
and the Birck Nanotechnology
Center,
West Lafayette,
Indiana 47907 USA
rtung@purdue.edu

Roland Wiesendanger
University of Hamburg/Institute
of Applied Physics,
Jungiusstrasse 11, 20355 Hamburg,
Germany
rwiesend@physnet.uni-hamburg.de

Hirofumi Yamada
Kyoto University/Department
of Electronic Science
and Engineering,
Katsura,
Nishikyo, Kyoto 615-8510,
Japan
h-yamada@kuee.kyoto-u.ac.jp

1

Introduction

Seizo Morita

Abstract. Since the publication of *Noncontact Atomic Force Microscopy* in 2002, the noncontact atomic force microscope (NC-AFM), which can image even insulators with atomic resolution, has achieved remarkable progress. This second volume deals with the following outstanding results obtained with atomic resolution after the publication of the previous books: (1) *Force Spectroscopy and Force-Mapping with Atomic Resolution*, (2) *Tuning Fork/qPlus Sensor*, (3) *Atomic Manipulation*, (4) *Magnetic Exchange Force Microscopy*, (5) *Atomic and Molecular Imaging in Liquids*, (6) *New Technologies in Dynamic Force Microscopy*. These results and technologies are now varying the NC-AFM with imaging function on an atomic scale toward characterization and manipulation tools of individual atoms/molecules and nanostructures with atomic/subatomic resolution. Therefore, the NC-AFM is now becoming a crucial tool for nanoscience and nanotechnology.

1.1 Rapidly Developing High Performance AFM

In the previous book published in 2002 [1], we mentioned that the atomic force microscope (AFM) is a unique microscope based on a mechanical method with the following features:

- True atomic resolution
- Observation of insulators
- Three-dimensional (3D) measurements of atomic-forces (atomic force spectroscopy [AFS])
- Control of atomic forces
- Measurement of mechanical response
- Mechanical manipulation of individual atoms
- Atom-by-atom mechanical assembly

In fact, the previous book reported true atomic resolutions on various semiconductor surfaces [Si(111)7 $\times$ 7, Si(100)2 $\times$ 1, Si(111)-c(4 $\times$ 2), GaAs(110), InP(110), InAs(110), Si(111)$\sqrt{3} \times \sqrt{3}$-Ag, Si(100)2 $\times$ 1:H, Si(100)1 $\times$ 1:2H,

S. Morita et al. (eds.), *Noncontact Atomic Force Microscopy*,
NanoScience and Technology,
DOI: 10.1007/978-3-642-01495-6_1, © Springer-Verlag Berlin Heidelberg 2009

Si(111)$5\sqrt{3} \times 5\sqrt{3}$-Sb, Ge/Si(111)] and HOPG. Besides, it observed atomic structures even on various ionic crystals [NaCl(100), KCl(100), KBr(100), SrF_2(111), CaF_2(111), BaF_2(111), $KCl_{0.6}Br_{0.4}$, NaCl/Cu(111), $CaCO_3$] and various metal oxides [NiO(001), $\alpha-Al_2O_3$(0001), TiO_2(110), TiO_2(100), SnO_2(110), Al_2O_3/NiAl(110), CeO_2(111), (H, K)/TiO_2(110)1×1]. Further, it achieved molecular/submolecular resolution on various molecules {(RCOO-/TiO_2) [R=H, CH_3, $C(CH_3)_3$, $C \equiv CH$, CHF_2, CF_3], C_{60}, adenine/HOPG, thymine/HOPG, DNA/mica, octanethiol, hexadecanthiol, alkanethiol/Au(111), dimethylquinquethiophene (DN5T), VDF oligomer, poly (vinylidene fluoride) [PVDF]}. Thus the previous book fully proved the ability of NC-AFM on true atomic resolution and observation of insulators with atomic resolution.

To measure three-dimensional (3D) atomic-forces (atomic force spectroscopy [AFS]), the previous book introduced two methods. In one method, the site-dependence of the site-specific frequency shift curve at atomically specified sites (A, B, C) was measured as shown in Fig. 1.1a, while, on the other method, the tip–sample distance dependence of the NC-AFM image at different atomic spacing (a, b, c) was measured as shown in Fig. 1.1b. Thermal

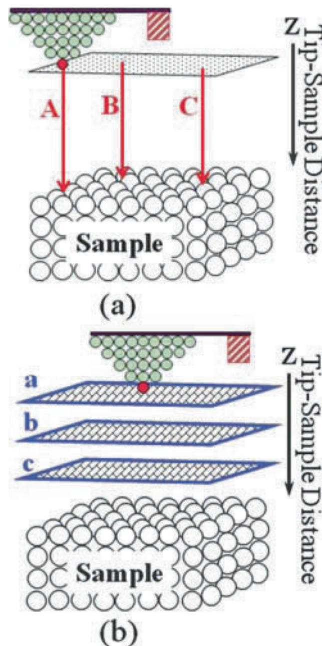

Fig. 1.1. Schematic model of atomic force spectroscopy to obtain a three-dimensional force-related map [1]. (**a**) The method using the site-dependent frequency-shift curves obtained at sites A, B, C, etc. (**b**) Alternating method using the tip–sample distance dependence of the NC-AFM images obtained at tip–sample distance a, b, c, etc.

drift along the sample surface at room temperature (RT), however, gradually shifted the tip apex outermost atom away from the atomically specified site and thus disturbed the former method that obtains the precise site-specific frequency shift curves at atomically specified sites. As a result, only at low temperature (LT) without thermal drift, the site-specific frequency shift curve measurements were achieved at atomically specified sites on a few limited samples such as Si(111)7×7 and graphite in 2002. Similarly, thermal drift perpendicular to the sample surface at RT gradually changed the atomic spacing and thus disturbed the latter method that obtains the tip–sample distance dependence of the NC-AFM image. As a result, atomically resolved NC-AFM images were acquired only at $2 \sim 3$ limited tip–sample distance in 2002. Now we can carry out precise force spectroscopy measurements and force-mapping with atomic resolution even at RT on various samples as introduced in this second volume.

To control atomic forces, measure mechanical response, and mechanically manipulate individual atoms, we have to precisely decrease and also control the tip–sample distance by varying the tip-to-sample gap from noncontact region toward nearcontact region as shown in Fig. 1.2. Precise control of tip–sample distance, however, was incomplete in 2002. As a result, control of atomic forces, measurement of mechanical response, and mechanical manipulation of individual atoms were tentatively investigated in 2002. Now we can precisely control tip–sample distance, and thus carry out precise control of atomic forces, measurement of mechanical response, and mechani-

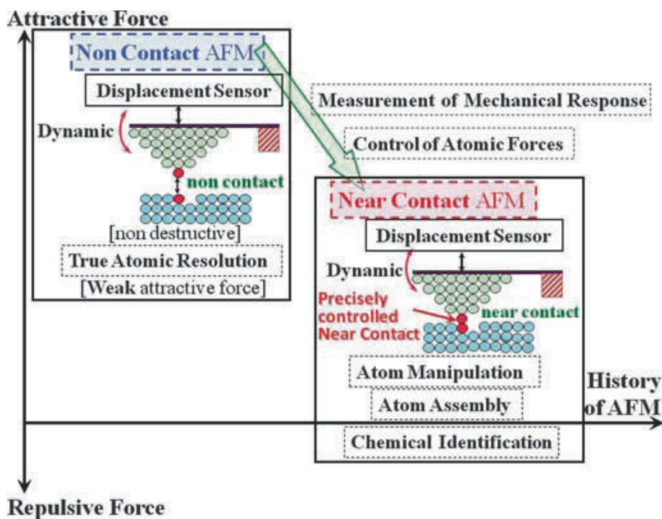

Fig. 1.2. Transition from noncontact AFM (NC-AFM) region for nondestructive topographic imaging to nearcontact (or precisely controlled contact) AFM region for atom manipulation, atom-by-atom assembly, and chemical identification using atomic force spectroscopy

cal manipulation of individual atoms even at RT as introduced in this second volume.

In 2002, we could not build nanostructures by mechanical atom manipulation with AFM. Therefore, atom-by-atom mechanical assembly (true bottom-up nanostructuring) was a dream in AFM field at that time. Now we can construct "Atom Inlay," that is, embedded atom letters, consisting of two atom species even at RT using AFM as introduced in this second volume. Thus, now, all above special features inspired in the previous book are fulfilled by AFM and such rapid development of AFM are completely introduced in this second volume.

1.1.1 Present Status of High Performance AFM

Here we will shortly introduce a few important results in relation with present-day high performance AFM. Those are spatial resolution, chemical coordination effect, and mechanical atom manipulation.

NC-AFM Spatial Resolution Beyond STM

Before 2004, spatial resolution of STM was entirely superior to AFM, because of better signal-to-noise ratio (S/N) of STM with better rigidity and tip–sample distance regulation in conjunction with the tunneling effect. AFM, however, measures chemical bond localized more than moving (spreading) delocalized electron measured by STM. Furthermore, difference of S/N between AFM and STM became smaller recently, so that we achieved AFM spatial resolution better than STM in a few samples [2, 3]. Figure 1.3a–d show successive AFM topographic images of Sn/Si(111)- $(2\sqrt{3} \times 2\sqrt{3})$ surface obtained by decreasing tip–sample distance [3]. Rhombuses indicate the unit cell of $2\sqrt{3} \times 2\sqrt{3}$ surface lattice structure. As unveiled by Fig. 1.4a expanded from Fig. 1.3d and cross-sectional line profile (Fig. 1.4b) obtained along the solid line in Fig. 1.4a [3], by approaching the tip apex toward the sample surface, number of atom observed in the unit cell increases from 4 to 8, because AFM can achieve the highest spatial resolution just before the contact [1]. In case of STM, however, only four atoms were found in the unit cell [4].

Thus, we already achieved AFM spatial resolution beyond STM in a few samples. AFM already demonstrated the possibility to attain even subatomic resolution [5].

Chemical Coordination Effect in NC-AFM Topographic Image

It was found that, in the filled state STM image of (Sn, Pb)/[Si(111), Ge(111)]-$(\sqrt{3} \times \sqrt{3})$ surfaces, relative atom heights of (Sn, Pb) adatoms become higher by increasing the number of the nearest neighbor heterogeneous (Si, Ge) adatoms [6–8]. This is the chemical coordination effect in STM topographic

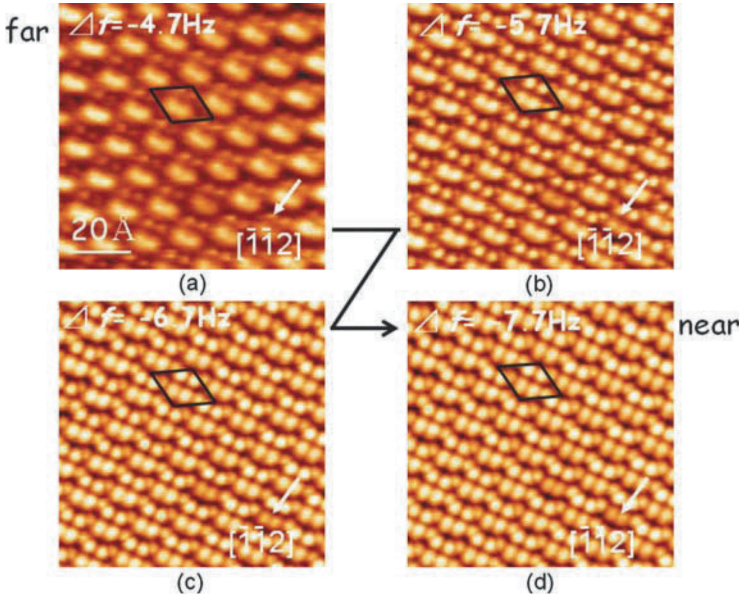

Fig. 1.3. Tip-to-sample distance dependence of NC-AFM topographic image of Sn/Si(111)-($2\sqrt{3} \times 2\sqrt{3}$) surface from (**a**) far distance to (**d**) near distance, through (**b**) and (**c**) [3]. Rhombuses indicate the unit cell of $2\sqrt{3} \times 2\sqrt{3}$ surface lattice structure. By approaching the tip apex toward the sample surface, number of atom observed in the unit cell increases from 4 to 8

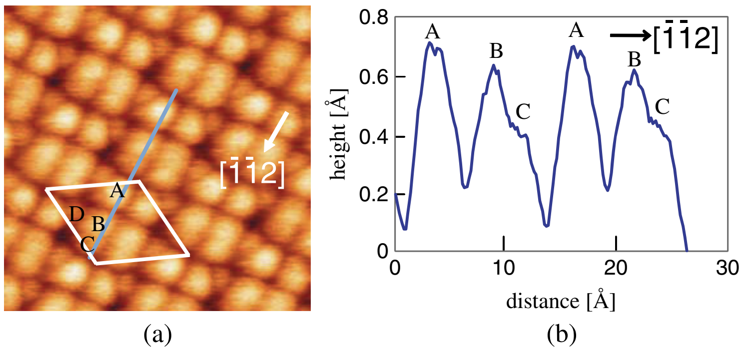

Fig. 1.4. (**a**) NC-AFM image expanded from Fig. 1.3d, and (**b**) cross-sectional line profile obtained along the *solid line* in (**a**) [3]

image. Therefore, its mechanism has been intensely investigated [6–8], and was attributed to the effects induced by electron transfer from (Si, Ge) dangling bond orbital to the nearest neighbor (Sn, Pb) dangling bond orbital. By investigating such coordination effect in NC-AFM topographic images, the imaging mechanism of NC-AFM will be clarified in more detail, but there was

no report in 2002. To measure such chemical coordination effect, NC-AFM with a single pm vertical resolution is crucial.

Experimentally, surrounding atom dependence of relative atom height of Sn adatom (open square) in filled state STM topographic image of Sn/Si(111)-($\sqrt{3}\times\sqrt{3}$) surface [6] is very clear and agrees well with the calculated one (filled square) [7] as shown in Fig. 1.5. On the other hand, theoretical simulation on Pb/Si(111)-($\sqrt{3} \times \sqrt{3}$) surface [8] suggests that the dangling bond of Si adatom has always empty orbital regardless of the coordination number, and that there is no corresponding coordination effect for Si adatom (open circle, filled circle) [6, 7].

In case of NC-AFM topographic image of Sn/Si(111)-($\sqrt{3} \times \sqrt{3}$) surface [9, 10] as well as Pb/Si(111)-($\sqrt{3} \times \sqrt{3}$) surface [10], however, relative atom height of Si adatom (filled triangle) shows clear coordination number dependence as shown in Fig. 1.5. Thus, NC-AFM has different chemical coordination mechanism. Accordingly, by investigating such surrounding atom

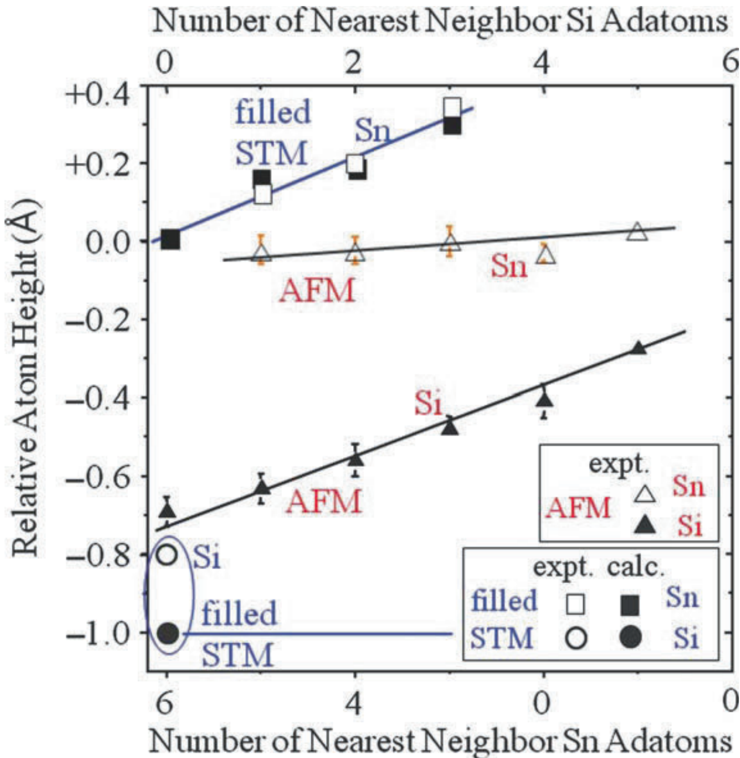

Fig. 1.5. Relative atom height of Si and Sn adatoms in Sn/Si(111)-($\sqrt{3} \times \sqrt{3}$) intermixed surface measured by filled state STM topographic image and NC-AFM topographic image as a function of the chemical coordination number at RT. [expt.] and [calc.] show experimental and theoretically calculated results

dependence of relative atom heights in NC-AFM topographic images, the imaging mechanism of NC-AFM will be clarified in more detail. On the other hand, such chemical coordination effect in intermixed heterogeneous surface will deteriorate chemical discrimination potential of NC-AFM topographic image (so-called atom selective image) using height difference between heterogeneous atoms.

Mechanical Atom Manipulation Under Nearcontact Region

In 2002, by decreasing the tip–sample distance and by varying the noncontact region to the nearcontact region (Fig. 1.2), vertical atom manipulation (removal of Si adatom) by mechanical vertical contact of AFM tip apex with Si(111)7×7 sample surface was tentatively realized at 9.3 K [1]. Immediately, both removal and deposition of Si adatom were successfully demonstrated at 78 K [11]. Then, by precisely controlling the tip–sample distance and by alternately changing the noncontact region and the nearcontact region, site-by-site lateral atom manipulation of single Ge atom adsorbed on Ge(111)-c(2×8) surface was carried out using the raster scan under the nearcontact region at 80 K [12]. Finally, novel atom manipulation phenomena were discovered at RT. Those are lateral and vertical atom interchange manipulations. By using the lateral atom interchange manipulation combined with the vector scan under the nearcontact region, substituted Sn adatoms embedded in Ge(111)-c(2×8) substrate were laterally interchanged 120 times with the selected adjacent Ge adatoms. Then a protruded "Atom Inlay," that is, embedded atom letters consisted of a little large Sn atoms embedded in a little small Ge atoms was constructed at RT as shown in Fig. 1.6a [13]. On the other hand, by using the vertical atom interchange manipulation induced by mechanical vertical contact, tip apex Si atoms were directly interchanged 11 times with the selected Sn adatoms of Sn/Si(111)-$(\sqrt{3} \times \sqrt{3})$ surface. As a result, a hol-

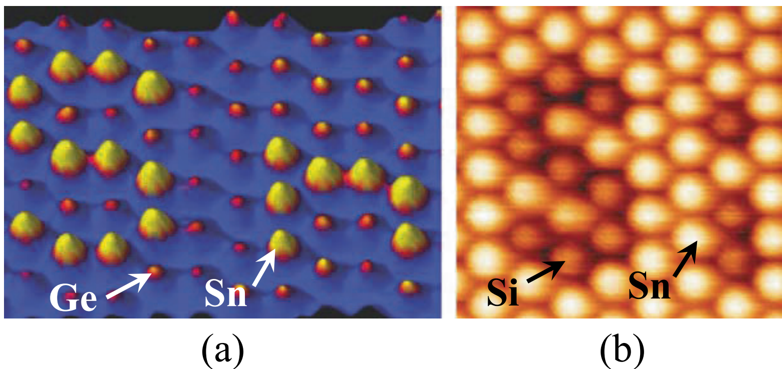

Fig. 1.6. (**a**) A protruded "atom inlay" [13] and (**b**) a hollowed "atom inlay" [14] constructed by atom-by-atom assembly

lowed “Atom Inlay” consisting of a little small Si adatom embedded in a little large Sn adatom was constructed at RT as shown in Fig. 1.6b [14]. The latter is a true single atom pen method using a Si tip apex.

Thus, AFM can construct embedded atom letters consisting of two atom species even at RT. Furthermore, AFM can measure the force needed to move single atom/molecule [15, 16].

1.2 Future Prospects for High Performance AFM

As written in Table 1.1, many topics continuously appeared in annual non-contact AFM conference. Thus, high performance AFM field are still rapidly growing every year. Here, we will briefly introduce several significant regions in relation with future AFM fields.

1.2.1 Atomic and Molecular Imaging in Liquids

In 2002, true atomic resolution was possible only under ultrahigh vacuum (UHV) environment. In air and liquid environments, Q-factor of mechanical resonant oscillation of cantilever drastically reduces and the small Q-factor gets disturbed to obtain atomic resolution. In 2005, by improving frequency noise in frequency modulation (FM) detection method and using small oscillation amplitude of cantilever, vertical and lateral resolutions of 2-6 and 300 pm were achieved, respectively, even with a low Q-factor in water [17]. Such true atomic resolution in water with the minimum deflection noise density of $5.7\,\mathrm{fm}/\sqrt{\mathrm{Hz}}$ in air and $7.3\,\mathrm{fm}/\sqrt{\mathrm{Hz}}$ in water [18] will open the door to atomic scale imaging of biological materials in liquids and atomic scale science taking place at the liquid/solid interface.

1.2.2 Magnetic Exchange Force Microscopy

In the previous book, the short-range magnetic exchange force interaction between a ferromagnetic Fe-coated tip and a NiO(001) surface was explored at RT by using a magnetic tip as a force sensor. As a result, atomically resolved NC-AFM topographic image showed topographic asymmetry of the different directions on oxygen sites, which seems to have a correlation with the spin alignment of NiO(001) surface. This early attempt, however, did not use an external magnetic field to align the magnetic polarization at the tip apex and also low temperature. As a result, topographic asymmetry of the different directions was uncertain and less than a value of about 1%. Besides, they could not observe asymmetry by Fourier transforms of their raw data because of insufficient S/N. Recently, by applying an external magnetic field of $B_{\mathrm{ext}} = 5\,\mathrm{T}$ perpendicular to the sample surface for the magnetic polarization of the iron film of the tip, the topographical asymmetry increased up to about

Table 1.1. Noncontact AFM conferences

Year Date	Location	Papers/ Persons	Topics
1998 July 21–23	Osaka, Japan	47/104	True Atomic Resolution [TiO_2, Ag, Cu, NaCl, TGS, HOPG at LT], Atomically resolved (KPFM, dissipation), Force curve, Theory, Tip-sample dependence of image [Si(111)$\sqrt{3}\times\sqrt{3}$-Ag, InAs at LT], C_{60}
1999 Sept. 1–4	Pontresina, Switzerland	99/134	Alkanethiol, NiO, (Au^-, Al^-)/Si(111)7×7, Higher flexural mode, Submolecule resolution (adenine, thymine), Bias dependence
2000 July 16–19	Hamburg, Germany	93/176	Imaging mechanism [negative or positive tip] of insulators (CaF_2), Cu^-TBPP/Cu(100), $HCOO^-$, CH_3COO^-/TiO_2, (Xe/HOPG, NiO) at LT, Dissipation, Si(111)2×1-Sb
2001 Sept. 2–5	Kyoto, Japan	101/163	($RCOO^-/TiO_2$)[R=H, CH_3, $C(CH_3)_3$, C≡CH, CHF_2, CF_3], qPlus sensor, Alkali halides, CeO_2, Imaging mechanism of molecules
2002 August 11–14	Montreal, Canada	88/121	Vertical atom manipulation, Chemical identification using height difference, KPFM of Si(111)5$\sqrt{3}\times5\sqrt{3}$-Sb, NC-AFM/STM of Cu(100)-c(2×2)N, MgO, Sub-Å oscillation amplitude, BCO SAM, Oxygen adsorbed Si(111)7×7, Vortex
2003 Aug. 31– Sept. 3	Dingle, Ireland	84/111	Subatomic resolution, Theory of Si(111)$\sqrt{3}\times\sqrt{3}$-Ag, Simulated force curves of CaF_2, Submolecule resolution of CuPc, Lateral mode image of Si(111)7×7, (O_2, CH_3OH, NO_2)/CeO_2, Na/TiO_2
2004 Sept. 12–14	Seattle, USA	92/109	Lateral interchange atom manipulation, Embedded atom letters, Lateral atom manipulation, Laser cooling of cantilever, (Atomic image, Force curves) of SWCNT, (Sub Å resolution, CaF_2) with qPlus sensor, Surrounding atom effect on NC-AFM topography, Molecular resolution in air, Scanning nonlinear dielectric microscopy (SNDM)

(*continued*)

Table 1.1. (continued)

2005 August 15–18	Bad Essen, Germany	104/150	Lateral Mnipulation of atomic defects on (CaF_2, KCl) at RT, Lateral manipulation of Si(111)7×7 adatom at RT, Molecular resolution in liquid, Atom tracking for force spectroscopy, H_2O dissociation/TiO_2, O_2 dissociation/CeO_2, SNDM data storage
2006 July 16–20	Kobe, Japan	128/229	Single-atom chemical recognition, Vertical interchange atom manipulation, Si(111)7×7 by SNDM, Magnetic exchange force microscopy, Rapid scan AFM, Potential mapping of Si(111)7×7 at RT, Photoswitching single-molecular tip, Atomic resolution in liquid, Subatomic resolution of tip-atom by CO on Cu(111)
2007 Sept. 16–20	Antalya, Turkey	96/102	Force measurement during atomic manipulation at LT, Tip effect on (TiO_2, MExFM, PTCDA), Alumina oxide on NiAl, Subsurface oxygen vacancy ordering on reduced CeO_2, Force mapping of NaCl, Theory of MExFM, Local solvation force, Laser cooling of cantilever down to 44 mK, (C_{60}, STO, HOPG) with SNDM, Short-range electrostatic force in KPFM
2008 Sept. 16–19	Madrid, Spain	131/180	3D Force and damping maps on nanotube peapods, Theory of vertical interchange atom manipulation, Water chemistry on (CeO_2, CaF_2), Charge state and imaging of a single atom, Si-tip imaging of TiO_2, Vertical and lateral force mapping, MExFM of Fe/W(001), Hydration structures, Atom-manipulation on Cu(111)-O at LT, High- speed AFM in liquid with atomic resolution, Short-range chemical interaction driven zero tunneling current, Superstructure in KBr/(Cu, NaCl)
2009	(New Haven, USA)		
2010	(Kanazawa, Japan)		

17% on the nickel atom sites [19]. Both atomically resolved unfiltered data sets and the Fourier transformed sets for 30 pm difference of tip–sample distance clearly showed the 1×1 at far distance and the (2×1) at near distance, respectively [19]. The (2×1) is antiferromagnetic surface unit cell of NiO(001). Magnetic exchange force microscopy based on AFM can detect the short-range magnetic exchange force interaction between a magnetic tip and a magnetic sample, and observe the arrangement of spins with atomic resolution even on insulating surface. Therefore, such spin imaging based on AFM will contribute to understanding magnetism on the atomic scale.

1.2.3 Rapid Growth of Tuning Fork/qPlus Sensor

AFM based on tuning fork (cf. qPlus sensor) now demonstrated several advantages. It is a kind of self-detection AFM so that it is compatible with conventional STM instrument with atomic resolution. In other words, AFM with atomic resolution can be incorporated with conventional STM instrument with atomic resolution. As a result, it progresses from a simple STM instrument to combined AFM/STM instrument with atomic resolution. Therefore, it can simultaneously observe atomically resolved AFM and STM images and has the potential ability of simultaneous spectroscopy (AFS and STS) [20]. Further, it can use small amplitude less than 10 pm and hence achieve high signal-to-noise ratio (S/N). It can achieve subatomic resolution [5,21]. Besides, it can mechanically manipulate metal atom/molecule [16]. Therefore, we can expect rapid growth of such AFM/STM based on tuning fork (cf. qPlus sensor) that will incorporate STM field with AFM field.

1.2.4 Differentiation of Atomic Force

Atomic force in AFM means chemical force between tip apex atom/molecule and sample surface atom/molecule. Besides chemical force between interacting atoms/molecules includes various kinds of force such as covalent bonding force, ionic bonding force, metallic bonding force, van der Waals force, and hydrogen bonding force. Therefore, by investigating the imaging mechanism of AFM with various samples and tips in more detail, differentiation of atomic force will progress at the atomic scale. In case of ionic crystals such as $CaF_2(111)$ surface, we already know that short-range electrostatic force is the origin of atomically resolved image. In this case, tip will pick up small cluster of ionic crystal, and then picked-up tip works as positive or negative tip depending on topmost ion species with positive or negative charge. As a result, because of the attractive force imaging method in noncontact AFM, positive tip can image only negative surface ion (anion), while negative tip can image only positive surface ion (cation) [22]. In case of $TiO_2(110)$ surface, however, quite seldom Si tip that can form covalent-like bond and hence image the real topographic structure of the surface was found in addition to positive and negative tip [23]. In case of molecular samples, van der Waals force and

polarization force contribute to AFM imaging [1]. Thus, by investigating the imaging mechanism of AFM with various samples and tips in more detail, difference of imaging mechanism will become clearer and hence differentiation of atomic force in AFM will progress at the atomic scale. Besides, such investigation will disclose the bonding nature between various atom pairs in more detail.

1.2.5 Atom-by-Atom Assembly of Complex Nanostructure at RT

The nanostructure is the base of the quantum effect. On the other hand, multi atom species are a key issue for functional materials. Therefore, complex nanostructures consisting of multiatom species will combine the quantum effect with functional materials and hence deliver abundant novel functional materials/devices. To construct complex nanostructures, true bottom-up nanostructuring, that is, atom-by-atom assembly, is crucial. It requires, first, imaging and chemical identification of individual atoms [9, 10, 24] (Fig. 1.7a), second, atom manipulation of selected atom species to the designed site [11, 12, 15] (Fig. 1.7b), and finally, atom-by-atom assembly of complex nanostructures [13, 14] (Fig. 1.7c).

Recently, these three procedures were developed based on AFM. As a result, a kind of complex nanostructures consisting of two atom species, protruded "Atom Inlay" [13] (Fig. 1.6a) and a hollowed "Atom Inlay" [14] (Fig. 1.6b), were constructed at RT. Now we can try to construct complex atom clusters/wires consisting of multiatom species. Such research will disclose the bonding nature and chemical coordination effect of various atom species consisting complex nanostructures in more detail. In future, we may investigate the possibility to construct more complex nanostructures such as molecule and polymer.

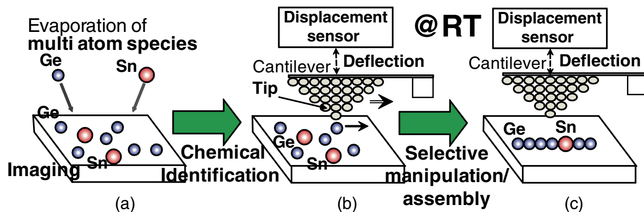

Fig. 1.7. Atom-by-atom assembly of complex nanostructure at RT. (**a**) Imaging and chemical identification of individual atoms, (**b**) atom manipulation of selected atom species to the designed site, and (**c**) atom-by-atom assembly of complex nanostructures

References

1. S. Morita, R. Wiesendanger, E. Meyer, *Noncontact Atomic Force Microscopy* (Springer, Berlin, 2002)
2. T. Eguchi, Y. Fujikawa, K. Akiyama, T. An, M. Ono, T. Hashimoto, Y. Morikawa, K. Terakura, T. Sakurai, M.G. Lagally, Y. Hasegawa, Phys. Rev. Lett. **93**, 266102 (2004)
3. Y. Sugimoto, M. Abe, S. Hirayama, S. Morita, Nanotechnology **17**, 4235 (2006)
4. L. Ottaviano, G. Profeta, L. Petaccia, C.B. Nacci, S. Santucci, Surf. Sci. **554**, 109 (2004)
5. F.J. Giessibl, S. Hembacher, H. Bielefeldt, J. Mannhart, Science **289**, 422 (2000)
6. S.T. Jemander, N. Lin, H.M. Zhang, R.I.G. Uhrberg, G.V. Hansson, Surf. Sci. **475**, 181 (2001)
7. W. Kaminski, P. Jelinek, R. Perez, F. Flores, J. Ortega, Appl. Surf. Sci. **234**, 286 (2004)
8. M. Švec, P. Jelinek, P. Shukrynau, C. Gonzalez, V. Chab, Phys. Rev. B **77**, 125104 (2008)
9. Y. Sugimoto, M. Abe, K. Yoshimoto, O. Custance, I. Yi, S. Morita, Appl. Surf. Sci. **241**, 23 (2005)
10. A. Ohiso, M. Hiragaki, K. Mizuta, Y. Sugimoto, M. Abe, S. Morita, e-J. Surf. Sci. Nanotechnol. **26**, 79 (2008)
11. N. Oyabu, O. Custance, I. Yi, Y. Sugawara, S. Morita, Phys. Rev. Lett. **90**, 176102 (2003)
12. N. Oyabu, Y. Sugimoto, M. Abe, O. Custance, S. Morita, Nanotechnology **16**, S112 (2005)
13. Y. Sugimoto, M. Abe, S. Hirayama, N. Oyabu, O. Custance, S. Morita, Nat. Mater. **4**, 156 (2005)
14. Y. Sugimoto, P. Pou, O. Custance, P. Jelinek, M. Abe, R. Perez, S. Morita, Science **322**, 413 (2008)
15. Y. Sugimoto, P. Jelinek, P. Pou, M. Abe, S. Morita, R. Perez, O. Custance, Phys. Rev. Lett. **98**, 106104 (2007) and its additional information
16. M. Ternes, C.P. Lutz, C.F. Hirjibehedin, F.J. Giessibl, A.J. Heinrich, Science **319**, 1066 (2008)
17. T. Fukuma, K. Kobayashi, K. Matsushige, H. Yamada, Appl. Phys. Lett. **86**, 193108 (2005)
18. T. Fukuma, S.P. Jarvis, Rev. Sci. Instrum. **77**, 043701 (2006)
19. U. Kaiser1, A. Schwarz, R. Wiesendanger, Nature **446**, 522 (2007)
20. M. Herz, C. Schiller, F.J. Giessibl, J. Mannhart, Appl. Phys. Lett. **86**, 153101 (2005)
21. S. Hembacher, F.J. Giessibl, J. Mannhart, Science **305**, 380 (2004)
22. C. Barth, A.S. Foster, M. Reichling, A.L. Shluger, J. Phys. Condens. Matter. **13**, 2061 (2001)
23. G.H. Enevoldsen, A.S. Foster, M.C. Christensen, J.V. Lauritsen, F. Besenbacher, Phys. Rev. B **76**, 205415 (2007)
24. Y. Sugimoto, P. Pou, M. Abe, P. Jelinek, R. Perez, S. Morita, O. Custance, Nature **446**, 64 (2007)

2

Method for Precise Force Measurements

Masayuki Abe and Ken-ichi Morita

Abstract. Quantitative force analysis using noncontact atomic force microscopy (NC-AFM) requires strict experimental conditions. Tip–sample positioning is an especially critical issue and thermal drift is a significant disturbance effecting precise force measurements. This chapter concentrates on techniques of tip–sample positioning at the atomic level for force measurements. Methods for compensating the thermal drift enable measurements of force spectroscopy and force mapping even at room temperature, for which precise force measurement had previously been thought impossible. The methods are also useful at low temperatures.

2.1 Quantitative Force Calculation

In the frequency modulation detection mode of non-contact atomic force microscopy (NC-AFM) [1], the observable is the frequency shift (Δf) of the cantilever resonance that results from the interaction force F between the tip apex and the sample surface. For a set force,[1] the frequency shift Δf depends on the resonance frequency f_0, spring constant k, and oscillation amplitude A of the cantilever. To normalize the variation caused by the measurement parameters, the normalized frequency shift γ is introduced, given by $\gamma(Z, A) = \frac{kA^{1.5}}{f_0}\Delta f(Z, A)$, where Z is the tip–sample displacement [3].

The force displacement (F–Z) curve can be obtained from the change of Δf with the tip–sample distance (Δf–Z) curve. The relation between the Δf–Z and F–Z curves is given by

$$\Delta f(Z) = \frac{f_0}{\pi k A} \int_{-1}^{1} F(Z + A(1+u)) \left(\frac{-u}{\sqrt{1-u^2}} \right) \mathrm{d}u \tag{2.1}$$

If A is small relative to the force region, (2.1) can be simplified to $\Delta f = f_0 \frac{1}{2k} \frac{\partial F}{\partial Z}$. For large amplitudes, we can use several deconvolution algorithms for

[1] Note that the interaction force F acting on the tip also depends on the structure and composition of the tip apex. For details, see [2] and Chap. 3.

S. Morita et al. (eds.), *Noncontact Atomic Force Microscopy*,
NanoScience and Technology,
DOI: 10.1007/978-3-642-01495-6_2, © Springer-Verlag Berlin Heidelberg 2009

force inversion [4–6]. Integration of the obtained F–Z curve in the Z direction gives the potential U–Z curve. It is expected that the inverted F–Z curve is a total superposition of the various forces acting on the AFM tip. By fitting and subtracting the long-range part of the F–Z curve, the short-range force F_s–Z curve, which dominates the interaction between atoms of the tip apex and the sample, can be extracted [7].

There has been a recent trend to map the Δf field in two or three dimensions and then convert this map to F and U fields (see Chap. 5). From U mapping, the lateral interaction force can be extracted by differentiating the U field in a lateral direction [8, 9]. The lateral force acting on the AFM tip during atom manipulation can be estimated using this analysis scheme at low temperatures [10]. Although quantitative force measurements provide insight into the mechanical properties at the atomic level, highly precise tip–sample positioning is required for the three orthogonal directions (X, Y, and Z).

2.2 Thermal Drift

Thermal drift is a problematic disturbance for precise force measurement causing unwanted shifts in the relative tip–sample position and is the main subject of consideration in this chapter. Even at low temperatures, some influence due to thermal drift remains. This unavoidable effect prevents site-specific and quantitative force measurements, especially at room temperature. In the direction of the tip–sample displacement (Z direction), conventional integral feedback for keeping Δf constant can compensate the thermal drift. In this case, the influence of thermal drift is included in the acquired image and can be removed by off-line processing. In the horizontal X and Y directions, however, it is difficult to compensate for the thermal drift with a conventional NC-AFM experiment setup. The influence of thermal drift is commonly observed in continuous imaging. Figure 2.8d–f show NC-AFM images of a Si(111)-(7 $\times$ 7) surface obtained at room temperature at 4 min intervals. Despite the fact that the same area is imaged, the three images are shifted slightly (see the triangles in the figures). This phenomenon is particularly problematic for experiments that require precision and quantitative accuracy, such as site-specific force spectroscopy.

2.3 Three-Fold Feedback for Precise Tip–Sample Positioning

To perform precise force measurements, a method for compensating for thermal drift at the atomic level is required. One successful method for positioning the tip and sample is to use threefold feedback, in the X, Y, and Z directions [11,12]. In this scheme, conventional Z feedback in the vertical direction is used to maintain the tip–sample displacement. To control the lateral (X and Y)

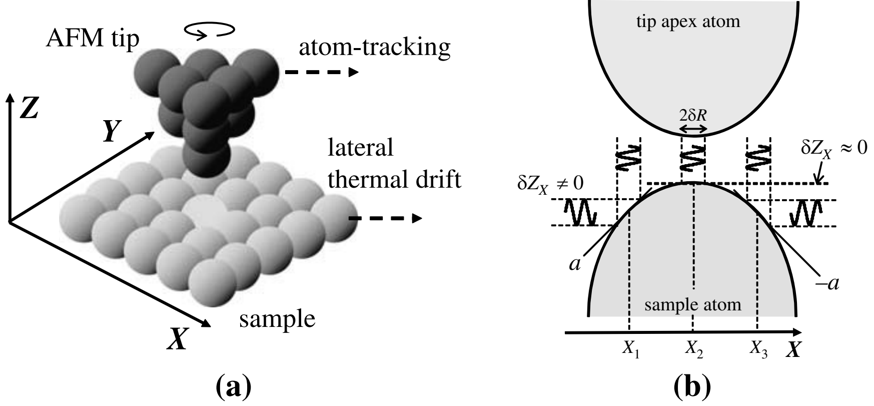

Fig. 2.1. (**a**) Concept of atom-tracking and (**b**) its principles, illustrating the one-dimensional case

position at the atomic level, the atom-tracking technique proposed by Pohl and Möller [13] is applied (Fig. 2.1).

2.3.1 Principle of Atom-Tracking

In atom-tracking, the response of the force interaction to lateral tip–sample modulation is detected and used for positioning feedback. In fact, there are two independent feedback loops, for the X and Y controls. For simplicity, we consider only one lateral direction. The principle of control in two lateral directions can be extrapolated from the one-direction case. Figure 2.1b shows the principle of atom-tracking in which the atoms of the AFM tip apex and sample surface are drawn in the interaction force region.[2] Consider a modulation of the AFM tip (or the sample) in a lateral direction (X) with a small amplitude δR in the interaction force region. When the AFM tip apex is shifted laterally from the apex of a sample surface atom ($X = X_1$ in Fig. 2.1b), the lateral modulation induces a synchronous response in the vertical (Z) direction δZ_X. If δR is much smaller than the atomic size, the magnitude of δZ_X is proportional to the differentiated value a. When the tip is at the apex of a surface atom ($X = X_2$), there is no response at the modulation frequency ($\delta Z_X \simeq 0$) because the inclination a is zero. At $X = X_3$, where the absolute distance from the tip apex is the same but at the opposite symmetric side ($|X_2 - X_1| = |X_2 - X_3|$), we obtain a response of the same amplitude δZ_X but with a phase shift of $\theta_X = \pi$. In this case, the relative tip–sample position from the apex of the sample surface atom can be determined from the

[2] The concept of atom-tracking is the same as Kelvin probe force microscopy (KPFM). In KPFM experiments, the Δf–V_s space is considered (here V_s is the bias voltage at the sample or tip). In the atom-tracking, the same scheme is used in real space and expanded to two dimensions (X and Y).

amplitude and phase of δZ_X. When the tip–sample position is controlled so that the response is zero, the tip can be fixed at the position where $a \simeq 0$ top. In the one-dimensional case in Fig. 2.1b, the tip can be positioned on top of a surface atom and the same positioning scheme can be used in the Y direction.

We can then compensate for thermal drift in three dimensions by using a conventional Z feedback to maintain Δf. This operation mode also allows us to position the AFM tip with equal precision at other surface sites such as vacancies or saddle points by changing the polarities of the X and Y feedbacks.

2.3.2 Experimental Setup

Figure 2.2 shows an NC-AFM setup with an atom-tracking module added. In this setup, the AFM tip is fixed and the sample is allowed to move in the three orthogonal spatial directions. Since independent X and Y positioning controls are required for atom-tracking, the modulation signals in the X and Y directions should be orthogonal to each other. In this experimental setup, orthogonal modulation signals $\delta X = \delta R \sin \omega t$ in the X direction and $\delta Y = \delta R \cos \omega t$ in the Y direction are employed. Here, δR, ω, and t are the amplitude, angular frequency of the atom-tracking modulation, and time. A $\pi/2$ phase difference in the modulation signals creates a circular movement (Fig. 2.1a) with radius δR above the probed atom.[3] This radius should be smaller than the dimensions of the detected protrusions of the surface atoms. As the AFM tip is in the interaction region, there is a response δZ [4] in the Z direction due to the X–Y modulation.

For a single, smooth topographic protrusion and for small δR, the time evolution of the signal in the vertical direction (δZ) during the circular motion oscillates with the same frequency ω as the reference signal. Thus, it can be broken down into the in-phase and the quadrature terms:

[3] The circular motion is not essential for the atom-tracking implementation. Atom-tracking can be performed using modulation signals with two different frequencies ($\delta X = \delta R_X \sin \omega_X t$ and $\delta Y = \delta R_Y \cos \omega_Y t$). In this case, two lock-in amplifiers are required. Moreover, if ω_X and ω_Y are similar, interference can arise between the two frequencies. It is also important to consider the band-width of the FM-demodulator when using two different frequencies. In the experimental setup shown in Fig. 2.2, we believe that interference between the in-phase and quadrature components can be neglected, and a two-phase lock-in amplifier is sufficient for detection of the two components.

[4] The lateral modulation frequency ω should be optimized by setting the experimental conditions and parameters, especially the cut-off frequency ω_Z of the filter for Z feedback. In Fig. 2.2, δZ is detected from the Z feedback output, meaning that the ω component from the topographic signal is detected as δZ. The value of ω must be smaller than ω_Z. In other words, the setup is in the topographic mode where this circular movement evolves into a contour line of constant Δf. If this condition is not held, that is, $\omega > \omega_Z$, the input signal of the Z feedback, that is, the output signal of the FM demodulator, should be measured as δZ. Of course, the larger ω becomes, the faster the response is to large thermal drift.

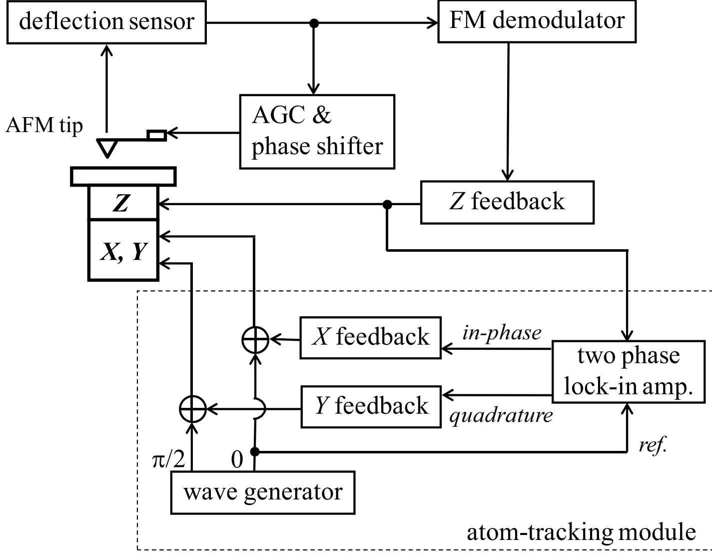

Fig. 2.2. The combination of atom-tracking and NC-AFM. The atom-tracking module consists of a two-phase oscillator, two feedback circuits, and a two-phase lock-in amplifier

$$\delta Z \simeq \delta Z_X \ \sin(\omega t + \theta_X) + \delta Z_Y \ \cos(\omega t + \theta_Y) \tag{2.2}$$

where δZ_X and δZ_Y are the respective amplitudes, and the phases θ_X and θ_Y have two possible values, 0 or π, depending on the position of the tip over the probed adatom (Fig. 2.1b). According to the signals received by the lateral scanner, the first and second terms of (2.2) can be respectively associated with the topographic response to the oscillations in the X and Y directions, and they can be separated using the two-phase synchronous detection method. For small δR values, the vertical amplitudes δZ_X and δZ_Y can be considered to be proportional to the slope of the topographic signal of the probed surface atom along the X and Y directions, respectively (Fig. 2.1b), and their values depend on the relative position between the outermost atom of the tip and the atom at the surface. When the tip is exactly above the probed atom, $\delta Z_X \cos\theta_X$ and $\delta Z_Y \cos\theta_Y$ are very close to zero. In the atom-tracking implementation, the lateral tip–sample position is controlled using two independent feedbacks so that $\delta Z_X \cos\theta_X \simeq Z_Y \cos\theta_Y \simeq 0$.

Figure 2.3 shows an example application of atom-tracking for the compensation of thermal drift at room temperature. The images in Fig. 2.3a show NC-AFM topographic images of a Si(111)-(7 × 7) surface before and after the atom-tracking implementation. After acquisition of the upper-left image, the tip was positioned over the Si(111)-(7 × 7) corner adatom indicated by the white arrow in the image and atom-tracking was activated. The two feedbacks of the atom-tracking implementation gave the required DC voltages to

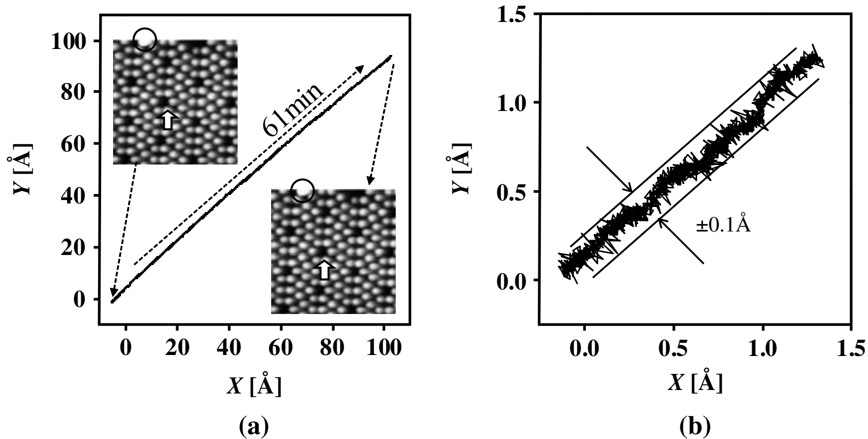

Fig. 2.3. Compensation of the lateral thermal drift by tracking an Si adatom of an Si(111)-(7 × 7) surface at room temperature. (**a**) Topographic images. After acquisition of the topographic image (*left*), the AFM tip was positioned on the arrowed Si adatom and the atom-tracking is activated. The graph shows the total displacement in the orthogonal lateral scan directions (X and Y) obtained from the output voltages of the atom-tracking feedbacks. The atom-tracking was operated for 61 min, after which the topographic image on the *right* was obtained. (**b**) Enlargement of a part of the X–Y track in (**a**) to illustrate the precision of the atom-tracking. The atom-tracking oscillation amplitude and frequency for the X and Y feedback were $\delta R = 43\,\text{pm}$ and $\omega/2\pi = 10\,\text{Hz}$

correct the sample lateral positions X and Y against thermal drift so that the tip was continuously maintained over the same surface spot. In this experiment, a total displacement of 138 Å larger than the image lateral dimensions was obtained by continuously tracking the Si adatom for slightly more than 1 h, yielding a thermal drift velocity of $v_{\text{td}} = 2.3\,\text{Å}\,\text{min}^{-1}$. In Fig. 2.3b, a magnification of the initial part of the X and Y lateral displacements is shown. This magnification shows that the atom-tracking can reach a precision of positioning control better than $\pm 0.1\,\text{Å}_{\text{pp}}$ even at room temperature. The lateral stability is comparable to that for inelastic electron tunneling spectroscopy (IETS) measurements at cryogenic temperatures [14].

2.3.3 Site-Specific Force Spectroscopy at Room Temperature

Through the compensation process for thermal drift and precise lateral positioning of the AFM tip over a surface atom, the atom-tracking technique provides the necessary stability required for force spectroscopic measurements, at both room and low temperatures. However, as atom-tracking requires a signal of the Z component (frequency shift or surface topographic signal) for its

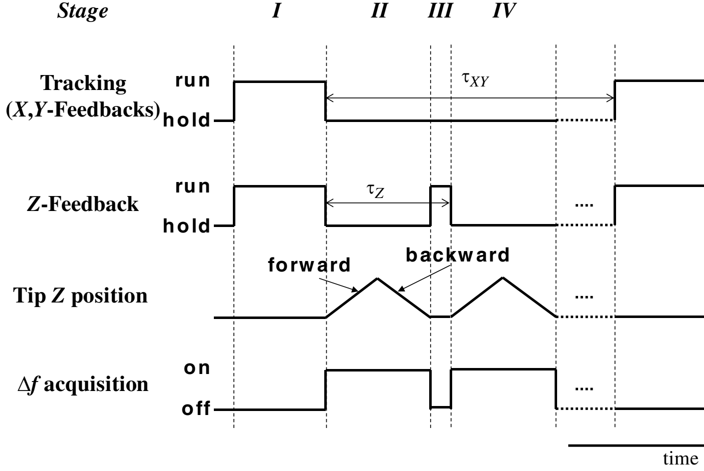

Fig. 2.4. Timing diagram for site-specific force spectroscopy at room temperature

operation, Δf–Z curves should be acquired over several short intervals in which the atom-tracking feedbacks and Z feedback are momentarily open. Thus, a protocol is required with thermal drift velocity as the main limiting factor for the repeated acquisition of equivalent Δf–Z curves at room temperature.

For obtaining reproducible Δf–Z curves, an example timing diagram is shown in Fig. 2.4. A precise position with atom-tracking is achieved and, together with topographic Z feedback, maintained for precise three-dimensional positioning of the tip on the probed atom (stage I). For the acquisition of a Δf–Z curve, atom-tracking and the topographic feedbacks are open and the voltage ramps for the forward and backward vertical tip–sample relative displacement are applied while recording the Δf variation (stage II). At room temperature, after the acquisition of a set of forward and backward Δf–Z curves, it is convenient to restore the topographic feedback for a very short time interval in order to compensate the vertical thermal drift (stage III). Additionally, to minimize the voltage-induced creep in the vertical piezoelectric ceramic, a group of several sets of forward and backward scans should be performed (repeating stage III–IV).

At room temperature, the number of sets that can be acquired during an interval in which the atom-tracking is deactivated is limited by the drift velocity and the lateral positioning precision. The largest interval τ_{XY} in which the atom-tracking can be maintained for the acquisition of a group of n forward and backward sets, each measured in a time τ_Z, is determined by the relation

$$\tau_{XY} \simeq n \times \tau_Z < N_{\mathrm{AT}}/v_{\mathrm{td}}, \qquad (2.3)$$

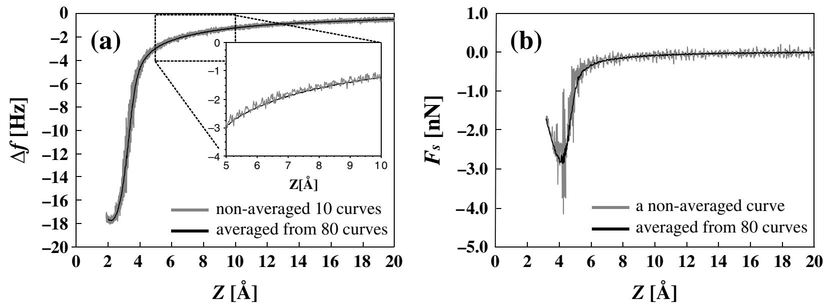

Fig. 2.5. (**a**) Δf–Z curves acquired over an Si(111)-(7×7) corner adatom at room temperature using the method proposed in the text. Ten of a total of 80 Δf–Z curves measured during tracking of the adatom are shown in *gray*. The average curve from these 80 Δf–Z curves is shown in *black*. The inset shows a comparison of a single Δf–Z (*gray*) with the averaged curve (*black*). (**b**) Short-range force F_s–Z curves calculated from the Δf–Z curve obtained in (**a**). The averaged curve (*black*) and the nonaveraged single curve (*gray*) are shown

where v_{td} is the thermal drift velocity and N_{AT} is the precision of the lateral positioning. After the acquisition of a set of Δf–Z curves, the atom-tracking feedbacks are close for repositioning of the AFM tip above the probed surface atom. Applying the timing diagram of Fig. 2.4 and the limitations imposed by (2.3), room temperature spectroscopic measurements on an Si(111)-(7×7) surface are demonstrated in Fig. 2.5 [11]. In this experiment, 80 curves were acquired. Ten of these Δf–Z (a forward and a backward curve from each acquisition interval) are displayed in Fig. 2.5a by gray lines. They overlap with a very low dispersion. In the absence of tip apex and/or surface changes, this close similarity among the curves allows us to average them in a single curve for a further reduction of noise. The averaged Δf–Z curve resulting from the 80 curves is shown in Fig. 2.5a as a black line. Comparing the noise between the averaged and the nonaveraged single curves, as in the inset of Fig. 2.5a, we can clearly see an improvement of a factor of 5–10.

Noise reduction of the Δf–Z signal is critical to avoid possible amplification in inverting the frequency shift to force. Figure 2.5b shows short-range force curves calculated from a nonaveraged Δf–Z curve (gray) and the averaged curve in Fig. 2.5a.[5] We can clearly see that the magnitude of the noise in the nonaveraged curve is greater than that of the averaged curve. Smoothing or performing a running-average of the Δf–Z curve is one method for reducing noise. However, care should be taken in heavy filtering because the

[5] To obtain the short-range force to displacement F_s–Z curves in Fig. 2.5b, Δf–Z curves are inverted to F–Z curves using the method in [6]. Then, long-range van der Waals force are subtracted from the F–Z curve. Electrostatic forces are minimized by controlling the sample bias voltage before the data acquisition. The procedure is the same as that in [7].

shape of the curve may change, especially after the inversion to force. Taking an arithmetic average of several Δf–Z curves is an appropriate method of noise reduction. From this point, reproducibility of positioning and measuring is important for precise force measurement.

2.4 Thermal Drift Compensation for Force Field Mapping

2.4.1 Concept of Feedforward

As mentioned earlier, the atom-tracking technique enables precise tip positioning on a probed surface atom for precise force measurements with force spectroscopy even at room temperature. This technique is very effective, as previously it was thought that site-specific force spectroscopy could only be performed at low temperatures where the effect of thermal drift is small. In the experimental scheme presented in Sect. 2.3.3, atom-tracking must be stopped temporarily, which causes a relative shift in the tip–sample position due to thermal drift during data acquisition. This means that as the force measurements owe their reproducibility to precise positioning of the tip apex, a smaller drift velocity is preferable. Practically, according to the (2.3), it is difficult to perform force spectroscopy with a thermal drift velocity of $v_{\mathrm{td}} > 5\,\text{Å}\,\mathrm{min}^{-1}$. Also, using only atom-tracking is not effective for NC-AFM applications such as force mapping and atom manipulation. Moreover, although atom-tracking allows the same area to be imaged repeatedly, as shown in Fig. 2.3a, the obtained images are distorted. As atom-tracking is feedback, the AFM tip must be in the force region of a specific surface atom during its activation for precise positioning.

An effective way to improve the performance and precision of NC-AFM is to add feedforward to the AFM. Feedforward is a system operation technique normally used in control engineering. Figure 2.6 shows the concept of NC-AFM with feedforward. For precise positioning, the atom-tracking technique and conventional Z control are feedback controls corresponding to $K(s)$ in Fig. 2.6. Relative position differences in three directions are detected at the NC-AFM (controlled object $P(s)$) and controlled with $K(s)$. Various types of disturbances $d_i (i = 1, 2, \ldots)$, such as instabilities in the system, internal and external vibrations, outside ambient sound, and tip–surface position change due to thermal drift, enter the NC-AFM system. If a disturbance can be modeled as $F(s)$ in Fig. 2.6, we can cancel the real disturbance by adding the modeled disturbance into the system. Although most of the disturbances are not predictable, some are, including thermal drift. For large data acquisition of force spectroscopy and force mapping at room temperature, feedforward is essential. Note that under real experimental conditions, we cannot detect the difference between the output of the feedforward and the real system variation caused by model errors. Nonetheless, even when a nonlinear disturbance

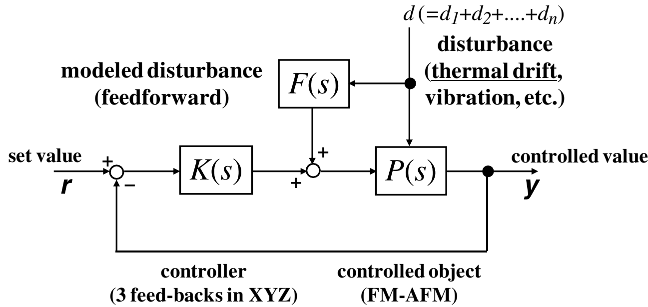

Fig. 2.6. Control diagram of NC-AFM. To perform NC-AFM (given in $P(s)$), feedback ($K(s)$) is used to maintain a set value $y = r$. $F(s)$ is a modeled disturbance for feedforward activation

enters the system, the feedforward lightens the burden on the atom-tracking feedback control and improves the system response to reduce positioning error.

2.4.2 Force Mapping at Room Temperature with Feedforward

Figure 2.7 shows an example of time variations of lateral thermal drift [9]. The data were logged from the output of atom-tracking feedbacks for an adatom of a Si(111)-(7 × 7) surface. We observe a linear change in each lateral direction of at least 10 min. This means that the thermal drift velocity $v_{\text{td}}(v_X, v_Y, v_Z)$ is constant for this period. Therefore, v_{td} can be used as a model parameter for the feedforward. Applying a voltage corresponding to $v_{\text{td}} \times t$ to the system as in Fig. 2.6 compensates for the thermal drift.

To observe the performance of the feedforward implementation, NC-AFM topographic imaging at room temperature where thermal drift exists is shown in Fig. 2.8.[6] Figure 2.8a–c shows a series of NC-AFM images of the same area obtained over 256 s with feedforward activated at room temperature [9]. On the same surface and with the same AFM tip but with the feedforward switched off, the area imaged in the series scan is shifted, as can be seen in Fig. 2.8d–f. Even for heavy thermal drift condition ($v_X = 6.9\,\text{Å}\,\text{min}^{-1}$ and $v_Y = 3.2\,\text{Å}\,\text{min}^{-1}$), as in Fig. 2.8g, the feedforward provides effective compensation. In Fig. 2.8g, image acquisition was started from the upper part with the feedforward activated. At the middle of the image (dotted line), the feedforward was turned off. Comparing the shapes of the unit cells in the upper and lower areas shows that the distortion in the upper area is negligible. These results indicate that the thermal drift compensation using

[6] In previous studies and in commercial controllers for scanning probe microscopy, a method for thermal drift compensation has been used, where a final image of a region is obtained by comparing a series of acquired images. In this scheme of pattern recognition, atomic level precision cannot be expected.

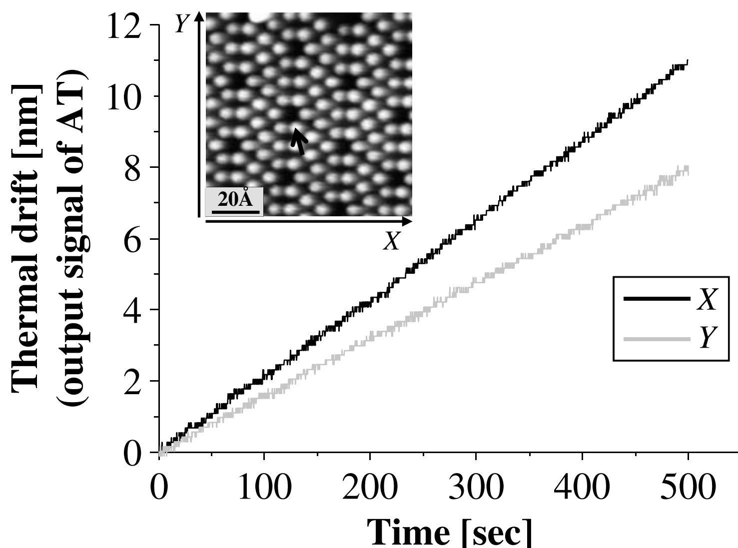

Fig. 2.7. Time variation of lateral thermal drift measured at room temperature. Output signals were logged of atom-tracking feedback performed on an adatom of Si(111)-(7 × 7)

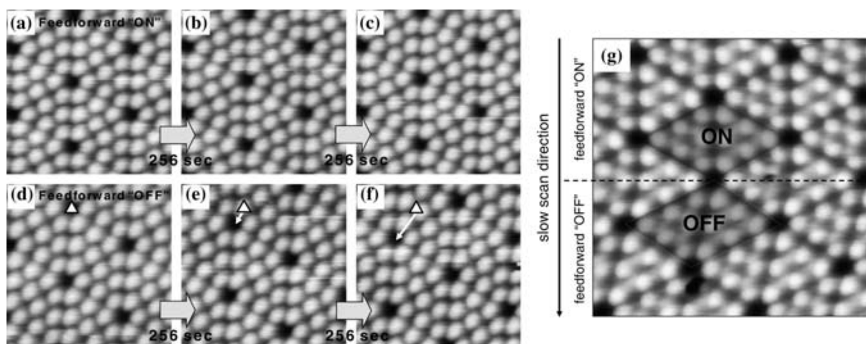

Fig. 2.8. NC-AFM topographic images of a Si(111)-(7 × 7) surface acquired at room temperature. The scan area was 85 × 85 Å^2. The images (**a**–**f**) were obtained at 256 s intervals: (**a**–**c**) were obtained with feedforward implementation and (**d**–**f**) were obtained without feedforward. In (**d**–**f**), the *open triangles* indicate the position of a corner hole imaged in (**d**). The *arrows* in (**e**) and (**f**) show the shift due to the lateral thermal drift of the hole. (**g**) NC-AFM topographic image obtained under heavy thermal drift condition [9]. The feedforward was switched from "ON" to "OFF" during a scan, with the area above the *dotted line* scanned with feedforward and the area below without feedforward

feedforward simulates the condition of quasi-low temperature even at room temperature.

2.4.3 Force Mapping with Feedforward

As mentioned in the first textbook on NC-AFM [15], in a low thermal drift condition such as at low temperature, a narrow bandwidth setting of the NC-AFM system improves the signal-to-noise ratio. In a similar manner, at room temperature, compensation of the three-dimensional tip–sample position with feedforward enables a reduction in the bandwidth of the Z and the atom-tracking feedbacks, which improves the image quality of NC-AFM operated at room temperature. The feedforward data acquisition approach also enables force mapping with atomic resolution. Force mapping is a method for visualizing a force field [16, 17] and can be used to visualize phenomena on surfaces such as atom identification, direction of dangling bonds, friction, and relaxation. For force mapping experiments, a condition of sufficient stability of the instrument is required, including high lateral resolution, sensitivity, and low thermal drift. In addition, at room temperature, the measurement time needs to be small due to the possibility of slight changes in the thermal drift velocity and positioning error due to nonlinear thermal drift that cannot be modeled. Also, numerous sampling points are preferable for high spatial resolution mapping. We present here two examples of force mapping. For both examples, if the experimental conditions satisfy the requirements for data acquisition, we can ignore the effect of nonlinear thermal drift that cannot be compensated with the techniques above.[7]

Example 1: Numerical Analysis for Potential and Lateral Force

Figure 2.9 shows experimental and analytical results of two-dimensional force mapping [18]. The frequency shift map $(\Delta f_Z(X, Z))$[8] acquired with

---

[7] However, note that there are remnant errors (in the author's case, these are at most 0.8, 0.8, and 0.6 Å during data acquisition in the X, Y, and Z directions, respectively, at room temperature.). These were the results of inaccuracies due to quick drift measurements before the feedforward activation. To minimize the effect of remnant errors, fast scans were performed along the X direction by changing the tip–sample displacement Z in the data acquisition of Figs. 2.9b and 2.10b. The data acquisition in the examples consisted of 1024×1024 points and were taken over about 3.5 min. These experimental conditions and the use of atom-tracking and feedforward meet the requirements for force mapping at room temperature.

[8] In the discussion earlier in this chapter, we implicitly assumed the interaction forces F and resulting frequency shift Δf to be in the vertical Z direction. In this subsection, as the interaction force in the lateral (X) direction is also discussed, subscripts are introduced to indicate the direction of the force. For example, Δf_Z denotes the frequency shift due to the vertical (Z) force.

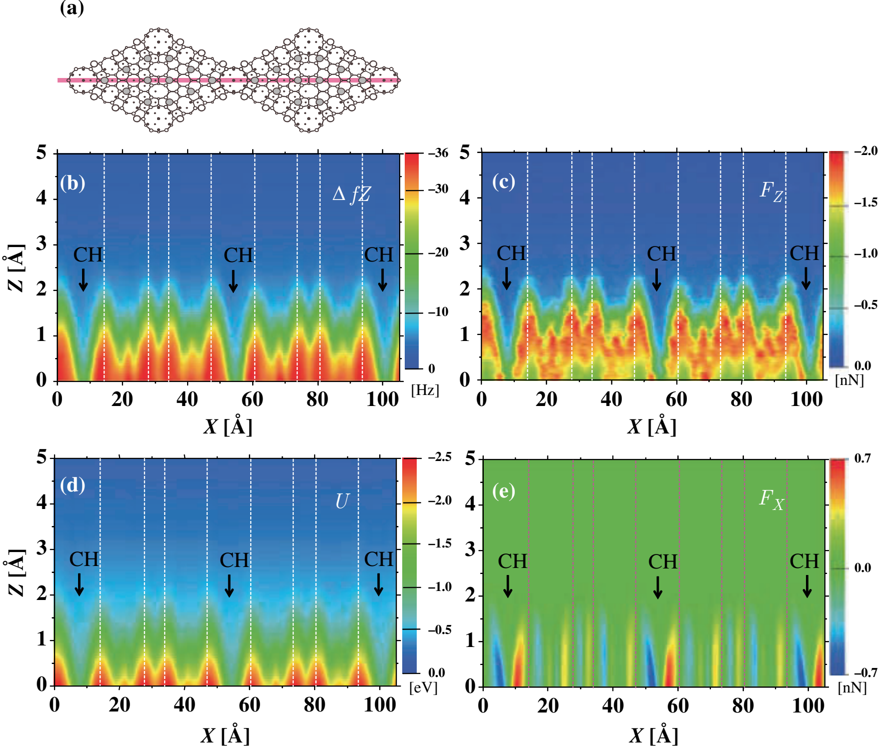

Fig. 2.9. Experimental and analytical results of two-dimensional force mapping on the Si(111)-(7×7) surface [18]. (**a**) Structure model of the Si(111)-(7×7) surface. Two unit cells are drawn. (**b**) Two-dimensional Δf_Z maps on a Si(111)-(7×7) surface. After the feed-forward was activated, data acquisition of the Δf_Z map was performed along the horizontal line connecting the three corner holes (CH) by changing the tip–sample distance. The maps include two unit cells, with the left and right halves corresponding to the unfaulted and faulted halves in each unit cell. (**c**) Force (F_Z) map calculated using the protocol of Sader and Jarvis [6] (**d**) Potential (U) map calculated from (**c**). (**e**) Lateral force (F_X) obtained by differentiating (**d**). The dotted lines indicate Si adatom sites

feedforward activated at room temperature is shown in Fig. 2.9b.[9] As the line profiles in the vertical direction in Fig. 2.9b correspond to the $\Delta f_Z - Z$ curves, all the profiles in the Z direction can be inverted to $F_Z - Z$ curves by deconvolution using (2.1). We obtain a force map ($F_Z(X, Z)$) by compiling the

[9] The actual data acquisition needed to be determined so that we could correctly invert the frequency shift Δf_Z to force F_Z. That is, the measurement was performed until a certain distance where the Δf_Z became almost zero. In Figs. 2.9a and 2.10b, the obtained Δf_Z map was cut such that the visible map appears in the vicinity of the surface.

inverted $f_Z - Z$ curves, as shown in Fig. 2.9c. Assuming that the interaction force is conservative (energy dissipation is negligible), we can calculate the interaction potential map $(U(X,Z) = -\int_{\infty}^{Z} F_Z(X,Z')\,\mathrm{d}Z')$, as in Fig. 2.9d, and also the lateral force map $\left(F_X(X,Z) = -\frac{\partial U(X,Z)}{\partial X}\right)$, as in Fig. 2.9e [8,9].

Mapping allows more than just visualizing the force (or the potential) field [18]. Once the $F_Z(X,Z)$ (or integrated $U(X,Z)$) map is obtained, we can acquire topographic signals for a range of experimental parameters (e.g., amplitude, spring constant, resonant frequency of cantilevers). Even torsional mode [19] images can be acquired. Moreover, numerical analysis of force mapping gives the lateral force for manipulating single atoms [10].

Example 2: Surface Atom Discrimination

Figure 2.10a shows an NC-AFM topographic image of a surface alloy composed of Si, Sn, and Pb atoms on a Si(111) surface. Although three different species are present on the surface, two contrast patterns (bright and dim spots) appear. The Δf_Z map in Fig. 2.10b was acquired along the arrow in

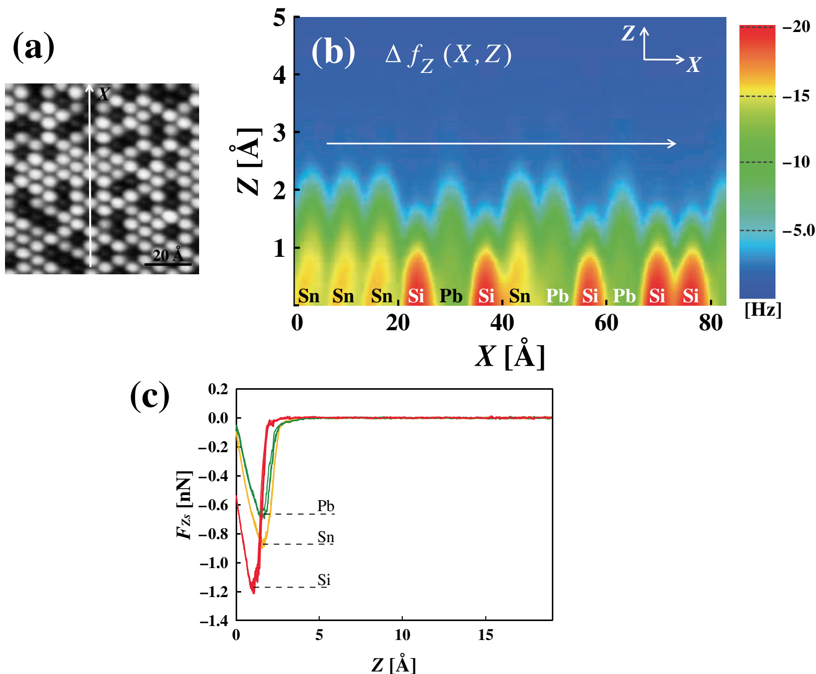

Fig. 2.10. (**a**) NC-AFM topographic image of a surface alloy composed of Si, Sn, and Pb atoms on a Si(111) substrate. (**b**) Two-dimensional Δf_Z map acquired along the arrow in (**a**). (**c**) Short-range force to displacement $(F_{Zs} - Z)$ curves above the twelve adatoms mapped in (**b**). The colors of the curves correspond to the colors of the maximum attractive Δf_Z values in (**b**). The red, yellow, and green curves are for Si, Sn, and Pb, respectively

the NC-AFM topographic image [20]. In the Δf_Z map, three patterns (peaks with red, yellow, and green bases) are clearly resolved. The different colors indicate that they have different maximum Δf_Z values due to the presence of different atom species.

An analysis of the Δf_Z map (and also the inverted F_z map) reveals considerable information useful for visualizing the surface and understanding interaction forces, as well as providing data for determining atomic differences. One useful piece of information is the color contour lines in Fig. 2.10b, which correspond to topographic signals. Since relaxation at both the AFM tip and the sample is small in the small Δf region [21], we can investigate the atom height and interaction force simultaneously. Comparing the contour lines shows that the atomic height is small between the peaks with yellow and green bases. However, there is a clear color contrast in the Δf_Z map for these two types of peak. Comparing the minimum values of the short-range force $F_{Z\mathrm{s}}$, the determined ratios of Sn to Si and Pb to Si are the same as those determined from force spectroscopy on the same surface system (see [2] and Chap. 3). This means that we can assign the red regions, which have the largest attractive Δf, as representing silicon, while the yellow and green regions represent Sn and Pb, respectively. In this way, force mapping not only yields significant information on the surface atoms, but also allows quantitative analysis for atom discrimination.

2.5 Summary

Force spectroscopy and force mapping have provided physical and chemical insights at the atomic scale. For precise force measurements, experiments require strict conditions, with tip–sample positioning being an especially critical issue. Usually, a low temperature environment is more suitable because thermal drift is negligible. However, in some fields, such as biophysics and catalysis, kT can be an important factor. It is difficult to build AFM instruments that are not subject to thermal drift at room temperature or higher. Atom-tracking and feedforward techniques can compensate for thermal drift motion, which can be useful in a low temperature environment. Finally, it should be noted that atom-tracking and feedforward do not improve the stability of the instruments and only function fully with a stable AFM instrument.

References

1. T.R. Albrecht, P.Grütter, D. Horne, D. Rugar, J. Appl. Phys. **69**, 668 (1991)
2. Y. Sugimoto et al., Nature **446**, 64 (2007)
3. F.J. Giessibl, Phys. Rev. B **56**, 16010 (1997)
4. U. Dürig, Appl. Phys. Lett. **76**, 1203 (2000)

5. F.J. Giessibl, Appl. Phys. Lett. **78**, 123 (2001)
6. J.E. Sader, S.P. Jarvis, Appl. Phys. Lett. **84**, 1801 (2004)
7. M.A. Lantz et al., Science **291**, 2580 (2001)
8. A. Schwarz, H. Hölscher, S.M. Langkat, R. Wiesendanger, in *Scanning Tunneling Microscopy/Spectroscopy and Related Techniques.* AIP Conference Proceedings No. 696 (AIP, New York, 2003), p. 68
9. M. Abe et al., Appl. Phys. Lett. **90**, 203103 (2007)
10. M. Ternes et al., Science **319**, 1066 (2008)
11. M. Abe, Y. Sugimoto, Ó. Custance, S. Morita, Appl. Phys. Lett. **87**, 173503 (2005)
12. M. Abe, Y. Sugimoto, O. Custance, S. Morita, Nanotechnology **16**, 3029 (2005)
13. D. Pohl, R. Möller, Rev. Sci. Instrum. **59**, 840 (1988)
14. C. Stipe, M.A. Rezaei, W. Ho, Science **279**, 1907 (1998)
15. S. Morita, R. Wiesendanger, E. Meyer (eds.), *Noncontact Atomic Force Microscopy* (Springer, Berlin, 2002)
16. H. Hölscher, S.M. Langkat, A. Schwarz, R. Wiesendanger, Appl. Phys. Lett. **81**, 4428 (2002)
17. A. Schirmeisen, D. Weiner, H. Fuchs, Phys. Rev. Lett. **97**, 136101 (2006)
18. Y. Sugimoto et al., Phy. Rev. B **77**, 195424 (2008)
19. S. Kawai, S. Kitamura, D. Kobayashi, H. Kawakatsu, Appl. Phys. Lett. **87**, 173105 (2005)
20. Y. Sugimoto, T. Namikawa, M. Abe, S. Morita, Appl. Phy. Lett. **94**, 023108 (2009)
21. Y. Sugimoto et al., Phys. Rev. B **73**, 205329 (2006)

3

Force Spectroscopy on Semiconductor Surfaces

Oscar Custance, Noriaki Oyabu, and Yoshiaki Sugimoto

Abstract. In this chapter, we introduce recent works on force spectroscopy performed using the frequency modulation detection method that have contributed to widen the knowledge and applicability of atomic force microscopy (AFM) for the study of surfaces with atomic resolution. We first introduce some experimental considerations regarding force spectroscopy acquisition. Then, we discuss how the combination force spectroscopy and first-principle calculations has contributed to clearly identify a channel for the dissipation of energy from the cantilever oscillation, as well as to clarify the interplay between atomic relaxations and differences in the tip–surface short-range interaction detected over atoms populating heterogeneous semiconductor surfaces. We introduce a protocol for single-atom chemical identification using AFM, which is based on the precise quantification of the tip–surface short-range interaction forces. Finally, anticipating the future general use of small cantilever oscillation amplitudes, we discuss force spectroscopy acquisition using higher flexural modes of rectangular cantilevers and oscillation amplitude values as small as 3.6 Å.

3.1 Introduction

Soon after its invention, the atomic force microscope (AFM) [1] demonstrated to be a very versatile tool for exploring and interacting with matter at the micro- and nanoscale, in different environments and with multiple applications in fields ranging from biology to semiconductor industry. Depending on the research field, the AFM is renamed as scanning force microscope, surface force microscope, and alike. However, the name selected by Binnig, Quate, and Gerber to succinctly refer to their invention [1] was probably chosen to stress that with this apparatus it could be possible to detect interatomic forces, and therefore, explore surfaces with true atomic resolution. It took almost a decade to beat all the technical adversities and demonstrate that AFM can certainly detect interatomic forces and obtain atomically resolved images of

S. Morita et al. (eds.), *Noncontact Atomic Force Microscopy*,
NanoScience and Technology,
DOI: 10.1007/978-3-642-01495-6_3, © Springer-Verlag Berlin Heidelberg 2009

highly reactive surfaces [2–4]. This breakthrough was in part possible, thanks to the development of the frequency modulation detection method by Albrecht and co-workers [5]. Since the achievement of true-atomic resolution with AFM, there was an increasing number of groups and researchers showing interest in frequency modulation atomic force microscopy (FM-AFM) not only for the study of conducting an insulating surfaces at the atomic scale, but for many other additional possibilities that this highly sensitive detection scheme offers to study different kind of phenomena at surface. There are excellent reviews that describe pioneering works in FM-AFM [6–8], that have instructed and inspired new generations of researchers excited by the possibilities offered by this technique.

Since the publication of these reviews, there has been significant progress in the field. One of the subjects that has undertaken an extraordinary development in recent years is force spectroscopy, which is the technique that allows us to quantify very precisely the tip–surface interaction forces exerted on the cantilever. In FM-AFM, these forces are indirectly obtained from variations of the cantilever resonant frequency as the tip–surface distance is continuously explored.

One of the first attempts to quantify the tip–surface interaction force as a function of the tip–surface distance in FM-AFM was performed by Gotsmann and co-workers [9–11]. Almost at the same time, important contributions were also performed by the group at Hamburg University [12–15]. However, it was the group of Basel University the one who achieved the breakthrough of quantifying the short-range forces associated with a single bond formation between the outermost atom of the tip and the atoms probed at the surface [16]. These pioneering works inspired and encouraged us to implement and make use of force spectroscopy in our AFM experiments.

In this chapter, we will introduce recent works on force spectroscopy performed on semiconductor surfaces, which have contributed to widen our knowledge on phenomenology of FM-AFM and have broaden the applicability of AFM for the study of surfaces with atomic resolution. We will first introduce some experimental considerations regarding force spectroscopy acquisition. Then, we will discuss how the combination force spectroscopic measurements and first-principle calculations has contributed to clearly identify a channel for the dissipation of energy from the cantilever oscillation, as well as the interplay between atomic relaxations and differences in the tip–surface short-range interaction of atoms populating heterogeneous semiconductor surfaces. We will introduce a protocol for single-atom chemical identification using AFM based on the precise quantification of the tip–surface short-range interaction forces. And finally, anticipating the future general use of small cantilever oscillation amplitudes, we will discuss force spectroscopy acquisition using higher flexural modes of rectangular cantilevers and oscillation amplitude values as small as 3.6 Å.

3.2 Experimental Considerations

In FM-AFM, the cantilever is constantly excited at resonance keeping the oscillation amplitude constant. In this detection scheme, the main observable is the frequency shift: the variation of the cantilever resonant frequency with respect to the free oscillation value upon the presence of an inhomogeneous force field between the cantilever tip and the surface.

Scanning the surface maintaining constant a frequency shift value chosen as image set point gives access to topographic maps of the surface, when properly adjusting the feedback parameters to obtain a minimal error in the frequency shift signal with respect to the set point value. It is convenient to record in every moment the cantilever oscillation amplitude – to corroborate that it is kept constant – and the excitation signal applied to the piezo actuator that drives the cantilever oscillation (which is related to the additional amount of energy one has to put into the cantilever oscillation to keep the oscillation amplitude constant under the presence of nonconservative tip–surface interaction, see Sect. 3.3 for more details).

Atomic resolution experiments normally require operation of the AFM in ultrahigh vacuum (UHV) environment. In UHV, the common forces sensed by the cantilever tip are the electrostatic interaction due to the presence of a charge difference between tip and surface; the van der Waals interaction, which is originated by dipole fluctuations at tip and surface; and the short-range forces between the closest tip–surface atoms responsible of atomic contrast [17–19]. For magnetic tips or surfaces, there may be also magnetic forces involved even at atomic level [20]. To maximize sensitivity to the short-range forces, a bias voltage between tip and sample is normally applied to cancel the tip–surface contact potential difference to minimize the long-range electrostatic interaction [21, 22], and cantilevers with sharp tips at their free end – tips with typical radius of a few nanometers – are used to reduce the van der Waals contribution to the total interaction force.

Sharp yet atomically reactive tips are required to explore semiconductor surfaces. To this end, prior the experiments, it is convenient to prepare a new cantilever tip by ion Ar sputtering. We use an ion energy of $\sim$0.6 keV for our Si cantilevers, adjusting the partial pressure of Ar to get a typical ion current of $\sim$0.2 μA measured at the cantilever holder, setting the sputter time to obtain reactive yet sharp tips giving high quality atomic resolution images (the sputter time must be recalibrated for a given cantilever wafer). Sometimes, gentle contacts with the surface are required to improve atomic resolution image quality or to stabilize the tip apex after unintended modifications during scanning or force spectroscopy measurements. If the tip is producing stable imaging and good force spectroscopy data, it can be used over several measurement sessions without any further cleaning treatment.

When using cantilevers and a detection system based on optical interferometry, higher sensitivity is obtained by positioning the laser spot as close as possible to the cantilever-free end, while keeping a good and stable oscillation

signal coming out from the interferometer and the frequency demodulator. This optimum positioning of the laser spot can be easily performed by looking at the diffraction patterns provided by the output signal from the interferometer when longitudinally and transversally scanning the laser spot over the cantilever-free end. This requires a system of piezoelectric motors capable of moving the laser spot in three dimensions [23].

Site-specific force spectroscopy is performed by recording the frequency shift signal over a surface atomic site while decreasing the relative tip–sample distance. It is convenient to explore a distance range from the free oscillation region (absence of any force exerted on the cantilever) to distances beyond the onset of significant short-range interaction responsible of atomic contrast [17–19]. A set of forward and backward curves is usually acquired upon approach (retraction) of the tip towards (from) the surface and, under normal acquisition conditions, the curve upon retraction should match – within the experimental noise – the one acquired during the approach. After the acquisition of force spectroscopic characteristics, the surface should be imaged to assure that neither the tip nor the surface has changed. High degree of precision and reproducibility in positioning the tip over the top most part of a surface atom at both cryogenic and ambient temperatures can be achieved by using the atom tracking technique [24,25]. In UHV experiments at room temperature, this tool can also be applied for the prediction and compensation of constant thermal drift in the three spatial dimensions [26] (for more details see Chap. 2).

3.2.1 Extraction of the Short-Range Force from the Frequency Shift

In FM-AFM, the frequency shift is proportional to a weighted average of the tip–surface interaction force over one cantilever oscillation cycle. For small enough perturbations of the harmonic behavior of the cantilever oscillation, the frequency shift (Δf) can be expressed as [14,27,28]

$$\Delta f = \frac{f_\mathrm{r}}{\pi k_\mathrm{s} A_0} \int_{-1}^{1} F_\mathrm{int}[z' + A_0(1+u)] \left(\frac{-u}{\sqrt{1-u^2}} \right) \mathrm{d}u, \tag{3.1}$$

(where f_r is the free-oscillation cantilever resonant frequency, k_s is the cantilever stiffness, A_0 is the cantilever oscillation amplitude, F_int is the tip–surface interaction force, and $z' = z - q$ is the tip–surface distance, with q being the generalized coordinate of the point-mass model that describes the harmonic oscillation of the tip [11,14]). The kernel function

$$K(u) = \left(\frac{-u}{\sqrt{1-u^2}} \right) \quad u \in \{-1, 1\} \tag{3.2}$$

has important consequences when operating FM-AFM at either large or small oscillation amplitudes. For large oscillation amplitudes, this kernel assures

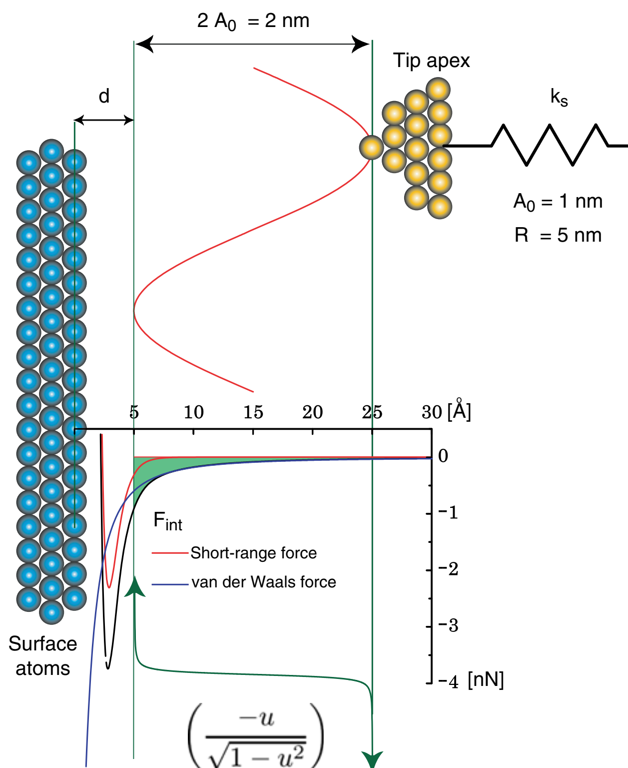

Fig. 3.1. A total interaction force (F_{int}) comprised by the short-range forces associated with a Si–Si interatomic interaction and the van der Waals force for a Si tip of 5 nm nominal radius. The behavior of the kernel function shown in (3.2) over a cantilever oscillation amplitude of 1 nm (total cantilever oscillation path of 2 nm) and a closest tip–surface distance approach (d) of 5 Å is also displayed

that the main contribution to the frequency shift comes from the point of closest proximity of the tip to the surface, as at the divergence for $u = 1$, the tip–surface interaction is normally negligible [28] (see Fig. 3.1). For small oscillation amplitudes, the kernel is responsible for the partial cancelation of the long-range interaction upon a small enough variation of these forces over a distance range equivalent to the total cantilever oscillation path [29, 30].

Force spectroscopy is based on (3.1), and obtaining the tip–surface interaction force from the measured frequency shift requires the inversion of this expression. This is, however, a nontrivial mathematical operation. Gotsmann [10], Durig [28], Giessibl [29], and Sader [31] have proposed different inversion procedures to obtain the tip–surface interaction force from (3.1). We have found that the methods proposed by Giessibl and Sader are more robust against the presence of experimental noise. While Giessibl's method requires powerful mathematical routines – commercially available – to invert a matrix

of $(n \times n)$ elements, with n the number of points of the frequency shift vs. tip–sample distance curve, the method proposed by Sader can be easily implemented having basic computational programing skills. Proper extraction of the tip–surface interaction force with Sader's method requires, however, exploring a tip–surface distance range extending to the free oscillation region; otherwise, the whole force curve will be shifted as a unit to smaller absolute force values. In cases where it is not possible to reach tip–surface distances entering in the free oscillation region, Giessibl's method may provide more accurate force values as the separation from the short-range interaction region is increased. In an overall evaluation, when reaching tip–sample distances corresponding to the free oscillation region, we have obtained a better performance using the method proposed by Sader and Jarvis [31]. The force extracted from frequency shift curves presenting significant instabilities loses its meaning as (3.1) is not well defined upon the presence of jumps in the frequency shift [14, 27, 32], and an alternative analysis is then required [33].

The tip–surface interaction forces extracted from the frequency shift vs. tip–sample distance curves include both long- and short-range interactions. The short-range forces can be obtained by subtracting the long-range contribution from the total force [22]. As during data acquisition the electrostatic force is minimized by compensating the tip–surface contact potential difference, the main long-range contribution comes from the van der Waals interaction. When possible, the long-range contribution should be characterized over surface sites not showing an apparent short-range interaction over a significant tip–surface distance range close enough to the surface, like, for example, over holes or vacancies [16, 24, 34]. In heterogeneous surfaces, upon the absence of surface sites for the direct characterization of the long-range interaction, it can be assumed that the long-range region embraces a distance from the free-oscillation regime to the position at which the total force curve for the different atomic species populating the surface starts deviating from a common behavior [35] (care about possible topographic offsets due to the acquisition protocol has to be taken [36], see Sect. 3.4 for details). An appropriate fitting of the total force over the long-range region to a Hamaker-like analytic model for the van der Waals interaction of a sphere over a plane [16] provides a good approximation to characterize the long-range contribution. Finally, the short-range interaction force is obtained by the subtraction of this fit evaluated over the whole tip–sample distance range explored to the total force curve.

3.2.2 Determination of Relevant Acquisition Parameters

The accuracy quantifying the tip–surface interaction force essentially depends on a proper characterization of the relevant acquisition parameters in FM-AFM. These are the cantilever oscillation amplitude, the cantilever stiffness, and the quality factor (Q) of the cantilever oscillation (in case that the

quantification of the energy dissipated from the cantilever would be also required).

The Q-value can be determined by the ring-down method, in which the excitation driving the cantilever at resonance is suddenly interrupted and the evolution of the square of the amplitude with time follows an exponential decay with a time constant given by $Q/2\pi f_0$, where f_0 is the cantilever resonant frequency. The Q-value can be also obtained from the width of the resonant peak of the power spectral density of the cantilever thermal motion measured with a spectrum analyzer.

For rectangular Si cantilevers operated in UHV, the method proposed by Cleveland and co-workers [37] produces a fair estimation of the cantilever stiffness. In this method, the equivalent static stiffness for the fundamental oscillation mode of the cantilever can be expressed as a function of the resonant frequency and the length and width dimensions of the cantilever. These geometrical dimensions are well defined during the cantilever production process, normally presenting a very low dispersion with respect to the corresponding nominal values, in comparison with the cantilever thickness. In case that it would be impossible to directly measure the cantilever dimensions, good estimations of the length and width values of the cantilevers can be obtained from the quality-control data provided with each cantilever wafer.

The main contribution to the uncertainty in the estimation of the tip–surface interaction force comes, by far, from the determination of the cantilever oscillation amplitude. In an optical interferometer detection scheme, the measured cantilever oscillation amplitude depends on the position of the laser spot along the cantilever longitudinal axis. Values closer to the real oscillation amplitude will be obtained when positioning the laser spot as close as possible to the cantilever free end, over the tip position; otherwise, corrections considering the distance of the laser spot from the cantilever free end must be undertaken. The magnitude of the cantilever oscillation amplitude is normally obtained from the detector output in volt units. A conversion factor to distance units can be calculated using the normalized frequency shift [27]. For an identical tip–surface interaction force and large enough cantilever oscillation amplitudes (see Sect. 3.6), the normalized frequency shift remains constant independently of the oscillation amplitude [13]. Thus, a calibration of the cantilever oscillation amplitude can be performed by tracing the relative tip–sample distance while changing the oscillation amplitude, keeping constant the normalized frequency shift over the same spot on the surface (this requires readjustment of the frequency shift set point for each oscillation amplitude) [24, 38]. A set of several pairs of oscillation amplitude values and corresponding relative tip–sample displacements should follow a linear behavior with slope as the calibration constant. To minimize the influence of piezo creep and assure reproducibility, several cycles increasing and decreasing the cantilever oscillation amplitude can be measured. This calibration should be performed at tip–surface distances corresponding to a significant long-range interaction force, avoiding possible contributions from atomic-scale variations

of the surface. Since the determination of the cantilever oscillation amplitude depends on the position of the laser spot, the calibration should be performed for each experimental session or after repositioning the laser spot on the cantilever.

3.3 Energy Dissipation and Force Spectroscopy

The combination of force spectroscopy and first-principles calculations has contributed in a decisive way to further clarify the enhancement of atomic contrast in the dissipation signal upon increasing the tip–surface short-range interaction force when probing semiconductor surfaces [39].

The dissipation signal is the additional amount of energy that the cantilever requires to keep the oscillation amplitude constant and at resonance under the presence of nonconservative tip–surface interaction forces. This additional energy is put into the cantilever by increasing the voltage amplitude of the harmonic signal applied to the piezoelectric actuator that drives the cantilever oscillation [14]. This voltage is determined by the feedback controller that keeps the oscillation amplitude constant in a FM-AFM detection scheme [5]. The extra excitation applied to compensate reductions in the cantilever oscillation amplitude can be fairly related to the energy dissipated from the cantilever within an oscillation cycle, as it was shown by Cleveand and coworkers [40]. An interesting review on phenomenology and first observations of dissipation signal at atomic scale in FM-AFM together with explanations about the possible origins of this atomic contrast can be found in Chaps. 19 and 20 of the first NC-AFM volume [6].

In those pioneering works, a puzzling experimental observation was that the contrast in the dissipation signal shows a dramatical variability upon modifications of the tip apex [41, 42], indicating a clear dependence of the atomic contrast in the dissipation signal with the nature and structure of the tip termination. It was later suggested that this contrast could even be an artifact due to the electronics regulating the oscillation amplitude [43].

3.3.1 Tip-Apex Characterization Combining Force Spectroscopy and First-Principles Calculations

To contribute to the understanding of the mechanics for the atomic contrast in the dissipation signal, we elaborated force spectroscopy experiments on the Ge(111)-c(2×8) surface. Similar to the Si(111)-(7×7) surface, this germanium reconstruction presents both adatoms and rest atoms terminating the surface [44, 45]. In preliminary experiments on the Ge(111)-c(2×8) surface with AFM, we obtained typically two atomic patterns in topography [46]: one displaying both adatoms and rest atoms (A pattern), usually with a clear dissipation signal registered over the adatom positions; the other showing only the adatoms (B pattern), normally accompanied of a faint atomic contrast

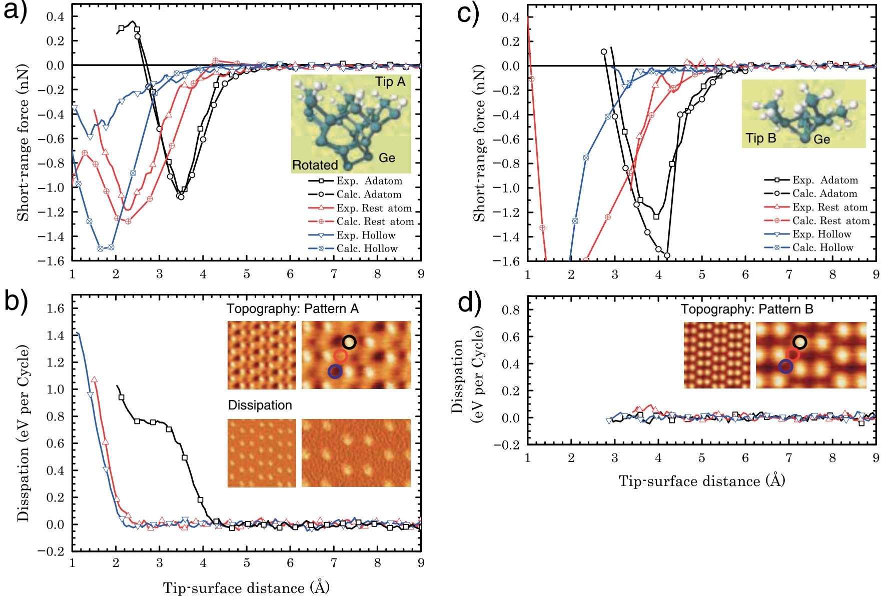

Fig. 3.2. Measured and calculated short-range forces over specific positions of the Ge(111)-c(2 × 8) surface with two tip terminations producing different atomic patterns. (**a**) and (**b**) Simultaneously measured short-range force and dissipation signal with the tip resolving both adatoms and rest atoms. Simultaneous topographic and dissipation images (A pattern) are displayed as insets. (**c**) and (**d**) Similar data as in (**a**) and (**b**) for a tip resolving only the adatoms of the Ge(111)-c(2 × 8) surface (B pattern). Acquisition parameters were $f_0 = 183{,}663\,\mathrm{Hz}$, $k = 44 : 3\,\mathrm{N\,m^{-1}}$, $A_0 = 182\,\text{Å}$, $Q = 259{,}500$ in both cases. Experiments were performed at 80 K tip–surface temperature. The most probable candidates to reproduce the tip termination during the experiments, together with the short-range forces calculated over the adatom, rest atom, and hollow sites using the corresponding tip model are displayed in (**a**) and (**c**), respectively. Figure adapted from [39]

in the dissipation signal, if any. Representative images of these atomic are displayed in Fig. 3.2.

Trying to clarify the origin of these two types of topographic contrast and the presence of atomic contrast in the dissipation signal only in one of them, we measured site-specific force spectroscopic characteristics – simultaneously recording the frequency shift, the cantilever oscillation amplitude, and the dissipation signal – over the adatom, rest atom, and hollow sites of the Ge(111)-c(2 × 8) surface. We started the measurements with a tip termination producing A pattern imaging. Then, we intentionally modified the tip by producing gentle and controlled contacts with the surface until obtaining a tip termination only resolving the adatoms of the surface and giving no contrast in the dissipation signal. Finally, we repeated the force spectroscopic

measurements with this tip producing B pattern imaging over the same surface sites but at a different location on the surface, keeping exactly the same experimental – resonant frequency, oscillation amplitude, cantilever stiffness, and Q-value – and cantilever dynamic regulation parameters as for the force spectroscopic series acquired with the tip producing A pattern imaging. Only the frequency shift set point was varied from $-15.5\,\mathrm{Hz}$ for imaging with the tip producing A patterns to $-13.4\,\mathrm{Hz}$ for the tip producing B patterns. This corresponds to imaging at very similar maximum total force values (including the long range interaction) of -1.4 and $-1.2\,\mathrm{nN}$, respectively. This procedure rules out possible artifacts in the dissipation signal coming out from the cantilever dynamics regulation electronic.

The short-range force and the dissipation energy measured in these experiments are summarized in Fig. 3.2. Despite the resemblance of the short-range force in both cases (especially over the adatom site), the behavior of the energy dissipated from the cantilever is completely different. A dramatic increment in the dissipation signal is obtained for the tip termination producing A pattern imaging, while complete absence of additional dissipation with respect to the intrinsic energy losses associated with the cantilever oscillation is obtained for the tip providing B patterns, even at the closest tip–sample distances. Interestingly, there is a plateau-like behavior for the dissipation signal over the adatom positions for the tip showing A pattern imaging, in contrast to the monotonic growth for the rest atom and hollow sites.

To elucidate the origin of this behavior in the dissipation signal, we undertook a characterization of the tip–apex termination for each spectroscopic series. This tip characterization is based on an extensive and methodical comparison of the measured short-range forces with the calculated ones using atomically extended and well-tested models to describe the tip–apex structure and composition. For the tip–apex characterization, a set of many possible tip were tested over the adatom and the rest atom positions. Some of these tip models were chosen from the experience gained in previous atomistic simulations [17, 18], others were produced after sharpening a bulk structure by cleaving over different crystalline plane directions, and the rest were the result of heating and quenching process of some of the tip models generated by the cleaving method. Some of these tip terminations are shown in Fig. 3.3.

We found that most of these structures can be grouped into very few families based upon the qualitative force and dissipation characteristics they exhibit, as it also happens in the experiments. A comparison of the calculated force upon approach over the adatom and rest atom positions with the corresponding experimental forces allowed us to perform a first screening. An analysis of the contribution to the interaction force of the different parts of the remaining tip models enabled us to discard some of the structures and to look for an optimum orientation with respect to the surface. Small variations regarding composition and atomic coordination at the very apex enable us a final selection that was based on the best reproduction of the force minima and the attractive and repulsive regions of the experimental curves (Fig. 3.2).

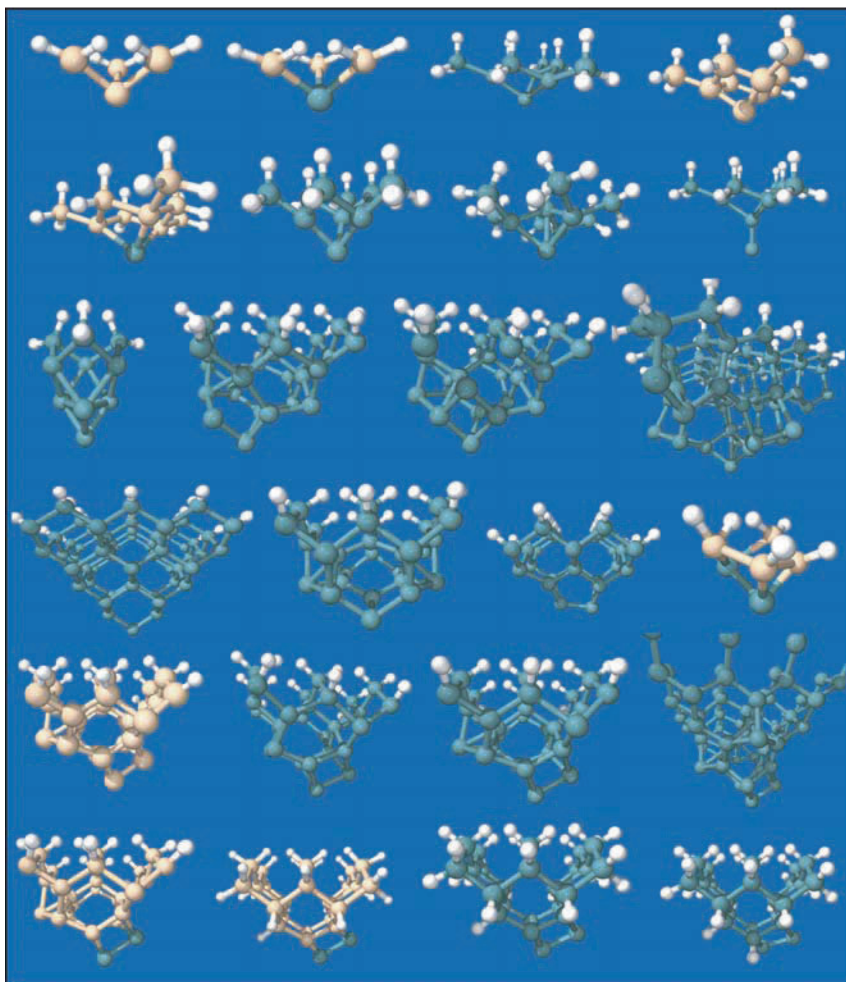

Fig. 3.3. Some of the tip models tested for the characterization of the AFM tip termination during the experiments. The tip characterization is based on an extensive and methodical comparison of the measured and calculated short-range forces. The color code for the tip-model composition is *green* for Ge atoms, *cream* for Si atoms, and *white* hydrogen. Figure adapted from [39]

The tip models satisfying the overall best fit to the experimental curves of both spectroscopic series were selected as candidates to simulate the AFM tip apex during the corresponding experiments.

This tip characterization yielded to an asymmetric Ge dimer terminated tip (tip A in Fig. 3.2) as the most probable candidate to reproduce the tip–apex termination for pattern A imaging. Although the tip A reproduced the force value and the stiffness of the attractive and repulsive regions of the

experimental curve over the adatom, an excessive attractive force over the rest atom was obtained due to the interaction of the tip–apex body with the surrounding Ge adatoms. By rotating the tip A with the dimer line oriented 30° clockwise with respect to the adatom row direction, both the value at the force minimum, and the stiffness of the attractive and repulsive regions were also well reproduced for the rest atom site. In contrast, pattern B imaging was probably produced by a symmetric tip apex terminated in a single atom with a T_4 coordination and a dangling bond pointing perpendicular towards the surface (tip B in Fig. 3.2). The excellent agreement in the comparison of the calculated and the experimental short-range forces for each of these tip models is shown in Fig. 3.2.

3.3.2 Identification of an Energy Dissipation Channel

In previous works, Durig [47], Sasaki, and Tsukada [48] predicted that atomic contrast in the energy dissipated from the cantilever oscillation may be originated by hysteresis in the tip–surface interaction force. Later, Kantorovich and Trevethan [49] elaborated this idea further by applying the soft-mode concept and transition state theory to FM-AFM. In atomistic simulations, these authors showed that energy dissipation of similar values to the ones recorded during experiments can be obtained considering the hysteresis originated by the existence of two or more solutions in the tip–surface interaction force upon approach and retraction of the tip over the surface [49].

In practice, however, it is very difficult to experimentally discern the existence of several solutions in the tip–surface interaction force over one oscillation cycle of the AFM tip. If different force solutions occur, their presence should be blurred when measuring frequency shift curves alone, as the frequency shift is basically a weighted average of the total tip–surface interaction over one oscillation cycle [27, 32]. Thus, experimental forces obtained from continuous frequency shift curves reflect, under normal conditions, only the conservative part of the tip–surface interaction [14]. We have to rely on atomistic simulations to investigate the existence of several force solutions and to corroborate whether there is hysteresis between them that may develop in energy dissipation from the cantilever oscillation.

The characterization of the most probable termination of the tip apex during the experiments described in Sect. 3.3.1 enables to clarify the existence of different force solutions during an approach and retraction cycle of the tip over the surface. Figure 3.4 displays the calculated short-range forces upon the approach and retraction of the tip A and tip B displayed in Fig. 3.2 over an adatom site of the Ge(111)-c(2×8) surface, together with the calculated potential energy as a function of the adatom vertical displacement perpendicular to the surface for different height positions of the corresponding tip model. While in the case of tip B both force curves are very similar, clear hysteresis between two solutions upon approach and retraction appears for the tip A. These two force solutions are associated with a bistability [47, 48] of the

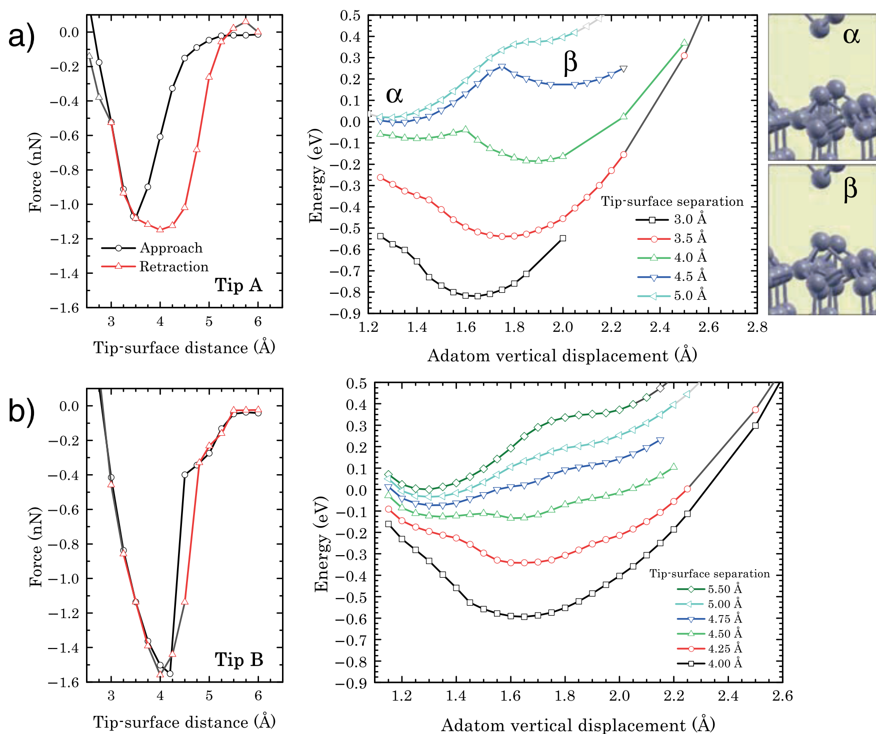

Fig. 3.4. Calculated short-range forces upon a tip approach and retraction cycle over an adatom site of the Ge(111)-c(2 × 8) surface, and potential energy as a function of the adatom vertical displacement perpendicular to the surface for different tip height positions. (**a**) and (**b**) correspond to calculations performed with the tip A and tip B models displayed in Fig. 3.2, respectively. Figure adapted from [39]

potential energy of the surface adatom due to the tip–apex proximity. The first force solution corresponds to a situation in which the adatom is perfectly sited at its surface position during the tip approach, while the second solution is associated with a situation in which the adatom is slightly pulled out from the surface following the tip retraction (see details of the respective atomic configurations in the images displayed in Fig. 3.4a). The evolution of these two solutions are closely related to the development of two minima at the potential energy curve, labeled as α and β in Fig. 3.4a, upon the surface adatom vertical displacement. The stability of the second force solution during the retraction of the tip model A is originated by the existence of apparent energy barriers between these two minima for a significant tip–surface distance range. The presence of these barriers is favored by structural changes that take place at the apex of tip A during the approach, which lead to a sharpening of the apex structure. Moreover, the accumulation of charge at the lower atom of the dimer at the tip apex reinforces its interaction with the surface adatom

upon retraction. These effects are not present in the single-atom apex of tip B, as it is shown in the potential energy of the surface adatom calculated using the tip B (Fig. 3.4b), leading to almost negligible energy barriers.

Upon these results, the behavior of the measured dissipation signal with the tip–sample distance over a surface adatom with the tip producing A pattern imaging can be explained by taking into account the finite temperature at which the experiments were performed. At zero temperature, a step-like behavior of the dissipation would be expected, as the transition between the two force solutions cannot take place until reaching the tip–surface distance where the barrier goes to zero (around 3.5 Å at the energy plot in Fig. 3.4a). Upon retraction, the system would stay in the second force solution until the barrier for the transition back to the original structure disappears (around 6 Å), following the whole hysteresis cycle shown in the force plot. However, at the tip–sample temperature the experiments were performed (80 K), the system has a probability to overcome these barriers and to jump by thermally activated processes between the two energy minima. This originates transitions between the two force solutions at larger tip–surface distances during the approach and at shorter tip–surface distances during the retraction, completing in this case only a fraction of the whole hysteresis cycle in the force. This situation explains the onset of dissipation at 4.4 Å and the steady increase of the dissipation signal for distances below 3.5 Å in Fig. 3.2b. At tip–surface distances where the barrier for the transition during approach vanishes (below 3.5 Å), the system completes the relevant part of the whole hysteresis cycle by following the first force solution during the tip approach towards the surface and the second solution upon the tip retraction. Under these conditions, the energy dissipation is to be almost steady, reaching the plateau regime. Notice that the energy associated with the hysteresis between the two force solution for the tip A is ∼0.53 eV; a value close to the dissipation signal at which the plateau in the dissipation curve recorded over the adatom is observed (∼0.75 eV, see Fig. 3.2b). Further raising of the dissipation signal after the plateau is originated by the onset of a second dissipation channel involving significant distortions of the tip apex and the adatom configuration, as well as bonding interactions beyond two atoms. This second dissipation channel is closely related to processes, leading to vertical atomic manipulation [50,51] (see Sect. 3.3.4 and Chap. 8), and to tip apex or surface permanent modifications.

The behavior of the dissipation signal with the tip–sample distance for the tip termination producing A pattern imaging at the rest atom and hollow sites in Fig. 3.2b might be originated by a concomitant dissipative interaction between the nearby tip–apex atoms and the neighboring surface adatoms, similar to the adatom case.

Upon these calculations, the energy dissipated from the cantilever oscillation when probing a Ge adatom – located in a T_4 bonding configuration – with a tip producing A pattern imaging is mainly related to the breaking and remaking of the bond with the beneath surface atom, as it is highlighted by

the different bonding configurations for the Ge adatom in the atomic models shown in Fig. 3.4a. The energy dissipation observed at the plateau in Fig. 3.2b might be therefore considered as an estimation of the adhesion associated with this single atomic bond of the Ge adatom with the surface atom underneath.

3.3.3 Surface Adhesion Maps at Atomic Scale

The results described in Sect. 3.3.2 suggest that energy dissipation imaging and spectroscopy measured at atomic scale with FM-AFM may provide information about the adhesion response of surface atoms to a single atomic contact with the tip apex. This information may then be related to the specific nature of the different atomic species forming an heterogeneous surface – leading to an additional channel for atomic recognition – or to variations of the local atomic structure. In this context, the constant height scan and dissipation images of the Si(111)-(7 × 7) surface shown in Fig. 3.5 are of most interest. While in the constant height scan image, the contrast of the Si atoms shows an homogeneous appearance at the respective faulted and unfaulted half unit cells [16, 52], in the dissipation image, the contrast on the corner adatoms considerably differs from that of the center adatoms. Furthermore, while the center adatoms of both half-unit cells present similar contrast in the dissipation signal, the corner adatoms of the faulted-like half-unit cell display less contrast than the corner adatoms of the unfaulted-like half-unit cell. Taking into account the mechanism for the energy dissipation channel described in Sect. 3.3.2, this dissipation image could be considered a map of the adhesion response of the surface adatoms to a single atomic contact with the tip apex, which clearly reveals subtle local structural differences between the adatoms that are imperceptible to the frequency shift. Upon this assumption, the corner adatoms of the faulted-like half-unit cell should be more strongly bonded to the surface than the ones of the unfaulted-like half-unit cell. In addition, a higher vertical mobility of the center adatoms – nearly equal for both half-unit

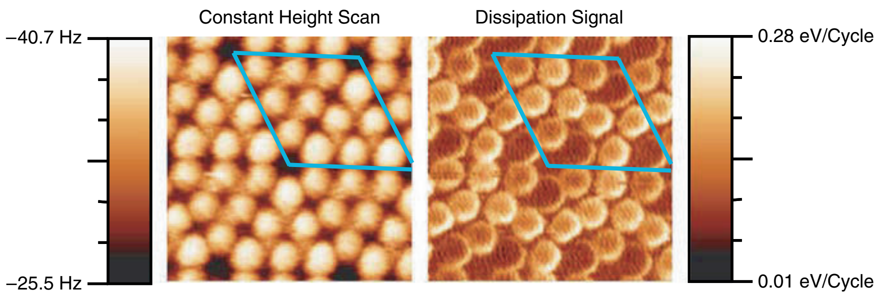

Fig. 3.5. Constant height scan (*left*) and simultaneously measured energy dissipation images of the Si(111)-(7 × 7) surface acquired at 10 K tip–surface temperature. Image size is $(5 \times 5)\,\mathrm{nm}^2$. Acquisition parameters were $f_0 = 173,833.1\,\mathrm{Hz}$, $K = 37.5\,\mathrm{N\,m}^{-1}$, $A = 133\,\mathrm{Å}$, $Q = 91,700$. Figure adapted from [39]

cells – due to a softer interaction with the underlying atoms is expected, in good agreement with previous experimental observations [50,53]. There is also an increment of the dissipation signal in the right-lower part of each adatom independently of its location. These asymmetric structures can be ascribed to the tip apex (because they are common to all the adatoms), and they denote an increment of the adhesion response due to a preferred directionality in the tip–apex configuration, as it has been pointed out in [54, 55].

With a proper tip–apex characterization, atomically resolved dissipation imaging in FM-AFM may develop in quantitative surface adhesion maps at atomic scale.

3.3.4 Signatures of Energy Dissipation in Frequency Shift and Force Curves

In FM-AFM, the frequency shift is proportional to a weighted average of the tip–surface interaction force over one oscillation cycle [14, 27, 32] (see (3.1) and Fig. 3.1). If several force solutions with apparent energy barriers for transitions between them are explored at the closets tip–surface distances, then the presence of these force solutions is going to be smeared off in the frequency shift signal. Thus, frequency shift curves (and the tip–surface interaction forces obtained from them) should not contain information about the nonconservative processes that lead to energy dissipation from the cantilever orcillation [39,48,49]; they are only to reflect the conservative part of the tip–surface interaction [14, 27, 32]. However, in some cases, it is possible to find signatures of nonconservative processes at the tip–surface interface in both frequency shift and force curves, which are subtler than mere discontinuities associated with atomic instabilities either at the tip [33] or at the surface. One example is the spectroscopic curves obtained during vertical interchange manipulation processes [51].

Figure 3.6 shows the variation of the frequency shift, the short-range interaction force, the cantilever oscillation amplitude, and the energy dissipated from the cantilever oscillation, simultaneously recorder during the approach and retraction of the sample over the AFM tip, corresponding to the deposition of a tin atom (Fig. 3.6a) and a silicon atom (Fig. 3.6b) in two consecutive vertical interchange atom manipulation processes, respectively.

A characteristic feature of the frequency shift curves in vertical interchange atom manipulation experiments is the appearance of a shoulder at close tip–surface distances. This shoulder develops into a double well structure in the corresponding short-range interaction force, with similar maximum attractive force values and that seem to concur with a significant increase in the dissipation signal (see Fig. 3.6b and Fig. S2 in [51]). These structures are originated by thermally activated jumps between different force solutions – associated with several energy branches available for the system – as the tip explore distances close to the repulsive regime of the tip–surface short-range interaction,

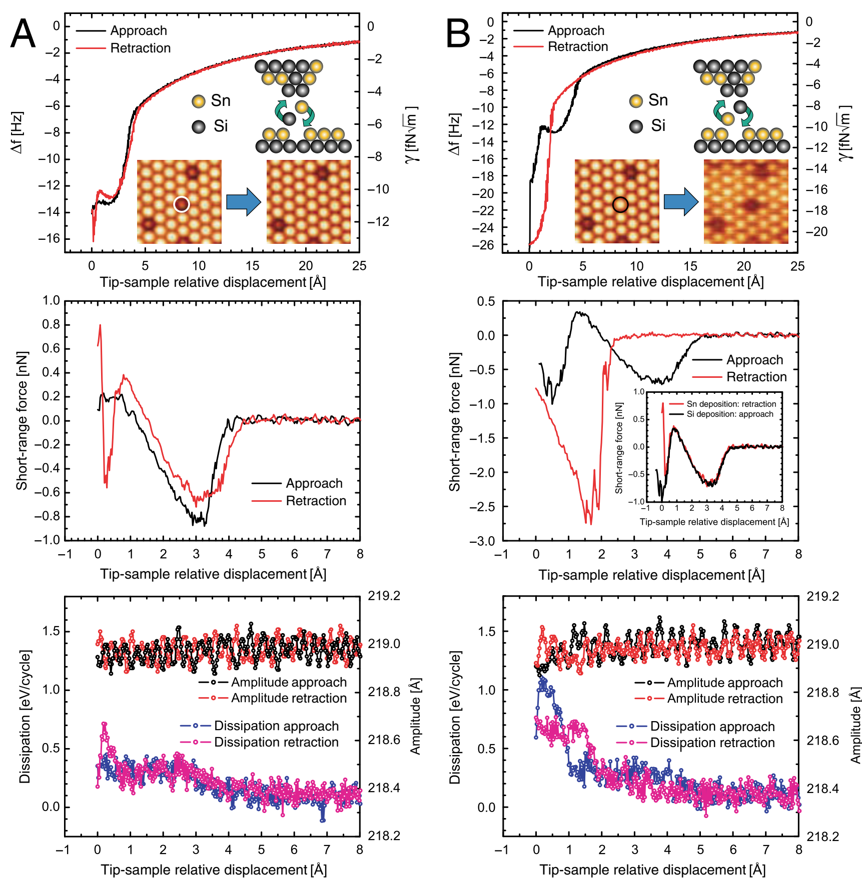

Fig. 3.6. Frequency shift, short-range force, cantilever oscillation amplitude, and energy dissipation per oscillation cycle characteristics simultaneously acquired during the deposition of tin atom (**a**) and a silicon atom (**b**) coming from the AFM tip in two consecutive vertical interchange atom manipulation processes on a Sn/Si(111)-($\sqrt{3} \times \sqrt{3}$)R30° surface. Acquisition parameters were $f_0 = 193{,}738.0$ Hz, $k = 48.8\,\mathrm{N\,m^{-1}}$, $A = 219$ Å, $Q = 13{,}000$. The experiments were performed at room temperature. Figure adapted from [51]

where the atomic rearrangements in the contact area leading to atom manipulation take place [51]. In particular, a double minima in the experimental force curve is an indication of the system evolving between two different bonding configurations during the approach and retraction cycle (see Chap. 11 and the Supplementary Online Material of [51]).

Similar behavior of the tip–surface interaction force has been also observed in force spectroscopy experiments on insulating surfaces like NaCl(100) [56] or MgO(100) (see Fig. 3.7), where a double minima in the force curve appears only over a specific site at the surface. As in the case of the spectroscopic

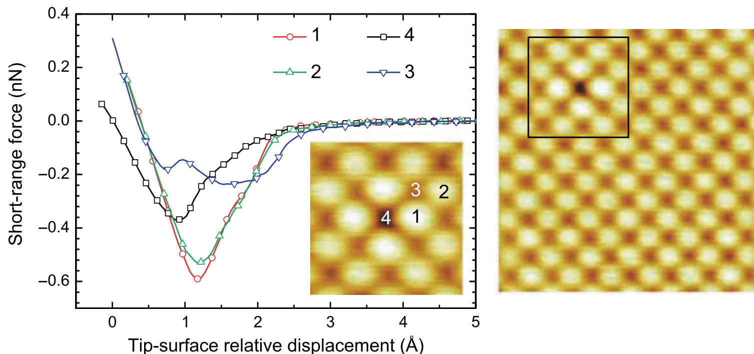

Fig. 3.7. Site-specific force spectroscopy over atomic positions in the vicinity of an atomic defect at the (100) surface of an MgO single crystal. At the sadle-point over the ionic species not resolved in the topographic images (*position 3*), a double-well structure in the short-range force is clearly observed. These minima can be ascribed to transitions between different force solutions accessible for the tip–surface system. Acquisition parameters were $f_0 = 175{,}048.0\,\mathrm{Hz}$, $k = 38.3\,\mathrm{N\,m^{-1}}$, $A = 24\,\mathrm{Å}$, $Q = 186{,}857$. Experiments were performed at 80 K tip–sample temperature. Image sizes are $(2.5 \times 2.5)\,\mathrm{nm}^2$ and $(1.0 \times 1.0)\,\mathrm{nm}^2$

curves in vertical interchange atom manipulation experiments, the presence of these double minima may be ascribed to transitions between different force solutions accessible for the tip–surface system. The energy barriers for the transitions between these different force solutions as a function of the tip–surface distance dictate where the system jumps during either approach or retraction in an stochastic process driven by the available thermal energy and, thus, determine the details of both frequency shift and force curves.

3.4 Force Spectroscopy and Atomic Relaxations

The combination of interatomic force measurements on heterogeneous semiconductor surfaces and first-principle calculations has also enabled to clarify the relation between striking observations of the topographic contrast at close tip–surface distances, the real surface structure, and role played by atomic relaxations of the closest tip and surface atoms [36].

Figure 3.8 summarizes the behavior of the topographic contrast when imaging silicon defects (protrusions with diminished contrast) at the perfect single-atomic later of tin atoms (bright protrusions) that form the Sn/Si(111)-$(\sqrt{3} \times \sqrt{3})R30°$ surface [57, 58]. For a low density of defects, these Si atoms are usually equally surrounded by six Sn atoms, showing an identical height difference with respect to the Sn atoms. We have found, however, a reduction of the relative topographic height between Sn and Si upon increasing the tip–surface interaction force. This effect is shown in Fig. 3.8d, where the

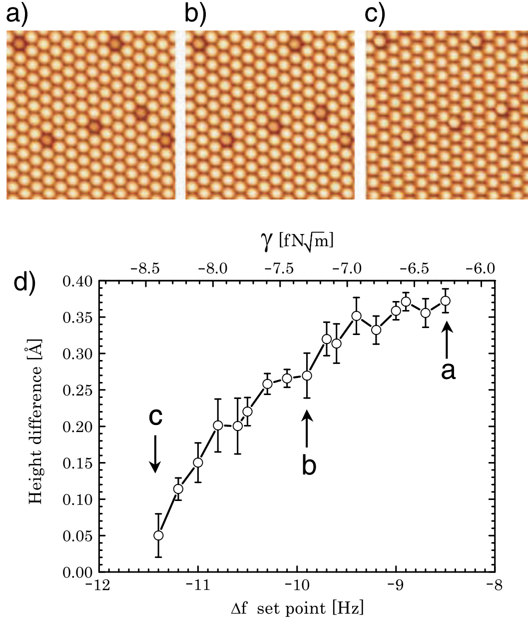

Fig. 3.8. (**a**)–(**c**) Images showing the reduction of the topographic height difference between substitutional silicon defects and the tin atoms of the Sn/Si(111)-($\sqrt{3} \times \sqrt{3}$)$R30°$ surface when decreasing the tip–sample distance. Image dimensions are $(8.5 \times 8.5)\,\mathrm{nm}^2$. (**d**) Dependence of the Sn–Si topographic height difference with the frequency shift image set point. Acquisition parameters were $f_0 = 162{,}285.8$ Hz, $k = 30.5\,\mathrm{N\,m}^{-1}$, and $A = 200$ Å. Figure adapted from [36]

topographic height difference between Sn and Si is quantified from a series of images measured – over the same surface area and with the same tip apex termination – consecutively increasing the absolute value of the frequency shift imaging set point. As is evidenced by the images depicted in Fig. 3.8a–c, the Sn–Si height difference decreases almost up to disappearance at the closest tip–surface distances.

The atomically resolved topography images displayed in Fig. 3.8 are consequence of the forces associated with the bonding interaction between the outermost atom of the tip apex and the surface atoms [17, 18]. It has been demonstrated that atoms on heterogeneous semiconductor surfaces occupying nonequivalent positions provide a different force response to the interaction with the AFM tip [59, 60]. This is not the case in the surface under consideration here, as both Sn and Si are occupying equivalent T_4 adsorption positions over the Si(111) surface, each atom having four valence electrons in a sp^3-like-hybridization and one dangling bond pointing outwards from the surface plane. Thus, the reduction of the Sn–Si topographic height difference when decreasing the tip–surface distance suggests several possible scenarios:

one, that there is a different chemical interaction between the Sn and the Si atoms, respectively, with the tip apex; other, that the interaction with the AFM tip produces structural vertical distortions of the atoms that manifest in a reduction of the topographic height difference; finally, there may occur a combination of these two cases depending on the strength of the interaction force. Information to further clarify this matter can be obtained by the analysis of site-specific force spectroscopic measurements.

Figure 3.9a shows frequency shift curves measured over the Sn and the Si atoms pointed out in the inset image. These curves were measured using the atom tracking technique to assure a precision in positioning the AFM tip over the topmost part of the surface atoms better than ± 0.1 Å [24–26]. Measuring site-specific force spectroscopic characteristics with the atom tracking technique requires locking onto the top-most par of the surface atom using the topographic signal (see Chap. 2 for details). In the case of heterogeneous surfaces with atoms showing variability in the topographic contrast, this procedure causes variations in the absolute tip–surface distance at which the acquisition of the frequency shift curve starts for the different atoms. For instance, when probing an Si adatom using a set point close to the onset of significant short-range interaction force, the tip is going to be closer to the sample than in the case of an Sn atom. This effect manifests in a different trend in the long-range interaction region of the frequency shift curves, which in principle should be common to all the curves measured with the same AFM tip in a surface area where local variations of the long-range interaction are not expected. This different trend in the long-range interaction is apparent in the curves shown in Fig. 3.9a. These curves meet at a frequency shift value of -5.4 Hz (the set point for the topographic feedback during both imaging and atom-tracking operation), point that corresponds to the origin of the relative tip–sample displacement (see the upper scale). A fair comparison of these curves, as well as the force curves obtained later on, requires compensation of this topographic effect associated with the acquisition protocol. Common values in the tip–sample displacement with respect to the surface plane are obtained by shifting the curve measured over the Si atom by a distance that matches the measured Sn–Si height difference at the given frequency shift topographic set point at which the curves were acquired. From the image recorded after the spectroscopic acquisition (inset in Fig. 3.9a), this distance corresponds to 0.54 Å (see the topographic profile displayed in Fig. 3.9b). The frequency shift curves after the topographic effect compensation are shown in Fig. 3.9b; now both curves share the same behavior over the long-range interaction region up to reaching the tip–surface distance where the contribution of the short-range interaction over the Sn atom becomes dominant.

The new crossing point of the frequency shift curves displayed in Fig. 3.9b provides an explanation for the reduction of the topographic height difference between Sn and Si upon decreasing the tip–surface distance (Fig. 3.8). According to the curves in Fig. 3.9b, the difference in topography at a given imaging set point should gradually decrease when increasing the absolute value of the

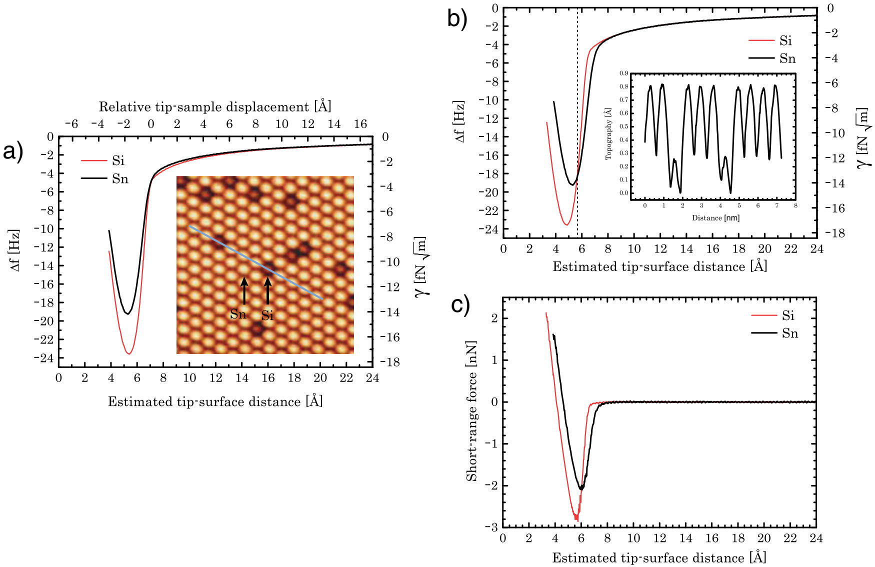

Fig. 3.9. (**a**) and (**b**) Force spectroscopic measurements over the Si and the Sn atoms pointed out the inset image. In (**b**), the frequency shift curve for the Si atom has been shifted by the height difference between Sn and Si (measured from the image in (**a**) and shown in the inset profile) to compensate the topographic effects associated with acquisition using the atom tracking technique. The *dotted line* highlight the position of the crossing point between both curves. Acquisition parameters were $f_0 = 162285.8$ Hz, $k = 30.5$ N/m, and $A = 259$ Å. The frequency shift set point for imaging and atom-tracking operation was -5.4 Hz. Image size is (8.5×8.5) nm^2. (**c**) Short-range forces corresponding to the frequency shift curves shown in (**b**). The tip–surface distance in estimated by assuming the surface position at the divergence for the fitting to the long-range contribution. Figure adapted from [36]

frequency shift up to reaching the crossing point, at which both atomic species would present the same height. This behavior is due to a different strength in the bonding interaction of Sn and Si, respectively, with the outermost atom of the tip apex, as it is evidenced by the corresponding short-range force characteristics displayed in Fig. 3.9c: the bonding force over the Sn atom is sensed at farther tip–surface distances, and, additionally, the value of the maximum attractive force is larger for the Si atom.

Contributions from atomic relaxations due to the interaction with the tip apex cannot be neglected as possible origin of the topographic height differences between Sn and Si. To investigate their influence, we have relied on atomistic simulations and the ability to characterize the most probable tip–apex termination during the experiments by the combination of force spectroscopic measurements and first-principles calculations (see Sect. 3.3.1).

Figure 3.10a shows the comparison of the short-range forces obtained from first-principles calculations upon approaching the tip model depicted in

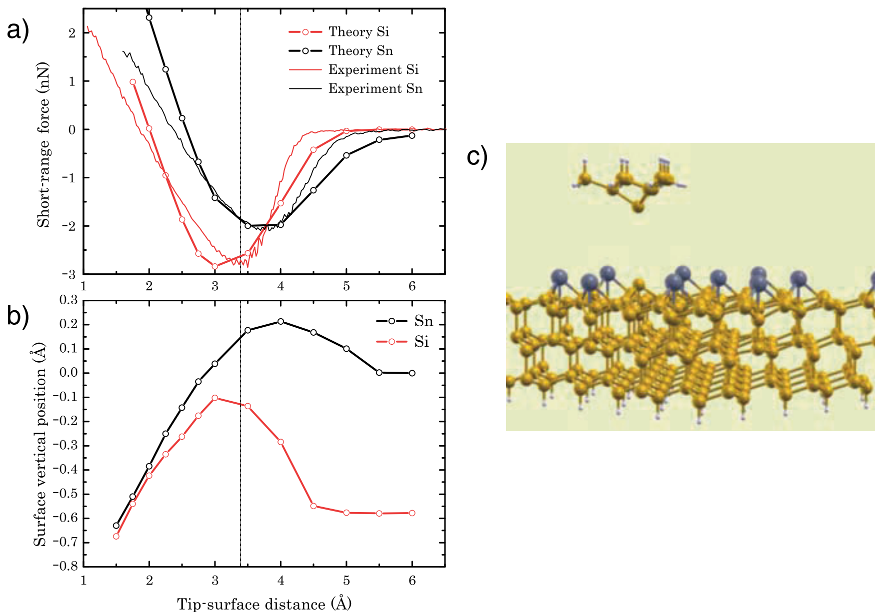

Fig. 3.10. (**a**) Comparison of the measured short-range forces displayed in Fig. 3.9c with the calculated interaction force of the tip model depicted in (**c**) with a Sn and a Si atom of the Sn/Si(111)-($\sqrt{3} \times \sqrt{3}$)$R30°$ surface, respectively. (**b**) Induced relaxations of the vertical position of the surface atoms due to the interaction with the tip model. The *dotted lines* denote the position of the crossing point between the frequency shift curves in Fig. 3.9b. For a proper comparison with the theoretical curves, the experimental force curves and the dotted line were shifted as a unit by 2.25 Å with respect to Fig. 3.9c, to align the minima of the force curves obtained over the Sn atom. Figure adapted from [36]

Fig. 3.10c – representing a quite stiff tip-apex termination – on a Sn and a Si atom of the Sn/Si(111)-($\sqrt{3} \times \sqrt{3}$)$R30°$ surface with the corresponding experimental curves (shown in Fig. 3.9c) over the closest tip–surface distance rage. Although the agreement between the force values at the minima is excellent, the stiffness of the attractive and repulsive interaction regions (i.e., the slope of the force curve in each of these two regimes) slightly differs from those of the experimental curves. This difference may be originated by a higher softness of the real tip apex during the experiments, which would allow atomic relaxations beyond the atomic positions considered in the tip model to accommodate the stress caused by the interaction with the surface, either in the attractive or the repulsive regime. Simulations using more realistic tip models [39, 55] have provided short-range force curves in a notable good agreement with the experimental ones, in both the maximum attractive force and the stiffness of the attractive and repulsive regimes [39] (see Sect. 3.3.1). The excellent agreement between the maximum attractive force values of the experimental and calculated short-renge force curves in Fig. 3.10a suggests, however, a tip-apex

termination during the experiment in the form of a Si atom with a single dangling bond pointing perpendicular towards the surface plane.

The analysis of the vertical displacements of the surface atoms upon proximity of the tip model (Fig. 3.10b) indicates that the attractive interaction with the tip originates local distortions that lift the Si atom upwards slightly more than for the Sn atom. At very low interaction forces, the height difference between Sn and Si remains close to the value for the isolated surface (∼0.5 Å). Upon increasing the attractive interaction force, both surface adatoms experience a vertical relaxation towards the tip, which is more prominent in the case of the Si atom. The onset of the covalent bonding with the tip outermost atom provides extra charge to the surface Si atom (that initially has a charge deficiency due to a charge transfer to the neighboring Sn atoms [61]), favoring a larger vertical displacement than that of the Sn atom. At a tip–surface distance close to the force minimum, there is a strong relaxation of both the tip outermost atom and the surface atom in order to accommodate an atomic separation between them similar to the sum of the corresponding covalent radii. This situation has important consequences for the single-atom chemical identification capability of AFM, as it is discussed in Sect. 3.5. At tip–surface separations smaller than the distance for the maximum attractive force, the surface atoms relax back towards the surface due to Pauli repulsion of the electron clouds of the interacting tip and surface atoms.

These results suggest that when imaging heterogeneous semiconductor surfaces, FM-AFM can provide a fairly direct access to the true structure of the surface. In principle, topographic measurements does not correspond to the real height difference between surface atoms, as the topography measured with FM-AFM is a complicated convolution of the total tip–surface interaction (which shows variability upon different tip-apex terminations, see Sect. 3.5) and the structure of the surface (that can also be affected by the interaction with the tip). However, the results described here show that when imaging at the onset of the short-range interaction (exploring weak forces that barely disturb the surface structure), the registered corrugation seems to closely reproduce the real atomic height differences expected for the free surface. At smaller tip–surface separations, the tip–surface interaction gradually produces significant displacements of both tip and surface atoms during every oscillation cycle, and differences in the strength of the short-range interaction intrinsic to each of the atomic species composing the surface start to dominate over the distance dependence; under these conditions, the measured topographic contrast cannot be related anymore to the geometry of the free surface.

3.5 Single Atom Chemical Identification

When exploring semiconductor surfaces with FM-AFM, atomic contrast is obtained by detecting the forces associated with the onset of a bond formation between the outermost atom of the AFM tip and the atoms at the surface

[17, 18]. In the case of heterogeneous surfaces, these short-range forces will show small variations for the different atomic species composing the surface. An example of this behavior can be seen in Figs. 3.9 and 3.10. Thus, these inter-atomic forces should contain information about the chemical nature of the different surface atoms, and, in principle, the precise quantification of the tip–surface short-range force over each atom at the surface should lead to the possibility of chemically identifying them.

The realization of this concept is, however, quite complex as the short-range forces obtained with FM-AFM ultimately depend on the tip-apex termination. This variability of the measured forces with the AFM tip is shown in Fig. 3.11b–f, where several sets of short-range force curves obtained over Sn and Si atoms of the Sn/Si(111)-($\sqrt{3} \times \sqrt{3}$)R30° surface are displayed. These sets of force curves were obtained over Sn and Si atoms in an equivalent local surface configuration similar to the one shown in Fig. 3.11a, using identical acquisition and analysis protocols (see [62] for details) but over multiple measurement sessions involving different tip–apex terminations. Some of these sets were even measured with the same cantilever and acquisition parameters – resonant frequency, oscillation amplitude, cantilever stiffness, and Q-value – but after intentionally modifying the tip apex by producing gentle tip–surface contacts. The comparison of all these sets of force curves (Fig. 3.11g) reveals a strong tip dependence of both the registered maximum attractive force values and the distance dependence of the forces over the attractive and repulsive regimens.

In spite of the variability of the measured forces with the AFM tip, we have found a parameter that remains nearly constant, independently of the tip–apex termination [62]. This parameter is the relative interaction ratio of the maximum attractive short-range force within a set of force curves measured with the same tip. A graphical visualization of this parameter can be obtained by normalizing the two curves within each set by the absolute value of the maximum attractive force registered over the Si atom ($|F_{\mathrm{Si(Set)}}|$). Doing so, the curves corresponding to the Si atom will present their minimum value at the unit, and the curves measured over the Sn atoms will display their minimum value at the relative interaction ratio. The result of applying this normalization for all the sets of force curves shown in Fig. 3.11 is displayed in Fig. 3.11h, revealing an average value of the relative interaction ratio for Sn calibrated against Si of 0.77 ± 0.02.

These findings have been reproduced on other surfaces with similar structure but different chemical composition, like the Pb/Si(111)-($\sqrt{3} \times \sqrt{3}$)R30° and the In/Si(111)-($\sqrt{3} \times \sqrt{3}$)R30° surfaces. Sets of short-range force curves were also obtained for these surfaces over structurally equivalent atoms to the ones pointed out in the insets of Figs. 3.12a and b, using identical acquisition and analysis protocols as for the Sn and Si case. Again, different behavior of the maximum attractive force value and the distance dependence of the force over the attractive and repulsive regions is obtained for different

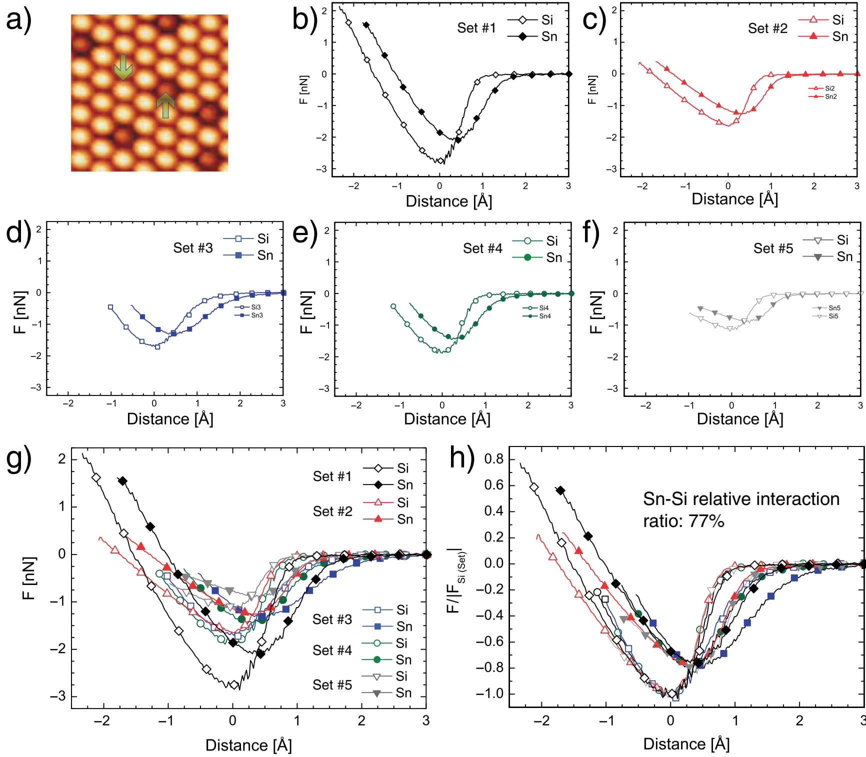

Fig. 3.11. (**a**) Topographic image of the Sn/Si(111)-($\sqrt{3} \times \sqrt{3}$)R30° surface. (**b**)–(**f**) Sets of short-range force curves obtained over structurally equivalent Sn (bright protrusions) and Si atoms as the ones pointed out in (**a**), using identical acquisition and analysis protocols but different tip terminations. (**g**) Comparison of all the sets of force curves. (**h**) Curves shown in (**b**)–(**f**) normalized to the corresponding absolute value of the maximum attractive short-range force registered over the Si atom ($|F_{Si(Set)}|$) within each set. The acquisition parameters are available in the supplementary information accompanying the publication from which the figures are adapted [62]

tip–apex terminations. There is only one apparent common feature to all the sets of force curves shown in Figs. 3.11 and 3.12: the curve obtained over the Si atom provides the stronger attractive interaction force. When performing the same normalization as in the Sn and Si case over the sets measured on the Pb/Si(111) and In/Si(111) surfaces, identical behavior is confirmed: the curves measured over the Si atoms meet at the force minima, and the curves obtained over Pb and In atoms coincide again at the corresponding minima, revealing an average relative interaction ratio for Pb calibrated against Si of 0.59 ± 0.03 (Fig. 3.12a), and a relative interaction ratio for In calibrated also against Si of 0.72 ± 0.04 (Fig. 3.12b).

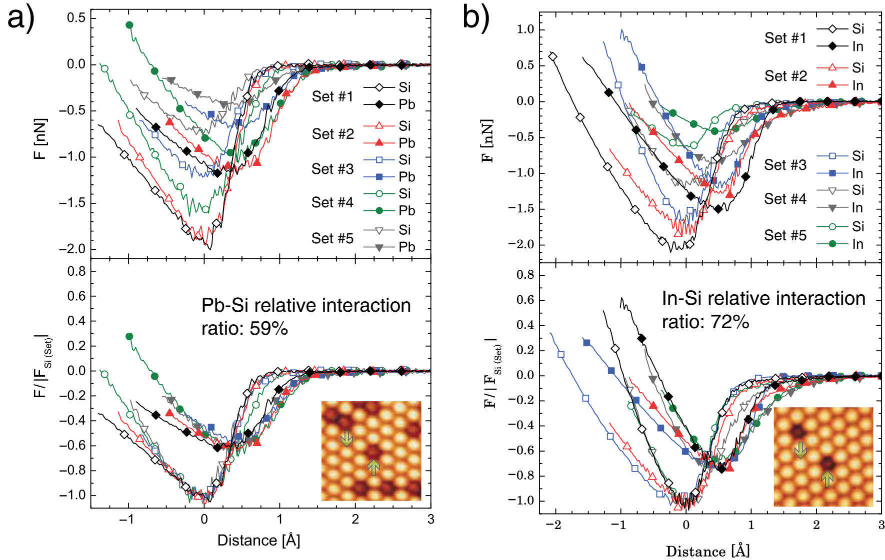

Fig. 3.12. Sets of short-range force curves obtained over Pb and Si atoms of the Pb/Si(111)-($\sqrt{3} \times \sqrt{3}$)R30° surface (**a**), and In and Si atoms of the In/Si(111)-($\sqrt{3} \times \sqrt{3}$)R30° surface (**b**), using identical acquisition and analysis protocols as in the experiments shown in Fig. 3.11. These measurements reproduce the findings described in detail for the Sn/Si(111) system yet in other surfaces with similar structure but different chemical composition. From these experiments, it is obtained an average relative interaction ratio for Pb and In calibrated against Si of 59 and 72%, respectively. The acquisition parameters are available in the supplementary information accompanying the publication from which the figures are adapted [62]

Insights into the behavior of the force curves upon acquisition with different tip–apex terminations, and into the essence of the relative interaction ratio, can be gained from first-principles simulations and modeling [62]. Calculations of the short-range interaction force over a Sn and a Si atom of the Sn/Si(111)-($\sqrt{3} \times \sqrt{3}$)R30° surface using different tip-apex terminations are shown in Fig. 3.13. Sets of force curves calculated with homogenous tip apexes made of Si but with different structure (Tip 1 and Tip 3 in Fig. 3.13) reveal a strong variability of the force values with the tip–surface distance, pointing towards a clear dependence of the measured forces on the structure and elasticity response of the tip apex. Sets of force curves calculated with tip models of identical structure but different chemical termination among the reasonable species involved in the experiments (that is Sn and Si) also produce disparities in the behavior of the short-range interaction. Weaker force values are obtained for Sn terminated tips, as it is evidenced by the comparison of the curves calculated with Tip 2 and Tip 4 with the ones obtained using Tip 1 and Tip 3 in Fig. 3.13, respectively. In all these cases, the strongest interaction is always registered over the Si atom, as it is observed also in the experiments.

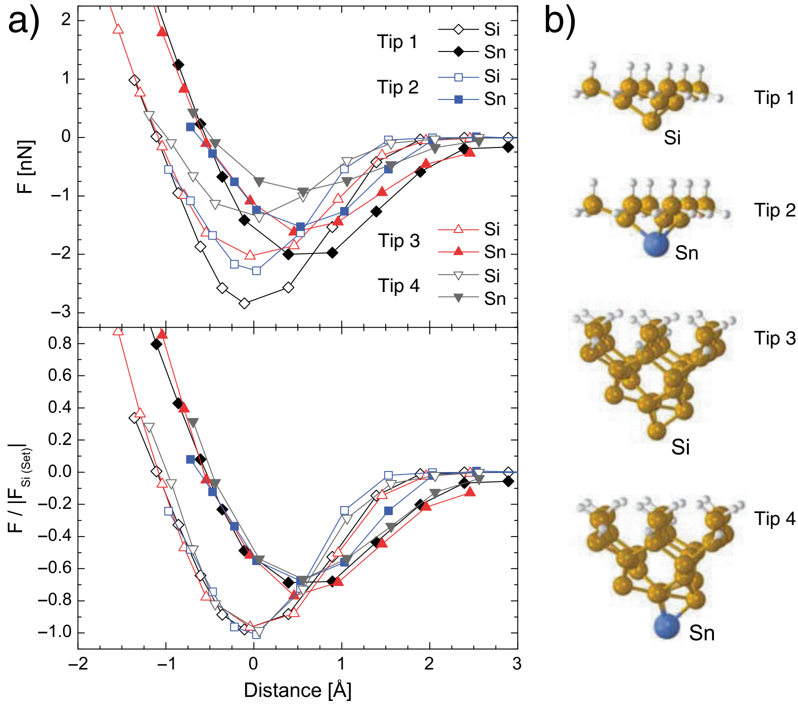

Fig. 3.13. (**a**) Sets of short-range force curves calculated over Sn and Si atoms of the Sn/Si(111)-($\sqrt{3} \times \sqrt{3}$)R30° surface using the tip models shown in (**b**). The force curves are depicted before (*upper graph*) and after (*lower graph*) the normalization of both curves within each set to the corresponding absolute value of the maximum attractive force obtained over the Si atom. Figure adapted from [62]

In spite of these differences, and independently of the tip–apex structure and chemical termination, when applying the same normalization procedure as in Fig. 3.11 to each set of force curves, all the curves calculated over Si and Sn atoms meet at the minima, leading to an average relative interaction ratio for Sn calibrated against Si of 0.71 ± 0.07 (Fig. 3.13); value quite close to the experimental one. These calculations suggest that, for tips providing a short-range interaction of enough strength to obtain atomic resolution, the relative interaction ratio seems to be independent of the chemical termination of the tip apex.

A basic interpretation of the relative interaction ratio can be gained from our current understanding of the imaging mechanism on semiconductor surfaces. As it is shown in Sect. 3.4, when probing the surface close to the onset of the short-range interaction, the surface structure is almost unperturbed [36]. However, close to tip–surface distances that correspond to the maximum attractive short-range force, there are important distortions of the interacting atoms at both tip and surface (see Sect. 3.4) [36]. In this situation, the dom-

inant contribution to the interaction comes from the bonding between the outermost atom of the AFM tip and the atom probed at the surface, which can be considered as they were almost forming a dimer-like structure. This dimer-like interaction could be roughly associated with the bond stretching (or pair-wise) term that is used as the fundamental energetic contribution in many approximate descriptions of the atomic bonding [63]. Under this approximation, the heterogeneous covalent interaction potential between a pair of elements t and α can be estimated as the geometric mean of the homogeneous interaction potential of the corresponding elements, $t-t$ and $\alpha-\alpha$, that is, $E^0_{t-\alpha} \approx \sqrt{E^0_{t-t} \times E^0_{\alpha-\alpha}}$. According to the bond stretching properties, the maximum attractive force $F_{t-\alpha,\max}$ should be proportional to the dissociation energy $E^0_{t-\alpha}$ divided by a characteristic decay length $R^*_{t-\alpha}$ of the interaction, that is, $F_{t-\alpha,\max} \propto E^0_{t-\alpha}/R^*_{t-\alpha}$. Thus, for a given tip–apex of unknown chemical termination, when considering the short-range interaction force of the tip outermost atom t with two separate surface atoms α and β evaluated at the force minima ($F_{t-\alpha,\max}$ and $F_{t-\beta,\max}$, respectively), if the differences between $R^*_{\alpha-t}$, $R^*_{\beta-t}$, $R^*_{\alpha-\alpha}$, $R^*_{\beta-\beta}$ and R^*_{t-t} are small enough, the relative interaction ratio could be approximated by the expression:

$$\frac{F_{t-\alpha,\max}}{F_{t-\beta,\max}} \approx \frac{\sqrt{F_{t-t,\max} \times F_{\alpha-\alpha,\max}}}{\sqrt{F_{t-t,\max} \times F_{\beta-\beta,\max}}} \approx \sqrt{\frac{F_{\alpha-\alpha,\max}}{F_{\beta-\beta,\max}}} \tag{3.3}$$

where $F_{t-t,\max}$, $F_{\alpha-\alpha,\max}$, and $F_{\beta-\beta,\max}$ denote the homogeneous short-range interaction force of the corresponding elements evaluated at the maximum attractive force.

The short-range force curves acquired over a given surface atom are expected to depend on the elastic response of tip and surface [36, 39, 55, 64], the chemical composition and structure of the tip apex [62], and its relative orientation with respect to the surface [65, 66]. However, when taking the relative interaction ratio of the maximum attractive short-range forces for two atomic species probed with the same tip, the common features associated with the structural characteristics of the tip–apex cancel out, and the influence of the chemical nature of the tip–apex outermost atom is minimized. Upon the presence of a certain covalent component in the tip–surface short-range interaction, the relative interaction ration becomes a quantification of the relative strength the surface atoms have to interact with the outermost atom of the tip, as it is pointed out by (3.3). This property can be generalized to multielement systems, as when individually probing different atoms at a surface with a given tip–apex termination, interactions between pairs of atomic species are to be obtained.

The independence of the relative interaction ratio from the tip–apex termination provides the basis for the formulation of a single-atom chemical identification protocol with FM-AFM. The identification procedure requires first the calibration of the relative interaction ratio for the atomic species involved with respect to one of them, typically the one providing the strongest interaction force. The determination of the maximum attractive short-range

force over each surface atom and comparison of their ratio with the tabulated values of the relative interaction ratio will allow them to identify the atomic species composing a multielement system, upon enough precision in both the quantification of the short-range interaction forces and the calibration of the corresponding relative interaction ratios.

We have demonstrated this protocol by merging Sn, Pb, and Si atoms on the same surface under equal proportions. An image of such system is displayed in Fig. 3.14a. The analysis of the topographic height difference between the atoms in Fig. 3.14a reveals nothing more than what is evident by simple inspection: there are only two visible groups of atoms, one presenting a bright contrast and other showing a diminished contrast. From the experience gained in the study of the Sn/Si(111), Pb/Si(111), and In/Si(111) surfaces, one could predict that the atoms with lessen contrast would correspond to Si (see images in Figs. 3.11 and 3.12); however, a priori, there is no clue to discern what protrusions correspond to Pb atoms and which ones to Sn. After systematically performing force spectroscopic measurements over each atom of the image, the quantification of the maximum attractive force values clearly reveals three groups of forces (Fig. 3.14d). When evaluating the ratios between the average force values representing these groups of forces, they match with the relative interaction ratio for Sn and Pb calibrated against Si, obtained from previous experiments (Figs. 3.11 and 3.12). This comparison allows us to correlate each group of forces with one of the atomic species (Fig. 3.14d), and, therefore, identity each surface atom as it is shown in Fig. 3.14c, where blue, green, and red colored atoms correspond to Sn, Pb, and Si, respectively.

Our initial hypothesis that protrusions showing lesser contrast correspond to Si atoms was right. Nevertheless, not always atoms with diminished contrast are Si. Figures 3.14e–h present a similar analysis performed over another area of this surface alloy composed by a mixture of Sn, Pb, and Si atoms. In this case, Pb atoms almost completely surrounded by Si (atoms marked in Fig. 3.14e by a darker shade of green) present identical topographic contrast to most of the Si atoms in the image. These variations in the topographic height of Pb atoms with the number of first-neighboring Si atoms have been attributed to a subtle coupling between charge-transfer and atomic-relaxations [61], which also influence the chemical response of the Pb atom with respect to the interaction with the AFM tip. The identification method described here was, however, robust enough to identify these Pb atoms even upon variations of their chemical properties.

We believe that the capability of AFM for the identification of individual atoms holds substantial promise for widening the applicability of this techniques to studies on heterogeneous surfaces, in which important functional properties are controlled by the chemical nature and short-range ordering of individual atoms, defects, adsorbates, or dopants. In particular, the combination of this identification method with the ability of the AFM for the atom manipulation [51,67,68] may bring future atom-based technological enterprises closer to reality. Furthermore, correlations between chemical specificity, short-

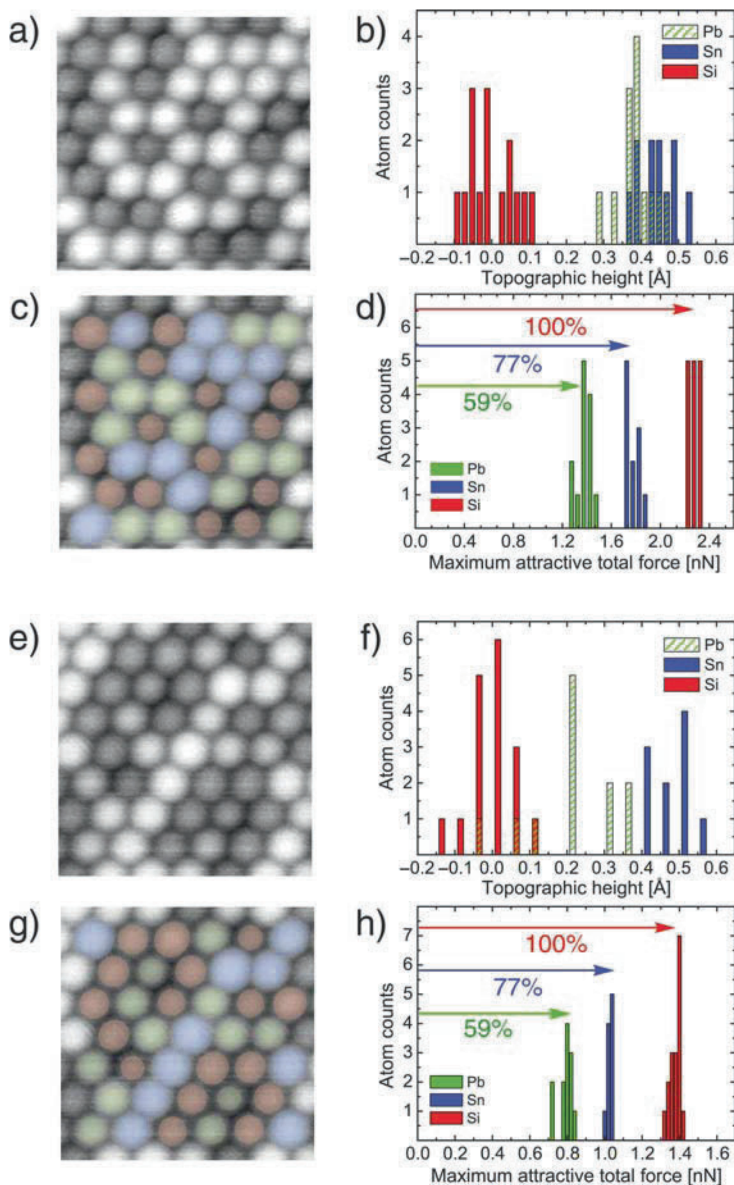

Fig. 3.14. Series of figures demonstrating chemical specificity of AFM. See text for details. Acquisition parameters can be found in the supplementary information of [62], from which the figure has been adapted

range interaction forces, Kelvin probe force microscopy, and energy dissipation measurements at atomic scale on heterogeneous surfaces may provide new insights into AFM phenomenology, and even help to develop a new and more refined identification protocol, as all these magnitudes are sensitive to the chemical nature of the surface atoms.

3.6 Force Spectroscopy with Higher Flexural Modes

Currently, there is a clear trend to operate FM-AFM using small cantilever oscillation amplitudes. It has been predicted improvements in both force sensibility and spatial resolution by reducing the cantilever oscillation amplitude to values close to the decay length of the short-range interactions responsible for atomic contrast in FM-AFM [69, 70]. Nevertheless, there is a limit on the reduction of the oscillation amplitude, which is imposed by the need of keeping the cantilever oscillation stable at close proximity to the surface [71].

Stable cantilever oscillation requires a restoring force at the closest tip–surface distance greater than the tip–surface interaction, to avoid snap to contact of the tip over the surface [8, 71]:

$$k_{\mathrm{s}} A_0 > \max(-F_{\mathrm{int}}),$$

where k_{s}, A_0, and F_{int} denote the cantilever static stiffness, the cantilever oscillation amplitude, and the tip–surface interaction force, respectively.

In addition, the presence of nonconservative interactions at small tip–surface separations generates dissipation of energy from the cantilever oscillation (see Sect. 3.3). This energy dissipation can create fluctuations of the oscillation amplitude that may reflect in an increment of the noise in the frequency shift signal due to slight variations of the tip–surface distance [71], and eventually they might develop into an unstable cantilever oscillation. Thus, proper control of the oscillation amplitude requires that the energy dissipated from the cantilever oscillation per cycle (ΔE_{TS}) should be smaller than the intrinsic energy lost by the cantilever oscillation (E_0) within the time lag in which the amplitude feedback responds to a variation of the oscillation amplitude [71]:

$$E_{\mathrm{TS}} < E_0 = \frac{\pi k_{\mathrm{s}} A_0^2}{Q}.$$

Fulfillment of these stability criteria and pursuance of high sensibility in force detection with small oscillation amplitudes demand the use of cantilevers with (i) high resonant frequencies; (ii) large static stiffness; (iii) high Q values (yet not excessively large so that it could make difficult controlling the oscillation amplitude).

Nowadays, there are several implementations that meet these requirements. One is the use of small cantilevers and special optical interferometers to focus the laser beam on them [72, 73]. A more popular approach is the

implementation of the qPlus sensor [74, 75]. But for an AFM based on standard cantilevers and optical interferometric detection, a straight forward solution may be to operate FM-AFM using the cantilever higher flexural modes [76,77]. These modes are characterized by a considerably larger effective static stiffness, higher resonant frequencies, and moderated Q values [78, 79]. The presence of nodes along the cantilever geometry for the higher flexural modes produces an effective shortening of the cantilever length that manifest in an notable increment of the associated resonant frequency and stiffness. Details about the predicted geometry and parameters of the second and third eigenmodes of a rectangular cantilever with respect to the fundamental mode are summarized in Fig. 3.15.

An open question is whether the equation that relates the frequency shift with the tip–surface interaction force (3.1) still holds to perform force spectroscopy using the cantilever higher flexural modes. Notice that (3.1) is derived under the assumption that a point-mass model correctly describes the dynamics of a continuous cantilever [14, 27, 32]; and this is the case for the first flexural mode, while an appropriate parametrization is required for higher eigenmodes [79].

To confirm the validity of (3.1) for force spectroscopy using higher flexural modes, we have compared force spectroscopic measurements acquired over the same atom and with the same tip–apex termination alternately using the first and second flexural modes of a rectangular cantilever [80]. These results are displayed in Fig. 3.16. We first measured a frequency shift curve over a corner adatom of the Si(111)-(7 × 7) surface using the fundamental mode, then we retracted the tip from the surface, switch to operation using the

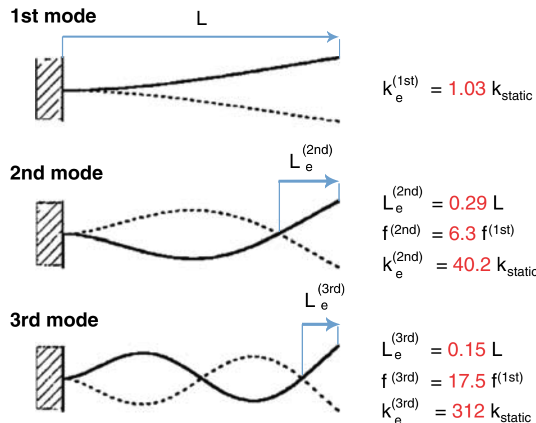

Fig. 3.15. Predicted geometry, effective length, effective static stiffness, and resonant frequency for the first, second, and third flexural modes of a rectangular cantilever, excluding effects associated with the mass and position of the cantilever tip

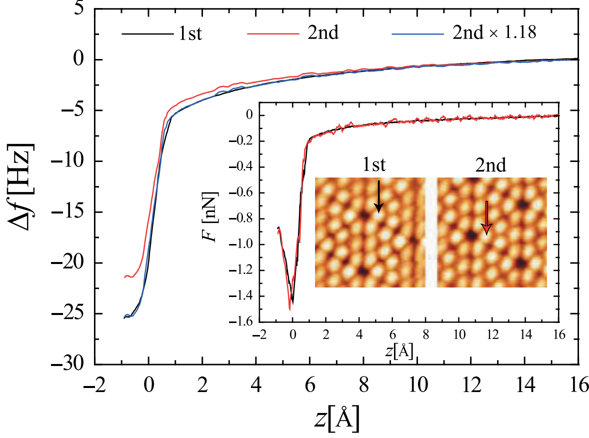

Fig. 3.16. Force spectroscopic measurements performed using the first and second flexural modes of a rectangular cantilever over the same surface atom with an identical tip termination. The *blue curve* corresponds to the frequency shift characteristic measured with the second eigenmode scaled by a 1.18 factor. Acquisition parameters for the first (second) flexural mode were $f_{1(2)} = 157{,}403\,(978{,}904)$ Hz, $k_{s(2nd)} = 26.9$ (1968) N m^{-1}, and $A_0 = 132$ (28.5) Å. Figure adapted from [80]

second mode, and finally we performed again spectroscopic measurements over the same surface atom using relative large oscillation amplitudes. During the acquisition of these spectroscopic series, the position of the laser spot (located close to the cantilever free end) for the detection of the cantilever dynamics was exactly the same, and the calibration of the oscillation amplitude [24, 38] was independently performed for each flexural mode after concluding the measurements.

Surprisingly, while the ratio of resonant frequencies was in good agreement with the theoretical predictions ($f_2/f_1 = 6.2$) [78, 79], we have found that a scaling of the frequency shift curve obtained with the second mode (Fig. 3.16) leads to an experimental estimation of the equivalent stiffness for the second mode which is 73 ± 17 times larger than that of the first mode, in contrast with a theoretically predicted ratio $k_{2nd}/k_{1st} \approx 40.2$. This discrepancy in the k_{2nd}/k_{1st} ratio may be attributed to the presence of the tip.

In the inset plot of Fig. 3.16, it is displayed the total tip–surface interaction forces obtained from the frequency shift curves measured with the first and the second flexural mode, respectively. As predicted in [79], the estimation of the equivalent stiffness for the point-mass model associated with the corresponding cantilever eigenmode is sufficient condition to validate (3.1) for force spectroscopy using the cantilever higher eigenmodes. The effective stiffness of higher flexural modes can be estimated by fitting the corresponding thermal noise spectra, and independently evaluating the Q-value of the cantilever oscillation in the corresponding mode.

As it has been stated earlier, the larger equivalent stiffness of the cantilever higher flexural modes enables operation of FM-AFM using small oscillation amplitudes. Driving the cantilever oscillation at the second mode, we have been able to measure force spectroscopic characteristics with oscillation amplitudes as small as 3.6 Å. Interestingly, at such small oscillation amplitudes, the normalized frequency shift [27] does not follow an $A_0^{3/2}$ scaling [13] anymore [38, 80]. This is evidenced in a series of frequency shift curves displayed in Fig. 3.17, and measured using the second flexural mode over the same surface atom with an identical tip–apex termination but at cantilever oscillation amplitudes ranging from 32.7 to 3.6 Å. While all the frequency shift curves provide an identical tip–surface interaction force independently of the oscillation amplitude, the normalized frequency shift (γ) of curves acquired with small amplitudes gradually diverges from the ones measured with larger oscillation amplitudes. The normalized frequency shift scaling fails because the approximation of (3.1) for large oscillation amplitudes [81]

$$\Delta f \approx \frac{f_\mathrm{r}}{\sqrt{2}\pi k_\mathrm{s} A_0^{3/2}} \int_0^\infty \frac{F_\mathrm{int}(z' + x)}{\sqrt{x}}\,\mathrm{d}x$$

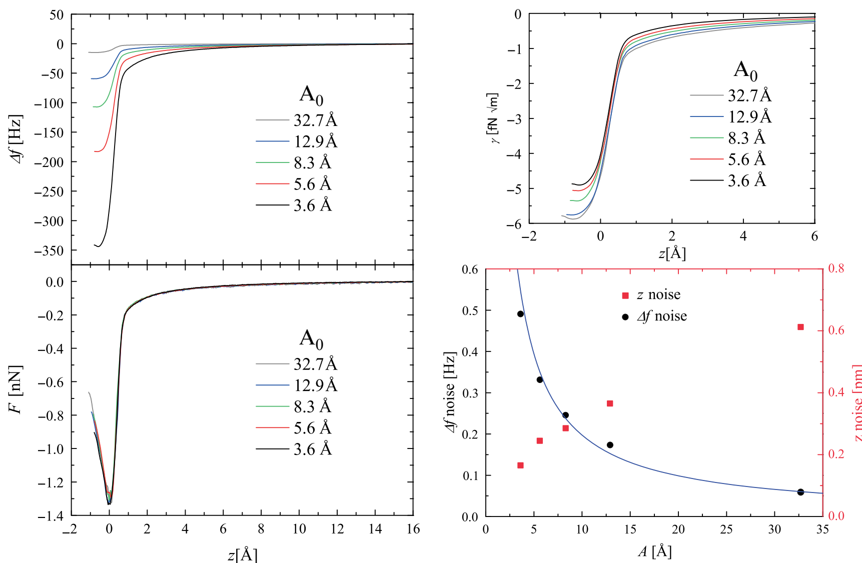

Fig. 3.17. Series of frequency shift curves acquired over the same adatom of a Si(111)-(7 × 7) surface with identical tip–apex termination using the second flexural mode of a rectangular cantilever driven at different oscillation amplitudes. The other panels show the corresponding normalized frequency shift (γ) [27] and tip–surface interaction force curves, as well as the dependence of the frequency shift and tip–sample distance noise with the cantilever oscillation amplitude (in this graph the curve is a A_0^{-1} fit to the frequency shift noise data). Acquisition parameters were $f_2 = 987,155$ Hz and $k_{2\mathrm{nd}} = 2,062\,\mathrm{N\,m^{-1}}$. Figure adapted from [80]

[with $x = A_0(1+u)$ from (3.1)], where the prefactor gives rise to the γ-scaling, does not longer hold. Therefore, comparison of frequency shift values measured with different cantilever oscillation parameters through the normalized frequency shift is not valid for small oscillation amplitudes. Another consequence of this behavior is that the precise calibration of the cantilever oscillation amplitude using the normalized frequency shift method [24, 38, 75] requires setting large enough oscillation amplitudes.

The set of frequency shift curves shown in Fig. 3.17 enables quantifying the improvement in the signal-to-noise ratio associated with the reduction of the cantilever oscillation amplitude. The noise analysis from these curves (see details in [80]) shows a good agreement with theoretical predictions [5, 8, 69]: the noise in the frequency shift increases inversely proportional to the oscillation amplitude, while the noise in the tip–sample distance reduces as the oscillation amplitude becomes smaller (Fig. 3.17). Although the noise in the frequency shift increases, the absolute value of the frequency shift signal obtained at small oscillation amplitudes for an identical tip–surface interaction force is considerably larger than the one measured at bigger oscillation amplitudes, leading to an overall improvement of the signal-to-noise ratio. Thus, operation of FM-AFM at small oscillation amplitudes seems to represent a refinement of sensitivity to tip–surface interaction forces and spatial resolution.

3.7 Summary

In this chapter, we have described examples of how force spectroscopy performed over individual atomic positions provides valuable information about the mechanical properties of the tip–surface interface, and facilitates the possibility of disclosing the chemical composition of a surface at atomic scale. The potential and opportunities offered by force spectroscopy will see a revolution in the near future with the application of this technique to a widen spectrum of surfaces and scientific problems, as well as with an increasing number of groups adapting and further developing the technique. Very promising achievements and an exciting panorama are foreseen with the ability of quantifying forces not only over individual atoms but mapping them over a line [15, 26, 56, 68, 82] or even over a surface area (see Chaps. 2, 5, and 9). Without any doubt, simultaneous measurements of forces and tunneling currents performed at small oscillation amplitudes over atoms, molecules, and nanostructures will bring new and exciting breakthroughs in nanoscience.

Acknowledgments

The authors are very grateful to friends and colleagues who decisively contributed to the works and achievements summarized in this chapter: Masayuki Abe, Pablo Pou, Pavel Jelinek, and Ruben Perez. The authors are specially

grateful to Prof. Seizo Morita for guidance, mentoring, and constant and unconditional support.

References

1. G. Binnig, C.F. Quate, C. Gerber, Phys. Rev. Lett. **56**(9), 930 (1986)
2. F. Giessible, Science **267**, 68 (1995)
3. Y. Sugawara, M. Ohta, H. Ueyama, S. Morita, Science **270**, 1646 (1995)
4. S. Kitamura, M. Iwatsuki, Jpn. J. Appl. Phys. **34**(1B), L145 (1995)
5. T.R. Albrecht, P. Grütter, D. Horne, D. Rugar, J. Appl. Phys. **69**(2), 668 (1991)
6. S. Morita, R. Wiesendanger, E. Meyer, *Noncontact Atomic Force Microscopy.* NanoScience and Technology (Springer, Berlin, 2002)
7. R. García, R. Pérez, Surf. Sci. Rep. **47**(6–8), 197 (2002)
8. F.J. Giessibl, Rev. Mod. Phys. **75**(3), 949 (2003)
9. B. Gotsmann, D. Krüger, H. Fuchs, Europhys. Lett. **239**(2), 153 (1997)
10. B. Gotsmann, B. Anczykowski, C. Seidel, H. Fuchs, Appl. Surf. Sci. **140**, 314 (1999)
11. B. Gotsmann, C. Seidel, B. Anczykowski, H. Fuchs, Phys. Rev. B **60**(15), 11051 (1999)
12. H. Hölscher, W. Allers, A. Schwarz, U.D. Schwarz, R. Wiesendanger, Phys. Rev. Lett. **83**(23), 4780 (2003)
13. H. Hölscher, A. Schwarz, W. Allers, U.D. Schwarz, R. Wiesendanger, Phys. Rev. B **61**(19), 12678 (2000)
14. H. Hölscher, B. Gotsmann, W. Allers, U.D. Schwarz, H. Fuchs, R. Wiesendanger, Phys. Rev. B **64**(7), 075402 (2001)
15. H. Hölscher, S.M. Langkat, A. Schwarz, R. Wiesendanger, Appl. Phys. Lett. **81**(23), 4428 (2002)
16. M.A. Lantz, H.J. Hug, R. Hoffmann, P.J.A. van Schendel, P. Kappenberger, S. Martin, A. Baratoff, H.J. Güntherodt, Science **291**(5513), 2580 (2001)
17. R. Pérez, M. Payne, I. Štich, K. Terakura, Phys. Rev. Lett. **78**(4), 678 (1997)
18. R. Pérez, I. Štich, M. Payne, K. Terakura, Phys. Rev. B **58**(16), 10835 (1998)
19. A.I. Livshits, A.L. Shluger, A.L. Rohl, A.S. Foster, Phys. Rev. B **59**(3), 2436 (1999)
20. A.S.U. Kaiser, R. Wiesendanger, **446**, 522 (2007)
21. R. Bennewitz, M. Bammerlin, M. Guggisberg, C. Loppacher, A. Baratoff, E. Meyer, H.J. Güntherodt, Surf. Interface Anal. **27**, 462 (1999)
22. M. Guggisberg, M. Bammerlin, C. Loppacher, O. Pfeiffer, A. Abdurixit, V. Barwich, R. Bennewitz, A. Baratoff, E. Meyer, H.J. Güntherodt, Phys. Rev. B **61**(16), 11151 (2000)
23. N. Suehira, Y. Tomiyoshi, Y. Sugawara, S. Morita, Rev. Sci. Instrum. **72**(7), 2971 (2001)
24. M. Abe, Y. Sugimoto, O. Custance, S. Morita, Appl. Phys. Lett. **87**(17), 173503 (2005)
25. M. Abe, Y. Sugimoto, O. Custance, S. Morita, Nanotechnology **16**(12), 3029 (2005)
26. M. Abe, Y. Sugimoto, T. Namikawa, K. Morita, N. Oyabu, S. Morita, Appl. Phys. Lett. **90**(20), 203103 (2007)
27. F.J. Giessibl, Phys. Rev. B **56**(24), 16010 (1997)

28. U. Dürig, Appl. Phys. Lett. **76**(9), 1203 (2000)
29. F.J. Giessibl, Appl. Phys. Lett. **78**(1), 123 (2001)
30. F.J. Giessibl, H. Bielefeldt, S. Hembacher, J. Mannhart, Ann. Phys. (Leipzig) **10**(11–12), 887 (2001)
31. J.E. Sader, S.P. Jarvis, Appl. Phys. Lett. **84**(10), 1801 (2004)
32. U. Dürig, Appl. Phys. Lett. **75**(3), 433 (1999)
33. R. Hoffmann, A. Baratoff, H.J. Hug, H.R. Hidber, H. v Löhneysen, H.J. Güntherodt, Nanotechnology **18**(39), 395503 (2007)
34. Y. Sugimoto, P. Jelinek, P. Pou, M. Abe, S. Morita, R. Pérez, O. Custance, Phys. Rev. Lett. **98**(10), 106104 (2007)
35. R. Hoffmann, L.N. Kantorovich, A. Baratoff, H.J. Hug, H.J. Güntherodt, Phys. Rev. Lett. **92**(14), 146103 (2004)
36. Y. Sugimoto, P. Pou, O. Custance, P. Jelinek, S. Morita, R. Pérez, M. Abe, Phys. Rev. B **73**(20), 205329 (2006)
37. J.P. Cleveland, S. Manne, D. Bocek, P.K. Hansma, Rev. Sci. Instrum. **64**(2), 403 (1993)
38. G. Simon, M. Heyde, H.P. Rust, Nanotechnology **18**, 255503 (2007)
39. N. Oyabu, P. Pou, Y. Sugimoto, P. Jelinek, M. Abe, S. Morita, R. Pérez, O. Custance, Phys. Rev. Lett. **96**(10), 106101 (2006)
40. J.P. Cleveland, B. Anczykowski, A.E. Schmid, V.B. Elings, Appl. Phys. Lett. **72**(20), 2613 (1998)
41. C. Loppacher, R. Bennewitz, O. Pfeiffer, M. Guggisberg, M. Bammerlin, S. Schär, V. Barwich, A. Baratoff, E. Meyer, Phys. Rev. B **62**(20), 13674 (2000)
42. R. Bennewitz, A.S. Foster, L.N. Kantorovich, M. Bammerlin, C. Loppacher, S. Schär, M. Guggisberg, E. Meyer, A.L. Shluger, Phys. Rev. B **62**(3), 2074 (2000)
43. M. Gauthier, R. Perez, T. Arai, M. Tomitori, T. M, PRL **89**(14), 146104 (2002)
44. R.S. Becker, B.S. Swartzentruber, J.S. Vickers, T. Klitsner, Phys. Rev. B **39**, 1633 (1989)
45. N. Takeuchi, A. Selloni, E. Tosatti, Phys. Rev. Lett. **69**, 648 (1992)
46. M. Abe, Y. Sugimoto, S. Morita, Nanotechnology **16**(3), S68 (2005)
47. H.J. Güntherodt, E.M. D. Anselmetti, *Forces in Scanning Probe Methods*, *NATO ASI, Ser. E*, vol. 286 (Kluwer, Dordrechet, 1995)
48. N. Sasaki, M. Tsukada, Jpn. J. Appl. Phys. **39**(12B), L1334 (2000)
49. L.N. Kantorovich, T. Trevethan, Phys. Rev. Lett. **93**(23), 236102 (2004)
50. N. Oyabu, O. Custance, I. Yi, Y. Sugawara, S. Morita, Phys. Rev. Lett. **90**(17), 176102 (2003)
51. Y. Sugimoto, P. Pou, O. Custance, P. Jelinek, M. Abe, R. Pérez, S. Morita, Science **322**, 413 (2008)
52. M.A. Lantz, H.J. Hug, P.J.A. van Schendel, R. Hoffmann, S. Martin, A. Baratoff, A. Abdurixit, H.J. Güntherodt, C. Gerber, Phys. Rev. Lett. **84**(12), 2642 (2000)
53. B.C. Stipe, M.A. Rezaei, W. Ho, Phys. Rev. Lett. **79**(22), 4397 (1997)
54. H.J. Hug, A. Baratoff, *Noncontact Atomic Force Microscopy* (Springer, Berlin, 2002), chap. 20, pp. 395–432
55. S.A. Ghasemi, S. Goedecker, A. Baratoff, T. Lenosky, E. Meyer, H.J. Hug, Phys. Rev. Lett. **100**(23), 236106 (2008)
56. A. Schirmeisen, D. Weiner, H. Fuchs, Phys. Rev. Lett. **97**(13), 136101 (2006)
57. W. Kamiński, P. Jelinek, R. Pérez, F. Flores, J. Ortega, Appl. Surf. Sci. **234**, 286 (2004)

58. S.T. Jemander, N. Lin, H.M. Zhang, R.I.G. Uhrberg, G.V. Hansson, Surf. Sci. **475**, 181 (2001)
59. P. Dieska, I. Štich, R. Pérez, Phys. Rev. Lett. **95**(12), 126103 (2005)
60. S.H. Ke, T. Uda, I. Štich, K. Terakura, Phys. Rev. B **63**(24), 245323 (2001)
61. A. Charrier, R. Pérez, F. Thibaudau, J.M. Debever, J. Ortega, F. Flores, J.M. Themlin, Phys. Rev. B **64**(11), 115407 (2001)
62. Y. Sugimoto, P. Pou, M. Abe, P. Jelinek, R. Pérez, S. Morita, O. Custance, Nature **445**, 64 (2007)
63. L. Pauling, *The Nature of the Chemical Bond*, 3rd edn. (Cornell University Press, New York, 1960)
64. V. Caciuc, H. Hölscher, S. Blügel, H. Fuchs, Phys. Rev. Lett. **96**(1), 016101 (2006)
65. S.H. Ke, T. Uda, R. Pérez, I. Štich, K. Terakura, Phys. Rev. B **60**(16), 11631 (1999)
66. S. Hembacher, F.J. Giessibl, J. Mannhart, Science **305**(5682), 380 (2004)
67. Y. Sugimoto, M. Abe, S. Hirayama, N. Oyabu, O. Custance, S. Morita, Nat. Mater. **4**(2), 156 (2005)
68. M. Ternes, C. Lutz, C. Hirjibehedin, F. Giessibl, A. Heinrich, **319**(5866), 1066 (2008)
69. F.J. Giessibl, H. Bielefeldt, S. Hembacher, J. Mannhart, Appl. Surf. Sci. **140**, 352 (1999)
70. F.J. Giessibl, H. Bielefeldt, Phys. Rev. B **61**(15), 9968 (2000)
71. F.J. Giessibl, S. Hembacher, M. Herz, C. Schiller, J. Mannhart, Nanotechnology **15**, S79 (2004)
72. J.L. Yanga, M. Despontb, U. Drechsler, B.W. Hoogenboom, P.L.T.M. Frederix, S. Martin, A. Engel, P. Vettiger, H.J. Hug, Appl. Phys. Lett. **86**(13), 134101 (2005)
73. B.W. Hoogenboom, P.L.T.M. Frederix, J.L. Yang, S. Martin, Y. Pellmont, M. Steinacher, S. Zäch, E. Langenbach, H.J. Heimbeck, A. Engel, H.J. Hug, Appl. Phys. Lett. **86**(7), 074101 (2005)
74. F.J. Giessibl, Appl. Phys. Lett. **73**(26), 3956 (1998)
75. F.J. Giessibl, Appl. Phys. Lett. **76**(11), 1470 (2000)
76. S. Kawai, S. Kitamura, D. Kobayashi, S. Meguro, H. Kawakatsu, Appl. Phys. Lett. **86**(19), 193107 (2005)
77. S.Kawai, H. Kawakatsu, Appl. Phys. Lett. **88**(13), 133103 (2006)
78. S. Rast, C. Wattinger, U. Gysin, E. Meyer, Rev. Sci. Instrum. **71**(7), 2772 (2000)
79. J. Melcher, S. Hu, A. Raman, Appl. Phys. Lett. **91**(5), 053101 (2007)
80. Y. Sugimoto, S. Innami, M. Abe, O. Custance, S. Morita, Appl. Phys. Lett. **91**(9), 093120 (2007)
81. H. Hölscher, B. Gotsmann, A. Schirmeisen, Phys. Rev. B **68**(15), 153401 (2003)
82. Y. Sugimoto, T. Namikawa, K. Miki, M. Abe, S. Morita, Phys. Rev. B **77**(19), 195424 (2008)

4

Tip–Sample Interactions as a Function of Distance on Insulating Surfaces

Regina Hoffmann

Abstract. Recent advances in the measurement methods of scanning force microscopy (SFM) in the dynamic mode allow experimental access to site-specific short-range forces. Either the tip is moved to a particular site, or the full three-dimensional frequency shift field of the oscillating tip is recorded while scanning a small surface area. Then the frequency shift is converted to force, and the long-range forces are fit by models and subtracted. The remaining short-range forces measured on a well-known surface CaF_2 (111) can be used to learn more about the tip structure and chemical composition. On NaCl (001)-type crystal surfaces, where there is a full symmetry of the local distribution of the positive and negative charge, the measurement of the force as a function of distance allows to identify unambiguously identify the positively and negatively charged sublattices on the surface. If additionally, the full three-dimensional force field is measured, information about the chemical nature of the tip-terminating cluster and about lateral forces are obtained. SFM measurements of site-specific force–distance curves further allow a deeper insight into mechanisms of energy dissipation at tips and surfaces.

One of the key techniques for characterizing insulating surfaces on the atomic scale is scanning force microscopy (SFM), where the force between tip and sample is measured (for recent reviews, see [1], Chaps. 4–10). In addition, for insulating materials, many well-known experimental approaches often used for surface characterization cannot be applied in a straightforward way because the methods often rely on the interaction of charged particles with the sample. Atomic resolution in SFM has first been achieved on the 7×7 reconstruction of Silicon (111) [2], InP (110) [3], and two years later on NaCl (001) [4] in the dynamic mode: an atomically sharp tip attached to a cantilever beam is oscillated while a piezo-electric scanner brings the tip apex in close proximity to the surface. The attractive interaction between tip and surface upon approach lowers the eigenfrequency of the cantilever. This change of the eigenfrequency is related to the force acting between tip and sample and varies on the atomic scale. The dynamic measurement mode allows to avoid hard contact between the tip apex and the sample surface, which could damage both tip and surface and is therefore often called noncontact mode.

S. Morita et al. (eds.), *Noncontact Atomic Force Microscopy*,
NanoScience and Technology,
DOI: 10.1007/978-3-642-01495-6_4, © Springer-Verlag Berlin Heidelberg 2009

Advances in experimental techniques now additionally allow access to the force F as a function of tip–sample distance, called z in this chapter, at specific atomic sites [5], which is important to understand chemical bond formation between the tip and the surface as well as the relaxation of atomic positions in the tip and the sample (see Chaps. 2–7 of this book). By varying the distance of the tip and sample, the contact between them, one of the most important and disputed subjects in scanning force microscopy, can be studied in a controlled way and sometimes chemical bond formation can be studied [6]. At large tip–sample distances, the interaction is conservative. At small tip–sample distances, in the course of forming a contact, hysteretic motion of atoms causes energy dissipation [7, 8]. The possibility of precisely measuring forces as a function of distance has also strongly influenced the measurement techniques themselves (Chaps. 2, 6, 16, and 17) and has first facilitated manipulation of atoms [9], which is an important subject in this book (Chaps. 8–12). Furthermore, the full three-dimensional force fields have been measured on all sites of a grid on the surface, and thus access to the full information including lateral forces has been obtained. Such lateral forces are not only a key issue in atomic scale friction [10], but also during lateral manipulation experiments, in SFM as well as in scanning tunneling microscopy [11].

In this chapter, the measurement of tip–sample interactions as a function of distance on insulating surfaces is reviewed.

4.1 Experimental Evaluation of Short-range Forces

4.1.1 Measurement Techniques

As the dynamic mode allows to obtain true atomic resolution during imaging, all approaches to measure the tip–sample interaction as a function of distance at the atomic scale so far rely on dynamic measurement modes (for a sketch of the working principle of a SFM, see Fig. 4.1). It has been shown that oscillating the tip indeed reduces experimental noise [13]. Two main dynamic measurement modes are used: amplitude modulation and frequency modulation techniques [14]. In the latter measurement mode, the cantilever oscillation amplitude is kept constant, and the eigenfrequency of the oscillating cantilever is detected. It has been shown that in the frequency modulation mode, it is simpler to extract the force from the measured signal, that is, the frequency shift Δf, in particular in the case where dissipative tip–sample interactions occur [15]. Therefore, this mode has more widely been used than amplitude modulation. To measure the tip–sample interaction as a function of distance, it is in principle possible to either vary the tip–sample distance or to vary the oscillation amplitude [16]. Although varying the oscillation amplitude is experimentally simpler, because piezoelectric drift and creep are essentially avoided, varying the tip–sample distance is conceptually simpler and has thus mostly been used.

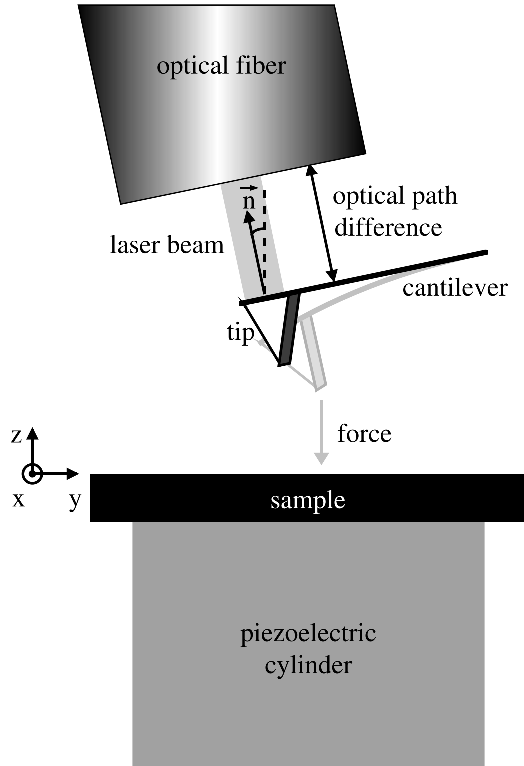

Fig. 4.1. Principle of an SFM similar to the one described in [12]. Upon approach, an attractive force acts between the sharp tip and the surface. The resulting deflection of the cantilever changes the optical path difference in the interferometer, which is measured while the sample is precisely moved using a piezoelectric cylinder. The coordinate system in this chapter is chosen such that the z-direction is perpendicular to the surface

When the tip–sample distance is varied, the effect of piezolectric drift on the measured results is much more severe than during imaging. During imaging a flat surface, a feedback loop keeps the tip–sample interaction constant, and thus allows only small variations of the tip–sample distance. If the sample surface is oriented precisely perpendicular to z, the tip height varies less than about 10^{-1} nm during the measurement, and thus piezoelectric drift in the z direction can be neglected. If the sample is tilted, a steady state is reached during imaging, where x (the fast scanning axis), y (the slow scanning axis), and z are varied in a systematic, repetitive way. In such a steady state, any deviations from the expected positions caused by piezo-electric creep can be compensated by applying corrected voltages to the piezolectric cylinder [12]. During acquisition of the force as a function of distance, the tip–sample distance is varied, and the feedback loop that keeps the tip–sample

interaction constant must of course be switched off. Piezoelectric drift and/or creep in the z direction perpendicular to the surface might therefore cause the tip to indent the sample surface. In the x and y directions, piezoelectric drift and/or creep might induce a loss of information of the precise position where the tip–sample interaction has been measured.

When measuring the tip–sample interaction as a function of distance, great care is thus taken to reduce the effects of piezoelectric drift and creep as much as possible. Two main experimental approaches are known: in the first approach, using essentially drift-free scanning force microscopes (as an example see [12]), in general at low temperatures, single positions, for example, above individual atoms, chosen by the experimentalist are addressed [5]. For this approach, extreme stability and reproducibility of the piezoelectric positioning is required. In this situation, full control of the tip allows to avoid specific points at the surface where the tip–sample interaction is destructive to either the tip or the sample or both. Thus the tip–sample distance can be reduced to below the point where imaging becomes unstable due to strong tip–sample interaction. In the second approach, frequency vs. distance data are collected at points of a scanned grid above the surface [17]. This approach offers the advantage that the full three-dimensional information of the force field is obtained, which gives access also to lateral forces, which is by definition the derivative of the tip–sample interaction in the lateral directions x and y [18,19]. Furthermore, it allows to confirm the lateral position of the tip after the measurement.

4.1.2 Conversion of Frequency Shift to Force

As the tip oscillates, its frequency shift arises from the average interaction over one complete oscillation cycle. The tip oscillation amplitude is typically on the order of several nanometers, while the part of the tip–sample interaction that is most interesting in this context, the short-range interaction due to chemical bonding, decays on the order of a few tenths of a nanometer. Therefore, the tip and sample interact strongly only during a rather short period of time, while the tip comes close to the lower turning point of its oscillation.[1] For this situation, usually called the large-amplitude limit, the frequency shift is roughly proportional to $\sqrt{UF}$, that is, the geometric means both taken at the lower turning point of the oscillation of the tip–sample interaction U and its derivative with respect to z, the force F [20–22]. This means that although the frequency shift results from an average of the force over a rather large distance range, there is still an exact relationship between the frequency shift and the force. The normalized frequency shift has been defined [23]

[1] This measurement mode is chosen to ensure that the cantilever restoring force is larger than the tip–sample attraction at all distances to avoid a snap-in. During a snap-in, the tip is pulled to the sample surface, a process during which large forces are applied to the sensitive tip apex, potentially leading to considerable damage of the tip and surface.

$$\gamma = \frac{\Delta f c_{\mathrm{L}} A_{\mathrm{osc}}^{3/2}}{f_0}, \tag{4.1}$$

which is independent of the respective resonance frequency f_0, longitudinal cantilever spring constant c_{L}, and tip oscillation amplitude A_{osc} used and thus allows to compare the frequency shift obtained in different experiments.

Recently, three main methods for calculating numerically the force from the input of the measured frequency shift data points have been proposed. Historically, the first one, by Dürig [15], is an iterative method, where the mathematically precise result is reached only after an infinite number of iterations. Each iteration enhances the measurement noise. In general, one or two iterations are sufficient, that is, after one or two iterations, the measurement noise exceeds the deviation from the exact result. This method inspired a second approach, by Giessibl [24], slightly modified by Baratoff [25, 26], in which the tip–sample interaction is extracted directly using numerical methods. The precision of the result depends only on the amount and precision of experimental data available.

If large spring constants are used, in particular in experiments where a piezoelectric quartz tuning fork replaces the commonly used microfabricated Silicon cantilevers, the oscillation amplitude of the tip can be reduced and the large amplitude limit discussed above is no longer valid. For smaller oscillation amplitudes, the fraction of the oscillation during which the tip and sample interact strongly is larger. However, even though this technique significantly reduces the noise in the measurement [13], the oscillation amplitude is typically not reduced enough to reach the small amplitude limit, in which the frequency shift is proportional to the force gradient.

4.1.3 Separation of Short-range and Long-range Forces

The tip is an inherently macroscopic object because it is important to support the imaging atom/ion or cluster by a stiff solid to avoid mechanical instabilities. The supporting part of the tip also generates tip–sample interactions: all materials generate van der Waals forces, and on insulating surfaces, electrostatic forces resulting from surface charge can sometimes not be avoided. The expected overall shape of the force as a function of distance is shown in Fig. 4.2. It is one of the unavoidable challenges of SFM measurements of the tip–sample interaction as a function of distance to separate the contribution resulting from the tip apex from the contribution resulting from the macroscopic part of the tip. For electrostatic attractive forces occurring between SFM tips and periodic arrangements of objects (e.g., atoms) on surfaces, as a rule of thumb, the decay length is roughly similar to the size of the force generating element (see Sect. 4.2.1). Therefore, separation of short-range and long-range forces means in practice that forces decaying on the scale of a few nanometers to a few tens of nanometers (due to the macroscopic part of the

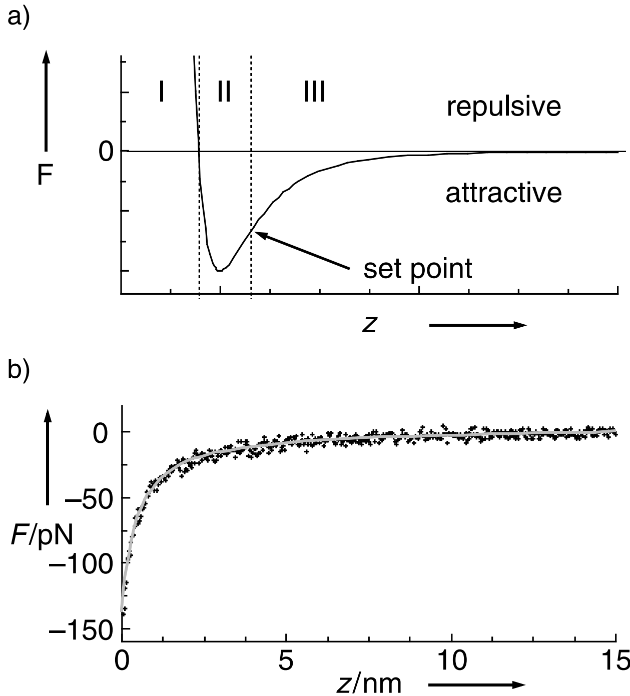

Fig. 4.2. (**a**) Expected overall shape of the force. Upon approach, the force is first attractive (region III). One then reaches the region where the setpoint for imaging is usually chosen. The force then reaches a minimum (region II) and quickly becomes repulsive (region I). (**b**) Typical long-range force measured on a CaF_2 (111) surface. The *black dots* are the measured data. The *grey line* results from a fit to the model shown in Fig. 4.3, including long-range electrostatic and van der Waals forces. From [27]

tip–apex) have to be separated from forces that decay on the order of a few tenths of a nanometer (due to an atom).

The main difficulty in this process arises from the fact that the exact tip shape as well as its chemical composition is unknown in most experiments. The tip is either a small silicon crystal or an etched wire glued to a piezoelectric tuning fork, or it is microfabricated from a silicon wafer. In all cases, the tip is exposed at least to air, water vapor, and possibly chemical solvents before it is used for measurement. Therefore, it is in most cases covered with oxide, which is either native or influenced by the microfabrication process. As corner or kink atoms have a lower coordination, and lower coordinated atoms are known to be chemically more reactive than surface atoms, it is thought that the tip apex is rounded during oxide formation. In some experiments, after introducing the tip into ultrahigh vacuum, the oxide is removed by sputtering, although it is possible that sputtering increases the tip radius. In some experiments, the tip

is heated to remove the water layer. This is plausible, but its effectiveness is in general not checked.

Several methods have been proposed to better understand and correctly quantify the measured long-range forces. One approach is to measure the force as a function of distance above a surface position where the tip is far from any interacting atom even at close tip–sample distances [5]. This approach requires a vacancy that can clearly be identified on the surface, for example, the corner hole of the Si(111) 7×7 reconstruction. However, this method is hardly applicable to insulating surfaces where vacancies are rare, and if one is found, an independent proof would be needed that the observed defect is not of a different type.

Another approach that is more widely used and applicable to different sample types relies on models of the long-range van der Waals and electrostatic forces [28]. In general, a conical tip with a spherical cap (Fig. 4.3) describes undamaged unsputtered tips reasonably well if one assumes a "nanotip" at its apex that accounts for short-range forces. It is important to measure the long-range part of the force in the distance regime of up to about 10–20 nm from the surface in order to tell the difference between electrostatic and van der Waals forces. The model forces diverge near the surface. The exact relative position of the tip and the surface and thus the onset of the short-range forces is unknown. The model is used to fit the long-range forces in the distance regime where one estimates short-range forces to be negligible. The fit must then be extrapolated into the

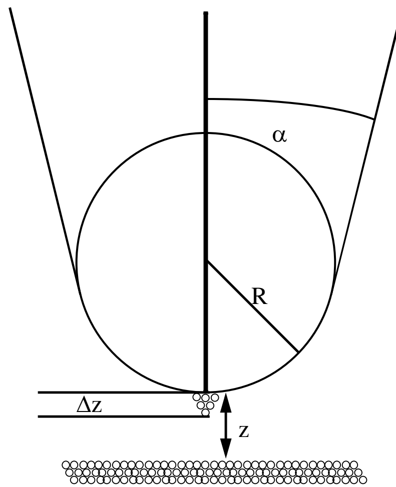

Fig. 4.3. Conical tip with a spherical cap used to model the long-range forces. It is thought that at the tip apex a sharp nanotip is located, which due to its sharpness facilitates atomic resolution. The tip radius of the conical tip in relation to the size of the atoms in the nanotip is to scale.

region where the short-range forces are important and its accuracy cannot be tested.

A third method is to look at force differences between two sites instead of the absolute force [29]. As for forces acting between rigid objects, the superposition principle is valid, and the frequency shift is a linear function of the force, the site-specific and the non-site-specific contribution to the frequency shift can be separated with this method if relaxation of the atomic positions is negligible. In practice, atomic positions do relax under the influence of the non-site-specific forces applied; however, if the long-range contribution to the total force is small, one can use this approximation.

4.2 Short-range Forces on Insulating Surfaces

The short-range forces on ionic and oxide materials arise from the short-range chemical bonding forces that comprise atomic-scale van der Waals forces, electrostatic forces, an overlap of electronic wavefunctions, and repulsive forces due to the Pauli exclusion principle. The electrostatic forces arise from the periodic distribution of charge at the surface, which is, even in ionic crystals, partly delocalized. On insulating surfaces, both electrostatic forces as well as the overlap of electronic wavefunctions can be important. However, the electrostatic forces usually give the surface its characteristic appearance in scanning force microscopy images (Fig. 4.4), because these forces can be attractive as well as repulsive: one type of atoms, which interacts attractively with localized charge on the tip apex appears as bright (a local maximum), the other type appears as dark (a local minimum). The electrostatic contribution to the chemical bonding force is thus crucial for the understanding of the short-range tip–sample interaction. Also, it is an essential problem to better understand the origin and the polarity of the localized charge at the tip apex. Studying tip–sample interactions as a function of distance can contribute to such an understanding.

4.2.1 Simple Model for Electrostatic Forces

In a simple (toy) model (see [31] for a similar treatment of the analogous magnetic problem, see also [32]), we model the surface as a plane of periodically arranged rigid ions of alternating sign and we model the tip as a point-like charge (Fig. 4.5). From solving the Laplace equation

$$\Delta\Phi(\boldsymbol{x}) = \rho(\boldsymbol{x}), \tag{4.2}$$

where $\Phi(\boldsymbol{x})$ is the electrostatic potential and $\rho(\boldsymbol{x})$ the electrostatic charge distribution, it becomes clear that the tip–sample forces decay exponentially as a function of tip–sample distance, with a decay constant related to the lattice constant of the surface. As the arrangement of charge at the surface is

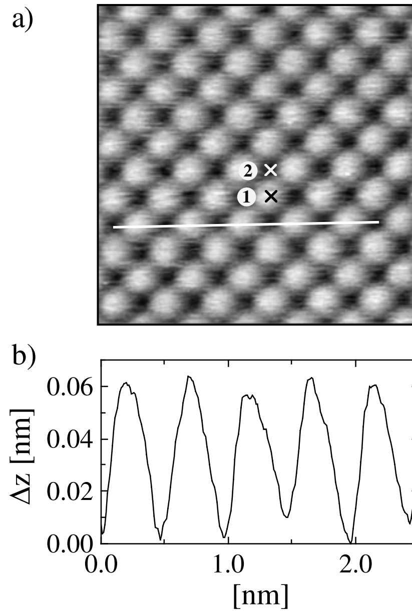

Fig. 4.4. (**a**) Atomic resolution SFM image of an NaCl(001) surface prepared by cleaving a NaCl crystal in ultrahigh vacuum. From symmetry arguments and from the lattice constant measured, it follows that one atomic site (Na^+ or Cl^-) is imaged as a local maximum (1) and the other is imaged as a local minimum (2). (**b**) Linecut along the line indicated in the image (**a**). From [30]

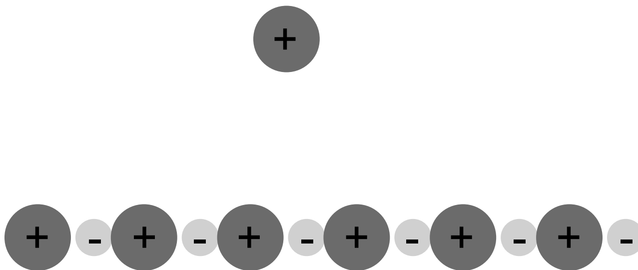

Fig. 4.5. Toy model used for a rough estimate of the decay length of the electrostatic force: the surface is represented by periodically arranged rigid ions of alternating sign and the tip is represented by a point-like charge.

periodic with lattice constants k_x in x-direction, and k_y in y-direction, taking the derivative of $\Phi(\boldsymbol{x})$ reduces to multiplying by ik_x or ik_y, respectively. As in the vacuum above the surface, there is no charge, and the interaction must be zero at infinite distances from the surface, one obtains

$$\left(-k_x^2 - k_y^2 + \frac{\partial^2}{\partial z^2}\right)\Phi(\boldsymbol{x}) = 0, \tag{4.3}$$

which can be solved easily. With $k = \sqrt{k_x^2 + k_y^2}$, the solution becomes

$$\Phi(\boldsymbol{x}) = \Phi(x, y)\, \mathrm{e}^{-kz}. \tag{4.4}$$

This gives a rough understanding of the decay rate of the short-range electrostatic forces, although the macroscopic extension of the tip, relaxation of atoms as well as other contributions to the chemical bonding forces have been neglected.

4.2.2 Relaxation and Realistic Electrostatic Interactions

For a basic understanding of the short-range forces measured on insulating surfaces, it is important that the atoms generating the forces are also held at their respective positions by forces of similar magnitude. Therefore, it is expected that the atomic positions change under the influence of such forces while the tip is approached to or scanned over a surface. Generally speaking, under the influence of the attraction experienced by the frontmost tip atom upon approach to the surface (at the transition between region III and II in Fig. 4.2a), the tip atom is approached closer to the surface than in the rigid case (Fig. 4.6). The force as a function of distance thus looks steeper than expected for rigid ions in this region. In contrast, at the onset of repulsion, around zero force, which corresponds to the bonding distance, the curve is flatter than that the rigid ion model suggests.

At close tip–sample distances, repulsive forces quickly become larger than the maximal attractive forces an ion can experience and can thus cause hopping of atoms, that is, displacement of atoms to nearby sites. This has an important effect on the repulsive branch of the force law measured: in this part, often hopping of atoms is observed, which manifests in abrupt changes of the force at a particular distance. A typical short-range force measured on KBr(001) where atomic hops at close tip–sample distances are avoided is shown in Fig. 4.7 (see also [17, 33–35]).

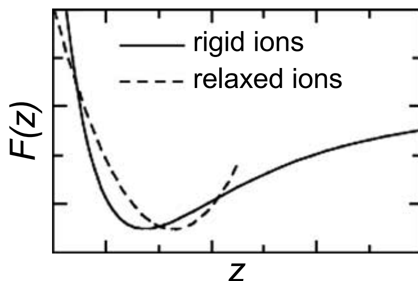

Fig. 4.6. Typical effect of relaxation. Relaxation distorts the measured curve with respect to the one expected for rigid ions such that the attractive part becomes steeper and the part where repulsive forces become important, around zero force, becomes flatter.

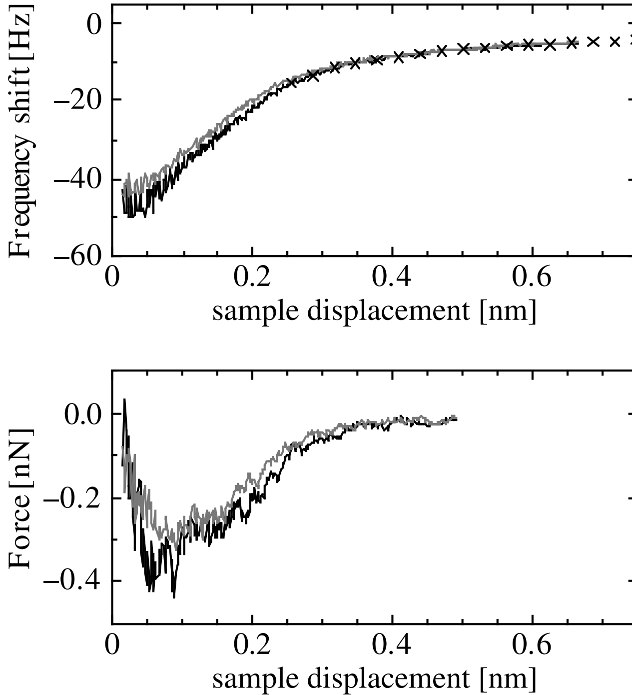

Fig. 4.7. Typical site-specific short-range force obtained from measurements on KBr(001). The *upper panel* shows the total measured frequency shift on the maximum and minimum of the observed contrast (*black* and *grey curves*). The *black crosses* represent a model for the long-range forces. The lower panel shows the typical short-range forces after converting the frequency shift to force and after subtracting the model long-range forces. From [33]

A more precise view on the atomistic processes during approach of the tip to the sample can be obtained from simulations [36]. The tip is modeled with several atoms or ions. The lower part of these atoms facing the sample can relax their positions while the upper part is kept fixed. In an iterative method, the total energy of the system is minimized. As for ionic materials of the NaCl type, the energy of a cluster is minimal when the cluster has a cuboid shape ("magic cluster"), often a cuboid is used as a tip. The surface is in general modeled by a slab of several layers of sample material where the center atoms are allowed to relax. It is important to keep some of the tip atoms as well as surface atoms fixed to be able to calculate the total force acting between tip and sample. These atoms keep the tip from relaxing excessively until it touches the surface. These atoms also represent the bulk part of tip and surface. Various calculation methods are used. For ionic crystalline materials, as the electrons are strongly localized, atomistic calculations (i.e., molecular dynamics simulations at zero temperature) are often sufficient,

where given potentials are used. The relatively simple treatment of the interactions between individual atoms then allows to increase the number of atoms in the simulation, which is important if atomic relaxation should be modeled properly, especially in the tip. In such simulations, for the tip, either sample material is used, because it is likely that the tip is covered by sample material in the course of the measurement, or MgO as a reasonable representative for SiO_x tips concerning the forces generated at the tip apex. For more thorough studies, or if semiconducting materials, in particular Si and its compounds as tip materials, are included in the problem, density functional theory is used. For some oxide materials, for example NiO, even the bulk is not yet fully understood, and simulations of the SFM setup are therefore difficult [37]. For these materials, reliable experimental results are therefore of special interest.

Simulations also allow to estimate the relative offset of the z scale in a particular experiment. This is achieved after a careful subtraction of the long-range forces and through comparison of measured results with simulations and also yields the tip–sample distance at which images are acquired.

4.2.3 Interaction of a Tip with a Well-known Surface

One of the key problems in scanning force microscopy is that the atomistic structure as well as the chemical composition of the tip cannot be characterized as thoroughly as the surface. The overall macroscopic tip structure can be analyzed, for example, using scanning electron microscopy or using specially designed samples. As any SFM image results from a convolution of tip and sample shapes, ideally one would prefer a delta peak on the surface to learn as much as possible about the tip apex. However, on the atomic scale, naturally, delta peaks are not available and it is thus much more difficult to learn about the detailed tip apex structure. Additionally, the tip apex is not flat, and it is thus difficult to image the tip apex with scanning probe techniques. STM tips have been investigated with field ion microscopy, which works best on conductive tips [38] and experimental efforts have been undertaken to use time of flight mass spectroscopy to characterize SFM tips [39]. However, this requires a rather sophisticated experimental set-up, which is in most experiments not available. As the tip interacts with the sample surface, it is possible that it acquires sample material. Therefore, a number of possibilities for the chemical nature of the tip material arise: Si, SiO_x, water, air, and sample material have to be considered.

It is therefore important to investigate the interaction of the tip with well-known surfaces in order to learn as much as possible about the tip. An ideal surface for this purpose is CaF_2 (111). In scanning force microscopy images on this surface, similar to NaCl (001), only one type of atoms (Ca^{2+} or F^-, resp.) is imaged as bright, the other type is imaged as a local minimum. However, the spatial arrangement of the positive charge is different from the

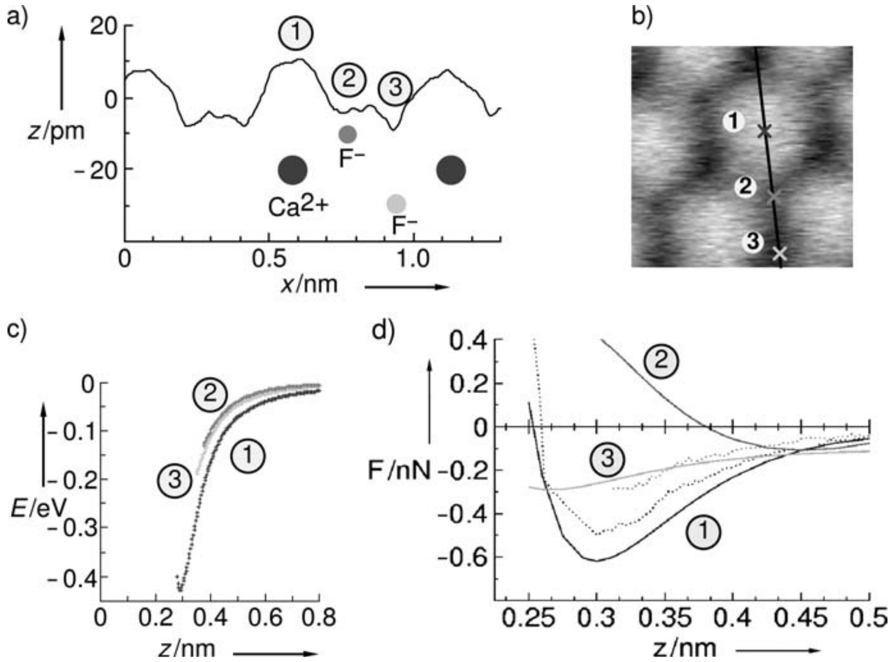

Fig. 4.8. Surface topography and tip–sample interaction on $CaF_2(111)$: (**a**) Linecut along $[\bar{2}11]$ through a typical image (**b**) measured with a negatively terminated tip: the attraction is strongest where the partial positive charge is located on the Ca^{2+} site (1). On the F^- sites (2 and 3), local repulsive forces weaken the overall attraction, these sites are imaged as local mimima. (**c**) Binding energy as a function of distance obtained on all three sites from the measured frequency shift. (**d**) Measured force (*dotted curves*) compared with results from simulations (*lines*). From [27]

spatial arrangement of the negative charge. On this surface, a careful comparison between measured and simulated images has allowed to learn about the tip apex ion polarity from the shape of the contrast in images combined with the appearance of a linecut in the $[\bar{2}11]$ direction [40]. For a negatively terminated tip, the positively charged Ca^{2+} is imaged as a protrusion, giving disk-like contrast (Fig. 4.8b). For positively terminated tips, the negative charge distributed at the F^- atoms is imaged as triangular shaped protrusions. For a negatively terminated tip, identified from images as well as line-cuts, the tip–sample interaction was studied as a function of distance [27]. The binding energy between the tip apex cluster and the Ca^{2+} site was determined to be 0.43 eV. However, the physical meaning of this binding energy is well-defined only if the nature of the tip apex is known.

Therefore, simulations using various tip models were performed. As the tip was exposed to air prior to the measurements, a pure silicon tip was not considered. Additionally, in the simulations, silicon tips could not account for

the disk-like contrast in the images. We therefore studied possible tip models representing oxidized silicon tips. These have often been sufficiently well modeled using MgO. However, for the quantitative precision required here, this was not sufficient. A hydrogen saturated silicon tip covered with a single oxygen atom at its apex showed a reasonable agreement with the experimental data (Fig. 4.8d). However, this tip yielded repulsion on the fluorine sites, where clearly attraction is observed experimentally. Additional calculations with a larger silica tip showed that the additional atoms on larger tips can indeed lead to attractive forces on the fluorine sites, and that extensive studies are needed to obtain complete agreement.

4.2.4 Sublattice Identification on Alkali Halide Surfaces

For crystals of the NaCl type, the spatial charge distribution of the positively charged and the negatively charged sublattices on the (001) easy cleavage plane are similar, in particular if the difference in the ionic radii is small as in, for example, KBr (K^+ ionic radius: 152 pm, Br^- ionic radius: 182 pm [41]). The atoms generate either attractive or repulsive short-range electrostatic forces that are superposed locally to the overall attractive non-site-specific force between tip and sample, and give the surface its characteristic appearance in SFM images. One type of atom is imaged as a local maximum, the other as a local minimum, but from images alone it is not clear which feature corresponds to which type of atom (Fig. 4.9).

It has been proposed to investigate the radii of the protrusions to identify the tip apex polarity. The radii of the observed protrusions in SFM images depend strongly on the magnitude of the long-range forces, and the frequency shift chosen for the particular image [42]. It is therefore difficult to draw a conclusion about the tip apex polarity solely from SFM images [43]. For the case of KBr and NaCl, the experimentally obtained force as a function of tip–sample distance has been carefully compared to atomistic simulations to identify the tip apex polarity [29].

To unambiguously eliminate non-site-specific long-range forces, the force differences between two neighboring atomic sites have been calculated both from the experimental and from the simulated data. On the repulsive site, that is, the topographic minimum observed in images, the simulations showed that the tip bends sideways because the tip apex ion is attracted to the next nearest neighbor ion of opposite sign. The direction in which the tip bends strongly depends on the details of the atomic arrangement on the tip as well as the relative crystallographic orientation of the tip and the surface. This bending concerns a relatively large number of atomic layers in the tip. It is therefore possible that differences between the experimental tip and the one used for the simulations play an important role. On the bridge site, atoms of both types are roughly at the same distance from the tip apex ion, and their attractive/repulsive electrostatic contributions to the total force roughly

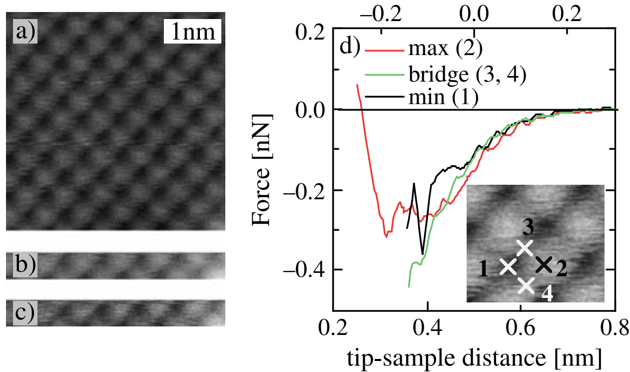

Fig. 4.9. (**a**) SFM image of the KBr surface. It was carefully checked after the acquisition of each set of frequency vs. distance that the surface drift had been negligible on the atomic scale. Indeed, the position of a defect in the lower right corner of the image (**b**) and (**c**) remained the same. (**c**) Forces obtained on the minimum (1), the maximum (2), and the bridge sites. As the two available bridge sites (3) and (4) are symmetric with respect to the surface, any differences measured between those two sites result from asymmetries in the tip. Such differences are measured only at tip–sample distances smaller than 0.35 nm on the lower z scale. This z scale results from a comparison with simulations and is the same as in Fig. 4.10. From [29]

cancel. On the maximum site, where electrostatic attraction dominates, relaxation is at least symmetry-conserving. Therefore, the interpretation relies on the results obtained above the topographic maximum and on the bridge site.

The force difference calculated from the force at the topographic maximum minus the force at the bridge site shows a clear difference between negative and positive tip apex polarity: for a positively terminated K^+ tip, negative force differences are calculated at a tip–sample distance of about 0.3–0.4 nm, while positive force differences are calculated in this distance regime for the negatively terminated Br^- tip. The experimental data is well represented by the positively terminated K^+ tip (Fig. 4.10).

Similar results have been obtained with density functional calculations, where a smaller tip has been used [43]. It has been shown that the method also works for NaCl (001) [30]. Additionally, the interaction of nonideal tips with NaCl (001) surfaces has been investigated [44].

4.2.5 Full Three-Dimensional Force Field

Measuring the full three-dimensional force field allows to compare calculations and measurements on all sites of the surface within the experimental resolution. It therefore gives a more complete view of the interaction of the tip and the surface. In several publications, using single force curves, quantitative

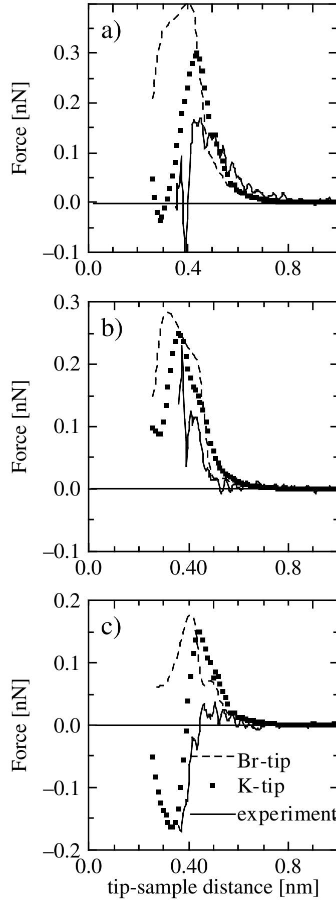

Fig. 4.10. Measured and calculated force differences above (**a**) sites 1 and 2, (**b**) sites 1 and 3, and (**c**) sites 3 and 2 as defined in Fig. 4.9. The force measured on the minimum site is strongly affected by lateral relaxation in the simulations. On this site, it is not clear whether the simulations represent well the atomistic details of the tip. On the bridge site, however, the tip experiences attractive forces from one type of atom, and repulsive forces from the other type of atom of roughly the same magnitude. Relaxations are therefore small and do not crucially depend on the tip model. On the maximum, the relaxations due to the strong attractive forces remain symmetry-conserving. Therefore, we rely on the data shown in panel (**c**) and conclude that the tip used in the experiment was positively terminated as the K-tip used for the simulations. From [29]

agreement between simulations and experiment has been found on the attractive sites only [27, 29]. On the repulsive site, in simulations, repulsive forces have been found, while in the experiment, attraction has been measured. One of the reasons is that on the repulsive site, lateral relaxation of the tip occurs, which is sensitive to the detailed atomic positions of several layers of tip apex

atoms. Therefore, it is more likely on the repulsive site that a given model does not fully represent the tip used in a particular experiment [29]. Furthermore, it has been pointed out that larger tip models can explain attractive forces even on sites where the dominant interaction with the tip is repulsive [27]. With an analysis of the full three-dimensional force field, one can check the agreement between simulations and experiments more thoroughly for different models of the non-site-specific forces.

Recently, for the KBr (001) surface, this method has been used to compare atomistic simulations and measurements [58]. To obtain the vertical force field at room temperature, the frequency shift was measured as a function of the relative tip–sample distance on a grid. Before and after each individual frequency shift vs. distance measurement, the feedback loop (keeping the frequency shift constant by adjusting the tip–sample distance) was switched on to stabilize the system. The atomistic simulations are described in detail in [29]. Excellent agreement on all sites between experiment and simulations was found, which can only be explained by a rather good match between the positively terminated K^+ model tip and the tip used in the experiment (Fig. 4.11). In

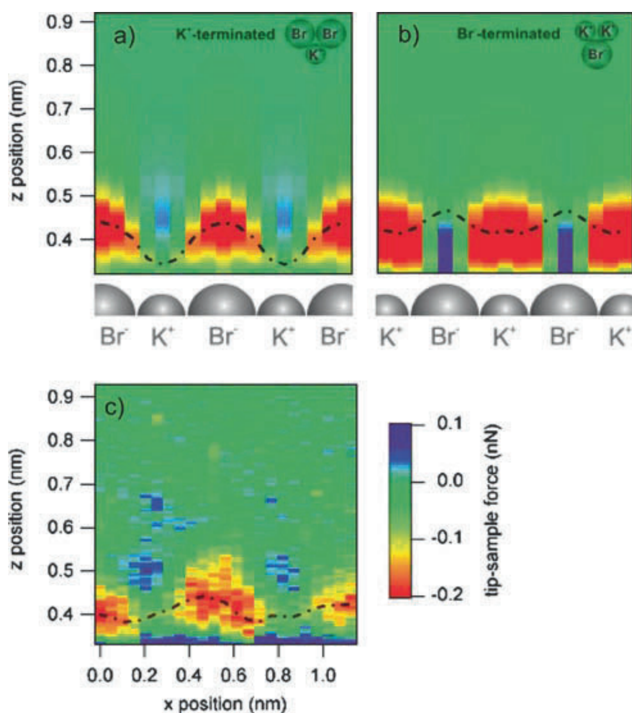

Fig. 4.11. Simulated three-dimensional force fields for (**a**) the positively terminated K^+ model tip and (**b**) the negatively terminated Br^- model tip. Panel (**c**) shows the results obtained from measurement on the same color coded scale. There is reasonable agreement between experiment and the positively terminated tip, whereas there is a clear disagreement for the negatively terminated tip. From [58]

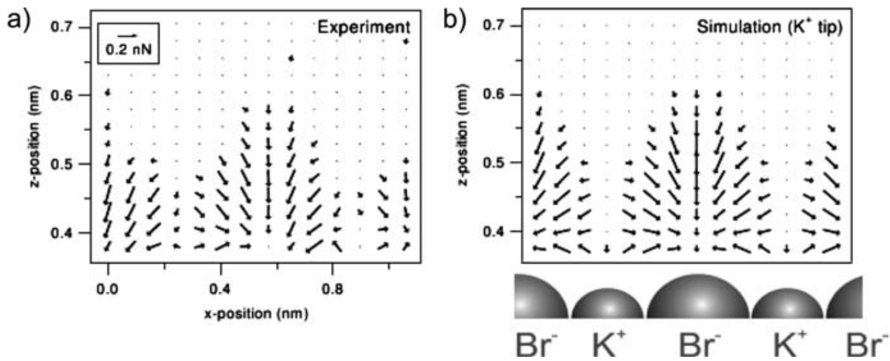

Fig. 4.12. Lateral forces extracted from (**a**) experimental three-dimensional force field data, and (**b**) simulations using a positively terminated K^+ model tip. From [58]

particular, the triangular-shaped attractive areas in red are well reproduced in the simulations. In contrast, clear differences are observed between the measurement and the negatively terminated Br^- model tip. Additionally, the course of the position where strongest attraction is obtained has been studied as a function of lateral displacement (*black line*). This course shows characteristic differences between positively and negatively terminated tips: in the positively terminated tip, the curve is closest to the sample surface for the position with strongest repulsion (above K), while for the negatively terminated tip, the curve is closest to the surface for the position with strongest attraction (above K).

Such an analysis also gives access to the lateral forces (Fig. 4.12), which are important for lateral atom manipulation as well as friction. As expected, the positively terminated tip is attracted by the negatively charged surface atoms.

4.2.6 Atomic Jumps and Energy Dissipation

So far in this chapter only energy conserving tip–sample interactions have been discussed. In the dynamic frequency modulation mode, the tip is oscillated at resonance and additionally the cantilever oscillation amplitude is kept constant using a feed-back loop. In this measurement mode, the excitation amplitude necessary to keep a constant oscillation amplitude is a measure of the intrinsic energy dissipation of the cantilever. It is observed that, upon approach to the surface, the excitation amplitude is increased by the feed-back loop, meaning that the surface damps the cantilever oscillation [45]. The energy dissipation shows atomic scale contrast. The mechanisms that can lead to such an energy dissipation have attracted a lot of attention recently. Energy dissipation by the surface is also observed during frequency vs. distance measurements. Frequency vs. distance measurements on insulating surfaces have contributed to this discussion as shown in this section.

Energy dissipation is best known as viscous damping observed in soft materials, or as damping by liquids or gases. However, in the context of atomic resolution SFM, the experiments are performed in ultrahigh vacuum, with small base pressures, where great care is taken to avoid the presence of liquids such as water. The tips and samples generally studied are hard; viscous damping is therefore not expected to occur. Also any mechanisms proposed must account for the observed atomic scale contrast. First, as for any SFM measurement, it is carefully checked that the contrast does not depend on the scan direction, and that the feedback loops work as intended. Often, in energy dissipation images, a lowered symmetry compared to the undisturbed surface symmetry is observed although the contrast appears symmetric in the topography images. Such a lowered symmetry reflects the asymmetry of the tip. The measured energy dissipation is very sensitive to the atomic configurations of both the tip and the surface. This becomes clear at tip changes: often the magnitude of the contrast and the symmetry of the features in energy dissipation images change strongly with tip rearrangements that leave the topography images nearly unaltered [8]. Also at defect sites, where the atomic structure of the surface differs locally from the ideal one, local changes in energy dissipation are observed (see Fig. 4.13).

Recently, for hard, clean, nonmagnetic tips, three main mechanisms have been discussed: apparent energy dissipation, that is, artifacts by the cantilever oscillation and detection electronics, energy dissipation by the Brownian motion of atoms, and energy dissipation attributed to hysteretic atomic jumps [8]. Apparent energy dissipation can be excluded by a careful experimental setup [46]. Brownian motion of atoms causes energy dissipation [47]. Because of thermal motion, the exact positions of the interacting tip and surface atoms during retraction in one particular oscillation cycle differ from the positions held during approach. The force between tip and sample therefore shows a small hysteresis between approach and retraction related to a certain amount of energy dissipated, which can be calculated as the area between the two force curves in a $F(z)$ plot. The effects calculated are, however, usually much smaller than the ones observed experimentally. The main reason is that the typical frequency of the moving atoms (typical phonon frequencies) are much larger than the cantilever oscillation frequency. At surfaces and on tips, the phonon frequencies can be lowered due to the lowered coordination between the atoms. Taking this effect into account, calculations still fail to explain the magnitude of the energy dissipation observed experimentally [48, 49].

It is therefore likely that hysteretic atomic jumps is the most important mechanism of energy dissipation in the context of atomic resolution SFM [7]. The atomistic configuration of either the tip or the sample or both is changed by an atomic jump at close tip–sample distances. The tip–sample interaction is thus strongly altered within one oscillation cycle, and energy is dissipated. Such a single event should cause an observable change both during imaging and in frequency vs. distance measurements. As energy dissipation is also

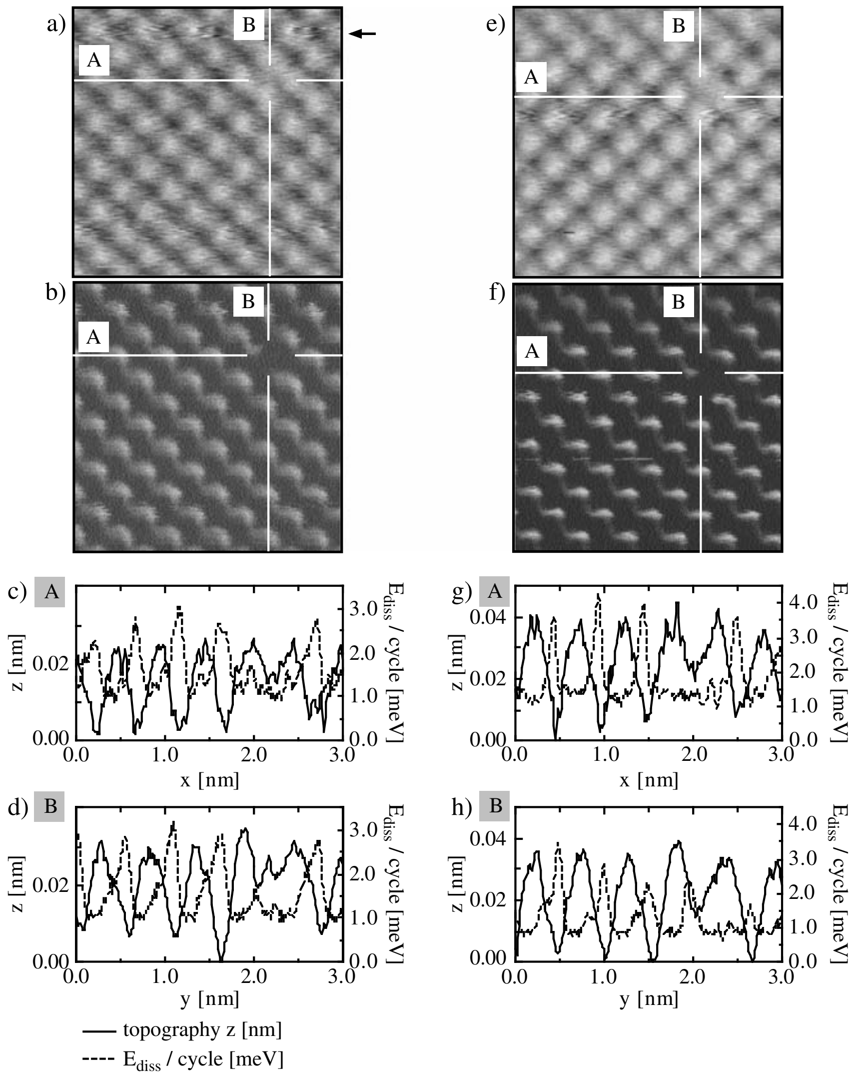

Fig. 4.13. Two subsequent SFM images (**a**) and (**e**) of an atomic scale defect on a KBr (001) surface. (**a**) First topographic image. The defect is a missing minimum located at the center of the two line-cuts A and B. (**b**) Energy dissipation image recorded alongside image (**a**). Note that the intrinsic energy dissipation of the free cantilever has been set to zero in this figure. The defect is observed more clearly than in the topographic image. (**c**) and (**d**) line-cuts A and B taken from the images (**a**) and (**b**). (**e**) Subsequent image acquired immediately after finishing image (**a**). The defect appears moved by approximately one lattice site along the diagonal direction ((110)-direction). Also the positions of the maxima and minima of the undisturbed surface have moved with respect to image (**a**) presumably due to a tip change near the arrow in image (**a**). (**f**) Energy dissipation image recorded alongsite image (**e**). (**g**) and (**h**) line-cuts A and B taken from images (**e**) and (**f**). From [42]

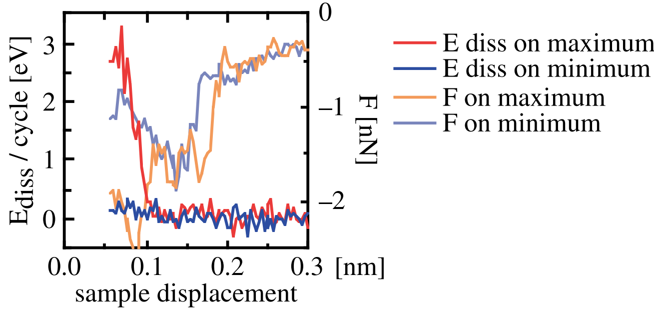

Fig. 4.14. Force and energy dissipation as a function of distance on NiO (001). On the maximum, where a plateau is observed, at about the same tip–sample distance, energy dissipation occurs. In contrast, on the minimum, a smooth force curve is measured, and the additional energy dissipation is only slightly larger than the intrinsic energy dissipation of the cantilever corresponding to zero in this graph. From [50]

observed in the absence of such detectable changes, it is a postulate that the atom or the group of atoms that has jumped hops back to its original position soon after. The dissipated energy is maximal if there is one jump forward and one jump back to the original state in each oscillation cycle; that is, if the rate of the jumps is equal to the cantilever oscillation frequency, which is the case if the jumps are induced by the oscillating tip. It has been the goal of a number of theoretical as well as experimental efforts to examine these postulates.

On NiO (001), strong energy dissipation has been observed at close tip–sample distances on only the atomic site that corresponds to a local maximum [50].[2] In Fig. 4.14, frequency vs. distance measurements are shown together with energy dissipation vs. distance measurements. On one atomic site, the force shows a plateau structure: the attractive (negative) force increases first when the tip interacts with the surface, then remains constant in a certain distance regime, and then increases again at closer distances. At the position where the force first increases, the tip apex atom interacts with the surface. The plateau and the second increase is a typical sign for the interaction of other tip and surface atoms that becomes important at closer distances. Calculations have suggested that the second increase of the force results from an interaction of the frontmost tip ion with the next nearest surface atoms [37]. It is, however, also possible that other tip atoms (excluding the tip apex ion) located near the tip apex interact with nearby surface atoms. The plateau structure is associated with a rise in the energy dissipation. We believe that hysteretic motion becomes more likely if the number of moving

[2] As the tip apex polarity cannot unambiguously be determined on this surface, it is not clear whether this corresponds to the Ni or the O site.

atoms increases, because the number of local minima in the energy landscape increases.

The energy dissipation is, however, not required to monotonically increase upon approach to the surface. It has been shown for small oscillation amplitudes of 0.25 nm, energy dissipation occurs only for a limited distance range. At large tip–sample distances, energy dissipation is negligible, it then increases at closer distances, shows a plateau, and then decreases again at even closer tip–sample distances [51]. This can be explained by hysteretic motion of atoms in the distance range where the plateau is observed. This hysteretic motion of atoms is suppressed when the tip remains at too close tip–sample distances even at its upper (i.e., large z) turning point. The tip never reaches the point where the jumping atom causing the hysteresis recovers its initial state.

Three different causes of energy dissipation by hopping atoms must be discerned: hopping on the sample, hopping between tip and surface, and hopping on the tip. Hopping on the sample is in general not expected because diffusion energy barriers within a low-indexed (easy cleavage plane) surface are usually rather high. There are, however, special cases where a movable entity is part of a particular surface structure such as the case of Si (001) [52]. On the Si (001) surface, two neighboring Si adatoms with dangling bonds form a dimer, which is tilted with respect to the surface, that is, one Si atom is located closer to the surface than the other. The flip where the two atoms of one dimer change their respective roles has a small energy barrier and is therefore thermally excited at room temperature. Previously in this chapter, we have discussed hopping with a rate given by the cantilever oscillation frequency, that is, hopping induced by the oscillating tip. In Si (001), in contrast, the dimer flips with a rate determined by the energy barrier $\Delta\varepsilon$ and by temperature T

$$\nu = \nu_0 \, \mathrm{e}^{-\Delta\varepsilon/(k_\mathrm{B}T)}, \tag{4.5}$$

where ν_0 is the attempt frequency. If the tip approaches such a naturally flipping entity, the energy dissipated is maximal if the rate of flipping is similar to the cantilever oscillation frequency. This phenomenon is called "stochastic resonance" [45, 53]. At low temperatures, atomic hops manifest as jumps in force vs. distance measurements, whereas at elevated temperatures, these jumps are softened by statistical averaging [34, 54].

Energy dissipation due to adhesion of the frontmost tip apex atom at the surface is the main mechanism currently discussed to explain experimental findings [55]. An atom loosely bound to the tip snaps to the surface at small tip-sample distances, and jumps back to the tip at larger tip–sample distances while the cantilever is swinging back. This scenario is interesting because, in addition to the average force obtained from the frequency shift, information about the hysteretic tip–sample interaction can be obtained from another source of information, the dissipated energy. However, to unambiguously interpret measured results, the third scenario, hopping on the tip, must be excluded. For rarely occurring jumps, it is experimentally rather simple to discern the two latter scenarios: in the case of hopping between

tip and sample, the energy barrier between the two states of the hopping atom strongly depends on the tip–sample distance. The hopping rate, which depends exponentially on this energy, is therefore expected to strongly depend on the tip–sample distance. For lateral hops on the tip, in contrast, a roughly constant hopping rate is expected. Such a hopping rate, which is roughly constant with tip–sample distance, has been observed experimentally (Fig. 4.15), and the jumps have been attributed to hops on the tip [56]. The tip–sample

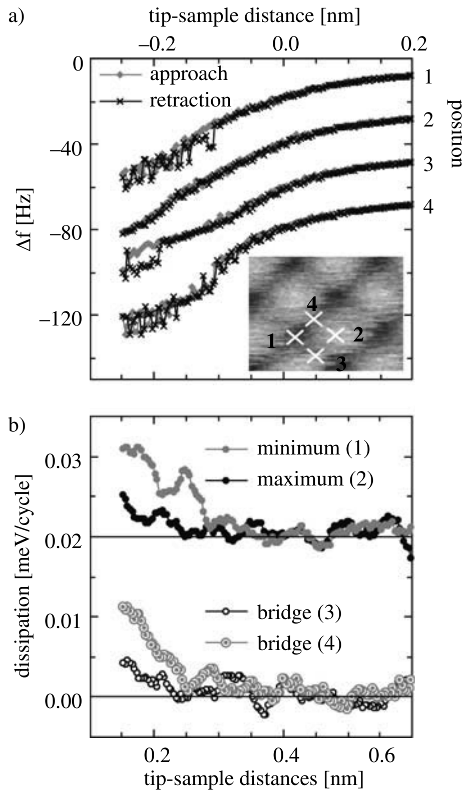

Fig. 4.15. Frequency shift measured during approach and retraction on different atomic sites on KBr (001). On the minimum (site 1) and on one of the bridge sites (site 4), at very small tip–sample distances, repeated jumps occur that result from atomic hops. On the maximum (site 2), no jumps occur, while on the other bridge site (3), only one jump occurs during approach and only three jumps occur during retraction. The energy dissipation rises upon approach to the surface only on sites 1 and 4, where a significant amount of jumps is observed. A careful estimate allows to relate the order of magnitude of the observed additional energy dissipation to the amount of energy dissipated by the repeated atomic hops. The inset shows locations 1–4 where the data were acquired on a small area from a larger undisturbed SFM image. The data obtained at different positions are vertically offset by 20 Hz in (**a**) and by 0.02 meV in (**b**). From [56]

interaction forces have been measured in both states of the hops, which made it possible to estimate the dissipated energy and relate it to the experimental value. Reasonable agreement was found and thus it is thought that the energy is indeed dissipated by the atomic hops observed.

Additionally, hopping on the tip has recently been investigated using large Si tips [57]. Indeed, it was observed that the tip assumes different configurations in different approaches to the surface, which leads to energy dissipation. To even better understand the tip–sample interaction for insulating surfaces, it is now important to check the atomistic configuration of real tips used in experiments and to learn about the chemical nature of the atoms composing the tip apex.

Acknowledgement

I am grateful for the continuous support of my work by Hans-Joachim Güntherodt, H.J. Hug, and A. Baratoff. Additionally, I thank in particular C. Barth, A. Foster, L.N. Kantorovich, M.A. Lantz, M. Reichling, K. Ruschmeier, A. Schirmeisen, A.L. Shluger, P.J.A. van Schendel, H.V. Löhneysen, and D. Weiner, and also numerous additional colleagues and members of the NC-AFM community for enlightening discussions. I thank A. Foster, H. Hölscher, J.M. Mativetsky, A. Schirmeisen, and T. Tomanić for critically reading the manuscript. Financial support by the DFG-Center for Functional Nanostructures and the Landesstiftung Baden-Württemberg in the framework of its excellence program for postdoctoral fellows is gratefully acknowledged.

References

1. S. Morita, R. Wiesendanger, E. Meyer (ed.), *Noncontact Atomic Force Microscopy* (Springer, Berlin, 2002)
2. F.J. Giessibl, Science **267**, 68 (1995); S. Kitamura, M. Iwatsuki, Jpn. J. Appl. Phys. **34**, L145 (1995)
3. H. Ueyama, M. Ohta, Y. Sugawara, S. Morita, Jpn. J. Appl. Phys. **34**, L1086 (1995)
4. M. Bammerlin, et al., Probe Microscopy **1**, 3 (1997)
5. M.A. Lantz, H.J. Hug, R. Hoffmann, P.J.A. van Schendel, P. Kappenberger, S. Martin, A. Baratoff, H.-J. Güntherodt, Science **291**, 2580 (2001)
6. T. Filleter, S. Maier, R. Bennewitz, Phys. Rev. B **73**, 155433 (2006)
7. N. Sasaki, M. Tsukada, Jpn. J. Appl. Phys. **39**, L1334 (2000)
8. H.J. Hug, A. Baratoff, in *Noncontact Atomic Force Microscopy*, ed. by S. Morita, R. Wiesendanger, E. Meyer (Springer, Berlin, 2002), p. 395
9. N. Oyabu, O. Custance, I.S. Yi, Y. Sugawara, S. Morita, Phys. Rev. Lett. **90**, 176102 (2003)
10. A. Socoliuc, E. Gnecco, S. Maier, O. Pfeiffer, A. Baratoff, R. Bennewitz, E. Meyer, Science **313**, 207 (2006)

11. M. Ternes, C.P. Lutz, C.F. Hirjibehedin, F.J. Giessibl, A.J. Heinrich, Science **319**, 1066 (2008)
12. H.J. Hug, B. Stiefel, P.J.A. van Schendel, A. Moser, S. Martin, H.-J. Güntherodt, Rev. Sci. Instrum. **70**, 3625 (1999)
13. F.J. Giessibl, Rev. Mod. Phys. **75**, 949 (2003)
14. R. Garcia, R. Perez, Surf. Sci. Rep. **47**, 197 (2002)
15. U. Dürig, Appl. Phys. Lett. **76**, 1203 (2000)
16. H. Hölscher, in *Noncontact Atomic Force Microscopy*, ed. by S. Morita, R. Wiesendanger, E. Meyer (Springer, Berlin, 2002), p. 349
17. H. Hölscher, S.M. Langkat, A. Schwarz, R. Wiesendanger, Appl. Phys. Lett. **81**, 4428 (2002)
18. A. Schwarz, H. Hölscher, S.M. Langkat, R. Wiesendanger, AIP Conf. Proc. **696**, 68 (2003)
19. S.M. Langkat, H. Hölscher, A. Schwarz, R. Wiesendanger, Surf. Sci. **527**, 12 (2003)
20. S.H. Ke, T. Uda, K. Terakura, Phys. Rev. B **59**, 13267 (1999)
21. F.J. Giessibl, H. Bielefeldt, Phys. Rev. B **61** 9968 (2000)
22. U.D. Schwarz, H. Hölscher, R. Wiesendanger, Phys. Rev. B **62**, 13089 (2000)
23. F.J. Giessibl, Phys. Rev. B **56**, 16010 (1997)
24. F.J. Giessibl, Appl. Phys. Lett. **78**, 123 (2001)
25. O. Pfeiffer, R. Bennewitz, A. Baratoff, E. Meyer, and P. Grütter, Phys. Rev. B **65**, 161403(R) (2002)
26. O. Pfeiffer, Dissertation, University of Basel (2004)
27. R. Hoffmann, C. Barth, A. S. Foster, A. L. Shluger, H. J. Hug, H.-J. Güntherodt, R. M. Nieminen, and M. Reichling, J. Am. Chem. Soc. **127**, 17863 (2005)
28. M. Guggisberg, M. Bammerlin, Ch. Loppacher, O. Pfeiffer, A. Abdurixit, V. Barwich, R. Bennewitz, A. Baratoff, E. Meyer, and H.-J. Güntherodt, Phys. Rev. B **61**, 11151 (2000)
29. R. Hoffmann, L. N. Kantorovich, A. Baratoff, H. J. Hug, and H.-J. Güntherodt, Phys. Rev. Lett. **92**, 146103 (2004)
30. M. A. Lantz, R. Hoffmann, A. S. Foster, A. Baratoff, H. J. Hug, and H.-J. Güntherodt, Phys. Rev. B **74**, 245426 (2006)
31. P. J. A. van Schendel, Dissertation, University of Basel (1999)
32. R. P. Feynman, R. B. Leighton, M. Sands, *The Feynman Lectures on Physics II*, Addison-Wesley Publishing Group, Reading, Massachusets (1964)
33. R. Hoffmann et al., Appl. Surf. Sci. **188**, 238 (2002)
34. A. Schirmeisen, D. Weiner, and H. Fuchs, Phys. Rev. Lett. **97**, 136101 (2006)
35. M. Heyde, G. H. Simon, H.-P. Rust, H.-J. Freund, Appl. Phys. Lett. **89**, 263107 (2006)
36. A. Foster, A. Schluger, C. Barth and M. Reichling, in Ref. [2], p. 305
37. A. S. Foster, and A. L. Shluger, Surf. Sci. **490**, 211 (2001)
38. G. Cross, A. Schirmeisen, A. Stalder, P. Grütter, M. Tschudy, and U. Dürig, Phys. Rev. Lett. **80**, 4685 (1998)
39. A. Wetzel, A. Socoliuc, and E. Meyer, R. Bennewitz, E. Gnecco, and C. Gerber, Rev. Sci. Instr. **76**, 103701 (2005)
40. A. S. Foster, C. Barth, A. L. Shluger and M. Reichling, Phys. Rev. Lett. **86**, 2373 (2001); A. S. Foster et al., Phys. Rev. B **66**, 235417 (2002).
41. M. J. L. Sangster and R. M. Atwood, J. Phys. C: Solid State Phys. **11**, 1541 (1978)

42. R. Hoffmann, Dissertation, University of Basel (2001)
43. O. H. Pakarinen, C. Barth, A. S. Foster, R. M. Nieminen, and C. R. Henry, Phys. Rev. B **73**, 235428 (2006)
44. R. Oja and A. S. Foster, Nanotechnology **16**, S7 (2005)
45. P. Hoffmann, S. Jeffery, J. B. Pethica, H. Ö. Özer, and A. Oral, Phys. Rev. Lett. **87**, 265502 (2001)
46. Ch. Loppacher, R. Bennewitz, O. Pfeiffer, M. Guggisberg, M. Bammerlin, S. Schär, V. Barwich, A. Baratoff, and E. Meyer, Phys. Rev. B **62**, 13674 (2000)
47. M. Gauthier and M. Tsukada, Phys. Rev. B **60**, 11716 (2000)
48. L. Kantorovich, Appl. Surf. Sci. **210**, 27 (2003) and refererences therein
49. T. Trevethan and L. Kantorovich, Nanotechnology **15**, S44 (2004)
50. R. Hoffmann, M. A. Lantz, H. J. Hug, P. J. A. van Schendel, P. Kappenberger, S. Martin, A. Baratoff, and H.-J. Güntherodt, Phys. Rev. B **67**, 085402 (2003)
51. S. Hembacher, F. J. Giessibl, J. Mannhart, and C. F. Quate, Phys. Rev. Lett. **94**, 056101 (2005)
52. L. Kantorovich, and C. Hobbs, Phys. Rev. B **73**, 245420 (2006)
53. R. Boisgard, J. P. Aimé and G. Couturier, Appl. Surf. Sci. **188**, 363 (2002)
54. L. N. Kantorovich and T. Trevethan, Phys. Rev. Lett. **93**, 236102 (2004)
55. N. Oyabu, P. Pou, Y. Sugimoto, P. Jelinek, M. Abe, S. Morita, R. Perez, and O. Custance, Phys. Rev. Lett. **96**, 106101 (2006)
56. R. Hoffmann, A. Baratoff, H. J. Hug, H. R. Hidber, H. v. Löhneysen, and H.-J. Güntherodt, Nanotechnology **18**, 395503 (2007)
57. S. Alireza Ghasemi, S. Goedecker, A. Baratoff, T. Lenosky, E. Meyer, and H. J. Hug, Phys. Rev. Lett. **100**, 236106 (2008)
58. K. Ruschmeier, A. Schirmeisen, and R. Hoffmann, Phys. Rev. Lett. **101**, 156102 (2008)

5

Force Field Spectroscopy in Three Dimensions

André Schirmeisen, Hendrik Hölscher, and Udo D. Schwarz

Abstract. Atomic resolution images in noncontact atomic force microscopy (NC-AFM) reflect planes of constant frequency shift. To draw conclusions on the chemical activity at specific surface sites, however, the force acting between tip and sample should be known locally rather than the frequency shift. This is not an easy translation due to the nonlinear nature of the relationship between the two.

To overcome this problem, several groups have developed an extension to NC-AFM, dynamic force spectroscopy, which allows the precise, distance-dependent measurement of tip–sample forces. The forces are determined from frequency shift vs. distance curves by mathematical analysis. By combining many of these curves in a raster grid, the full three-dimensional surface force field can be probed with atomic resolution as it extends into vacuum. This chapter reviews experiments performed on NiO, NaCl, KBr, and graphite that illustrate the strengths and weaknesses of the different experimental approaches as well as the type of results that can be obtained.

5.1 Introduction

Since its invention in 1986 [1], the success of atomic force microscopy (AFM) roots in its combination of high resolution imaging capabilities and broad versatility, as it is capable of imaging almost any type of surface without the need for tedious sample preparation. Force microscopy relies on the detection of interaction forces between a raster-scanned sharp tip and the investigated surface, with the corresponding signal being recorded as a function of the tip's lateral position. Typically, finite tip–sample contact areas cause the net interaction to be averaged over the often dozens or even hundreds of atoms involved in the process of contrast formation, with individual atom–atom interactions not explicitly being exploited in conventional AFM imaging modes.

By employing atomically sharp tips in conjunction with the right experimental approach, it is nevertheless possible to measure signals that are dominated by interatomic forces caused by just the tip's foremost atom. To avoid the above-mentioned averaging effect due to the formation of tip–sample

S. Morita et al. (eds.), *Noncontact Atomic Force Microscopy*,
NanoScience and Technology,
DOI: 10.1007/978-3-642-01495-6_5, © Springer-Verlag Berlin Heidelberg 2009

contact areas comprising multiple atoms, "dynamic" modes, that is, modes where the tip is oscillated close to the surface, are usually being applied [2,3]. If the tip is scanned in a horizontal raster, the corresponding approach is called *dynamic force microscopy* (DFM) and enables atomic resolution imaging on many different material classes, including metals [4–6], semiconductors [3, 7–10], and insulators [11–14]. Alternatively, dynamic mode operation also allows the measurement of the distance-dependent tip–sample forces ("force distance curves") at specific lattice sites, which is then referred to as *dynamic force spectroscopy* (DFS) [15–19]. Recently, combination of the two abilities has culminated in the chemical identification of surface atoms [20]. Moreover, it has been demonstrated how a systematic acquisition of adjacent force distance curves allows to determine three-dimensional (3D) atomic force fields above the sample surface [21, 22].

The recent growing interest [23–28] in the force field technique stems from several aspects. From the technical perspective, the availability of 3D atomic-scale force field maps facilitates assessing lateral relaxations of the tip–sample contact occurring during the approach as well as experimental artifacts like piezoelectric drift. From the scientific viewpoint, characterization of the vertical force field allows to calculate the potential energy barriers [23] and landscapes [27].

Experimental access to the spatial variation of the potential energy with sublattice resolution is difficult. Conventional techniques [29] rely on the measurement of the dynamic behavior of test adsorbates by, for example, diffusion experiments and field emission techniques [30]. Direct observation of adatom motion with the field ion microscope [31] or the scanning tunneling microscope [32] is possible, but limited to conducting surfaces. Potential energy barriers can be extracted from those experiments (cf. Fig. 5.1a), but the full spatial characterization of the energy landscape remains a challenge. Ideally, one would measure the site-specific variation of the interaction energy between a test molecule and the substrate. A viable technical solution is the measurement of forces between a single atom-terminated sharp asperity and a flat surface, a basic geometry that is naturally instantiated by scanning probe microscopy techniques (Fig. 5.1b).

An added benefit of this approach is that it also recovers lateral atomic forces [22, 24], which has been exploited to determine the lateral force needed to move an atom on a surface [27]. A combination of the simultaneously measured lateral and vertical forces allows to obtain atomic scale force vector fields [33]. Finally, high-precision, low-drift measurements performed at low temperature could successfully probe the 3D force field of graphite with picometer resolution in x, y, and z and piconewton force resolution [34]. From this dense three-dimensional raster, force maps in all directions could be obtained at all locations within the covered space. This lead in particular to atomically resolved true force images in topview perspective rather than just to vertical xz maps.

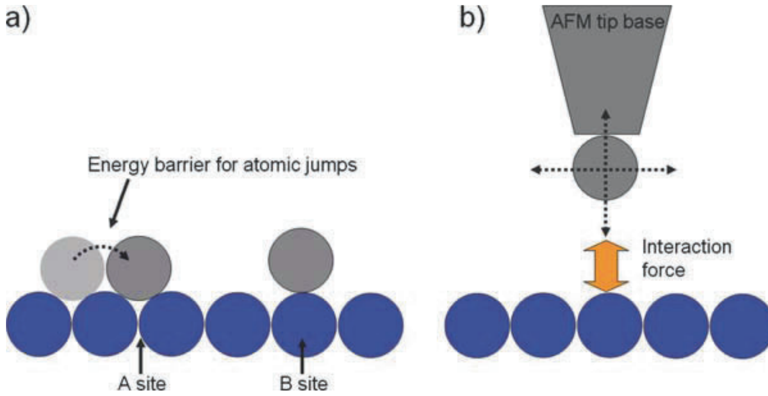

Fig. 5.1. Basic principle of potential energy landscape measurements. **(a)** Surface atoms are adsorbed at lattice sites where the potential energy exhibits a local minimum ("A sites"). During surface diffusion, lateral motion manifests as jumps over the barriers between adjacent energy minima ("B sites"). **(b)** By measuring the interaction forces between a single atom-terminated tip and the surface, the potential energy landscape can be recovered

5.2 Three-Dimensional Force Field Spectroscopy: The Technique

To achieve high resolution, most DFM experiments are performed in ultrahigh vacuum (UHV), where clean surfaces without unwanted adsorbates can be prepared. Because of the high quality factors Q that oscillating AFM cantilevers exhibit in vacuum, it is advantageous to apply the *frequency modulation* (FM) *scheme* introduced by Albrecht et al. [2] to excite the cantilever and detect its motion. In this scheme, the cantilever is "self-oscillated," that is, an electronic feedback system is used to drive the cantilever at its actual resonance frequency f. As f depends on the forces acting on the tip, the difference Δf between f and the eigenfrequency of the undisturbed cantilever f_0 is a measure for the strength of the tip–sample interaction and ultimately the tip–sample distance. This differs from amplitude modulation (AM) based imaging modes [36–38], where the cantilever is externally driven with a fixed driving frequency, which are best used in low-Q conditions such as in air or liquids. In this section, we discuss the experimental set-up of FM-AFM, explain the origin of the detected frequency shift Δf, and present methods that allow tip–sample forces to be recovered from distance-dependent Δf measurements.

5.2.1 Experimental Set-up

Figure 5.2 shows schematically the basic set-up of an atomic force microscope operated in frequency modulation mode. The movement of the cantilever with spring constant c_z is measured by detecting the position of a laser beam

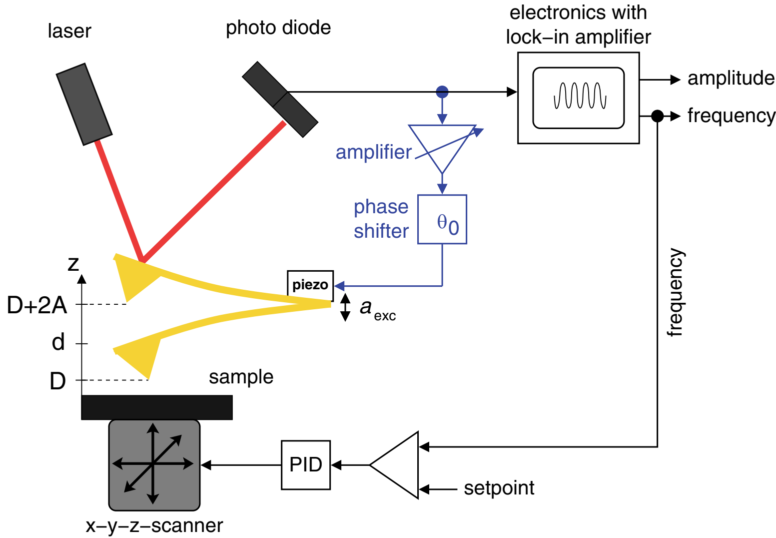

Fig. 5.2. A dynamic force microscope operated in frequency modulation mode, as it is often realized for UHV applications. The key feature is the positive feedback used to "self-oscillate" the cantilever. A laser beam is reflected at the backside of a cantilever that has an integrated sharp tip at its free end. Bending of the cantilever causes a deflection of the reflected beam, which is detected by a photo diode. The resulting signal is subsequently amplified and phase-shifted before it is used to drive the dither piezo exciting the cantilever. The measured quantity is the frequency shift $\Delta f = f - f_0$ caused by the tip–sample interaction, which serves as the feedback signal controlling the tip–sample distance

reflected from the cantilever backside on a photo diode. This signal is then fed into an amplifier featuring the possibility of *automatic gain control* (AGC) [2] and subsequently used to excite a piezo that drives the cantilever. The time delay between the excitation signal and cantilever deflection is adjusted to a phase shift of 90°, leading to an oscillation at resonance. The measured quantity is the *frequency shift* Δf representing the difference between the actual resonance frequency f and the eigenfrequency f_0 of the free cantilever, that is, $\Delta f = f - f_0$. Two different modes have been established: The *constant amplitude* mode [2], where the excitation amplitude a_{exc} of the dither piezo is regulated by the AGC electronics to maintain a constant value of the oscillation amplitude A, and the *constant excitation mode* [39], where a_{exc} is kept constant. In the following, we focus on the constant amplitude mode, which is the dominant mode of operation in most studies published to date.

For imaging, the frequency shift Δf is used to control the tip–sample distance D (distance of closest approach during an oscillation cycle, cf. Fig. 5.2). Thus, if the system's feedback loop regulates the frequency shift to remain on a constant setpoint value, the acquired data reflects planes of constant Δf.

Usually regarded as representing the "topography" of the surface, such planes of constant frequency shift are in reality hard to interpret in terms of physical quantities, as constant Δf does not equal constant force. Even worse, the determination of tip–sample interaction forces solely from DFM images is generally impossible. Therefore, we concentrate in this section on the earlier introduced *dynamic force spectroscopy* (DFS) approach, where the recording of the frequency shift Δf as a function of the tip–sample distance D ("frequency shift curves" or "$\Delta f(D)$ curves") is used to determine the tip–sample force with high resolution.

An example for such measurements is given in Fig 5.3a, where $\Delta f(D)$ curves acquired at different oscillation amplitudes are depicted. All curves

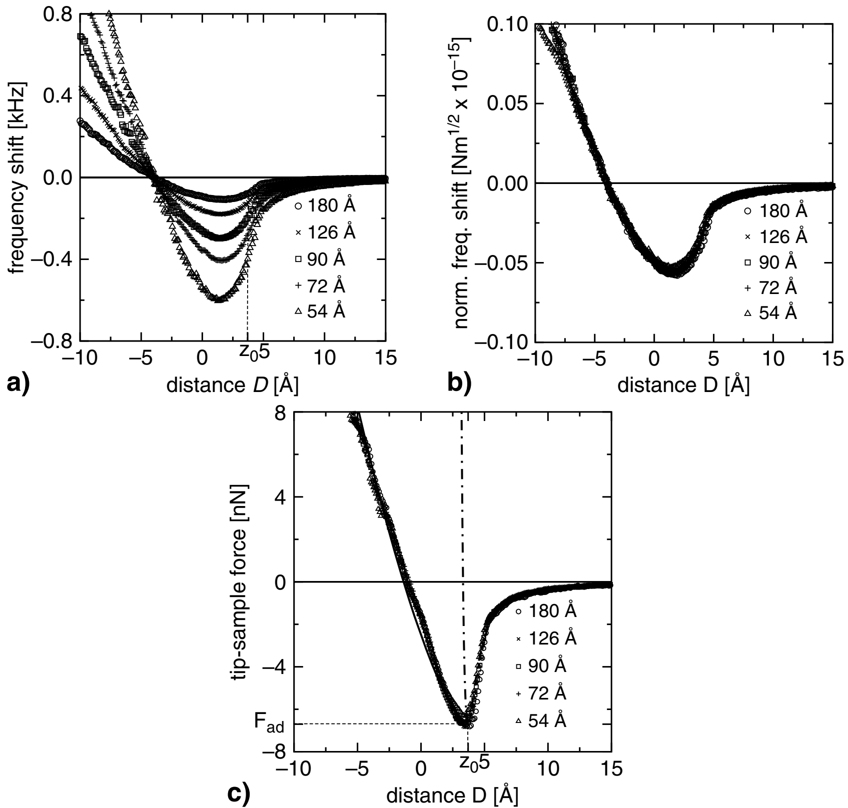

Fig. 5.3. **(a)** Experimental frequency shift vs. distance curves acquired with a silicon tip and a graphite sample for different oscillation amplitudes A (54–180 Å) in UHV at 80 K [40]. The curves are shifted along the D axis to make them comparable. **(b)** Application of (5.5) to the frequency shift curves shown in (**a**). The normalized frequency shift γ is almost identical for all amplitudes. **(c)** Example for the application of dynamic force spectroscopy. The *grey symbols* reflect the tip–sample force as calculated from the experimental data of panel (**a**) using (5.6)

exhibit a similar overall shape, but differ in magnitude depending on the oscillation amplitude A and tip–sample distance D. During the approach of the tip towards the sample surface, the frequency shift decreases and reaches a minimum. With a further reduction of the nearest tip–sample distance, the frequency shift increases again and becomes positive. In the next subsection, we will explain how these data can be used to recover the tip–sample forces.

5.2.2 The Interrelation Between Frequency Shift and Tip–Sample Forces

A quantitative formula for the frequency shift can be obtained by the application of different mathematical treatments based on the assumption that the tip oscillations are still nearly sinusoidal, that is, the tip position z as a function of the time t can be still described by $z(t) := A \cos(2\pi f t)$. Such an approach is justified if the tip–sample interaction force F_{ts} is much smaller than the retracting cantilever force and results in the equation

$$\Delta f = -\frac{f_0^2}{A c_z} \int_0^{1/f_0} F_{\mathrm{ts}}\left[z(t), \dot{z}(t)\right] \cos(2\pi f_0 t)\, \mathrm{d}t \tag{5.1}$$

$$= -\frac{f_0}{\pi A^2 c_z} \int_{-A}^{A} \frac{F_{\rightarrow} + F_{\leftarrow}}{2} \frac{z'}{\sqrt{A^2 - z'^2}}\, \mathrm{d}z', \tag{5.2}$$

where $F_{\rightarrow}$ and $F_{\leftarrow}$ describe the tip–sample force during approach and retraction, respectively. In most cases, these two forces are considered to be equal, that is, hysteresis-free behavior is assumed. Nonetheless, as the frequency shift is a measure of the complete oscillation cycle of the cantilever, it is determined by the averaged tip–sample force $F_{\mathrm{ts}} = (F_{\rightarrow} + F_{\leftarrow})/2$. For completeness, we also give the formula for the calculation of the energy ΔE that is dissipated per oscillation cycle:

$$\Delta E(A) = \pi c_z \left(A\, a_{\mathrm{exc}} - \frac{A^2}{Q} \right). \tag{5.3}$$

For a more detailed derivation of these formulas see, for example, [41–43].

The integral in (5.2) can be further simplified with the assumption that the decay length of the tip–sample interaction is much smaller than the oscillation amplitude. This so-called *large amplitude limit* was first analyzed by Giessibl [41] and is typically reached if the oscillation amplitudes are larger than 5 nm. Because of the assumed large amplitude, the weighting term in the integral (5.2) can be expanded at $z' = -A$ to $\approx -\sqrt{A/2(A+z')}$. By shifting the origin of the z-axis to $z = z' + D + A$ and extending the upper limit of the integral to infinity, the frequency shift can be simplified to [45]

$$\Delta f^{\mathrm{la}} = \frac{1}{\sqrt{2}\pi} \frac{f_0}{c_z A^{3/2}} \int_D^\infty \frac{F_{\mathrm{ts}}(z)}{\sqrt{z-D}}\, \mathrm{d}z. \qquad (5.4)$$

The index "la" highlights the restriction of the formula to the large-amplitude limit.

It is interesting to note that the integral in this equation is independent of the amplitude, as it depends solely on the tip–sample force F_{ts} and the tip–sample distance D. The experimental parameters (c_z, f_0, and A) appear only as prefactors. Therefore, Giessibl [41] defined the *normalized frequency shift*

$$\gamma(z) = \frac{c_z A^{3/2}}{f_0} \Delta f(z), \qquad (5.5)$$

which is a useful quantity if experiments obtained with different oscillation amplitudes and/or cantilevers ought to be compared. Additionally, it allows to elegantly link theoretical calculations with experiments. The validity of (5.5) is nicely demonstrated by its application to the frequency shift curves presented earlier in Fig. 5.3a. As shown in Fig. 5.3b, all curves obtained for different amplitudes collapse into one universal γ curve, which depends only on the actual tip–sample distance D. This scaling law is also useful to calibrate the oscillation amplitude [44].

For typical DFM set-ups, it is straightforward to measure the frequency shift with a fixed oscillation amplitude A as a function of the actual tip–sample distance D. From such an experiment, the calculation of the tip–sample interactions is possible by reversing the integral in (5.4). As shown by Dürig [45], this results in

$$F_{\mathrm{ts}}^{\mathrm{la}}(D) = -\frac{\partial}{\partial D} \int_D^\infty \sqrt{2} \frac{c_z A^{3/2}}{f_0} \frac{\Delta f(z)}{\sqrt{z-D}}\, \mathrm{d}z, \qquad (5.6)$$

allowing a direct calculation of the tip–sample interaction force from frequency shift vs. distance curves.

Application of this formula to the experimental frequency shift curves of Fig. 5.3a is shown in Fig. 5.3c. The obtained force curves are almost identical although obtained with different oscillation amplitudes. The fact that tip–sample forces (or, alternatively, potentials) can be determined with high accuracy and without the discontinuity due to the so-called *jump-to-contact* observed in conventional force curves [46] demonstrates the advantage of dynamic force spectroscopy compared to force–distance curves acquired without oscillating the cantilever.

As (5.4) was derived with the condition that the oscillation amplitude is considerably larger than the decay length of the tip–sample interaction, the same restriction applies to (5.6). However, using more complex algorithms, it is also possible to determine forces from dynamic force spectroscopy experiments without the restriction to large amplitudes. The numerical approach of

Gotsmann et al. [47, 48], for example, works in every regime, as do the semi-analytical methods introduced by Dürig [49], Giessibl [50], and Pfeiffer [51]. The method of Sader and Jarvis [52], finally, results into the formula

$$F_{\mathrm{ts}}(D) = -\frac{\partial}{\partial D}\int_D^\infty \sqrt{2}\frac{c_z A^{3/2}}{f_0}\frac{\Delta f(z)}{\sqrt{z-D}} + 2c_z\frac{\Delta f}{f_0}(z-D) + \frac{c_z}{2}\frac{\Delta f}{f_0}\sqrt{\frac{A}{\pi}}\sqrt{z-D}\,\mathrm{d}z, \tag{5.7}$$

which is easy to implement as an extension of (5.6) because only two additional terms have to be included into the integral. This equation is a good approximation for all amplitudes, but especially helpful if very small amplitudes are used such as it is frequently the case for quartz crystal sensors (see, e.g., [26, 53–55]). Note that the numerical solution of (5.6) and (5.7) is greatly improved if the square-root singularity at the lower integration limit D of the denominator of the first term in the integral is eliminated by a change of variables $z \rightarrow D + t^2$ (see Chap. 4.4 in [56] for a discussion of this issue).

5.2.3 Extending Dynamic Force Spectroscopy to Three Dimensions

The above described concept can be extended to achieve three-dimensional force spectroscopy, that is, the probing and subsequent mapping of the complete force field above the sample surface [21]. As the acquisition of a three-dimensional force field with atomic resolution requires high stability, high lateral resolution, and high force sensitivity, a home-built low-temperature UHV force microscope optimized for atomic scale experiments was used to perform the experiment presented in this Sect. [40, 57]. In particular, low temperatures significantly reduce thermal drift and distortions due to piezo nonlinearities ("piezo creep").

Measurements were performed with a commercial single-crystalline silicon cantilever with an eigenfrequency of $f_0 = 195\,\mathrm{kHz}$ and a force constant of $c_z = 48\,\mathrm{N\,m^{-1}}$. After insertion into vacuum, the tip was first cleaned by argon ion sputtering to remove the silicon oxide layer and subsequently coated with an iron layer of 12.5 nm thickness by thermal evaporation. The sample was a nickel oxide single crystal, which had been cleaved in situ along its (001) plane. Note that due to NiO's rock salt structure, both atomic species (Ni and O) are present at the (001) surface.

To record a three-dimensional force field with atomic resolution on the lateral scale, the following procedure was applied. First, all scanning parameters, in particular the frequency shift Δf, were optimized to obtain atomic resolution during regular "topographic" imaging (acquisition of a plane of constant frequency shift). Immediately after scanning such an image, two times $32 \times 32 \times 256$ frequency shift values were captured in a box of $1 \times 1 \times 10\,\mathrm{nm}^3$ above the same scan area. The time needed to record this data set

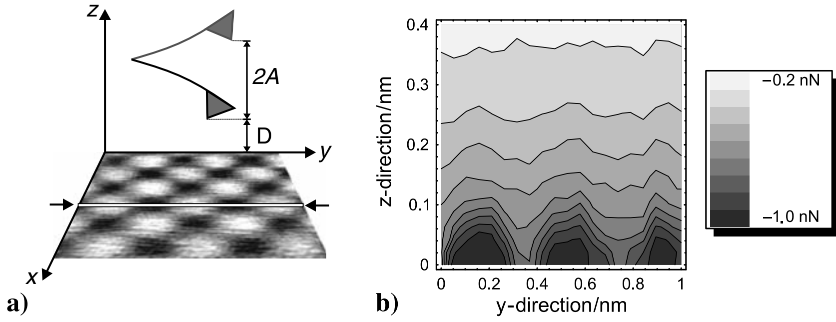

Fig. 5.4. The principle of 3D force spectroscopy, illustrated with the example of NiO (001). (**a**) The cantilever oscillates near the sample surface and measures the frequency shift at all locations defined by a dense raster grid inside an xyz box. The surface topography of the NiO sample, as obtained immediately before recording the spectroscopy field, is displayed in a perspective representation (image size: $10 \times 10\,\text{Å}^2$). (**b**) The reconstructed force field of NiO (001) taken along the line indicated in (**a**). The positions of the atoms are clearly visible

was about 80 min. Directly after recording this data array, a control image using the same scanning parameters in the constant frequency shift mode was acquired (see [22, 58] for details).

The data acquisition technique for the spectroscopy data array is schematically illustrated in Fig. 5.4a. A grid of equidistant points was defined at the scan area of $1 \times 1\,\text{nm}^2$. Using a specialized software routine, the procedure started in the lower left corner and continued line-by-line until the upper right corner was reached. At each grid position, the cantilever was first stabilized at a frequency shift of $\Delta f = -32.2\,\text{Hz}$, which had been set to obtain atomic resolution in Fig. 5.4a. The corresponding absolute z value was recorded to define an absolute z scaling. The cantilever was subsequently retracted by 9.80 nm from that point before it was approached by 9.93 nm ("trace") and retracted again ("retrace"). Consequently, the oscillating tip came nominally 130 pm closer to the sample surface at its point of closest approach during the recording of the topographic image of Fig. 5.4a. During both trace and retrace, 256 frequency shift values were recorded. After that, the cantilever was stabilized and moved to the next scan position, where the recording procedure was repeated. As a result, one obtains two $\Delta f(x, y, z)$ data arrays with $32 \times 32 \times 256$ frequency shift values, with each $\Delta f(x, y, z)$ array consisting of 1,024 individual $\Delta f(z)$ curves.

Using the method introduced earlier, it is now straightforward to determine the tip–sample interaction force F_{ts} from the $\Delta f(z)$-curves, that is, the $\Delta f(x, y, z)$ data array can be transformed into a $F_{\text{ts}}(x, y, z)$ force field. Figure 5.4b displays a two-dimensional cut along one scan line of the complete three-dimensional force field $F_{\text{ts}}(x, y, z)$ during retraction. This corresponds nearly to the crystallographic [100] direction. As the tip–sample distance is

stabilized at the same frequency shift $\Delta f = -32.2\,\mathrm{Hz}$ at every image point, the minimum tip–sample distance between the tip and an imaginary flat plane parallel to the surface is different at every image point. Therefore, the z scale of all curves within the line were adjusted with the recorded z position during stabilization at each image point. The lateral distances between the maxima in the force map are identical to those in Fig. 5.4a, that is, atomic resolution has been obtained close to the sample surface.

Considering the measurement procedure, it is clear that thermal and electronic drift can significantly distort the data. In fact, a detailed analysis [22,58] of the data set revealed that there was lateral drift of about one lattice constant in [110] direction during the experiment. This drift rate can be attributed to a slight temperature increase of $\approx 4\,\mathrm{mK\,h^{-1}}$ due to the slowly decreasing helium level in the bath cryostat. Moreover, electronic drift in the analogue electronics measuring the frequency shift resulted into a continuous drift of Δf of $-1.1\,\mathrm{Hz\,h^{-1}}$. Nonetheless, as the time needed to record a single $\Delta f(z)$ curve ($\approx 2.4\,\mathrm{s}$) or a complete scan line of curves ($\approx 150\,\mathrm{s}$ per line) is comparatively short, the amount of drift within one line is negligible.

5.3 Force Field Spectroscopy on Ionic Crystals

5.3.1 Force Fields and Energy Dissipation on NaCl

As shown earlier, the systematic mapping of tip–sample forces as a function of the tip position in three dimensions requires great experimental efforts. Most importantly, drift rates must be exceptionally low if a large number of individual force curves should be collected within a single experiment, which usually is only possible with intricate AFM set-ups operating at low temperature. We will show in this section that the 3D force spectroscopy technique can nevertheless be employed at room temperature with atomic precision, thus opening up its possibilities to a large community of scientists and engineers. Prerequisite for a successful application, however, is that the number of curves collected overall is relatively low so that the measurement is completed on a time scale faster than typical drift rates. Here we focus on ionic crystals and in particular NaCl, as single crystals of this material proved to be well suited for atomic-scale investigations under ultrahigh vacuum conditions [59, 60].

Experiments were performed with an ultrahigh vacuum AFM operated at room temperature [23]. Prior to the collection of the force curves, the tip was intentionally brought several times into intimate contact with the surface. This procedure most likely resulted in a tip with an NaCl cluster termination [16]. An atomic resolution topographic image of the NaCl surface is shown in Fig. 5.5. On a surface area of $2 \times 2\,\mathrm{nm}^2$, 3D force mapping was performed as described in the previous section by measuring the force-induced frequency shift as a function of relative tip–sample distance z on a predefined

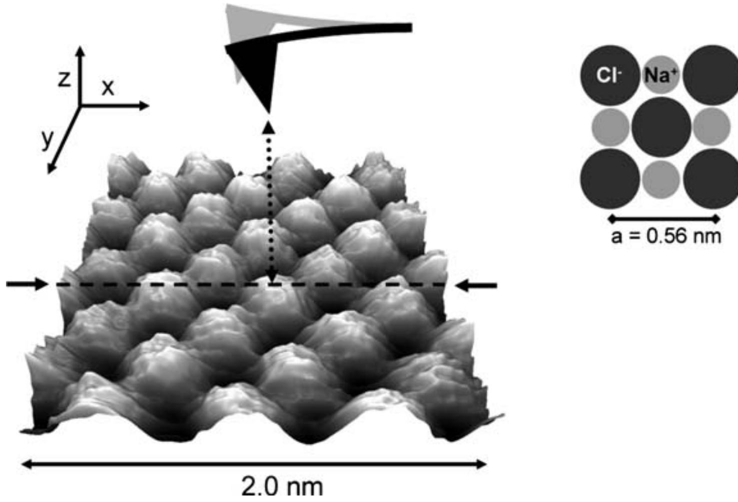

Fig. 5.5. Grayscale height image showing the surface topography (raw data) at a constant frequency shift of $\Delta f = -138\,\mathrm{Hz}$ obtained in conventional scan mode of NC-AFM on NaCl (100) in ultrahigh vacuum with an oscillation amplitude of $A = 4.5\,\mathrm{nm}$. For the subsequent 3D spectroscopy, the frequency shift was acquired as a function of tip–sample distance z for 34 points along the x direction and for 10 equidistant y positions. The force map analysis described below was performed for a y position along the *dashed line*. Inset in the upper right corner: The NaCl (001) surface

grid, consisting of 34 equidistant points along the x axis for 10 equidistant positions along the y axis.

Figure 5.6a shows the resulting raw data image of the frequency shift as a function of the vertical tip–sample distance and the lateral x position along the dashed line shown in Fig. 5.5, thus representing one slice in real space. The circular areas at around $z = 0.22\,\mathrm{nm}$ indicate the molecular lattice sites, separated by the NaCl lattice constant of 0.56 nm. For further reference, we distinguish the two atomic sites in the center of the circles and in between the circles, which correspond to the lattice positions of the two ionic species of NaCl, by referring to them as A and B sites, respectively (cf. Fig. 5.6).

Simultaneously with the frequency shift, the dissipated energy was measured (see Fig. 5.6 b), which shows atomic-scale contrast only at distances of $z < 0.2\,\mathrm{nm}$. As stable feedback operation during scanning is usually restricted to the parts of the frequency shift curves with positive slope (i.e., the frequency shift becomes more positive with increasing tip-sample distance), atomic contrast in the dissipation develops here only far beyond the point of stable scan operation. This shows that interpretation of atomic-scale contrast in energy dissipation images must carefully consider the influence of the distance control loop.

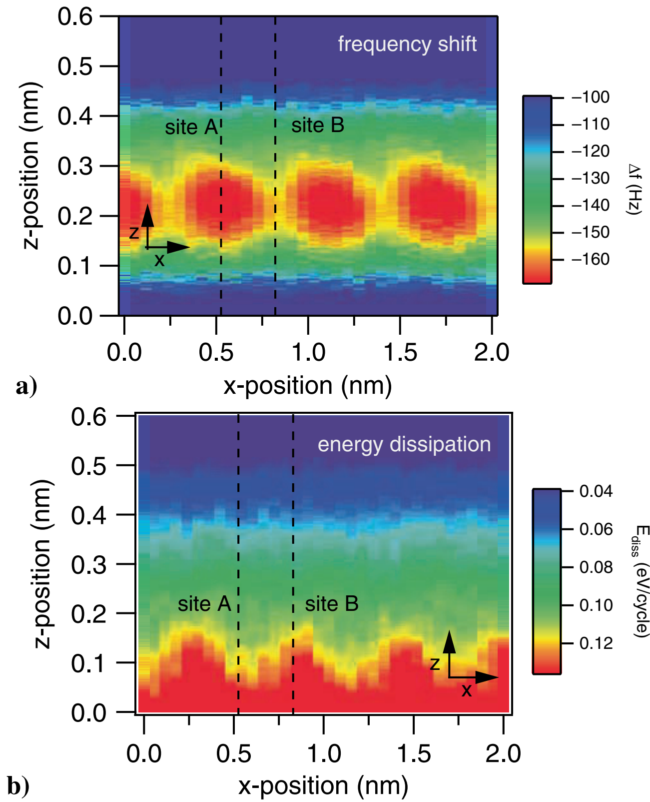

Fig. 5.6. (a) Plot showing the measured frequency shift Δf (unprocessed raw data) as a function of both the horizontal position along the x axis as well as the relative tip–sample separation z. The image comprises 34 spectroscopy curves, each covering a range of $\Delta z = 1.1$ nm. Long-range force interactions were measured up to distances of $z = 3$ nm. **(b)** Simultaneously acquired "dissipation map," featuring the energy that is dissipated per oscillation cycle

The tip–sample interaction potential energy map calculated from the frequency shift curves [45] is presented in Fig. 5.7a. The image shows the exact position and quantitative values for the potential energy minima, which are not only relevant for surface diffusion processes [29, 61], but also for atomic-scale friction models. According to the Prandtl–Tomlinson model [62, 63], the tip is trapped in the local energy minima of a sinusoidal interaction potential corresponding to site A. Upon lateral movement of the tip base, the tip apex will move sidewards either in a discontinuous stick-slip motion or by smoothly following the potential profile; which motion will be realized depends mainly on the ratio between the stiffness of the tip–surface contact and the height of the energy barrier [60].

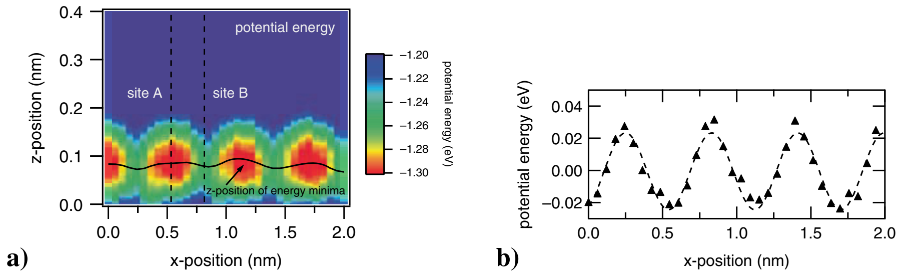

Fig. 5.7. (a) Image of the tip–sample potential energy as a function of horizontal and vertical tip position. The *solid black line* indicates the z positions of the potential energy minima. **(b)** Plot of the experimental values of the potential energy (*triangles*) collected along the black line in (**a**), recalibrated so that the average energy is zero. Their values can be approximated by a sinusoidal curve (*dashed line*), yielding an effective potential energy barrier of $\Delta E_{\mathrm{barrier}} = 48\,\mathrm{meV}$

The equilibrium z position of the tip atom is in the minimum of the individual $E(z)$ curves, indicated by the black solid line in Fig. 5.7a. Those minima are almost independent of the x position of the tip, showing only a small corrugation of 10 pm. Considering a lateral displacement of the tip base, the tip apex atom would be dragged along the potential minima (Fig. 5.8) and experience the strongly varying potential energy depicted in Fig. 5.7b. From this energy profile, we can directly determine the effective energy barrier $\Delta E_{\mathrm{barrier}} = 48\,\mathrm{meV}$, which is the fundamental parameter in atomic friction models [62–65]. From atomic-scale friction experiments, effective energy barriers in the range from 0.1 to 0.5 eV have been reported on NaCl crystals [60] depending on the applied effective load. The above value represents the potential energy barrier experienced by a single atom terminated tip apex, as opposed to the multiatom contacts typically encountered in conventional friction force experiments. Interestingly, the shape of the potential energy barrier in Fig. 5.7b is well described by a sinusoidal curve (*dashed line*), which is often assumed in simple atomic friction models, but has been questioned lately [66] in the analysis of friction experiments on mica surfaces.

Those energy barriers are comparable to typical diffusion energy barriers determined from the dynamics of surface adsorbates [29, 61]. The experimentally determined effective energy barrier suggests a considerable mobility of adsorbates on an NaCl surface at room temperature, which is in fact observed experimentally. However, one has to keep in mind that the tip atom is connected to a large tip base, which might influence the overall mechanical behavior of the contact. In fact, evidence for the complex mechanical behavior of the investigated single-atom contact can be derived from the following analysis of the tip–sample forces.

For a more detailed analysis of the interaction forces acting in z direction, we turn to Fig. 5.9a, which shows the vertical force map calculated from

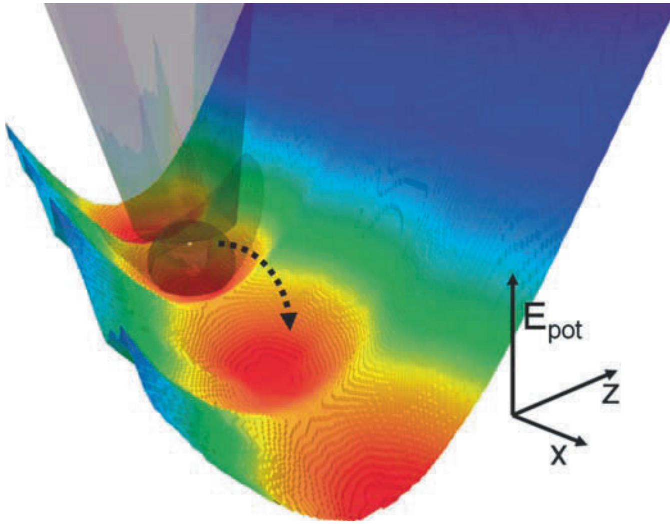

Fig. 5.8. Figure showing a 3D representation of the interaction energy map, visualizing the local energy minima. The last tip atom, which would jump from minimum to minimum during a lateral sliding movement along the x axis (*dashed arrow*), is represented by a *grey sphere*

the potential energy map by taking the partial derivative $F_{\mathrm{vertical}}(z,x) = -\frac{\partial E(z,x)}{\partial z}$. The onset of repulsive forces is characterized by a minimum in the force curves [67], emphasized by the black circles in the force map. In contrast to the energy map, the force map shows two distinct minima per lattice constant, corresponding to the two ionic species in the NaCl crystal. From the potential energy map we can also deduce the lateral force map by taking the partial derivative with respect to the horizontal axis $F_{\mathrm{lateral}}(z,x) = -\frac{\partial E(z,x)}{\partial x}$. The resulting force map in Fig. 5.9 b shows no significant lateral forces for tip–sample distances larger than $z = 0.37\,\mathrm{nm}$. Below this distance, the lateral forces reach values up to 40 pN in both directions, pointing towards the energy minima.

In Fig. 5.10a, the vertical (i.e., normal) forces are shown as a function of tip–sample distance above site A and site B. While the repulsive force part of curve A shows a monotonically increasing characteristic with an effective contact stiffness of $3.2\,\mathrm{Nm}^{-1}$, force curve B shows a transition point at $F_{\mathrm{trans}} = -0.34\,\mathrm{nN}$, where the curve is horizontally shifted. After this transition point curves A and B become almost identical. This transition is reminiscent of load relaxations due to defect creation in a subsurface volume during nanoindentation experiments [68, 69]. In this case, the mechanical relaxation most likely takes place at the tip apex. Without an additional compliant mechanism, the repulsive part of the force curve B would continuously increase, as for instance the dashed curve shows, which we refer to as the unrelaxed site B

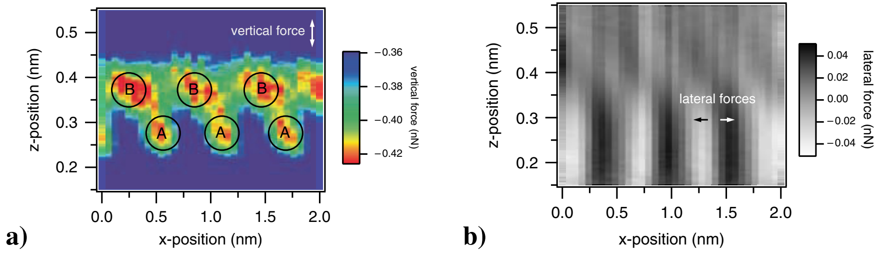

Fig. 5.9. (a) Image showing the force acting in the vertical z direction (i.e., the normal force) as a function of both the x and z position of the tip. The onset of repulsive forces is at different vertical and horizontal positions for the two ionic species (*black circles* at the site A and site B positions). **(b)** The lateral forces as a function of x and z position of the tip derived from the potential energy diagram. The maximum lateral forces reach values of 40 pN

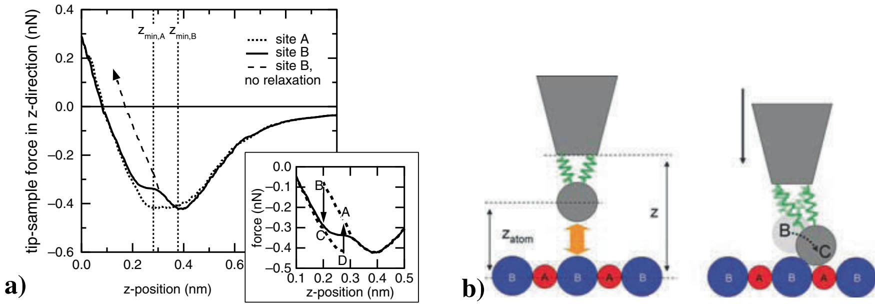

Fig. 5.10. (a) Normal forces as a function of relative tip–sample distance z taken at the x positions labeled A and B. The *dashed curve* was constructed for the purpose of demonstration from the left part ($z < 0.2\,\text{nm}$) of the solid curve, shifted by 0.9 nm to the right. The inset shows the experimental site B force (*solid*) compared with the force curves expected from a double well potential energy model (*dotted*), indicating the resulting hysteresis due to different forces during the forward and backward movement of the oscillating tip. **(b)** *Left*: Tip atom approaching site B of the surface. *Right*: Beyond a certain distance the tip atom relaxes towards site A, which is represented by the sudden force drop from B to C in the inset of (**a**)

curve. As the precise atomic configuration of the tip and the sample remains unchanged, as evidenced by the reproducibility of the subsequent force curves, the mechanical relaxation at the tip–sample interface must be fully reversible.

A simple model of the single atom contact is used to rationalize this observation: the tip apex is modeled by a stiff tip base with one atom connected by effective vertical and horizontal springs, while the surface consists of a periodic arrangement of the two ionic species, which are considered infinitely stiff (see Fig. 5.10b). The mechanical stiffness of the tip base was calculated by a finite element simulation using FEMlab, where the tip was approximated by a silicon cone of height 200 nm with an apex radius of $R = 4\,\text{nm}$ and a half

opening angle of 10°. The resulting compliances were $c_{\mathrm{vertical}} = 37\,\mathrm{N\,m^{-1}}$ and $c_{\mathrm{lateral}} = 8.8\,\mathrm{N\,m^{-1}}$, and therefore indicating that the tip base can be regarded as stiff in comparison to the experimentally observed force gradients for the vertical and lateral tip–sample interaction.

When approaching the tip above site A, the repulsive forces will compress mainly the effective vertical spring. Above site B, however, the lateral compliance of the tip apex atom will lead to a mechanical relaxation of the tip apex atom away from site B towards site A, which occurs at the transition force F_{trans}. The emergence of a tip atom relaxation also explains the different image contrast in the energy and force maps, yielding one and two minima per lattice constant, respectively. The minima in the energy map represent the total energy minimum, taking into account the mechanical tip atom relaxation. The force minima, on the other hand, are characterized by the onset of repulsive forces, where the relaxation has not yet occurred, therefore clearly indicating separate minima at both sublattice sites.

Because the tip is oscillating in DFS, the measured forces are an average of the forces acting during the forward and backward movement (cf. Sect. 5.2.2). During the forward cycle, the force will follow the dashed curve until a threshold force is reached. Then the curve will drop vertically to the shifted curve, as the atom suddenly relaxes to its new position while the tip base position stays constant. This behavior is sketched in the inset of Fig. 5.10a (dotted curve) by the vertical transition from B to C. During the retraction cycle, the tip atom will jump back to the initial force curve at a different position as before (from D to A), and a hysteresis develops.

The best agreement for the instability position predicted by the energy diagram with the experimentally observed transition point B to C is obtained by adjusting the only left unknown parameter $c_{\mathrm{lateral}} = 0.4 \pm 0.1\,\mathrm{N\,m^{-1}}$. This value coincides with a typical lateral contact stiffness obtained from atomic scale friction experiments [60]. A comparison of the effective experimental force curve, which is inherently an average of the forward and backward movement of the tip during the oscillation cycle, and the corresponding predicted hysteresis loop is shown in the inset of Fig. 5.10a. This should leave a significant fingerprint in the energy dissipation [70, 71]. The dissipation map in Fig. 5.6b shows enhanced values exactly at the B sites, with contrast developing beyond the transition point ($z < 0.2\,\mathrm{nm}$), in excellent agreement with the simple model. The above analysis demonstrates that force field spectroscopy with simultaneous measurement of conservative and dissipative is a powerful technique to understand mechanical relaxation processes at the atomic level.

5.3.2 Force Vector Fields on KBr

We have seen above that not only normal forces but also the forces acting horizontally along the specific direction that the xz map is following can be derived. By superposition of theses vertical and lateral atomic force fields, a vector field can be constructed that represents the magnitude and direction of

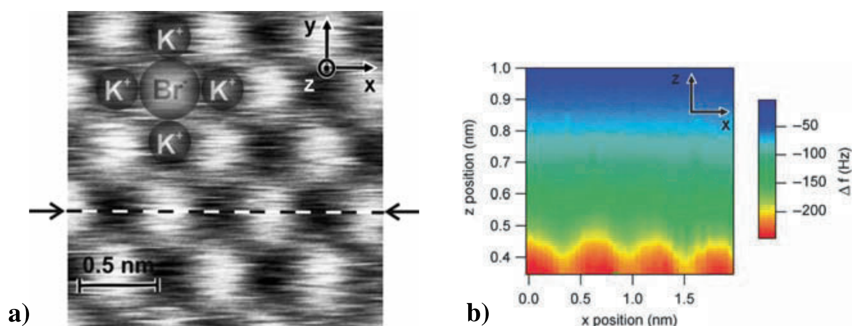

Fig. 5.11. (a) Surface topography of a KBr (001) sample. The overlay indicates the positions of K^+ and Br^- surface ions as they have been determined by the force field analysis. The *dashed line* marks a representative y position along the sites of topography maxima at which the force field measurements were performed. **(b)** Measured frequency shift (unprocessed raw data) displayed as a function of the relative tip–sample distance z and the horizontal tip position along the x axis. Each of the 38 individual Δf curves comprised in this plot covers a distance of 0.65 nm in z direction

forces acting between the terminating tip apex atom and the surface atoms as a function of their relative position in real space. This ability is illustrated in this section with the example of a KBr (001) single crystal that was cleaved in situ to assure an atomically clean surface and heated to 420 K for 60 min to equilibrate residual charges. The measurements were carried out with the same system as described earlier.

Figure 5.11a shows an atomically resolved area of $2 \times 2\,\text{nm}^2$ on the KBr (001) surface. To obtain the vertical force field, the frequency shift was measured as a function of the relative tip–sample distance on a grid of 38 equally spaced points in the x and 6 equidistant positions in the y direction. Before and after each individual frequency shift vs. distance measurement, the feedback loop (keeping the frequency shift constant by adjusting the tip–sample distance) was switched on to stabilize the system at a reference tip–sample distance for 104 ms. The frequency shift was measured over a range of 1.1925 nm in steps of 0.0025 nm with a time constant of 5.12 ms for each data point. Together with the time needed for feedback stabilization, this resulted in a total acquisition time of 1.7 min per x-z slice. Positional drift during these room temperature measurements was $\approx 0.001\,\text{nm}\,\text{s}^{-1}$, which is negligible in the z direction, as the z position is stabilized by the feedback every 2.44 s. In lateral direction, this drift amounts to an uncertainty in the y position of one slice of 0.1 nm.

A two-dimensional map shows the unprocessed frequency–distance data as a function of lateral and vertical tip position along the corrugation maxima (Fig. 5.11b). The individual force curves, which were calculated from the frequency shift curves, in Fig. 5.12a contain the site-specific forces that are

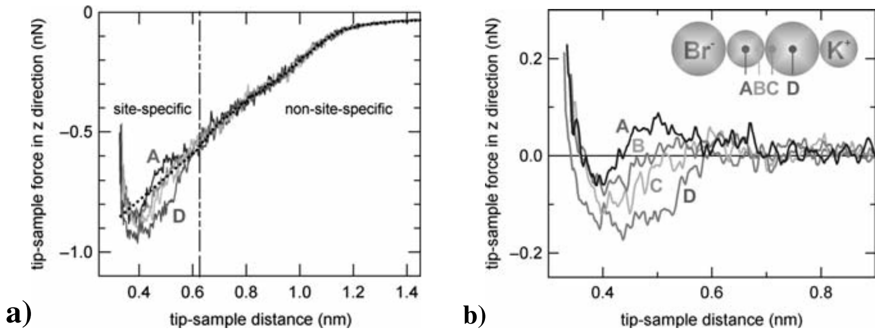

Fig. 5.12. (**a**) Experimental force curves recorded on KBr (001) along a line between the positions of the two ionic species; the exact lattice positions are labeled A–D in the inset in (**b**). The *black dotted curve* represents the average over all force curves with a linear extrapolation into the regime of site specific behavior. (**b**) Site-specific part of the short-range regime for the same force curves as in (**a**), where the nonsite-specific contributions have been subtracted

responsible for the atomic scale image contrast as well as site-independent long range forces. The latter typically is a superposition of van der Waals and electrostatic forces, whereas the site-specific part is dominated by short-range chemical binding forces. The forces on different lattice sites labeled A–D along a line between the two ionic species in Fig. 5.12a match within the noise up to $z = 0.62\,\text{nm}$, while site-specific differences occur in the range $0.30\,\text{nm} < z < 0.62\,\text{nm}$. The precise force law for the nonsite-specific force contribution is unknown, but those forces are sufficiently well approximated by a line fit for $0.62\,\text{nm} < z < 1.10\,\text{nm}$, which can be extrapolated into the site-specific regime. This first-order approximation is justified as any long-range background force is expected to show a continuous curve shape and should not contribute to atomic scale features. Figure 5.12b shows the resulting short range forces, which was derived by subtracting the dotted curve (i.e., nonsite-specific forces) from the experimental force curves.

The corresponding site-specific vertical force field is illustrated in Fig. 5.13a, which is based on 23 adjacent force curves. The areas of attractive forces up to $F = -0.18\,\text{nN}$ at the x position of one ionic species on the surface show a roughly triangular shape in the force map. In between the attractive force areas, we find small circularly shaped areas with repulsive forces up to $F = 0.07\,\text{nN}$ around $z = 0.50\,\text{nm}$ at the location of the oppositely charged surface ion. In fact, the direct comparison of these experimental force maps with simulated force maps revealed excellent quantitative agreement for the case of a K^+ terminated tip [33].

In a next step, the lateral tip–sample forces were calculated from the force fields by integration in z direction and subsequent differentiation in x direction [22, 24]. Combining the vertical and lateral forces allows one to extract the corresponding force vectors in the x-z plane. Those vectors quantify

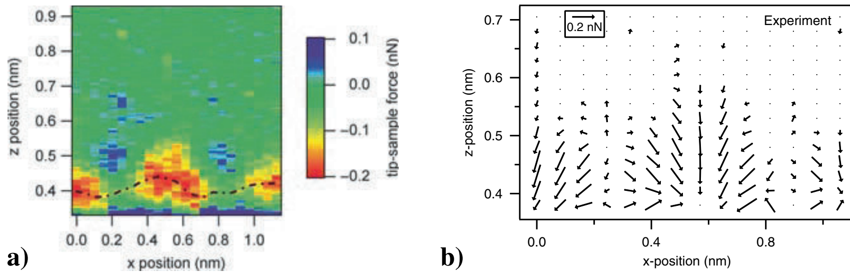

Fig. 5.13. (**a**) The two-dimensional map of the site-specific vertical tip–sample forces. (**b**) Atomic scale force vector field on KBr (001) determined from the AFM experiment. Individual arrow length and orientation represents the magnitude and direction of the site-specific force experienced by the atomically sharp tip at the respective position in the x-z plane

magnitude and direction of the site-specific force experienced by an atomically sharp tip at the respective position in the x-z plane above the surface. Figure 5.13b shows the resulting experimental force vector field. The force vector maps show that approaching the tip directly above a K^+ ion leads to no lateral forces, whereas the lateral forces are strongest at the position between the K^+ and the Br^- sample ions, always pointing towards the Br^- ion. This is a direct consequence of the local energy minimum of the tip–sample system at the Br^- sites.

5.4 True 3D Force Field Spectroscopy on Graphite

We have seen in the previous chapter that even though impressive results can be obtained with 3D force field spectroscopy performed at room temperature, the number of force curves that can practically be acquired within a single experiment is limited to a couple of hundred individual curves due to thermal drift. Therefore, 3D resolution in such measurements is usually poor, and experimentalist focus on collecting individual xz planes as shown above rather than full dense $(x, y, z, F_{\mathrm{ts}})$ data sets. However, xy force maps featuring directly tip–sample interaction forces or potential energies instead of the "planes of constant frequency shift" that regular "topographic" NC-AFM imaging delivers would be highly beneficial for many applications. This is because constant-frequency shift images are difficult to interpret, while force and energy fields can be directly understood and compared to theory.

In this section, we are reporting results that comprise 256 × 119 pixels laterally, equivalent to the acquisition of 30,464 $\Delta f(z)$ curves. The original data presented in this section has been published in [34]. Overall, one pixel was recorded every 6.8 pm laterally and ≈2 pm vertically, resulting in a covered xy area of 1,750 × 810 pm^2. Key for the successful acquisition of this data in such a dense grid, which took 40 h to complete, were two main components:

first, the use of a home-built high-resolution, low drift microscope operating in ultrahigh vacuum ($p \approx 4 \times 10^{-11}$ mbar) and at low temperatures ($T \approx 6$ K), which showed drift rates as low as one unit cell per day once in equilibrium [26]. Second, by carefully characterizing the thermal drift during data acquisition, we were able to remove the remaining drift after the data acquisition had been completed. This resulted in a virtually drift-free array of $(x, y, z, F_{\mathrm{ts}})$ data despite much higher pixel density and much longer measurement times than demonstrated in the above sections. In addition, the potential energy E, the energy dissipated during an individual oscillatory cycle E_{diss}, and the tunneling current I have been recorded simultaneously. As a consequence, cuts along *any plane* within the covered 3D space (including xy planes) can be produced, delivering high-resolution maps of F_{ts}, E, E_{diss}, and I from any angle. Details on the data acquisition and analysis procedures have been described in [35].

The experiments presented here were performed on highly oriented pyrolytic graphite (HOPG). The sample was cleaved in air, transferred into vacuum, and heated to 450 K for 30 min before being moved into the microscope. The microscope's force sensor was a quartz tuning fork in the so-called Q-plus configuration [53], featuring an eigenfrequency and quality factor of f_0=29,023 Hz and $Q\approx$21,000, respectively. Oscillation amplitude was 0.23 nm.

Visualizations of the full 3D data sets for the normal force (a), potential energy (b), and energy dissipated during an individual oscillation cycle (c) are displayed in Fig. 5.14. The z axis was arbitrarily calibrated to be zero at the height given by the lowest plane that has been recorded during data acquisition, and so z values do not directly coincide with an absolute distance from the surface. The arrays shown are cut off at about 0.3 nm height although the full sets cover 3.5 nm in that direction, as the data does not include any lateral contrast for larger distances. To increase the contrast for the eye, the average force/energy in each plane of constant z was subtracted for all diagrams, rendering the atomic-scale contrast clearly visible. Note that the force corrugation caused by the atoms, for example, is only about 3% of the total force acting on the tip (the maximum attractive force measured between tip and sample was about -2.34 nN at the distance of closest approach).

Having full 3D data available, it is possible to produce actual force images on the atomic scale. Figure 5.15a, b show force images at 7 pm (a) and 44 pm (b) above the plane of closest approach. With these images and the dozens of images that can be generated at intermediate heights, it can be studied how the contrast changes with distance, giving valuable insight into the strength of local interactions. By an analysis presented elsewhere [34], the positions of all atoms in the lattice can be determined, as indicated by the hexagon in Fig. 5.15a, b.

Other useful information can be drawn from vertical force maps, which illustrate how the force field of individual atoms extends into vacuum. Figures 5.15c–e show three examples of such plots, which have been recorded within the area marked by the grey rectangle in Fig. 5.15a. It is especially

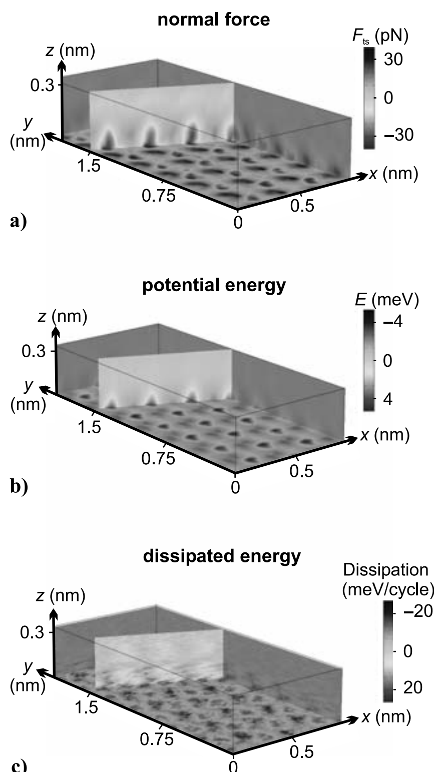

Fig. 5.14. Representations of the three-dimensional data sets for the normal tip–sample interaction force F_{ts} **(a)**, the tip–sample potential energy E **(b)**, and the energy dissipated per cycle E_{diss}**(c)** recorded on graphite. The average force/energy was removed in each plane of constant z to make the respective atomic-scale contrasts visible. To highlight the fact that full 3D data is available and cuts in any direction can be produced, a plane normal to the surface along a row of maxima has been included in the figure. In this projection, it can be seen how the force and energy fields extend into vacuum

interesting to note that in Fig. 5.15c, the positions of the force maxima are changing with the height. However, this is not visible in the other cuts.

The ability to collect (x, y, z, F_{ts}) arrays in such a dense raster and virtually drift-free opens the door to analyze more effects on the atomic scale than ever before. It might find application in all fields of science where site-specific atomic-scale information on interaction forces and potential energies is important, such as chemical imaging, catalysis, thin film growth, device fabrication, or nanotribology. Not only height-dependent changes on the atomic scale can be made visible, but also changes between "regular" tips and tips that are functionalized with specific atomic species of molecules to show enhanced reactivity with the surface. Such information might be very helpful as input for improving theoretical models and to verify numerical analysis.

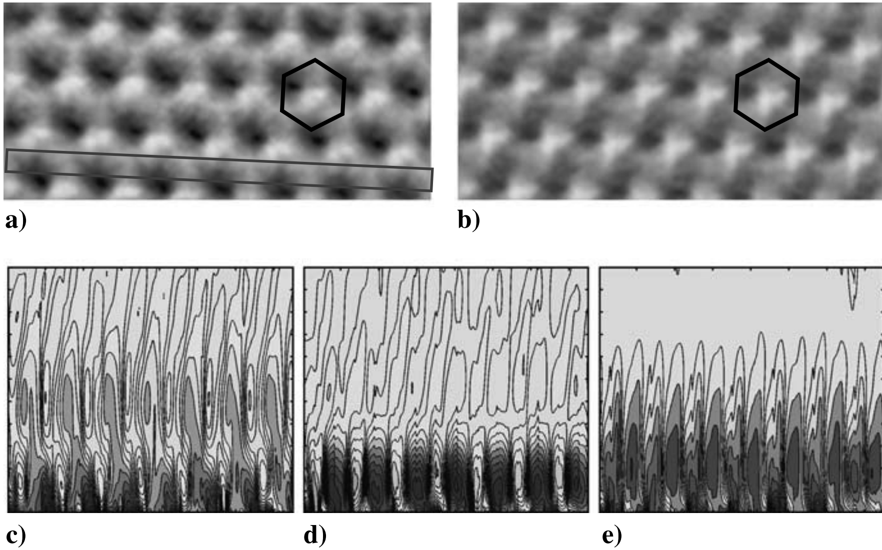

Fig. 5.15. Different slices of the force data set shown in Fig. 5.14a. **(a)** and **(b)**: Force images for different heights above the surface: **(a)** 7 pm above lowest imaged plane, **(b)** 44 pm above lowest imaged plane. Image sizes are 1,750 pm × 810 nm. In contrast to conventional "topographical" NC-AFM images, which show planes of constant frequency shift, the contrast in the images is given by the actual force acting between tip and sample at the specific height indicated above. The corrugation in (**a**) is about 60 pN and in (**b**) about 40 pN. **(c)**–**(e)**: Vertical force maps projected (roughly) onto the xz plane taken at three different locations within the *grey rectangle* given in (**a**). Note that the precise orientation relative to the lattice as given by the rectangle includes a rotation by about 15° relative to the xz plane to be in line with rows of force maxima. To enhance contrast, the average force was removed for each height z as described earlier for Fig. 5.14a. Map sizes are x by z 1,750 × 220 pm^2 each, and the force scale spreads from −30 to +30 pN

Acknowledgements

The authors thank all colleagues who contributed to this work with their experimental results: Wolf Allers, Shenja Langkat, and Alexander Schwarz (University of Hamburg), Domenique Weiner and Kai Ruschmeier (University of Münster), as well as Boris J. Albers, Mehmet Z. Baykara, Todd C. Schwendemann, and Nicolas Pilet (Yale University). A. S. acknowledges financial support from the Deutsche Forschungsgemeinschaft (DFG SCHI 619/1-2 and TRR 61 project B7), U. S. from the National Science Foundation (grant No. MRSEC DMR 0520495), the Department of Energy (grant No. DE-FG02-06ER15834), and the Petroleum Research Fund (grant No. 42259-AC5).

References

1. G. Binnig, C.F. Quate, C. Gerber, Phys. Rev. Lett. **56**, 930 (1986)
2. T.R. Albrecht, P. Grütter, D. Horne, D. Rugar, J. Appl. Phys. **69**, 668 (1991)
3. F.J. Giessibl, Science **267**, 68 (1995)
4. S. Orisaka, T. Minobe, T. Uchihashi, Y. Sugawara, S. Morita, Appl. Surf. Sci. **140**, 243 (1999)
5. C. Loppacher, M. Bammerlin, M. Guggisberg, S. Schär, R. Bennewitz, A. Baratoff, E. Meyer, H.-J. Güntherodt, Phys. Rev. B **62**, 16944 (2000)
6. V. Caciuc, H. Hölscher, D. Weiner, H. Fuchs, A. Schirmeisen, Phys. Rev. B **77**, 045411 (2008)
7. S. Kitamura, M. Iwatsuki, Jpn. J. Appl. Phys. **34**, L145 (1995)
8. H. Ueyama, M. Ohta, Y. Sugawara, S. Morita, Jpn. J. Appl. Phys. L **34**, 1086 (1995)
9. Y. Sugawara, M. Ohta, H. Ueyama, S. Morita, Science **270** 1646 (1995)
10. A. Schwarz, W. Allers, U.D. Schwarz, R. Wiesendanger, Phys. Rev. B **61**, 2837 (2008)
11. M. Bammerlin, R. Lüthi, E. Meyer, A. Baratoff, J. Lü, M. Guggisberg, C. Gerber, L. Howald, H.-J. Güntherodt, Probe Microsc. **1**, 3 (1997)
12. W. Allers, A. Schwarz, U.D. Schwarz, R. Wiesendanger, Europhys. Lett. **48**, 276 (1999)
13. C. Barth, M. Reichling, Nature **414**, 54 (2001)
14. R. Hoffmann, M.A. Lantz, H.J. Hug, P.J.A. van Schendel, P. Kappenberger, S. Martin, A. Martin, A. Baratoff, H.-J. Güntherodt, Phys. Rev. B **67**, 085402 (2003)
15. M.A. Lantz, H. Hug, R. Hoffmann, P.J.A. van Schendel, P. Kappenberger, S. Martin, A. Baratoff, H.-J. Güntherodt, Science **291**, 2580 (2001)
16. R. Hoffmann, L.N. Kantorovich, A. Baratoff, H.J. Hug, H.-J. Güntherodt, Phys. Rev. Lett. **92**, 146103 (2004)
17. M. Abe, Y. Sugimoto, O. Custance, S. Morita, Appl. Phys. Lett. **87**, 173503 (2005)
18. S. Hembacher, F.J. Giessibl, J. Mannhart, C.F. Quate, Phys. Rev. Lett. **94**, 056101 (2005)
19. Y. Sugimoto, S. Innami, M. Abe, O. Custance, S. Morita, Appl. Phys. Lett. **91**, 093120 (2007)
20. Y. Sugimoto, P. Pou, M. Abe, P. Jelinek, R. Perez, S. Morita, O. Custance, Nature **446**, 64 (2007)
21. H. Hölscher, S.M. Langkat, A. Schwarz, R. Wiesendanger, Appl. Phys. Lett. **81**, 4428 (2002)
22. A. Schwarz, H. Hölscher, S.M. Langkat, R. Wiesendanger, AIP Conf. Proc. **696**, 68 (2003)
23. A. Schirmeisen, D. Weiner, H. Fuchs, Phys. Rev. Lett. **97**, 136101 (2006)
24. M. Abe, Y. Sugimoto, T. Namikawa, K. Morita, N. Oyabu, S. Morita, Appl. Phys. Lett. **90**(20), 203103 (2007)
25. M. Heyde, G.H. Simon, H.P. Rust, H.J. Freund, Appl. Phys. Lett. 263107 (2006)
26. B.J. Albers, M. Liebmann, T.C. Schwendemann, M.Z. Baykara, M. Heyde, M. Salmeron, E.I. ALtman, U.D. Schwarz, Rev. Sci. Instrum. **79**, 033704 (2008)
27. M. Ternes, C.P. Lutz, C.F. Hirjibehedin, F.J. Giessibl, A.J. Heinrich, Science **319**, 1066 (2008)

28. M. Ashino, D. Obergfell, M. Haluska, S. Yang, A.N. Khlobystov, S. Roth, R. Wiesendanger, Nat. Nanotechnol. **3**, 337 (2008)
29. R. Gomer, Rep. Prog. Phys. **53**, 917 (1990)
30. E.W. Müller, Ergebn. exakt. Naturwiss. **27**, 290 (1953)
31. E.W. Müller, Z. Phys. **131**, 136 (1951)
32. G. Binnig, H. Rohrer, C. Gerber, E. Weibel, Phys. Rev. Lett. **49**(1), 57 (1982)
33. K. Ruschmeier, A. Schirmeisen, R. Hoffmann, Phys. Rev. Lett. **101**, 156102 (2008)
34. B.J. Albers, T.C. Schwendemann, M.Z. Baykara, N. Pilet, M. Liebmann, E.I. Altman, and U.D. Schwarz, Nat. Nanotechnol. **4**, 307 (2009)
35. B.J. Albers, T.C. Schwendemann, M.Z. Baykara, N. Pilet, M. Liebmann, E.I. Altman, and U.D. Schwarz, Nanotechnol. **20**, 264002 (2009)
36. Q.D. Zhong, D. Inniss, K. Kjoller, V.B. Elings, Surf. Sci. Lett. **290**, L688 (1993)
37. P.K. Hansma, J.P. Cleveland, M. Radmacher, D.A. Walters, P.E. Hillner, M. Bezanilla, M. Fritz, D. Vie, H.G. Hansma, C.B. Prater, J. Massie, L. Fukunaga, L. Gurley, V.B. Elings, Appl. Phys. Lett. **64**, 1738 (1994)
38. C.A.J. Putman, K.O. Vanderwerf, B.G. Degrooth, N.F. Vanhulst, J. Greve, Appl. Phys. Lett. **64**, 2454 (1994)
39. H. Ueyama, Y. Sugawara, S. Morita, Appl. Phys. A **66**, S295 (1998)
40. W. Allers, A. Schwarz, U.D. Schwarz, R. Wiesendanger, Rev. Sci. Instrum. **69**, 221 (1998)
41. F.J. Giessibl, Phys. Rev. B **56**, 16010 (1997)
42. H. Hölscher, B. Gotsmann, W. Allers, U.D. Schwarz, H. Fuchs, R. Wiesendanger, Phys. Rev. B **64**, 075402 (2001)
43. H. Hölscher, B. Gotsmann, A. Schirmeisen, Phys. Rev. B **68**, 153401 (2003)
44. R.H. Simon, M. Heyde, H.P. Rust, Nanotechnology **18**, 255503 (2007)
45. U. Dürig, Appl. Phys. Lett. **75**, 433 (1999)
46. Y. Seo, W. Jhe, Rep. Prog. Phys. **71**, 016101 (2008)
47. B. Gotsmann, B. Ancykowski, C. Seidel, H. Fuchs, Appl. Surf. Sci. **140**, 314 (1999)
48. B. Gotsmann, H. Fuchs, Phys. Rev. Lett. **86**, 2597 (2001)
49. U. Dürig, Appl. Phys. Lett. **76**, 1203 (2000)
50. F.J. Giessibl, Appl. Phys. Lett. **78**, 123 (2001)
51. O. Pfeiffer, Quantitative dynamische Kraft- und Dissipationsmikroskopie auf molekularer Skala. Ph.D. thesis, Universität Basel, 2004
52. J.E. Sader, S.P. Jarvis, Appl. Phys. Lett. **84**, 1801 (2004)
53. F.J. Giessibl, Appl. Phys. Lett. **73**, 3956 (1998)
54. J. Jersch, T. Maletzky, H. Fuchs, Rev. Sci. Instrum. **77**, 083701 (2006)
55. M. Heyde, M. Kulawik, H.P. Rust, H.J. Freund, Rev. Sci. Instrum. **74**, 2446 (2006)
56. W.H. Press, S.A. Tekolsky, W.T. Vetterling, B.P. Flannery, *Numerical Recipes in C* (Cambridge University Press, Cambridge, 1992)
57. A. Schwarz, U.D. Schwarz, S. Langkat, H. Hölscher, W. Allers, R. Wiesendanger, Appl. Surf. Sci. **188**, 245 (2002)
58. S.M. Langkat, H. Hölscher, A. Schwarz, R. Wiesendanger, Surf. Sci. **527**, 12 (2003)
59. E. Gnecco, R. Bennewitz, T. Gyalog, C. Loppacher, M. Bammerlin, E. Meyer, H.-J. Güntherodt, Phys. Rev. Lett. **84**, 1172 (2000)
60. A. Socoliuc, R. Bennewitz, E. Gnecco, E. Meyer, Phys. Rev. Lett. **92**, 134301 (2004)

61. H. Brune, Surf. Sci. Rep. **31**, 121 (1998)
62. G.A. Tomlinson, Philos. Mag. S. 7 **7**, 905 (1929)
63. L. Prandtl, Z. Angew. Math. Mech. **8**, 85 (1928)
64. G.M. McClelland, in *Adhesion and Friction*, ed. by M. Grunze, H.J. Kreuzer (Springer, Heidelberg, Germany, 1989), pp. 1–16
65. Y. Sang, M. Dubé, M. Grant, Phys. Rev. Lett. **87**, 174301 (2001)
66. E. Riedo, E. Gnecco, R. Bennewitz, E. Meyer, H. Brune, Phys. Rev. Lett. **91**, 084502 (2003)
67. H. Hölscher, A. Schwarz, W. Allers, U.D. Schwarz, R. Wiesendanger, Phys. Rev. B **61**, 12678 (2000)
68. J. Kiely, J. Houston, Phys. Rev. B **57**, 12588 (1998)
69. G.L.W. Cross, A. Schirmeisen, P. Grütter, U.T. Dürig, Nat. Mater. **5**, 370 (2006)
70. N. Sasaki, M. Tsukada, Jpn. J. Appl. Phys. **39**, L1334 (2000)
71. L.N. Kantorovich, T. Trevethan, Phys. Rev. Lett. **93**, 236102 (2004)

6

Principles and Applications of the qPlus Sensor

Franz J. Giessibl

Man sollte die Dinge so einfach wie möglich machen, aber nicht einfacher.

(Things should be made as simple as possible, but not one bit simpler.)

Albert Einstein (1879–1955)

Abstract. The concept of the atomic force microscope (AFM) is a very simple one: map the surface of a sample by a sharp probe that scans over the surface similar to the finger of a blind person that reads Braille characters. In AFM, the role of that finger is taken by the probe tip that senses the presence of the sample surface by detecting the force between the tip of the probe and a sample. The qPlus sensor is a self sensing cantilever based on a quartz tuning fork that supplements the traditional microfabricated cantilevers made of silicon. Quartz tuning forks are used in the watch industry in quantities of billions annually, with the positive effects on quality and perfection. Three properties of these quartz-based sensors simplify the AFM significantly: (1) the piezoelectricity of quartz allows simple self sensing, (2) the mechanical properties of quartz show very small variations with temperature, and (3) the given stiffness of many quartz tuning forks is close to the ideal stiffness of cantilevers. The key properties of the qPlus sensor are a large stiffness that allows small amplitude operation, the large size that allows to mount single-crystal probe tips, and the self-sensing piezoelectric detection mechanism.

6.1 Motivation: qPlus Versus Si Cantilever

The first atomic force microscope utilized a cantilever that was built by hand in the laboratory from gold foil and a small piece of diamond acting as a tip [1]. Soon after, MEMS (micro electronic and mechanical systems) capabilities offered by the semiconductor industry were utilized to mass-fabricate cantilevers from silicon.

S. Morita et al. (eds.), *Noncontact Atomic Force Microscopy*,
NanoScience and Technology,
DOI: 10.1007/978-3-642-01495-6_6, © Springer-Verlag Berlin Heidelberg 2009

Initially, Si-based cantilevers were built from SiO_2 and Si_3N_4 [2]. Later, cantilevers with integrated tips were machined from silicon-on-insulator wafers [3]. The most common cantilevers in use today are built from all-silicon with integrated tips pointing in a [001] crystal direction and go back to Wolter et al. [4], followed by a number of companies that offer Si cantilevers with integrated sharp tips on wafers, including a few hundred cantilevers each.

The qPlus sensor still requires manual assembly and it is fair to ask why two decades after the introduction of AFM, manual assembly of its key component is still practiced. Manual assembly was even practiced in manufacturing transistors years after its invention [5] – the reason why manual production of cantilevers is still warranted is outlined in this chapter.

6.1.1 Specifications of an Atomic Force Probe

Imagine the ideal properties of that tiny finger that should probe a surface without destructing it. One first obvious quality of that probe is to be very sharp that ideally a single atom sits at its end. Second, the probe needs to be sensitive enough to be able to feel the tiny forces that act between single atoms. The first AFMs were mostly operated in "contact" mode, and for this mode the stiffness of the cantilever should be significantly smaller than the interatomic spring constants of atoms in a solid [6], which amounts to $k \leq 10\,\mathrm{N\,m^{-1}}$. For nondestructive imaging, the forces between tip and sample should be small compared to the maximal forces that can be sustained by single bonds. Also, it is desired to keep artifacts due to elastic deformations of tip and sample small [7]. It has to be kept in mind, though, that elastic effects will occur in imaging. There is a tradeoff between maximizing the signal-to-noise level by imaging at very close distances and by minimizing tip and sample distortion by imaging at large distances where forces are small. This tradeoff can be somehow relaxed by reducing the noise level in the force measurements – a pursuit that pervades all progress in AFM.

Figure 6.1 shows a schematic view of a probe tip close to a sample. The bonds within the sample (and similar the bonds within the probe tip) have a stiffness k_{ss}, which amounts to roughly $170\,\mathrm{N\,m^{-1}}$ in the case of silicon. The bond between the front atom of the tip and the sample atom next to it is depicted by k_{ts}, which strongly depends on the distance between tip and sample.

For an illustration of the magnitude of typical tip sample bonds, we use the Stillinger–Weber potential [8] that has been devised to describe the bonding in silicon. The Stillinger–Weber potential not only depends on the distance between two silicon atoms, but also on the mutual alignment of next nearest neighbor atom. In the case of perfect tetragonal bonding symmetry, the bonding energy $V_{\mathrm{Si-Si}}$, the force $F = -\partial V_{\mathrm{Si-Si}}/\partial z$ and stiffness $k_{\mathrm{Si-Si}} = \partial^2 V/\partial z^2$ is only a function of the interatomic distance z. These functions are shown in Fig. 6.2. The Stillinger–Weber potential is often used as a model for describing covalent bonds, but it has some constraints. A very serious constraint

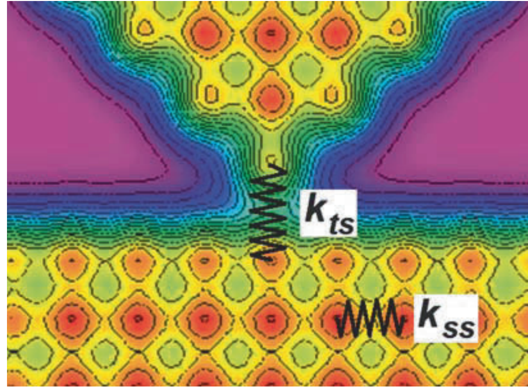

Fig. 6.1. A sharp tip close to a sample. The bonds of the atoms in tip and sample are characterized by a stiffness k_{ss}. For silicon, $k_{ss} \approx 170\,\mathrm{N\,m^{-1}}$. The stiffness of the "bond" between the front atom of the tip and the sample atom next to it is given by k_{ts}, which strongly depends on the tip sample distance

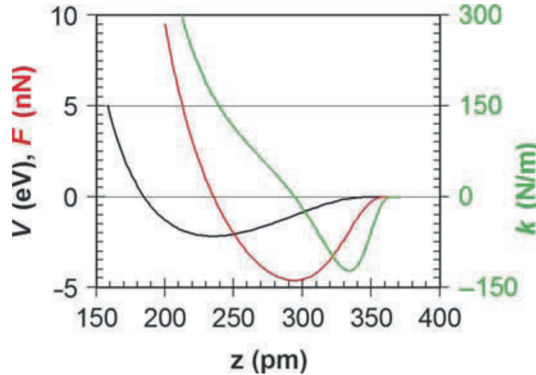

Fig. 6.2. Potential energy V, force F, and stiffness k for a single Si–Si bond after the Stillinger–Weber potential. The potential reaches its minimum of $-2.17\,\mathrm{eV}$ for an equilibrium distance of $z_{eq} = 235\,\mathrm{pm}$. The maximum attractive force reaches $-4.6\,\mathrm{nN}$ at a distance of 296 pm and the stiffness at z_{eq} is $k_{eq} = 170\,\mathrm{N\,m^{-1}}$. For distances $z > 296\,\mathrm{pm}$, the stiffness k_{ss} is negative, reaching a minimal value of $-120\,\mathrm{N\,m^{-1}}$

is the artificial limitation of the bonding length to 376 pm – the potential is assumed to be zero for greater distances. The key reason for that is that the nearest neighbors in Si are 384 pm apart, and the calculation of lattice energies becomes simpler if only the nearest neighbors have to be taken into account. This artificial limitation causes the rather strong maximal attractive force of more than $-4\,\mathrm{nN}$ and the rather large force gradient of $-120\,\mathrm{N\,m^{-1}}$. Nevertheless, the Stillinger–Weber potential describes the experimental phonon spectrum of Si very well and even though the actual Si bonds

may be somewhat weaker (see, e.g., total energy pseudopotential calculations by Perez et al. [9]) it has to be anticipated that single atomic bonds in semiconductors have a stiffness on the order of $\pm 100\,\mathrm{N\,m^{-1}}$. The stiffness of bonds in solids can be estimated from the frequencies of optical phonons [10]. Silicon has an optical phonon at a wavenumber of $520\,\mathrm{cm^{-1}}$ (at the Gamma point where $\boldsymbol{k} = 0$), every Si atom in the bulk is embedded in bonds with an effective spring constant of $447\,\mathrm{N\,m^{-1}}$. Diamond, in contrast, has an optical phonon at a wavenumber of $1{,}200\,\mathrm{cm^{-1}}$ and every C atom in diamond is embedded in bonds with an effective spring constant of $1{,}020\,\mathrm{N\,m^{-1}}$. This value is very high compared to the stiffness of the mainly used commercial silicon cantilevers.

6.1.2 Cantilevers in Dynamic Force Microscopy

In dynamic force microscopy, the cantilever is oscillating and amplitude changes [11] or frequency shifts [12] are utilized to probe the forces acting between tip and sample. Atomic resolution on reactive surfaces was first obtained in frequency modulation AFM with very large cantilever oscillation amplitudes of 34 nm [19]. Initially, it was not clear why these huge amplitudes were required, but the simple picture shown in Fig. 6.3 explains that situation.

The eigenfrequency f_0 of the cantilever is given by

$$f_0 = \frac{1}{2\pi}\sqrt{\frac{k}{m}}, \tag{6.1}$$

and when the stiffness of the tip sample bond k_{ts} is taken into account, the new frequency is

$$f = \frac{1}{2\pi}\sqrt{\frac{k + k_{\mathrm{ts}}}{m}}. \tag{6.2}$$

Equation (6.2) is correct only if k_{ts} is constant during the oscillation cycle. For large amplitudes, this is certainly not the case.

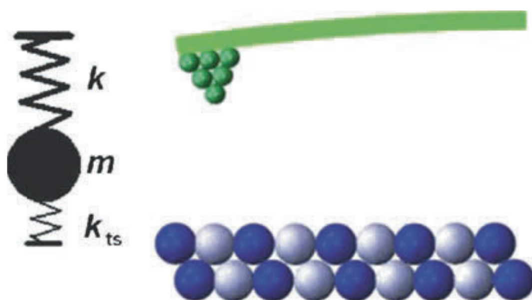

Fig. 6.3. Mass and spring model (*left*) as a mechanical analog of an oscillating cantilever next to a surface (*right*)

When the oscillation amplitude A is large, we have to generalize (6.2) by

$$f = \frac{1}{2\pi}\sqrt{\frac{k + \langle k_{\mathrm{ts}}\rangle}{m}}. \tag{6.3}$$

When $\langle k_{\mathrm{ts}}\rangle$ is small compared to k, we can express the frequency shift $\Delta f = f - f_0$ as

$$\Delta f(z) = f_0 \frac{\langle k_{\mathrm{ts}}(z)\rangle}{2k}, \tag{6.4}$$

with

$$\langle k_{\mathrm{ts}}(z, A)\rangle = \frac{2}{\pi}\int_{-1}^{1} k_{\mathrm{ts}}(z - Au)\sqrt{1 - u^2}\,\mathrm{d}u. \tag{6.5}$$

Also, we note that for small tip sample distances, k_{ts} can become quite large (see Fig. 6.2). In this case, the stiffness of the cantilever k would need to be significantly larger than $100\,\mathrm{N\,m^{-1}}$; otherwise, stable oscillation would become impossible [14]. In frequency modulation AFM, the cantilever is part of an oscillator that has to oscillate at a precisely determined amplitude A, as any amplitude fluctuations show up as noise in the AFM data. The creation of a stable oscillator is difficult enough (for a block diagram of the oscillator circuit of an FM-AFM, see, e.g., [15]) and stability is easier to obtain if the oscillation frequency does not vary too much around f_0, in other words, we demand that $\mid \Delta f \mid \ll f_0$ thus $\mid \langle k_{\mathrm{ts}}\rangle \mid \ll k$. For small amplitude operation, $\langle k_{\mathrm{ts}}\rangle \approx k_{\mathrm{ts}}$ and thus we demand that $k \gg \mid k_{\mathrm{ts}} \mid$.

6.1.3 Advantages of Small Amplitude Operation

In the scanning tunneling microscope (STM), the tunneling current is used to probe the presence of a sample surface. As the tunneling current increases by a factor of ten for every distance reduction of 100 pm, there is only one current path that mainly originates from the front atom of the tip. In AFM, forces of various origin are acting on the probe of the tip, but ideally only the short range contributions originating from the front atom would be measured. In frequency modulation AFM, there is a way to discriminate force contributions by their decay length. In large amplitude AFM, it has been shown that the frequency shift is dominated by long-range forces. The normalized frequency shift γ, which is defined by

$$\gamma := \frac{\Delta f}{f_0} k A^{3/2}, \tag{6.6}$$

can be expressed as

$$\gamma \approx 0.4 \times \sum_{i=1}^{N} F_{\mathrm{ts}}^{i}\sqrt{\lambda_i}, \tag{6.7}$$

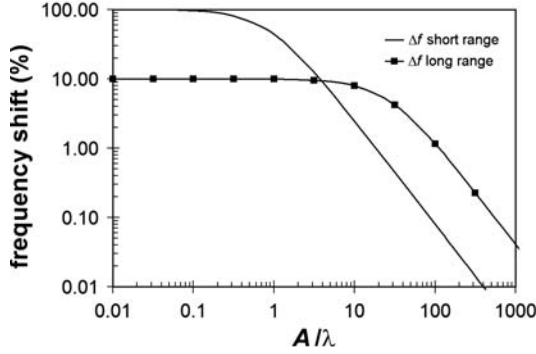

Fig. 6.4. Frequency shift contributions of short- and long-range force components as a function of amplitude

where i is an index denoting the force channel. For example, let us assume the interaction consists of a short range force with a magnitude of 1 nN and a range of 100 pm and a long range force with a magnitude of 3 nN and a range of 3 nm. The long-range forces are mainly caused by van der Waals interactions that can be reduced by using sharp tips [16–18]. In this case, the contribution of the long-range force to the frequency shift is $3 \times \sqrt{30} \approx 16$ times as large as the short range contribution.

For oscillation amplitudes that are small compared to the range of the short-range interaction λ, the frequency shift is proportional to the force gradient (see (6.4)) and the long-range contribution is only 10% of the short-range contribution. The crossover from small- to large amplitude operation is shown in Fig. 6.4. This figure shows how the frequency shift becomes smaller as the amplitude is increased. It is important to note that the minimum distance (lower turnaround point of the cantilever) is held constant when the amplitude is varied. When the amplitude reaches the range of the short-range interaction λ, the frequency shift component originating from the short range force starts to decrease while the long-range component still remains constant. For $A \approx 3 \times \lambda$, the contributions of long- and short-range force match, while for $A > 3 \times \lambda$, the long-range contributions dominate Δf. In summary, large amplitude FM-AFM requires the use of very sharp tips, while small amplitude AFM can cope with blunt tips as well.

The cost of using small amplitudes is an increase in frequency noise. Albrecht et al. [12] have calculated the thermal noise of a cantilever and found

$$\frac{\delta f_{\text{thermal}}}{f_0} = \sqrt{\frac{k_{\text{B}} T B}{\pi f_0 k A_{\text{rms}}^2 Q}}, \tag{6.8}$$

that is, the thermal noise ratio is roughly given by the square root of the ratio between the thermal energy $k_{\text{B}}T$ and the mechanical energy stored in the cantilever $kA^2/2$ divided by the quality factor Q and multiplied by the ratio between bandwidth and frequency ($A^2 = 2A_{\text{rms}}^2$).

Often times, the thermal noise is smaller than the detector noise. Detector noise is described by the precision at which we can measure the cantilever deflection. Good interferometers as well as electrical detection of the qPlus deflection reach deflection noise densities of $n_{q'} = 100\,\mathrm{fm}/\sqrt{\mathrm{Hz}}$. A deflection noise density of $n_{q'} = 100\,\mathrm{fm}/\sqrt{\mathrm{Hz}}$ means that the position of the cantilever can be determined with a precision of 100 fm in a 1 Hz bandwidth and with a 1 pm deflection noise for a bandwidth of 100 Hz.

The corresponding frequency noise is [19, 20]

$$\frac{\delta f_{\mathrm{detector}}}{f_0} = \frac{n_{q'}}{\pi A f_0} B_{\mathrm{FM}}^{3/2}, \tag{6.9}$$

where B_{FM} is the bandwidth of the frequency detector. Because the two noise sources are statistically independent, we find

$$\delta f = \sqrt{\delta f_{\mathrm{thermal}}^2 + \delta f_{\mathrm{detector}}^2}. \tag{6.10}$$

Here it is important that detector noise increases dramatically with B_{FM}; therefore, slow scanning reduces noise sharply. Both thermal and detector frequency noise vary inversely with amplitude. The signal-to-noise ratio is thus given by dividing the signal level shown in Fig. 6.4 by the $1/A$ dependence of the frequency noise. The result is displayed in Fig. 6.5. The signal-to-noise ratio is optimal when the amplitude is tuned to the interaction that is to be used for imaging. In the first application of FM-AFM [12], magnetic dipole forces on recording media have been probed and the use of large amplitudes was helping to obtain good quality images. However, the analysis above shows that for probing atomic interactions with force ranges in atomic dimensions, amplitudes in the 100 pm range are preferred.

The use of small amplitude suppresses long-range contributions to the frequency shift and optimizes the signal-to-noise ratio.

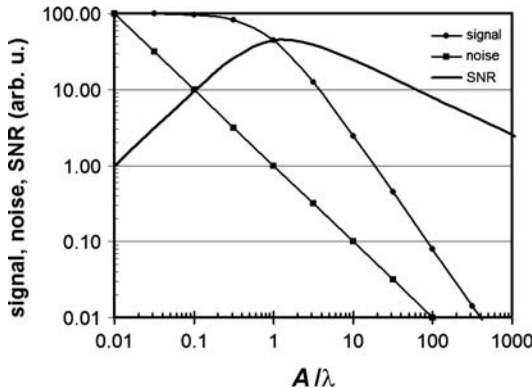

Fig. 6.5. Signal-to-noise ratio (SNR) in FM-AFM as a function of amplitude

6.1.4 Ideal Physical Properties of Cantilevers

Three physical properties of cantilevers are relevant in force microscopy:

1. Stiffness k
2. Eigenfrequency f_0
3. Quality factor Q

Because of the considerations outlined in Sect. 6.1.2, we want the stiffness k to be on the order of $1\,\mathrm{kN\,m^{-1}}$ to allow stable small amplitude operation.

The eigenfrequency f_0 should be as high as possible to minimize frequency noise (see (6.9) and (6.8)). However, there is a tradeoff that depends on the specific implementation of the deflection sensor. Usually, the deflection noise $n_{q'}$ increases with frequency for a given detector and so the optimal value depends on the detection method.

The quality factor Q should be as high as possible, according to (6.8). However, there is a practical consideration. One way to express the quality factor is to compare the energy loss per cycle $\Delta E_{\mathrm{cycle}}$ in a damped oscillator to the energy stored in the cantilever $E = kA^2/2$:

$$Q = \frac{2\pi E}{\Delta E_{\mathrm{cycle}}}. \tag{6.11}$$

If Q is extremely large, amplitude control can become very difficult because the interaction of the probe tip with a sample is in general dissipative and the relative change of the energy loss per cycle is inversely proportional to Q.

In practice, it is also important how these parameters depend on the medium (liquid, gaseous, vacuum) and temperature. One of the main reasons why frequency standards are often built from quartz tuning forks is their superiority to silicon with respect to frequency stability vs. temperature [21]. Also, for practical considerations, it is very important to consider the type of probe tips that can be used with a given cantilever.

6.2 Theory of qPlus Versus Tuning Fork Sensors

Quartz tuning forks are wonderful inventions. They allow to produce watches at very low cost that keep time much more precise than mechanical watches that are prized orders of magnitude higher [22]. Here, we explain the principle of quartz tuning forks and explain how they can be rebuilt to act as powerful force sensors.

6.2.1 Quartz Tuning Forks

Quartz tuning forks are etched from single crystal quartz that is oriented in a $X + 5^\circ$ orientation [23]. This orientation ensures that the frequency variation

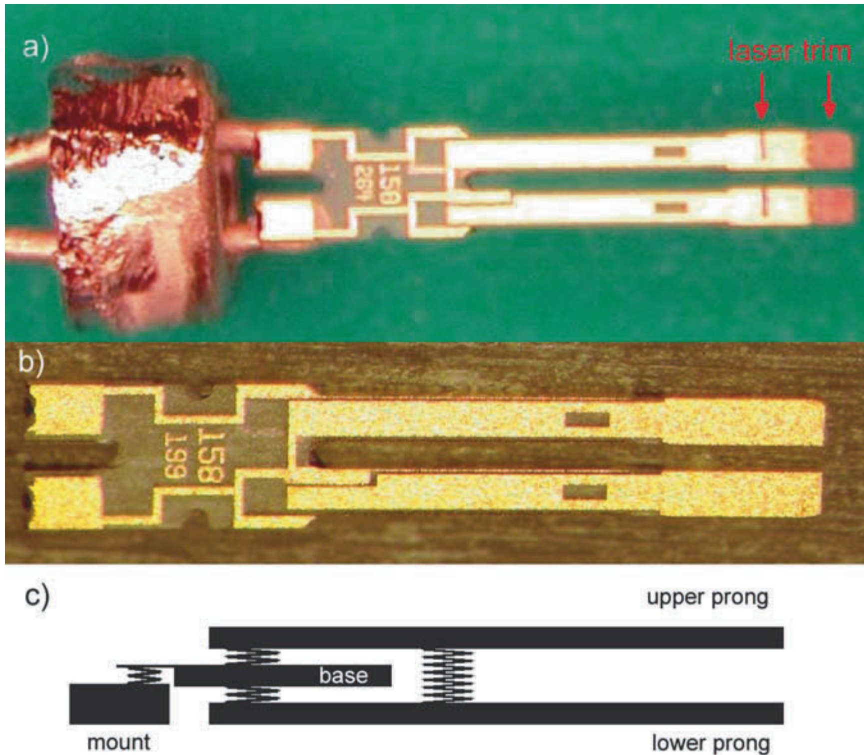

Fig. 6.6. Quartz tuning forks. (**a**) A tuning fork as used in watches with an opened metal case. The arrows point to an area where the gold plating has been partially removed to trim the mass of the prongs such that an eigenfrequency of exactly 32,768 Hz arises. (**b**) Untrimmed tuning fork as taken out of a wafer. The trimming procedure has not been done on this fork as can be seen by the undamaged gold plating at the end of the fork. (**c**) Mechanical analog of the tuning fork: in principle, the fork is a quite complex mechanical system with many oscillation modes and eigenfrequencies. When both prongs are symmetric, the antiparallel mode where one prong oscillates opposite to the other one has a very high Q value

with temperature is almost zero at 28° C – the typical temperature of a watch mounted on a wrist. The piezoelectricity of quartz allows for a simple transformation of the mechanical oscillation of the quartz fork to an electrical signal. Incidentally, the piezoelectric effect and its inversion that are instrumental for the whole field of scanning probe microscopy have been first observed in quartz by the Curie brothers (see the instructive report in Chen's introduction to STM [76]). Quartz tuning forks have surprisingly large Q-values – on the order of 10^5. Therefore, frequency stability is excellent and power consumption is very low – ideal for watch applications. Figure 6.6a shows a quartz tuning fork as used in Swatch watches. The metal case of the device has been opened

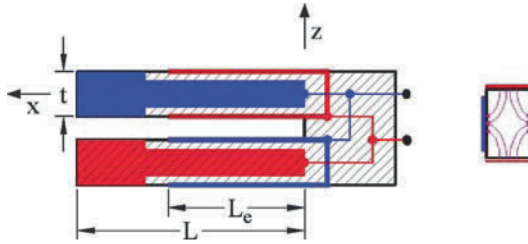

Fig. 6.7. Electrode configuration of the quartz tuning forks shown in Fig. 6.6

and one can see the transparent quartz fork as well as the gold electrodes. The gold electrodes have been removed partially at the ends of the prongs to adjust the eigenfrequency to exactly 2^{15} Hz (32.768 kHz). Figure 6.6b shows a similar tuning fork that has not yet been trimmed. The prongs are rectangular and are surrounded by gold electrodes – two vertical and two horizontal layers of gold (see Fig. 6.7). Figure 6.6c is a mechanical analog to the tuning fork. When both prongs have exactly the same mass and stiffness, an oscillation mode where both prongs oscillate opposite to each other evolves that has extremely little losses and thus with (6.11) a very high Q value.

Because of their useful properties, quartz tuning forks have been applied in scanning probe microsocopy quite early. Guethner et al. [25] has used a quartz tuning fork for scanning near field acoustic microscopy, and Karrai et al. [26] used tuning forks to sense the distance of near field optical microscopes. Rychen has used tuning forks to probe forces in low temperatures and high magnetic fields [27–29]. However, the high symmetry of tuning forks has to be given up when a probe is attached to one of the prongs as required for using the fork as a sensor. Dransfeld et al. [30] have proposed to attach a counterweight to the prong that does not carry a tip, and Rychen et al. use extremely lightweight tips [29]. The influence of adding mass to one of the prongs on the Q value has been analyzed in Rychen's Ph.D. thesis [31] and it is found that the Q-value drops considerably when the added mass reaches about 1% of the mass of one prong. The piezoelectric effect results in the generation of surface charges upon mechanical stress. To convert the mechanical stress within the prongs of the tuning forks into surface charges that are collected by metal electrodes on the quartz material, two designs are in use: thick prongs where the width w (y-coordinate in Fig. 6.7) and the thickness t (z-coordinate in Fig. 6.7) of the cross-section of one prong are on the same order of magnitude and thin prongs where the thickness is much greater than the width [23]. For thick prongs such as the ones shown in Fig. 6.6, the electrode configuration is usually as shown in Fig. 6.7. The cross section in the right side of Fig. 6.7 shows the electrodes and the electric field lines within the quartz material. When one beam of the fork is deflected by an amount z, the charge q that is collected on the electrode is given by

$$q = z d_{21} k L_{\mathrm{e}} (L_{\mathrm{e}}/2 - L)/t^2, \tag{6.12}$$

where d_{21} is the piezoelectric coupling constant ($d_{21} = 2.31\,\mathrm{pC\,N^{-1}}$ for quartz), k is the spring constant, L_e is the length of the electrodes (see Fig. 6.7), L is the length of the prongs, and t is the thickness of the prongs [32]. The sensitivity of the E158 fork shown here is $q/z = 2.8\,\mathrm{\mu C\,m^{-1}}$.

Two observations deserve to be mentioned: (a) the sensitivity is proportional to the spring constant and (b) the electrodes do not need to reach until the very end of the fork to get good sensitivity – for $L_\mathrm{e} = 0.8L$ we still get 96% of the maximum sensitivity at $L_\mathrm{e} = L$. Thus we can afford to leave the end of the prongs free of electrodes for contacting a tip.

For the type of forks used here, the dimensions are given by $L = 2.4\,\mathrm{mm}$, thickness $t = 214\,\mathrm{\mu m}$, and width $w = 130\,\mathrm{\mu m}$. The theoretical stiffness of one beam is given by

$$k = \frac{1}{4} E w \frac{t^3}{L^3}, \tag{6.13}$$

where E is the elastic modulus ($E = 78.7\,\mathrm{GPa}$ for quartz) and w is the width of the prongs. The formula is derived for a beam that is fixed to massive material. In the tuning fork configuration, a slightly smaller spring constant is expected. Heyde et al. [33] have performed finite element analysis to calculate the expected spring constant. Here, we follow a different approach: the quantities that can be measured with great precision are w and L. In contrast, it is harder to measure t. The frequency f_0 can be measured with great precision. For a clamped beam, f_0 is given by [76]

$$f_0 = 0.161 \sqrt{\frac{E}{\rho}} \frac{t}{L^2}, \tag{6.14}$$

where ρ is the mass density ($\rho = 2{,}650\,\mathrm{kg\,m^{-3}}$ for quartz). Thus, we can use (6.14) to measure the effective thickness t and get a more precise value for k. For the forks we use here the theoretical spring constant is $k = 1{,}800\,\mathrm{N\,m^{-1}}$.

6.2.2 qPlus Sensor

Even when the mass of a tip attached to one of the prongs is compensated by attaching a similar mass to the other prong, the asymmetry that affects the prong that interacts with a surface cannot be lifted easily. Therefore, we attach one prong to a heavy substrate such that we end up with a quartz cantilever instead of a quartz tuning fork. Even the use of heavy tips or a strong interaction with a surface bond will not cause a collapse of the Q factor. Therefore, we call this arrangement the qPlus sensor configuration as opposed to a tuning fork configuration [34, 35]. Essentially, the qPlus sensor is a cantilever made of quartz with various favorable properties

1. A stiffness close to the optimal value as found in Sect. 6.1
2. A high Q value
3. Self sensing

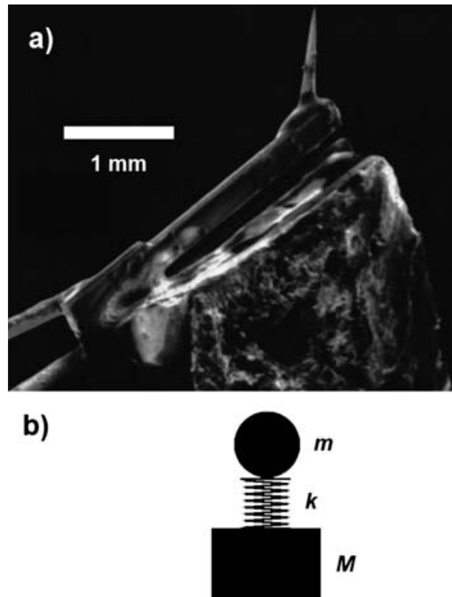

Fig. 6.8. A quartz tuning fork is glued onto a heavy substrate, turning the tuning fork into a qPlus sensor. In this first prototype of a qPlus sensor shown in (**a**), the free prong of the tuning fork is glued to a piece of Pyrex glass. The tip is an etched tungsten wire with a wire diameter of approx. 200 μm. The mechanical analog to the qPlus sensor is shown in (**b**). It is much simpler than in the case of the tuning fork, because only the free prong is allowed to oscillate. The mass of the mount M should be large compared to the effective mass of the fork, where $M > 1{,}000\,m$ is a reasonable value

The sensor shown in Fig. 6.8 has been used for high speed imaging in ambient conditions [36]. The electrical connections of the fork were connected to an instrumentation amplifier with a high gain. The charges that are collected on the electrodes when the sensor is deflected cause a voltage change in the input of an instrumentation amplifier. The charges q that collect on the electrodes change the potential difference at the input terminal.

6.2.3 Manufacturing High Quality qPlus Sensors

After the proof of principle was reached, the resolution limits that could be probed with the new sensor were investigated. First, the manufacture of the sensor needed to be simplified. On that behalf, a ceramic substrate that simplifies the building of the sensor was designed. The substrate is made of alumina with vias and conductive leads as well as mounting holes. Substrates of this kind are used in hybrid electronics design and can be ordered as custom designs [37].

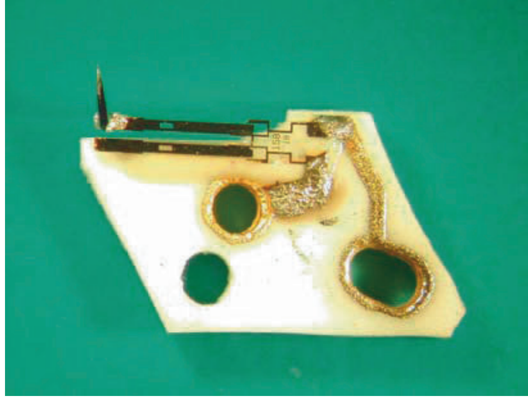

Fig. 6.9. Second generation qPlus sensor. The sensor consists of three parts: the tuning fork, a ceramic substrate, and the tip. Electrical connections are made using conductive epoxy [38]

Fig. 6.10. Third generation qPlus sensor. A different ceramic substrate is used that allows to isolate the tip potential from the electrodes of the sensor. The tip is contacted with a squeezed gold wire (diameter 10 µm). The Q-value still remains on the order of a few thousand. The two electrodes of the tuning fork are fed into a single amplifier, see Sect. 6.2.4

To obtain a sensor with a high Q-value, it is important to create a very stiff bond between the fork and the substrate. This can be achieved by using a very thin layer of glue and by taking care that the area where the free prong meets the base part of the fork remains free of glue (see Fig. 6.9). This sensor design can also be used to build a lateral force sensor by rotating the tip by 90° and oscillating the tip parallel to the surface [39]. The third generation of qPlus sensors is shown in Fig. 6.10. Here, the tip is connected via a dedicated terminal. This allows to apply high voltages for tip annealing or field emission without affecting the deflection sensors amplifiers. Both electrodes of the fork

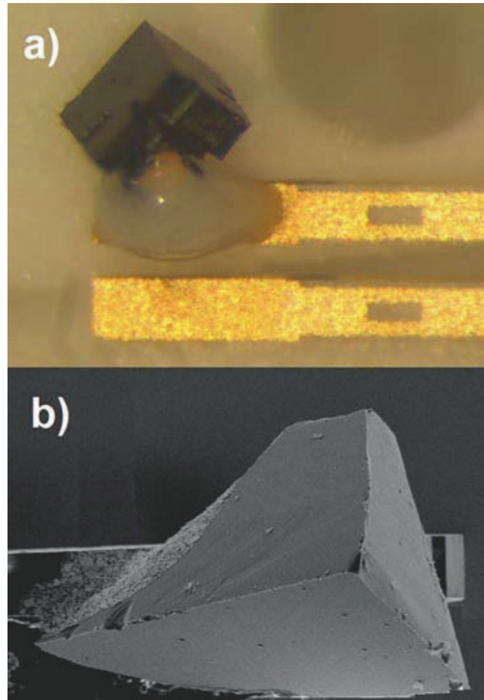

Fig. 6.11. Single-crystal tips for the qPlus sensor. (**a**) NiO single crystal tips for in situ cleavage. The cuts in the crystal are designed to facilitate cleaving such that a tip with three freshly cleaved NiO {001} surfaces arises [41]. (**b**) Si single crystal tips for ex situ cleavage. An Si tip terminated by three {111} faces emerges [42, 43]

are fed into a current-to-voltage amplifier and the difference between the two signals has much less interference noise than a single deflection electrode. [40]

The tip of the force sensor is a crucial part. Ideally, we want a single atom at the front with a well defined atomic neighborhood. A single crystal tip appears to be ideal. Tips from silicon have been cleaved ex situ, exposing three {111} faces [42,43]. NiO tips that are bound by {001} cleaved ex situ [44] and in situ [41] have been created as well.

6.2.4 Preamplifiers for qPlus Sensors

The qPlus sensor needs only one more component to produce an electrical deflection signal: a current-to-voltage converter that converts the flowing charges generated at the oscillating prongs into a voltage. Because cable capacity has an adverse effect on the noise performance of the deflection measurement, the amplifier should be located as close as possible to the sensor. For vacuum and low-temperature applications, it is challenging to design an amplifier that is compatible with these demanding environments.

Figure 6.12 shows the evolution of amplifiers we went through. The first type shown in Fig. 6.12a is an instrumentation amplifier. This type was used in the first qPlus experiments in ambient environments. The principle of operation is the following: when the qPlus sensor is deflected, charges accumulate on the electrodes as given in (6.12). These charges cause a voltage increase in the capacitor (qPlus electrodes plus cable capacity) and the voltage differential is measured with the instrumentation amplifier. To define the input potentials of the instrumentation amplifier and to avoid long-term charging effects, the inputs need to be connected to ground with a very large resistivity (at least 100 MΩ).

The second type shown in Fig. 6.12b) is a traditional transimpedance amplifier as used in current amplifiers of STMs. To obtain a high bandwidth, it is important to use a resistor that has little stray capacitance. Surface-mount-device (SMD) resistors work well here. The case of the amplifier should be vacuum compatible, for example, the amplifier should be available in a metallic or ceramic case, although we have used plastic cases in UHV without

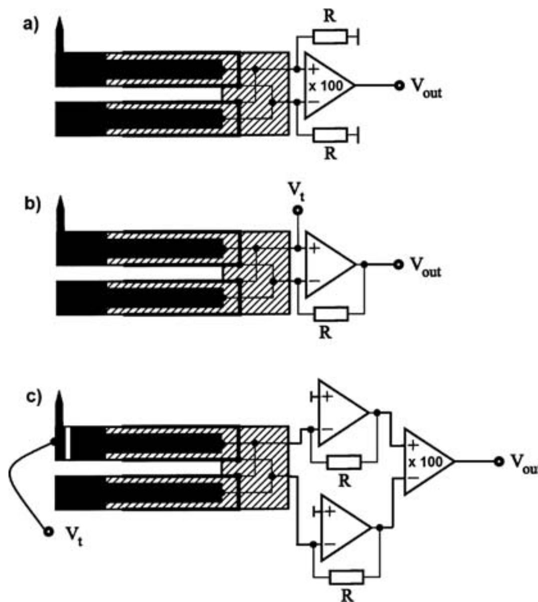

Fig. 6.12. Three types of preamplifiers for qPlus sensor. (**a**) First generation, an instrumentation amplifier (AD 624 [45]) with two resistors. (**b**) Second generation, a current-to-voltage converter or transimpedance amplifier, similar to the ones used in STM current amplification. Operational amplifiers that work well here are the AD711, AD744, and AD823 [45]. (**c**) Third generation, a dual current-to-voltage converter with an instrumentation amplifier (e.g., AD823 for the I/V converter and AD624 as an instrumentation amplifier). The resistor values are all on the order of 100 MΩ, with a small and low capacity SMD design

apparent additional outgassing and adverse effects on vacuum pressure. In STM, a bandwidth B_{IVC} of 1 kHz is usually sufficient, but here we need at least 10 kHz. Assuming an ideal operational amplifier, the gain of the amplifier is given by

$$V_{\text{out}} = \frac{I_{\text{in}} R}{1 + \text{i}2\pi f RC}, \tag{6.15}$$

where R is the feedback resistor and C is its stray capacitance.

Proper heat sinking is important if the amplifier operates in vacuum, especially if small cases are used, because the cooling effect of air is of course missing in vacuum. Generally, it is a good idea to operate the amplifiers close to the lower threshold of the operating voltage to minimize heat introduction caused by the electric power that is consumed in the amplifier. To avoid uncontrolled oscillations ("motor boating" [46]), it is advisable to put buffer capacitors close to the power terminals of the operational amplifier [47].

The third type of preamplifier shown in Fig. 6.12c uses two channels for the deflection measurement. The advantage of this approach is that the signal becomes twice as large, and uncorrelated noise is only a factor of $\sqrt{2}$ larger and so an increase in signal-to-noise ratio of $\sqrt{2}$ is expected. Correlated noise, such as interference noise, even cancels completely because of the differential stage at the output of the two current amplifier channels. Also, the tip bias is completely free, allowing high-voltage tip treatment or field emission while the sensor is attached to the microscope [40].

Figure 6.13 shows an amplifier in the most demanding environments: vacuum and low temperatures. The operational amplifier in use is of type AD823 [45]. This device can be reliably operated with a very low voltage of ±1.5 V at a quiescent current of typically 5 mA. At low temperatures and 3 V operating voltage, the current is only about 2 mA, thus the heat production is

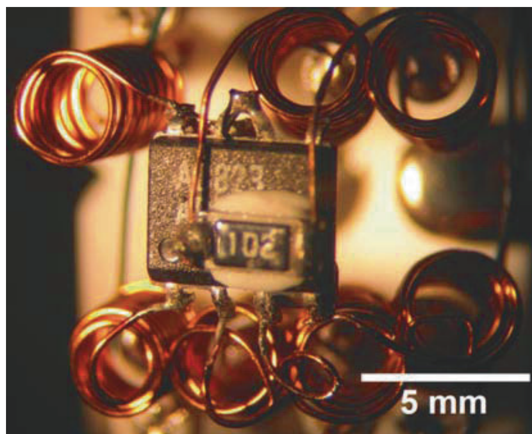

Fig. 6.13. A low temperature preamplifier (AD 823 [45]) with an attached heating resistor

6 mW – tolerable in many 4 K microscopes. The manufacturer quotes a minimal operating temperature of 233 K, but experience shows that the device already works at around 130 K. To keep the amplifier at this temperature in a 4 K environment, it is important to isolate it thermally from the 4 K parts. As can be seen in the photograph, this is achieved by connecting the chip with wire loops wound from a copper alloy with low heat conduction. When the amplifier does not operate, the temperature falls to the one of the 4 K environment. The charge carriers freeze out at this temperature and turning on power will not cause a current flow. The 1 kΩ resistor that is glued onto the SMD type plastic case is used to "jump-start" the amplifier from cold temperatures. When applying about 5 V to the heating resistor, after about 1 min, the quiescent current starts to flow and the heater can be turned off – the amplifier keeps itself warm by its power dissipation. The buffer capacitors (0.1 μF) are also glued to the amplifier case, because ceramic capacitors might only have 4% of their nominal capacitance at 4 K. The 100 MΩ feedback resistor, in contrast, is mounted firmly to a 4 K connection to minimize Johnson noise [46].

6.3 Applications

The applications of the qPlus sensor are potentially all the cases of traditional AFM. Combined STM and AFM is a special feature of qPlus technology.

6.3.1 Own Results

Initially, the main objective to utilize small amplitude AFM and qPlus technology was to see how far the spatial resolution of AFM could be taken. In 2000, subatomic resolution, that is, the resolution of spatial features within a single atom, was performed as can be seen in Fig. 6.14a [43]. Figure 6.14b shows the first result of atomic resolution by lateral AFM, also obtained using a qPlus sensor [39]. Sub-Angstrom resolution by AFM has been obtained in 2004 by operating a qPlus sensor in a higher harmonic mode [48], see Fig. 6.14c. When oscillation amplitudes are very small, the tunneling current between a conductive tip and a sample is quite large and simultaneous STM and AFM is easy to do. Surprisingly, STM and AFM yield different image data as can be seen in Fig. 6.14d [49]. Finally, the forces that act during atomic manipulation have been measured in a collaboration between the IBM Almaden Research Laboratory and our group [50]. Figure 6.14e shows the lateral force data acting between a metallic tip and a Co adatom. Note that the height difference between the last and second last force curve is only 5 pm.

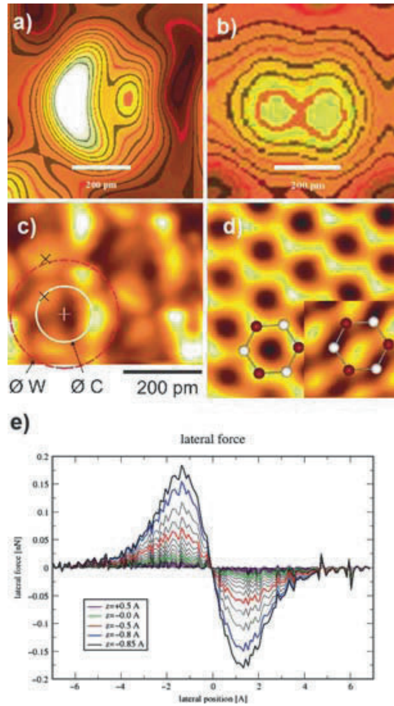

Fig. 6.14. (**a**) First sub-atomic resolution data, showing two maxima in the image of a single atom that are explained by the orbital structure of the tip [43], (**b**) a dual maximum in lateral force microscopy caused by a tip that oscillates laterally [39], (**c**) sub-Angstrom resolution using higher harmonic AFM [48], (**d**) simultaneous STM and AFM on graphite [49], and (**e**) lateral forces over a cobalt adatom [50 and Markus Ternes et al.'s chapter in this book]

6.3.2 External Groups

One of the first groups who adapted the qPlus principle was King et al. [51,52] who imaged DNA in ambient conditions. Several companies have implemented the qPlus sensor in their microscopes (see Fig. 6.15). Udo Schwarz from Yale University and Markus Heyde from the Fritz-Haber Institute in Berlin also utilized the qPlus principle (see also their chapters in this book).

6.4 Outlook

Einstein's request to make things as simple as possible is appealing and promises to not only simplify the technique, but also might help to perform new types of experiments. The question is whether force sensing can be made even simpler – or whether some things have already been made too simple.

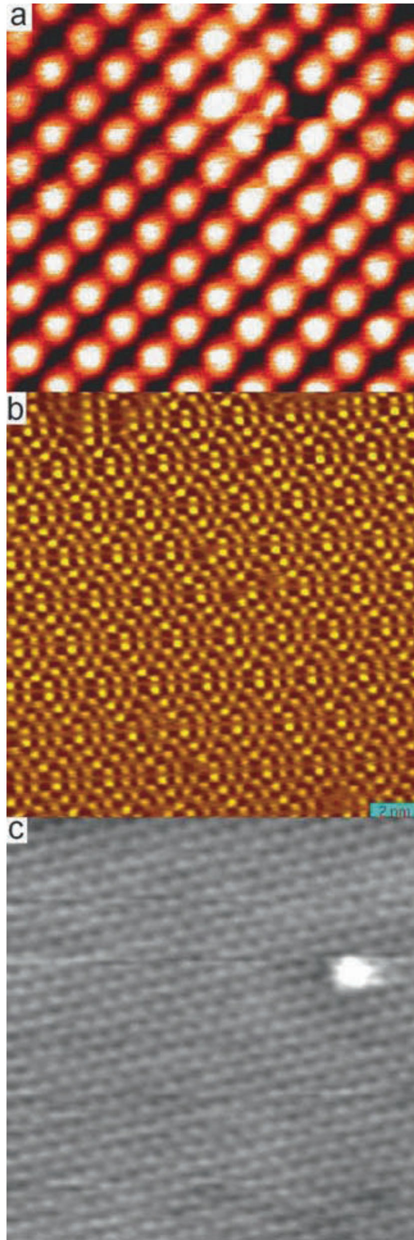

Fig. 6.15. Results obtained by commercial manufacturers of scanning probe microscopes: (**a**) Topographic image of NaCl imaged with the Omicron QPlus LT STM/AFM at 5 K showing an atomic defect [53]. (**b**) Constant-height frequency shift image of Si(111)-(7×7) imaged with an RHK 300 UHV STM/AFM (tuning fork configuration) [61]. (**c**) Constant-height frequency shift image of a Cu (111) surface with a defect imaged with a Createc UHV LT STM/AFM using a qPlus sensor [62]

This question will be answered in the future when more scientists start to look into the forces that act in atomic science and engineering. Various new results were derived with the qPlus sensor that would be difficult to obtain with traditional FM-AFM. With the commercial availability of the qPlus sensor and other research groups using it (see Chaps. 5, 7 and 9 of this book), it can be expected that further progress will be obtained, for example, when the thriving field of STM studies on surfaces is enriched with the force aspects that occur in parallel.

Acknowledgment

I wish to thank my students Stefan Hembacher, Markus Herz, Martina Schmid, Martin Breitschaft, Elisabeth Köstner, Thorsten Wutscher, Martin Smolka, Maximilian Schneiderbauer as well as the post doctoral fellows Hartmut Bielefeldt, Toyoaki Eguchi, and Sebastian Gritschneder for helping to bring qPlus AFM to its current status. McKinsey & Company, Inc. as well as T.W. Hänsch have supported the first steps towards the creation of the qPlus sensor and Jochen Mannhart from Augsburg University provided support and freedom to explore the key possibilities of small-amplitude AFM.

References

1. G. Binnig, C.F. Quate, C. Gerber, Phys. Rev. Lett. **56**, 930 (1986)
2. T.R. Albrecht, S. Akamine, T.E. Carver, C.F. Quate, J. Vac. Sci. Technol. A **8**, 3386 (1990)
3. S. Akamine, R.C. Barrett, C.F. Quate, Appl. Phys. Lett. **57**, 316 (1990)
4. O. Wolter, T. Bayer, J. Greschner, J. Vac. Sci. Technol. **9**(2), 1353 (1991)
5. L. Berlin, *The man behind the microchip: Robert Noyce*, 1st edn. (Intel, Santa Clara, USA, 2005)
6. D. Rugar, P. Hansma, Physics Today **43**(10), 23 (1990)
7. W.A. Hofer, A.J. Fisher, R.A. Wolkow, P. Grutter, Phys. Rev. Lett. **87**, 236104 (2001)
8. F.H. Stillinger, T.A. Weber, Phys. Rev. B **31**(8), 5262 (1985)
9. R. Perez, I. Stich, M.C. Payne, K. Terakura, Phys. Rev. B **58**, 10835 (1998)
10. N.W. Ashcroft, N.D. Mermin, *Solid State Physics* (Saunders College, Philadelphia, 1981)
11. Y. Martin, C.C. Williams, H.K. Wickramasinghe, J. Appl. Phys. **61**(10), 4723 (1987)
12. T.R. Albrecht, P. Grutter, H.K. Horne, D. Rugar, J. Appl. Phys. **69**, 668 (1991)
19. F.J. Giessibl, Science **267**(5194), 68 (1995)
14. F.J. Giessibl, S. Hembacher, M. Herz, C. Schiller, J. Mannhart, Nanotechnology **15**, S79 (2004)
15. F.J. Giessibl, in *Noncontact Atomic Force Microscopy*, ed. by S. Morita, R. Wiesendanger, E. Meyer (Springer Berlin Heidelberg New York, 2002), chap. 2, pp. 11–46
16. F.J. Giessibl, Phys. Rev. B **56**, 16010 (1997)

17. M. Lantz, H.J. Hug, R. Hoffmann, P. van Schendel, P. Kappenberger, S. Martin, A. Baratoff, H.J. Guentherodt, Science **291**, 2580 (2001)
18. T. Eguchi, Y. Fujikawa, K. Akiyama, T. An, M. Ono, T. Hashimoto, Y. Morikawa, K. Terakura, T. Sakurai, M. Lagally, Y. Hasegawa, Phys. Rev. Lett. **93**(26), 266102 (2004)
19. U. Duerig, H.P. Steinauer, N. Blanc, J. Appl. Phys. **82**, 3641 (1997)
20. F.J. Giessibl, Rev. Mod. Phys. **75**(3), 949 (2003)
21. S. Hembacher, F.J. Giessibl, J. Mannhart, Appl. Surf. Sci. **188**, 445 (2002)
22. E. Momosaki, Proc. 1997 IEEE Interntl. Freq. Contr. Symp. **56**, 552 (1997)
23. F.L. Walls, in *Precision Frequency Control*, ed. by E. Gerber, A. Ballato (Academic Press, Orlando a.o., 1985), pp. 276–279
76. C.J. Chen, *Introduction to Scanning Tunneling Microscopy* (Oxford University Press, New York, 1993)
25. P. Guethner, U.C. Fischer, K. Dransfeld, Appl. Phys. B **48**, 89 (1989)
26. K. Karrai, R.D. Grober, Appl. Phys. Lett. **66**(14), 1842 (1995)
27. J. Rychen, T. Ihn, P. Studerus, A. Herrmann, K. Ensslin, Rev. Sci. Instr. **70**(6), 2765 (1999)
28. J. Rychen, T. Ihn, P. Studerus, A. Herrmann, K. Ensslin, H.J. Hug, P.J.A. van Schendel, H.J. Guentherodt, Rev. Sci. Instr. **71**, 1695 (2000)
29. J. Rychen, T. Ihn, P. Studerus, A. Herrmann, K. Ensslin, H.J. Hug, P.J.A. van Schendel, H.J. Guentherodt, Appl. Surf. Sci. **157**(4), 290 (2000)
30. K. Dransfeld, U. Fischer, P. Guethner, K. Heitmann, US Patent 5212987 (1991)
31. J. Rychen, Combined low-temperature scanning probe microscopy and magneto-transport experiments for the local investigation of mesoscopic systems. Ph.D. thesis, ETH Zuerich, Switzerland, ETH Diss No. 14119 (2001)
32. F.J. Giessibl, Appl. Phys. Lett. **76**, 1470 (2000)
33. M. Heyde, M. Kulawik, H.P. Rust, H.J. Freund, Rev. Sci. Instrum. **75**(7), 2446 (2005)
34. F.J. Giessibl, German Patent p. DE 196 33 546 (1996)
35. F.J. Giessibl, US. Patent pp. 6, 240, 771 (2001)
36. F.J. Giessibl, Appl. Phys. Lett. **73**, 3956 (1998)
37. CeramTec, CeramTec AG, Marktredwitz, Germany (2008)
38. EpoTek, Norwood, MA 02062-9106, U.S.A., (2008)
39. F.J. Giessibl, M. Herz, J. Mannhart, Proceedings of the National Academy of Sciences (USA) **99**(19), 12006 (2002)
40. M. Smolka. Rasterkraftmikroskopie. Diploma Thesis, Universitaet Regensburg, Germany (2008)
41. T. Wutscher. Einkristalline spitzen fuer die rasterkraftmikroskopie. Diploma Thesis, Universitaet Regensburg, Germany (2007)
42. F.J. Giessibl, H. Bielefeldt, S. Hembacher, J. Mannhart, Ann. Phys. (Leipzig) **10**(11-12), 887 (2001)
43. F.J. Giessibl, S. Hembacher, H. Bielefeldt, J. Mannhart, Science **289**, 422 (2000)
44. M. Schmid, J. Mannhart, F.J. Giessibl, Phys. Rev. B (2008)
45. Analog Devices, One Technology Way, P.O. Box 9106, Norwood. MA 02062-9106, U.S.A., (2008)
46. P. Horowitz, W. Hill, *The Art of Electronics* (Cambridge University Press, Cambridge, New York, 1989, 2nd ed.)
47. M. Breitschaft. Low-temperature afm. Diploma Thesis, Universitaet Augsburg, Germany (2006)

48. S. Hembacher, F.J. Giessibl, J. Mannhart, Science **305**, 380 (2004)
49. S. Hembacher, F.J. Giessibl, J. Mannhart, C.F. Quate, Proc. Natl. Acad. Sci. (USA) **100**, 12539 (2003)
50. M. Ternes, C.P. Lutz, C.F. Hirjibehedin, F.J. Giessibl, A. Heinrich, Science **319**(5866), 1066 (2008)
51. G.M. King, J. G. Nunes, Rev. Sci. Instrum. **72**(11), 4261 (2001)
52. G.M. King, J.S. Lamb, J. G. Nunes, Appl. Phys. Lett. **79**(11), 1712 (2001)
53. Omicron, *Omicron UHV AFM/STM.* Omicron Nanotechnology GmbH, Limburger Str. 75, D-65232 Taunusstein, Germany (2002)
54. Nanosurf, *easyPLL, easyPLL Sensor Controller.* Nanosurf AG, Grammetstr. 14, CH-8804 Liestal (2002)
55. K. Kobayashi, H. Yamada, H. Itoh, T. Horiuchi, K. Matsushige, Rev. Sci. Instrum. **72**(12), 4383 (2001)
21. R. Bennewitz, C. Gerber, E. Meyer, Appl. Surf. Sci. **157**(4), 207 (2000)
23. C. Barth, M. Reichling, Nature **414**, 54 (2001)
63. A. Livshits, A. Shluger, A. Rohl, Appl. Surf. Sci. **140**, 327 (1999)
71. G. Binnig, H. Rohrer, C. Gerber, E. Weibel, Phys. Rev. Lett. **50**, 120 (1983)
73. G. Binnig, H. Rohrer, C. Gerber, E. Weibel, Phys. Rev. Lett. **49**, 57 (1982)
61. RHK Technology, 1050 East Maple Road, Troy, MI 48083, USA
62. CreaTec Fischer & Co. GmbH, Industriestr. 9, 74391 Erligheim, Germany

7

Study of Thin Oxide Films with NC-AFM: Atomically Resolved Imaging and Beyond

M. Heyde, G.H. Simon, and T. König

Abstract. Results presented in the following show structural analysis of metal-oxide surfaces and the extraction of physical quantities from the force field above such a surface by noncontact atomic force microscopy (NC-AFM). The measurements have been performed with our dual mode NC-AFM/STM in ultrahigh vacuum at 5 K. The introduction will be followed by a description of the experimental setup, including the ultrahigh vacuum cryogenic environment and our tuning fork tunneling current and force sensor. The sensor parameters affecting the measurements are given together with an amplitude characterization method. In the next section, a structure determination of ultrathin Alumina/NiAl(110) is shown. Atomic resolution could be achieved throughout both reflection domain unit cells. NC-AFM reveals details of morphological features, interconnections to substrate–film interactions, and comparability to theory also with respect to topographic height. In the last section, we present measurements beyond imaging, namely spectroscopy data taken on thin MgO films grown on Ag(001). Force–distance measurements based on atomically resolved NC-AFM images of these films have been taken. Inequivalent sites could be resolved and their effect on nucleation and adsorption processes is considered. Furthermore, work function shift measurements on different MgO film thicknesses grown on Ag(001) are studied and the impact of this shift on the catalytic properties of adsorbed metal species is discussed.

7.1 Introduction

In the last few years, it has been demonstrated that noncontact atomic force microscopy (NC-AFM) can be the bridge to nanoscale science on insulating surfaces in general and metal-oxide surfaces in particular. Our work is focused on examples of the latter. Atomic resolution imaging of oxide surfaces gives access to their structural details including, atomic positions, point and line defects as well as to their morphology within certain limits. Additionally, the specific nature of the interaction that enables force microscopy permits the study of physical and chemical material properties of samples and tip–sample combinations, respectively. This may be possible down to the atomic level

S. Morita et al. (eds.), *Noncontact Atomic Force Microscopy*, NanoScience and Technology,
DOI: 10.1007/978-3-642-01495-6_7, © Springer-Verlag Berlin Heidelberg 2009

depending on the measured quantity and is achieved by the examination of the force field between tip and sample in one, two or three dimensions, which are lines, planes, and volumes above the surface. Contact potential difference, charging, and comparative chemical identification are just three examples that can be addressed with this quickly developing class of techniques. Fortunately, they can be implemented in just one experimental setup. With this, the desired comparability among the techniques and to theory can be facilitated even on a quantitative level. Further, the development of functionalized tips and defined oxide surfaces offers great freedom in the study of surface processes. Such knowledge provides a toolkit for surface science and especially surface chemistry where NC-AFM can be involved in the study of structure, adsorption, initial growth, as well as reaction mechanisms and dynamics on oxide surfaces, for example, in the interesting field of model catalysis. Paramount questions in that field are the nature, vitality, and structure of the proclaimed "active sites" and their selectivity mechanisms in heterogeneously catalyzed chemical reactions. The fundamental interactions of metal atoms, clusters, and molecules with metal-oxide supports studied in this context are in fact relevant to several technological fields. An understanding of growth mechanisms and parameters of the respective geometric and electronic structures are of huge importance [1].

Atomic resolution has been a focus of scanning probe methods for the last two decades. With our low temperature microscope, we have achieved atomic resolution in NC-AFM and in the scanning tunneling microscopy (STM) mode. This includes the small and highly symmetric unit cell of the thin MgO(001) on Ag(001) as well as the two large and complex reflection domain unit cells of the thin alumina overlayer on NiAl(110) with its site distances comparable to those on closed packed metal surfaces.

Our results obtained for the Alumina/NiAl(110) surface shed light on a recent density functional theory (DFT) model from a new angle and show that NC-AFM is capable of giving new insight and different perspectives on experimental and theoretical results obtained with other techniques. In particular, results different from STM are shown, which spark interest in similarity and complementarity of results from both methods. The mapping and study of samples like complex oxide surfaces with densely packed sites require extreme stability and high sensitivity if one is to reach sub-Ångström spatial and adequate force resolution. In recent years, there have also been considerable efforts towards clarification of how to handle individual frequency shift curves that vary depending on the microscopic tip and of how to best extract unbiased results from these data. In this context, new in situ amplitude characterization techniques emerged during our studies [2]. However, providing the ultimate level of understanding requires developments in NC-AFM itself.

Atomic resolution on MgO/Ag(001) as well as the small unit cell are perfect starting points for measurements beyond imaging. For example, a detailed force field analysis revealing physical information of different sites is of great interest in catalysis especially for adsorption experiments. The chemical

activity of adsorbed metal particles depends strongly on their charge. Neutrally deposited Au atoms on MgO films might in some cases be charged and thus become chemically active [3]. Since a shift in the metal work function turns out to be the key factor for the charge transfer, we determined this shift with our dual mode NC-AFM/STM.

At this point, a comment may be necessary. In our publications, we use the nomenclature frequency modulation dynamic force microscopy (FM-DFM) for the FM mode in NC-AFM. It displays the implemented method and identifies it as a dynamic technique in contrast to the static bending of the first atomic force microscopes [4]. The historic notion of noncontact, however, can lead to conceptual difficulties when analyzing the details of the imaging mechanisms and to confusion between different implementations of force microscopy. Nevertheless, it has to be acknowledged that the word NC-AFM has gained a huge uniting power in the field of force microscopy, bringing together such different areas as biological studies under physiological conditions and works on single crystals at cryogenic temperatures with atomic resolution. We therefore think that the title for this book is not only well chosen, but that it has an appealing sound to it. In the following, we use NC-AFM synonymously for FM-DFM.

7.2 Methods and Experimental Setup

Our instrument (Fig. 7.1) is optimized for high resolution imaging in both NC-AFM and STM. The microscope operates in ultrahigh vacuum (UHV) at cryogenic temperature (5 K), which reduces damping of the force sensor and enhances it with respect to tip stability as well as to reduction of thermal drift, piezo creep, and piezo hysteresis. The setup ultimately enables atomic-resolution imaging and ultrastable spectroscopy of conducting and insulating surfaces by recording tunneling current and frequency shift with the same microscopic tip and if desired at the same time. Besides detailed investigation of surface structures, the high stability allows site-specific spectroscopy measurements, atom transfer, and single adatom contacts to be performed. However, meaningful conditions for such measurements can best be achieved at cryogenic temperatures. Therefore, evaporation of metals onto samples at low temperature is implemented beside the standard facilities for metal crystal and oxide film preparation. All measurements presented in this chapter were performed in UHV at 5 K [5]. More details on the particular equipment can be found in [5–7].

7.2.1 Quartz Tuning Fork-based Sensor for Dual-Mode NC-AFM/STM

The sensor in use is a quartz tuning fork as presented in [8] with a cut Pt/Ir wire as a NC-AFM/STM tip (see Fig. 7.2). Tip preparation can be performed in situ by field emission and/or dipping the tip into and pulling necks from

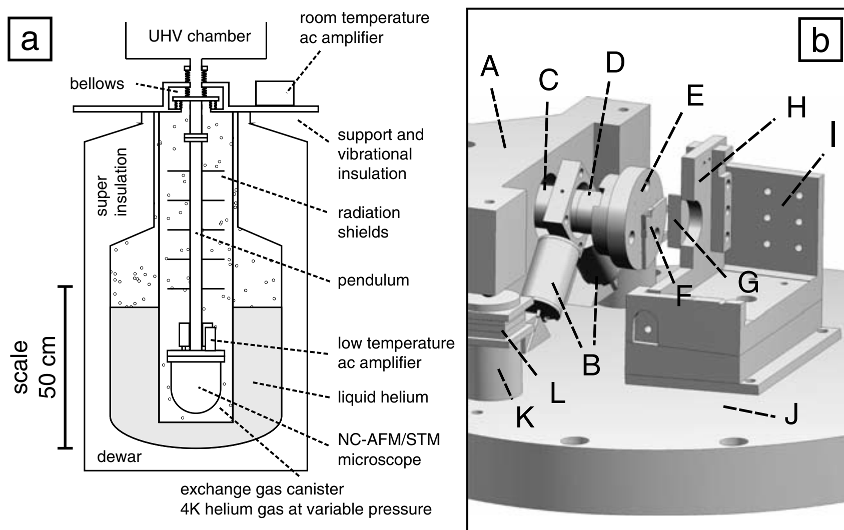

Fig. 7.1. (**a**) The experimental setup. An evacuated pendulum of about 1 m length suspended with steel bellows from the main UHV chamber is the central design feature for providing mechanical vibration insulation for the microscope. At its end, the NC-AFM/STM head is mounted in an UHV environment. The pendulum is placed inside an exchange gas canister filled with helium gas, which is surrounded by a liquid helium bath. The helium gas chamber prevents acoustic noise from perturbing the microscope while permitting thermal coupling to the liquid cryogen (helium or sometimes nitrogen). The low temperature ac amplifier is situated near the NC-AFM/STM head while the room temperature ac amplifier is mounted outside the dewar. (**b**) The microscope on its support stage: (A) Walker unit, (B) x-, y-piezo and (C) z-piezo of the tripod scanner unit, (D) z dither piezo, (E) sensor carrier, (F) tuning fork assembly, (G) sample (not fully drawn), (H) sample holder (not fully drawn), (I) sample stage, (J) microscope stage, (K) walker support, and (L) shear stack piezos. The support stage has a diameter of 100 mm

the sample surface. This removes residual oxide contaminants, produces good tip configurations, and has proven to be particularly useful with respect to the time consuming handling of UHV and low temperatures. The tuning fork assembly and electronics are capable of simultaneous recording of tunneling current I_t and frequency shift Δf while controlling the z-position of the tip via either of them [7]. The tip–wire has a diameter of 250 µm and is electrically connected to the signal electronics through a thin Pt/Rh wire with a diameter of 50 µm. Both, tip and contact wire are electrically insulated from the tuning fork and its electrodes. The frequency shift is directly recorded via the tuning fork electrodes while the tunneling current is taken independently from the contact wire of the tip (Fig. 7.2). Excitation of the tuning fork along the tip axis is done with a separate slice of piezo (dither piezo) on top of the z-piezo. The force sensor parameters spring constant $k \approx 22{,}000\,\mathrm{N\,m^{-1}}$, resonance

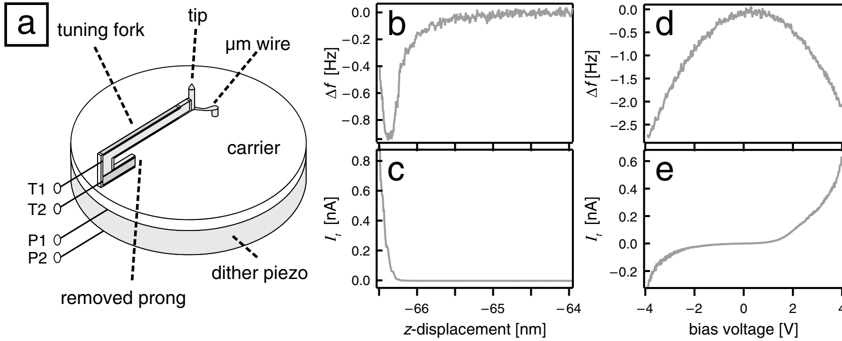

Fig. 7.2. (**a**) The sensor setup for NC-AFM and STM operation in UHV at low temperatures: dither piezo with connections P1, P2 for mechanical excitation in z-direction along the tip–axis. Quartz tuning fork on a ceramic carrier plate. Electronically separated signal wires for force (T1, T2 contacts of the tuning fork) and current (μm wire) detection. The same tip senses both signals. (**b**–**e**) Pairs of simultaneously recorded signal curves from the frequency shift and the current channel: (**b**–**c**) Signal–distance curves at constant bias voltage, (**d**–**e**) signal–bias voltage curves at constant height

frequency f_0 = 17–22 kHz, quality factor Q = 8,000–25,000 depend on the individual tuning forks. The oscillation amplitude A_{osc} has been set to values within the range 1–20 Å. The spring constant of the tuning fork sensor is significantly higher than typical interatomic force constants. This prevents a sudden "jump-to-contact" of the cantilever even at very small tip–sample distances and oscillation amplitudes. Also, the often observed instability and breakdown of oscillation amplitude after contact formation in the repulsive regime is reduced.

The great advantage of this setup is the simultaneous data acquisition from frequency modulation (FM) force detection in combination with the tunneling current. This enables, for example, the detection of insulating contaminants on the tip via a shift of the NC-AFM signal to larger distances off the surface with respect to the I_{t} signal than without such contaminants. In general, it is interesting to measure the two signals as they may complement each other, and the use of the very same microscopic tip enables direct comparison. A pair of curves from both channels recorded in a sweep in z-direction and another one recorded at varying bias voltage are shown in Fig. 7.2. The sensor is operated by the sensor controller/FM-detector easyPLLplus from Nanosurf [9] in the self-exciting oscillation mode [10] at constant oscillation amplitude. The detected oscillation amplitude signal is fed into an automatic gain control circuit and is used to self-excite the quartz tuning fork mechanically by the dither piezo. A phase shifter ensures that the spring system is excited at its resonance frequency. This operation mode of constant oscillation amplitude allows even to probe the regime of strong repulsive force in contrast to an operation mode at a constant excitation amplitude, where the oscillation amplitude decays

as the vibrating tip penetrates the repulsive interaction regime [11]. It furthermore readily facilitates theoretical analysis of the technique and results obtained with it. An additional custom-built analog FM detector has been used for the frequency shift recording based on [12]. The signal electronics has been described in [7]. A unit by Nanotech Electronics [13] as well as one by Nanonis [14] have been used for scan control and data acquisition.

7.2.2 Concepts for Force and Energy Extraction and Sensor Characterization

For the proper interpretation of tip–sample interaction forces and energies in NC-AFM, one naturally needs to make efforts in their precise extraction from experimental frequency shift data. Formulas (7.1) and (7.2) from [15] allow a determination of tip sample force F and potential energy U from the frequency shift. They are valid for the entire oscillation amplitude range accessible to sensors, that is, large and small amplitude regimes, and also cover the intermediate amplitude range below 1 nm in which we operate our tuning fork. The expression for the force in terms of the frequency shift is given by

$$F(D) = \frac{2k}{f_0} \int_D^\infty \left(1 + \frac{A_{\mathrm{osc}}^{1/2}}{8\sqrt{\pi(z-D)}} - \frac{A_{\mathrm{osc}}^{3/2}}{\sqrt{2(z-D)}} \frac{\mathrm{d}}{\mathrm{d}z} \right) \Delta f(z)\, \mathrm{d}z, \quad (7.1)$$

where D is the distance of closest approach between tip and sample, z is the tip–sample distance, A_{osc} the oscillation amplitude, k and f_0 the sensor constants, $\Delta f(z)$ the recorded frequency shift, and $F(D)$ is the interaction force between tip and sample. Integrating equation (7.1) gives the corresponding expression for the interaction energy $U(D)$ between tip and sample

$$U(D) = \frac{2k}{f_0} \int_D^\infty \left(z - D + \frac{A_{\mathrm{osc}}^{1/2}}{4} \sqrt{\frac{z-D}{\pi}} + \frac{A_{\mathrm{osc}}^{2/3}}{\sqrt{2(z-D)}} \right) \Delta f(z)\, \mathrm{d}z. \quad (7.2)$$

However, other formulas for the large and small amplitude limits, respectively, have already existed earlier [16, 17]. Equation (7.1) shows the dependence of derived force data on the frequency shift and equally important the dependence on sensor parameters. In particular, the oscillation amplitude assumed for force calculation from $\Delta f(z)$ has a crucial influence on the derived force and energy curves, while resonance frequency and spring constant of the sensor are simply proportionality constants. Therefore, we have developed methods for cantilever parameter determination for force sensors with an emphasis on in situ oscillation amplitude determination [2] and evaluated a standard measurement procedure for the spring constant with respect to our much stiffer tuning fork sensor with its particular geometry. For UHV

operation, but also in general, it will be beneficial to have a sensor characterization at hand that can be performed in situ and most important without damaging the microscopic tip. Our proposed amplitude characterization methods rely therefore on characteristics of the tip–sample interactions in frequency modulation NC-AFM or STM and the general response of sensors to them. They can be performed without laser interferometry, which may be desirable in low cooling-power cryostats. The first hurdle towards proper characterization is actually the determination of relative or possibly absolute distances. Relative motion is commonly quantified with monoatomic steps on several clean calibration specimens like low index metal surfaces. Access to absolute values may be achieved (if the sensor permits) via monitoring the conductivity within the tip–sample gap and transferring this to the force channel. For the amplitude determination schemes presented here, only relative positioning is relevant and z-calibration is assumed to be done.

The spring constant determination follows the well known Cleveland method, where frequency changes upon attachment of test masses allow determination of the spring constant from linear regression [18]. For tuning forks, one has to consider the influence of the elastic bearing of the oscillating prong at the base of the tuning fork. It effectively extends the prong into the basis leading to lower values of k than predicted by calculations based on prong geometry. Many other methods, like the static deflection methods, play no role because static deflection of the stiff tuning forks by calibration devices yields too small deflections and does not seem reasonable.

The oscillation amplitude A_{osc} of a tuning fork force sensor or other force sensor can be determined in situ from the characteristic change of signal–distance curves for a measured quantity upon amplitude variation at large amplitudes. The signal of choice can be the average tunneling current $\langle I_{\text{t}} \rangle$ as well as normalized frequency shift γ, frequency shift Δf or its derivative $\Delta f'$. Upon stabilizing the sensor and tip in the vicinity of the sample surface, a set of force– or current–distance curves is recorded at various oscillation amplitudes. A plot of the cantilevers changing relative equilibrium positions at constant $\langle I_{\text{t}} \rangle$, constant Δf, constant γ, or constant $\Delta f'$ vs. the corresponding values for A_{osc} gives the calibration curve. Alternatively, the calibration curve can be recorded by sweeping the amplitude and recording z-displacement while keeping the signal, then typically $\langle I_{\text{t}} \rangle$ or Δf, at a constant value. During the procedure, no tip changes must disturb the measurement. Important for amplitude determination are the larger values of A_{osc}, while the calibration factor is valid also at intermediate or small A_{osc} as long as the deflection varies linearly with excitation. The reason for this is the direct linear correspondence between amplitude increase and change in the sensor's equilibrium position in the large amplitude regime. It has unity slope. This holds, because from a certain value of A_{osc}, the signal interaction occurs solely in the half-period during which the tip is closest to the sample, while the half-period away from the surface gives vanishing contributions. This is the case for all A_{osc} at a constant signal value for which the equilibrium position of the sensor already resides in

the flat curve section of the measured quantity. Any further increase of A_{osc} at a certain equilibrium position then means a deviation from the preset constant signal value, which can then obviously be compensated by a retraction of the sensors equilibrium position that equals the initial increase of A_{osc} in size. Thus one can expect unity slope for the z-displacement of points at constant signal plotted over the A_{osc} they have been recorded with – at least in the large amplitude region. Relating the experimentally determined slope to unity gives the calibration factor for A_{osc}. What amplitude size can actually be considered large depends on the quantity used for characterization and the error that is accepted by the experimenter [2]. Performing the calibration with $\langle I_{\mathrm{t}} \rangle$ or $\Delta f'$ at oscillation amplitudes of several nanometers gives theoretical errors for the calibration factor of a few percent. Therefore, amplitude measurements of reasonable quality are feasible.

7.3 Atomic Resolution Imaging

After years of significant improvements in NC-AFM and after atomic resolution has been obtained on metal, semiconductor, and insulator surfaces [19–22], insulating surfaces with larger and much less symmetric unit cells are being studied. However, the amount of data from these systems is still very limited. Recent work on bulk alumina or associated thin films on NiAl and Ni_3Al surfaces has been promising though [23–27]. Being the very basis for more detailed insight into physical and chemical properties of a surface by NC-AFM, atomic resolution needs to be extended further towards more complex surface unit cells, larger corrugations (steps, kinks, molecules), and to bulk samples. Progress on thin films can be considered as a stepping-stone towards resolving all positions in large complex reconstructed surface unit cells of bulk insulators. Our sample system, the ultrathin alumina film on NiAl(110), with its high density and large number of inequivalent surface sites constitutes a good test for the resolution of our ultrahigh vacuum, low temperature NC-AFM. We present detailed images of the complex microstructure for both reflection domains of the thin alumina obtained with our microscope [28]. Resolution is such that atomic positions can be determined by simple graphical analysis in real space without application of filtering or correlation methods, emphasizing the potential of NC-AFM on complex oxide surfaces (Fig. 7.3).

Thin (5 Å) crystalline alumina overlayers can be grown on (110) surfaces of the ordered (CsCl-structure) intermetallic compound NiAl [29]. Film preparation has been carried out according to the recipe presented in the literature [29,30] and resulted in the usual flat topography with long range order on extended terraces and reflection as well as antiphase domain boundaries. Despite a large bandgap of about 6.7 eV [31], the limited thickness allows electron flow through the film into the substrate and therefore the application of electron based analysis techniques. Extensive studies in the context of model catalysis with many such surface science techniques [29–38] and a recent STM

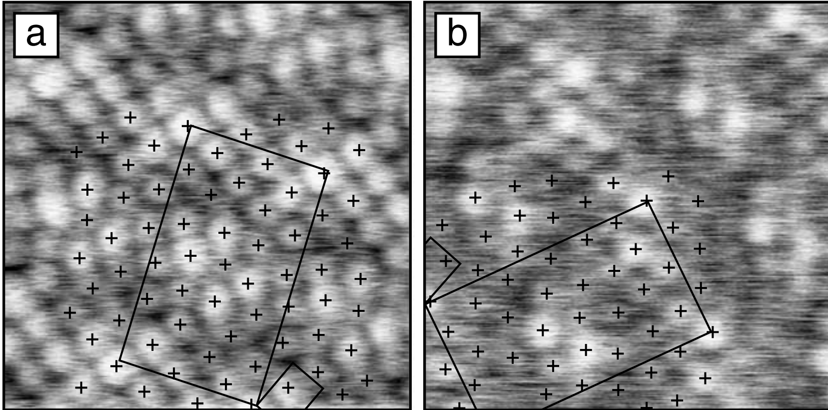

Fig. 7.3. High resolution NC-AFM images of the ultrathin alumina film on NiAl(110). (**a**) Domain B, (**b**) domain A. The geometrical relation between the oxide and the small NiAl(110) surface unit cell as well as overlays of atomic positions with crosses are indicated. Images were leveled and equalized. Scan area $3 \times 3\,\text{nm}^2$ each. (**a**) $\Delta f = -6.2\,\text{Hz}$, $A_{\text{osc}} = 1.4\,\text{Å}$; (**b**) $\Delta f = -6.7\,\text{Hz}$, $A_{\text{osc}} = 1.7\,\text{Å}$

and DFT study converged into an atomistic model of the film that matches many of the experimental findings [39]. The accumulated data give so far evidence for a nickel-free structure with two aluminum and oxygen double layers. It is oxygen terminated towards the vacuum with the next lower layer of 24 aluminum atoms 40 pm underneath. This aluminum layer sits on top of an oxygen interface layer with the equal number of 24 atoms. The bottom-most layer accommodates 16 aluminum atoms and anchors the film to the substrate. Lattice constants of the film's large, slightly parallelogram-shaped surface unit cells as determined by low energy electron diffraction are $b_1 = 10.55\,\text{Å}$ and $b_2 = 17.88\,\text{Å}$ enclosing an angle $\alpha = 88.7°$. Each oxide surface unit cell covers 16 of the $2.89 \times 4.08\,\text{Å}^2$ sized rectangular NiAl(110) surface unit cells. Dimensions, geometry, and orientation between the two oxide reflection domains and the substrate are illustrated in Fig. 7.4c. However, because of technical constrains, the DFT model [39] assumes a commensurate structure (10.93 Å, 17.90 Å; $\alpha = 88.16°$) for the film which is incommensurate in the [001] direction of the NiAl substrate. Extreme tunneling conditions in underlying STM data for the topmost oxygen layer give rise to speculations over substrate influence, mixed contributions from different atomic layers to images assigned to only one layer, and force interactions in the images. Therefore, the atomic surface structure is still under discussion and more real space information with atomic resolution is desirable.

Low noise, as achieved by low temperature pre-amplifiers, all measures for mechanical and electrical noise reduction, operation in UHV and at low temperature, is self speaking a fundamental prerequisite for highest resolution and stability. Another is a common set-point for the frequency shift across the

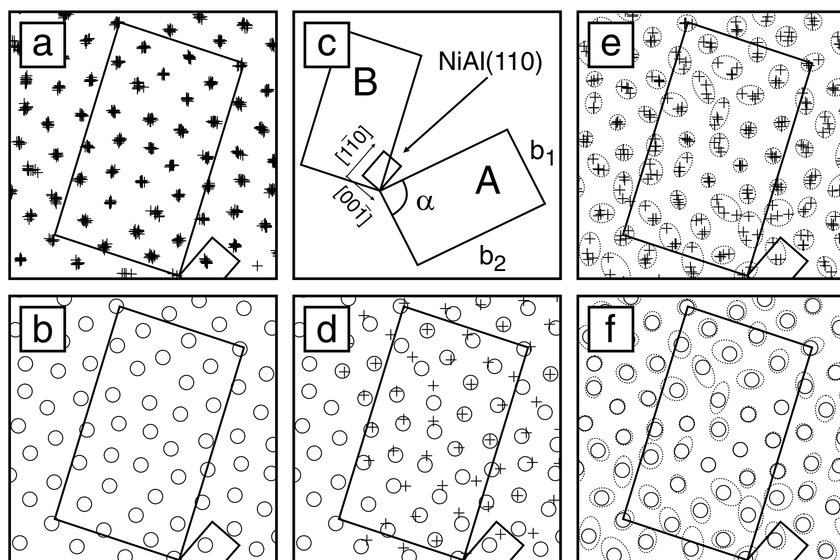

Fig. 7.4. (**a**) Stack of ten superimposed overlays with crosses of the surface unit cell taken from NC-AFM image in Fig. 7.3a of domain B. The spread in each set of crosses indicates the uncertainty due to imaging noise, weak contrast, and reading errors. (**b**) Average for overlays from (**a**) being the mean positions of the groups of crosses. (**c**) Geometry and dimensions of the two oxide overlayer domains A and B, their orientation relative to each other and to the NiAl(110) substrate ($b_1 = 10.55$ Å, $b_2 = 17.88$ Å, $\alpha = 88.7°$). (**d**) Average positions of domain A (*crosses*) reflected onto result for domain B (*circles* from (**b**)) for comparison. (**e**) Positions for the averaged overlays of several images (domain B). The spread here (given by *dotted loops*) allows to check reproducibility. (**f**) Average of positions from (**e**)

surface structure, which gets increasingly difficult with stronger corrugation and dissimilar interaction atop different sites. Large terraces reduce problems with features outside the scan frame and also small amplitudes have turned out to be advantageous. Last, but not least, one is to address the tip with the inherent uncertainties around its structure, stability, and chemical composition. Recorded surface structures have to be verified with another microscopic tip in each case. In our scheme, this is facilitated by in situ preparation of the tip with field emission and/or dipping (see Sect. 7.2.1).

Atomic resolution NC-AFM images of the ultrathin alumina film on NiAl(110) are shown in Fig. 7.3. Several such images of both the film's surface unit cells have been obtained. They have been leveled (subtraction of a parabola from each line in the image) and equalized (selected height range to enhance the image contrast), but no filtering has been necessary. However, long acquisition times required minor lateral corrections to be performed to account for slight drift. Clearly resolved are 28 individual protrusions visible in the surface unit cell of each reflection domain. This is in agreement with

the number of oxygen sites in the topmost layer of the DFT model and differs from the predicted number of 24 aluminum atoms in the second layer, which is in line with earlier experimental data on oxygen termination of the film. To show that the lateral structure is reproducibly obtained from the images, the following has to be confirmed:

- Scattering of positions related to reading error, noise, and reduced contrast in the images has to allow separation of all protrusions within each image.
- Lateral spread among positions of protrusions from different images assigned to the same site has to allow separation from all other sites. Here images should be recorded with different tips to guarantee reproducibility.
- A structure derived for one domain has to match the mirror image of the respective reflection domain.

To check the images for these requirements, they have been evaluated with respect to bright protrusions (Fig. 7.4). After identification of an identical surface unit cell in all images of both domains, overlays of the observed protrusions with crosses have been produced. Several overlays for the same image give a measure for the statistical reading error and uncertainty due to noise and weak contrast, while a comparison of overlays from different images (recorded after tip change or tip preparation) gives an idea of the imaging contribution and condition, that is, scanning parameters, shape, and atomic composition of the tip as well as atomic contrast mechanisms, to the uncertainty in position. Recurrent structures from such different and independent images indicate therefore reproducibility. The average positions in both cases are taken as mean positions of the sets of crosses belonging to individual positions in different overlays. Average overlays are shown in Fig. 7.4(b, d, f). The rather regular shapes of the areas covered by the groups of crosses belonging to the individual and averaged positions in different images – as given by dotted loops – emphasize that the found overlays are quite well defined (Fig. 7.4(e, f)). Most of the positions can be distinguished without any doubt. The evaluated images, which have been recorded with different microscopic tips on different surface sites, show that equal patterns and reproducibility are established. This is supported by the finding that the structure in one domain is reproduced by the mirrored positions from the other reflection domain (Fig. 7.4(d)), as required.

Each surface unit cell contains 28 observable protrusions matching the number proposed for the topmost oxygen layer by the DFT model. Figure 7.5 shows a direct graphical comparison with that oxygen layer of the model given in the supplement to [39]. We find the similarity rather striking. To first approximation, they indicate individual atomic sites marked with crosses in Fig. 7.3. One can also see that positions interconnecting the characteristic squares and rectangles of eight oxygen sites in the model are among the brightest protrusions in the NC-AFM images. On the other hand, protrusions at points with lower contrast naturally exhibit larger scattering of the crosses in Fig. 7.4e. These points fall into the troughs of the wave-like feature visible

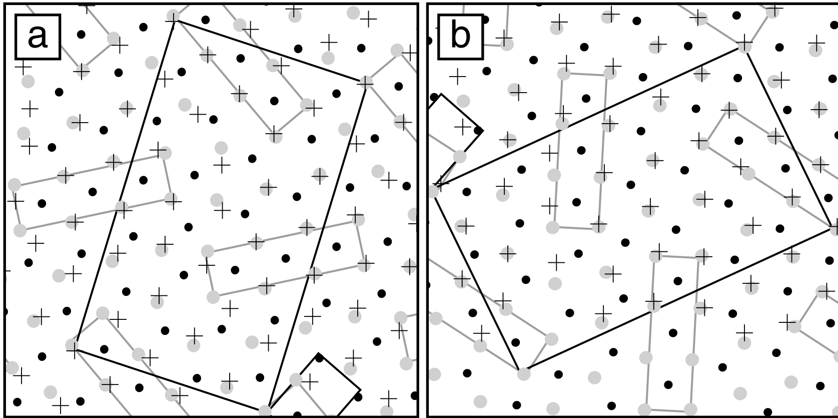

Fig. 7.5. Comparison of the atomic positions from averaged overlays for both domains (*crosses*) with those of the topmost oxygen (*grey dots*) and aluminum (*black dots*) atoms in the DFT model. Large black parallelograms indicate the oxide unit cell as chosen already in Fig. 7.3. Attached is the small black rectangle of the NiAl(110) unit cell. *Grey rectangles* highlight characteristic blocks of 8 surface oxygen atoms in the model. (**a**) Domain B, (**b**) domain A

in NC-AFM images (Fig. 7.3 and 7.6). It consists of alternating bright and dark rows: crests and troughs. This wave-like topography of the surface unit cells is in fact typical for the film [40] and related to strain and commensurability [41, 42]. As observed by NC-AFM before [24], the crests are 9 Å apart but the full repeat unit has a length of 18 Å, that is, that of an oxide unit cell. Each two of the protruding rows differ slightly in apparent structure, height, and contrast, making them inequivalent as shown in Fig. 7.6. However, a row pairing in lateral direction has not been found.

As the lateral structures can be resolved, the topography of the characteristic rectangular arrangements of eight oxygen atoms has been evaluated in detail (Fig. 7.7). The two opposing rectangular arrangements in the surface unit cell should be laterally equivalent due to the glide mirror plane in the structure's symmetry. With respect to average height and corrugation, however, they could differ. And indeed one sees a different spread in z-direction for the eight oxygen sites on inequivalent crests. This can be seen from each two parallel rows of four protrusions within the two opposing blocks. They are contrarily inclined with respect to each other. This is shown in Fig. 7.7 and compared with height values for the calculated oxygen sites of the DFT model. The experimental data are in reasonable qualitative and quantitative agreement with the theoretical result. Also, the DFT coordinates exhibit a mean height that is 6 pm smaller for the eight oxygen in the less pronounced crests compared to the stronger crests. In agreement with this, one finds a difference in mean height of 2.5 pm between inequivalent crests. If one now

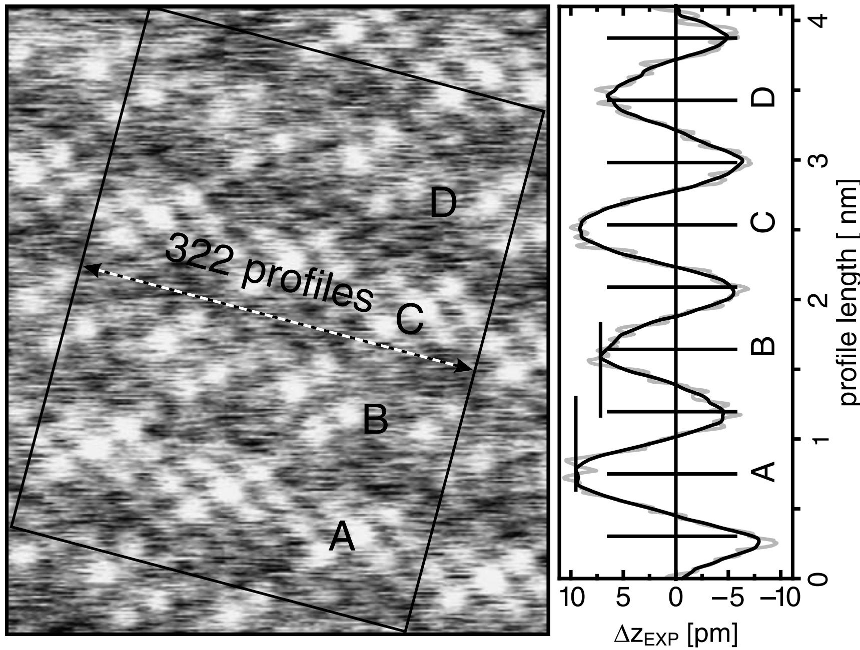

Fig. 7.6. NC-AFM image of a B domain (scan range $4.1 \times 4.8\,\text{nm}^2$, $\Delta f = -5.5\,\text{Hz}$, $A = 1.4\,\text{Å}$). The wave-like topographic feature of the oxide film exhibits two inequivalent but equidistant crests. They differ in the arrangement, contrast, and number of their brightest protrusions. The length of a complete period of the feature is 18 Å. The right part shows an average of 322 line profiles (*grey curve*) lined up along the short end (indicated by the *dashed double arrow line*) of the three unit cells broad rectangle marked in the image. The *black curve* has been smoothed. Every second crest is less pronounced. Line segments in the line profile are set to spacings of a quarter of a unit cell length

considers the orientation of these oxygen blocks with respect to the substrate, one finds those on the more pronounced crests to be rotated about 7° off the NiAl[001] axis. A similar result has been found for short gold chains adsorbed at low temperatures onto this film system. Their alignment at about 5° off the NiAl[001] symmetry axis results from a minimization of the mismatch towards the surface aluminum rows of the oxide film as well as to those of the substrate [43, 44].

Results in the lateral directions are consistent with a published density functional theory model and connect directly to other experimental data from the literature. For two prominent structural features, agreement with theory is found even for topographic height. Results reveal that structural analysis with sub Ångström resolution can allow insight into details beyond the atomic surface arrangement itself.

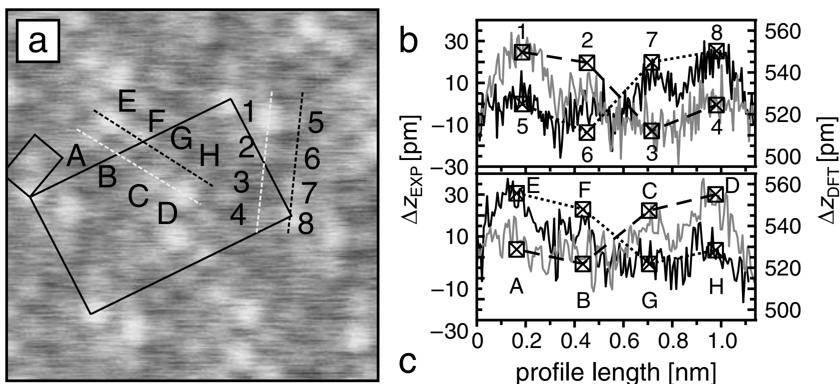

Fig. 7.7. (**a**) Topography of rectangular blocks of 8 protrusions. Scan range $3 \times 3\,\mathrm{nm}^2$. The parallel rows of four positions are inclined in opposite directions along the rectangle. (**b**–**c**) Line profiles in comparison to absolute heights for corresponding oxygen positions from the DFT model (*boxes with crosses*)

7.4 Beyond Imaging: Spectroscopy

In this section, we focus on site-specific spectroscopy measurements. Here we benefit from the great advantage of the dual mode NC-AFM/STM capabilities. The ability to sensitively detect forces as well as the local density of states with spatial resolution down to the atomic scale, at the same position and at the same time, is of great interest, as forces and effects related to electronic structure are fundamental quantities in physics. Concepts for force and energy extraction and sensor characterization are provided in Sect. 7.2.2. In the NC-AFM mode, the detected tip–sample force interaction can be used to generate a laterally resolved image (see Sect. 7.3) or to determine its distance dependence (see Sect. 7.4.1). During these measurements, the tunneling current is mapped simultaneously. The term spectroscopy might be irritating as it is usually related to energies and not to distance dependencies. Nevertheless, we will use it throughout the text, because it is somehow established in this sense throughout the literature. The basic parameters that can be varied in the experimental setup are the lateral and vertical displacement in x-, y-, and z-direction, the sample voltage V_s, and the oscillation amplitude A_osc, while measuring the frequency shift Δf, A_osc, dissipation, and the tunneling current I_t.

A wide variety of physical questions has been tackled with the help of scanning tunneling spectroscopy (STS) on its own. It provides the possibility to study electronic effects on a local scale. The analysis of Landau and spin levels [45], vibrational levels [46], Kondo resonances [47] as well as the imaging of electronic wave functions, like Bloch waves [48], drift states, and charge density waves [49], are only a few examples. As STS reflects the sum of squared wave functions, it is an obvious task to measure the local appearance of such

wave functions on solid surfaces. The combination of NC-AFM and STM provides therefore an extremely powerful tool to study local effects on oxide film surfaces.

For the spectroscopic measurements in this section, it seems useful to change the sample system from the complex surface structure of the thin alumina film to the rather simple structure of MgO films. Presented are a few topics and exemplary results performed with our setup on thin MgO(001) films deposited on Ag(001), which aim at characterization of properties of a certain area on the sample surface. The oxide film has been investigated with our STM and STS capabilities in the context of the analysis of localized electronic defects. Depending on the location (kink, edge, corner) of the defect, for the first time different defect energy levels have been observed in the band gap of MgO. The charge state of defects has been shown to be manipulable by the STM tip. Comparison with ground state energy levels of color centers on the MgO surface obtained from embedded cluster calculations supports the assignment of the defects to singly and doubly charged color centers [50].

Furthermore, adsorption properties of single gold and palladium atoms have been explored with respect to the thickness of supported MgO films underneath [51]. For Au on different MgO film thicknesses (3 and 8 ML), significant differences in the distribution of Au adsorption sites and in the Au cluster geometry have been found, which are in line with recent calculations and electron paramagnetic resonance experiments. On the surface of thick MgO films or unsupported MgO, Au adsorbs on O sites [52], and the equilibrium cluster geometry is three dimensional. In contrast, the calculations performed for thin MgO films predict a change of the preferred Au nucleation site [53] and a stabilization of two-dimensional Au cluster geometries [54]. While Pd atoms are arranged in a random fashion, Au forms an ordered array on the surface. The long-range ordering as well as the STM appearance of single Au atoms on a 3 monolayer thin MgO film can be explained through partial charge transfer from the substrate to Au atoms as predicted recently by density functional theory calculations [53]. In contrast to that, Au atoms on a thick film were found to be essentially neutral.

In the following, we present measurements beyond the imaging capabilities of NC-AFM. In the first section, we show z-spectroscopy measurements on individual atomic MgO sites followed by work function shift measurements on different MgO film thicknesses in the second section.

7.4.1 z-Spectroscopy on Specific Atomic Sites

Here precise measurements at 5 K, where the frequency shift is measured as a function of z and lateral displacement, are presented in detail. From these spatially resolved frequency shift spectra, the interaction force and energy can be directly derived. For the analysis and interpretation of NC-AFM images, it is important to measure the full interaction potential between probe and sample. Instead of keeping the frequency shift constant, it becomes necessary

to map the frequency shift at different z-displacements over the sample surface. Such a type of measurement allows to search for the largest interaction potential and to analyze the variation of the interaction potential at specific surface sites.

Frequency shift vs. distance curves can be measured at specific lattice sites or can be acquired in every point corresponding to a pixel of a NC-AFM image. Different types of modes for the force mapping have already been discussed in the literature for atomic force microscopes under ambient conditions operated in a static mode [55–57]. Measurements of site-dependent frequency shift curves on an atomic scale as a function of the tip–sample surface distance have been reported by several authors, for example, [8,58,59]. Moreover, distance dependent NC-AFM images [60], giving the possibility to acquire three-dimensional force related maps by NC-AFM, have been presented. Complete three-dimensional force fields with atomic resolution by NC-AFM have been shown by Hölscher et al. [61,62], where the force fields have been derived from frequency shift curves aligned at the previously acquired topography image.

Figure 7.8a shows an image with atomic resolution, which has been obtained on a flat terrace of the MgO film. The largest difference in contrast corresponds to adjacent next-neighbor ions in the (010) direction. A schematic illustration of the MgO/Ag(001) growth model is provided in Fig. 7.8b. After acquisition of the NC-AFM image, frequency–distance measurements were performed above the center of the two inequivalent labeled sites (Fig. 7.8d, position 1, 2), which will be discussed later on in more detail.

For the acquisition of two- or three-dimensional force or energy maps, the frequency shift needs to be measured, while moving the oscillating tip in x-, y-, and z-direction over a selected scan field. In principle, it should not matter in which direction one first moves the tip over the scan field. The order is defined by the needed precision in the spatial resolution and drift aspects of the scanner unit. A schematic view of this method is provided in Fig. 7.8c. The three dimensions in x-, y-, and z-direction can be independently addressed. The movement of the tip is adjusted by time synchronized triangular voltage cycles for the different scan directions. Here we have chosen to acquire the data set in the sequence of x-, z-, and y-direction, where x has the fastest and y the lowest scan speed. A single x-, z-scan is marked by a gray shaded area in Fig. 7.8c. With this setup we achieve a very high spatial resolution of the frequency shift in x-, z-direction. Such a frequency shift map is provided in Fig. 7.8d, where the frequency shift is color-coded and plotted across the x-, z-direction. The onset of atomic resolution can be seen by the lateral variation of the potential.

In Fig. 7.8e, a pseudo three-dimensional view of such a data set is plotted to illustrate the measured interaction potential in more detail. The atomically resolved contour lines show the variation in the interaction strength of the tip–sample surface potential. From these data sets, it is possible to derive the

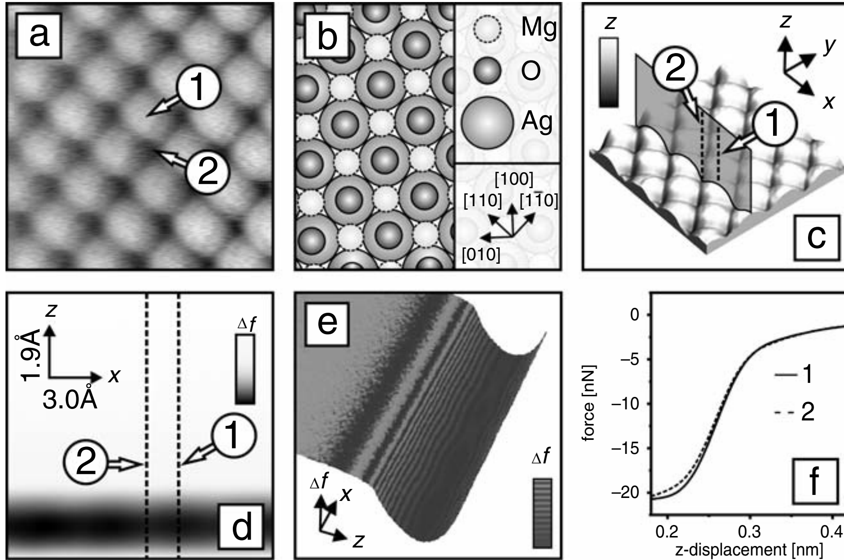

Fig. 7.8. (a) NC-AFM image of MgO on Ag(001) with atomic resolution. Scan area 1.5×1.5 nm, $\Delta f = -8.5$ Hz, oscillation amplitude $A_{\mathrm{osc}} = 0.35$ nm, $T = 5$ K, approximately 30 pm corrugation. The labels 1 and 2 indicate the position of frequency shift distance measurements (see text). (**b**) The MgO/Ag(001) growth model, schematic illustration of the configuration: Mg-atoms occupy hollow sites, that is, they continue the Ag fcc lattice ($a = 0.409$ nm), O-atoms occupy top sites. Schematic of the NC-AFM spectroscopy method. (**c**) During the data acquisition, the oscillating tip is moved in x-, z-, and y-direction over the selected scan field. A single x-, z-scan is marked by a *gray shaded area*. (**d**) Frequency shift image map of the selected x-, z-plane (1.5×0.95 nm). (**e**) A pseudo three-dimensional view of the frequency-shift measured in the x-, z-direction. (**f**) Selected force vs. distance curve calculated by the given formula (7.1) from the frequency shift image map at specific lattice sites marked in (**c**–**d**)

interaction force F between tip and sample as well as the according energy U by using formulas (7.1) and (7.2) [15].

Figure 7.8f displays two site-specific force distance curves (labeled 1 and 2) calculated from the frequency shift map in Fig. 7.8d. The selected curves are equivalent and in full agreement with single frequency shift vs. distance curves taken at the corresponding surface sites. Beside further quantification, we can now compare the features of the image obtained at a constant frequency shift (Fig. 7.8a) with the site-specific frequency-shift curves (Fig. 7.8f). One type of ion is imaged as a protrusion while the other one is imaged as a depression, which is a typical finding for ionic surfaces imaged by NC-AFM [22,63]. Here, the tip seems to prefer one atomic species. The comparison of the two force distance curves calculated from frequency shift vs. distance curves (Fig. 7.8f) clarifies that the deepest minimum, that is, the strongest tip–sample

interaction occurs at the protrusion. As the electron density on the MgO surface is maximal above the oxygen atoms [64], it is likely that the maxima in the NC-AFM image correspond to the position of the oxygen atoms. Moreover, electron paramagnetic resonance spectra have shown the possibility to determine the adsorption site of Au atoms, namely, adsorption on top of oxygen ions on the terrace of the MgO surface [52]. The hyperfine coupling constants measured by electron paramagnetic resonance spectroscopy are comparable to density functional theory calculations, indicating a good qualitative agreement of the theory with the experimental results. We can now consider a metallic tip apex to correspond to a metal atom or cluster, which probes the sample surface for adsorption sites of equilibrium force or energy interaction. With this measurement characteristics, we have an additional tool, which probes inequivalent surface sites to extract atomic-scale information on surface chemical reactivity and possible adsorption sites for metal atoms and small clusters. The combination with the highly resolved interaction potential in x- and z-direction furthermore allows one to derive the full shape of the interaction potential for further comparison with theoretical calculations.

7.4.2 Work Function Shift Measurements

In this section, we present three independent techniques to determine the metal work function shift of Ag(001) covered by different thickness of MgO films. The influence of the work function shift on charge transfer from a metal support through the thin MgO oxide film to neutrally deposited Au particles will be discussed. Finally, the experimental data will be compared to DFT calculations.

Charged particles and clusters adsorbed on metal supported thin oxide films are of high interest in the research area of catalysis. For example, Au particles that are rather inert become chemically active when they are charged. It has been shown that Au_8 clusters deposited on MgO are active in the $CO + 1/2\ O_2 \rightarrow CO_2$ conversion [3, 65] if stabilized at color centers (two electrons trapped in an oxygen vacancy) providing the charge. A typical defect concentration is about 1% of a monolayer [65], and as a consequence, charge transfer is not as likely as desired for catalytic processes. Recently, Pacchioni et al. [53] proposed charge transfer from a metal support through a thin MgO film to adsorbed Au particles also in the absence of defects [53, 66]. STM measurements in combination with DFT calculations confirmed the charge transfer for Au monomers and dimers adsorbed on defect poor thin MgO films grown on Ag(001) [51, 67]. Charge transfer depends on a variety of different mechanisms and effects. The most important ones are now briefly presented. With increasing MgO film thickness, the tunneling probability decreases. Thus the oxide film thickness must not exceed the tunneling length of the electrons, otherwise the charge transfer is shut off. Therefore, the film thickness might be used as a parameter to tune the catalytic properties of the adsorbed Au as discussed by Freund [68]. Furthermore, the electron affinity of the adsorbed

species should be high. A key factor for the charge transfer is a shift in the metal work function, resulting in a reduction of the tunneling barrier and thus an increase of the tunneling probability. This work function shift results mainly from the metal/oxide bonding distance. The oxide film reduces the surface electron density overspill into the vacuum and thus the surface dipole that the electrons, tunneling from the substrate to the adsorbed particle, have to overcome. This is clearly resolved for MgO/Mo(001) having a seven times larger adhesion energy than MgO/Ag(001), thus resulting in a shorter oxide-metal bond followed by a higher surface electron density compression and consequently a larger work function shift than for MgO/Ag(001) [66]. Moreover, the work function shift depends on metal induced gap states. Such states arise from penetration of metal electron wave functions into the oxide overlayer and from chemical bonds between metal and oxide [69, 70]. To determine the shift in the metal work function of Ag(001) with respect to different MgO film thicknesses, here nominal 0.5 ML MgO (effectively 1 ML MgO islands), 3 ML MgO, and 8 ML MgO (Fig. 7.9(a–c)), we applied three different methods.

The tunneling current as a function of z-displacement of the tip ($I_t(z)$), field emission resonances (FER) as well as contact potential differences (CPD) have been measured at defined lateral tip positions on terraces of the mentioned sample surfaces. While the first two methods are related to the tunneling current, the third method is related to the electrostatic force between tip and sample. Here we benefit from the possibility of our setup to directly switch between the three methods. At this stage, the three methods will be briefly introduced and publications for further reading will be stated, followed by the analysis of the data.

Method 1: $I_t(z)$-spectroscopy

During these measurements, the tip is located laterally at a fixed position. The feedback is off and the tip is moved towards the sample surface. Simultaneously, the z-displacement and the tunneling current are detected. During these measurements, the tip is not oscillated. The tunneling current $I_t(z)$ depends exponentially on the z-displacement as described by Binnig et al. [71]

$$I_t(z) \propto \exp\left(-\kappa \sqrt{\Phi_{ap}}\, z\right), \tag{7.3}$$

where κ is a constant, z is the displacement of the tip perpendicular to the surface, and Φ_{ap} is the apparent barrier height. It is not straightforward to extract the work function from the apparent barrier height as we will discuss later. A typical tunneling current vs. z-displacement curve is shown in Fig. 7.9d. From the slope in the logarithmic plot, we can calculate the apparent barrier height. Because of the fact that the tunneling current shows an exponential behavior, the lateral resolution is quite high. This is also true for the second method.

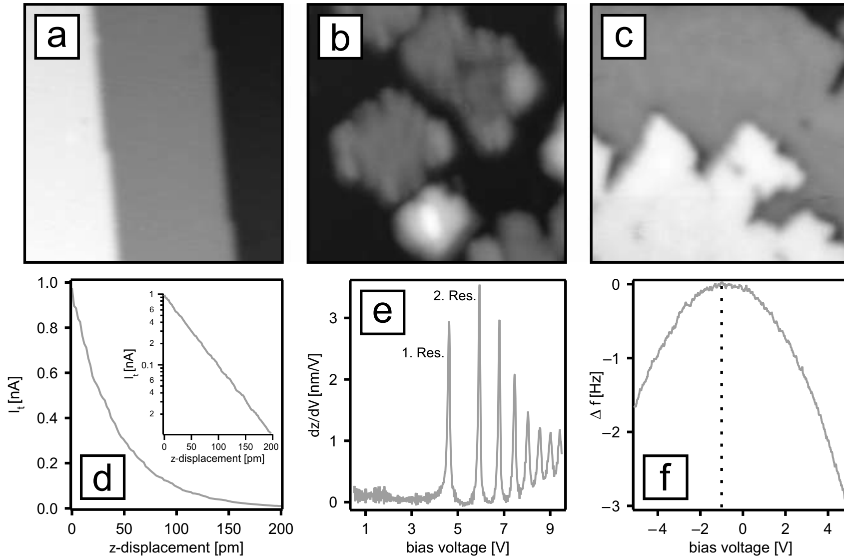

Fig. 7.9. Experiments in spectroscopy modes on top of thin MgO films on Ag(001) with varying thickness. (**a**) Bare Ag(001), $20 \times 20\,\mathrm{nm}^2$, $V_\mathrm{s} = 10\,\mathrm{mV}$, $I_\mathrm{t} = 1\,\mathrm{nA}$. (**b**) MgO patches (0.5 ML) grown on Ag(001), $50 \times 50\,\mathrm{nm}^2$, $V_\mathrm{s} = 3.5\,\mathrm{V}$, $I_\mathrm{t} = 400\,\mathrm{pA}$. (**c**) Several layer thick MgO film on Ag(001), $30 \times 30\,\mathrm{nm}$, $V_\mathrm{s} = 3.5\,\mathrm{V}$, $I_\mathrm{t} = 200\,\mathrm{pA}$. The rotated growth of MgO on Ag(001) is revealed by comparison with (**a**). (**d**) Current distance relation (inset shows the log-plot). (**e**) Field emission resonances on Ag(001). The first two resonances are indicated. (**f**) Parabolic voltage dependence of the electrostatic force component. Offset along the vertical axis due to other force components (subtracted) and along the horizontal axis due to work function difference as indicated by the *dotted line*

Method 2: FER-spectroscopy

Field emission resonances result from interfering electron wave functions. When the applied bias voltage exceeds the work function, electrons can enter a regime between tunneling barrier and sample surface. Electron waves are to some extent reflected at the borders of this regime. As a consequence, standing waves occur representing the eigenstates. The existence of FER was first theoretically predicted by Gundlach et al. [72] and experimentally confirmed by Binnig et al. [73]. To avoid tip changes, which are likely in the constant height mode because of the high electric field when going to high voltages, we measured in the constant current mode with a closed feedback loop. The tip was not oscillating and the lateral position of the tip was constant while the bias voltage was swept (see Fig. 7.9e). For the evaluation of the data, we assumed a 1D trapezoidal potential between tip and sample. Within this approximation, the FER can be described by [74]

$$eV_n = \Phi + \left(\frac{3\pi\hbar e}{2\sqrt{2m}}\right)^{2/3} E^{2/3} n^{2/3}, \tag{7.4}$$

where e is the charge of an electron, V_n is the voltage of the nth resonance, Φ is the work function, E is the electric field, and n is the number of the nth resonance. This equation does not take the image potential into account. The image potential rounds the corners of the barrier off [72]. Furthermore, the barrier is reduced, resulting in an increase of the tunneling current. As the image potential affects mainly the resonances with small n [74], we did not take the first resonance into account for the evaluation of the data. By fitting equation (7.4) to V_n vs. n, we can determine the work function of the sample system. The work function shift is then determined by the work function difference of the MgO film and the bare Ag(001).

Method 3: CPD-spectroscopy

This method is related to contact potential differences, which can be measured with a NC-AFM. From the collection of different forces acting between tip and sample, the long range electrostatic force is the force of interest, which is given by

$$F_{\text{el}} = -\frac{1}{2}\frac{\partial C}{\partial z}\left(U_{\text{bias}} - \frac{\Delta\Phi}{e}\right)^2, \tag{7.5}$$

where C is the capacitance, depending on the tip and sample geometry, U_{bias} is the applied bias voltage, e is the charge of an electron, and $\Delta\Phi$ is the work function difference of tip and sample, also known as the contact potential difference. Since the electrostatic forces are always attractive, the resonance frequency shift of the oscillating tip is always negative, see Fig. 7.9f. It shows a parabolic behavior due to the square term in the equation. During the measurements, the x-, y-, and z-position of the oscillating tip were constant, while the bias voltage U_{bias} was swept and the resonance frequency shift was detected (Fig. 7.9f). In this capacitor model involving the tip and sample, there is a vacuum gap when measuring on the bare Ag(001), while in the case of MgO/Ag(001) an additional dielectric is present. This dielectric will change the capacitance between tip and sample and thus it can influence the force between tip and sample, leading to an offset in the resonance frequency shift (Fig. 7.9f offset along the vertical axis). Furthermore, non-electrostatic forces, always present between tip and sample, influences this offset too. As this offset is not carrying the desired information, it can simply be subtracted. The important information arising from the work function difference is the shift of the maximum position of the parabola with respect to the zero bias position, as indicated by the dotted line in Fig. 7.9f (offset along the horizontal axis). By subtracting the work function difference taken on MgO/Ag(001) from the work function difference measured on Ag(001), we can eliminate

Table 7.1. Comparison of experimental and theoretical data [66]

Number of MgO layers on Ag(001)	Theory $\Delta\Phi$ (eV)	$I_t(z)$ $\Delta\Phi_{ap}$ (eV)	Experiment FER $\Delta\Phi$ (eV)	CPD $\Delta\Phi$ (eV)
MgO island	−1.01[a]	−2.0	−1.2	−0.5
3	−1.18	−1.4	−1.4	−1.1
8		−1.2	−1.3	−1.1

[a]Calculated for 1 monolayer

the contribution from the tip and end up with the work function difference between the different MgO films grown on Ag(001) and the bare Ag(001).

Table 7.1 shows the results of the measurements. Column 1 represents the number of MgO layers on Ag(001), column 2 shows theoretical values calculated by density functional theory using the generalized gradient approximation (PW-91 functional) [66]. Columns 3–5 present the experimental data taken with the three presented methods.

As already mentioned, it is not straightforward to extract the work function from the apparent barrier height Φ_{ap}. Controversial statements have been made in the past. Lang [75] claims in his theoretical considerations, a convergence of Φ_{ap} to Φ for large z-displacements, while Chen [76] in his theoretical approach shows that Φ_{ap} stays constant till point contact. The latter has been confirmed by Olesen et al. [77] in an experiment. The apparent work function Φ_{ap} calculated from the $I_t(z)$ measurements shows a large deviation compared to CPD, FER, and the calculated values from DFT. Especially for the MgO islands, Φ_{ap} is overestimated. In the case of the FER, the agreement between experimental and theoretical data is quite convincing. Because of the high lateral resolution, the work function shift derived on the 1 ML high MgO islands is comparable to the calculated DFT values. This high lateral resolution is not available in the third method.

The contact potential difference measurements in the NC-AFM mode on MgO islands reveal a value of $\Delta\Phi = -0.5\,\text{eV}$. This value seems to be too small compared to the theoretical value of $\Delta\Phi = -1.1\,\text{eV}$ for one monolayer of MgO. The underestimation of this value might arise from a large surface area involved in this measurements, thus the lateral resolution is fairly low, resulting in an average of the bare metal and the MgO patch area. However, this averaging effect seems to have only an influence on patched films and not on closed monolayers of MgO. The work function shift on 3 and 8 ML MgO films turns out to be the same $\Delta\Phi = -1.1\,\text{eV}$, which is in close agreement with the theoretical predictions.

In conclusion, the analysis, the shift in the metal work function as calculated by Giordano et al. [66] could be confirmed by CPD- and FER-spectroscopy. The agreement between theory and experiment is excellent. As the work function shift is already set up by the first monolayer MgO, the effect seems to be dominated by the metal/MgO interface.

7.5 Conclusion

In summary, these experiments demonstrate different applications, opportunities, and the potential of NC-AFM and combined NC-AFM/STM measurements. For the first time, atomically resolved images of the complex surface unit cells of the ultrathin alumina film on NiAl(110) have been obtained in NC-AFM mode. It has been possible to observe all individual atomic positions in the surface unit cells for both reflection domains of the topmost oxygen layer unambiguously. Our results confirm the combined STM and DFT model [39] and complement earlier NC-AFM images [24] from the literature. For selected structural elements, quantitative agreement for the corrugation has been found. Graphical evaluation of the images and line profiles of spot patterns in the surface unit cell has been sufficient to derive the positions. No application of any filtering or correlation techniques has been necessary. The results are a promising step towards high resolution real space atomistic surface characterization of thick insulating films and eventually bulk surfaces of wide band insulators with complex surface unit cells.

Atomically resolved NC-AFM images of MgO films have been combined with site-specific frequency shift vs. distance measurements. The frequency shift has been measured as a function of z and the lateral displacement [8]. With these measurement characteristics, we have probed inequivalent surface sites on thin MgO films to extract atomic-scale information on surface chemical reactivity and possible adsorption sites for metal atoms and small clusters. Furthermore, the metal work function shift as a key parameter for charge transfer and therefore for the catalytic properties of adsorbed particles has been determined with contact potential differences and field emission resonances spectroscopy. The results are in good agreement with DFT calculations.

Acknowledgements

The authors thank Hans-Peter Rust and Gero Thielsch for major contributions to the development and maintenance of the experimental setup. Hans-Joachim Freund is gratefully acknowledged for his help and advise. Furthermore, we acknowledge Marek Nowicki and Thomas P. Pearl for fruitful discussions.

References

1. H.-J. Freund, Faraday Discuss. **114**, 1 (1999)
2. G.H. Simon, M. Heyde, H.-P. Rust, Nanotechnology **18**, 255503 (2007)
3. B. Yoon et al., Science **307**, 403 (2005)
4. G. Binnig, C.F. Quate, G. Gerber, Phys. Rev. Lett. **56**, 930 (1986)
5. M. Heyde, M. Kulawik, H.-P. Rust, H.-J. Freund, Rev. Sci. Instrum. **75**, 2446 (2004)

6. M. Heyde, M. Sterrer, H.-R. Rust, H.-J. Freund, Appl. Phys. Lett. **87**, 083104 (2005)
7. H.-P. Rust, M. Heyde, H.-J. Freund, Rev. Sci. Instrum. **77**, 043710 (2006)
8. M. Heyde, G.H. Simon, H.-P. Rust, H.-J. Freund, Appl. Phys. Lett. **89**, 263107 (2006)
9. Nanosurf AG, Grammetstrasse 14, CH-4410 Liestal, Swiss.
10. K. Kobayashi et al., Rev. Sci. Instrum. **72**, 4383 (2001)
11. B. Gotsmann, H. Fuchs, Appl. Surf. Sci. **188**, 355 (2002)
12. T.R. Albrecht, P. Grütter, D. Horne, D. Rugar, J. Appl. Phys. **69**, 668 (1991)
13. Nanotec Electronica, Parque Cientifico de Madrid, Pabellon C, campus UAM, Cantoblanco, E-28049 Madrid, Spain.
14. Nanonis GmbH, Technoparkstrasse 1, CH-8005 Zurich, Swiss.
15. J.E. Sader, S.P. Jarvis, Appl. Phys. Lett. **84**, 1801 (2004)
16. U. Dürig, Appl. Phys. Lett. **75**, 433 (1999)
17. F.J. Giessibl, Appl. Phys. Lett. **78**, 123 (2001)
18. J.P. Cleveland, S. Manne, D. Bocek, P.K. Hansma, Rev. Sci. Instrum. **64**, 403 (1993)
19. F.J. Giessibl, Science **267**, 68 (1995)
20. C. Loppacher et al., Appl. Surf. Sci. **140**, 287 (1999)
21. R. Bennewitz et al., Phys. Rev. B **62**, 2074 (2000)
22. C. Barth, C.R. Henry, Phys. Rev. Lett. **91**, 196102 (2003)
23. C. Barth, M. Reichling, Nature **414**, 54 (2001)
24. C.L. Pang, H. Raza, S.A. Haycock, G. Thornton, Phys. Rev. B **65**, 201401(R) (2002)
25. G. Hamm et al., Phys. Rev. Lett. **97**, 126106 (2006)
26. S. Gritschneder, C. Becker, K. Wandelt, M. Reichling, J. Am. Chem. Soc. **129**, 4925 (2007)
27. S. Gritschneder et al., Phys. Rev. B **76**, 014123 (2007)
28. G.H. Simon et al., Phys. Rev. B **78**, 113401 (2008)
29. R.M. Jaeger et al., Surf. Sci. **259**, 235 (1991)
30. M. Kulawik, N. Nilius, H.-P. Rust, H.-J. Freund, Phys. Rev. Lett. **91**, 256101 (2003)
31. S. Andersson et al., Surf. Sci. **442**, L964 (1999)
32. H. Isern, G.R. Castro, Surf. Sci. **211**, 865 (1989)
33. J.-P. Jacobs et al., J. Vac. Sci. Technol. A **12**, 2308 (1994)
34. J. Libuda et al., Surf. Sci. **318**, 61 (1994)
35. A. Sandell et al., J. Electron Spectrosc. Relat. Phenom. **76**, 301 (1995)
36. G. Ceballos et al., Chem. Phys. Lett. **359**, 41 (2002)
37. S. Ulrich, N. Nilius, H.-J. Freund, Surf. Sci. **601**, 4603 (2007)
38. T. Nishimura, Y. Hoshino, T. Okazawa, Y. Kido, Phys. Rev. B **77**, 073405 (2008)
39. G. Kresse et al., Science **308**, 1440 (2005)
40. T. Bertrams, A. Brodde, H. Neddermeyer, J. Vac. Sci. Technol. B **12**, 2122 (1994)
41. K.F. McCarty, J.P. Pierce, B. Carter, Appl. Phys. Lett. **88**, 141902 (2006)
42. M. Schmid et al., Phys. Rev. Lett. **97**, 046101 (2006)
43. M. Kulawik, N. Nilius, H.-J. Freund, Phys. Rev. Lett. **96**, 036103 (2006)
44. N. Nilius et al., Phys. Rev. Lett. **100**, 096802 (2008)
45. M. Morgenstern et al., Phys. Rev. B **62**, 7257 (2000)

46. B.C. Stipe, M.A. Rezaei, W. Ho, Science **280**, 1732 (1998)
47. A. Hewson, *From the Kondo Effect to Heavy Fermions* (Cambridge University Press, Cambridge, 1993)
48. H.A. Mizes, J.S. Foster, Science **244**, 559 (1989)
49. C.G. Slough et al., Phys. Rev. B **34**, 994 (1986)
50. M. Sterrer et al., J. Phys. Chem. B **110**, 46 (2006)
51. M. Sterrer et al., Phys. Rev. Lett. **98**, 096107 (2007)
52. M. Yulikov et al., Phys. Rev. Lett. **96**, 146804 (2006)
53. G. Pacchioni, L. Giordano, M. Baistrocchi, Phys. Rev. Lett. **94**, 226104 (2005)
54. D. Ricci, A. Bongiorno, G. Pacchioni, U. Landman, Phys. Rev. Lett. **97**, 036106 (2006)
55. M. Radmacher et al., Biophys. J. **66**, 2159 (1994)
56. D.R. Baselt, J.D. Baldeschwieler, J. Appl. Phys. **76**, 33 (1994)
57. D.D. Koleske et al., Rev. Sci. Instrum. **66**, 4566 (1995)
58. S. Morita, Y. Sugawara, K. Yokoyama, T. Uchihashi, Nanotechnology **11**, 120 (2000)
59. A. Schirmeisen, D. Weiner, H. Fuchs, Phys. Rev. Lett. **97**, 136101 (2006)
60. T. Minobe et al., Appl. Surf. Sci. **140**, 298 (1999)
61. H. Hölscher, S.M. Langkat, A. Schwarz, R. Wiesendanger, Appl. Phys. Lett. **81**, 4428 (2002)
62. S.M. Langkat, H. Hölscher, A. Schwarz, R. Wiesendanger, Surf. Sci. **527**, 12 (2003)
63. A.I. Livshits, A.L. Shluger, A.L. Rohl, A.S. Foster, Phys. Rev. B **59**, 2436 (1999)
64. P.V. Sushko, A.L. Shluger, C.R.A. Catlow, Surf. Sci. **450**, 153 (2000)
65. A. Sanchez et al., J. Phys. Chem. A **103**, 9573 (1999)
66. L. Giordano, F. Cinquini, G. Pacchioni, Phys. Rev. B **73**, 045414 (2005)
67. V. Simic-Milosevic et al., J. Am. Chem. Soc. **130**, 7814 (2008)
68. H.-J. Freund, Surf. Sci. **601**, 1438 (2007)
69. J. Goniakowski, C. Noguera, Interface Sci. **12**, 93 (2004)
70. Y.-C. Yeo, T.-J. King, C. Hu, J. Appl. Phys. **92**, 7266 (2002)
71. G. Binnig, H. Rohrer, Surf. Sci. **126**, 236 (1983)
72. K.H. Gundlach, Solid-State Electron. **9**, 949 (1966)
73. G. Binnig, H. Roherer, Helv. Phys. Acta **55**, 726 (1982)
74. O.Y. Kolesnychenko, Y.A. Kolesnichenko, O. Shklyarevskii, H. van Kempen, Physica B **291**, 246 (2000)
75. N.D. Lang, Phys. Rev. B **37**, 10395 (1988)
76. C.J. Chen, *Introduction to Scanning Tunneling Microscopy* (Oxford University Press, New York, 1993)
77. L. Olesen et al., Phys. Rev. Lett. **76**, 1485 (1996)

8

Atom Manipulation on Semiconductor Surfaces

Yoshiaki Sugimoto

Abstract. Since the sophisticated atom manipulation experiment reported by Eigler, single atom manipulation and assembly by scanning tunneling microscopy (STM) has attracted much attention because of the intriguing applications in nanofabrication and nanoscience. In recent years, we have developed an atom manipulation technique using atomic force microscopy (AFM), which has proven to be a powerful tool for imaging individual atoms on insulating as well as conducting surfaces, force spectroscopic measurements between single atoms, and even chemical identification. After the first demonstration of the vertical and lateral manipulation of single atoms using AFM at low temperature, we have achieved well-controlled atom manipulation and assembly on semiconductor surfaces even at room temperature. The new method to enable us to rearrange surface adatoms at room temperature is based on an interchange of different atom species.

8.1 Introduction

The ability to engineer nanostructures with unique and specific properties is a key technology for developing the next generation of novel nanoelectronic devices. For this tremendous goal, major success is anticipated through the bottom-up approach: an attempt to create such nanodevices from the atomic or molecular level instead of miniaturizing from the macroscopic world. In the bottom-up approach, the ultimate limit is to engineer artificial nanostructures on surfaces by manipulating single atoms or molecules one by one. In 1990, Eigler reported that single atoms can be laterally manipulated on a surface to create an artificial nanostructure using a scanning tunneling microscope (STM) [1]. Since then, only a few groups worldwide have developed the required STM technology for nanostructuring on a surface by precisely allocating single atoms and molecules at desired positions [2,3]. The technique has developed to a point that it is possible to build a logic gate [4] based on a few hundred molecules, or to complete the initial stage of wiring a single molecule and to study the electrical properties of this metal–molecule–metal junction [5]. Most of these technologically promising experiments [1–14], however,

S. Morita et al. (eds.), *Noncontact Atomic Force Microscopy*,
NanoScience and Technology,
DOI: 10.1007/978-3-642-01495-6_8, © Springer-Verlag Berlin Heidelberg 2009

must be performed at low temperature (LT), where the low thermal energy of the atoms at the surface guarantees the stability of the artificially created nanostructure, avoiding diffusion or desorption. To achieve nanodevices operative in ambient conditions, strategies for atom-by-atom construction of stable nanostructures at room temperature (RT) are highly desirable.

STM was the only tool with all the necessary capabilities for manipulating single atoms and molecules and arranging them on a surface at will until true atomic resolution using an atomic force microscope (AFM) was achieved [15–17]. Our group has developed an atom manipulation technique using AFM and it was demonstrated that AFM can manipulate atoms, even at RT, with high precision, comparable to previous STM studies [18, 19].

In this chapter, we review atom manipulation experiments on semiconducting surfaces that our group has performed during the past several years. The first experimental evidence of reproducible mechanical vertical manipulation of selected single atoms of a surface using AFM was reported in 2003 [20]. In vertical atom manipulation, atoms are vertically transferred between tip and surface. Atom extraction from a surface is illustrated in Fig. 8.1a. In 2005, lateral manipulation of single atoms that adsorbed on a surface at LT was reported [21]. In lateral atom manipulation, single atoms that always stay on the surface are laterally manipulated as shown in Fig. 8.1b. Then atom

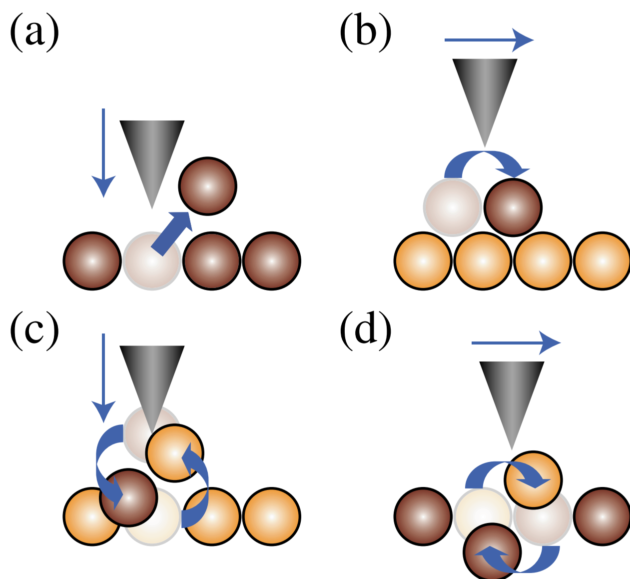

Fig. 8.1. Classification of atom manipulation modes demonstrated by AFM. (**a**) Vertical atom manipulation, (**b**) lateral atom manipulation, (**c**) interchange vertical atom manipulation, and (**d**) interchange lateral atom manipulation. The latter two methods enable us to manipulate single atoms at room temperature

manipulation and assembly at RT with similar precision to that obtained in LT manipulation experiments using STM was demonstrated [18]. This RT technique is based on a novel method that we call interchange lateral atom manipulation, in which two different atomic species are interchanged in the plane of a heterogeneous surface, as shown in Fig. 8.1d. In 2007, a combination of conventional lateral atom manipulation experiments and first-principle calculation clarified the mechanism of mechanical lateral atom manipulation on the Si(111)-(7×7) surface at RT [22]. Moreover, in 2008, we demonstrated a novel method for engineering nanostructures on surfaces at RT by vertically interchanging tip apex atoms and single surface atoms as shown in Fig. 8.1c [19], a technique we call interchange vertical atom manipulation.

The remainder of this chapter is organized as follows. First, the experimental method is described in Sect. 8.2. Second, we present vertical atom manipulation in Sect. 8.3, lateral atom manipulation at LT in Sect. 8.4, interchange lateral atom manipulation in Sect. 8.5, lateral atom manipulation at RT in Sect. 8.6, and interchange vertical atom manipulation in Sect. 8.7. Finally, concluding remarks are presented in Sect. 8.8.

8.2 Experimental

We have used two similar types of ultrahigh vacuum AFM, of which one works at RT and the other at LT [23]. The deflection of commercial Si cantilevers with a typical spring constant of $30\,\mathrm{N\,m^{-1}}$ and first resonant frequency of 160 kHz (NanoWorld AG, Neuchatel, Switzerland) was detected using a home-built interferometer. A sharp, clean Si tip apex was prepared by Ar ion sputtering in ultrahigh vacuum. The cantilever dynamics were detected and regulated using phase-locked loop-based commercial electronics (Nanosurf AG, Liestal, Switzerland). A constant amplitude mode was applied for cantilever oscillation, except for the vertical atom manipulation experiments in Sect. 8.3, where a constant excitation mode was used. The cantilevers were oscillated at relatively large amplitudes (on the order of 10 nm) to maintain a stable oscillation amplitude [24]. The shift in the cantilever's first mechanical resonant frequency (frequency shift, Δf) was the observable used for controlling the tip–surface distance. Data acquisition, microscope operation, force spectroscopy, and single atom manipulation processes were performed through a very versatile commercial scanning probe controller based on digital signal processor technology (Nanotec Electronica S.L., Madrid, Spain) [25].

We used two substrates of Si(111) and Ge(111) for atom manipulation experiments. A clean Si(111)-(7×7) surface was obtained from an n-type single crystal Si wafer by direct current heating, flashing the sample up to 1,200°C with subsequent slow cooling from 900°C to RT. During sample preparation, vacuum pressure was kept below 1×10^{-10} Torr. This surface was used for vertical atom manipulation in Sect. 8.3 and lateral atom manipulation at RT in Sect. 8.6. Sn/Si(111)-($\sqrt{3} \times \sqrt{3}$), In/Si(111)-($\sqrt{3} \times \sqrt{3}$), and

Sb/Si(111)-(7×7) surfaces were used for the interchange lateral atom manipulation described in Sect. 8.5. These surfaces were prepared by evaporating Sn, In, or Sb atoms on the Si(111)-(7×7) surface followed by annealing the sample [26, 27]. The Sn/Si(111)-$(\sqrt{3} \times \sqrt{3})$ surface was also used for interchange vertical atom manipulation, as described in Sect. 8.7.

Clean reconstructed Ge(111)-c(2×8) surfaces were prepared by successive cycles of Ar ion sputtering while heating the sample at 500°C. Typical ion bombardment parameters were 1 keV of ion beam energy, with an ion current measured at the sample of approximately 4 µA and a 45° of incidence angle. After the ion bombardment, upon recovering a vacuum pressure of less than 1×10^{-10} Torr, a further sample annealing at 750°C for 3 min followed by a slow cool-down to RT completed the surface preparation. Ge(111)-c(2×8) surfaces were used for lateral atom manipulation at LT in Sect. 8.4. Sn/Ge(111)-c(2×8) surfaces were prepared for interchange lateral atom manipulation in Sect. 8.5. This surface was prepared by evaporating a small number of Sn atoms on the Ge(111)-c(2×8) surface and then annealing the surface [28].

8.3 Vertical Atom Manipulation

First, we present the first experimental evidence, to our knowledge, of the reproducible mechanical vertical manipulation of selected single atoms of a surface by using AFM [20]. The method is based on a carefully controlled soft nanoindentation process at a constant excitation mode of the cantilever oscillation using LT-AFM (80 K). The results of vertical manipulation of Si adatoms on the Si(111)-(7×7) surface are shown in Fig. 8.2. After taking an atomically resolved image over a region centered on one terrace of the surface [Fig. 8.2a], a specific Si adatom in the imaged area was selected for manipulation, as shown by the circle. The tip was positioned directly above this target Si adatom, and the tip–sample distance was gradually decreased from the imaging distance by applying a ramp voltage to the electrode of the piezo-electric scanner with the feedback loop open. Since the cantilever was oscillating at its first resonant frequency, multiple nanoindentation processes took place during the sample approach. The nanoindentation process was carefully controlled by simultaneously monitoring both the variations of the cantilever oscillation amplitude and Δf. Upon further indentation, a sudden jump in Δf was normally detected. At this point, the ramp was stopped, the tip–sample distance was increased to the initial distance, and the feedback was reactivated. Figure 8.2b is the image obtained with the same parameters used for taking the initial image. The selected Si center adatom marked with a circle in Fig. 8.2a was removed from its initial position, and a vacancy was created without additional perturbation of the Si(111)-(7×7) unit cell. This fact implies that at least three strong covalent bonds that fixed the Si adatom to the surface were broken during nanoindentation. Moreover, the deposition of a single atom can be performed over the created vacancy in Fig. 8.2b by the

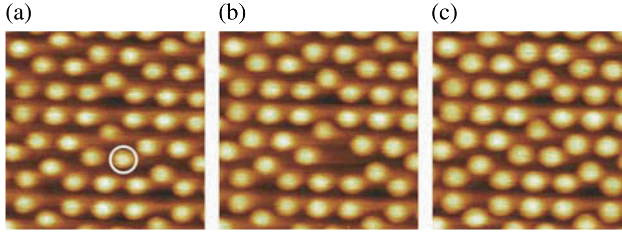

Fig. 8.2. Sequence of AFM topographic images showing mechanical vertical atom manipulation. A single Si adatom marked with a circle in (**a**) was removed by vertical approach of the tip toward the Si adatom. A single atom was deposited on the created vacancy site visible in (**b**). As a result, the perfect surface was restored as shown in (**c**). Image size is $47 \times 47\,\text{Å}^2$. The cantilever oscillation amplitude (A) and Δf were 257 Å and -4 Hz, respectively [20]

same method as that applied for atom extraction. Figure 8.2c shows that a single atom transferred from the tip restored the initial unperturbed structure of the Si(111)-(7×7) half-cell. This result implies the possible formation of three new covalent bonds, as the deposited atom adapted to a central adatom position of the Si(111)-(7×7) reconstruction.

This experiment proved that AFM has enough precision to perform vertical manipulation of single atoms. Soon after, it was demonstrated that the same technique can be used for vertical atom manipulations on the same surface even at RT [29].

Previous STM studies on manipulation of the bare Si(111)-(7×7) surface suggested that the mechanism for removing single Si adatoms at RT was thermally activated field ion emission due to a high electric field between tip and sample during the application of a voltage pulse [14,30,31]. This could also be the mechanism for the modification of the Si(111)-(7×7) surface performed at LT using AFM by applying a voltage pulse between tip and sample [32]. An alternative mechanism was proposed for the lateral displacement of single Si adatoms on the same surface performed by LT-STM, where tunneling electrons from the STM tip, temporally occupying a surface resonance state, could play a fundamental role [33]. Nevertheless, a completely different mechanism for manipulating Si adatoms should be involved in the mechanical atom manipulation presented here, because neither a bias voltage nor a voltage pulse was applied between the AFM tip and the sample during the manipulation process. See Chap. 11 for the detailed mechanism of mechanical vertical atom manipulation.

8.4 Lateral Atom Manipulation at Low Temperature

The first lateral atom manipulation using AFM has been demonstrated using the same LT apparatus as that used for the first vertical atom manipulation experiment in Sect. 8.3. An adsorbate deposited from the tip on a clean

Ge(111)-c(2×8) surface was laterally manipulated at 80 K [21]. The adsorbate was imaged as a bright spot in AFM images, as shown in Fig. 8.3a. Individual Ge adatoms on the Ge(111)-c(2×8) substrate were also observed with slight contrast. Scanning at a far enough tip-surface distance, characterized by a Δf set point for imaging ($\Delta f_{\mathrm{image}}$), it can be seen that this adsorbate remained unperturbed at the surface during imaging (Fig. 8.3a). In contrast, two bright spots instead of one were observed in a subsequent image (Fig. 8.3 b). In this image, the tip was scanned from the bottom to the horizontal dotted line with slightly reduced tip–surface distance by changing the set point to the value for manipulation (Δf_{move}). Then from the horizontal dotted line to the top, the tip–surface distance was increased by restoring the $\Delta f_{\mathrm{image}}$ set point. A possible explanation of the double protrusions observed in Fig. 8.3b is that after the adsorbate at the initial position was imaged, it jumped to the next stable adsorption position in the same direction as the slow scan, and then the same adsorbate was imaged again. No additional atom movement was observed after recovery of the tip–surface distance.

In the same way, the adsorbate was consecutively manipulated along the $[1\bar{1}0]$ direction as shown in Figs. 8.3 (c)–(h). The arrows indicate the slow scan direction; the solid (dotted) arrows correspond to imaging at Δf_{move} ($\Delta f_{\mathrm{image}}$), respectively. Dotted lines indicate the slow scan position at which the set point was switched from Δf_{move} to $\Delta f_{\mathrm{image}}$. As Fig. 8.3b–h illustrates, the adsorbate was manipulated as following the slow tip scan when imaging at high attractive interaction force (Δf_{move}), and it stopped near the line at which the interaction force was released. While in Fig. 8.3b–d, f, and g, the adsorbate was manipulated to the next stable adsorption position, in Fig. 8.3e, h, the atom was manipulated along the $[1\bar{1}0]$ direction repeatedly until the tip–surface distance was increased. Additionally, while in Fig. 8.3b–e, g, the adsorbate was displaced upwards, in Fig. 8.3f, h, it was manipulated downward according to the set slow scan direction. Finally, in Fig. 8.3h, the adsorbate was manipulated until it was almost returned to the surface position where it was initially deposited (Fig. 8.3a). These experimental results showed that this atom hopping can be controlled by tuning the distance between the sample and the oscillating AFM tip.

The lateral atom manipulations shown in Fig. 8.3 were performed by forward and backward fast line scans parallel to the $[11\bar{2}]$ crystallographic direction. In tip-induced movement of an adsorbate placed in a homogeneously distributed surface potential, one should expect lateral displacements along the fast line scan direction too. These lateral displacements were, however, not observed (Fig. 8.3); thus, the adsorbate movement should be confined along the adatom rows by greater diffusion energy barriers in the $[11\bar{2}]$ crystallographic direction than in the $[1\bar{1}0]$ one.

This manipulation process can be categorized as the pulling mode proposed in previous lateral atom manipulation using LT-STM [34], because this jump occurs after imaging the adatom as it followed the slow tip scan. The experiment demonstrated in Fig. 8.3 is the first clear evidence of the AFM

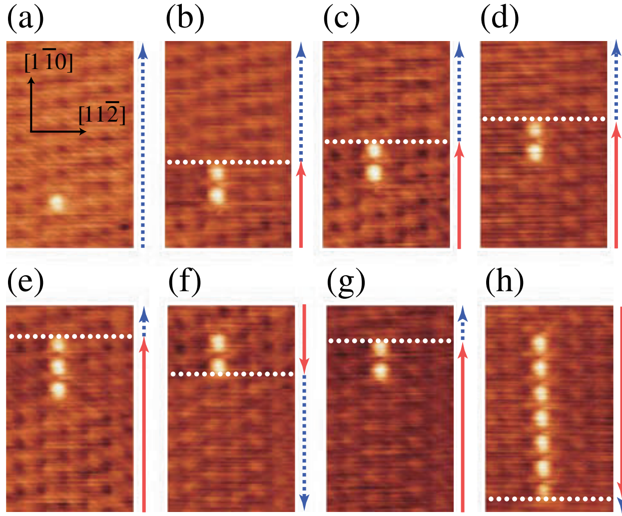

Fig. 8.3. (**a**)–(**h**) Sequence of consecutive topographic AFM images showing the lateral manipulation of an adsorbate deposited on top of a Ge(111)-c(2×8) surface. This adsorbate is manipulated by changing the slow scan direction and the tip–surface distance as indicated by the arrows beside each image. Scanning at a close tip–surface distance (*solid arrows*) corresponds to $\Delta f_{\mathrm{move}} = -32.0$ Hz. Scanning at a distance at which the adatom remains unperturbed (*dotted arrows*) corresponds to $\Delta f_{\mathrm{image}} = -28.8$ Hz. The scan line at which the change between these two Δf values was made is indicated by a *dotted line* in each image. The image size is 2.2×3.5 nm^2. The spring constant (k), the first mechanical resonance frequency (f_0), and A are 33.2 N m^{-1}, 167,485.8 Hz, and 9.3 nm, respectively. The temperature of the tip and sample was kept at 80 K [21]

capability for laterally manipulating adsorbates deposited on top of a surface, and it opened up new and very exciting perspectives for this technique.

8.5 Interchange Lateral Atom Manipulation

After the first demonstration of the vertical and lateral manipulation of single atoms using AFM at LT as described earlier, we discovered a new method that enables us to manipulate single atoms even at RT. As a result, we have achieved well-controlled atom manipulation and assembly on the Sn/Ge(111)-c(2×8) surface at RT [18]. In this method, which we call interchange lateral atom manipulation, substitutional Sn adatoms in the plane of the Ge surface can be individually manipulated by a tip-induced interchange with the surrounding surface Ge adatoms. This novel atom manipulation can be controlled by an appropriate selection of the tip scan direction, and by tuning the attractive interaction force acting between tip and surface.

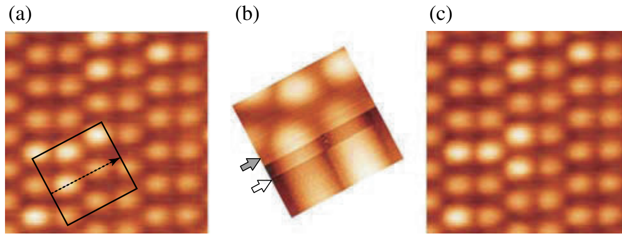

Fig. 8.4. Sequence of AFM topographic images showing the method for interchange lateral manipulation of substitutional Sn adatoms on the Ge(111)-c(2×8) surface. (**a**) After imaging the surface at tip–surface interaction forces that do not activate the interchange between Sn and Ge adatoms, the scan size was reduced and the tip fast-scan direction was aligned with the line connecting the centers of the adatoms selected for manipulation, as indicated by the square and the dotted arrow, respectively. (**b**) The surface was imaged until the slow scan reached the line connecting the centers of the adatoms (marked with a *gray arrow*), and the slow scan was stopped at this line. Successive topographic scans over this line with gradually reduced tip–surface distance led to the adatom interchange. This process is monitored by a swap in the height signals associated with each adatom type (see the *white arrow*). These line-scans were performed by lifting the oscillating tip, typically 1 Å above the surface, on the way back. (**c**) The surface area was imaged again without perturbing the adatoms. Image size is $4.6 \times 4.6\,\text{nm}^2$ for (**a**) and (**c**), and $1.9 \times 1.9\,\text{nm}^2$ for (**b**). AFM acquisition parameters were $A = 176$ Å with a cantilever of $k = 34.8\,\text{N m}^{-1}$ and $f_0 = 169.430$ kHz. Δf value is -8.3 Hz for (**a**) and (**c**), and -11.3 Hz in (**b**) [18]

Figures 8.4 show the procedure for manipulating a substitutional Sn adatom on the Ge(111)-c(2×8) surface. First, we obtain an AFM topographic image of the Sn/Ge(111)-c(2×8) surface, as shown in Fig. 8.4a. In this initial image, where Sn adatoms appear slightly brighter than Ge adatoms, an Sn adatom and a first neighboring Ge adatom are chosen for manipulation. Next, a small area is scanned by rotating the scan angle, as indicated by the square in Fig. 8.4a. The scan direction is selected such that the fast scan direction is aligned with the vector that connects the positions of the selected Sn and Ge adatoms. The fast scan begins near the position occupied by the Sn adatom, and ends near the Ge adatom position. At this time, the tip is lifted, typically 1 Å above the surface, on the way back before subsequent scans in the fast scan direction. The result of this scan is shown in the upper half of the image in Fig. 8.4b. The slow tip-scan is stopped when the tip reaches the line connecting the centers of the two adatoms (the gray arrow). The tip successively scans the same line above the arrow in Fig. 8.4a. Then the attractive interaction force acting between the outermost atoms of the tip and the atoms at the surface is gradually increased by reducing the tip–surface distance. At a certain closest approach distance, the attractive interaction force overcomes the threshold value needed for activating the interchange between Sn and Ge adatoms during the line-scan, making the Sn adatom follow the

tip. Successful manipulation can be confirmed by checking the height signals associated with each adatom type, which change in location after the adatom interchange as shown by the white arrow in Fig. 8.4b, in subsequent line-scans. Finally, reducing the attractive interaction force to values at which the adatoms remain unperturbed at their adsorption positions, the surface is imaged again (Fig. 8.4c). By comparing Fig. 8.4a, c, one can confirm that the target Sn adatom is manipulated. The tip–surface interaction force involved in this manipulation is associated with the onset of covalent bond formation between the outermost atom of the tip and the adatoms at the surface, as expected for AFM image formation on a semiconductor surface [17].

To demonstrate the reproducibility of the new lateral manipulation method found at RT, we created an artificial nanostructure atom-by-atom. Figures 8.5 display a selection of sequential AFM images acquired while constructing an "atom inlay," which is an in-plane nanostructure composed of several embedded atoms on a surface. The white arrow in each image indicates the same Sn adatom. By consecutively rearranging substitutional Sn adatoms on the Ge surface, the letters "Sn," the atomic symbol of the element tin, were constructed at RT (Fig. 8.5i). The creation of these nanostructures required more than 120 interchange lateral atom manipulations with continuous AFM operation for 9 h. This new lateral manipulation method is proven to be well controlled even at RT.

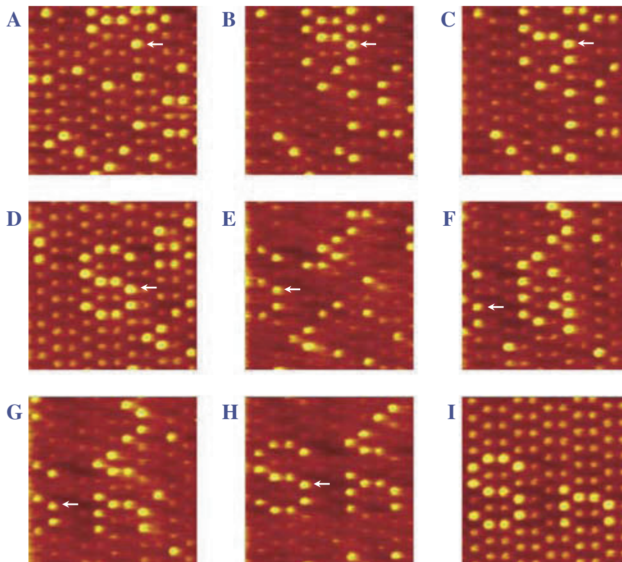

Fig. 8.5. Sequence of AFM images of the process of rearranging single atoms for the construction of an "atom inlay" at RT. Image size is $7.7 \times 7.7\,\mathrm{nm}^2$. The image was acquired with $A = 157\,\text{Å}$, using a Si cantilever of $k = 29.5\,\mathrm{N\,m^{-1}}$, setting a Δf value of $-4.6\,\mathrm{Hz}$ with respect to $f_0 = 160.450\,\mathrm{kHz}$ [18]

Although an atomistic picture of this manipulation mechanism has not been clarified yet, phenomenologically, atom interchange can be attributed to the diffusion process by a tip-induced reduction of the energy barrier. It was reported that substitutional Pb adatoms on the Pb/Ge(111)-c(2×8) surface, which is similar to the Sn/Ge(111)-c(2×8) surface, diffuse by interchanging the positions of Pb and Ge adatoms even at RT [35, 36]. In contrast, the energy barrier for diffusion of substitutional Sn adatoms on the Ge(111)-c(2×8) surface is higher than that for Pb/Ge(111)-c(2×8). We measured the diffusion rate of the substitutional Sn adatoms at RT by continuously imaging the same surface area for more than 6 h with a weak enough tip–surface attractive interaction force [18]. We found that the diffusion rate is less than 5.7×10^{-7} jumps per s per atom. The lower limit of the energy barrier value is determined to be 1.1 eV, which is higher than 0.54 eV, the measured activation energy value for the Pb/Ge(111)-c(2×8) system [36]. We suggest that bonds between Sn adatoms and the first layer of Ge atoms are stronger than those between Pb adatoms and Ge atoms. Nevertheless, the chemical bonding force between the AFM tip apex atoms and the surface adatoms can reduce the energy barrier associated with the Sn-Ge interchange. Additionally, the tip-induced reduction in this energy barrier is very localized, because when the fast tip-scan is properly aligned with the vector connecting the centers of the two adatoms, almost no interchange events with other first neighboring Ge adatoms out of this direction have been detected.

From the diffusion measurements of the Sn adatoms, we can estimate the minimum mean lifetime of the artificial nanostructures shown in Fig. 8.5i. Let us consider that the nanostructure is destroyed when one of the adatoms that compose it thermally diffuses and changes its position. Assuming that this change in position is a statistically independent process, the minimum mean lifetime of the artificial nanostructure would be the minimum mean lifetime of an unperturbed substitutional Sn adatom placed in a well-reconstructed area of the Ge(111)-c(2×8) surface times the number of atoms that compose the nanostructure. Taking into account that the minimum mean lifetime of an unperturbed substitutional Sn is the inverse of the upper limit for the diffusion rate, that is, 1.75×10^6 s, in principle, artificial nanostructures formed in this way could remain stable on the surface at RT for relatively long periods of time. For the nanostructures reported here, a minimum mean lifetime of 25 h is estimated.

In addition, we confirmed that interchange lateral atom manipulation can be applied not only to Sn/Ge(111)-c(2×8) surfaces but also to other alloy systems, such as Sn/Si, In/Si, and Sb/Si systems, even on different surface structures [19, 37]. Sn, In, and Sb atoms are group IV, III, and V elements in the periodic table, respectively. Figure 8.6 shows the results of manipulation on the Sn/Si(111)-($\sqrt{3} \times \sqrt{3}$), In/Si(111)-($\sqrt{3} \times \sqrt{3}$), and Sb/Si(111)-(7×7) surfaces. The upper images (Fig. 8.6a–c) are the AFM topographies before manipulation, and the lower images (Fig. 8.6d–f) are those after manipulation. Two different atomic species marked by dotted rectangles were interchanged

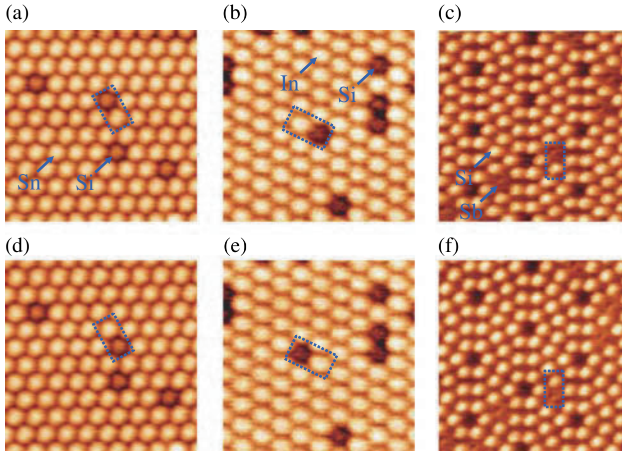

Fig. 8.6. AFM images demonstrating interchange lateral atom manipulation on the various surfaces. (**a**), (**d**) Sn/Si(111)-($\sqrt{3}\times\sqrt{3}$) surface, (**b**), (**e**) In/Si(111)-($\sqrt{3}\times\sqrt{3}$) surface, and (**c**), (**f**) Sb/Si(111)-(7×7) surface. (**a**–**c**) are before manipulations and (**d**–**f**) are after manipulations [19,37]

by the method described above. Note that while the Sn/Ge(111)-c(2×8) and Sb/Si(111)-(7×7) surfaces have restatoms, Sn/Si(111)-($\sqrt{3}\times\sqrt{3}$) and In/Si(111)-($\sqrt{3}\times\sqrt{3}$) do not: all dangling bonds of the first-layer Si atoms are saturated. Thus, this result clarifies that restatoms are not requisite for the atomic interchange process. The experimental results imply that the in-plane atomic interchange process is based on a common mechanism independent of the surface structure and elements.

The experiments described here show the capability of AFM for engineering nanostructures by rearranging surface adatoms on various semiconductor surfaces at RT. Since nanostructures incorporated into the surface remain stable for relatively long periods of time even at RT, the study presented here paves the way for various applications, such as the construction of artificial nanodevices and dopant arrangement in semiconductor surfaces with atomic precision.

8.6 Lateral Atom Manipulation at Room Temperature

Despite the success of AFM manipulation at RT, resulting from the discovery of interchange lateral atom manipulation, the atomistic mechanism of this new method remained unclear. To shed some light on the mechanism of RT manipulations on semiconductors using AFM, we carried out standard lateral atom manipulation experiments. Intrinsic Si adatoms on the Si(111)-(7×7) surface in the presence of a single atomic vacancy were chosen for the lateral atom manipulation experiments [22,38]. The line profiles during atom manipulation,

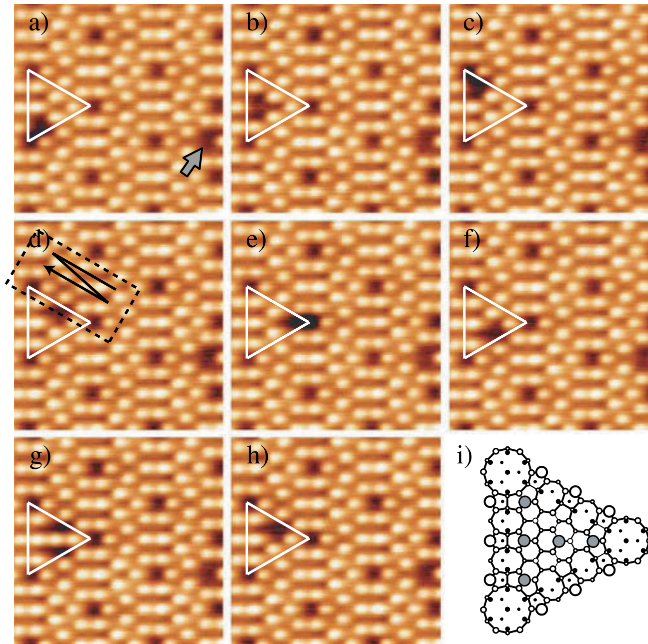

Fig. 8.7. (**a**–**h**) Topographic images selected from a series of vacancy-mediated manipulations of Si adatoms of the Si(111)-(7 × 7) surface. The vacancy indicated by the *gray arrow* in (**a**) is a marker. Image dimensions are 8.0 × 8.0 nm^2. The acquisition parameters are $f_0 = 162{,}295.8$ Hz, $A = 282$ Å, and $k = 28.7\,\mathrm{N\,m^{-1}}$. Imaging ($\Delta f_{\mathrm{image}}$) and manipulation ($\Delta f_{\mathrm{move}}$) frequency shift set points were −3.9 and −5.1 Hz, corresponding to an attractive chemical bonding force at closest approach of −0.15 and −0.47 nN, respectively. In (**i**), a model of the atomic configuration for the highlighted unit cell in (**g**) is displayed [22]

which include useful information as described further, were analyzed. Furthermore, the chemical bonding force between the AFM tip and the manipulated Si adatom, which was associated with moving the Si adatom, was measured using the same tip as that used for the manipulation.

Figure 8.7a–h shows a selection of AFM images from a series of sequential lateral manipulations of Si adatoms on the Si(111)-(7 × 7) surface. These figures show exactly the same place; the vacancy used as a marker is indicated by the gray arrow in Fig. 8.7a. We manipulated the Si adatoms in a faulted half-unit cell (white triangles) in the presence of an atomic vacancy, which was used as an open space for manipulation at RT. These atomic vacancies can be created [20, 29, 39] or occasionally found. Figure 8.7 shows that the vacancy in the white triangle changes its position, which originates from the manipulation of an Si adatom into the vacancy site. The adatoms adjacent to a vacancy can be individually manipulated along the dimer rows (Fig. 8.7a–f), and across the half-unit cell (Fig. 8.7f–h). The Si adatom can be deposited on

unusual adsorption positions (M sites), as shown in Fig. 8.7g. The model in Fig. 8.7i illustrates the M site, in which the adatom sits in a T_4 configuration bonded to one of the three original surface rest atoms. Si adsorption on this site is stable enough to allow imaging of the Si atom for hours at weak tip–surface interaction forces.

These manipulations have been performed using a similar protocol to the method for interchange lateral atom manipulation described in the previous section. For example, lateral manipulation of an Si adatom from the corner adatom site to the center adatom site, which was performed between Fig. 8.7d and e, is carried out as follows. After obtaining the initial image (Fig. 8.7d), the scan angle is rotated so that the fast scan direction is aligned parallel to the line connecting the vacancy and the Si adatom to be manipulated, and the smaller area indicated by the dotted rectangle is scanned. The tip is scanned near the surface in one direction and lifted 1 Å on the way back to cause directional migration of the atom. Then the slow scan is stopped when the tip scan reaches the line connecting the target adatom and the vacancy. Decreasing the tip–surface distance by changing the setpoint to Δf_{move} induces atom movement. Finally, the initial imaging set point ($\Delta f_{\mathrm{image}}$) is restored, and we obtain the final image shown in Fig. 8.7e. The Si adatom is manipulated in the direction parallel to the fast scan direction.

We found that lateral manipulation strongly depends on the tip asymmetry, as predicted by theoretical calculation [40]. In the series partially shown in Fig. 8.7, the same Δf_{move} set point was used for all the manipulations in the various directions. It is rare to encounter such a highly symmetric tip apex; different Δf_{move} set points are normally required for each manipulation direction. Recent statistical experiments of lateral atom manipulation on the same system using AFM clearly show that the probability of successful atom movements depend dramatically on the scan direction with respect to the tip apex asymmetry, even for crystallographically equivalent directions [38].

The profiles of AFM line scans during manipulation provide information, such as the path of atom hopping and the manipulation mechanism. Figure 8.8c shows the AFM topography during the manipulation carried out between the images in Fig. 8.7d and e. The slow scan is from bottom to top, and the fast scan is from left to right. After imaging the area enclosed by the dotted rectangle in Fig. 8.8c, the slow scan is stopped, and the tip–surface distance is reduced by changing the setpoint to Δf_{move} at the line indicated by the gray arrow. Successive tip scanning on the same line with stronger tip–surface interaction induces atom manipulation. The white arrow indicates the line where the tip–surface distance is restored by changing the setpoint to $\Delta f_{\mathrm{image}}$. Five profiles from successive line scans are displayed in Fig. 8.8b. Profiles B–D obtained with Δf_{move} are sequential, and they correspond to three different stages of the process: before (B), during (C), and after (D) the manipulation. Profiles A and E are topographies with $\Delta f_{\mathrm{image}}$. In profile A, two adatoms are observed at the left corner (Co_{L}) and right corner (Co_{R}) sites and the vacancy is at the center (Ce) site. In profile B, once the left corner

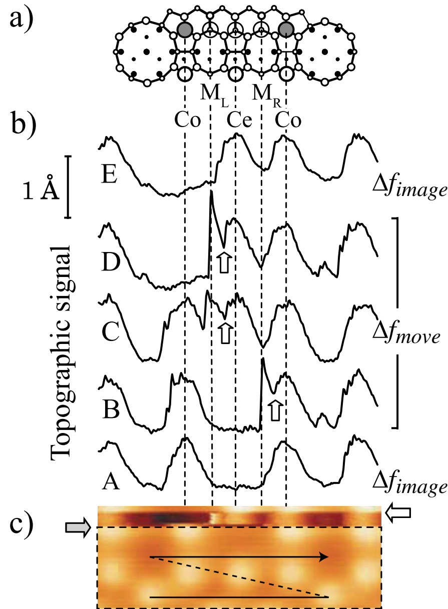

Fig. 8.8. (**a**) Ball-and-stick model of a partial Si(111)-(7×7) unit cell with a vacancy on a center (Ce) adatom site. The corner (Co) adatom sites, two equivalent M sites (M_L and M_R), and two H_3 adsorption positions are indicated. (**b**) Line profiles obtained from (**c**), where the topography associated with the manipulation process between the images in Figs. 8.7d, e is displayed. The fast scan velocity was $8.6\,\mathrm{nm\,s^{-1}}$ and the rectangle's dimensions are $4.3 \times 1.5\,\mathrm{nm}^2$ [22]

adatom and the vacancy have been imaged, feedback suddenly retracts the tip at the M_R position due to the jump of the right corner adatom toward the tip. The adatom adsorbs on the M_R site until it jumps back to the Co_R site at the tip location marked by the arrow. In profile C, the tip initially encounters and passes over the adatom on the Co_L site and, near the M_L position, it is suddenly retracted due to the jump of the adatom from the Co_L to the M_L site. Subsequently, the adatom jumps again to the Ce site at the tip location marked by the arrow. In profile D, just after the vacancy is imaged, the center adatom jumps toward the tip and adsorbs on the M_L site. Then, it returns to the Ce site at the tip location marked by the arrow. The same atom hopping process as that seen in profile D repeatedly occurs until the Δf_image set point is recovered. This is visualized as the bright feature near the M_L position in Fig. 8.8c. In profile E, the vacancy is finally at the Co_L site, in contrast with profile A.

The comparison of these profiles with previously reported manipulation experiments performed with LT-STM [34,41] indicates that the manipulations reported here can be classified into the so-called pulling mode [34], in which an attractive interaction force with the tip apex pulls the surface adatom

toward the tip position. An Si adatom is manipulated by a local reduction in the natural diffusion barrier that enables thermally activated hopping to adjacent adsorption sites by the attractive chemical bonding force between the tip and the adatom [42,43]. The directionality is imposed by the tip scan direction together with the asymmetric potential energy landscape created by the particular tip–apex structure [38,40]. These ideas are further substantiated with an extensive study by first-principles simulations of the energetics and stability of the Si(111)-(7 × 7) adatoms in the presence of a vacancy, as well as the modifications induced by the AFM tip. The detailed mechanism of mechanical lateral atom manipulation is discussed in Chap. 11.

An important feature of AFM is the ability to measure the chemical bonding force between the tip apex atoms and surface atoms. The site-specific force spectroscopic technique developed for RT is described in Chap. 2. This capability can be applied to measurements of the chemical bonding force associated with atom manipulation. In Fig. 8.9, a Δf vs. tip–sample distance ($\Delta f - z$) curve on top of the corner adatom is displayed (the dotted curve). This curve was obtained by averaging 80 curves that were repeatedly measured over the same site within a ±0.1 Å error using an atom tracking technique. The $\Delta f - z$ was converted into the force vs. tip–sample distance ($F - z$) curve by a conversion formula [44]. Then the short-range chemical bonding force displayed in Fig. 8.9 (the solid curve) was obtained by subtracting the long-range force that was estimated from the $F - z$ curve measured over the corner hole. The tip apex state was equivalent in both the force spectroscopy of Fig. 8.9 and atom manipulation of Fig. 8.7. By comparing the $\Delta f - z$ and $F - z$ curves, we can determine the value of the chemical bonding force at the tip–surface distance for both imaging and manipulation. The chemical bonding force exerting the tip just over the adatom during tip scanning with Δf_{image} is estimated to be −0.15 nN. On the other hand, this chemical bonding force becomes −0.47 nN

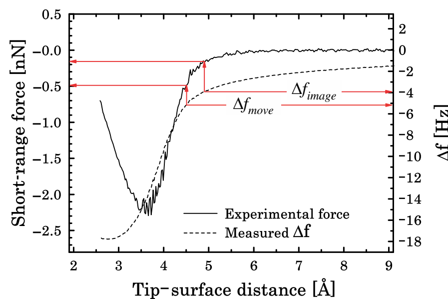

Fig. 8.9. The dotted curve is an averaged $\Delta f - z$ curve resulting from the force spectroscopic measurement on top of the corner adatom using the same tip as that used for the manipulation experiments illustrated in Fig. 8.7. The solid curve is a short-range chemical bonding force converted from the experimental $\Delta f - z$ curve [22]

at the tip–surface distance where an Si adatom can be manipulated during the AFM topographic scan.

8.7 Interchange Vertical Atom Manipulation

We have demonstrated nanostructuring at RT by interchange lateral atom manipulation, as explained in Sect. 8.5. Recently, we have reported a new method for effectively rearranging adatoms on a binary alloy system using interchange vertical atom manipulation. In this method, individual atoms on the tip apex can be deposited on a surface by interchange between a single atom on the tip and a single adatom on the surface. This technique can be regarded as an atomic version of dip-pen nanolithography [45], as one can write patterns on surfaces with atomic precision [19].

The atom manipulation experiments were performed on a Sn/Si(111)-($\sqrt{3} \times \sqrt{3}$) surface. In AFM topographic images of the surface, Sn adatoms and Si adatoms appear as bright and slightly dim spots, respectively, as shown in Fig. 8.10 [26]. Atom manipulation is based on the site-specific force spectroscopic measurement [27,46,47], as described later. First, an AFM image of the surface is acquired, and the target Si adatom is selected for manipulation (the center Si adatom in Fig. 8.10a). Next, the tip is positioned over the topmost part of the Si atom with a lateral precision better than ± 0.1 Å using an atom tracking technique [47]. Then the sample is moved toward the oscillating AFM tip until a jump in the Δf associated with a slight tip modification is observed, as indicated by the arrow in Fig. 8.11a. Scanning the same area as in the previous image after the tip retraction, we find that an Sn atom is deposited on the site that the Si adatom has occupied (Fig. 8.10b). This implies that the Si adatom on the surface has moved to the tip apex; an interchange between the tip apex Sn atom and the surface Si adatom has occurred. The same procedure can then be applied to the opposite process. By moving the tip toward the previously deposited Sn adatom, we can replace the Sn atom by an Si adatom coming from the tip, as shown in Fig. 8.10c. Although the image in Fig. 8.10c shows less contrast than in Fig. 8.10a, b, we can recover good image contrast by scanning a region that neighbors the imaged area at a slightly closer tip–surface distance than that used for imaging (Fig. 8.10d).

Figure 8.11 shows the $\Delta f - z$ curves during (a) the Sn deposition process and (b) the Si deposition process. The black (gray) curve corresponds to approach (retraction). The curves in Fig. 8.11a were obtained during the manipulation process carried out between Fig. 8.10a and b, while those in Fig. 8.11b were obtained between Fig. 8.10b and c. Atom interchanges occurred at the tip–surface distance where the Δf signal jumped, indicated by the arrows in Fig. 8.11. The approach and retraction curves during the Sn deposition process are similar, which implies that the tip apex is not significantly changed (Fig. 8.11a). This is also confirmed by the faint variation of the topographic signal before and after the Sn deposition, as shown in

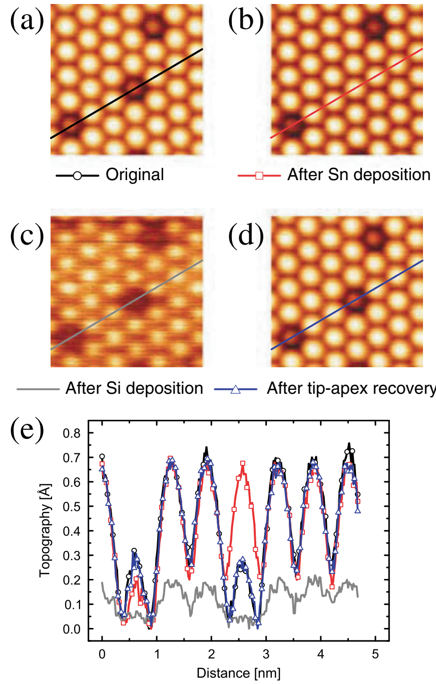

Fig. 8.10. (**a**–**d**) Sequence of AFM images of alternating interchange vertical atom manipulations. (**e**) Line profiles of images of (**a**)–(**d**). Acquisition parameters were $f_0 = 193{,}738.0\,\mathrm{Hz}$, $A = 219\,\text{Å}$, $k = 48.8\,\mathrm{N\,m^{-1}}$, and a cantilever quality factor (Q) of 13,000. A Δf set point value of $-6.3\,\mathrm{Hz}$ is common to all the topographic images. Experiments were performed at RT [19]

Fig. 8.10e. In contrast, Fig. 8.11b shows that $\Delta f - z$ completely changes after Si deposition: this process considerably modifies the tip apex state. This is also substantiated by the remarkable change in topographic contrast for the image acquired just after Si deposition (Fig. 8.10e). After tip recovery by scanning at slightly closer tip–surface distances, the line profile of Fig. 8.10d is in good agreement with the initial line profile in Fig. 8.10a (Fig. 8.10e). This indicates that the tip apex state can be initialized, and the sequential atom interchange process is completely reversible. The chemical bonding force during atom interchange calculated from the $\Delta f - z$ curves together with the dissipation signals is described in Chap. 3.

Vertical interchange differs from the atom transfer between the STM tip and sample surface previously reported [48]. In previous studies, an atom weakly bonded on a metallic surface was reversibly transferred between the STM tip and the surface by applying a bias voltage. In the present method, a tip apex atom and a surface atom strongly bound to the substrate are interchanged by soft nanoindentation using an AFM tip. Moreover, interchange

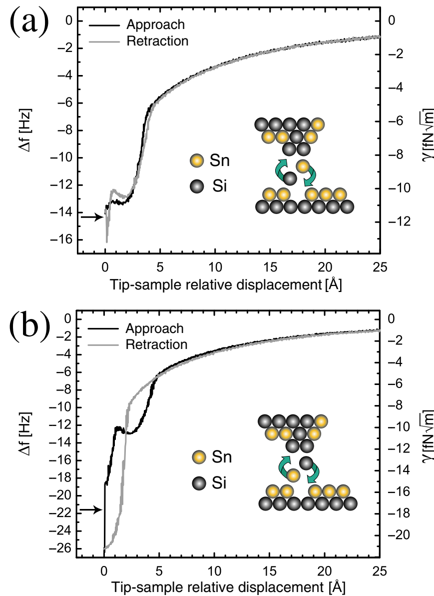

Fig. 8.11. (**a**) Force spectroscopic measurements ($\Delta f - z$ curves) associated with the Sn deposition process shown in Fig. 8.10a, b. (**b**) $\Delta f - z$ curves for the Si deposition shown in Fig. 8.10b, c. The *black* (*gray*) curves correspond to approach (retraction). In the Δf plots, the corresponding normalized frequency shift (γ) is displayed on the right axis [19]

vertical atom manipulation is also different from other mechanical atom manipulation using AFM [18, 22, 49], in which the relatively weak attractive interaction force between tip and sample plays an important role. Vertical atom interchange is induced by a small repulsive interaction force at very close tip–surface distances (see Chap. 3). At such a close distance, a larger contact involving several atoms is expected, leading to a very complex energy landscape. However, the reproducibility of vertical atomic interchange and the resemblance of recorded Δf and force curves in experiments performed with different tips point toward a common basic microscopic mechanism [19]. Details of the manipulation mechanism, including the atomic process, are described in Chap. 11.

From our extensive force spectroscopic measurements on this surface [26, 27], we have found that 29% of the tips can induce atom interchange between tip and surface atoms. Once a tip that produces atom interchange is found, manipulation can be performed in a reproducible way. Moreover, the tips that can produce atom interchange can be classified into three types. The first type can alternately deposit Sn and Si atoms as in Fig. 8.10; the second type can deposit only Sn atoms, and the third can deposit only Si atoms. The tip statistics shows that it is almost equally probable to find tips

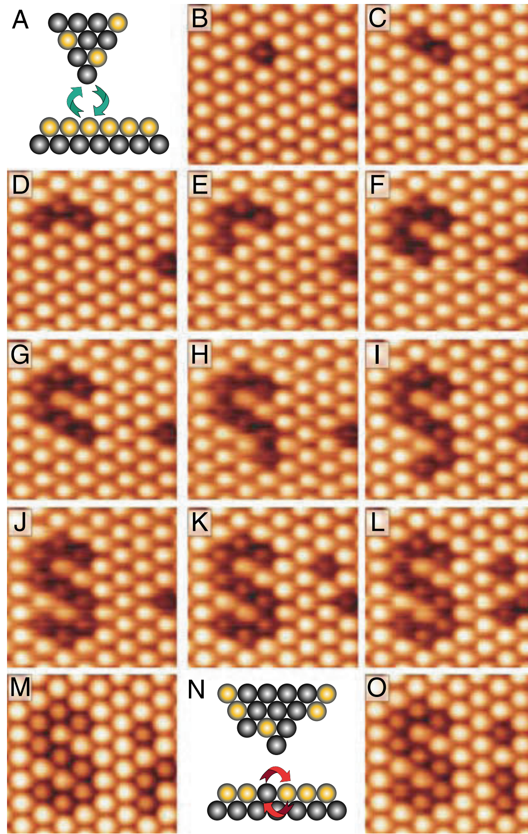

Fig. 8.12. Complex atomic patterning by interchange vertical atom manipulation at RT. (**a**) Illustration of the vertical interchange of atoms between the tip and surface. (**b**–**m**) Series of topographic images showing the creation of atomic patterns displaying the symbol of silicon. These patterns were constructed by the successive deposition of Si atoms coming from the tip onto the Sn monolayer. (**n**) Illustration of the lateral interchange of surface atoms. (**o**) The Si atom adjacent to the "i" character in (**m**) was relocated to a nearby position in several in-plane interchange lateral atom manipulations. Acquisition parameters were $f_0 = 193,744.2\,\mathrm{Hz}$, $A = 226\,\mathrm{Å}$, and $k = 48.8\,\mathrm{N\,m^{-1}}$, with imaging Δf set point values between -5.5 and $-6.6\,\mathrm{Hz}$

producing either Si deposition or alternate deposition of Sn and Si atoms, and less probable to find one depositing only Sn atoms. By using soft tip–surface contact, we can switch among the three tip types even using the same cantilever, although at present, we have not yet been able to develop a systematic way of producing tips of each type.

To show reproducibility and high precision, we have demonstrated that a nanopattern with atomic precision can be created by interchange vertical atom

manipulation. Figure 8.12 shows the processes of creating the letters "Si" written by Si adatoms embedded on the Sn monolayer. To create these complex atomic patterns, individual Si atoms coming from Si tips were successively deposited on the surface. Since the tip used to create these atomic patterns was type that can only deposit Si atoms, the Si adatom beside the "i" character in Fig. 8.12m was moved away from the character by interchange lateral atom manipulations. Perturbation of the surface structure was not observed during the patterning, as shown in Fig. 8.12. It took 1.5 h to construct the atom letters; the construction time was drastically reduced compared with previous interchange lateral atom manipulation [18].

The study described earlier demonstrated interchange vertical atom manipulation on the Sn/Si(111)-($\sqrt{3} \times \sqrt{3}$) surface. This manipulation method was found to be possible on other semiconductor surfaces as well, such as the In/Si(111)-($\sqrt{3} \times \sqrt{3}$) and Pb/Si(111)-($\sqrt{3} \times \sqrt{3}$) surfaces [19]. Therefore, interchange vertical atom manipulation as well as interchange lateral atom manipulation are expected to be widely used in areas ranging from surface science studies to bottom-up nanotechnology.

8.8 Summary

In this chapter, we reviewed atom manipulation experiments on semiconductor surfaces using AFM. Beginning with vertical and lateral atom manipulation at LT, our group has demonstrated that AFM has the capability of atom manipulation even at RT. Atom manipulation at RT was successfully performed by using intrinsic or substitutional adatoms instead of adsorbates deposited on top of a surface. In particular, the new manipulation methods of interchange lateral/vertical atom manipulation enable us to rearrange adatoms strongly bonded to the substrate with the possibility of patterning complex atomic structures. This new capability of the AFM technique can contribute to the realization of selective semiconductor doping [50], practical implementation of quantum computing [51], or atomic-based spintronics [52]. The possibility of combining sophisticated atom manipulation with the capability of AFM for single-atom chemical identification [27] may bring the advent of future atomic-level applications closer, even at RT.

Acknowledgement

The authors thank their colleagues who contributed to this study: Seizo Morita, Masayuki Abe, Oscar Custance, Noriaki Oyabu.

References

1. D.M. Eigler, E.K. Schweizer, Nature (London) **344**, 524 (1990)
2. J.A. Stroscio, D.M. Eigler, Science **254**, 1319 (1991)
3. M.F. Crommie, C.P. Lutz, D.M. Eigler, Science **262**, 218 (1993)
4. A.J. Heinrich, C.P. Lutz, J.A. Gupta, D.M. Eigler, Science **298**, 1381 (2002)
5. G.V. Nazin, X.H. Qiu, W. Ho, Science **302**, 77 (2003)
6. J.I. Pascual et al., Nature **423**, 525 (2003)
7. N. Nilius, T.M. Wallis, W. Ho, Science **297**, 1853 (2002)
8. T. Komeda et al., Science **295**, 2055 (2002)
9. H.C. Manoharan, C.P. Lutz, D.M. Eigler, Nature **403**, 512 (2000)
10. S.-W. Hla, L. Bartels, G. Meyer, K.H. Rieder, Phys. Rev. Lett. **85**, 2777 (2000)
11. B.C. Stipe, M.A. Rezaei, W. Ho, Science **279**, 1907 (1998)
12. B.C. Stipe, M.A. Rezaei, W. Ho, Phys. Rev. Lett. **78**, 4410 (1997)
13. G. Meyer, S. Zophel, K.H. Rieder, Phys. Rev. Lett. **77**, 2113 (1996)
14. H. Uchida, D. Huang, F. Grey, M. Aono, Phys. Rev. Lett. **70**, 2040 (1993)
15. F.J. Giessibl, Science **267**, 68 (1995)
16. S. Kitamura, M. Iwatsuki, Jpn. J. Appl. Phys. **34**, 145 (1995)
17. S. Morita, R. Wiesendanger, E. Meyer (eds.), *Noncontact Atomic Force Microscopy* (Springer-Verlag, Berlin Heidelberg New York, 2002)
18. Y. Sugimoto et al., Nat. Mater. **4**, 156 (2005)
19. Y. Sugimoto et al., Science **322**, 413 (2008)
20. N. Oyabu et al., Phys. Rev. Lett. **90**, 176102 (2003)
21. N. Oyabu et al., Nanotechnology **16**, S112 (2005)
22. Y. Sugimoto et al., Phys. Rev. Lett. **98**, 106104 (2007)
23. N. Suehira, Y. Tomiyoshi, Y. Sugawara, S. Morita, Rev. Sci. Instrum. **72**, 2971 (2001)
24. F.J. Giessibl et al., Nanotechnology **15**, S79 (2004)
25. I. Horcas et al., Rev. Sci. Instrum. **78**, 013705 (2007)
26. Y. Sugimoto et al., Phys. Rev. B **73**, 205329 (2006)
27. Y. Sugimoto et al., Nature (London) **446**, 64 (2007)
28. M. Abe, Y. Sugimoto, S. Morita, Nanotechnology **16**, S68 (2005)
29. S. Morita et al., Appl. Surf. Sci. **241**, 2 (2005)
30. I.W. Lyo, P. Avouris, Science **253**, 173 (1991)
31. I.W. Lyo, P. Avouris, Science **259**, 1724 (1993)
32. Y. Sugawara, Y. Sano, N. Suehira, S. Morita, Appl. Surf. Sci. **188**, 285 (2002)
33. B.C. Stipe, M.A. Rezaei, W. Ho, Phys. Rev. Lett. **79**, 4397 (1997)
34. L. Bartels, G. Meyer, K.-H. Rieder, Phys. Rev. Lett. **79**, 697 (1997)
35. E. Ganz, S.K. Theiss, I.S. Hwang, J. Golovchenko, Phys. Rev. Lett. **68**, 1567 (1992)
36. I.S. Hwang, J. Golovchenko, Science **258**, 1119 (1992)
37. Y. Sugimoto, O. Custance, M. Abe, S. Morita, e-J. Surf. Sci. Nanotech. **4**, 376 (2006)
38. Y. Sugimoto, K. Miki, M. Abe, S. Morita, Phys. Rev. B **78**, 205305 (2008)
39. S. Kawai H. Kawakatsu, Appl. Phys. Lett. **89**, 023113 (2006)
40. L. Pizzagalli, A. Baratoff, Phys. Rev. B **68**, 115427 (2003)
41. S.W. Hla, K.F. Braun, K.H. Rieder, Phys. Rev. B **67**, 201402 (2003)
42. G. Meyer et al., Phys. Rev. Lett. **78**, 1512 (1997)
43. M.B. Watkins, A.L. Shluger, Phys. Rev. B **73**, 245435 (2006)

44. J.E. Sader, S.P. Jarvis, Appl. Phys. Lett. **84**, 1801 (2004)
45. R. Piner et al., Science **283**, 661 (1999)
46. M.A. Lantz et al., Science **291**, 2580 (2001)
47. M. Abe, Y. Sugimoto, O. Custance, S. Morita, Appl. Phys. Lett. **87**, 173503 (2005)
48. D.M. Eigler, C.P. Lutz, W.E. Rudge, Nature (London) **352**, 600 (1991)
49. M. Ternes et al., Science **319**, 1066 (2008)
50. T. Shinada, S. Okamoto, T. Kobayashi, I. Ohdomari, Nature **437**, 1128 (2005)
51. B. Kane, Nature **393**, 133 (1998)
52. D. Kitchen et al., Nature **442**, 436 (2006)

9

Atomic Manipulation on Metal Surfaces

Markus Ternes, Christopher P. Lutz, and Andreas J. Heinrich

Abstract. Half a century ago, Nobel Laureate Richard Feynman asked in a now-famous lecture what would happen if we could precisely position individual atoms at will [R.P. Feynman, Eng. Sci. **23**, 22 (1960)]. This dream became a reality some 30 years later when Eigler and Schweizer were the first to position individual Xe atoms at will with the probe tip of a low-temperature scanning tunneling microscope (STM) on a Ni surface [D.M. Eigler, E.K. Schweizer, Nature **344**, 524 (1990)].

Nowadays, such "atom manipulation" is used widely in research to build, probe, and manipulate objects at the scale of individual atoms. For example, two- and one-dimensional confined quantum structures were built atom-by-atom, and in those studies the STM was used to directly image the quantum nature of the electrons confined in those artificial structures [M.F. Crommie, C.P. Lutz, D.M. Eigler, Science **262**, 218 (1993); H.C. Manoharan, C.P. Lutz, D.M. Eigler, Nature **403**, 512 (2000); N. Nilius, T.M. Wallis, W. Ho, Science **297**, 1853 (2002); C.R. Moon, L.S. Mattos, B.K. Foster, G. Zeltzer, W. Ko, H.C. Manoharan, Science **319**, 782 (2008)]. Atom-manipulation has been used to build molecules from the constituting individual atoms or smaller molecules [S.-W. Hla, L. Bartels, G. Meyer, K.-H. Rieder, Phys. Rev. Lett. **85**, 2777 (2000); J. Repp, G. Meyer, S. Paavilainen, F.E. Olsson, M. Persson, Science **312**, 1196 (2006)]. And last, but not least, atom manipulation has been used to build devices on the atomic scale such as the molecules cascade [A.J. Heinrich, C.P. Lutz, J.A. Gupta, D.M. Eigler, Science **298**, 1381 (2002)] and atomic switches [D.M. Eigler, C.P. Lutz, W.E. Rudge, Nature **352**, 600 (1991); J.A. Stroscio, F. Tavazza, J.N. Crain, R.J. Celotta, A.M. Chaka, Science **313**, 984 (2006)].

However, in all this body of work, the fundamental question – "how much force does it take to move an atom on a surface?" – had eluded experimental access until the advent of atomic-resolution noncontact AFM. Only in the last few years has it become possible to manipulate matter atom-by-atom with AFM [N. Oyabu, O. Custance, I. Yi, Y. Sugawara, S. Morita, Phys. Rev. Lett. **90**, 176102 (2003); Y. Sugimoto, P. Jelinek, P. Pou, M. Abe, S. Morita, R. Pérez, O. Custance, Phys. Rev. Lett. **98**, 106104 (2007)], most prominently in the controlled exchange of atoms within a surface layer of alloyed semiconductors [N. Oyabu, Y. Sugimoto, M. Abe,

S. Morita et al. (eds.), *Noncontact Atomic Force Microscopy*,
NanoScience and Technology,
DOI: 10.1007/978-3-642-01495-6_9, © Springer-Verlag Berlin Heidelberg 2009

Ó. Custance, S. Morita, Nanotechnology **16**, S112 (2005); Y. Sugimoto, M. Abe, S. Hirayama, N. Oyabu, Ó. Custance, S. Morita, Nat. Mater. **4**, 156(2005)].

This chapter describes the use of a low-temperature scanning probe system that can be simultaneously operated as an STM and an AFM in the noncontact mode with sub-Angstrom oscillation amplitude. We will discuss how such a tool can be used to simultaneously measure the vertical and lateral forces exerted by the probe tip on the adsorbate before and during the controlled manipulation process.

Understanding the force necessary to move specific atoms on specific surfaces is one of the keys to further progress in nanoscience and will enable a deeper understanding of the atomic-scale processes at the heart of future nanotechnology endeavors, furthering progress toward nanoscale devices.

9.1 Introduction

Half a century ago, Nobel Laureate Richard Feynman asked in a now-famous lecture what would happen if we could precisely position individual atoms at will [1]. This dream became a reality some 30 years later when Eigler and Schweizer were the first to position individual Xe atoms at will with the probe tip of a low-temperature scanning tunneling microscope (STM) on a Ni surface [2].

Nowadays, such "atom manipulation" is used widely in research to build, probe, and manipulate objects at the scale of individual atoms. For example, two- and one-dimensional confined quantum structures were built atom-by-atom, and in those studies the STM was used to directly image the quantum nature of the electrons confined in those artificial structures [3–6]. Atom-manipulation has been used to build molecules from the constituting individual atoms or smaller molecules [7, 8]. And last, but not least, atom manipulation has been used to build devices on the atomic scale such as the molecules cascade [9] and atomic switches [10, 11].

However, in all this body of work, the fundamental question – "how much force does it take to move an atom on a surface?" – had eluded experimental access until the advent of atomic-resolution noncontact AFM. Only in the last few years has it become possible to manipulate matter atom-by-atom with AFM [12, 13], most prominently in the controlled exchange of atoms within a surface layer of alloyed semiconductors [14, 15].

This chapter describes the use of a low-temperature scanning probe system that can be simultaneously operated as an STM and an AFM in the noncontact mode with sub-Angstrom oscillation amplitude. We will discuss how such a tool can be used to simultaneously measure the vertical and lateral forces exerted by the probe tip on the adsorbate before and during the controlled manipulation process.

Understanding the force necessary to move specific atoms on specific surfaces is one of the keys to further progress in nanoscience and will enable a deeper understanding of the atomic-scale processes at the heart of future nanotechnology endeavors, furthering progress toward nanoscale devices.

9.2 Modes of Manipulation

In general, one can classify atomic manipulation techniques into two different categories, commonly referred as vertical (perpendicular to the surface) manipulation, and lateral (parallel to the surface) manipulation [16, 17]. The history of the vertical atom manipulation extends back to the work of Becker and coworkers who showed that it is possible to transfer atoms from the apex of an STM tip to the surface by applying a voltage pulse of a few volts between the tip and the surface, with the tip positioned laterally at the desired landing position for the manipulated atom [18].

This vertical manipulation method was later extended to a complete manipulation technique by the additional ability to transfer atoms or molecules from the sample onto the apex of the tip [2]. The principal steps of the vertical atom-manipulation are outlined in Fig. 9.1a. At the beginning, the tip is placed over the desired adsorbate on the surface. Then, usually by increasing the tip–sample voltage and decreasing the tip–sample distance, the adsorbate changes from being bound to the sample to being bound on the apex of the tip. Resetting the tip–sample voltage and height to the original nonperturbative imaging values allows one to move the tip to the desired final position for the adsorbate. Here, the adsorbate is transferred back from the tip to the surface in similar manner as the original "pick-up," but usually with inverted tip–sample voltage. The actual procedure to transfer the adsorbate to the tip and back to the surface depends critically on the sample–adsorbate system as well as on the atomic structure of the tip apex and sometimes involves more complex steps [19].

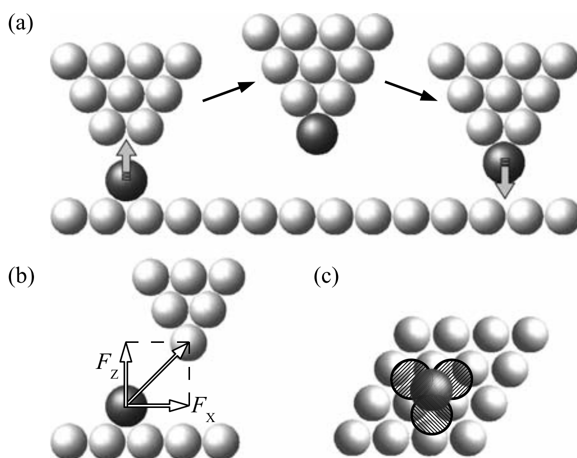

Fig. 9.1. Vertical (**a**) and lateral (**b**) atom manipulation. In lateral manipulation, the adsorbate can only move successively from the initial adsorption site to neighboring adsorption sites (**c**)

The key element of the vertical manipulation is the actual transfer of the adsorbate onto the tip, and subsequently back to the surface. This is in contrast to lateral manipulation, where the adsorbate always stays bound on the surface. In lateral manipulation, interaction forces between the tip apex and the adsorbate are used to apply a lateral force F_x. When this force becomes strong enough to overcome the energy barrier between two neighboring adsorption sites, the adsorbate moves from its initial binding site to a neighboring site as illustrated in Fig. 9.1b, c.

The origin of the tip–adsorbate force lies in the formation of a chemical bond between the tip apex and the adsorbate. The strength of this bond depends sensitively on the tip–sample distance. At the relatively large tip–sample distances used for imaging, the forces are too small to move the adsorbate. Reducing the tip–sample distance increases the attractive interaction force so that the tip can "pull" the adsorbate, which then follows the tip motion by hopping from one adsorption site to the next. Decreasing the tip–sample distance further, the repulsive regime of the interaction force can be reached in which the tip is "pushing" the adsorbate.

Typically, the adsorbate to be repositioned interacts primarily with the outermost atom of the tip apex, due to the short range nature of the chemical interaction forces. The detailed structure of the tip apex is not critical when the lateral force required to reposition an adsorbate is very small. For example, alkali metals and Van der Waals bonded atoms such as noble gasses typically have tiny lateral energy barriers between the binding sites on close-packed metal surfaces, so they can be repositioned easily [2,16]. For adsorbates requiring large manipulation forces, the detailed structure and chemical character of the tip apex are critical for successful atom manipulation.

The force necessary to manipulate the adsorbate must be smaller than the force to manipulate the last atom on the tip. Otherwise, the outermost atom on the tip will move to a new binding site instead of repositioning the adsorbate on the surface. For manipulation in the "pulling" mode, the tip–adsorbate interaction must also be strong enough to develop a sufficiently large lateral force. Reports of successful lateral manipulation in the "pulling" mode are confined primarily to movement of atoms or weakly bound molecules on flat and smooth metal surfaces [2,5,16,17,20,21], where the lateral barriers for adsorbate motion are often small. The "pushing" mode, which can apply larger lateral forces, allows one to manipulate also larger molecules, which bond with several ligands onto the surface [22–25].

Atom manipulation has also been used successfully to change the internal confirmation of molecules [26–28], to rotate molecules with respect to the surface [25,29,30], to perform chemical reactions between individual molecules [7], or to functionalize the tip apex by attaching the molecule on its end [31].

Since the first demonstration of atom manipulation, theoretical models have been explored to understand the physics behind the manipulation. Vibrational heating and the influence of the electric field in the junction have

been studied to model the pick-up and drop-off in the vertical manipulation process [32–35].

Describing the lateral atom-manipulation in a theoretical framework is especially challenging, because it has to account for the interactions between sample, adsorbate, and tip–apex not only in the vertical direction, but also in three-dimensional space. Computationally expensive total-energy calculations have been performed for several systems [36–39]. For a more detailed overview of the theoretical models of atom manipulation that have been investigated, we refer to recent overview articles [40, 41].

While the atomic short-range forces between tip apex and sample are responsible for controlled atom manipulation on surfaces, only recently were these forces measured directly [42]. In this chapter, we outline how we determine experimentally these driving forces and the corresponding energy landscape. We show how these techniques also allow one to study the interplay between lateral and vertical force components atom manipulation on metallic surfaces.

9.3 Instrumentation

All manipulation experiments discussed in this chapter were performed with a home-built, combined STM/AFM working at a cryogenic temperature of $T = 5\,\mathrm{K}$ and in ultra-high-vacuum ($p < 10^{-8}\,\mathrm{pa}$). We use frequency modulation AFM [43] with the q-plus sensor design [44] in which a metallic Iridium tip is mounted on one leg of a cantilever made from a quartz tuning fork, while the other leg is fixed on a three-axis piezoelectric scanner as shown in Fig. 9.2a (for more details on the q-plus sensor see Chap. 6).

The cantilever is excited to its first mechanical resonant frequency $f_0 = 21{,}860\,\mathrm{Hz}$ by applying an AC modulation voltage to the z piezo in addition to the feedback-loop voltage used to control the vertical tip position. A low-temperature preamplifier is mounted in UHV very close to the AFM to detect the piezoelectric cantilever deflection. The preamplifier is thermally weakly coupled to the cold AFM in order to allow self-heating to warm the preamplifier to its operating temperature of $T \approx 150\,\mathrm{K}$. The output signal of the preamplifier is proportional to the oscillatory tip motion in the z direction and is used as the input signal for a home-made regulation circuit, which adjusts the excitation signal for a constant z oscillation amplitude. Additionally, the preamplifier output is used to detect the cantilever frequency shift Δf from its free oscillation at f_0 by a commercial phase-lock-loop (PLL) from *Nanotek*.

Samples of Pt(111) and Cu(111) were prepared by repeated cycles of argon ion sputtering and thermal annealing. The cleanliness of the surface was checked with Auger-electron spectroscopy. The clean sample was transferred through vacuum onto the cold AFM, and metal adsorbates were then deposited onto the cold surface from degased metal evaporators. For the experiments with carbon monoxide, CO was deposited onto the cold sample surface

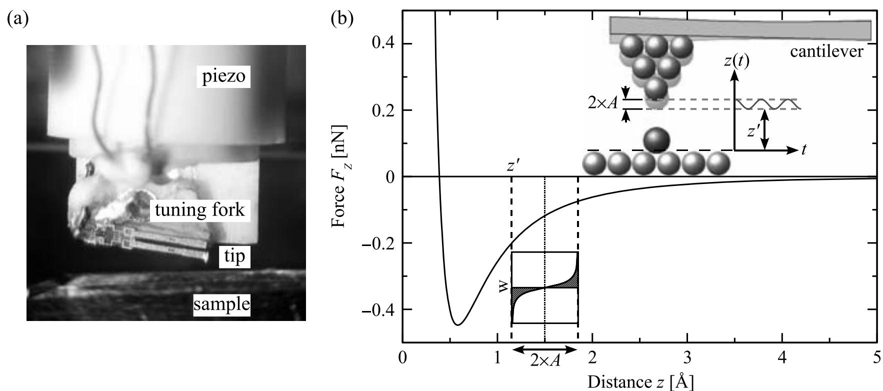

Fig. 9.2. (**a**) Image of the AFM/STM scanner with a tuning fork as force sensor. The tip mounted on the cantilever oscillates between z', the closest, and $z' + 2 \times A$, the furthest approach to the sample (inset in **b**). The detected frequency shift Δf depends on the force $F_z(z)$ during the tip oscillation weighted by $w(z)$

by admitting the purified gas through a leak valve into the room-temperature part of the chamber that house the AFM. A shutter held at $T \approx 6\,\mathrm{K}$ was opened to admit the adsorbates for dosing, and this shutter was closed during AFM operation to block room temperature radiation and residual vacuum contamination.

Iridium was chosen as the tip material based on its hardness, and on our previous success using iridium tips for STM spectroscopy and manipulation experiments. The tip was fabricated by mechanically fragmenting an Ir wire and selecting a small sharp fragment. The iridium tip was initially cleaned in vacuum by locally heating the apex at an applied voltage of $-600\,\mathrm{V}$ and a current of $\approx 5\,\mu\mathrm{A}$. During the experiments, different tips were produced by gently touching the tip to the sample surface. Thus, the actual chemical composition of the tip apex is unknown and might contain metal atoms from the sample metal.

The stiff cantilever design has a spring-constant of $k_0 = 1,800\,\mathrm{Nm}^{-1}$, which is about 100 times stiffer than a typical chemical bond [45], so it avoids snap to contact between sample and tip. This stiff design allows us to use very small modulation amplitudes of only $A = 25 - 30\,\mathrm{pm}$ normal to the surface. Small oscillation amplitudes are desirable when using the instrument as an STM because the strong exponential dependence of the tunneling current on the tip–sample distance, which changes by about one order of magnitude per 0.1 nm, would complicate or even inhibit the detection of the tunneling current at large oscillation amplitudes. Additionally, the stability and spatial resolution of the instrument, which was designed in particular for atom manipulation, has to be on the order of 1 pm. Achieving this stability with a larger oscillation amplitude might be more difficult because it requires a more accurate and responsive cantilever amplitude regulation.

9.3.1 Detected Signals

The resonant frequency of the free oscillating cantilever $f_0 = 1/2\pi\sqrt{k_0/m}$ depends only on the stiffness k_0 and on an effective mass m. If the tip apex interacts with the surface, the frequency shifts to

$$f = \frac{1}{2\pi}\sqrt{\frac{k_0 + \langle k_z \rangle}{m}}, \tag{9.1}$$

where $\langle k_z \rangle$ is the time average over one oscillation cycle of the tip motion of the vertical force gradient (i.e., the stiffness) $k_z = \partial F_z/\partial z$ of the tip–sample interaction [43]. This equation holds as long as $|k_z| \ll k_0$. Expanding (9.1) to first order in Taylor series allows one to associate the frequency shift $\Delta f = f - f_0$ with the stiffness between tip apex and sample,

$$k_z \approx \frac{2k_0}{f_0}\Delta f. \tag{9.2}$$

This approximation is only accurate as long as the vertical stiffness k_z does not change significantly during the oscillation cycle of the cantilever. In general, this assumption does not hold, so one must calculate the force F_z between tip and sample by inverting the following expression, which precisely relates force and frequency shift [46]:

$$\Delta f(z') = -\frac{f_0}{2k}\frac{2}{\pi A^2}\int_0^{2A} \mathrm{d}z \frac{z - A}{\sqrt{2Az - z^2}} F_z(z' + z). \tag{9.3}$$

Figure 9.2b illustrates relationship given by (9.3). This equation cannot in general be inverted to determine $F_z(z)$ analytically, but an excellent approximation is given by the analytical expression found by Sader and co-workers [47], and we regularly use this approximation. Equation (9.3) can also be inverted numerically instead [46].

Throughout this chapter we use two different measures of the tip–sample distance, z and z', to distinguish between the instantaneous and time-averaged quantities. We use z to indicate the instantaneous tip–sample distance. The oscillating tip moves between $z = z'$ at its closest approach to the sample during an oscillation cycle, and $z = z' + 2A$ at its greatest distance, as illustrated in Fig. 9.2b. We express values that are averages weighted over the tip oscillation cycle as functions of z'. For example, the measured vertical stiffness $k_z(z')$ is the time average of $k_z(z)$ as z oscillates between z' and $z' + 2A$. In contrast, the vertical force $F_z(z)$ calculated from $\Delta f(z')$ by inverting (9.3) stands for the instantaneous force F_z acting between tip and sample at a tip–sample separation z.

It is important to note that z represents the position of the macroscopic bulk of the tip relative to the bulk of the sample; changes in the distance between the atom at the tip apex and the nearest surface atom may be very

different from changes in z due to strain in the microscopic junction. Nonetheless, the determination of tip–sample forces presented here is valid even for cases where the strain in the tip apex and sample may be large.

In addition to the frequency shift, we also detect the conductivity $G = I/V$ of the junction by applying a small voltage of $V = 1\,\mathrm{mV}$ between tip and sample and detecting the tunneling current I. This allows us to assign an absolute height between tip and sample. We define $z \equiv 0$ throughout this chapter as the extrapolated tip height where the conductance between tip and bare surface G_B would equal the single-channel, spin-degenerate quantum of conductance $G_0 = 2e^2/h = (12,906\,\Omega)^{-1}$, where e is the elementary charge and h is Planck's constant (see Fig. 9.3). This height is determined by extrapolating the tunneling conductance from tip heights where this conductance is exponential in z. This approach provides a convenient reference for z that corresponds roughly to the point contact between the tip and the bare surface. We note that this assignment does not necessarily provide a precise comparison of the tip heights between two different surfaces. However, as long as metal surfaces and metal tips are used, the variations should be small.

The measured conductance is an average over the tip oscillation. As long as the tip–sample distance is in the tunneling regime the conductance is given by [48]

$$G(z) = G_0 \exp(-2\kappa z), \quad \text{with} \quad \kappa = \frac{2\pi}{h}\sqrt{m_0(\Phi_\mathrm{T} + \Phi_\mathrm{S})}. \tag{9.4}$$

The decay constant κ depends on the free electron mass m_0, and the work functions Φ_T and Φ_S of tip and sample, respectively. For metal–metal junctions with $\Phi \approx 4$–$6\,\mathrm{eV}$ [49], the decay constant is ≈ 10–$13\,\mathrm{nm}^{-1}$. Thus, for a tip oscillating at an amplitude $A = 30\,\mathrm{pm}$, the conductance between closest approach z and furthest approach $z + 2A$ changes by $\exp(4\kappa A) \approx 4$.

The strong exponential decay of the tunneling conductance allows to easily calibrate the oscillation amplitude A by detecting the ratio between the minimal and maximal conductance during an oscillation amplitude. The amplitude results then to $A = \ln(G_\mathrm{max}/G_\mathrm{min})/4\kappa$, whereby κ has to be determined by measuring $G(z)$ curves using (9.4). We note that for this calibration it is crucial that the bandwidth of the current amplifier is sufficiently larger than f_0.

The average conductance $\langle G(z')\rangle$ over one tip oscillation between z' and $z' + 2A$ is given by

$$\langle G(z')\rangle = G_0 \frac{1}{2\pi}\int_{-\pi}^{+\pi} \exp(2\kappa(z' + A(1 + \sin t)))\,\mathrm{d}t = G(z' + A) I_0(2\kappa A), \tag{9.5}$$

with $I_\alpha(\zeta)$ as the modified Bessel function of first kind. Because of our small modulation amplitude, $I_0(2\kappa A)$ is small (≈ 1.1) and can be neglected. This allows us to assign the measured average conductance at z' to the momentary conductance at $z = z' + A$ (see abscissa of Fig. 9.3). The resulting systematic error in the z height determination is only $\approx 5\,\mathrm{pm}$.

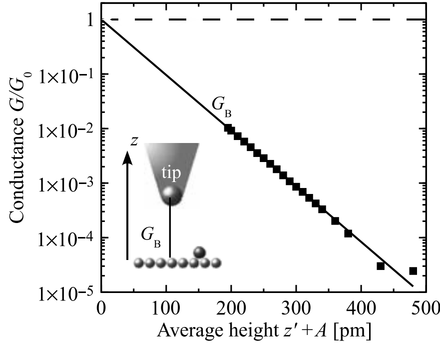

Fig. 9.3. The background conductance G_B between the bare surface and the tip shows an exponential dependence (*full line*) and determines $z \equiv 0$ as the extrapolated height where G_B equals the quantum of conductance G_0

Furthermore, we detect the power dissipation D of the cantilever by recording the excitation signal necessary to stabilize the oscillation at constant amplitude. In our experiments, the cantilever has a mechanical quality factor of $Q \approx 35{,}000$, which was determined by applying a random-noise excitation signal and measuring the resonance peak width around f_0 by means of a spectrum analyzer. The energy stored in the mechanical motion of the tip is $E = \frac{1}{2}k_0A^2$, which is only $\approx 5\,\mathrm{eV}$ for an oscillation amplitude of $A = 30\,\mathrm{pm}$ and $k_0 = 1{,}800\,\mathrm{N\,m^{-1}}$. Thus, the intrinsic energy loss per oscillation cycle $D_0 = 2\pi E/Q$ is less than 1 meV. Every dissipative energy transfer from the mechanical cantilever motion during its oscillation has to be compensated by the drive signal and can be recorded in our system with a resolution of approximately 1 meV per cycle.

We note that any *non*-dissipative energy transfer during the oscillation cycle as, for example, a vertical movement of an adsorbate due to the acting forces during the close approach of the oscillation cannot be detected. Also possible single dissipative events like sudden jumps of an adsorbate from its original to its neighboring adsorption site have to have a much higher dissipation to be detectable due to the relatively slow regulation speed of the amplitude regulation loop. With a loop-bandwidth of 100 Hz, only events of $\gtrsim$200 meV are distinguishable.

9.4 Forces During Adsorbate Manipulating

We chose cobalt on Pt(111) as example system to determine the forces that act on individual atoms during atom-manipulation. This adsorbate–sample system is known to have a relatively high diffusion barrier of $\approx 200\,\mathrm{meV}$ [50], which is much higher than the thermal energy at 5 K of $k_BT = 4.3\,\mathrm{meV}$. Random Brownian motion can thus be neglected, and relatively large and

easily detectable forces are expected to be necessary to move the cobalt atom along the Pt(111) surface.

Cobalt atoms adsorb on the hexagonal lattice of the smooth Pt(111) surface at hollow site positions. On the (111) crystal facet of Pt(111), there are two distinguishable hollow sites: the hexagonal close-packed (hcp) and face-centered cubic (fcc) lattice sites, which differ only by the presence or absence of a Pt atom in the second layer of the surface. It has been shown that these two different adsorption sites change the electronic structure of the atomic states on the Co atom slightly [51].

For comparison, we performed similar experiments with cobalt adsorbates on a Cu(111) surface [42]. This surface has the same hexagonal lattice structure as Pt(111), but a much lower diffusion barrier for cobalt atoms [52]. Additionally, and in difference to the Pt(111) surface, without the presence of the tip, the atoms adsorb only on the fcc hollow sites [53].

Furthermore, we compared the results obtained from single metal atoms with the manipulation forces measured on a more complex molecule. We choose carbon-monoxide on Cu(111) as a well studied system [9, 17, 54, 55], which has been found to be immobile up to 40 K [31].

To simplify the computation of the force calculations, all data were taken at constant z-height relative to the bare surface, that is, without regulating the tip–sample height for constant-current or constant-frequency-shift as in usual STM or AFM measurements. We note that it is crucial to align the surface plane parallel to the plane of motion of the probing tip in this operational mode.

Figure 9.4a–d shows images of a single cobalt atom on Pt(111) and a single carbon monoxide molecule on Cu(111) with constant tip-heights close to the threshold for atom manipulation. In these images, the vertical stiffness k_z and the conductance G show circular symmetry, without any sign of the threefold substrate symmetry. The images obtained from cobalt on Pt(111) show a narrow, Gaussian-like, dip in k_z and a peak in G.

In contrast, the images from a carbon monoxide molecule on Cu(111) have a more complex structure: the vertical stiffness k_z is flat around the central minimum, and G contains a central conductance peak within a broader conductance dip. For an asymmetric tip apex, k_z often deviates from circular symmetry for carbon monoxide [56]. In these images, the change in stiffness due to the adsorbate is $17\,\mathrm{N\,m^{-1}}$ on cobalt and $9\,\mathrm{N\,m^{-1}}$ on carbon monoxide, in the range of a metal–metal bond stiffness (10–$100\,\mathrm{N\,m^{-1}}$) [45].

We note that the applied voltage between tip and sample $|V| = 1\,\mathrm{mV}$, which is necessary to detect the conductance G, was here and in all following measurements small enough to have a negligible influence on the move threshold. At larger voltages ($|V| \gtrsim 5$–$10\,\mathrm{mV}$), the manipulation threshold is reduced due to the excitation of vibrational modes between the surface and the cobalt atom or the carbon monoxide molecule [9, 57]

We can derive the force to move an atom from the measurement of k_z as a function of both vertical and lateral tip position. Figure 9.5 shows "line scans"

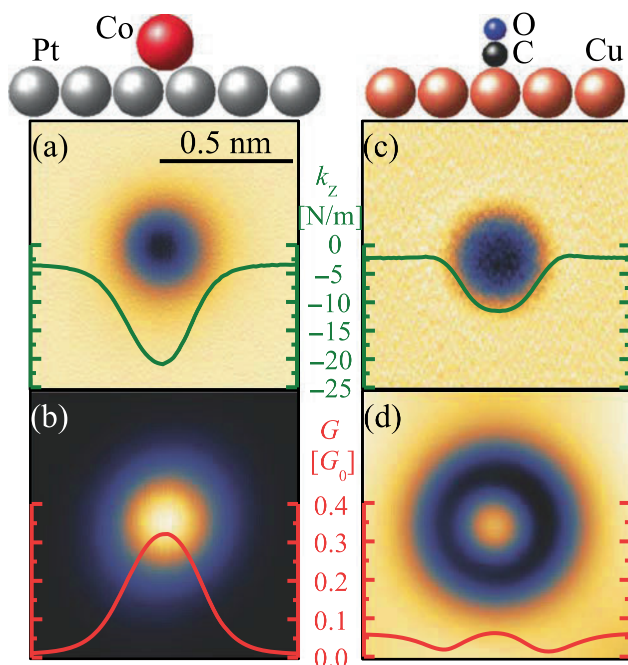

Fig. 9.4. Simultaneous AFM and STM measurements of individual adsorbates showing the tip–sample stiffness (**a**) and conductance (**b**) of a single Co atom on Pt(111), and the stiffness (**c**) and conductance (**d**) for a single CO molecule on Cu(111). The colored curves in the panels are horizontal cross sections through the centers of the images. The ball models of the surfaces are scaled to match the dimensions of the images

obtained by moving the tip parallel to the surface at constant height, passing over the top of an isolated cobalt atom on Pt(111). The direction of these scans corresponds to the direction of easiest motion on this substrate: it connects two neighboring threefold hollow adsorption sites (Fig. 9.5a). These scans were repeated at progressively smaller tip heights until the cobalt atom hopped to a neighboring adsorption site, as illustrated in Fig. 9.5b. Figure 9.5c, d shows that both G and $|k_z|$ increased as the tip height was decreased. At the smallest tip height and at a lateral position about halfway to the adjacent binding site, a sudden jump occurred in both k_z and G. At this tip position, the cobalt atom reproducibly hopped from its initial binding site to the next and was imaged again at its new position by the continuing line scan. In contrast, the atom reliably remained at its initial binding site when the tip was only 5 pm farther from the surface.

The vertical force F_z was determined by integrating k_z along z as discussed in Sect. 9.3.1 by removing the averaging due to the tip oscillation.

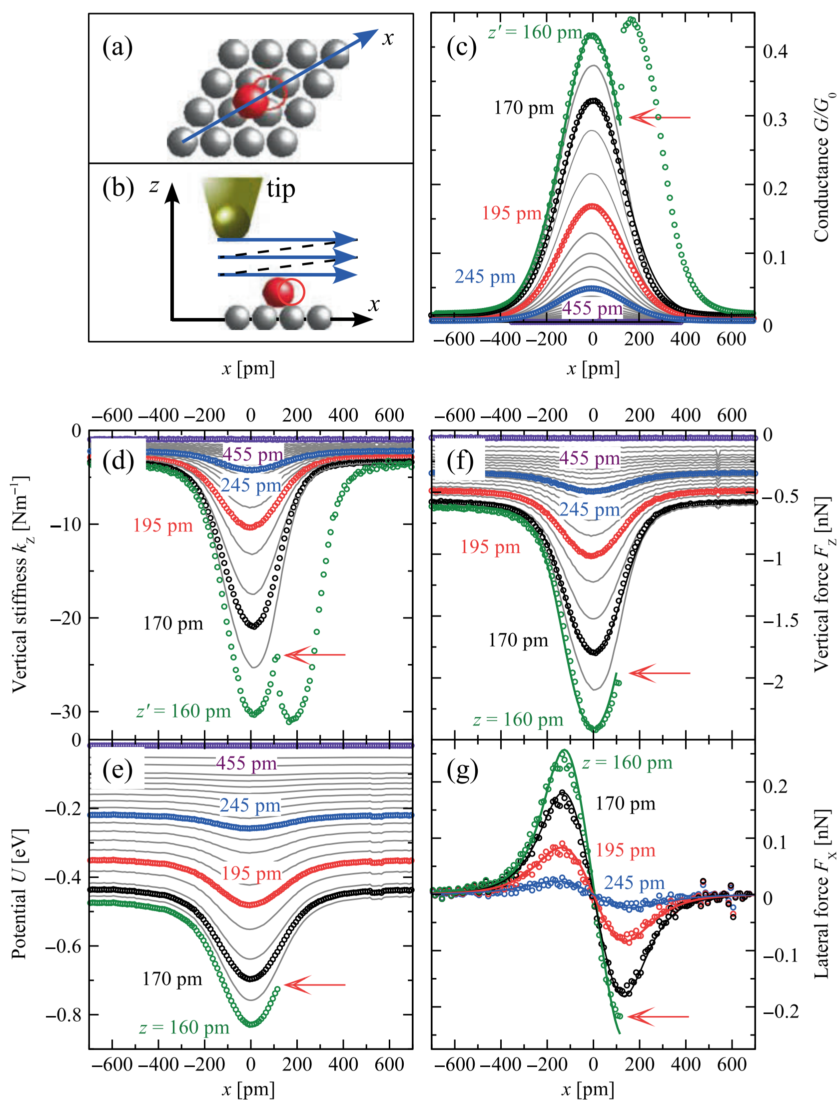

Fig. 9.5. Schematic top (**a**) and side view (**b**) of the Pt(111) surface atoms (*gray*) and the adsorbed Co atom (*red*). The *blue arrows* indicate the scan direction of the tip. Simultaneously measured conductance G (**c**) and stiffness k_z (**d**) (*circles* and *gray lines*). Tip–sample interaction energy U (**e**), vertical force F_z (**f**), and lateral force F_x (**g**) extracted from the stiffness data. Selected line scans are labeled with the tip height z or the closest approach z' during the oscillation. *Red arrows* indicate the hop of the Co atom to the neighboring binding site. Colored lines in (**c**), (**f**), and (**g**) are fits with the s-wave model (see Chap. 9.5)

We interpret F_z as the sum of two components: a background force F_B and the force F_z^* due to the presence of the adsorbate. The background force is in large part due to tip dependent long-range (van der Waals) forces and increases as the tip approaches the surface but does not depend on the lateral position. The vertical force F_z^* due to the adsorbate grows rapidly, doubling in magnitude as z is changed by only 15 pm near the move threshold (see Figs. 9.5f and 9.10a), indicating the short-range nature of this force.

We found the tip–sample interaction force to be nondissipative as long as the adsorbate did not hop to a new binding site. In this nondissipative range of tip positions, we calculated the tip–sample interaction potential U (Fig. 9.5e) by integration of F_z along z [58]. The lateral force F_x was then calculated by differentiation of U in the lateral x direction (Fig. 9.5g). This technique allowed us to determine forces in any direction, even though the cantilever only senses the vertical stiffness. The lateral force was zero with the tip placed above the adsorbate, grew as the tip was moved laterally until a maximum was reached, and vanished far from the adsorbate.

This procedure allows us to determine the force that it takes to move a single cobalt atom across a Pt(111) surface. At the point where the atom hopped, we found a lateral force $F_x = 210 \pm 30\,\mathrm{pN}$. At the same time, the vertical force $F_z^* = -1.4 \pm 0.2\,\mathrm{nN}$ was much larger than the lateral force and was nearly half as large as the bond-breaking force of 4 nN for a Pt point contact [59].

To understand the interplay between the vertical and horizontal force components, we decreased z below the threshold height for hopping and continued to measure the forces. As shown in Fig. 9.6, we found that the lateral force to move the atom remained constant, while the vertical force varied substantially. It might be of surprise that the lateral force F_x at $x \approx -120\,\mathrm{pm}$ and $z \leq 155\,\mathrm{pm}$ exceed the force necessary to move the atom at $x \approx 80\,\mathrm{pm}$, but at negative x the cobalt atom motion is hindered by a platinum surface atom as illustrated in Fig. 9.5a and requires a much higher manipulation force.

We further note that this measurement has been performed with a different tip (in the sense as described in Sect. 9.3) than that used to obtain the data shown in Fig. 9.5. This tip resulted in slight differences in the recorded forces such as a background force F_B between the tip and the bare sample as seen at $x = \pm 600\,\mathrm{pm}$, that is, by a factor of about 2 smaller than in Fig. 9.5.

Similar height dependent measurement have been performed with the tip approaching the cobalt atom from positive x. In this measurements, the threshold force is reached before the tip scans over the adsorbate and the atom jumps in a direction opposite to the tip motion (see Fig. 9.7a).

For the range of heights measured, the tip–adsorbate vertical force $F_z^* = F_z - F_\mathrm{B}$, with F_B defined as the background force at $x \pm 600\,\mathrm{pm}$, varied from $-0.45\,\mathrm{nN}$ (with the tip laterally far from the atom) to $-3.0\,\mathrm{nN}$ (with the tip nearly above the atom) at the point where the cobalt atom hopped. The tip can only exceed a lateral force large enough to manipulate the cobalt atom at tip–sample distances $\leq 160\,\mathrm{pm}$. For smaller heights than 160 pm, there are

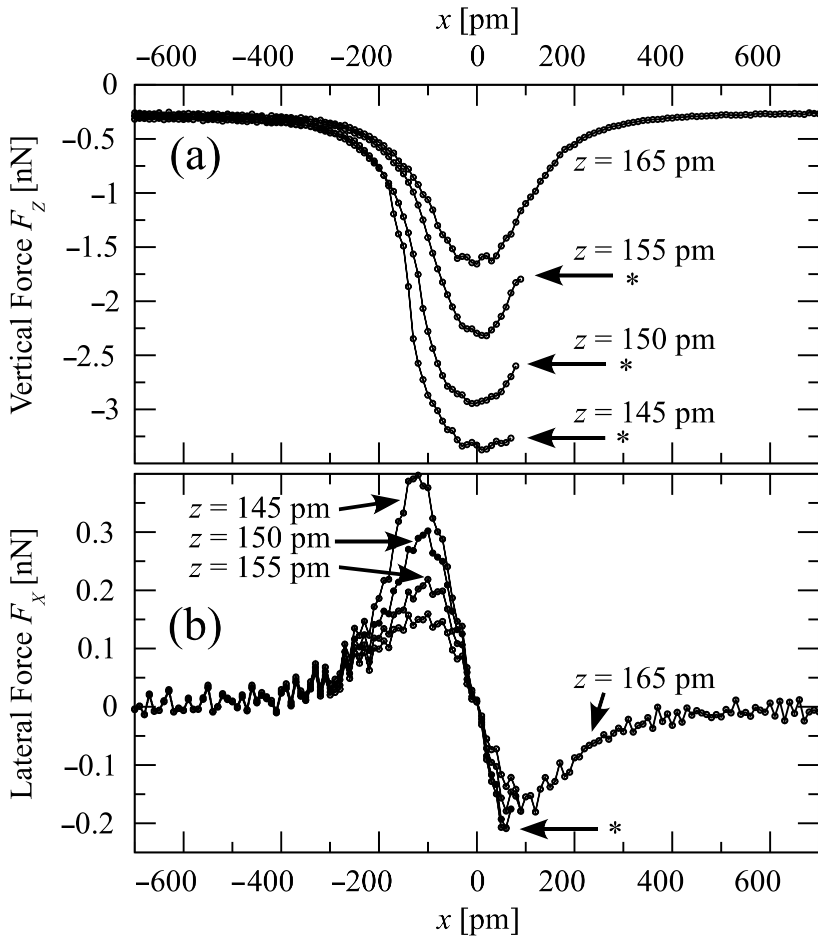

Fig. 9.6. Vertical (**a**) and lateral (**b**) force components when moving the tip over a Co atom on Pt(111) in direction of easiest adsorbate motion. Scans were performed with successively reduced tip height z even below the initial move threshold. Arrows with asterisks mark the point where the atom hops

two distinguish tip positions in x, which initialize the atom to hop. In the left-hand part of Fig. 9.7b–d, the tip is located between the initial ($x = 0$ and the final ($x = 160\,\text{pm}$) position of the cobalt atom. Additionally, a tip placed closely behind the final position is also capable to exceed sufficient lateral force to make the atom jump.

These results suggest that the lateral force F_x is the key for the manipulation of metal adsorbates on flat metal surfaces. This insensitivity to F_z^* is in contrast to the mechanism determined for moving Si atoms on Si(111) [13]. There, it was found that the vertical force plays a dominant role by causing

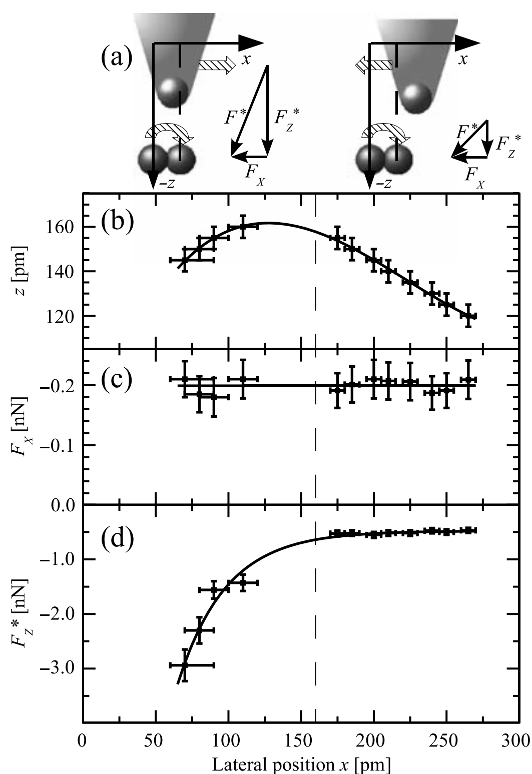

Fig. 9.7. (**a**) Schematic diagrams showing the two different lateral tip positions at which the Co atom hops when the tip height is below the threshold. (**b**) Tip positions at which the Co atom on Pt(111) hopped from its initial ($x = 0$) to its final binding site ($x = 160$ pm, *vertical dashed line* through panels). The lateral force F_x (**c**) and the vertical force F_z^* (**d**) for each data point of panel (**b**). *Solid lines* are guides to the eye

a reduction of the energy barrier between two adsorption sites as a result of relaxation of the Si adsorbate and surface. The force that is required to move an atom strongly depends on the supporting substrate. Much smaller forces were sufficient to manipulate cobalt atoms on Cu(111) as shown in Fig. 9.8. Here, the required lateral force was only 17 ± 3 pN, even though copper and platinum are both face-centered cubic (fcc) crystals and the cobalt atom binds at a threefold hollow site on both surfaces. This indicates that the nature of the chemical bonding plays a strong role. For copper, the bonding is dominated by hybridization of the electronic states of the cobalt adsorbate with the 4*s* metal band, which shows no discernible direction dependence. In contrast, extra bonding occurs on platinum, resulting from its partially filled and strongly directional 5*d* bonds [60], which apparently increase the forces necessary for manipulation.

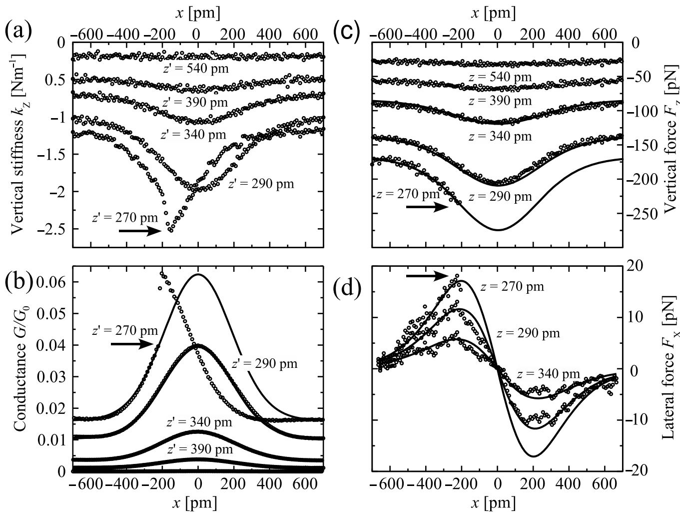

Fig. 9.8. Simultaneously recorded stiffness k_z (**a**) and conductance G (**b**) over a Co atom adsorbed on a Cu(111) surface at selected tip–sample separations z'. (**c**) and (**d**) show the computed vertical force F_z and lateral force F_x. *Arrows* indicate the hop of the Co atom. The conductance and the forces can be well described by the s-wave model (*full line*)

9.4.1 Manipulating a Small Molecule: CO on Cu(111)

The manipulation forces for cobalt and a small molecule, such as carbon monoxide, differ dramatically even though both adsorbates move on Cu(111) at a similar tunneling conductance in STM experiments [17]. We found that the lateral manipulation force for carbon monoxide molecules ($160 \pm 30\,\mathrm{pN}$) is an order of magnitude larger than that for Co atoms (Fig. 9.9). More importantly, the spatial dependence of the forces was markedly different. For example, F_z^* at closest tip–sample approach before hopping was almost independent of the lateral tip position around the center of the molecule and became weakly repulsive at $x \approx \pm 300\,\mathrm{pm}$.

It is not surprising that the CO molecule exhibits more complex interaction forces than metal atoms, because covalent bonds tend to be strongly directional, and the molecule has an angular orientation in addition to its position degrees of freedom.

The measured lateral stiffness at the threshold tip height for moving the CO molecule was $1.2\,\mathrm{N\,m^{-1}}$ (Fig. 9.9), which is slightly stiffer than a typical Van der Waals bond ($0.5-1\,\mathrm{N\,m^{-1}}$) [45] and comparable to the lateral stiffness for moving a Co atom on Pt(111). It is important to be aware that this measured stiffness reflects not just the adsorbate–surface interaction but also the combined effects of the tip–adsorbate stiffness and strain in the tip apex.

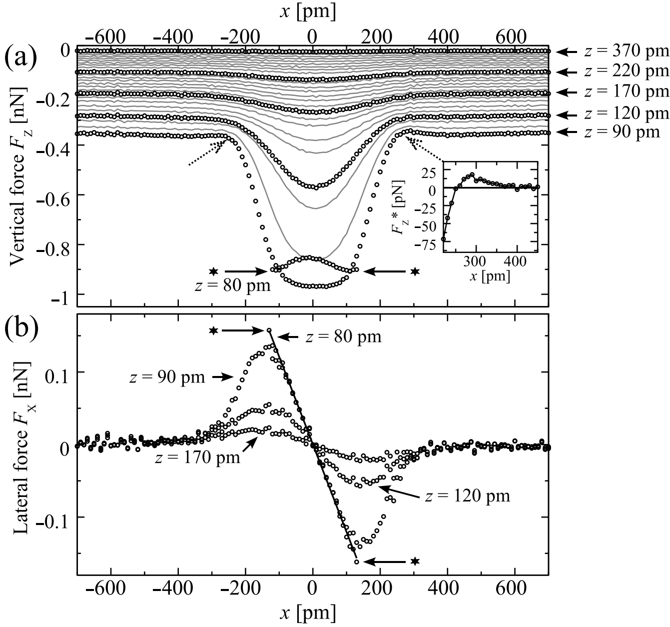

Fig. 9.9. Vertical (**a**) and lateral (**b**) force components when moving the tip over a CO molecule on Cu(111) for different tip heights z. The x direction corresponds to the easiest adsorbate motion from an on-top binding site to an adjacent one via a bridge site. At the positions marked with *arrows* and *asterisk*, the molecule hopped between neighboring binding sites. The full line in (**b**) at $z = 80\,\text{pm}$ is a linear fit to the lateral force with a slope of 1.2 N/m

9.5 Modeling Forces and Conductance

The forces and conductance between the cobalt adsorbate on Pt(111) and the tip show a high degree of symmetry (Fig. 9.5). As long as the cobalt atom is not moving, $|F_z|$ and G are symmetric around $x = 0$, and increase continuously for smaller $|x|$ and z values. The lateral force F_x is antisymmetric around $x = 0$ and also grows continuously for lower tip–sample separations z.

To explore this spatial symmetry, we model the tip–adsorbate force as depending only on the distance between the tip–apex and the adsorbate on the surface. For this model, the distance dependence of the force F^* was derived from the difference between the vertical force F_z measured directly on top of the atom at $x = 0$ and the vertical force at a distance ($x = \pm 600\,\text{pm}$), where F_z is no longer influenced by the adatom and thus equals the background force F_B

$$F^*(z) = F_z(x = 0, z) - F_\mathrm{B}(z). \tag{9.6}$$

We found that distance dependence of the force F^* as extracted from the data shown in Fig. 9.5f is well described by an inverse power-law (Fig. 9.10a)

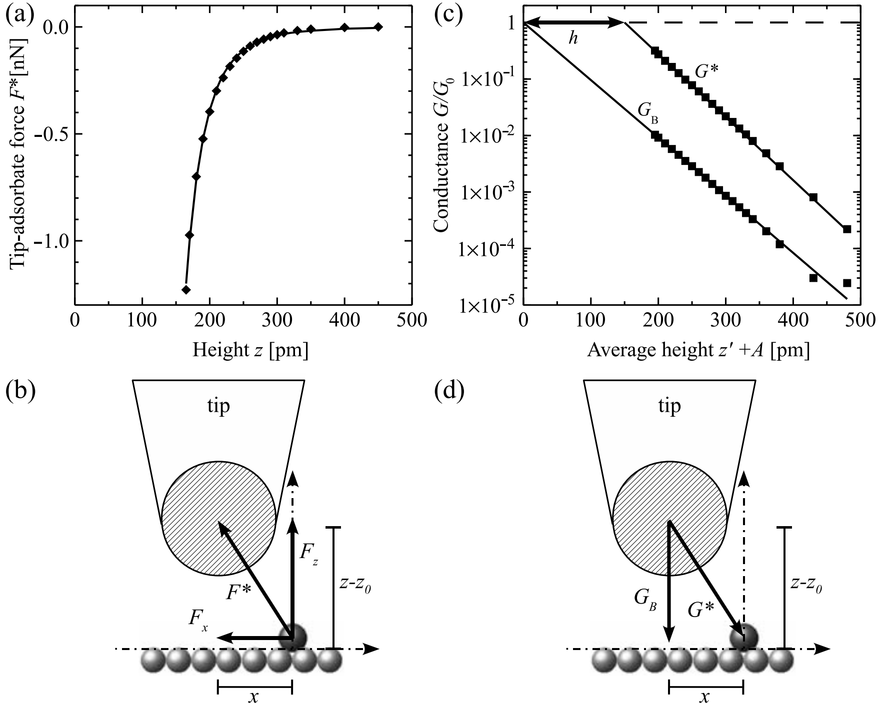

Fig. 9.10. (**a**) The tip-adsorbate force $F_z^* = F_z - F_B$ can be well described by an inverse-power law (*full line*). (**b**) Schematic diagram of the spherical symmetric model to describe the tip-adsorbate forces. (**c**) The background conductance G_{B} and tip-adsorbate conductance G^* show an exponential dependence (*full lines*). (**d**) Schematic diagram illustrating the two independent conductance channels used in the model

$$F^*(z) = -1.76 \times 10^7 \times (z + 39.2\,\mathrm{pm})^{-7}\,\mathrm{N} \times \mathrm{pm}^7. \quad (9.7)$$

This fitted function of F^* was assumed to be isotropic in space so that the vertical and lateral forces F_z and F_x are only geometric projections onto the corresponding axes as illustrated in Fig. 9.10b. Under this assumption, the equations

$$F_x(x, y, z) = \frac{x}{d} \times F^*(d + z_0) \quad (9.8)$$

and

$$F_z(x, y, z) = \frac{z + z_0}{d} \times F^*(d + z_0) + F_B(z) \quad (9.9)$$

describe all forces. Here $d = \sqrt{x^2 + y^2 + (z - z_0)^2}$ denotes the effective tip–adsorbate distance and z_0 is a fit parameter (see Fig. 9.10b).

Similarly, we model the conductance with two independent channels: a bare-surface conductance $G_\mathrm{B}(z) = G_0 \exp(-2\kappa_B z)$, which is not influenced by the adsorbate, and a conductance solely acting between tip and the adsorbate

$$G^*(x, y, z) = G_0 \exp(-2\kappa^*(h + d + z_0)). \tag{9.10}$$

The decay constants $\kappa_\mathrm{B} = 11.7\,\mathrm{nm}^{-1}$, $\kappa^* = 12.9\,\mathrm{nm}^{-1}$, and the effective atom height $h = 150\,\mathrm{pm}$ are extracted from the z-dependence of the measured conductance at $x = 0$ and $x = \pm 600\,\mathrm{pm}$, respectively, as shown in Fig. 9.10c.

The free parameter z_0 was then chosen to fit simultaneously (9.8)–(9.10) to the line-scans of F_z, F_x, and G at different heights. Despite the simplicity of this model, it agrees well with the data on Pt(111), as shown as solid colored lines in Fig. 9.5 using $z_0 = -580\,\mathrm{pm}$. This observed spherical symmetry of the force between the Co adsorbate and the tip apex suggests that the interaction occurs primarily via s-wave orbitals in both the tip–apex atom and the Co atom. For the different adsorbate–surface system, cobalt on Cu(111), we found that $z_0 = -480\,\mathrm{pm}$ produces a good fit as shown in Fig. 9.8.

We note that this model treats the two conductance channels independently and does not account for any interference between them, which might occur due to many-particle effects such as the Kondo effect [61]. Also any relaxations in tip, sample, or between the adsorbate and sample are only accounted for by the free parameter z_0. This parameter should not be misinterpreted as the apex radius of the tip as the schematic illustrations in Fig. 9.5b, d might suggest. The parameter z_0 is an effective response parameter of the whole tip, sample, and adsorbate system, which incorporates the tip geometry, the effective adsorbate radius, and linear relaxations in tip and sample.

Furthermore, the functions used in the model are determined by the obtained data at $x = 0$ and $x = \pm 600\,\mathrm{pm}$. Thus, it is evident that the fit is excellent for all data at these values. Nevertheless, this model provides insight into the geometry of the interacting orbitals and does not depend on any numerical calculations. We note that this proposed model is very similar to the one suggested by Hla and Braun [62] with one critical exception, in their case the force vs. distance curve has to be derived from numerical simulations, while here it is measured.

9.6 Mapping the Energy Landscape

In the previous sections, we described a method to determine the interaction forces and energies between the tip and the adsorbate–sample system. This allowed us to determine the threshold forces for manipulating atoms and molecules on flat metal surfaces. These measurements were done along the direction of easiest motion and at different tip–sample distances. Now, we will expand this measurements to determine the full three-dimensional energy landscape of the manipulation process.

At small tip heights, below the move threshold, the adsorbate follows the tip from binding site to binding site [17, 53]. Under these conditions, maps of the forces and the tip–sample interaction potential can be constructed by combining k_z images obtained at various tip heights both above and below the manipulation threshold.

To calculate the tip–sample interaction potential, we use parts of k_z images obtained above the move threshold. The part is chosen to include only the area in which the tip is closer to the adsorption site of the adsorbate than to any other possible adsorption site for that particular adsorbate. This area is marked as red triangle in Fig. 9.11a. This data is then replicated and laterally shifted to the locations of the binding sites nearest the tip and combined to a full data set, resulting in an image as shown in Fig. 9.11b. With this method, we approximate the effect of moving the atom so that it always occupies the binding site nearest the tip. A more accurate measurement would entail manually moving the atom to each successive binding site and then measuring the stiffness for the corresponding triangle-enclosed region.

Vertical stiffness maps produced with the above method are then combined with data measured at a sufficiently close tip–sample distance so that the cobalt atom follows the lateral tip motion by successively visiting all the threefold hollow binding sites, nearly always occupying the site nearest the tip (Fig. 9.11c, d). We used 25 images similar to the one shown in Fig. 9.11b obtained at different tip–sample distances, and an image as shown in Fig. 9.11d to calculate the energy landscape by integrating along the z direction each data point of the stack. The resulting energy map for cobalt on Pt(111) is shown in Fig. 9.11e.

The most stable adsorption sites for the cobalt atom are the threefold hollow sites, which appear as minima in the potential map. The two different types of hollow sites (fcc and hcp) are essentially indistinguishable. The energy landscape shows spherical symmetries around each binding site until they overlap. The barrier height along that direction of easiest motion is 250 ± 50 meV, which is consistent with the energy barrier of 200 meV measured in diffusion experiments [50]. The highest energy is detected around the high-symmetry on-top positions ($\geq$400 meV). The distortion from perfect sixfold symmetry at this point is presumably due to the tip–apex and small errors in the alignment of the individually recorded stiffness maps.

Simultaneous to the energy landscape, we recorded the power dissipation in the cantilever during the continuous atom manipulation at the closest tip–sample separation (Fig. 9.11f). The dissipation is $\approx$1 meV/cycle for most of the image, which is not detectably different ($\pm$0.5 meV) from the free cantilever dissipation. The dissipation due to the atomic scale junction becomes detectable only when the tip is equidistant (within 10 pm) from two cobalt binding sites. There the dissipation increases by $\approx$2 meV per cycle, because the oscillating tip can induce the atom to hop repeatedly between the two sites. The dissipation further rises to more than 30 meV per cycle when the tip is placed close to a high-symmetry site equidistant from six binding sites.

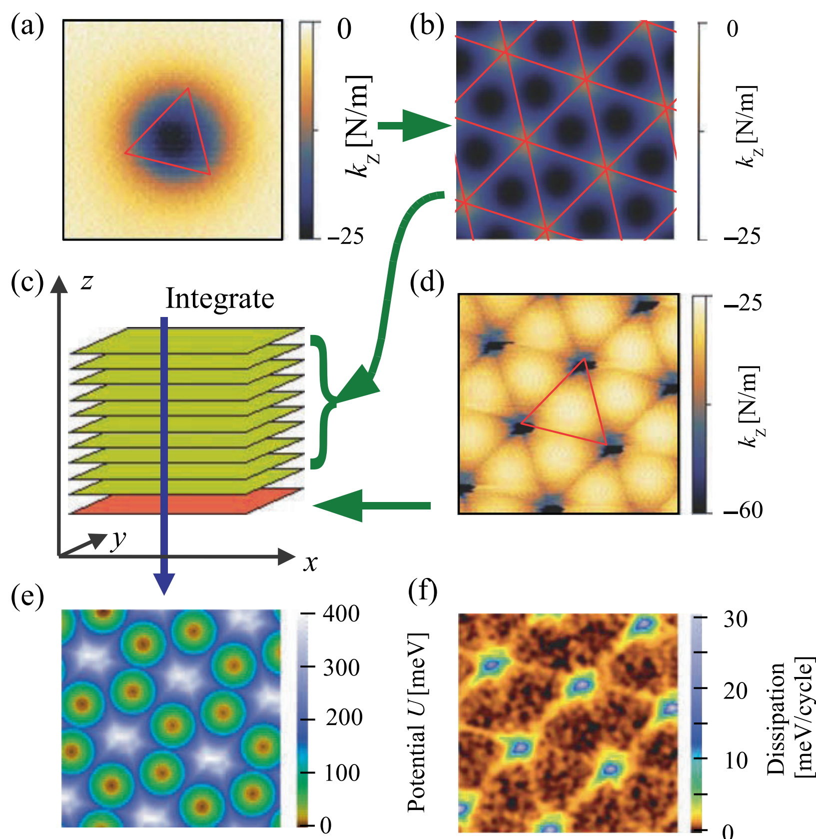

Fig. 9.11. (**a**) Vertical stiffness map at a height where the cobalt atom remains at one binding site on the Pt(111) surface. (**b**) Vertical stiffness map for use in computing the potential energy map. It is constructed by replicating the enclosed patch of data in (**a**). (**c**) Maps similar to the one in (**b**) are combined together with the k_z data obtained at a tip height where the Co atom follows the lateral tip motion (**d**). (**e**) Potential energy at constant height obtained by integrating the stiffness along z for each lateral position. (**f**) Power dissipation of the oscillating cantilever measured simultaneously with (**d**). Note that there is no detectable energy dissipation for tip heights where the atoms remain bound to one binding site as in (**a**). All images are $0.67 \times 0.67\,\text{nm}^2$ in size

Because dissipation occurred when the atom hopped, comparison of energies between two binding sites might not be valid under all circumstances, but energies within the basin around any one binding site are correct. We note that the noise in the dissipation signal is primarily due to noise in detecting the cantilever deflection amplitude.

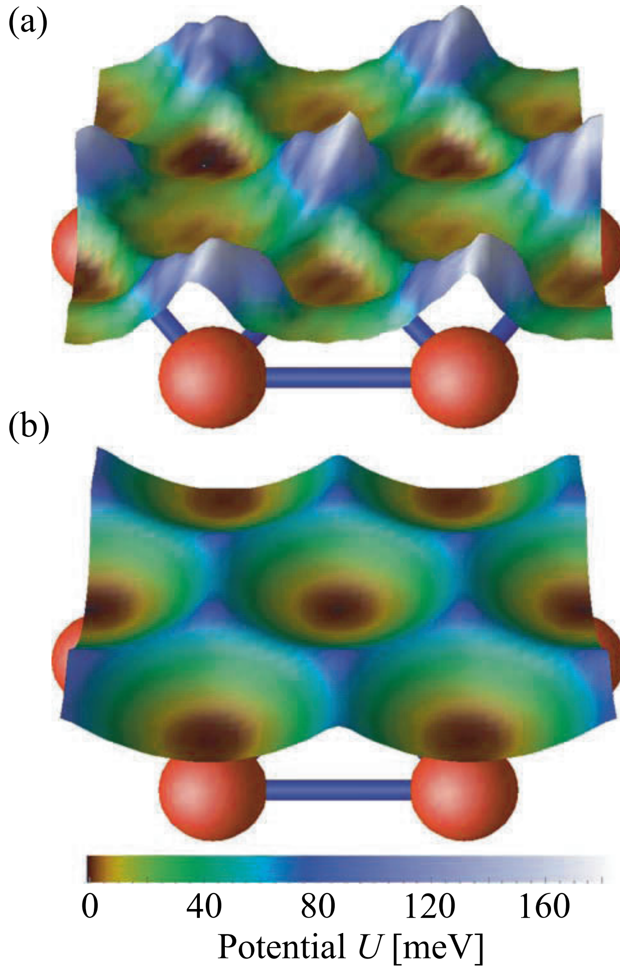

Fig. 9.12. Two-dimensional potential landscapes of the tip–sample interaction energies during manipulation of cobalt (**a**) and carbon-monoxide (**b**) on Cu(111). The underlying Cu(111) lattice is superimposed as a ball-and-stick model. The size of each image is $550 \times 480\,\mathrm{pm}^2$

In addition to cobalt on Pt(111), we also mapped the interaction potential for cobalt and for carbon monoxide on Cu(111). Figure 9.12a shows the result for cobalt manipulated on Cu(111). In contrast to the potential landscape of cobalt on Pt(111), the most stable adsorption sites are the fcc hollow sites only [53]. The neighboring hexagonal close-packed (hcp) sites have a slightly higher potential energy ($\approx 5\,\mathrm{meV}$). We note that the Co atom can only be stabilized on this binding site when the tip is in close proximity [53]. The fcc and hcp sites were separated by a potential barrier of $35 \pm 5\,\mathrm{meV}$.

The landscape for an adsorbed carbon monoxide molecule clearly reflects the different symmetry of the binding site (Fig. 9.12b). In this case, we found that the bridge site had the lowest barrier (70 ± 10 meV) between two on-top binding sites.

For all three systems, the measured potential barrier height for positioning the tip between two neighboring adsorption sites is in close agreement with the diffusion barrier for adsorbate motion as determined by density functional theory (37 meV for cobalt on Cu(111)) [52] and experiments performed without the presence of a probe tip (75 meV for carbon monoxide on Cu(111) [63] and 200 ± 10 meV for cobalt on Pt(111) [50]). Although diffusion experiments detect the lowest barrier of the adsorbate–surface potential landscape without the presence of a tip, our measurements determine the potential for moving the tip resulting from all interactions among tip, surface, and adsorbate.

9.7 Summary

The presented route to measure the forces necessary to manipulate atoms and molecules in arbitrary directions and to determine the full tip–sample potential landscape is an important step towards atomic-scale fabrication. We showed that these forces and energies depend strongly on the choice of adsorbate and surface. It provides complimentary information to STM manipulation experiments, the main tool for atom manipulation to date.

A systematic investigation of the manipulation forces on different surface–adsorbate combinations is now possible, and the driving mechanism to create future nanoscale devices can be explored in a quantitative manner, which might help to choose appropriate material combinations. We believe that friction, as observed in tribology experiments, and molecular diffusion can gain new impetus by the detailed understanding of forces and potentials involved in the contact between a single atom or molecule, the supporting surface, and a manipulating tip in proximity.

Acknowledgments

We thank B.J. Melior, G. Zeltzer, and M. Breitschaft for expert technical assistance and F.J. Giessibl, and C.F. Hirjibehedin for their help and the stimulating discussions on issues related to this work.

References

1. R.P. Feynman, Eng. Sci. **23**, 22 (1960)
2. D.M. Eigler, E.K. Schweizer, Nature **344**, 524 (1990)
3. M.F. Crommie, C.P. Lutz, D.M. Eigler, Science **262**, 218 (1993)
4. H.C. Manoharan, C.P. Lutz, D.M. Eigler, Nature **403**, 512 (2000)

5. N. Nilius, T.M. Wallis, W. Ho, Science **297**, 1853 (2002)
6. C.R. Moon, L.S. Mattos, B.K. Foster, G. Zeltzer, W. Ko, H.C. Manoharan, Science **319**, 782 (2008)
7. S.-W. Hla, L. Bartels, G. Meyer, K.-H. Rieder, Phys. Rev. Lett. **85**, 2777 (2000)
8. J. Repp, G. Meyer, S. Paavilainen, F.E. Olsson, M. Persson, Science **312**, 1196 (2006)
9. A.J. Heinrich, C.P. Lutz, J.A. Gupta, D.M. Eigler, Science **298**, 1381 (2002)
10. D.M. Eigler, C.P. Lutz, W.E. Rudge, Nature **352**, 600 (1991)
11. J.A. Stroscio, F. Tavazza, J.N. Crain, R.J. Celotta, A.M. Chaka, Science **313**, 984 (2006)
12. N. Oyabu, O. Custance, I. Yi, Y. Sugawara, S. Morita, Phys. Rev. Lett. **90**, 176102 (2003)
13. Y. Sugimoto, P. Jelinek, P. Pou, M. Abe, S. Morita, R. Pérez, O. Custance, Phys. Rev. Lett. **98**, 106104 (2007)
14. N. Oyabu, Y. Sugimoto, M. Abe, Ó. Custance, S. Morita, Nanotechnology **16**, S112 (2005)
15. Y. Sugimoto, M. Abe, S. Hirayama, N. Oyabu, Ó. Custance, S. Morita, Nat. Mater. **4**, 156(2005)
16. J.A. Stroscio, D.M. Eigler, Science **254**, 1319 (1991)
17. L. Bartels, G. Meyer, K.-H. Rieder, Phys. Rev. Lett. **79**, 697 (1997)
18. R.S. Becker, J.A. Golovchenko, B.S. Swartzentruber, Nature **325**, 419 (1987)
19. L. Bartels, G. Meyer, K.-H. Rieder, Appl. Phys. Lett. **71**, 213 (1997)
20. P. Zeppenfeld, C.P. Lutz, D.M. Eigler, Ultramicroscopy **42**, 128 (1992)
21. M.F. Crommie, C.P. Lutz, D.M. Eigler, Nature **363**, 524 (1993)
22. T.A. Jung, R.R. Schlittler, J.K. Gimzewski, H. Tang, C. Joachim, Science **271**, 181 (1996)
23. M.T. Cuberes, R.R. Schlittler, J.K. Gimzewski, Appl. Phys. Lett. **69**, 3016 (1996)
24. J. Lagoute, K. Kanisawa, S. Fölsch, Phys. Rev. B **70**, 245415 (2004)
25. M.J. Cromstock, J. Cho, A. Kirakosian, M.F. Crommie, Phys. Rev. B **72**, 153414 (2005)
26. J. Gaudioso, L.J. Lauhon, W. Ho, Phys. Rev. Lett. **85**, 1918 (2000)
27. C. Loppacher, M. Guggisberg, O. Pfeiffer, E. Meyer, M. Bammerlin, R. Lüthi, R. Schlittler, J.K. Gimzewski, H. Tang, C. Joachim, Phys. Rev. Lett. **90**, 066107 (2003)
28. B.-Y. Choi, S.-J. Kahng, S. Kim, H. Kim, H.W. Kim, Y.J. Song, J. Ihm, Y. Kuk, Phys. Rev. Lett. **96**, 156106 (2006)
29. F. Moresco, G. Meyer, K.-H. Rieder, Phys. Rev. Lett. **86**, 672 (2001)
30. N. Henningsen, K.J. Franke, I.F. Torrente, G. Schulze, B. Priewisch, K. Rück-Braun, J. Dojić, T. Klamroth, P. Saalfrank, J.I. Pascual, J. Phys. Chem. C **111**, 14843 (2007)
31. L. Bartels, G. Meyer, K.-H. Rieder, Surf. Sci. **432**, L621 (1999)
32. R.E. Walkup, D.M. Newns, P. Avouris, Phys. Rev. B **48**, 1858 (1993)
33. M. Brandbyge, P. Hedegard, Phys. Rev. Lett. **72**, 2919 (1994)
34. S. Gao, M. Persson, B.I. Lundqvist, Solid State Commun. **84**, 271 (1992)
35. S. Gao, M. Persson, B.I. Lundqvist, Phys. Rev. B **55**, 4825 (1997)
36. S. Ciraci, E. Tekman, A. Baratoff, I.P. Batra, Phys. Rev. B **46**, 10411 (1992)
37. U. Kürpick, T.S. Rahman, Phys. Rev. Lett. **83**, 2765 (1999)
38. L. Pizzagalli, A. Baratoff, Phys. Rev. B **68**, 115427 (2003)

39. K. Liu, S. Gao, Phys. Rev. Lett. **95**, 226102 (2005)
40. N. Lorente, J. Phys. Condens. Matter **17**, S1049 (2005)
41. R. Otero, F. Rosei, F. Besenbacher, Ann. Rev. Phys. Chem. **57**, 497 (2006)
42. M. Ternes, C.P. Lutz, C.F. Hirjibehedin, F.J. Giessibl, A.J. Heinrich, Science **319**, 1066 (2008)
43. T.R. Albrecht, P. Grütter, D. Horne, D. Rugar, J. Appl. Phys. **69**, 668 (1991)
44. F.J. Giessibl, Appl. Phys. Lett. **76**, 1470 (2000)
45. D.R. Lide (ed.), *Handbook of Chemistry and Physics*, 90th edn. (CRC, Boca Raton, Florida, 1999)
46. F.J. Giessibl, Appl. Phys. Lett. **78**, 123 (2001)
47. J.E. Sader, S.P. Jarvis, Appl. Phys. Lett. **84**, 1801 (2004)
48. N.D. Lang, Phys. Rev. B **34**, 5947 (1986)
49. H.B. Michaelson, J. Appl. Phys. **48**, 4729 (1977)
50. P. Buluschek, Dissertation, École Polytechnique Fédérale de Lausanne, 2007
51. Y. Yayon, X. Lu, M.F. Crommie, Phys. Rev. B **73**, 155401 (2006)
52. D.V. Tsivlin, V.S. Stepanyuk, W. Hergert, J. Kirschner, Phys. Rev. B **68**, 205411 (2003)
53. J.A. Stroscio, R.J. Celotta, Science **306**, 242 (2004)
54. G. Meyer, B. Neu, K.-H. Rieder, Appl. Phys. A **60**, 343 (1995)
55. L. Bartels, G. Meyer, K.-H. Rieder, D. Velic, E. Knoesel, A. Hotzel, M. Wolf, G. Ertl, Phys. Rev. Lett. **80**, 2004 (1998)
56. F.J. Giessibl, S. Hembacher, H. Bielefeld, J. Mannhart, Science **289**, 422 (2000)
57. T. Komeda, Y. Kim, M. Kawai, B.N.J. Persson, H. Ueba, Science **295**, 2055 (2002)
58. H. Hölscher, S.M. Langkat, A. Schwarz, R. Wiesendanger, Appl. Phys. Lett. **81**, 4428 (2002)
59. S.R. Bahn, K.W. Jacobsen, Phys. Rev. Lett. **87**, 266101 (2001)
60. B. Hammer, J.K. Norskov, Nature **376**, 238 (1995)
61. V. Madhavan, W. Chen, T. Jamneala, M.F. Crommie, N.S. Wingreen, Science **280**, 567 (1998)
62. K.-F. Braun, S.-W. Hla, Phys. Rev. B **75**, 033406 (2007)
63. K.L. Wong, B.V. Rao, G. Pawin, E. Ulin-Avila, L. Bartels, J. Chem. Phys. **123**, 201102 (2005)

10

Atomic Manipulation on an Insulator Surface

Sabine Hirth, Frank Ostendorf, and Michael Reichling

Abstract. The manipulation of atomic and molecular species on metal surfaces with the scanning tunneling microscope (STM) operated at low temperature is a well established method for bottom-up nanofabrication [G. Meyer et al., Single Mol. **1**, 79 (2000); N. Lorente, R. Rurali, H. Tang, J. Phys. Condens. Matter **17**, S1049 (2005)], but is limited in its understanding and applications by restrictions inherent to the STM technique. These limitations can be overcome by using a dynamic scanning force microscope (SFM) for atomic manipulation that offers three major advantages compared to STM. First, the force microscope allows a quantification of the forces applied during the manipulation process (see Chap. 9), second, it facilitates manipulation at room temperature (see Chaps. 8 and 11) and, third, the technique allows manipulation on electrically insulating surfaces. However, examples for force controlled manipulation of atomic size species on an insulator surface are still scarce regarding experimental evidence [S. Hirth, F. Ostendorf, M. Reichling, Nanotechnology **17**, S148 (2006); R. Nishi et al., Nanotechnology **17**, S142 (2006)] as well as theoretical explanation [T. Trevethan et al., Phys. Rev. Lett. **98**, 028101 (2007); T. Trevethan et al., Phys. Rev. B **76**, 085414 (2007)]. Here we demonstrate the force controlled manipulation of water related defects on a $CaF_2(111)$ surface by a raster scanning motion of the tip over a specific surface region. Manipulation is facilitated by repulsive forces exerted by approaching the tip very closely to the defects. We focus mainly on the presentation of manipulation results and discuss the circumstances that allow a control of the manipulation process. The $CaF_2(111)$ surface is specifically well suited for such studies as this surface has been very well characterized by NC-AFM in previous studies [M. Reichling, C. Barth, Phys. Rev. Lett. **83**, 768 (1999); C. Barth, M. Reichling, Surf. Sci. **470**, L99 (2000); F.J. Giessibl, M. Reichling, Nanotechnology **16**, S118 (2005); R. Hoffmann et al., J. Am. Chem. Soc. **127**, 17863 (2005)] and contrast formation is understood on a quantitative level [A.S. Foster et al., Phys. Rev. Lett. **86**, 2373 (2001); C. Barth et al., J. Phys. Condens. Matter **13**, 2061 (2001); A.S. Foster et al., Phys. Rev. B **66**, 235417 (2002)]. Furthermore, the geometric and electronic structures of this surface is well understood from a variety of theoretical simulations [A.V. Puchina et al., Solid State Commun. **106**, 285 (1998); V.E. Puchin et al., J. Phys. Condens. Matter **13**, 2081 (2001); Y. Ma, M. Rohlfing, Phys. Rev. B **75**, 205114 (2007); Y. Ma, M. Rohlfing,

S. Morita et al. (eds.), *Noncontact Atomic Force Microscopy*, NanoScience and Technology,
DOI: 10.1007/978-3-642-01495-6_10, © Springer-Verlag Berlin Heidelberg 2009

Phys. Rev. B **77**, 115118 (2008)]. Therefore, it can be expected that the experimental evidence of force controlled manipulation presented here will finally be fully explained by further theoretical modeling.

10.1 Introduction

The manipulation of atomic and molecular species on metal surfaces with the scanning tunneling microscope (STM) operated at low temperature is a well established method for bottom-up nanofabrication [1,2], but is limited in its understanding and applications by restrictions inherent to the STM technique. These limitations can be overcome by using a dynamic scanning force microscope (SFM) for atomic manipulation that offers three major advantages compared to STM. First, the force microscope allows a quantification of the forces applied during the manipulation process (see Chap. 9), second, it facilitates manipulation at room temperature (see Chaps. 8 and 11) and, third, the technique allows manipulation on electrically insulating surfaces. However, examples for force controlled manipulation of atomic size species on an insulator surface are still scarce regarding experimental evidence [3,4] as well as theoretical explanation [5,6]. Here we demonstrate the force controlled manipulation of water-related defects on a $CaF_2(111)$ surface by a raster scanning motion of the tip over a specific surface region. Manipulation is facilitated by repulsive forces exerted by approaching the tip very closely to the defects. We focus mainly on the presentation of manipulation results and discuss the circumstances that allow a control of the manipulation process. The $CaF_2(111)$ surface is specifically well suited for such studies as this surface has been very well characterized by NC-AFM in previous studies [7–10] and contrast formation is understood on a quantitative level [11–13]. Furthermore, the geometric and electronic structures of this surface is well understood from a variety of theoretical simulations [14–17]. Therefore, it can be expected that the experimental evidence of force controlled manipulation presented here will finally be fully explained by further theoretical modeling.

10.2 Basic Principles

10.2.1 Experimental Procedures

Manipulation experiments are performed in an ultra-high vacuum (UHV) chamber operated at a base pressure below 1.3×10^{-8} Pa. The system is equipped with a commercial dynamic scanning force microscope UHV 350 from RHK (Troy, Michigan, USA), providing highest resolution and stability during imaging and manipulation. Procedures of sample preparation and atomic resolution imaging are similar to those used in previous studies of the $CaF_2(111)$ surface [11,12]. The crystal is kept at room temperature during all experiments. For imaging and manipulation, commercial, uncoated,

conductive silicon cantilevers with resonance frequencies of 60–70 kHz and spring constants of a few Nm^{-1} are used. Q values are above 80,000 in the UHV. The cantilever oscillation amplitude is kept constant at a level of 18–25 nm. All tips can be assumed to be covered with a native silicon oxide layer when purchased. Tips are used without further treatment like sputtering or flashing; only a bakeout at 120°C overnight is performed to remove volatile surface contaminants. For best imaging contrast, the contact potential is minimized by adjusting the sample bias to a voltage of typically +0.6 V. The contact potential is determined via Kelvin probe force spectroscopy ($U_{\mathrm{mod}} = 100\,\mathrm{mV}$) [18, 19]. During imaging, the cantilever resonance frequency detuning is typically −20 Hz. The topography feedback is set to a very slow time constants (1.5 s), facilitating imaging in the quasi constant height mode [20]. Images are taken at a scan speed of 300 ms per line and, although the feedback is slow compared to the line acquisition time, we can readily pick up topography information under these circumstances. When manipulating defects, we follow a protocol based on regular line-by-line scanning of the surface as used for imaging. For manipulating defects present in a certain area, the respective region is raster-scanned, with the detuning increased to typically 35 Hz. Successful manipulation appears in the resulting high contrast images as a chain-like manipulation path with an overall direction that is not related to the scanning direction in a simple way. When the desired position is achieved, the tip is retracted from the surface by reducing the detuning to 20 Hz or even lower values. Under the latter conditions, the defect is not manipulated but can be imaged without severe perturbation. The $CaF_2(111)$ sample with a size of $2 \times 10 \times 3\,\mathrm{mm}^3$ (Korth Kristalle GmbH) is prepared by cleavage of a longer rod in UHV at base pressure and room temperature inside the microscope. A successful preparation yields large atomically flat terraces divided by steps having a height of integer multiples of the F–Ca–F triple layer height (315 pm). Immediately after cleavage, terraces are found to be absolutely clean and contamination at step edges that could result from trapping of diffusing molecules cannot be detected even in traces. In images shown below, the direction of slow scanning is indicated by the solid arrow (filled triangle) in the upper left or right corner. Fast scanning is performed perpendicular to this direction in alternating lines from left to right ($\Rightarrow$) and right to left ($\Leftarrow$).

10.2.2 Surface Characterization

The $CaF_2(111)$ surface is a prototype insulating surface that is well understood in its NC-AFM atomic contrast formation. The surface consists of stacked triple layers with a height of 315 pm. Fluoride forms the first and third layer and the cubic sites are filled by calcium ions that are missing in every second of the gap rows. It has been shown that contrast formation strongly depends on tip polarity as demonstrated in Fig. 10.1, combining

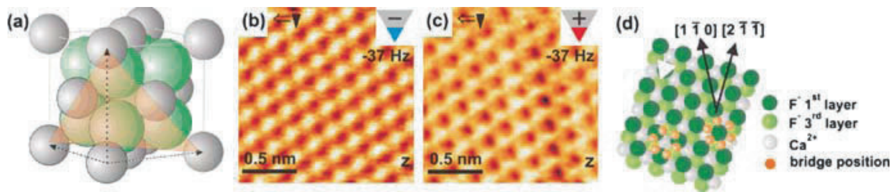

Fig. 10.1. Schematic representation and NC-AFM scanning results for the CaF_2(111) surface. (**a**) unit cell of CaF_2; small spheres represent calcium and large spheres the fluoride lattice. The (111) plane is represented by the shaded triangle. Images (**b**) and (**c**) demonstrate the two basic contrast patterns found in NC-AFM imaging for negatively and positively terminated nano tips, respectively. Pane (**d**) shows a model of the (111) surface with an assignment of surface directions as present in images (**b**) and (**c**). The small spheres indicate the positions bridging either fluorine or calcium sites. The orientation of the hexagon defined by the bridging sites is the same in both cases (From [3])

structural models of the crystal and the (111) surface with NC-AFM imaging results [11].

A negatively terminated tip images calcium ions as bright circular features, but the calcium sub-lattice does not provide unambiguous information about surface directions. When imaging with a positively charged tip, a triangular contrast is observed that is formed by a superposition of interactions between fluoride in the first and third row of a triple layer [12]. The corners of the triangle are determined by the low lying fluoride ions as depicted (white triangle) in panel (d). This ability of the NC-AFM to image both fluorine sub-lattices allows an unambiguous identification of all directions in the surface plane. NC-AFM images demonstrating results for both tip terminations shown in panels (b) and (c) have been taken on the crystal used for the manipulation experiments. From these images we can deduce the crystal orientation that is the same for all other images shown later. Therefore, we have an absolute coordinate system for the description of the different manipulation pathways on the surface. As will be shown later, the analysis of manipulation images reveals a point of maximum interaction at bridge positions between apparent protrusions. These positions are marked in red in panel (d) and can either represent positions bridging calcium or fluorine ions. A comparison of the two bridge positions observed for tips of different polarity shows that these positions are shifted by a small distance, but the angular orientation of the hexagon of bridge positions is the same in both cases. Therefore, the two bridge positions can be seen as equivalent for the following discussion. A careful analysis of the lattice contrast performed for many images reveals that in most cases imaging is performed with a negatively terminated tip. Hence, in the vast majority of images, a disk-like contrast is observed [12]. Furthermore, great care was taken to avoid and detect atomic tip changes that would strongly change lattice and defect contrast formation. Manipulation experiments involving strong

tip–surface interaction could in a reproducible manner only be performed with exceptionally stable, negatively terminated tips.

10.3 Experimental Results

10.3.1 Defect Preparation and Contrast Formation

It is well known from NC-AFM imaging experiments on CaF_2 crystals cleaved in air and on surfaces dosed with gases after vacuum cleavage that the (111) surface of CaF_2 is readily degraded by water and oxygen [7, 21]. This leads to the formation of randomly distributed nanometer-sized features protruding from the surface by typically less than 100 pm, that is, much less than the triple layer step height. When exposing the surface to small amounts of water, one observes the evolution of two types of atomic scale defects, namely stationary defects firmly pinned to a lattice site and mobile defects that may be moved from one site to another by the action of the scanning tip. The mobile species is found only after few days of measurement in the presence of a large number of stationary defects. We interpret this in a model proposing that water reacts with different types of vacancies on the surface and one type of reactive center is saturated after a while, and afterwards water reacts with the less abundant second type of vacancy. Based on preliminary theoretical studies of water molecules interacting with surface vacancy defects on $CaF_2(111)$, we associate the stationary defect with a hydroxyl group embedded into the surface at the site of a former neutral surface F center (F^0), while the mobile defect is associated with a water molecule attached to a charged surface F center (F^-). [22] An easy way of surface preparation for low dosages is simply exposing the surface to the residual gas of the vacuum system that mainly contains water. Phenomena observed in such an experiment do not differ qualitatively from those observed for deliberate water dosage but the formation of surface defects is very slow, facilitating a detailed observation of the development. The series of images taken over a total time of 144 h shown in Fig. 10.2 provides an overview of the degradation of $CaF_2(111)$ under UHV conditions in a frame size of 300 by 300 nm. Defects emerging with time are marked by circles for better visibility.

Occasionally, very few clusters cover the surface directly after cleavage (Fig. 10.2a) and as frames (b)–(d) show, contamination is continuously built up. The last two frames are assembled from four smaller panes as scanning larger frames became increasingly difficult with an increasing number of contaminants present. The last image of the series exhibits chain-like features that are indications for manipulation events. The manipulation paths extend over several tenth of nanometers and we note the preferential direction of manipulation in independently scanned panes. All manipulation paths are roughly parallel and deviations are caused by scanner piezo creep as the frames were taken consecutively at different positions without giving the piezo time to equilibrate after the previous scanning motion. Figure 10.3. is a study of contrast

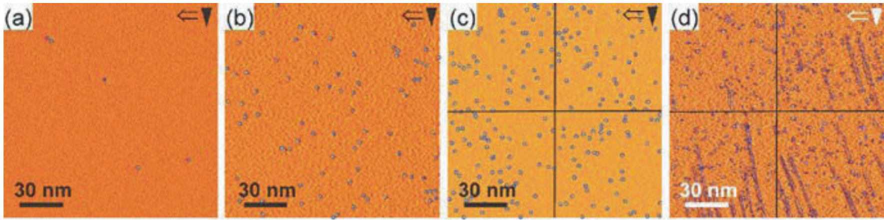

Fig. 10.2. Degradation of a $300 \times 300\,\text{nm}^2$ area on an atomically flat $CaF_2(111)$ surface observed in UHV as a function of time. Circles mark contaminants on the surface, a few resulting from the preparation but most of them developing under the influence of the residual gas. The black lines in frames (**c**) and (**d**) mark the boundaries of the four smaller images that were assembled to form the larger frame. Image (**a**) shows the surface directly after cleavage. Frame (**b**) shows an increased density of impurities after three days. In frame (**c**), the contamination level is further increased after the fifth day. Frame (**d**) shows a high density of impurities as observed on the ninth day after cleavage. The quasi-parallel lines indicate the manipulation of certain defects over distances of several ten nanometers (From [3])

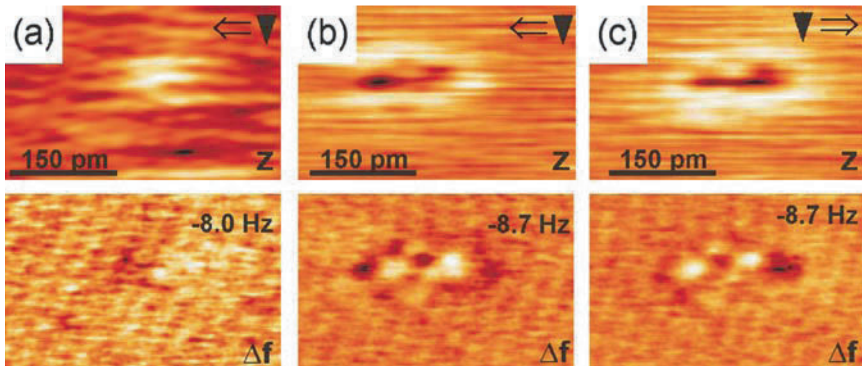

Fig. 10.3. Contrast formation studied on a stationary atomic size defect. Shown are simultaneously recorded topography and detuning images. Frames (**b**) and (**c**) have been recorded at an increased average detuning compared to frame (**a**). The increase of 0.7 Hz in detuning results not only in an increased contrast but also a contrast inversion. The apparent elongation of the defect and the characteristic pattern involving dark and bright contrast points to a repulsive interaction of the foremost tip ions with the defect (From [3])

formation for imaging a stationary defect at different tip–surface distance. When scanned with a relatively large tip–surface distance, defects appear as protrusions; however, they change their appearance to that of an indentation with a protruding rim when approaching the surface and scanning in a detuning range that resolves individual lattice sites. This predominant contrast is shown in frames (b) and (c) representing the same defect imaged in forward and backward scanning direction, respectively.

The apparent depth of defects ranges from 10 to 25 pm but as the topography feedback is quite slow, this number is not of great significance. We anticipate that contrast inversion is the result of a complex interaction of the negatively terminated tip with a hydroxyl group. At large tip–surface distance, the partially positive protruding hydrogen causes an enhanced attractive interaction with the tip and the defect appears as a protrusion. When decreasing the tip–surface distance, the interaction with the hydrogen may become repulsive and additionally there is a repulsive interaction with the oxygen that might be exposed as the hydrogen is pushed aside. This scenario is in line with a general model that has been developed for contrast inversion at protruding surface defects [23].

10.3.2 Manipulation of Mobile Defects

Defects found to be mobile on $CaF_2(111)$ can be moved by the interaction with the tip, in a fashion demonstrated in Fig. 10.4. Frames (a)–(g) are consecutively recorded images that have either been taken in the imaging mode at a detuning of -20 Hz or in the manipulation mode at a detuning of -35 Hz. In this experiment, apparently a group of defects is manipulated on the scale of several nanometers first upwards (frames (a)–(c)) and then downwards (frames (d) and (e)). To explore the dependence of the manipulation direction from

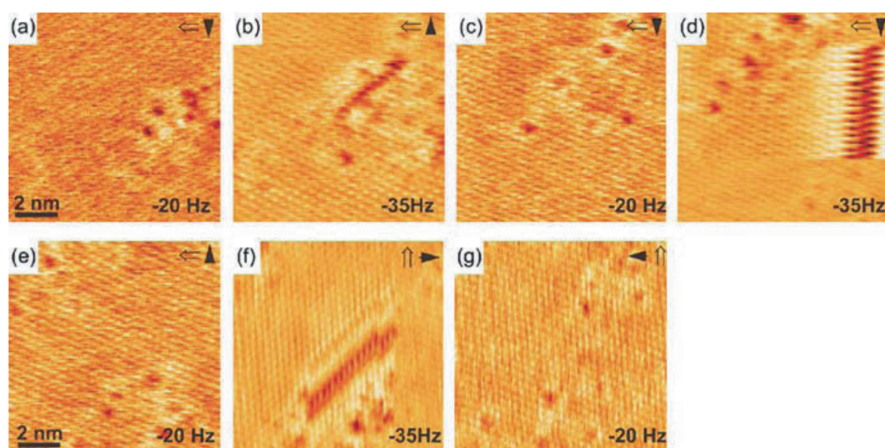

Fig. 10.4. Manipulation of a group of defects on the $CaF_2(111)$ surface. Frames (**a**), (**c**), (**e**), and (**g**) were taken in the imaging mode with an average detuning of -20 Hz. Frames (**b**), (**d**), and (**f**) show manipulation performed with an average detuning of -35 Hz. The chain structure is caused by the repeated imaging of the same defect in the course of manipulation. The direction of manipulation in frames (**b**) and (**f**) is identical despite the interchange of slow and fast scanning direction. The manipulation paths of images (**b**) and (**d**) recorded with opposite slow scanning direction enclose and angle of 120° (From [3])

the scanning direction, in a last manipulation step the fast and slow scanning directions are interchanged (frames (f) and (g)). As the group is initially close to one side of the imaging frame, defects are partially dispersed and the final pattern of the group of defects is different from the initial one. The strong interaction between tip and defect during scanning in the manipulation mode is apparent in the form of strong contrast features forming lines along the main manipulation direction. In none of the images, the direction of manipulation is related to the scanning direction in a trivial way. It is assumed that manipulation occurs via a hopping mechanism where consecutive positions are reached by the interaction of the defect with the tip and neighboring ions. By the action of the tip, defects are first weakly displaced in a potential trough associated with one ionic site. Hopping motion over trough wells results in an abrupt change of the contrast.

In this context it is interesting to investigate the manipulation pathways in frames (b), (d), and (f) of Fig. 10.4. These pathways appear as lines enclosing an angle of 120° with each other. This strongly indicates that defects move along specific crystallographic directions on the surface. Another interesting feature is the width of the manipulation paths. In frame (b), a chain of one minimum per position is observed while image (d) indicates at least two minima along the line, sometimes even three pronounced minima. Although the direction of manipulation in frames (b) and (f) is the same, the appearance of the pathway is different. The minimum along the line appears elongated, indicating a longer manipulation path along the fast scanning direction. We anticipate that this elongation is an effect of movement within the potential trough. Remarkably, mostly more than one defect is manipulated and we assume that this is due to the fact that manipulation is not only performed by the tip terminating cluster providing the atomically resolved image, but also by the force field of larger parts of the tip apex.

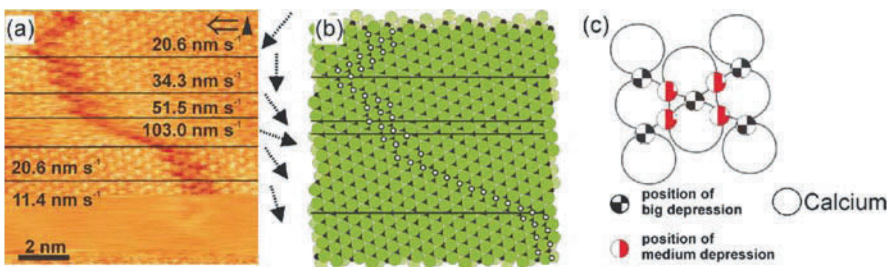

Fig. 10.5. Velocity dependence of the manipulation path. (**a**) A topography image recorded in the manipulation mode where the scanning speed is changed in a systematic manner. The image is taken at an average detuning of −35 Hz. The *dotted arrows* denote the preferential direction of movement as deduced from the resulting image. (**b**) The surface with indicators of preferential sites during manipulation. (**c**) Detailed schematic representation of bridging sites possibly attained during manipulation (From [3])

10.3.3 Velocity Dependence of Manipulation

The direction of manipulation can be influenced by a variation of the scanning speed as is illustrated in Fig. 10.5. The manipulation path is shown in pane (a), while in pane (b) a series of positions is marked that are presumably occupied during defect movement, and pane (c) describes two different bridging positions that apparently play a role for the manipulation process. At slow scanning speed, the path of the defects appears to be broader than that for fast scanning, and hopping occurs more often in the direction of the slow scanning direction for both, forward and backward scanning motion. With increased scanning speed, the visible manipulation path becomes more narrow but the manipulation is more directional. By a careful selection of scanning speed, virtually any manipulation direction is accessible as is indicated by the dotted arrows next to pane (a). Therefore, the method does not only allow the demonstration of simple manipulation events but could principally also be used to perform more sophisticated manoeuvres. The sketch shown in Fig. 10.5c demonstrates that the defect is confined in a rhomb defined by four calcium ions marked by segmented small circles. The quartered circles in image (c) mark positions that are deeper than those marked with half-filled circles. This indicates that the interaction with the tip at these positions is weaker or the defect is more mobile. Most probably, preferred hopping directions are along the threefold hollow sites between the calcium ions and the nearest bridging positions to a point of large depression.

With an orientation of the substrate as indicated in Fig. 10.5(c), the hopping to neighboring bridge sites is not equal for all directions. Because of the angle between a symmetry axis of the substrate and the fast scanning direction, it is likely that the potential energy path along those lines is not the same, effectively leading to different probabilities for a hopping event. When the scanning is very slow, the interaction time of tip and defect might be sufficient to trigger the jump to the left although that might not be the kinetically most favored route. Therefore, we expect that in more elaborate studies it will be possible to define the direction of manipulation by a proper choice of the scanning direction with respect to the crystallographic directions.

10.4 Conclusions

The experimental evidence presented here clearly demonstrates the possibility of force controlled manipulation of a water related defect on the $CaF_2(111)$ surface. While a detailed understanding of the manipulation mechanism requires many further efforts, here we outline a few important points providing a preliminary understanding of the process. The key assumption is that the main interaction resulting in the manipulation is repulsive and manipulation is facilitated by a series of hopping events during scanning in both directions. When the tip is relatively far away from the defect, repulsion causes a local relaxation in form of an evasion of the defect inside a potential trough associated with a neighboring lattice ion. Upon approach, the repulsive force

becomes increasingly stronger and when exceeding a certain limit, hopping motion occurs from one potential trough into another. However, the sequential formation of stationary and mobile defects strongly indicates that the manipulated defect is not simply a molecule but a complex formed by a molecule and a surface vacancy defect. Indeed, preliminary theoretical calculations indicate that water dissociates and forms hydroxide as a stationary defect when interacting with surface F^0 centers. On the other hand, a water molecule can bind to an F^- center and form a mobile defect. Mobility is created by lowering the diffusion barrier for the water/F^- complex in the force field of the scanning tip [22]. In the framework of this model, manipulation is a rather complex process involving surface relaxation and the motion of the adsorbed species together with a vacancy defect. Pinning the water molecule to the vacancy prevents diffusion at room temperature if the tip is absent, while manipulation is facilitated by thermal diffusion over a reduced barrier in the presence of the tip.

Acknowledgments

The authors are most grateful to A. Foster for many contributions to the interpretation of experimental results and sharing his simulation results with the authors and to R. Nishi, Y. Sugimoto, A. Shluger, and S. Gritschneder for stimulating discussions.

References

1. G. Meyer et al., Single Mol. **1**, 79 (2000)
2. N. Lorente, R. Rurali, H. Tang, J. Phys. Cond. Matter **17**, S1049 (2005)
3. S. Hirth, F. Ostendorf, M. Reichling, Nanotechnology **17**, S148 (2006)
4. R. Nishi et al., Nanotechnology **17**, S142 (2006)
5. T. Trevethan et al., Phys. Rev. Lett. **98**, 028101 (2007)
6. T. Trevethan et al., Phys. Rev. B **76**, 085414 (2007)
7. M. Reichling, C. Barth, Phys. Rev. Lett. **83**, 768 (1999)
8. C. Barth, M. Reichling, Surf. Sci. **470**, L99 (2000)
9. F.J. Giessibl, M. Reichling, Nanotechnology **16**, S118 (2005)
10. R. Hoffmann et al., J. Am. Chem. Soc. **127**, 17863 (2005)
11. A.S. Foster et al., Phys. Rev. Lett. **86**, 2373 (2001)
12. C. Barth et al., J. Phys. Condens. Matter **13**, 2061 (2001)
13. A.S. Foster et al., Phys. Rev. B **66**, 235417 (2002)
14. A.V. Puchina et al., Solid State Commun. **106**, 285 (1998)
15. V.E. Puchin et al., J. Phys. Condens. Matter **13**, 2081 (2001)
16. Y. Ma, M. Rohlfing, Phys. Rev. B **75**, 205114 (2007)
17. Y. Ma, M. Rohlfing, Phys. Rev. B **77**, 115118 (2008)
18. M. Nonnenmacher, M.P. O'Boyle, H.K. Wickramasinghe, Appl. Phys. Lett. **58**, 2921 (1991)
19. U. Zerweck et al., Phys. Rev. B **71**, 125424 (2005)
20. S. Gritschneder et al., Nanotechnology **16**, S41 (2005)
21. M. Reichling et al., Surf. Sci. **439**, 181 (1999)
22. A. Foster, private communication
23. P. Rahe et al., Phys. Rev. B **77**, 195410 (2008)

11

Basic Mechanisms for Single Atom Manipulation in Semiconductor Systems with the FM-AFM

Pablo Pou, Pavel Jelínek, and Rubén Pérez

Abstract. This chapter unveils the atomic-scale mechanisms that are responsible for the room temperature manipulations of strongly bound atoms on semiconductor surfaces. First-principles simulations, matching the experimental forces, identify the key steps in two paradigmatic examples: the lateral manipulation of single adatom vacancies on the Si(111)-7×7 reconstruction in the attractive regime and the vertical interchange of atoms between the tip and the Sn/Si(111)-($\sqrt{3} \times \sqrt{3}$)R30° surface by a gentle exploration of the repulsive force regime. Our calculations reveal that the outstanding experimental control of the manipulation under attractive forces comes from the localized reduction of the diffusion energy barriers induced by the tip for the different steps in the complex path followed by the Si adatom during the process. Using selective constraints, to face the difficulties posed by the complexity of a multi-atom contact and operation in the repulsive regime, our simulations illustrate how the vertical interchange can take place at the atomic scale, identify the crucial dimer structure formed by the closest tip and surface atoms, and discuss the role of temperature in the competition with other possible final outcomes (including atom removal or deposition by the tip).

11.1 Introduction

Scanning probe microscopes (SPM) have become the tool of choice for imaging and manipulation at the nanoscale. During SPM operation, the forces appearing due to accidental contact may lead to changes in the tip and surface structure. This experimental observation has triggered the efforts to convert the tip-induced removal, deposition, and lateral displacement of atoms into a controlled manipulation process, where the final outcome of the process can be determined at will with atomic-scale precision. Just a decade after the development of the scanning tunneling microscope (STM), Eigler and Schweizer started the era of man-made atomic patterns manipulating Xe atoms on an Ni(111) surface at cryogenic temperatures to form the IBM logo [1]. While

S. Morita et al. (eds.), *Noncontact Atomic Force Microscopy*,
NanoScience and Technology,
DOI: 10.1007/978-3-642-01495-6_11, © Springer-Verlag Berlin Heidelberg 2009

atomic-scale manipulations with the STM under low-temperature (LT) conditions have become routine in many laboratories, progress with the atomic force microscope (AFM) was hampered by the limitations in resolution.

The first atomically resolved images of the Si(111)-7×7 reconstruction taken with the AFM operated in the frequency modulation mode (FM-AFM, also known as noncontact AFM) [2] were published in 1995. After this breakthrough, it took only 7 years for the FM-AFM, operating at 78 K, to show its ability to remove single adatoms from this reconstruction and to fill these vacancies again with Si atoms coming from the tip [3] (see Fig. 11.7). At variance with similar experiments with the STM, no bias voltage or voltage pulse was involved in these atomic manipulations as both tip and sample were always electrically grounded. They are purely mechanical, and rely only on the exquisite control of the tip–sample interaction to extract from the surface a single adatom that is strongly connected by three covalent bonds to the underneath Si layer. These manipulations were followed by experiments at room temperature from two groups [4, 5] on the same surface. In 2005, lateral atomic manipulations at both LT and room temperature (RT) were reported on Ge(111) surfaces [6]. These experiments proved that adsorbates, as well as intrinsic adatoms of semiconductor surfaces, could be individually manipulated laterally using the tip–sample short-range interaction force. The interchange lateral manipulation of substitutional Sn adatoms – that are not mobile on the Ge surface at RT – allowed the formation of artificial nanostructures that are stable at RT [7]. Basic atomic manipulations at RT have also been achieved on insulating surfaces [8, 9].

The very precise control of the position of the tip-apex even at RT [10–12] as well as the ability to measure the tip–sample interaction in force spectroscopy experiments with outstanding accuracy (see [13,14] and Chap. 3) are behind the recent breakthroughs in FM-AFM manipulation: (1) The atomistic mechanism involved in the lateral manipulations at RT – the local tuning of energy barriers for tightly-bound atoms to allow thermally induced displacements – has been identified and put on a firm, quantitative basis by a combined theoretical and experimental study on the Si(111)-7×7 surface [15]; (2) The force required to move an atomic adsorbate on a metallic surface at LT has been determined [14]; and (3) an atomic dip-pen lithography technique based on the vertical interchange of single atoms between the tip-apex and the topmost layer of a semiconductor surface at RT has been developed [16].

All of the atomic manipulations mentioned so far can be grouped in terms of the character of the tip–sample interaction: lateral manipulations are performed in the attractive regime, while the deposition or removal of surface atoms and the vertical interchange correspond to the repulsive regime of the short-range interaction. The goal of this chapter is to unveil the atomic-scale mechanisms that are responsible for the RT manipulations of strongly bound atoms on semiconductor surfaces and to characterize the basic properties of the two interaction regimes. Our approach is based on a set of carefully designed, large-scale first-principle simulations. At variance with STM,

FM-AFM provides direct access to the forces during the manipulation process. This information can be exploited to reproduce the experimental conditions in our simulations, matching quantitatively the theoretical forces and those measured in force spectroscopy experiments.

The rest of the chapter is organized as follows: In Sect. 11.2, we summarize our theoretical approach for the calculation of the optimal atomic pathway in different manipulation processes. A detailed analysis of the interaction between a semiconductor surface and a silicon tip is provided in Sect. 11.3. Section 11.4 describes the study of the lateral manipulation of single adatom vacancies on the Si(111)-(7×7) surface at room temperature performed in the attractive interaction regime. In Sect. 11.5, we report theoretical simulations of the vertical atomic exchange taking place between the tip and sample in the strong-repulsive interaction regime.

11.2 Theoretical Approach: First-Principles Simulations

Atomic manipulations are directly accompanied by the breaking and formation of chemical bonds between the different atoms involved in the process. The inherent quantum character of the chemical bonding requires the use of first-principles methods based on density functional theory (DFT). Furthermore, atomic manipulations, mainly those performed in the repulsive regime, involve many atoms of both the surface and the probe. This multi-atom contact significantly increases the number of possible trajectories and their complexity in the configuration space. The efficient characterization of the potential energy surface (PES) and the search for optimal trajectories are challenging tasks that have attracted a lot of attention during the last few years [17,18].

Although several theoretical studies on atomic manipulation with FM-AFM [19, 20] have been carried out with a fully converged first-principles description using plane-wave (PW) DFT methods, an extensive search of the PES using PW methods is still precluded by their large computational demand. An interesting alternative is to resort to DFT methods based on a local orbital basis, specially those developed with the aim of computational efficiency, that allow first-principles studies of much more complex systems and trajectories. In the simulations presented in this chapter, we have used a fast local-orbital DFT-LDA technique (Fireball) [21,22]). This approach offers a very favorable accuracy/efficiency balance once the atomic-like basis set is carefully chosen [23].

We model the real tip–surface system using a supercell approach. In the simulations described later, the Si(111)-(7×7) and the Sn/Si(111)-($\sqrt{3} \times \sqrt{3}$) reconstructions were represented by a (7×7) and a (6×6) periodic slab that includes 7 Si layers and a total of 347 and 264 atoms, respectively. Due to the

large size of these surface unit cells, only the Γ point was used to sample the Brillouin zone.

The modeling of the tip is one of the key issues in AFM. This is a complex problem, where the lack of direct experimental information on the structure after tip preparation combines with the possibility of surface contamination during the AFM operation. Our long experience with semiconductor surfaces shows that, to simulate processes where the tip-apex does not interact strongly with the surface, i.e., in the attractive regime, a tip model that fairly reproduces the chemical reactivity of the few outermost atoms of the apex is appropriate. In particular, we have shown [13, 15, 24, 25] that it is possible to characterize the most probable structure and composition of the apex by a detailed comparison between the attractive short-range (SR) forces obtained in first-principles simulations with the experimental ones. However, in the strong-interaction regime, the role of the mechanical response of the tip becomes more important, and larger models would be required for a complete, quantitative study. This problem is further discussed in the context of the vertical manipulations presented in Sect. 11.5.

The vertical scanning operation in AFM was simulated in a stepwise, quasi-static manner by making small movements of the tip perpendicularly to the surface. The atoms of both tip and surface were allowed to relax to their ground state configuration – with convergence criteria for the total energy and forces of 10^{-6} eV and 0.05 eVÅ^{-1}, respectively – at each of these steps. Only the slab last layer with H atoms saturating it and the topmost part of the tip model were kept fixed. The quasi-static approximation provides a very good description of the imaging process due to the fact that the motion of AFM tip is much slower than the ongoing atomic processes in the system.

11.3 The Short Range Chemical Interaction Between Tip and Sample

Imaging [13,26] and manipulation [5,14,15,19] mechanisms on semiconductor and metal surfaces are mostly determined by the short-range chemical interaction between a surface atom and the outermost atoms of the probe. Therefore, a detailed knowledge of the character of the chemical forces acting between the tip and the sample, and its dependence on the tip–sample distance and their atomic and electronic structure, is a key ingredient to understand and control these processes.

Semiconductor surfaces often undergo a strong structural rearrangement of the upper surface atomic layers, with respect to an ideal surface, to minimize the number of unsaturated bonds – the so-called *dangling bonds* – and lower the total energy. Taking the Si(111)-7 × 7 case as an example, the reconstruction leaves only 12 adatoms in the upper layer, reducing the original 49 dangling bonds to only 19 (located on the 12 adatoms, the six rest atoms

in the second layer and the corner hole). These *dangling bond* states determine the strong chemical activity of most semiconductor surfaces. The atomic resolution obtained on semiconductors with the FM-AFM [26] was precisely attributed to the presence of a *dangling bond* state on the outermost atom of the silicon tip that interacts with the dangling bonds on the surface.

The strong covalent bonding of surface atoms in semiconductors significantly reduces their mobility and, therefore, to manipulate them, larger mechanical forces, used for weakly bound adsorbates on metal surfaces, are required. However, this problem in the manipulation process turns into an asset when considering stability issues: the strong interaction significantly extends the lifetime of the formed atomic patterns, and allows the existence of these assemblies at RT, which makes them much more relevant for technological applications. To illustrate the strength of the chemical interaction between the *dangling bonds* of a prototypical semiconductor tip and a surface adatom, we present results of a DFT simulation for the system considered in our study of the lateral manipulation (see Sect. 11.4): a corner Si adatom on the Si(111)-(7×7) reconstruction with a vacancy in the adjacent central adatom position in the half-unit cell. Due to the localized character of the interaction, these results can be generalized to an arbitrary semiconductor surface with strongly localized *dangling bonds*.

Figure 11.1 shows the evolution with the tip–sample distance of the atomic and electronic structure. At large tip–sample distances, there is a negligible vertical displacement of the adatom (see the left top plot in Fig. 11.1). A sudden upward movement of the adatom of $\sim$0.4 Å is observed for a tip–sample distances of $\sim$4.5 Å. A strong correlation between the onset of the short-range chemical force between tip and sample and the vertical displacement of the adatom can be clearly identified in the middle graphs in Fig. 11.1. Next, the vertical adatom displacement decreases until it reaches its initial value at a tip–sample distance near to 2.5 Å while, at the same time, the SR force increases linearly. A further decrease of the tip–sample distance, below 2 Å, induces substantial atomic rearrangements as too much elastic energy has been already stored in few bonds (for details see Fig. 11.6 and the discussion in Sect. 11.5).

These changes in the structure are coupled with significant changes in the electronic properties. A detailed analysis of the density of states projected on the adatom along the tip–sample distance (see Fig. 11.1) points out a strong modification of the *dangling bond* state [27]. In the far-distance regime, the dangling bond state remains in a similar energy as on the unperturbed surface. Reaching tip–sample distances of $\sim$4.5 Å, where the onset of the chemical bond between tip and sample takes place, we observe a strong modification of the local electronic state of the inspected surface adatom. At closer tip–sample distances, below 4.5 Å, the dangling bond state is completely wiped off from the Fermi level, as it can be seen in Fig. 11.1. These electronic modifications have significant implications for the transport properties as discussed in [27].

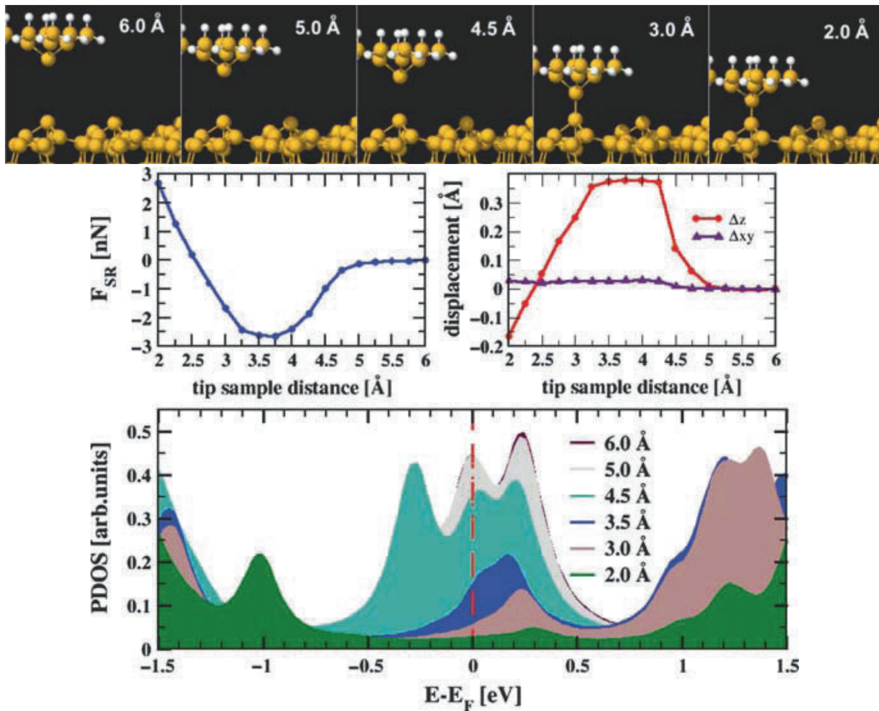

Fig. 11.1. (*Top*) Relaxed atomic structures at different tip–sample distances during the approach of a silicon tip toward a corner adatom on the Si(111)-(7 × 7) surface. (*middle*) Short-range force (*left*) and vertical and lateral displacement of the adatom (*right*) as a function of the tip–sample distance. (*bottom*) Projected density of states (PDOS) on the Si adatom below the tip apex at different tip–sample distances

To summarize, we have seen how the proximity of the tip and the consequent formation of the chemical bond between the outermost apex atom and the surface adatom, induces a strong modification of the atomic and electronic structure of the intrinsic adatom states on semiconductor surfaces. This effect leads to a weakening of the adatom surface bonds and, therefore, it facilitates its eventual transfer on the surface, as in further sections.

11.4 Manipulation in the Attractive Regime: Vacancies in the Si(111)-(7 × 7) Reconstruction

The vacancy-mediated lateral manipulation of intrinsic Si adatoms on the Si(111)-(7 × 7) surface at room temperature [15], represents a paradigmatic example of atomic manipulation performed in the attractive tip–sample interaction regime. A precise command of both the vertical and lateral position of the probe allows the controlled movement of individual Si adatoms on

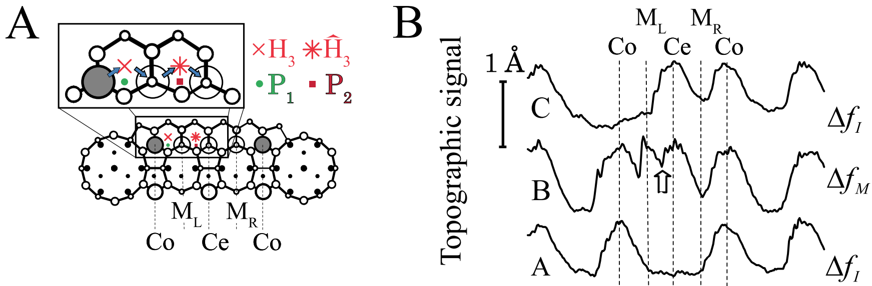

Fig. 11.2. (**a**) The optimal atomic pathway during the Co→Ce manipulation. (**b**) Topographic signals taken at different stages of the manipulation process obtained in two different, low (Δf_I) and high interaction (Δf_M), set points

semiconductor surfaces (see Fig. 11.2). The manipulation was performed using an experimental protocol similar to the one reported in [7] and described in Chap. 8: the process of imaging and manipulation itself was controlled by switching between a weaker (Δf_{I}) and a stronger interaction (Δf_{M}) set point while scanning along the direction of the desired movement (see Fig. 11.2b). Constant-frequency shift profiles A–C in Fig. 11.2b correspond to consecutive scans moving the tip from left to right over the same line of the surface. Profile A has been obtained before the manipulation at the low-interacting set point, Δf_{I}. The vacancy placed in the central (Ce) adatom position can be clearly identified. Profile C shows the position of the atoms after the manipulation: the corner (Co) adatom has been displaced to the center adatom position. Profile B, acquired at the stronger tip–sample interaction regime (Δf_{M}), corresponds to the manipulation process. This profile clearly illustrates that the single-atom manipulation process involves, at least, two consecutive jumps between adjacent sites: CoA → M and M → CeA (see Fig. 11.2a). The maximal attractive short-range force needed to move the silicon adatom, experimentally determined for the Δf_{M} operating conditions, was ∼0.5 nN. Notice that, in principle, a larger value – closer to the maximum strength of the covalent bonds between the adatom and the surface – could be expected.

To obtain a detailed picture of the atomic-scale processes involved in the lateral manipulation, we have carried out an analysis of the optimal atomic pathways using first principles DFT methods. We have considered the case illustrated in Fig. 11.2: an Si(111)-7 × 7 reconstruction, where an adatom initially located on the Co site is transferred to the Ce empty site. The PES for the vacancy pathway was characterized through an extensive set of DFT simulations, including the determination of the energetics for the vacancy on different adatom sites and the activation energy barriers for the adatom hopping toward available empty sites. To estimate the magnitude of the activation energy barriers on the surface, we have used a quasi-static approach where the adatom is moved in discrete steps along the most energetically favorable trajectory between two adjacent local minima, letting the system to relax to its

ground state keeping the adatom lateral (x, y) coordinates fixed. These calculations reveal that the apparent two-step manipulation is actually a much more complex process. We have identified the path $Co \rightarrow H_3 \rightarrow M_L \rightarrow \hat{H}_3 \rightarrow Ce$ (see Fig. 11.2a) as the optimal pathway to move the adatom from the Co site to the empty Ce site. The magnitude of the activation energy barriers of the individual jumps along the optimal trajectory, estimated from our constrained minimization calculations, are summarized in Fig. 11.3a. The large energy barriers for some of the steps (e.g., > 1.5 eV for the $Co \rightarrow H_3$ step) practically forbid the thermally activated diffusion of adatoms at RT, in agreement with the experimental observations under the normal imaging conditions (using the Δf_I set point).

In Sect. 11.3 we have shown how the proximity of a silicon tip weakens the adatom bonds with its neighboring surface atoms. It is evident that this effect must play a crucial role in the lateral manipulation processes discussed here. Therefore, we have analyzed in detail the influence of the tip–sample interaction (as determined by the relative position of the tip and the adatom) on the barriers associated with the different jumps in the adatom pathway from the Co to the Ce site. For these simulations, a well-tested Si(111) nanoasperity [26] was used as tip model. This tip, although small and consequently fairly rigid, correctly reproduces the *dangling bond* termination of the Si tips used in the experiments. In particular, this tip matches quantitatively the measured forces and provides a fairly symmetric interaction, in agreement with the experimental observation that identical Δf_{M} operating conditions are needed for manipulating the adatom in different directions. As shown later, these are the key ingredients to reproduce the role played by the tip in the atomic manipulations performed in the attractive regime. Nevertheless, other tip-apex structures (as the tip model showed in Fig. 11.9) were also tested. No significant differences with the results for the tip considered here were found.

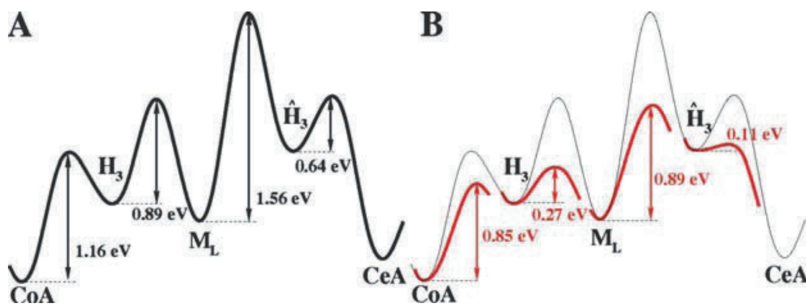

Fig. 11.3. (**a**) Energy barriers along the optimal atomic pathway for the diffusion of a silicon atom from the Co to the Ce site on the Si(111)-(7 × 7) without the presence of a tip. (**b**) Change of the energy barriers along the optimal atomic pathway induced by the proximity of a silicon tip at the tip–sample distance of 4.0 Å.

To estimate the influence of the tip on the energy barriers, we have performed a large set of constrained minimizations for several tip–sample distances and different tip lateral positions. Notice that during the energy minimization procedure all the atoms in the tip, apart from the last Si layer and the saturating H-layer, are allowed to relax. Figure 11.4 illustrates the reduction of the activation energy barriers with the increasing tip–sample interaction in the case of the two most difficult steps, the $Co \rightarrow H_3$ and the $M_L \rightarrow \hat{H}_3$, with the tip placed in the P_1 and P_2 horizontal positions respectively (see Fig. 11.2a). These points are located on the scan line followed during the manipulation experiments. Similar tendencies can be found in both cases: the reduction of the tip–sample distance below 4.5 Å is accompanied by a substantial reduction of the activation energy barriers. A total energy lowering of the final metastable positions, H_3 and $\hat{H}_3$ respectively, is also observed.

We have quantified the role of the horizontal position of the tip in the mechanism of the lateral adatom manipulation. We have calculated the activation energy barriers of the $Co \rightarrow H_3$ step varying the lateral position of the tip, see Fig. 11.5, while the tip height was kept constant at $z = 4.0$ Å. Figure 11.5a displays the change of the barrier according to the variation of the tip position in the direction perpendicular to the scan movement. Along this direction, only minor variations of the activation barrier are observed. However, the variation of the horizontal tip position in the direction from the Co to the H_3 site (see Fig. 11.5b), shows more dramatic changes in both the magnitude of the barrier and the total energy of the final state.

The results presented earlier provide a clear indication of the basic mechanism operating during atomic manipulations in the attractive regime. As Figs. 11.4 and 11.5 show, for tip–surface distances corresponding to calculated SR forces around the experimental values used during the manipulations, the barriers are reduced close to the value (∼0.8 eV) that enables spontaneous

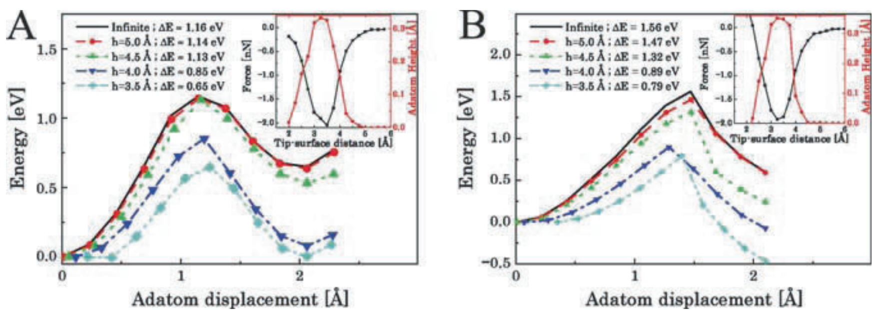

Fig. 11.4. Calculated diffusion barriers for the (**a**) $CoA \Rightarrow H_3$ and (**b**) $M \Rightarrow \hat{H}_3$ steps, when the tip is located at the P_1 and P_2 positions (see Fig. 11.2) at different tip–sample distances. The insets show the short-range force and the vertical displacement of the silicon surface adatom as a function of the tip–sample distance

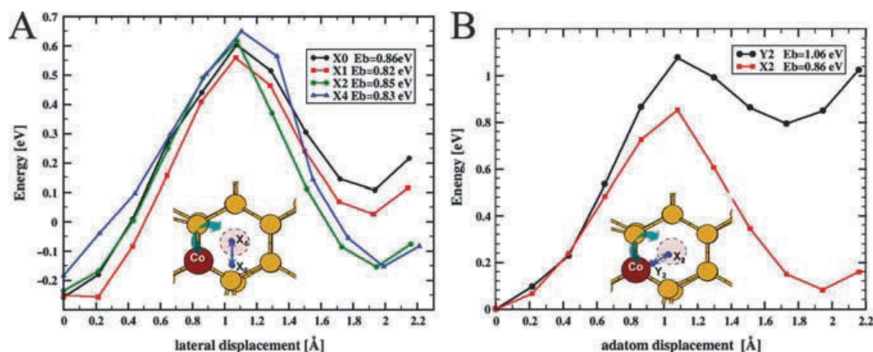

Fig. 11.5. Calculated diffusion barriers for the $CoA \Rightarrow H_3$ step for different horizontal tip positions (shown in the inset). The tip height was fixed, in all cases, at 4.0 Åwith respect to the corner Si adatom of the Si(111)-(7 × 7) faulted unit cell

thermally activated jumps between the two sites at RT during the long time (for typical oscillation frequencies around 100 kHz) that the tip spends close to the sample. Similar significant reductions on the calculated energy barriers (see Fig. 11.3) are also found for the rest of the transitions between adjacent adsorption sites when the tip is located close to the relevant lateral position along the manipulation path where the adatom jumps are observed.

This mechanism based on thermally activated hopping, already proposed for previous STM manipulation experiments, is now put on a firm quantitative basis. Surprisingly, our simulations confirm the experimental observation that atomic manipulations are possible at tip–samples forces that are quite small compared to the strength of the semiconductor covalent bonds. The explanation lies on the thermal energy available at RT and the long tip residence times. This combination allows a precise control of the atomic jumps by means of tip assisted diffusion, fine tuning the interaction strength through the tip–sample distance for a range of operating temperatures. Notice that this precise command on the atomic jumps would not be possible without the strong localization of the energy barrier reduction induced by the "sharp" *dangling bond* of the outermost atom of the tip, as illustrated by the results showed in Fig. 11.5. Blunter tips would reduce several barriers at the same time, making the controlled manipulations much more difficult. The unique combination of sharp tips and precise experimental control of the tip position found in FM-AFM, where the apex can be placed in a specific point to induce an atomic jump over a particular energy barrier, provides access to the atomic-scale manipulation at RT.

In summary, our DFT simulations have revealed the key for controlled lateral manipulation: the substantial local reduction of the diffusion energy barriers. The onset of significant attractive forces below 5 Å, directly associated with the covalent interaction between the tip and surface dangling bonds, induces pronounced vertical relaxations on the adatom (see the insets

of Fig. 11.4), the surrounding surface atoms and the outermost tip atoms. By gently tuning this interaction, it is relatively easily to reduce these barriers below the limit that enables instantaneous thermally activated diffusion at RT. The control of the net adatom displacement is then possible using the directionality imposed by the tip global movement.

11.5 Manipulation in the Repulsive Tip–Surface Interaction Regime

11.5.1 A Complex Phase Space Under Strong Tip–Surface Interactions

The theoretical simulation of the vertical manipulation processes described in Sect. 11.1 – and, in particular, the vertical atom interchange discussed later in Sect. 11.5.2 – represents a formidable challenge. These manipulations are produced by the gentle exploration of the repulsive part of the short-range chemical interaction between the closest tip–surface atoms. At variance with the simulations for lateral manipulation described so far, it is necessary to face the problems associated with working in the repulsive regime of the tip–surface short-range interaction and the intrinsic complexity of the phase space associated with a multi-atom contact. We understand, from our previous work on force spectroscopy [13], that the slope of the repulsive part of the interaction, that is controlled by the effective combined stiffness of the tip and surface, varies significantly for different tips on different experimental sessions. Our first-principles calculations for tips with quite different apex structure and chemical composition (even for large tips including 48 Si atoms) show a much smaller variability, with effective stiffnesses consistently larger than the experimental results. This systematic behavior is due to the constraint of fixed atomic positions for the last atomic layer of the tip imposed in first-principles calculations: we are losing the long-range elastic response of the tip, that is not dominated by the apex. One could argue that with an atomistic approach with classical potentials, we can consider much larger tips models and fix this problem with the elastic response. Unfortunately, these potentials performed very poorly in the description of the breaking and remaking of bonds that necessarily lies behind the vertical manipulation. This is the reason why we choose to stick to first-principles calculations, sacrifice the precise, quantitative description of the tip–elastic response, and focus on providing some clues about the feasibility of these processes and the atomic mechanisms involved.

To start the study of the relevant configurations that the closest tip and surface atoms can explore in this strong interaction regime, we first analyze the atom removal or deposition by the tip on the Si(111)-(7×7) achieved in the first FM-AFM manipulation experiments (see Fig. 11.7e, f). To this end, we have considered the same Si tip used in our simulations of the lateral manipulation in the attractive regime. We have performed DFT simulations

approaching the tip towards the Si(111)-(7 × 7) surface and then retracting the tip back to the starting position. These simulations illustrate how the removal of the adatom from the surface takes place at the atomic scale.

Our results for the case, where the tip-apex atom is positioned right on top of one of the corner adatoms are shown in Fig. 11.6. In the first steps of the tip excursion toward the surface, the system explores the attractive interaction regime discussed in detail in Sect. 11.3. Reducing the tip–sample distance further, below 2 Å, the apex atom is pushed into the tip (see Fig. 11.6b), increasing the mechanical strain of the system. At even closer tip–sample distance, ∼0.5 Å, the system is no longer able to sustain the applied mechanical load: it undergoes a substantial rearrangement of atoms in the contact area between tip and sample to minimize its total energy and to release the mechanical stress. The irreversible atomic deformation manifests in the characteristic jump in the total energy vs. distance. We should emphasize that, until reaching point B, the response of the system to the mechanical load is purely elastic and during tip retraction, the system returns to the original configuration with no significant energy dissipation [24,28]. However, crossing point B, a plastic deformation – associated with the breaking of few bonds where the stress was accumulated during the loading – takes place. The system no longer matches the original pathway on retraction and it undergoes different atomic rearrangements. On further retraction, a characteristic *dimer-like* structure with the apex atom and the surface adatom (see Fig. 11.6e) is formed. Finally, the adatom is picked up by tip (Fig. 11.6f) and removed from the surface.

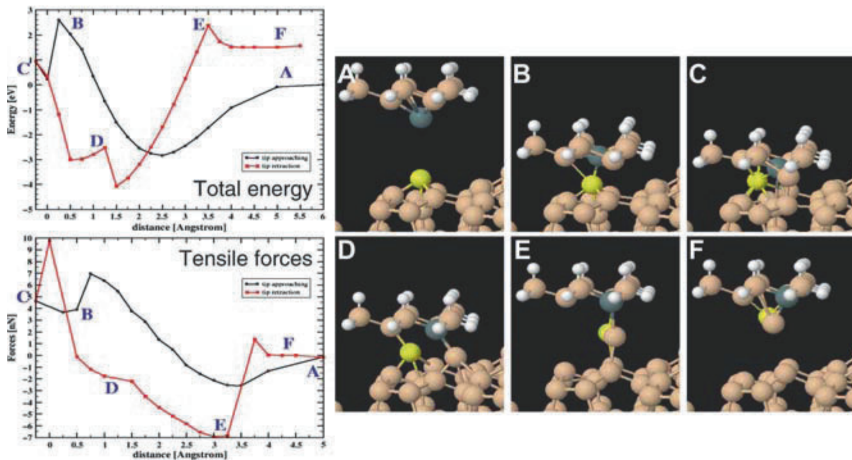

Fig. 11.6. Atomic pathway for the adatom extraction process: (*left*) Total energy and short-range force along the approach/retraction cycle of a Si tip over a corner silicon adatom on the faulted unit cell in the Si(111)-(7 × 7) surface. (*right*) Snapshots (**a**–**f**) show the evolution of the atomic structure during the approach (A–C) and the retraction (C–F)

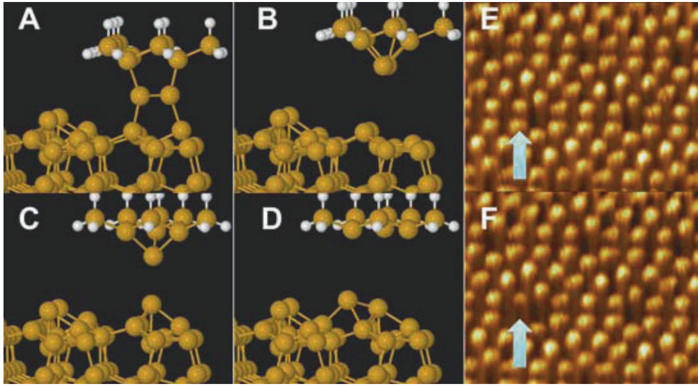

Fig. 11.7. Complexity of the phase space in the strong interaction regime. (**a**) Characteristic *dimer-like* structure that minimizes the energy of a tip–surface system at close tip–sample distances. (**b**)–(**d**) Possible final atomic structures after the tip approach/retraction cycle: (**b**) the tip extracts the surface adatom, (**c**) the tip and the surface keep their original structure, and (**d**) a tip atom is deposited on the surface. (**e**) and (**f**) the experimental formation of an atomic vacancy on the Si(111)-(7×7) surface using FM-AFM (for details, see [3]). The *arrows* mark the place where the manipulation process took place

The *dimer-like* configuration found in the process (Fig. 11.6e, and clearly illustrated in Fig. 11.7a), is very interesting, because it represents a bifurcation point in the phase space. This basic motif appears in all of the simulations that we have performed, starting from different initial conditions. However, from this atomic configuration, the system can branch out into quite distinct areas of the configuration space corresponding to different local energy minima and atomic structures. Our simulations show that, depending on several factors such as the initial tip position and the indentation depth, the system can reach, without crossing significant energy barriers, different final configurations on retraction. These possible scenarios include (1) the extraction of a surface adatom (Fig. 11.7b), (2) the return to the initial configuration (Fig. 11.7c), and (3) the deposition of a tip atom on the surface (Fig. 11.7d). These results illustrate, even with this relatively simple tip, the complexity of the phase space when exploring the repulsive regime, where subtle differences in the bonding configuration of the basic dimer structure lead to markedly different outcomes of the approach/retraction process. The presence of several atomic species further enlarges the phase space. As discussed in Sect. 11.5.2, the dimer motif plays also a central role in the microscopic understanding of the vertical atom interchange experiments performed at room temperature (Fig. 11.8), where a surface atom is replaced by a tip atom of a different chemical species after an approach/retraction cycle. This analysis will require the inclusion of temperature effects in the competition among different final states.

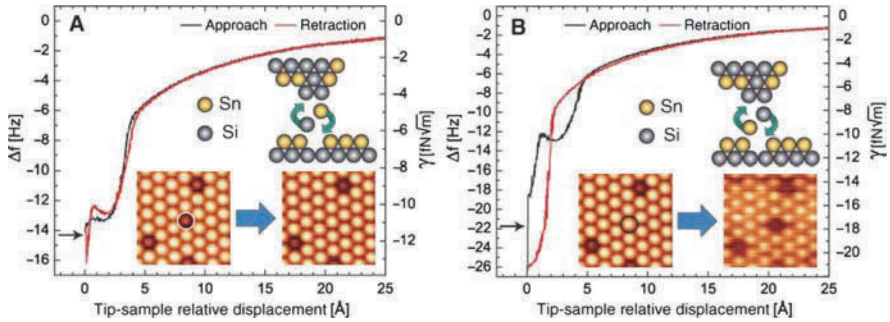

Fig. 11.8. (**a**) Characteristic frequency shift (Δf) signal on approach (*black*) and retraction (*red*) of the tip over an Si substitutional atom in an Sn/Si(111)-($\sqrt{3}\times\sqrt{3}$) surface during a vertical exchange manipulation. The *insets* display two consecutive topography images taken before and after the vertical manipulation, where the Si atom, marked with a *white circle*, was replaced by an Sn atom. (**b**) Characteristic frequency shift signal on approach (*black*) and retraction (*red*) of the tip above the Sn atom deposited in (**a**), pointed out by a *black circle*. In this case the Sn atom has been replaced by an Si atom coming from the tip

11.5.2 Dip-Pen Atomic Lithography: Vertical Atom Interchange Between the Tip and the Surface in the α-Sn/Si(111)-($\sqrt{3}\times\sqrt{3}$) Surface

The ability to incorporate individual atoms in a surface following predetermined arrangements might bring closer future atom-based technological enterprises. In this section, we discuss the basic atomistic mechanisms behind the recent experimental assembling of complex atomic patterns at RT by the vertical interchange of atoms between the tip-apex of an atomic force microscope and a semiconductor surface [16] (see Fig. 11.8). Our analysis will focus on the Sn/Si(111)-($\sqrt{3}\times\sqrt{3}$)R30° reconstruction, but these vertical interchange manipulations have also been reproduced in the Pb/Si(111)-($\sqrt{3}\times\sqrt{3}$)R30° and the In/Si(111)-($\sqrt{3}\times\sqrt{3}$)R30° reconstructions, where we expect the same mechanisms to be operative.

Although these experiments are discussed in detail in Chap. 8 of this volume, we provide here the basic experimental facts that are particularly relevant for the theoretical analysis. The inset of Fig. 11.8a shows topographic atomic resolution AFM images of a single atomic layer of tin atoms (bright protrusions) grown over a silicon (111) single crystal substrate. The dark spots correspond to substitutional silicon defects at the perfect tin surface layer. These Si defects can be vertically manipulated during force spectroscopy [13, 29] experiments. After imaging the surface and positioning the AFM tip with a lateral precision better than ±0.1 Å [10] on top of the marked Si atom, the sample was progressively approached toward the oscillating AFM tip. At a given tip–surface distance, an instability in the frequency shift occurs as highlighted by the arrow in the graph. In the image taken immediately after

the sample retraction, the targeted Si atom has disappeared, and an Sn atom occupies the corresponding lattice position instead (right image in Fig. 11.8a). The only reasonable hypothesis to explain this event is that the Si atom at the surface has been replaced by an Sn atom originally located at the tip-apex, as sketched out by the cartoon in Fig. 11.8a. The same procedure can be consecutively applied to the freshly deposited Sn atom (marked with a circle in the left image of Fig. 11.8b), resulting in the replacement of this surface atom by an Si atom coming from the tip, and in a partial loss of atomic contrast (right image in Fig. 11.8b). The resemblance of the characteristic frequency shift curves (see Fig. 11.8) recorded on vertical atomic interchange manipulations performed on different experimental sessions with different tips is truly remarkable [16]. In spite of the apparent complexity of the process, this extremely good reproducibility strongly indicates the presence of a common basic microscopic mechanism.

The extensive force spectroscopy experiments on this surface show that 29% of the tips produced vertical interchange atom manipulation, being almost equally probable to find tips producing either Si deposition or alternate deposition of Sn and Si atoms (this is the case illustrated in Fig. 11.8), and less probable to have a tip depositing only Sn atoms. The preparation of these tips relies on making a number of gentle tip–surface contacts using the same cantilever over different measurement sessions, but there is no systematic way of producing a priori a particular kind of tip. Once an atom exchanging tip is found, it is possible to perform the manipulations in a reproducible way. Therefore, these vertical interchange atomic manipulations require a tip-apex rigid enough to endure the high loads over the repulsive part of the short-range chemical interaction without undergoing major structural modifications.

The creation of these atomic patterns must involve not only the repeated interchange of atoms between tip and surface but also diffusion and segregation processes at the tip-apex to guarantee the presence of the required chemical species in the appropriate atomic arrangement. The simulation of the whole process is far beyond the capabilities of current first-principles methods. Thus, we focus our analysis on the feasibility of the vertical atom interchange and the identification of the common atomistic mechanisms involved.

At this point, we still have to face the complexity of the phase-space that the closest tip and surface atoms can explore, with different possible outcomes including atom removal or deposition by the tip, apart from the vertical interchange. We have used the possibility to impose constraints on the tip model to further simplify the complex scenario associated with the tip mechanical response and separate the discussion in two different steps. First, we model the experimental apex with a rigid tip where only the two atoms defining the apex are allowed to relax on interaction with the surface (see Fig. 11.9). These simulations illustrate how the vertical interchange can take place at the atomic scale, and identify the crucial dimer structure formed by the closest tip and surface atoms. In a second step, we relax some of these constraints to show the interplay with the other possible final outcomes and processes and the role

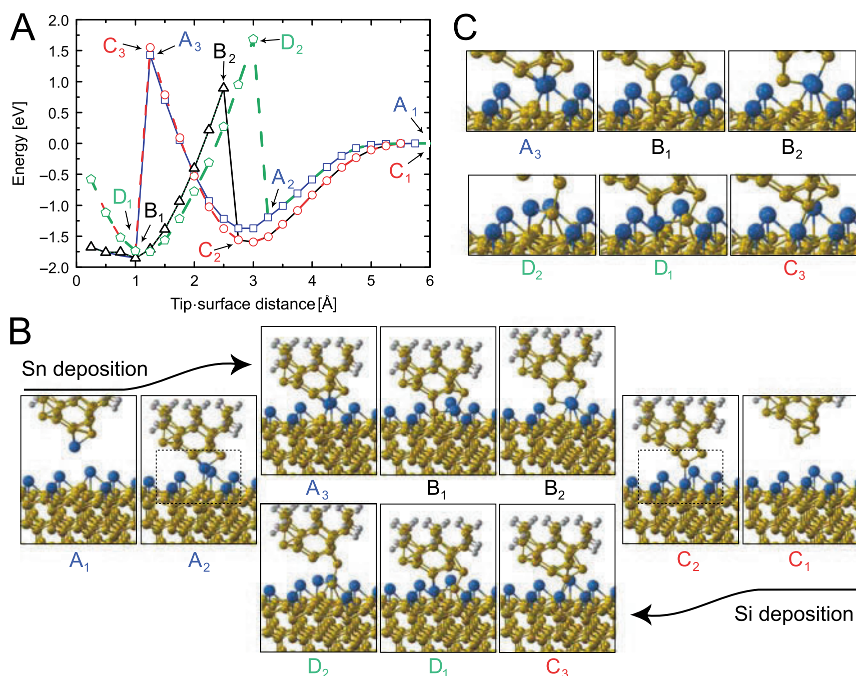

Fig. 11.9. First-principles simulations of the vertical interchange manipulation. (**a**) Evolution of the total energy on two consecutive tip approach and retraction cycles with a model rigid tip – only the two atoms in the dimer defining the apex are allowed to relax – over the same location of an Sn/Si(111)-($\sqrt{3} \times \sqrt{3}$)R30° surface resulting in the alternate deposition of an Sn atom (first cycle, *continuous lines*) and a Si atom (second cycle, *dashed lines*), respectively. (**b**) Atomic configurations associated with the transitions between energy branches labelled in (**a**) showing the relevant atomistic processes involved in the vertical interchange of atoms between tip and surface. (**c**) shows a zoom of the same selected configurations

of the temperature. In spite of its obvious limitations, our tip model captures an important property of the real tips, as a very robust apex is required to stand the high loads associated with the exploration of the repulsive part of the tip–surface short-range chemical interaction. This is the aspect that we have emphasized, sacrificing the quantitative description of the softer elastic response found in the experiments.

Figure 11.9 illustrates, using the total energy, the evolution of the system during an alternate deposition of an Sn (continuous lines) and an Si atom (dashed lines) using the rigid tip model. The most relevant atomic configurations during both processes are depicted in Fig. 11.9b. In the case of the Sn deposition, the system follows the branch A (squares), starting at A_1, where there is no significant interaction. At A_2, we are near the total energy minima and hence the zero of the short-range attractive force. Further tip–surface

approach leads to a repulsive force that increases up to structure A_3, where the atoms are significantly compressed but still keeping their original bonding topology. On retraction from any tip–surface distance larger than the one corresponding to A_3, the system follows the same energy curve back to the original structure A_1. On the contrary, approaching the tip beyond A_3, the system undergoes a discontinuous jump to a new energy branch B (triangles) with a significantly different bonding topology (panel B_1 in Fig. 11.9b). During further approach and consecutive retraction the system follows this energy branch up to B_2, where a new jump takes it to another energy solution (branch C, circles), leading to the final bonding topology (structure C_2) and the atomic interchange. The Si deposition case presents the same basic features. During approach, the system follows the C branch until reaching C_3, where it jumps to branch D (pentagons). Retraction from any distance along the D branch after this jump leads to a new jump from D_2 to A_2 and to the atom interchange. Comparing the two deposition cases, although the atomistic details are slightly different, overall, the atom interchange mechanism seems to be the same. The key step in these processes is to reach the earlier discussed *dimer-like* structure shown in panels B_1 and D_1. In these atomic configurations, the two original tip and surface closest atoms have now an "equal" number of bonds with the surrounding atoms, losing their identity as being part of the tip or the sample. Our simulations confirm that this dimer structure, that minimizes the stored elastic energy under compression, is the lowest energy configuration reached also with other tip–surface relative orientations and even with different tip structures.

Our DFT simulations using the rigid tip model reproduce the vertical interchange atom manipulations observed in the experiments and highlight the atomistic processes behind. The constraints imposed on the tip keep the energy barriers for all of the alternative processes – including tip modifications and extraction of atoms from the surface – quite high, while the barrier for the vertical interchange reduces significantly on loading. To further explore the role of the mechanical response of tip and the interplay among the different possible outcomes, we have approached our tip to a more realistic situation and carried out simulations with a setup, where the four outermost atoms of the tip-apex are allowed to relax. Figure 11.10a depicts the energy for an approach (squares) and retraction (triangles) cycle over an Si atom resulting in a tip change, where the Sn atom at the apex is lost and left on the surface. On retraction, the system crosses an energy branch (circles) that would result in the vertical interchange of these atoms – the Sn replaces the Si at the surface, while the Si atom incorporates into the dimer structure at the tip apex.

Given the complexity of the configuration space shown by these simulations, where an apparently small change in the tip leads to a completely different result for the approach/retraction curve, one may wonder about the feasibility of the vertical interchange. The important point to notice is also highlighted in Fig. 11.10a: all of the alternative outcomes lead the system to a final state of higher energy than the one associated with the vertical atom

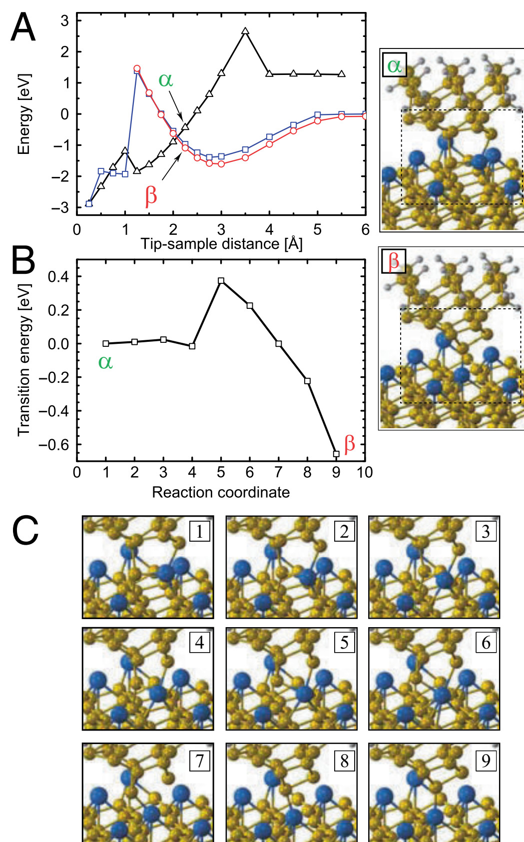

Fig. 11.10. (a) Total energy (*squares* and *triangles*) for a tip–surface approach and retraction cycle over an Si atom producing a tip modification where the Sn atom at the apex is lost and left on the surface. (**b**) Activation energy barrier between two atomic configurations close in total energy labelled as α and β in (**a**). The atomic configurations corresponding to the two α and β state are shown on the *right*. (**c**) Details of the bonding configurations along the minimum energy path for the transition from state α to state β

interchange. In the simulations discussed so far, where no temperature effects are included, the details of the tip structure and mechanical response determine which are the final states that can be reached without crossing significant energy barriers. However, in the experiments that are performed at room temperature, thermodynamics would favor the lowest energy final configurations. Therefore, the feasibility of the vertical interchange process is controlled by the energy barriers among the different local minima.

The calculation of the energy barriers in this multi-atom contact, where the structure of the transition state is difficult to guess, requires a more sophisticated approach that the constrained minimization used in the case of

the lateral manipulation. We have used the "Nudge Elastic Band" method [17], a well-established method for finding transition paths and the corresponding energy barriers between given initial and final states. In this method, a collection of intermediate sets of atomic configurations (or images) is created by a straight line interpolation of the coordinates of the atoms from the initial to the final state. Those images are connected together with springs to form a chain that provides a discrete representation of the path from the initial to the final state. This chain mimics an elastic band made of beads (the images) and springs. The total energy of the entire chain has to be minimized to find the minimum energy path (MEP). This total energy includes both the sum of the total energies of the different images and the contribution from the harmonic interaction between neighboring images along the direction of the path described by the chain. The minimization process involves the relaxation of the coordinates of the atoms in the different images subject to the constraints imposed by the springs. Any maximum along the MEP is a saddle point on the potential energy surface, and the energy of the highest saddle point gives the activation energy needed for the transition.

In our estimation of the typical barriers involved in vertical atom interchange processes, we have studied the transition of the system from an energy branch resulting in an Sn deposition to the one associated with the concerted vertical interchange. In particular, we have considered the transition energy between two atomic configurations very close in energy (points α and β in Fig. 11.10a) belonging to these two different branches: the starting atomic arrangement (α) is a dimer-like configuration in which both atoms have lost their identity as being part of the tip or the sample; the final state (β) is the deposition of the Sn atom. We have used nine images including the initial and final states labelled as α and β, respectively. Figure 11.10b displays the final energies for the sets of different atomic configurations defining the MEP. A zoom of the final relaxed structures over the relevant region of the tip–surface interface is displayed in Fig. 11.10c. We have found that there is an energy barrier of 0.4 eV for the transition between these two configurations (Fig. 11.10b), which is associated with the breaking of the remaining bond of the Si atom with the surface and the formation of a second bond of the Sn atom with the surface (see the panel labelled as 5 in Fig. 11.10c). With this relatively small energy barrier, these vertical interchange atom manipulations can easily take place at RT. It is not necessary to reach the high repulsive energies at which jumps between branches in Fig. 11.9 occur – energy values that would turn into extremely repulsive forces. In contrast, just driving the tip to tip–surface separations close (or slightly beyond) to the distance for the zero short-range force, we are very likely to obtain a vertical atomic interchange by a thermally activated jump near the crossing point of the different energy branches available for the system.

The simulations described earlier also shed light over some of the features exhibited by the associated experimental curves. The frequency shift signals (Fig. 11.8) display a shoulder at closer tip–surface distances, that develops into

a double well structure in the corresponding short-range chemical interaction forces (see Chap. 8). These features, together with the large energy dissipation measured at the closest tip–surface distances [24, 28] can be qualitatively explained in terms of the presence of several energy branches – and, thus, different tip–surface interaction forces – during the evolution of the system. The energy barriers between branches as a function of the tip–surface distance dictate where the system jumps during either approach or retraction and, thus, determine the details of both frequency shift and force curves [16]. Since the frequency shift is proportional to a weighted average of the tip–surface interaction force over one oscillation cycle [30, 31], the existence of these different force branches is blurred [24, 28] in both the frequency shift and the short-range chemical interaction force derived from it; magnitudes that, a priori, only reflect the average conservative part of the interaction [30, 32, 33]. However, the calculated energy landscape provides a clear indication that the striking presence of two force minima of very similar depth are due to the evolution of the system between two different bonding configurations during an approach and retraction cycle.

Figure 11.11 shows the theoretical results that explain the origin of the dissipation signal and the force spectroscopy results measured in the experiments. An oscillation cycle of the experimental approach curve shown in Fig. 11.8b, before reaching the point of maximum proximity between tip and surface, can be simulated by assuming that: (1) the tip approaches the surface following energy branch C in Fig. 11.9; (2) at a given tip–surface distance (C_3), the system jumps to the energy branch D; and (3) on retraction the

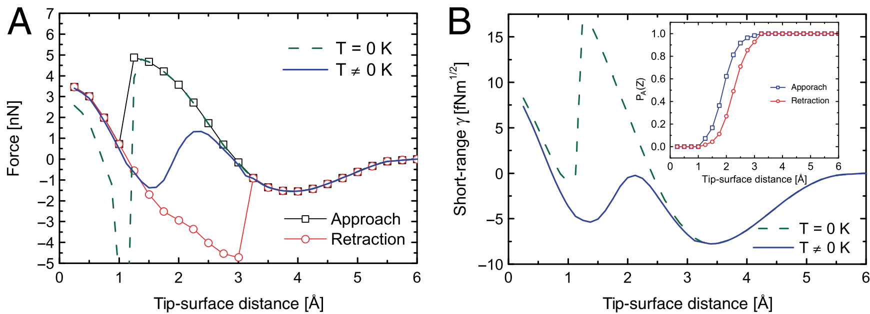

Fig. 11.11. (**a**) Short-range forces corresponding to the evolution and transitions between the energy branches C and D shown in Fig. 11.9; *squares* and *circles* denote the force upon approach and retraction, respectively. The theoretical forces that would be obtained from the inversion of the frequency shift at zero (*dashed*) and non-zero (*continuous*) temperature are also included. (**b**) Normalized frequency shift obtained from the short range force curves shown in (**a**) at zero (*dashed line*) and nonzero temperature (*continuous line*). The *inset* displays the probability of being in the C branch during the approach–retraction cycle used to incorporate the effect of a nonzero temperature in the frequency shift calculation

system jumps back (D_2) to the branch C. Notice that, in this case, there is not vertical atomic interchange and therefore the initial and final configuration upon approach and retraction are identical. The forces on approach (squares) and retraction (circles), assuming these transitions between energy branches, are shown in Fig. 11.11a. An approach and retraction cycle considering these two force solutions leads to a dissipated energy of $\sim$7 eV. The normalized frequency shift γ associated with this process is shown in Fig. 11.11b (dashed line). The step-like change of γ at the tip–surface distance where the atom reallocations take place is an expected consequence of the force hysteresis. The green dashed line of Fig. 11.11a is the force curve associated to this normalized frequency shift when it is calculated with the same inversion procedure used with the experimental results. This curve coincides with the force of the C branch before the jump (up to this point, the force over the oscillation cycle is conservative), but, for closer distances, a strong hysteresis (jump) appears and the short-range force calculated from the frequency shift inversion loses its meaning [30, 32, 33].

Both the force curve and the dissipated energy ($\sim$7 eV) associated with this process are still quite different from the experimental ones. The origin of this discrepancy lays on the role played by the temperature: our calculations so far are done at zero temperature while the experiments are performed at RT. At finite temperature, the system can overcome energy barriers between different energy solutions that smears out the steps and reduces the dissipation signal found at zero temperature [28]. To incorporate the effect of the temperature, we have calculated the normalized frequency shift (continuous line in Fig. 11.11b) using the force solutions on approach and retraction shown in Fig. 11.11a, but giving them some relative probabilities (see the inset of Fig. 11.11b) that reproduce the measured dissipation energy ($\sim$1.2 eV) at the closer tip–surface distances. The corresponding short-range force curve (continuous line in Fig. 11.11a) obtained from this frequency shift using the inversion procedure [31] now exhibits the main feature of the experimental forces: a double well with similar force minimum values. Therefore, this characteristic feature in the experimental short-range force curve is a clear signature of force hysteresis during the approach and retraction cycle.

11.6 Conclusion

This chapter unveils the atomic-scale mechanisms that are responsible for the RT manipulations of strongly bound atoms on semiconductor surfaces. First-principles simulations, matching the experimental forces, identify the key steps in two paradigmatic examples: the lateral manipulation of single adatom vacancies on the Si(111)-7 $\times$ 7 reconstruction in the attractive regime, and the vertical interchange of atoms between the tip and the Sn/Si(111)-($\sqrt{3} \times \sqrt{3}$)R30° surface by a gentle exploration of the repulsive force regime. Our calculations reveal that the outstanding experimental control of the

manipulation under attractive forces comes from the localized reduction of the diffusion energy barriers induced by the tip for the different steps in the complex path followed by the Si adatom during the process. Using selective constraints to face the difficulties posed by the complexity of a multi-atom contact and operation in the repulsive regime, our simulations illustrate how the vertical interchange can take place at the atomic scale, identify the crucial dimer structure formed by the closest tip and surface atoms, and discuss the role of temperature in the competition with other possible final outcomes (including atom removal or deposition by the tip).

Acknowledgements

The authors acknowledges the relevant experimental contribution from Oscar Custance, Yoshiaki Sugimoto, Masayuki Abe and Prof. Seizo Morita to the work described in this chapter. The work of P.P. and R.P. is supported by the Ministerio de Ciencia e Innovacion (MICINN, Spain) under Grants MAT2005-01298 and NAN2004-09183-C10, and by the VI Framework Programme of the European Union under the STREP project FORCETOOL (NMP4-CT-2004-013684). P.P. acknowledges the financial support by the Juan de la Cierva Programme (MICINN, Spain). P.J. acknowledges the financial support from COST P19-OC09028 and GAAV under the grants no. IAA 100100905 and GA CR 202/09/0775. Part of these calculations has been performed at the Centro de Computacion Cientifica of the UAM and the MareNostrum supercomputer at the BSC-CNS.

References

1. D. Eigler, E.K. Schweizer, Nature **344**, 524 (1990)
2. F. Giessibl, Science **267**, 68 (1995)
3. N. Oyabu, O. Custance, I. Yi, Y. Sugawara, S. Morita, Phys. Rev. Lett. **90**(17), 176102 (2003)
4. S. Morita, I. Yi, Y. Sugimoto, N. Oyabu, R. Nishi, O. Custance, M. Abe, Appl. Surf. Sci. **241**, 2 (2005)
5. S. Kawai, H. Kawakatsu, Appl. Phys. Lett. **89**, 023113 (2006)
6. N. Oyabu, Y. Sugimoto, M. Abe, O. Custance, S. Morita, Nanotechnology **16**(3), S112 (2005)
7. Y. Sugimoto, M. Abe, S. Hirayama, N. Oyabu, O. Custance, S. Morita, Nat. Mater. **4**(2), 156 (2005)
8. R. Nishi, D. Miyagawa, Y. Seino, I. Yi, S. Morita, Nanotechnology **17**(7), S142 (2006)
9. S. Hirth, F. Ostendorf, M. Reichling, Nanotechnology **17**(7), S148 (2006)
10. M. Abe, Y. Sugimoto, O. Custance, S. Morita, Appl. Phys. Lett. **87**(17), 173503 (2005)
11. M. Abe, Y. Sugimoto, O. Custance, S. Morita, Nanotechnology **16**(12), 3029 (2005)

12. M. Abe, Y. Sugimoto, T. Namikawa, K. Morita, N. Oyabu, S. Morita, Appl. Phys. Lett. **90**(20), 203103 (2007)
13. Y. Sugimoto, P. Pou, M. Abe, P. Jelinek, R. Pérez, S. Morita, O. Custance, Nature **446**, 64 (2007)
14. M. Ternes, C. Lutz, C. Hirjibehedin, F. Giessibl, A. Heinrich, Science **319**, 1066 (2008)
15. Y. Sugimoto, P. Jelinek, P. Pou, M. Abe, S. Morita, R. Pérez, O. Custance, Phys. Rev. Lett. **98**, 106104 (2007)
16. Y. Sugimoto, P. Pou, O. Custance, P. Jelínek, M. Abe, R. Pérez, S. Morita, Science **322**, 413 (2008)
17. G. Henkelman, H. Jónsson, J. Chem. Phys. **113**, 9901 (2000)
18. R. Martoňák, D. Donadio, A. Oganov, M. Parrinello, Nat. Mater. **5**, 623 (2006)
19. P. Dieska, I. Štich, R. Pérez, Phys. Rev. Lett. **95**(12), 126103 (2005)
20. P. Dieska, I. Stich, Nanotechnology **18**, 084016 (2007)
21. O.F. Sankey, D.J. Niklewski, Phys. Rev. B **40**(6), 3979 (1989)
22. P. Jelinek, H. Wang, J.P. Lewis, O.F. Sankey, J. Ortega, Phys. Rev. B **71**(23), 235101 (2005)
23. M. Basanta, Y.J. Dappe, P. Jelinek, J. Ortega, Comp. Mat. Sci. **39**, 759 (2007)
24. N. Oyabu, P. Pou, Y. Sugimoto, P. Jelinek, M. Abe, S. Morita, R. Pérez, O. Custance, Phys. Rev. Lett. **96**(10), 106101 (2006)
25. Y. Sugimoto, O. Custance, S. Morita, M. Abe, P. Pou, P. Jelínek, R. Pérez, Phys. Rev. B **73**, 205329 (2006)
26. R. Pérez, M. Payne, I. Štich, K. Terakura, Phys. Rev. Lett. **78**(4), 678 (1997)
27. P. Jelínek, M. Švec, P. Pou, R. Perez, V. Cháb, Phys. Rev. Lett. **101**, 176101 (2008)
28. L.N. Kantorovich, T. Trevethan, Phys. Rev. Lett. **93**(23), 236102 (2004)
29. M.A. Lantz, H.J. Hug, R. Hoffmann, P.J.A. van Schendel, P. Kappenberger, S. Martin, A. Baratoff, H.J. Güntherodt, Science **291**(5513), 2580 (2001)
30. F.J. Giessibl, Phys. Rev. B **56**(24), 16010 (1997)
31. J.E. Sader, S.P. Jarvis, Appl. Phys. Lett. **84**(10), 1801 (2004)
32. H. Hölscher, B. Gotsmann, W. Allers, U.D. Schwarz, H. Fuchs, R. Wiesendanger, Phys. Rev. B **64**(7), 075402 (2001)
33. U. Dürig, Appl. Phys. Lett. **75**(3), 433 (1999)

12

Multi-Scale Modelling of NC-AFM Imaging and Manipulation at Insulating Surfaces

T. Trevethan, N. Martsinovich, L. Kantorovich, and A.L. Shluger

Abstract. We present the results of calculations performed to simulate the process of atomic-scale imaging and manipulation that explicitly take into account dynamical processes occurring at the surface. These calculations are performed using a novel multi-scale method that combines a simulation of the experimental instrument coupled with a kinetic Monte Carlo simulation of the microscopic system that evolves in real time. This method is applied to three qualitatively different systems: the manipulation of a Pd atom adsorbed on the MgO (001) surface, the imaging of the thermally induced motion of a water molecule adsorbed on the CeO_2 (111) surface, and the manipulation of a C_{60} molecule on the Si (001) surface. The results of these simulations show how optimum protocols for controlled atomic-scale manipulation can be determined and how dynamical surface processes can significantly affect the contrast seen in NC-AFM images.

12.1 Introduction

The interpretation of the results of atomic resolution non-contact atomic-force microscopy experiments is a difficult and challenging task, due to both the complexity of the imaging mechanism and the unknown nature of the exact tip-apex structure [1]. Therefore, it is necessary to employ theoretical modelling to better understand the results produced by a particular experiment. The application of theory to modelling NC-AFM images has been able to explain the contrast patterns observed and identify features in many atomic resolution experiments [1–3] and has proved invaluable to the advance of the field over the past decade. The modelling of an NC-AFM experiment typically involves calculating a tip–surface force-field – for a particular tip and a particular surface – from atomistic simulations. This force-field, which gives the vertical force on the tip as a function of tip position in three-dimensions above the surface, can then be used to calculate the frequency-shift (also as a function of tip position) from the cantilever parameters and the amplitude

S. Morita et al. (eds.), *Noncontact Atomic Force Microscopy*,
NanoScience and Technology,
DOI: 10.1007/978-3-642-01495-6_12, © Springer-Verlag Berlin Heidelberg 2009

by integrating over the tip trajectory [4]. This in turn can then be used to create either a constant height image of frequency or a topography image at a given frequency shift set-point. This procedure, however, involves several important simplifying assumptions. The first of these is that the NC-AFM instrumentation controlling the cantilever oscillations and the surface position act ideally, i.e., that the tip follows a sinusoidal trajectory, and that the lateral scanning speed is slow enough that any finite response of the amplitude or frequency feed-back loops can be neglected; in other words, it is assumed that the instrumentation reacts instantaneously during the scan on the constantly undulating surface. The second assumption is that the tip-experiences a conservative force-field due to its interaction with the surface, and that there are no non-conservative processes i.e., no atomic-scale structural changes occur during the entire imaging process.

In many NC-AFM images of stable and well defined surfaces and systems, the assumptions described earlier are applicable and well tested [1,4,5]. However, there are many instances where this is not the case: e.g., when microscopic structural changes occur to the surface or tip during the imaging process. These structural changes may consist of the thermally driven diffusion of an adsorbate across a surface, or may be induced by the tip at close approach – something that is produced intentionally in an atomic-scale manipulation experiment [6–8]. When considering the effect of dynamical processes during the experiment, the interpretation and modelling becomes significantly more complex and challenging.

To understand the effect of various dynamical processes during an NC-AFM experiment, it is useful to consider the various time-scales involved. The chemical force that acts between the tip and the surface at close approach is sensitive to the thermal vibrations of individual atoms in both the surface and the tip, which typically have a characteristic frequency of 10^{12}–10^{14} Hz. The cantilever, however, oscillates with a frequency on the order of 10^5 Hz, and so atoms in the junction will vibrate billions of times over a single oscillation of the tip. It has been shown earlier that the force fluctuations of these fast lattice vibrations are effectively averaged over the tip trajectory, and the tip "feels" the system in its ground state configuration (within the harmonic approximation) resulting in a conservative tip–surface interaction [9,10]. Other processes that result in structural changes, may occur over a vast range of time-scales: rare hops and manipulation events may occur only a few times during the acquisition of an entire image (which occurs over the order of seconds to minutes) resulting in definite changes in contrast as the image is scanned. Faster diffusion processes may occur at a frequency comparable to the tip oscillations, and in this case the response of the instrument and the interplay between the diffusion and tip oscillations is difficult to predict. In all cases, the dynamical evolution of the surface processes and the motion of the tip are not independent of one another, but directly coupled and must be treated as a single interacting system.

In this contribution we explain how an explicit, real-time and multi-scale simulation of the entire NC-AFM experiment, including the dynamical evolution of the instrumentation at the macroscopic scale and atomistic processes at the microscopic scale, can help in understanding the imaging of complex process and how atomic- and molecular-scale manipulation can best be achieved and detected. Modelling the imaging process requires spanning both the time of acquiring an entire image and the characteristic time-scale of atomic-scale transitions – a complex task that requires the use of novel methods.

We apply this model to three realistic but qualitatively different systems: the manipulation and diffusion of a Pd adatom on the MgO (001) surface, the thermally induced structural change of an H_2O molecule on the CeO_2 surface and the manipulation of a C_{60} molecule on the Si (001) surface. In the first system, which consists of a metal adatom weakly bound to an ionic surface, we model how the atom can be manipulated at close approach and also the image contrast when the atom is freely diffusing across the surface. In the second system, we image the fast structural changes of a small molecule that is strongly bound and immobile on the surface but free to move between three equivalent states. In the final example, we model the manipulation by the tip of a much larger molecule that is strongly bound to the surface.

Section 12.2 outlines the details of the model and how this is implemented in the simulation. Section 12.3 then describes the application of the model to the three example systems. In Sect. 12.4 a discussion is given.

12.2 Methods

The simulation of the NC-AFM experiment is treated in two separate parts: the instrument and the microscopic system. These are then linked together to form a complete self-consistent simulation.

12.2.1 Modelling the Instrument

The NC-AFM instrumentation controls the amplitude of the cantilever oscillations and the position of the surface (and hence the frequency shift) with two feed-back loops: the automatic gain control (AGC) and the automatic distance control (ADC), respectively (see Fig. 12.1). These loops are implemented using a complex set-up of electronics, incorporating a digital phase locked loop as a frequency demodulator, and a laser diode detection system to measure the deflection of the cantilever [4]. The instrument outputs three signals that can be used for generating images: the sample height (topography), the frequency shift (detuning) and the excitation signal (dissipation).

To model the complex behaviour of this instrument we employ a Virtual atomic-force microscope (VAFM), which consists of an explicit numerical simulation of the entire experiment in real time, and is described in detail in [11, 12]. The VAFM, we employ, performs a numerical integration of the

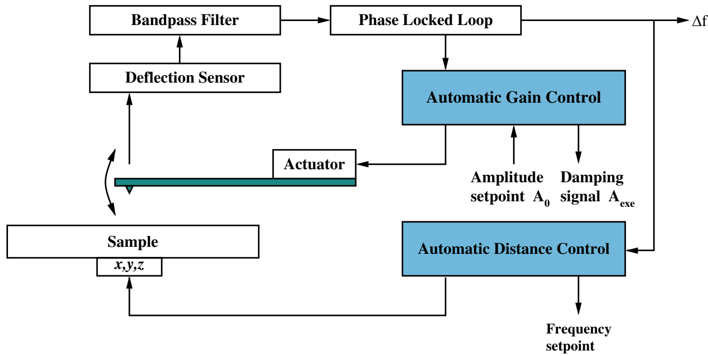

Fig. 12.1. Block diagram showing the interacting parts of the virtual AFM

trajectory of the cantilever, the control electronics and the driving signal with a fixed time-step, which is small compared with the motion of the tip (approximately 10^{-10} s). The tip moves in a three-dimensional force-field above the surface as the tip is oscillated and the surface is scanned. The scanning of the surface takes place continuously and the oscillating tip follows a lateral path collecting line scans to produce an image, in real time. The lateral trajectory in the calculations presented here consists of a raster scan without flyback – with the surface moving alternately in perpendicular fast and slow directions to build up all the lines for the complete image. Other implementations of dynamic AFM instrument simulations can be found in [13, 14].

By performing a complete real-time simulation of the instrument, the force-field experienced by the tip can be altered to reflect a structural change in the surface during the imaging process. The simulations including the trajectory of the tip, all the control mechanisms and the output signals, will react in a completely realistic way as the experiment progresses.

12.2.2 Modelling the Tip–Surface Junction

At the heart of all calculations to model NC-AFM experiments is the tip–surface force-field, which usually consists of two components: a macroscopic van der Waals force, which depends only on the tip–surface separation and a microscopic force-field which is sensitive to the atomic-scale structure of the surface and tip. The microscopic force-field depends strongly on the exact chemical nature and structure of the tip model used, and so the choice of this tip model is critical to the outcome of a simulation and the predicted contrast. The exact nature of the tip-apex used in the actual experiment is unknown: tips are usually fabricated from silicon, but are exposed to the atmosphere and so form an oxide layer and may be contaminated with other species. In addition the tip is most likely to be contaminated by material from the surface under investigation during the experiment.

The identity of the tip-apex can be determined by simulating an NC-AFM image with many different types of tips and selecting the tip that gives the closest match to the observed contrast pattern [15, 16]. In addition, force-curves over individual surface atoms can be determined from force-spectroscopy experiments and further used to characterize the tip–surface interaction [17,18]. However, to reach a qualitative understanding of the imaging process, model tips are often employed which significantly reduce the computational effort involved in calculating tip–surface interactions.

With a given tip model, the force-field can be calculated from a series of atomistic calculations. With the tip in a fixed position above the surface, the force on the tip is calculated after all free atoms in the tip–surface junction are relaxed. This is then repeated for an array of tip positions to obtain the force-field in three dimensions. The method used to calculate the tip force depends on the identity of the surface and the tip model: ideally an ab-initio method, such as density functional theory is employed [19–21]. However, depending on the system, high quality interatomic potentials can be used instead which drastically reduces the computational effort involved by several orders of magnitude. If the microscopic system retains the same structure throughout the experiment, a single force-field is required to model the imaging process. However, structural changes will change the force-field experienced by the tip during the experiment. In this case, a force-field for each structure that is accessible during the simulation is required.

Dynamical processes in the surface and the structural changes associated with them occur from transitions between minima on the potential energy surface (PES) of the tip–surface junction. These transitions (or jumps) are thermally induced and occur when the system crosses a potential energy barrier (or saddle point). Energy barriers for processes in the microscopic system can be calculated from atomistic calculations, employing the same methods used for calculating the force-field.

In many microscopic processes, such as e.g., atomic self-diffusion, the barriers, and hence the rates of transitions, remain constant. However, when the tip of an SPM is interacting with the surface, these barriers can be modified and will change as the tip is moved above the surface. This results in a PES that is a function of tip-position – giving rise to a potential energy barrier field. A "barrier field" then gives the activation energy for a certain process as a function of tip position. The presence of the tip may act to change the barrier for a process at close approach. In fact, as the tip moves in time (both due to vertical oscillations and the lateral scan), the "barrier field" becomes an explicit function of time as well. Manipulation occurs when a barrier that is insurmountable when the tip is far from the surface (and no transitions occur at a given temperature) is lowered by the presence of the tip, allowing a transition to proceed.

The frequency at which atomic-scale transitions occur in the system may be comparable to the tip motion, but the actual transition itself occurs on the time-scale of atomic relaxation (i.e., 10^{-12} s) i.e., effectively instantaneously

with respect to the tip motion. So, as far as the NC-AFM experiment is concerned, the dynamics of the individual transition is irrelevant – we are only interested in evaluating when they occur. Atomic-scale transitions are an inherently stochastic process that can be modelled realistically using a kinetic Monte Carlo (KMC) method [22], if the rates of the relevant transitions are known.

12.2.3 Kinetic Monte Carlo

Given the activation barrier (for a given tip position x, y, z), the transition rate for a particular process, k, can be calculated from the familiar Vineyard expression [23]:

$$r^k(x, y, z) = \nu^k \, \mathrm{e}^{-\beta \Delta E^k(x,y,z)}, \tag{12.1}$$

where ν is the attempt pre-factor, $E^k(x, y, z)$ the energy barrier field for process k and $\beta = 1/k_B T$. In the traditional KMC method, the rates for individual processes are constant and do not change in time [24]. Then, the simulation of the system dynamics is done by, firstly, choosing at random the time-step using the total rate of all possible "positive" processes, and, secondly, choosing, again at random, the particular process from the available list of processes which will take the system to the next state. The standard KMC algorithm is based on considering only "positive" processes which lead to the system changing its state.

To evaluate the dynamics of a system when the barriers (and rates) vary in time due to the motion of the tip, a more general KMC algorithm that employs a fixed time-step Δt must be employed [22]. In this method, a complete set of processes is considered including the one in which nothing happens, i.e., the system remains in its current state (see for example state A in Fig. 12.2b). Then, one considers the probability, $P_0(\Delta t)$, for the system to remain in the current state over the time Δt (which exponentially decays with increase of the time step), and the probabilities $P_k(\Delta t)$, to move to every available other state k over the same time (for example the four B states in Fig. 12.2b). By considering the complete system of possible states the system may jump into (including multiple jump events), one ensures that all probabilities add up to unity exactly, i.e.,

$$P_0(\Delta t) + \sum_k P_k(\Delta t) = 1. \tag{12.2}$$

A single random number is drawn to decide which particular state of all available states will be realized, including the remaining in the current state. To avoid complex calculations of all possible paths to reach available states from the current one over the finite time Δt (which should include also jumping to these states via intermediate states, i.e., multiple jump events), one can choose a very small time-step and simply disregard multiple events, in which

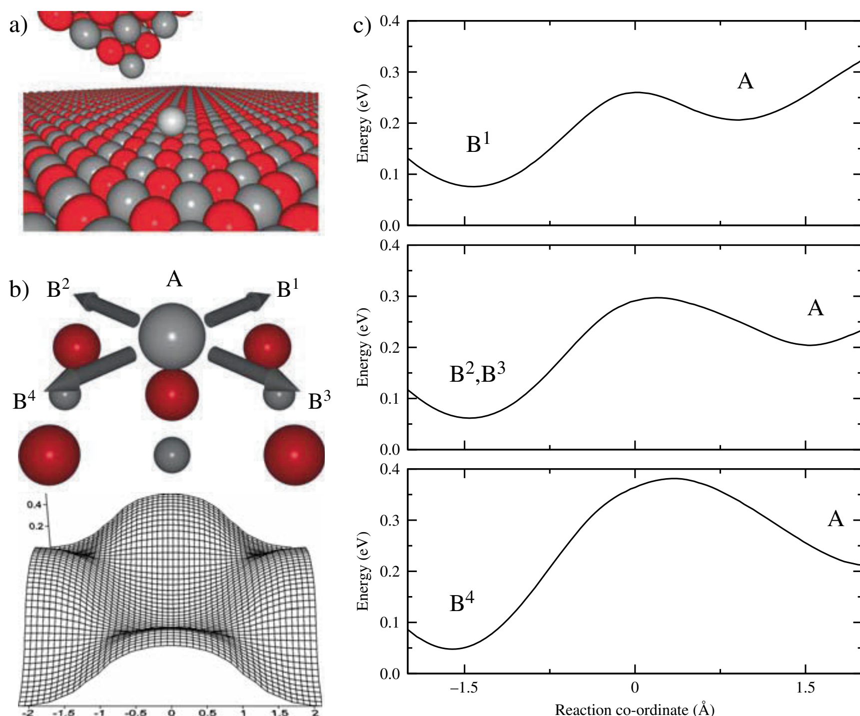

Fig. 12.2. (**a**) Configuration of the surface, adatom and tip (**b**) *Top*: Schematic of a single oxygen unit cell on the MgO (001) surface with the Pd atom adsorbed above the central O, showing the four equivalent transitions to neighboring oxygen sites. *Bottom*: 2-D potential energy surface for the Pd atom as a function of lateral position above the unit cell. The centre of the cell is located at lateral position $x = 0$ $y = 0$ and B^1 at $x = 2.122$ and $y = 2.122$. (**c**) Minimum energy paths along the four reaction coordinates for the Pd atom to move into each of the four neighboring minima with the Mg terminated MgO tip at a height of $z = 4.5$ Å and lateral position $x = -0.53$ Å $y = -0.53$ Å relative to the central O position

case the construction of the possible list of events is trivial. In the case of simulations of AFM induced diffusion of atoms on the surface, we can simply consider single jumps to all nearest lattice sites (e.g., see Fig. 12.2b).

For the given tip position the probabilities of these events can be explicitly calculated given the known energy barriers as functions of the tip position, and the known time step, Δt. Then, a random number is drawn to choose the particular process from the list, i.e., which atom to move and to which lattice site, or to keep the current configuration of the atoms on the surface unchanged (i.e., "do nothing"). Then, as the tip moves over the time Δt, the list of processes is compiled again, their probabilities are recalculated and it is decided what is the next state of the system. Thus, in this algorithm, for a given time-step in the simulation, the probability of the system crossing a

barrier is calculated based on the instantaneous rate, and a random number is drawn to determine whether the barrier is crossed or not.

The KMC simulation is run simultaneously with the VAFM calculation, with the potential energy barrier fields evolving in real time as the tip moves and the surface is imaged. This means the position and motion of the tip alters the dynamics of the surface processes. When a microscopic transition occurs the force-field will switch instantaneously to the corresponding new microscopic structure. In this way both the microscopic and macroscopic parts of the system evolve in-step and self-consistently.

12.3 Applications

12.3.1 Pd Adatom on MgO (001)

The adsorption and diffusive behaviour of individual Pd atoms and Pd clusters on the MgO (001) surface has been widely studied, with a variety of techniques, primarily as this system is an important catalyst [25]. However, as an example of a system consisting of adatoms weakly bound to an ionic surface, it is useful as model system to investigate the manipulation of individual atoms on an insulator. MgO has the rock-salt structure and the (001) surface is very stable and nearly flat. To model this system, we have employed a set of classical pair-wise inter-atomic potentials that have been derived from high-quality ab-initio calculations of the Pd/MgO interface [26]. The atomistic calculations have been performed using the SciFi code which has been specifically developed to model SPM tip–surface interactions [27].

A single Pd atom is adsorbed directly above the oxygen site on the MgO surface with an adsorption energy of approximately 1 eV. The Pd atom can diffuse on the surface via a nearest neighbor hopping mechanism, and the energy barrier to move to a neighbouring minimum (above a neighboring oxygen) is approximately 0.25 eV and will therefore be highly mobile at room temperature, but immobile at low temperatures (70 K being a convenient reference point). Figure 12.2a shows the configuration of an adsorbed Pd atom on the surface, along with the potential energy surface of this system as a function of the lateral position of the Pd atom (Fig. 12.2b). Here, it is clear that the Pd atom can move in one of four equivalent directions in a single transition. In the description that follows the initial adsorbed position of the Pd atom is labelled state A, and the four neighboring states B^1, B^2, B^3, and B^4.

It is apparent that the states B^1, B^2, B^3, and B^4 are equivalent, however when a tip is introduced to the system above the surface this symmetry may be broken and the barriers to move into the different states change. This is at the heart of the manipulation mechanism the potential energy surface of the system and hence the individual barriers are modified through the interaction with the tip. In the calculations presented here, the tip is represented by a 64 atom MgO cube oriented so that its threefold axis is perpendicular to the

surface plane and is terminated with a single Mg atom. The upper 32 atoms are frozen in bulk-like positions and the remaining atoms free to relax. This tip is chosen as a convenient model, however the MgO tip has been shown to be representative of a wide variety of polar tips [1]. The nature of the tip apex is crucial to the manipulation mechanism in this case: the Mg apex has a very weak attractive interaction with the Pd adatom (much weaker than the Pd–O interaction), and is therefore able to exert a force (through Pauli repulsion) to "push" the Pd atom at close approach.

The minimum energy path, and hence barrier, for the Pd atom to move from state A to states B^1, B^2, B^3, and B^4 can then be determined for a given position (x, y, z) of the tip above the surface, using a constrained minimisation procedure (described in [28]). For example, Fig. 12.2c shows each of the four minimum energy paths when the tip apex is positioned at a height of 4.5 Å above the surface and at a lateral position 0.75 Å in the direction to state B^4 from the position directly above state A. Here, the barrier to move to state B^1 is the smallest and the barrier to move to state B^4 the largest (the barriers to move to states B^2 and B^3 are equivalent due to the symmetry). This calculation is then repeated for a three-dimensional array of fixed positions of the tip above the Pd atom and surface to derive the four separate energy barriers as a function of tip position. The barriers are calculated for a grid of positions with 18×18 points laterally over the conventional unit cell and 50 tip heights vertically between 4 and 6 Å (a total of 16,200 points). With this complete grid, each of the four energy barriers can be determined for any arbitrary tip-position in three dimensions above the surface by interpolating between these points using a polynomial interpolation scheme. This results in four "energy barrier fields" – which in addition to the force-field of the system enable the complete description of the dynamical evolution for any arbitrary tip trajectory.

The dynamical evolution of this system can then be determined using the kinetic Monte Carlo algorithm, with rates calculated using a standard attempt pre-factor of 10^{12} Hz. The tip trajectory is controlled using the virtual AFM and the system will react in real time. When a jump of the Pd atom occurs (according to the KMC simulation), both the force-field and barrier-fields are instantaneously shifted to the new position of the Pd atom and the simulation continues. The jump of the atom and, hence, of the force-field occurs instantaneously with respect to the motion of the tip and the instrument will respond to the jump in a completely realistic and self-consistent way.

In the calculations presented here, a finite time-step of $\Delta t = 10^{-9}$ s is used for both the KMC algorithm and the VAFM trajectory. This is sufficiently large to assume that an atomic jump happens instantaneously. In addition to the atomistic tip–surface force-field, an attractive macroscopic van der Waals force (using a spherical tip model with a radius of 10 nm and a Hamaker constant of 1 eV) is added to replicate a realistic tip–surface interaction. The resonant frequency of the cantilever is $f_0 = 100$ kHz, the spring constant

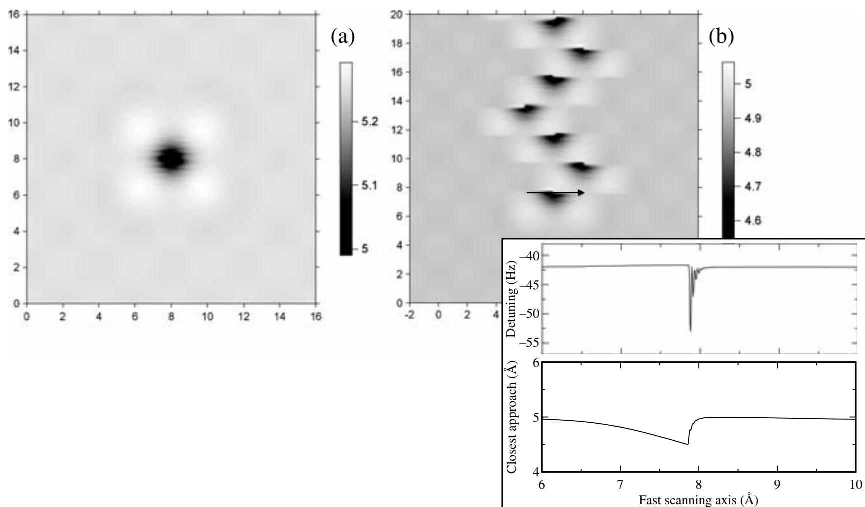

Fig. 12.3. (**a**) Constant frequency shift ($\Delta f_0 = -38$ Hz) topography image of the Pd atom at the centre of a $16 \times 16\,\text{Å}^2$ area of the MgO (001) surface at 10 K. (**b**) Constant frequency shift ($\Delta f_0 = -42$ Hz) topography image of the Pd atom on a $20 \times 20\,\text{Å}^2$ area of the MgO (001) at 10 K. The frequency detuning along the fast scan line indicated and the corresponding distance of closest approach (topography) are shown as an *inset*

20 N/m and the set-point amplitude $A_0 = 10$ nm. All the other parameters for the instrument are described in [28].

Figure 12.3a shows a topography scan of a Pd atom on the MgO (001) surface (scan area 16×16 Å), for the frequency set-point $\Delta f_0 = -38$ Hz and at 10 K, with the slow scanning direction going from top to bottom. The topography is low (dark) over Pd atom due to the short-range repulsion with the Mg terminated tip; however, the tip is not yet getting close enough to the surface to significantly lower any barrier to induce a jump of the adatom. To illustrate the time-scales involved, this image is acquired over several minutes of real time (although it takes many hours to calculate). Each scan line takes 0.4 s, during which the cantilever will have oscillated approximately 40,000 times over 4×10^8 simulation time-steps.

Figure 12.3b shows the same scan, but this time performed at a frequency shift set-point of $\Delta f_0 = -42$ Hz, which now brings the tip closer to the surface (and Pd atom) at close approach. Now the Pd atom is being pushed upwards as the scan progresses, resulting in the "half moon" shapes as the atom jumps to a neighboring site as a single line is scanned. Figure 12.3b also shows the instantaneous frequency shift (detuning) and topography as a jump occurs on the scan line indicated in the image. Here, when the jump occurs, the force-field changes and the instrument retracts the surface to maintain the set-point frequency shift, which happens over a finite time due to the response of the

instrument [29]. In an ideal instrument, the frequency shift would remain constant, however, in reality a spike occurs due to the instantaneous jump. This strong response signature can be used as a confirmation of successful manipulation and to identify the exact point a manipulation occurs. In addition, the jump of the atom (and force-field) will cause a difference in the tip–surface force during the approach and retraction over a single oscillation cycle that will lead to a spike in the dissipation (amplitude gain) signal, however in this case the effect is small (a peak of 5 meV) and is unlikely to be detected in a real experiment.

With this simulation it is now possible to determine the outcomes and success of various manipulation protocols, which can be used to guide experimental efforts. For example, it is the case that scanning in the (110) direction offers less control over the Pd atom (i.e., more uncertainty in the direction of manipulation) than scanning in the (100) direction [28]. However, both of these protocols demonstrate only limited control over the adatom and are also sensitive to the direction of the scanning. The lack of control is due to the fact that during *scanning* the tip on its trajectory is visits regions that will cause the manipultion in several different directions, only one of which is *desired*.

An alternative is to position the tip only in a "high success" region along a predetermined trajectory [29], through a vertical approach of the oscillating cantilever over a fixed lateral position to induce the manipulation in a specific direction. To achieve a high degree of control it is necessary to determine the "high success" manipulation regions from a series of simulations. Here, the probability of the system moving in a particular direction can be determined by repeating the evaluation of a given trajectory of the tip many times to build up statistics.

This manipulation procedure was simulated with the oscillating cantilever approaching the surface with a constant velocity of $v = 20\,\mathrm{nm\,s^{-1}}$ up to a distance of closest approach of 4 Å. The final state of the system (either A, B^1, B^2, B^3, or B^4) is recorded after the approach, and this is repeated 1,000 times. These calculations are then repeated for a grid of lateral positions over the oxygen unit cell shown in Fig. 12.2 (with the Pd atom at the centre) and the proportion of attempts resulting in each state was used to determine the corresponding probabilities.

Figure 12.4 shows lateral plots of probabilities for the protocol described, for temperatures $T = 10$ and 70 K, for achieving the manipulation in a specified direction (here, to state B^2) and also for manipulating the atom into one of the other three states. The lateral area for achieving a desired manipulation into the B^2 state is on the opposite side to the adatom (as is expected, from a "pushing" mechanism). The area for complete certainty of achieving the desired manipulation to B^2 (and not to any other state) is significantly larger at a lower temperature – showing that a lower system temperature will lead to greater degree of control with this protocol. As is the case with lateral scanning, when the atom jumps, the sudden change in force-field will cause

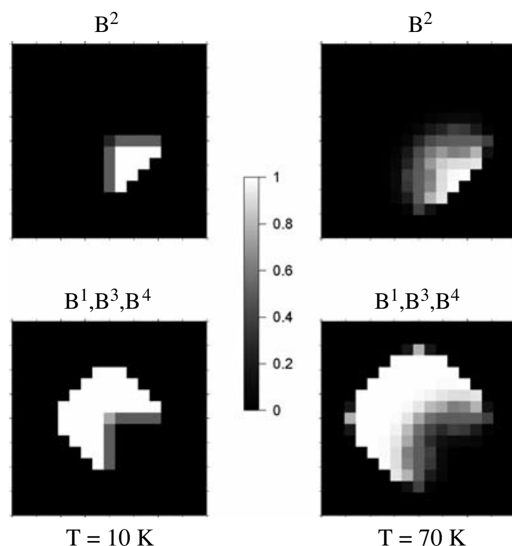

Fig. 12.4. Probabilities of manipulating the Pd adatom in different directions, for a constant velocity approach of the oscillating cantilever over a fixed lateral position (on a grid over the oxygen unit cell, where the Pd adatom is initially located in the centre of the cell) for temperatures of 10 and 70 K

a spike in the frequency shift – a signature that can be used to confirm the manipulation has occurred [29].

In the examples of different manipulation protocols earlier, at low temperatures, there are no spontaneous transitions when the tip is far from the surface, i.e., structural changes must be induced by the tip. At higher temperatures, this is no longer the case and the Pd atom may diffuse across the surface as it is scanned. Figure 12.5a shows a constant height (frequency shift) image of the same surface area at a temperature of 110 K, where the rate for a spontaneous jump of the Pd atom is approximately 20 Hz. Here, the atom is jumping between states several times during a single line-scan (even when the tip is not modifying the energy barriers) resulting in bright and dark "stripes" that pattern the image. In this case, the length of a stripe will be proportional to the residence time of the atom. The distribution of the lengths of the different stripes should reveal the average rate for the different processes for different relative positions of the tip and Pd atom.

Figure 12.5b shows an image of the same scan, but this time at a temperature of 180 K. In this image the underlying MgO lattice is visible but with "noise" concentrated over the oxygen sites. In this case, the Pd atom is diffusing on the surface very rapidly, with the rate for a spontaneous transition at 6 MHz which corresponds to an average of 60 jumps over a single oscillation of the cantilever. Figure 12.5c shows the corresponding dissipation (amplitude

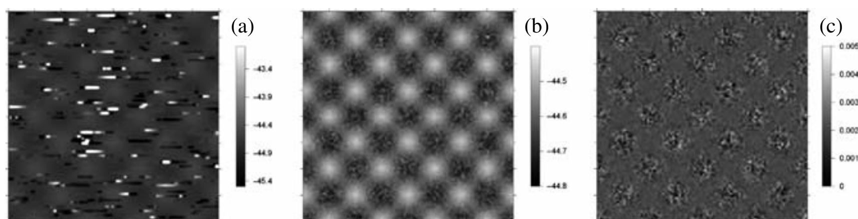

Fig. 12.5. Constant height frequency shift images (closest approach of 0.48 nm) of a 1.7×1.7 nm area of the MgO (001) surface (**a**) with the Pd atom diffusing at 110 K (**b**) 180 K. (**c**) dissipation image at 180 K, where the units are in eV/cycle

gain) image, where it is possible to see a small dissipation contrast centred around the oxygen sites. This contrast consists of enhanced "noise" and is due to the fact that the Pd rapidly jumping is resulting in many changes to the tip–surface interaction during a single oscillation cycle, so that the force distance curves on approach and retraction are different (and thus work is done by the tip).

12.3.2 H_2O Adsorbate on CeO_2 (111)

In the example above, we investigated the effect that a rapidly diffusing adatom has on NC-AFM images. In this case, the atom was free to diffuse across the surface, however there are many examples of systems where an adsorbate or surface structure is confined to a small number of accessible states [30]. In this case, the transitions of the system could have a significant effect on the contrast patterns observed.

Recently, experiments have shown images of water adsorbed on the CeO_2 (111) surface [31], which were taken at room temperature. The protrusions assigned to the water adsorbates were triangular in form and observed to encompass three adjacent top oxygen sites. Ab initio calculations were performed that show that a water molecule adsorbs dissociatively on the surface and that the dissociated proton can rotate around the hydroxyl group formed and occupy one of three equivalent states (see Fig. 12.6) [32]. The energy barrier separating these states is calculated to be 0.3 eV, which would result in the proton hopping with a frequency on the order of megahertz at room temperature. This is a qualitatively different behaviour to that displayed in the previous system since the adsorbate is confined to only three equivalent states and is not free to diffuse across the surface.

The force-field of the surface and adsorbed water molecule was determined for atomistic calculations that employed a modified Ceria shell-model potential (the full details of which can be found in [33]) and employed the GULP atomistic simulation code [34]. The tip used for imaging was a hydroxyl terminated MgO tip (in the same orientation as in the previous section), since the tip will have been exposed to water molecules. The fixed time-step KMC

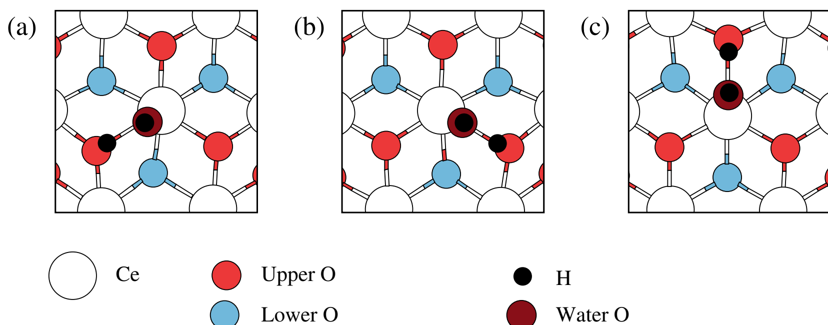

Fig. 12.6. Three equivalent accessible configurations of an adsorbed water molecule on the ceria (111) surface [35]

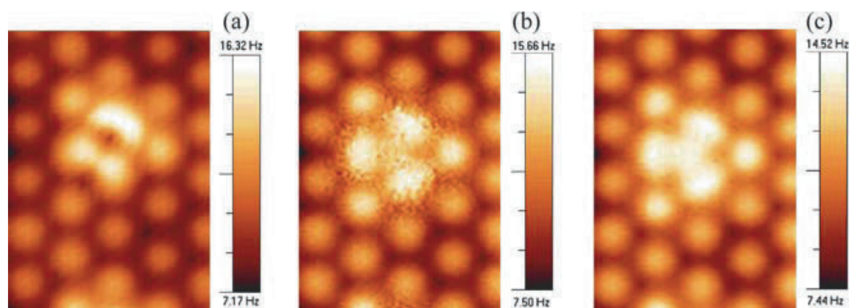

Fig. 12.7. Constant height mode images (closest approach of 4.2 Å) of H_2O adsorbed on the ceria (111) surface at (**a**) 4 K, (**b**) 200 K and (**c**) 300 K [35]

algorithm was used to determine the thermal transitions of the water molecule between the three configurations. When a jump occurs, the force-field is rotated about the centre of the water molecule by either 120 or 240°, i.e., the proton moves either clockwise or anti-clockwise. In these calculations, the barriers are not modified by the presence of the tip, which is an approximation that holds given that the tip does not come too close to the surface.

The parameters for the instrument and cantilever are taken from the corresponding experiment [31]. The resonant frequency of the cantilever is 71.4 kHz and the spring constant is 32 N/m. The amplitude set-point is set at 3.75 nm. As in the previous calculation, a macroscopic van der Waals force is added to the tip–surface interaction with a tip radius of 1.4 nm and a Hamaker constant of 0.4 eV. The scan is performed in the same way as described in Sect. 12.2, but with a scanning speed of 3 nm/s.

Figure 12.7a shows a constant height (frequency shift) image (at 4.2 Å) of the adsorbed water molecule at 4 K, where no transitions occur throughout the whole image (the structure is that of Fig. 12.6a). The lattice of bright spots in this image correspond to the top oxygen sites in the CeO_2 (111) surface,

and the water molecule appears as an asymmetric protrusion covering three oxygen sites. As the temperature is increased to 200 K the form of the image changes significantly, now the molecule is rotating rapidly with a transition rate of approximately 30 kHz, which is less than the oscillation frequency of the cantilever. The image now has threefold symmetry (Fig. 12.7b). At a temperature of 300 K, the rotation of the molecule is now much more rapid than the cantilever oscillation frequency. The image is similar to that at 200 K, but contains significantly less noise above the molecule.

These calculations indicate that there will be a characteristic "noise" in the frequency shift images due to a rapidly diffusing defect. When defects are immobile, they can be clearly seen in images and may be manipulated by a tip. However, when the temperature is such that defects can make rapid thermally activated hops this can significantly change the appearance of the image.

12.3.3 C_{60} on Si (001)

We have considered manipulation and thermal motion of adsorbed species which can jump between nearest lattice sites over a small barrier. Here, we shall discuss a different type of a manipulation experiment involving a C_{60} molecule adsorbed on the Si(001) surface. The peculiarity of this example is that the molecule is large, spherical and is also strongly bound to the surface.

We note that manipulation of C_{60} on this or any other surface has not yet been reported with AFM. However, it was achieved with scanning tunnelling microscopy (STM), both along and across the troughs formed on this surface by Si–Si dimer rows running parallel to each other [36–38]. The process of STM manipulation of C_{60} on the Si(001) surface has also been modelled theoretically using ab initio DFT calculations [37–39]. These studies show that the most stable adsorption sites of the C_{60} on this surface are those in which the molecule makes four chemical bonds with four Si atoms of the surface. This is possible if the molecule is adsorbed either on the dimer row or between two nearest rows (in the trough). There is a large number of possible adsorption configurations [37,40,41] with adsorption energies ranging between -0.87 and -2.63 eV. Furthermore, it was shown [37, 42] that the movement of the molecule on the Si(001) surface consists of elementary rolling events in which the molecule pivots over the front two Si–C bonds, while the back two Si–C bonds are broken and then two new Si–C bonds are formed at the front, which bring the molecule to a new adsorption site. Essentially the same rolling mechanism takes place when the molecule is either pushed [38, 39] or pulled [43] by the STM tip.

The barrier for diffusion of C_{60} is high, ~ 2.5 eV, and it is the STM tip that pushes (or pulls) the molecule over this barrier (which is reduced by the presence of the tip). Interestingly, it was revealed that the role of the STM tip was not only in reducing the energy barriers for the molecule to roll between two configurations; in fact, it was found that the crucial factor in the STM

manipulation is that the tip keeps a continuous covalent contact with the molecule along the whole manipulation path [38].

Obviously, this type of manipulation would not be possible in NC-AFM experiments due to their very nature: because of the oscillations the tip cannot maintain a continuous contact with the molecule. Therefore, a different mechanism was suggested [44] whereby the molecule thermally diffuses (via rolling) between two neighboring sites, and the role of the tip is in reducing the corresponding energy barrier when the tip is in the proximity of the molecule. In essence, this is the same manipulation mechanism as in the pushing manipulation of a Pd adatom on the Mg (001) surface described earlier.

To investigate the energies of the tip–molecule interaction and the effect of this interaction on the energy barriers for the C_{60} manipulation in the presence of the tip, we performed a series of calculations using a self-consistent density functional theory-based tight binding (DFTB) code [45, 46].

We considered a series of positions of the molecule along the transition path connecting two stable adsorption sites designated as $t4c$ and $t4g$ [41] In both configurations, the molecule sits in the trough making four C–Si bonds with Si atoms of four Si dimers (see Fig. 12.8c). To model the rolling of the molecule from $t4c$ to $t4g$ without the tip (self-diffusion of the molecule), we used a constrained minimization method similar to that used in the earlier ab initio DFT calculations [37, 42]; however, a much bigger surface cell was used. Briefly, a single C atom of the C_{60} was displaced in small steps along the trough; the displacement coordinate of this atom was fixed, while the rest of the system, apart from the lowest two layers of the Si slab, was allowed to relax, including the other two coordinates of the displaced atom. In this way, the energy barrier in the absence of the tip and the sequence of intermediate configurations for the C_{60} movement from the configuration $t4c$ to $t4g$ were obtained.

To obtain the energy barriers for the C_{60} manipulation in the presence of the tip, we considered, for each position of the tip, the discrete set of intermediate configurations of the molecule during the transition $t4c \rightarrow t4g$ as discussed earlier. Single-point energies, without geometry relaxation, were calculated for all these intermediate configurations with a tip present in the system, for a range of tip positions. We used an atomically sharp (111)-oriented Si tip used in the earlier studies of C_{60} STM manipulation [38, 39, 43] and in other theoretical studies of AFM processes [20, 21, 47]. Two coordinates, Y and Z, defined in Fig. 12.8b, determine the tip position relative to the initial $t4c$ configuration of the molecule. The tip apex height Z above the top of the C_{60} ranged between -1.6 and $2.0\,\text{Å}$, and the lateral tip position Y behind the C_{60} along the trough (calculated with respect to the centre of mass of the C_{60} in its starting position) ranged between 1.0 and $6.6\,\text{Å}$; both Z and Y were incremented with a step of $0.2\,\text{Å}$.

The relative energies of the C_{60} movement from the configuration $t4c$ to $t4g$ in the presence of the tip are shown in Fig. 12.8a for the lateral tip position

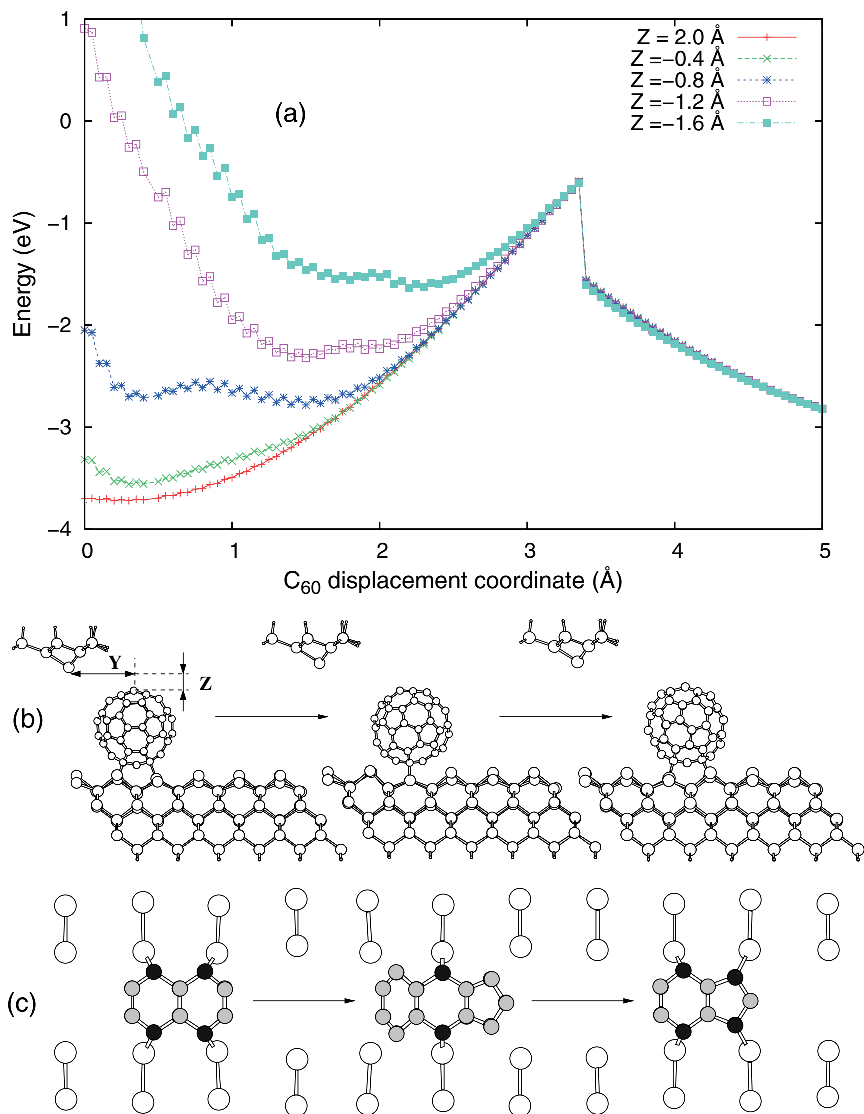

Fig. 12.8. (**a**) Energies of the C_{60} movement on the Si(001) surface in the presence of the tip at the lateral tip position $Y = 5$ Å and a range of tip heights Z. (**b**) The starting configuration of the C_{60}, the transition state and the final configuration, together with the definition of the coordinates Y and Z of the tip. (**c**) The top view of the bonding of the molecule to Si atoms of the surface dimers in the three geometries shown in (**b**); for clarity, only the lower part of the C_{60} is actually given. In (**c**), Si atoms are shown with *white circles*, while C atoms with *black* (C atoms bonded to Si) and *grey circles*

$Y = 5\,\text{Å}$ and a series of heights Z. The energies are calculated with respect to the isolated C_{60}, tip and the p(2 × 1) reconstructed Si(001) surface. The Figure also shows the initial and final adsorption configurations together with the intermediate transition (pivoting) configuration of the molecule.

We can see that the energies of the C_{60}-tip–surface system during the movement of the C_{60} depend strongly on the tip position. While the energy of the second (final) stable configuration and the maximum energy in the transition state (the pivoting point) practically do not depend on the position of the tip (at these points, the molecule is already far from the tip), the energy of the initial configuration and the actual position of the first energy minimum, when the molecule is rotated a little away from the tip, strongly depend on the tip position. The energy goes up if the tip is close to the C_{60} and down if it is far from it. Thus, the height of the energy barrier for the molecule going from the lowest-energy configuration to the transition state changes depending on the tip position: the barrier becomes smaller if the tip is low above the molecule (small Z), and larger, similar to the tip-free case, if the tip is high (large Z). Similarly, the Y position of the tip affects the initial lowest-energy configuration and hence the energy barrier: the barrier is higher if the tip is far from the molecule (large Y values) and lower if the tip is closer to the molecule.

We stress that these energies are semi-quantitative, since we used an approximate computational approach without relaxation of the system, however, they show the correct trend of energies as a function of the tip position. When the tip is closer to the molecule (small Z and/or Y), barriers become lower and it should be easier for the molecule to overcome them thermally.

We also calculated the force-field acting on the tip for each tip position during its oscillation, for use in explicit simulations of the NC-AFM tip movement. The vertical tip force can be calculated by numerical differentiation of the energy in the energy minima with respect to the tip height, Z. We find that the forces are repulsive for most of the tip positions near the C_{60} and become large when the tip is very close to the molecule. As the tip is placed further away from the molecule the interaction becomes weakly attractive and forces tend to zero.

Once the barriers for the molecule to move from one stable site to the other are available for each tip position, it is possible to calculate the corresponding transition rates. Therefore, the entire machinery of the dynamic calculation of the NC-AFM manipulation described in the earlier sections can be used.

For the real-time simulation of the manipulation of C_{60} by NC-AFM we used the KMC procedure implemented in the VAFM algorithm described earlier. Virtual AFM parameters used in our simulations follow the AFM setup used in an experimental study of the Si(001) surface [48]: $f_0 = 160$ kHz, spring constant $k = 40\,\text{N m}^{-1}$, $Q = 10{,}000$ and the amplitude set point $A_0 = 100\,\text{Å}$. The gain parameters for the amplitude control were $K_P^A = 0.1\,\text{N m}^{-1}$ and $K_I^A = 50\,\text{N m}^{-1}\,\text{s}^{-1}$, and for the distance control $K_P^D = 1 \times 10^{-13}\,\text{m s}$ and $K_I^D = 1 \times 10^{-9}\,\text{m}$. The tip–sample interaction consisted of a short-range

conservative force field obtained from our DFTB calculations as explained earlier, and of a macroscopic van der Waals force. The latter was calculated using a spherical tip model with the tip radius of 100 Å and a Hamaker constant of 1.165 eV estimated for the Si–Si interaction [49].

In the VAFM simulations, the vertically oscillating tip initially approaches the substrate from above, a large lateral distance away from the molecule, until the required frequency shift is achieved. Then, the tip is moved laterally towards the C_{60} along the line that passes through the centre of the molecule above the trough on the Si(001) surface (as a scan line). At each step of the VAFM simulation, the probability of a C_{60} jump is evaluated using the energy barriers calculated above. If the manipulation is successful, the molecule moves to its next stable adsorption site with the corresponding change of the tip force field and the subsequent reaction of the VAFM which would adjust the tip height in real time. After the first manipulation event, the tip continues to move forward until it comes close enough to the molecule so that it may jump again. This way, a continuous manipulation sequence can be calculated. In these calculations, to simulate each elementary translation of the molecule between two stable sites, we used the same force field and energy barriers as for the $t4c \rightarrow t4g$ elementary step. This is approximate since the initial and final configurations for each elementary translation may be different [37, 42]. Nevertheless, this approximation will not affect the qualitative picture of the NC-AFM manipulation we are interested in here.

Figure 12.9 shows the distance of closest approach of the tip (defined with respect to the top of the C_{60} molecule), the frequency shift and the dissipation signal obtained in the VAFM simulations of C_{60} manipulation at the fixed frequency shift of $\Delta f = -11$ Hz. The C_{60} centre of mass is initially at the point which corresponds to 4.8 Å on the horizontal axis of the graph. In Fig. 12.1a, we can see that after the tip has been lowered to the surface (the left part of the topography scan line), it approaches the molecule laterally and images it (the distance of closest approach slightly goes up) until the point indicated by the left arrow, when the molecule jumps. At this point, the tip is very close to the surface. However, after the molecule has jumped from the tip to the right by 3.8 Å (which is the lattice constant of the Si(001) surface),

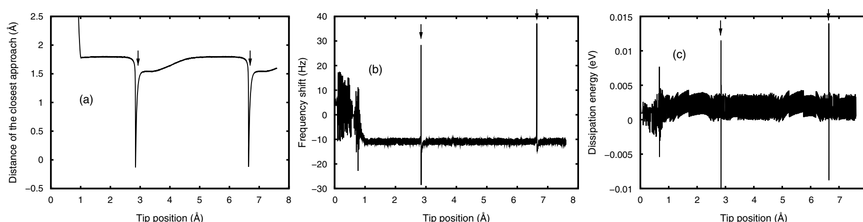

Fig. 12.9. (**a**) Distance of closest approach, (**b**) frequency shift and (**c**) dissipation signal during a VAFM scan of C_{60} on the Si(001) surface at $\Delta f = -11$ Hz and $T = 300$ K. The *arrows* in (**a**) show the points when manipulation occurs

the feedback system of VAFM raises the tip to the height of ∼1.6 Å above the molecule. A new lateral tip approach and imaging of the molecule takes place, until, 3.8 Å later, the tip again approaches the molecule close enough for manipulation to happen (the second arrow). Thus, the distance of closest approach (the topography scan line) has a characteristic shape with the abrupt dips of the tip height at the points of successful manipulation events.

The frequency shift line, Fig. 12.9b, after the initial stabilisation period during ∼1 Å of the tip displacement towards the molecule, also shows abrupt peaks at the points of manipulation. There are also peaks in the dissipation signal due to the manipulation events, see Fig. 12.9c, which can also serve to identify the event of successful C_{60} manipulation by NC-AFM.

We performed VAFM simulations at temperatures $T = 4$, 77, 300, and 600 K and found that the influence of the temperature on the VAFM scan lines (both the distance of the closest approach, frequency shift and dissipation signal) is small. The Y coordinate of the tip corresponding to the manipulation events is almost the same at different temperatures. On the other hand, the average value of Z (the height of the tip) at which manipulation is successful, depends strongly on temperature: lower values of Z are reached at lower temperatures. This is because lower temperatures require smaller barriers for the manipulation to occur.

To check the reproducibility of the C_{60} manipulation events, we simulated several scan lines, several hundred A long each, which resulted in successful manipulation of the molecule every time when the tip moved forward by one lattice constant. Thus, according to our calculations, the manipulation of C_{60} with an oscillating AFM tip is well reproducible, and the molecule can be manipulated over large distances. In real experiments, such long manipulation sequences may not be achievable due to possible competing processes, for example, the molecule jumping into the neighboring trough or onto the row and therefore getting away from the trajectory of the tip movement.

12.4 Discussion

We have presented calculations performed to simulate the NC-AFM imaging and manipulation of three qualitatively different systems, employing a novel multi-scale model of the entire imaging and manipulation process. The first of these involved a single atom adsorbed on an isotropic surface, which can be manipulated at low temperatures and is free to diffuse at higher temperatures. The second example consisted of an adsorbed molecule which was free to rotate on the surface, but confined to a single lattice position. The third example consisted of a very large molecule strongly bound to a surface, which can be manipulated by the tip at close approach. In the first and third examples, it was demonstrated how the adsorbate can be manipulated by the tip. In the first and second examples the effect of thermal motion on images was

determined and it was shown that rapid thermally induced structural changes can change the appearance of an image significantly.

The process of manipulation in this model is described in terms of the modification of the potential energy surface (and hence activation barriers) for the system by the tip at close approach. In both of the two examples of manipulation described earlier, this barrier modification arises due to the repulsive interaction between the tip and the adsorbate. In this case, the adsorbate always moves away from the tip – analogous to "pushing." However, in other systems manipulation may also occur via a "pulling" mechanism – where an object is manipulated towards the tip through an attractive interaction with the tip apex, as is the case with vacancy manipulation on the MgO (001) surface [29]. In both these cases, manipulation is achieved through modification of the barrier, however the mechanism causing the barrier modification is fundamentally different.

As shown above, our approach can be used to predict optimum protocols for manipulating adsorbed species on surfaces using only the force exerted by an AFM tip apex on the adsorbate. These may guide experimental efforts in achieving control over and adsorbed species: for example, our calculations indicate that manipulation protocols based on scanning provide only limited degree of control that strongly depends on the scanning direction. Choosing the manipulation trajectory and "hitting" the right spot allows a much higher degree of control over the manipulated atom. However, for all the systems, the mechanism for manipulating an object on the atomic scale will always be highly dependent on the exact nature of the termination of the tip apex, as is the case for contrast in images. Quantitative predictions for optimum manipulation protocols will only be accurate so long as the tip used matches that in the actual experiments, which is very difficult to achieve in practise.

The model that has been developed captures both the dynamical evolution of processes occurring in the tip–surface junction as well as the real-time response of the NC-AFM instrument, which represents an extension to the traditional method of modelling NC-AFM images in the conservative regime. This approach provides a reliable "window" into atomic-scale processes during imaging and manipulation, and combined with experimental data may give an important insight into atomic scale surface processes. Experiments exploiting this will significantly broaden the scope of application of the NC-AFM from analyzing static structures to retrieving information about dynamical processes.

Acknowledgements

We thank J. Polesel Maris and S. Gauthier for their contribution and advice with the Virtual AFM. We would also like to thank M. Watkins, M. Reichling and O. Custance for their advice and valuable discussions.

References

1. W.A. Hofer, A.S. Foster, A.L. Shluger, Rev. Mod. Phys. **75**, 1287 (2003)
2. A.S. Foster, C. Barth, A.L. Shluger, M. Reichling, Phys. Rev. Lett. **83**, 2373 (2001)
3. Y. Sugimoto, P. Pou, M. Abe, P. Jelinek, R. Perez, S. Morita, O. Custance, Nature **446**, 1287 (2007)
4. F.J. Giessibl, Rev. Mod. Phys. **75**, 957 (2003)
5. R. Garcia, R. Perez, Surf. Sci. Rep. **47**, 197 (2002)
6. Y. Sugimoto, M. Abe, S. Hirayama, N. Oyabu, O. Custance, S. Morita, Nat. Mater. **4**, 156 (2005)
7. Y. Sugimoto, P. Jelinek,P. Pou, M. Abe, S. Morita, R. Perez, O. Custance, Phys. Rev. Lett. **98**, 106104 (2007)
8. S. Hirth, F. Ostendorf, M. Reichling, Nanotechnology **17**, S148-S154 (2006)
9. L. Kantorovich, Phys. Rev. B **64**, 245409 (2001)
10. T. Trevethan, L. Kantorovich, Surf. Sci. **540**, 497 (2003)
11. J. Polesel-Maris, S. Gauthier, J. Appl. Phys. **97**, 1 (2005)
12. L.N. Kantorovich, J. Polesel-Maris, T. Trevethan, Virtual atomic force microscope simulation code. See EPAPS Document No. E-PRLTAO-98-020702 for the manual and further information.
13. J. Melcher, S.Q. Hu, A. Raman, Rev. Sci. Instrum. **79**, 061301 (2008)
14. G. Couturier, R. Boisgard, L. Nony, J.P. Aime, Rev. Sci. Instrum. **74**, 2726 (2003)
15. G.H. Enevoldsen, H.P. Pinto, A.S. Foster, M.C.R. Jensen, A. Kuhnle, M. Reichling, W.A. Hofer, J.V. Lauritsen, F. Besenbacher, Phys. Rev. B **78**, 045416 (2008)
16. A.S. Foster, A.L. Shluger, R.M. Nieminen, Nanotechnology **15**, S60 (2004)
17. R. Hoffmann, A.S. Foster, A. Baratoff, H.J. Hug, H.R. Hidber, H.J. Guntherodt, Phys. Rev. B **74**, 245426 (2006)
18. R. Hoffmann R, L.N. Kantorovich, A. Baratoff, H.J. Hug, H.J. Guntherodt, Phys. Rev. Lett. **92**, 146103 (2004)
19. A.S. Foster, A.Y. Gal, J.D. Gale, Y.J. Lee, R.M. Nieminen, A.L. Shluger, Phys. Rev. Lett. **92**, 036101 (2004)
20. R. Perez, M.C. Payne, I. Ŝtich, K. Terakura, Phys. Rev. Lett. **78**, 678 (1997)
21. L. Kantorovich, C. Hobbs, Phys. Rev. B **73**, 245420 (2006)
22. L. Kantorovich, Phys. Rev. B **75**, 064305 (2007)
23. G.H. Vineyard, J. Phys. Chem. Solids **3**, 121 (1957)
24. A.F. Voter, in *Radiation Effects in Solids*, ed. by K.E. Sickafus, E.A. Kotomin, B.P. Uberuaga (Springer, Berlin, 2007)
25. J.A. Venables, L. Giordano, J.H. Harding, J. Phys.: Condens. Matter **18**, S411 (2006)
26. Y. Long, N.X. Chen, H.Y. Wang, J. Phys.: Condens. Matter **17**, 6149 (2005)
27. L. Kantorovich, T. Trevethan, A. Foster, Self-Consistent Image Force Interaction code, http://www.cmmp.ucl.ac.uk/lev/codes/SciFi/manual-3-51/index.html
28. T. Trevethan, M. Watkins, L. Kantorovich, A.L. Shluger, Phys. Rev. B **76**, 085414 (2007)
29. T. Trevethan, M. Watkins, A. Shluger, L. Kantorovich, J. Polesel-Maris, S. Gauthier, Nanotechnology **17**, 5866 (2006)

30. N. Sasaki, S. Watanabe, M. Tsukada, Phys. Rev. Lett. **88**, 046106 (2002)
31. S. Gritschneder, M. Reichling, Nanotechnology **18**, 044024 (2007)
32. M. Watkins, A.L. Shluger, J. Phys. Chem. B (in press)
33. T.X. Sayle, S.C. Parker, C.R. Catlow, Surf. Sci. **316**, 329 (1994)
34. J. Gale, A. Rohl, Mol. Simul. **29**, 291 (2003)
35. M. Watkins, T. Trevethan, A.L. Shluger, L.N. Kantorovich, Phys. Rev. B **76**, 245421 (2007)
36. P. Moriarty, Y.R. Ma, M.D. Upward, P.H. Beton, Surf. Sci. **407**, 27 (1998)
37. N. Martsinovich, C. Hobbs, L. Kantorovich, R.H. Fawcett, M.J. Humphry, D.L. Keeling, P.H. Beton, Phys. Rev. B **74**, 085304 (2006)
38. N. Martsinovich, L. Kantorovich, R.H. Fawcett, M.J. Humphry, P.H. Beton, Small **4**, 765 (2008)
39. N. Martsinovich, L. Kantorovich, Nanotechnology **19**, 235702 (2008)
40. P.D. Godwin, S.D. Kenny, R. Smith, Surf. Sci. **529**, 237 (2003)
41. C. Hobbs, L. Kantorovich, J. Gale, Surf. Sci. **591**, 45 (2005)
42. D.L. Keeling, M.J. Humphry, R.H. Fawcett, P.H. Beton, C. Hobbs, L. Kantorovich, Phys. Rev. Lett. **94**, 146104 (2005)
43. N. Martsinovich, L. Kantorovich, Phys. Rev. B **77**, 115429 (2008)
44. N. Martsinovich, L. Kantorovich, in preparation
45. D. Porezag, T. Frauenheim, T. Köhler, G. Seifert, R. Kaschner, Phys. Rev. B **51**, 12947 (1995)
46. M. Elstner, D. Porezag, G. Jungnickel, J. Elsner, M. Haugk, T. Frauenheim, S. Suhai, G. Seifert, Phys. Rev. B **58**, 7260 (1998)
47. C. Hobbs, L. Kantorovich, Surf. Sci. **600**, 551 (2006)
48. T. Uozumi, Y. Tomiyoshi, Y. Sugawara, S. Morita, Appl. Surf. Sci. **188**, 279 (2002)
49. T.J. Senden, C.J. Drummond, Colloids Surf. A **94**, 29 (1995)

13

Magnetic Exchange Force Microscopy

Alexander Schwarz, Uwe Kaiser, Rene Schmidt, and Roland Wiesendanger

Abstract. Magnetic exchange force microscopy is a novel noncontact atomic-force microscopy based technique to image the arrangement of magnetic moments at surfaces with atomic resolution using sharp magnetic tips. Recent results obtained with iron coated silicon tips on two magnetically different antiferromagnetic surfaces are reviewed: NiO(001), an insulator, where the localized spin-carrying d-electrons are localized and interact via superexchange and Fe/W(001), a metal with delocalized itinerant spin-carrying d-electrons. The experimental findings are discussed with respect to the tip configuration, the role of an applied magnetic field, the magnitude of the magnetic signal as well as the interplay between chemical and magnetic forces.

13.1 Introduction

New developments in the field of magnetic imaging are fueled by demands of novel magnetic data storage and sensor devices as well as a fundamental interest in magnetic phenomena. This tendency is generally evident in the history of scanning probe microscopy. Thus, shortly after the invention of scanning tunneling microscopy (STM) in 1982 [1] and atomic force microscopy (AFM) in 1986 [2], their high resolution capabilities were utilized for magnetic sensitive imaging by implementing magnetic tips. One year after the invention of AFM, magnetic force microscopy (MFM) was established [3], and is now widely used [4]. It senses the long-range dipolar magnetostatic force between a ferromagnetic tip and a ferromagnetic sample. Imaging is performed in the constant height mode. Typical tip–sample distances are larger than 10 nm to separate the magnetic signal from topographical features. This relatively large scan height as well as the spreading of the stray field emanating from the tip limits the resolution to about 10 nm [5].

A much higher resolution is possible with spin-polarized scanning tunneling microscopy (SP-STM), which was invented in 1990 [6], and is nowadays routinely used to image metallic magnetic surfaces with atomic resolution [7]. A method based on force detection, which therefore can also be applied to

S. Morita et al. (eds.), *Noncontact Atomic Force Microscopy*,
NanoScience and Technology,
DOI: 10.1007/978-3-642-01495-6_13, © Springer-Verlag Berlin Heidelberg 2009

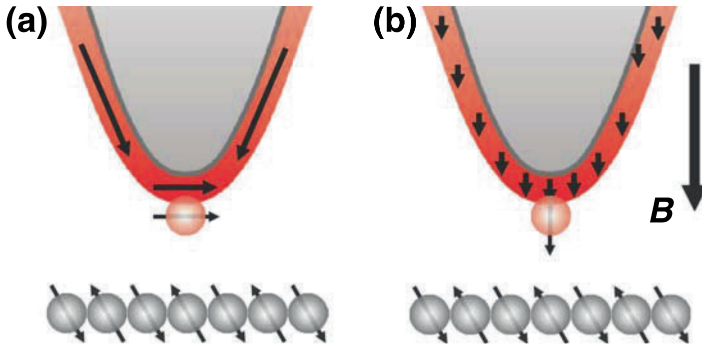

Fig. 13.1. Concept of MExFM on antiferromagnetic surfaces. The magnetic exchange force between tip and sample can be unambiguously discriminated from the chemical force, if atoms, which are chemically and structurally identical, possess oppositely oriented magnetic moments. (**a**) In-plane sensitive tip apex. If shape anisotropy dominates, ferromagnetic thin film tips are in this configuration. (**b**) Out-of-plane sensitive tip apex. Such a configuration can be realized by applying a sufficiently large external flux density B perpendicular to the surface

insulating surfaces, i.e., magnetic exchange force microscopy (MExFM), was proposed as early as 1991 [8]. However, it was not realized until 2007 [9], when atomic-scale imaging with magnetic sensitivity on the antiferromagnetic NiO(001) was reported for the first time.[1] The general set-up resembles that of an NC-AFM experiment [11], except that for MExFM the atomically sharp tip, which is approached close to the surface, has to be magnetically sensitive as well (cf. Fig. 13.1). At sufficiently small distances the spin-carrying electronic states of the foremost tip atom and the surface atom directly underneath overlap resulting in a significant magnetic exchange interaction. In the simplest approximation, the magnetic exchange interaction between magnetic moments of the foremost tip atom and the surface atom directly underneath, can be described by a Heisenberg model, i.e., $E_{\text{ex}} = -J\boldsymbol{S}_{\mathbf{t}}\boldsymbol{S}_{\mathbf{s}}$, where J is the exchange coupling constant between tip and sample spins $\boldsymbol{S}_{\mathbf{t}}$ and $\boldsymbol{S}_{\mathbf{s}}$, respectively. Magnitude and sign of the magnetic exchange energy E_{ex} depends on the relative orientation between $\boldsymbol{S}_{\mathbf{t}}$ and $\boldsymbol{S}_{\mathbf{s}}$ as well as on the the sign of J, i.e., positive for ferromagnetic coupling and negative for antiferromagnetic coupling. Hence, on antiferromagnetically ordered surfaces (see sketch in Fig. 13.1) an alternating contrast that varies on the atomic scale is expected.

[1] Previous reports of a magnetic contrast on NiO(001) [10] were ambiguous and probably even wrong, because (1) no magnetic signal could be seen in the raw data, (2) a Fourier transform to prove that the antiferromagnetic periodicity was really detected was never presented, and (3) the claimed magnetic contrast in an unit cell averaged image was seen between neighboring rows of oxygen atoms and not between neighboring rows of nickel atoms.

In the following sections, we review MExFM experiments performed at low temperatures in ultra-high vacuum with our home-built microscope (*Hamburg design*) [12] using ferromagnetic iron tips on two antiferromagnetic sample systems: NiO(001) [9,13] and the Fe monolayer on W(001) [14–16]. On these two samples chemical and magnetic interactions, which are both electron mediated and short-ranged, can be unambiguously distinguished from each other, because the antiferromagnetically ordered magnetic moments are located at chemically and structurally equivalent atomic sites. Moreover, an external magnetic field can be applied to align the magnetic moments of the ferromagnetic tip into a favorable direction without altering the antiferromagnetic structure of the sample. We will discuss mainly the experimental aspects of MExFM, e.g., contrast pattern, magnitude of chemical and magnetic signal, tip properties, etc. First-principles calculations based on density functional theory, which go far beyond the simple Heisenberg model mentioned earlier, are presented in Chap. 14 of this book [16].

13.2 Tip Preparation

The precise atomic configuration at the tip-apex region plays an important role for atomic resolution imaging, e.g., it will influence the magnitude of the corrugation amplitude and whether a certain chemical species appears as protrusion or depression. The situation is obviously even more complex, if one has to consider magnetic exchange interactions as well. Unfortunately, not much is usually known about the actual configuration of atoms at the tip apex. In fact, the sample is often much better characterized than the tip in most scanning probe experiments. Nevertheless, some general assumptions regarding the configuration at the tip-apex can be inferred.

The direction of the magnetic moment of the foremost tip atom depends on magnetic exchange energy, magneto-crystalline anisotropy energy, shape anisotropy energy and Zeeman energy. In bulk iron the easy axis of magnetic polarization is along ⟨001⟩-directions due to the magneto-crystalline anisotropy energy. If silicon tips are coated with a thin iron film, e.g., about 10–20 nm, shape anisotropy favors a magnetic polarization parallel to the surface at the tip apex (cf. Fig. 13.1a), but with no a priori preferred orientation within this plane [5]. A magnetic polarization perpendicular to the surface can be induced by an external magnetic flux density oriented parallel to the tip axis (cf. Fig. 13.1b). However, some of our experimental results indicate that even if the applied external magnetic flux density (e.g., 5 T) is larger than the saturation magnetic polarization of iron (2.187 T), the foremost tip atom is not necessarily aligned accordingly [13]. Probably, local magnetic anisotropy energies dominate at the tip-apex, where atoms are certainly not in a bulk-like configuration.

During atomic resolution imaging in NC-AFM experiments spontaneous tip changes are frequently observed due to the strong interaction between tip

and sample at small distances. Particularly, one tip configuration might be suitable for atomic resolution, but another one might not be, e.g., because the tip-apex does not end in a single atom. In MExFM experiments tip changes can additionally switch between magnetically sensitive and magnetically insensitive tip configurations. For example, after a collision between tip and sample either a non-magnetic adsorbate could be picked up or all magnetic atoms at the tip apex could be lost. However, even if the tip apex is covered with magnetic material and atomically sharp, it might still be impossible to resolve the magnetic structure. For example, the direction of the magnetic moment of the tip is not stable, e.g., it rotates randomly on a time scale much faster than the data acquisition time or it aligns itself always parallel (or antiparallel) to the surface magnetic moments. Another possibility is a too low signal-to-noise ratio. For example, the angle between magnetic moments of foremost tip-apex atom and surface atoms could be close to 90°, the magnetic moments could be too small or the tip–sample distance could be too large.

Although spontaneous unwanted tip changes are bothersome in general, intented collisions between tip and sample can be utilized to provoke tip changes. This is routinely done in NC-AFM experiments to achieve atomic resolution with an initially blunt tip-apex. Similarly, it is also possible to obtain a magnetically sensitive tip configuration in this manner. Whatever the real configuration at the tip-apex is, if atomic resolution is obtained in the noncontact regime, one can at least infer that the tip-apex is atomically sharp.

The easiest way to unambiguously distinguish between magnetic insensitive and magnetic sensitive tip configurations is to perform measurements on surfaces, where structurally and chemically identical atoms are antiferromagnetically ordered. On ferromagnetic surfaces the situation is more delicate. One way is to look for domain walls, where the direction of the magnetic moments change continuously. Another possibility would be to either reverse the magnetic polarization of the sample or the tip (but not both simultaneously), which would result in a contrast reversal between two MExFM images recorded on precisely the same area. However, to assure registry on the atomic level, a marker defect, e.g., a vacancy or an adsorbate, has to be present in the imaged area.

13.3 NiO(001)

Nickel oxide (cf. Fig. 13.2a), crystallizes in the rock salt structure ($a = 417\,\text{pm}$) and exhibits a nearly perfectly bulk terminated (001) surface [17] with a (1×1) chemical surface unit cell. Below its Néel temperature of 525 K, it is a collinear antiferromagnet. Magnetic moments point in $\langle 211\rangle$ directions and are coupled ferromagnetically in $\{111\}$ planes, which are stacked in an antiferromagnetic order due to the superexchange of the localized nickel d-electrons via the bridging oxygen atoms. Since the magnetic order is bulk terminated as well [18], the (001) surface shows a row-wise antiferromagnetic order with a (2×1)

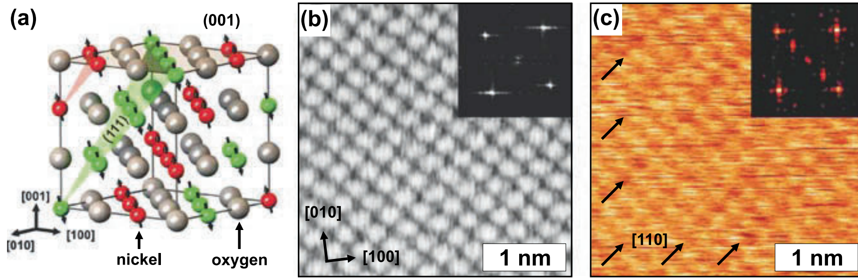

Fig. 13.2. (**a**) Rock salt structure of nickel oxide. The (001) surface exhibits a checkerboard pattern of Ni- and O-atoms with an antiferromagnetic ordering between neighboring rows of Ni-atoms along ⟨110⟩-directions. (**b**) NC-AFM image on NiO(001). Oxygen atoms are imaged as protrusions and nickel atoms as depressions. The fourier transform (*inset*) shows four peaks, representing the chemical surface unit cell. (**c**) MExFM image of NiO(001). Neighboring rows of depressions, i.e., nickel atoms, exhibit slightly different contrast levels, which shows up as an additional pair of peaks in the fourier transform (inset). Parameters: (**b**) $f_0 = 165\,\text{kHz}$, $c_z = 36.0\,\text{N/m}$, $A_0 = \pm 15\,\text{nm}$, $\Delta f = -11.0\,\text{Hz}$ and (**c**) $B = 5\,\text{T}$, $f_0 = 159\,\text{kHz}$, $c_z = 36.0\,\text{N/m}$, $A_0 = \pm 6.7\,\text{nm}$, $\Delta f = -23.4\,\text{Hz}$

magnetic surface unit cell. Clean NiO(001) samples with some 10 nm wide and clean terraces separated by monatomic steps (cf. Fig. 13.2a), are prepared by in situ cleavage of single crystals and subsequent heating to remove surface charges.

Figure 13.2b displays a typical NC-AFM image recorded with a non-magnetic tip [19–21]. The arrangement of maxima and minima as well as the four peaks in the Fourier transform, cf. inset, clearly reflects the (1×1) chemical surface unit cell. It is most likely that maxima correspond to the position of the oxygen atoms, where the total valence charge density is largest [22], and hence the electron mediated chemical interaction responsible for the atomic scale contrast is expected to be largest as well [23]. The chemical corrugation amplitude of about 20 pm is well above the noise level of our instrument.

On the other hand, Fig. 13.2c shows an MExFM image recorded with an iron coated tip. First, the overall corrugation amplitude of about 5 pm is much lower compared to Fig. 13.2a. Second, the raw data exhibit a small contrast between neighboring rows of minima, which shows up as additional pair of peaks in the Fourier transform, cf. inset, and corresponds to the larger (2×1) magnetic surface unit cell. Even though the signal-to-noise ratio in the raw image data is low, these two peaks in the Fourier transform unambiguously prove the detection of the antiferromagnetic structure. To determine the corrugation amplitude quantitatively, we performed a unit cell averaging procedure.[2] For a better visualization of the periodicity of the antiferromag-

[2] All unit cells in the raw data of a periodic image can be averaged to obtain a single averaged unit cell of much better signal-to-noise ratio. This procedure to enhence the image quality is well established in the field of electron microscopy.

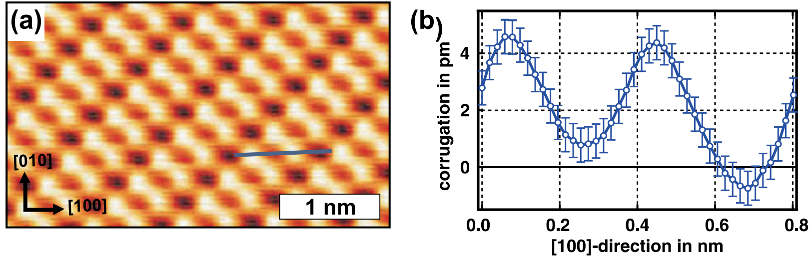

Fig. 13.3. (**a**) Unit cell averaged image of the raw data displayed in Fig. 13.2c. (**b**) Line section along the [001] direction of NiO(001). The magnetic contrast between neighboring rows of Ni-atoms (minima) is about 1.5 pm. No contrast is visible between neighboring rows of O-atoms (maxima)

netic structure the image in Fig. 13.3a is tiled from the averaged unit cell and clearly shows the row-wise modulation due to the magnetic exchange interaction between the ferromagnetic iron tip and the antiferromagnetic NiO(001) surface. From the line section along the [100]-direction, cf. Fig. 13.3b, a chemical corrugation amplitude of $z_{\text{chem}} = \frac{1}{2}|(\text{Ni}\uparrow -\text{O}) - (\text{Ni}\downarrow -\text{O})| = 4.5\,\text{pm}$ and a magnetic corrugation amplitude of $z_{\text{mag}} = |\text{Ni}\uparrow -\text{Ni}\downarrow| = 1.5\,\text{pm}$ can be measured.

Interestingly, we found that on approaching the surface by adjusting larger negative frequency shifts we first see only a chemical contrast but at smaller distances the magnetic contrast appears as additional modulation on top of the nickel atoms [9]. The origin of this distance dependent contrast are the localized spin-carrying *d*-electrons, which do not reach as far as the *s*- and *p*-electrons into the vacuum region. Peculiarly, the chemical contrast in the MExFM experiment, cf. Fig. 13.2b, is much lower than in the normal NC-AFM experiments, cf. Fig. 13.2a. Since we always observe a rather small chemical corrugation amplitude in our MExFM experiment on NiO(001), tips with a small chemical interaction might be required to approach close enough to the surface to probe the localized *d*-electrons. A large chemical interaction might otherwise lead to a tip instability before any magnetic signal is detectable.

The contrast pattern in Fig. 13.2c is the regular MExFM contrast on NiO(001), which is in qualitative agreement with theoretical predictions of a significant magnetic exchange force between the magnetic moments of a single atom iron tip and the nickel atoms in NiO(001) [24]. However, in Fig. 13.4a a modulation of the corrugation height is not only visible between neighboring rows of nickel atoms, but also between neighboring rows of oxygen atoms. We can interpret this contrast pattern in terms of a magnetic double tip (see [13] for a detailed discussion). If two magnetic atoms next to each other contribute significantly to the atomic scale contrast, one of them could interact magnetically with a nickel atom while the other one is already on top of an oxygen atom. The presence of a magnetic double tip is supported by two peculiar features visible in the line section along the [100]-direction, cf. Fig. 13.4b: (1)

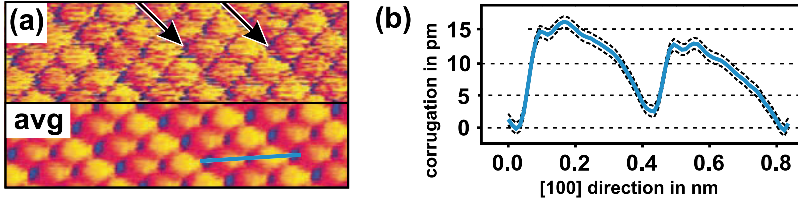

Fig. 13.4. (**a**) MExFM image (*top*) and the corresponding unit cell averaged image (*bottom*) obtained with a magnetic double tip on NiO(001). The *arrows* indicate the darker rows of Ni-atoms. (**b**) Line section along the [100] direction. The apparent magnetic contrast on neighboring oxygen rows and the asymmetric shape of the minima, which are also much narrower than the wide maxima, indicate the presence of a wedge-shaped blunt two atom tip apex. Parameters: $B = 5\,\mathrm{T}$, $f_0 = 159\,\mathrm{kHz}$, $c_z = 34.0\,\mathrm{N/m}$, $A_0 = \pm 6.3\,\mathrm{nm}$, $\Delta f = -20.5\,\mathrm{Hz}$

the maxima are wider than the minima and (2) the line shape is asymmetric. Feature (1) indicates a blunt tip and feature (2) a wedge-shaped tip. Subsuming (1) and (2) a tip apex consisting of two laterally and vertically displaced Fe atoms would explain the observed line shape. Note that none of these features are found in the symmetric line section of Fig. 13.3b, which indicates a single atom tip-apex. We can exclude a superexchange mechanism between the nickel atoms below the surface oxygen atoms and the iron tip as well as a direct magnetic exchange due to a small magnetic moment on the oxygen atoms, as it has been predicted in [24], because such a modulation must be always visible, but it is, e.g., not visible in Fig. 13.2c.

In Sect. 13.2 we already pointed out that even an external flux density of 5 T, which is much larger than the saturation magnetic polarization of the tip material, is not necessarily sufficient to fully align the magnetic moment of the foremost tip atom. This is shown in Fig. 13.5. Both images show the same area on NiO(001) with an atomic scale defect in the lower left corner, which can be used as a marker. Comparing (a) and (b) one can clearly detect a contrast reversal, i.e., darker rows of nickel atoms in (a) appear brighter in (b) and vice versa. Such a contrast reversal can be explained by a change of the orientation of the foremost tip atom. Since we neither observed a bump or a hole in the imaged area, we have no indication of a material transfer between tip and surface. In this context, it is important to remember that atomic structure and orientation of atomic magnetic moments are interrelated via spin–orbit coupling, which is the origin of the magneto-crystalline anisotropy energy. Hence, a reconfiguration in the tip apex region was most likely responsible for the reorientation of the magnetic moment of the foremost tip apex atom.

Note that the magnetic moments on NiO(001) are canted. Thus, if the magnetic moment at the tip-apex is canted as well, a contrast reversal does not require a flip of the magnetic moment of the foremost tip atom by 180° [13].

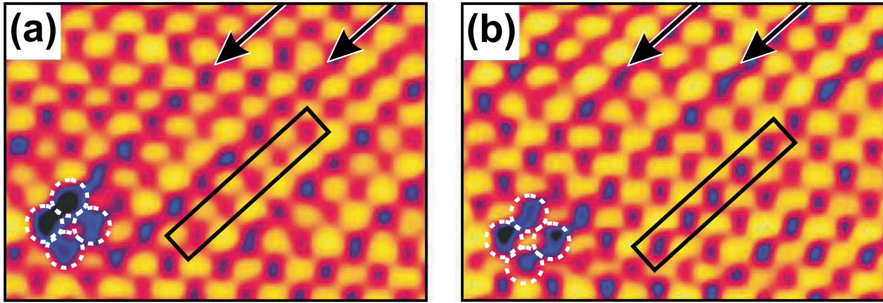

Fig. 13.5. Two low pass filtered MExFM images of NiO(001). After recording image (**a**) and before recording image (**b**) a tip reconfiguration occurred, which resulted in a reversal of the magnetic contrast, i.e., darker rows of nickel atoms appear brighter and vice versa with respect to the *encircled marker* defect in the *lower left corner* (see *arrows* and *rectangles* in the images). Parameters: $B = 5\,\mathrm{T}$, $f_0 = 159\,\mathrm{kHz}$, $c_z = 34.0\,\mathrm{N/m}$, $A_0 = \pm 6.3\,\mathrm{nm}$, $\Delta f = -21.0\,\mathrm{Hz}$

Furthermore, even a large external magnetic flux density does not exclude such a reorientation of the magnetic moment due to a reconfiguration, because the magnetic exchange energy between neighboring atoms at the tip apex can be much larger than the Zeeman energy of the external flux density.

13.4 Fe/W(001)

As a second specimen, we studied the iron monolayer (ML) on tungsten. Unlike the insulating NiO(001) sample Fe/W(001) is an itinerant metallic system. Surprisingly, an ML of Fe pseudomorphically grown on W(001) is not ferromagnetic. Due to strong hybridization with the substrate, it exhibits an antiferromagnetic c(2×2) order with out-of plane anisotropy, cf. Fig. 13.6a [25]. However, already two atomic layers show the prototypical ferromagnetism of this material. In the ML of Fe electrons are not as strongly correlated as in NiO. Hence, density functional calculations are less complex, which allows implementing realistic multi-atom tips and relaxation effects [14, 14a, 15]. Moreover, since an Fe coated tip is used here, only one relevant chemical species is present in this tip–sample system leading to an experimentally easier situation than for NiO(001). As an itinerant two-dimensional antiferromagnetic metal with delocalized *d*-electrons, the Fe ML is magnetically quite different from the insulating NiO, where the *d*-electrons are strongly localized and coupled via superexchange. Therefore, it is very interesting to compare the experimental findings for both systems with each other.

To prepare a suitable sample it is mandatory to start with a clean W(001) substrate. This is achieved by flashing the substrate at 2,100°C for 10 s and by annealing at 1,300°C in oxygen ($\approx 10^{-6}$ mbar). After such a treatment of the substrate, we deposited slightly more than one atomic layer of Fe at

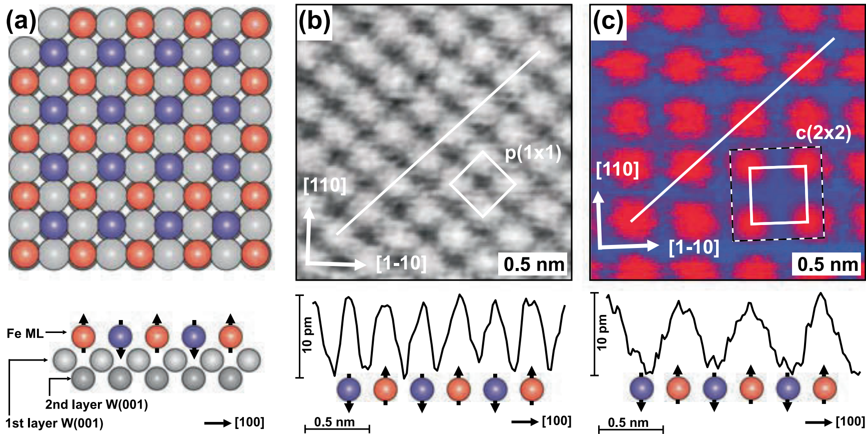

Fig. 13.6. (**a**) Structure of the Fe/W(001) sample. The ML of Fe grows pseudomorphically on W(001) as shown in the side view and exhibits a checkerboard antiferromagnetic order. (**b**) NC-AFM image of the Fe ML obtained with a magnetically insensitive tip. The contrast pattern reflects the p(1 × 1) chemical unit cell, i.e., every Fe atom is represented by a protrusion, (**c**) MExFM image of the Fe ML. The c(2 × 2) arrangement of protrusions with respect to the underlying tungsten substrate reflects the magnetic surface unit cell obtained with a magnetically sensitive tip. The enframed inset displays the result of a simulation employing density functional theory (DFT) based on first principles calculations, which is in very good agreement with the experimental data [14–16]. Note that the magnetic signal of 10 pm is much larger than on NiO(001), cf. line section. Parameters: (**b**) $B = 5\,\mathrm{T}$, $f_0 = 156\,\mathrm{kHz}$, $c_z = 32.5\,\mathrm{N/m}$, $A_0 = \pm 5.0\,\mathrm{nm}$, $\Delta f = -28.5\,\mathrm{Hz}$; (**c**) same except $\Delta f = -14.8\,\mathrm{Hz}$

an elevated temperature of about 600 K onto the substrate. As a result, the substrate is completely covered by a pseudomorphically grown wetting layer, i.e., the antiferromagnetic ML with out-of-plane anisotropy. Excess iron forms ferromagnetic second layer islands with fourfold in-plane anisotropy [26] and stripes along substrate steps (step flow growth).

Atomically resolved data on the Fe ML revealed two different contrast patterns. In Fig. 13.6b protrusions are arranged in a p(1 × 1) array with respect to the W(001) substrate. Thus, every Fe atom is imaged as protrusion as expected for a purely chemical contrast of a pseudomorphically grown ML. On the other hand, protrusions in Fig. 13.6c are arranged in a c(2 × 2) array with respect to the W(001) substrate, i.e., only every second Fe atom is imaged as protrusion. This contrast pattern reflects the symmetry of the antiferromagnetic surface unit cell. Both images were actually recorded with the same iron coated tip, but in between tip changes occurred. These tip changes resulted in a magnetically sensitive, cf. Fig. 13.6b, and a magnetically insensitive, cf. Fig. 13.6c, tip configuration. Possible mechanisms for such tip changes are explained in Sect. 13.2.

One important and very encouraging result on the Fe ML is the large magnetic corrugation amplitude of 10 pm, cf. line section of Fig. 13.6c. It is in fact as large as the chemical corrugation amplitude, cf. line section of Fig. 13.6b. Compared to the magnetic corrugation amplitude of 1.5 pm on NiO(001), such a large signal is readily detectable and promising with respect to future investigations using MExFM (see Sect. 13.5). The origin of the larger signal is the farther extension of the spin-carrying *d*-electrons into the vacuum region of the Fe ML compared to the localized *d*-electrons in nickel oxide. Another possible reason is the out-of-plane orientation of the magnetic moments of the Fe ML. If the tip magnetic moments are oriented parallel to the external magnetic flux density, i.e., perpendicular to the surface, the resulting magnetic signal is larger than for canted magnetic moments as on NiO(001).

Comparing the line sections of MExFM data on NiO(001), cf. Fig. 13.2c, and the Fe ML on W(001), cf. Fig. 13.6c, reveals a surprising difference. On NiO(001) the magnetic exchange interaction is added on top of the chemical interaction, i.e., oxygen atoms are imaged as protrusions and nickel atoms are imaged as depressions, but with a height modulation on neighboring rows of nickel atoms, which reflects the row-wise antiferromagnetic order. On the other hand, only every second iron atom of the ML is imaged as protrusion. This is surprising, because magnetic exchange and chemical interaction are both electron mediated and of short range. Therefore, each iron atom should appear as protrusion due to the chemical interaction and the additional magnetic exchange interaction should result in a height modulation, which reflects the checkerboard type antiferromagnetic order.

The origin of this peculiar contrast pattern is revealed by theoretical studies, which are presented in more detail in Chap. 14 of this book [16]. By employing a multiatom iron tip with magnetic moment pointing toward the surface, distance dependent force curves could be calculated on the three high symmetry points, i.e., on top of iron atoms with parallel and antiparallel magnetic moments, respectively, and in between at the hollow sites. In an intermediate distance regime these curves exhibit a cross over, where the total short-range electron mediated force, i.e., chemical plus magnetic exchange force, on the parallel and hollow site is equal. Therefore, only the iron atoms with antiparallel aligned magnetic moments appear as protrusions. Using these force data and long-range van der Waals forces stemming from a tip with 8 nm radius the experimentally observed contrast pattern could be reproduced, cf. enframed inset in Fig. 13.6c. Thus, we can conclude that the missing maxima on every second iron atom are due to a competition between magnetic exchange and chemical interaction, but not because of an absence of the latter [14].

13.5 Future Perspectives

What can be expected in future from MExFM? One can think of many interesting experiments, e.g., investigating the structure of domain walls or more complex magnetic structures like spin spirals in electrically insulating systems with atomic resolution. Note that recently such spin spirals have been observed on metallic surfaces by SP-STM and attracted a lot of attention [27]. Magnetic sensitive force spectroscopy allows to study the distance dependence of the various types of magnetic exchange forces (e.g., superexchange, double exchange, RKKY, etc.), which can be directly compared with theory. Moreover, apart from MExFM only SP-STM can obtain a magnetic contrast with atomic resolution, but the latter can only be applied to electrically conductive surfaces. Such a limitation does not exist for a force based technique, which is particularly useful, if magnetic properties of single atoms or molecules on surfaces should be investigated. On metallic substrates strong hybridization occurs, which can be avoided if insulating substrates are utilized instead. Even on conductive samples MExFM is very useful, because it is sensitive to a different quantity, i.e., forces instead of the local density of states (LDOS). Hence, complementary information can be extracted.

We would like to thank U.H. Pi and acknowledge financial support from the Deutsche Forschungsgemeinschaft (SFB 668-A5 and Graduiertenkolleg 611).

References

1. G. Binnig, H. Rohrer, Helv. Phys. Acta. **55**, 726 (1982)
2. G. Binnig, C.F. Quate, C. Gerber, Phys. Rev. Lett. **56**, 930 (1986)
3. Y. Martin, H.K. Wickramasinghe, Appl. Phys. Lett. **50**, 1455 (1987)
4. U. Hartmann, Annu. Rev. Mater. Res. **29**, 53 (1999)
5. A. Schwarz, R. Wiesendanger, Nano Today **3**, 28 (2008)
6. R. Wiesendanger, G. Güntherodt, H.J. Güntherodt, R.J. Gambino, R. Ruf, Phys. Rev. Lett. **65**, 247 (1990)
7. M. Bode, Rep. Prog. Phys. **66**, 523 (2003)
8. R. Wiesendanger, D. Bürgler, G. Tarrach, A. Wadas, D. Brodbeck, H.J. Güntherodt, G. Güntherodt, R.J. Gambino, R. Ruf, J. Vac. Sci. Technol. B **9**, 519 (1990)
9. U. Kaiser, A. Schwarz, R. Wiesendanger, Nature **446**, 522 (2007)
10. H. Hosoi, K. Sueoka, K. Hayakawa, K. Mukasa, in *Noncontact Atomic Force Microscopy*, ed. by S. Morita, R. Wiesendanger, E. Meyer (Springer, Berlin, 2002), p. 126; Hosoi, K. Sueoka, K. Mukasa, Nanotechnology **15**, 505 (2004)
11. F.J. Giessibl, in *Noncontact Atomic Force Microscopy*, ed. by S. Morita, R. Wiesendanger, E. Meyer (Springer, Berlin, 2002), p. 11
12. M. Liebmann, A. Schwarz, S.M. Langkat, R. Wiesendanger, Rev. Sci. Instrum. **73**, 3508 (2002)
13. U. Kaiser, A. Schwarz, R. Wiesendanger, Phys. Rev. B **77**, 104418 (2008)
14. R. Schmidt, C. Lazo, H. Hölscher, U.H. Pi, V. Caciuc, A. Schwarz, R. Wiesendanger, and S. Heinze, Nano Lett., **9**, 200 (2009)

15. C. Lazo, V. Caciuc, H. Hlscher, and S. Heinze, Phys. Rev. B **78**, 214416 (2008)
16. C. Lazo, V. Caciuc, H. Hlscher, and S. Heinze, in *First Principles Simulation of Magnetic Exchange Force Microscopy on Fe/W(001)*, ed. by S. Morita, F.-J. Giessibl, R. Wiesendanger (Springer-Verlag Berlin-Heidelberg, 2009) pp. 287–302
17. T. Okazawa, Y. Yagi, Y. Kido, Phys. Rev. B **67**, 195406 (2003)
18. F.U. Hillebrecht, H. Ohldag, N.B. Weber, C. Bethke, U. Mick, M. Weiss, J. Bahrdt, Phys. Rev. Lett. **86**, 3419 (2001)
19. H. Hosoi, K. Sueoka, K. Hayakawa, K. Mukasa, Appl. Surf. Sci. **157**, 218 (2000)
20. W. Allers, S. Langkat, R. Wiesendanger, Appl. Phys. A **72**, S27 (2001)
21. R. Hoffmann, M.A. Lantz, H.J. Hug, P.J.A. van Schendel, P. Kappenberger, S. Martin, A. Baratoff, H.J. Güntherodt, Phys. Rev. B **67**, 085402 (2003)
22. M.R. Castell, S.L. Dudarev, G.A.D. Briggs, A.P. Sutton, Phys. Rev. B **59**, 7342 (1999)
23. S. Ciraci, A. Baratoff, I.P. Batra, Phys. Rev. B **41**, 2763 (1990)
24. H. Momida, T. Oguchi, Surf. Sci. **590**, 42 (2005)
25. A. Kubetzka, P. Ferriani, M. Bode, S. Heinze, G. Bihlmayer, K. von Bergmann, O. Pietzsch, S. Blügel, R. Wiesendanger, Phys. Rev. Lett. **94**, 087204 (2005)
26. K. von Bergmann, M. Bode, R. Wiesendanger, Phys. Rev. B **70**, 174455 (2004)
27. M. Bode, M. Heide, K. von Bergmann, P. Ferriani, S. Heinze, G. Bihlmayer, A. Kubetzka, O. Pietzsch, S. Blgel, R. Wiesendanger, Nature **447**, 190 (2007)

14

First-Principles Simulation of Magnetic Exchange Force Microscopy on Fe/W(001)

Cesar Lazo, Hendrik Hölscher, Vasile Caciuc, and Stefan Heinze

Abstract. Based on density functional theory, we analyze the contrast mechanisms in magnetic exchange force microscopy (MExFM) and present first-principles calculations of the magnetic exchange force between an iron tip and an Fe monolayer on W(001), which is a model system of a two-dimensional antiferromagnet. Our study reveals that a single Fe atom is not an adequate tip model and we use Fe pyramids of five and 14 atoms. We find that the magnetic exchange forces on the tip atoms in the nearest layer from the apex atom are non-negligible and can be opposite to that on the apex atom. In addition, the apex atom interacts not only with the surface atoms underneath but also with the nearest-neighbors in the surface. We show that structural relaxations of tip and sample due to their interaction depend sensitively on the magnetic alignment of the two systems. As a result, the onset of significant magnetic exchange forces is shifted toward larger tip–sample separations which facilitates their detection in MExFM.

14.1 Introduction

Recent advances in magnetic microscopy techniques [1, 2] allowed spectacular new insights into magnetic properties of nanostructures at surfaces. Among these the spin-polarized scanning tunneling microscope (SP-STM) fascinated many scientists because it is capable to image magnetic structures with atomic resolution [3–9]. However, a scanning tunneling microscope is limited to conducting surfaces and it took many years until the idea presented by Wiesendanger et al. [10] in 1990 was realized: the direct measurement of the magnetic exchange forces between a magnetic tip and a nonconductive magnetic sample. This technique, denoted as magnetic exchange force microscopy (MExFM)[1] is in principle applicable to all magnetic surfaces, i.e., conducting

[1] Please, note that MExFM is different to the often applied *magnetic force microscopy* (MFM) which is well suited to image ferromagnetic domain structures but cannot achieve atomic resolution because data acquisition is based on the detection of long-range magnetostatic forces.

S. Morita et al. (eds.), *Noncontact Atomic Force Microscopy*,
NanoScience and Technology,
DOI: 10.1007/978-3-642-01495-6_14, © Springer-Verlag Berlin Heidelberg 2009

as well as insulating systems, which is a valuable advantage compared to the SP-STM technique, e.g., to study molecular magnets. However, the interpretation of measurements by MExFM is not straightforward and the development of theoretical models and tools to understand them is essential.

In the past, first-principles calculations based on density functional theory (DFT) have become indispensable and versatile tools to study nanostructures and to gain an understanding of their electronic, structural, chemical, and magnetic properties. However, within these methods one is frequently limited by the size of the system which can be considered and the level of approximation which is used. To model atomic force microscopy (AFM) experiments, it is essential to calculate the forces between the sample and the tip. For this purpose one has to include, besides the sample, some kind of model tip in the calculations. This fact makes the first-principles simulation of AFM experiments much more challenging than the simulation of STM experiments, in particular, if one allows structural relaxations of tip and sample which can often be crucial. Such realistic theoretical modelling of the interaction between tip and sample has become an integral and essential part of many AFM experiments [11–16]. Nevertheless, there have been only few studies in the past focussing on MExFM [17–22].

The first theoretical study of MExFM was based on a semi-empirical tight-binding calculation by Ness et al. [17] and showed that the magnetic exchange forces between an iron tip and a chromium or a nickel surface should be well below 1 nN. Nonetheless, such forces should be detectable with an atomic force microscope. In this work, however, relaxation of the apex atom and the sample were neglected, and only the *d*-electrons of the system were considered. Later on, Nakamura et al. [18, 19] employed a more sophisticated approach based on DFT to calculate the magnetic exchange force between two Fe(001) surfaces. Forces of a few nN were obtained at a distance of 3 Å. Additionally, it was found that the forces exhibited an oscillatory RKKY-interaction-like behavior as a function of distance. Even above 4 Å, the forces should still be within the experimental resolution limit of AFM. A more recent first-principles study [21, 22] of the magnetic exchange force between a single-iron atom, representing the tip, and the NiO(001) surface has been carried out within the framework of DFT. The calculated MExFM images show a magnetic contrast on the atomic-scale when the single Fe atom tip approaches the surface within 1 Å above the contact point. Therefore, this work predicted the possibility of using MExFM for magnetic imaging with atomic resolution.

These theoretical studies encouraged many experimental attempts to demonstrate MExFM, focussing especially on the (001) surface of the antiferromagnetic insulator NiO [23–28]. However, it took many years before the first successful experiment for NiO(001) was reported [29, 30].

Here, we apply density functional theory using the highly accurate full-potential linearized augmented plane wave (FLAPW) method to study the interaction of a magnetic tip and a magnetic sample which is measured in MExFM but also occurs in SP-STM. We consider one monolayer Fe on W(001) as a model sample system which exhibits a c(2$\times$2) antiferromagnetic structure

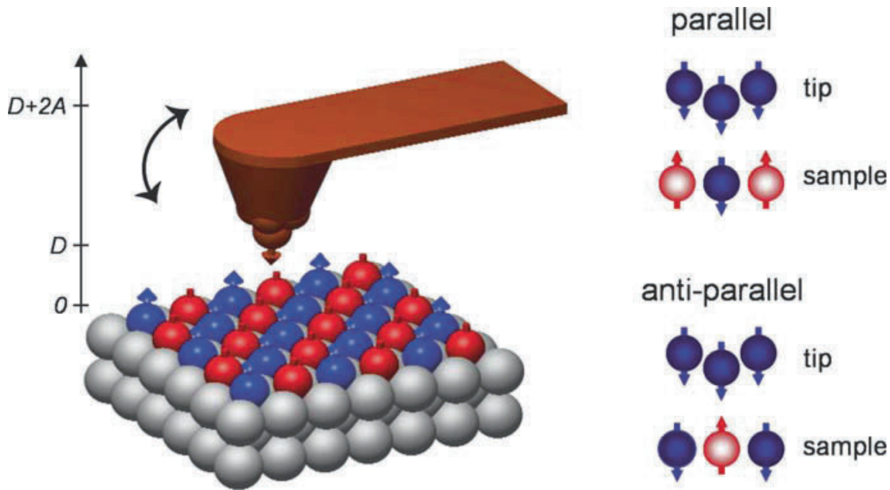

Fig. 14.1. The experimental set-up in magnetic exchange force microscopy. A cantilever with magnetic coating (a few layers of iron for example) oscillates close to the sample surface. The tip–sample forces cause a change of the resonance frequency of the cantilever. Under optimal imaging conditions (UHV, low temperatures, ...) the difference of the forces acting between a parallel or antiparallel configuration of the magnetic moments of the tip-apex and the sample surface atoms may be detected

(Fig. 14.1) and has been resolved by both SP-STM [6] and MExFM [31, 32]. The iron tip is modeled by an Fe pyramid consisting of five atoms and structural relaxations of both tip and sample due to their interaction have been included. Our results show that the relaxations depend sensitively on the magnetic configuration between tip and sample, i.e., whether the tip magnetization is parallel or antiparallel to the moment of the Fe surface atom below. We calculate the magnetic exchange forces, and demonstrate that their measurement in MExFM for this tip–sample system is feasible and even facilitated due to relaxations as their onset is shifted to larger tip–sample separations. We analyze the dependence of the calculated magnetic exchange forces on the tip size and find that a single Fe atom is an inadequate tip model while increasing the tip to 14 atoms changes the forces only quantitatively. By simulating MExFM images, we can explain the contrasts observed in recent experiments [31, 32] and show that they are due to a competition between chemical and magnetic forces.

14.2 Computational Method

To gain insight into the magnetic interactions which occur in an MExFM experiment between an Fe tip and a monolayer of Fe on W(001), we have performed first-principles calculations based on density functional theory within the generalized gradient approximation (GGA) [33] to the exchange-

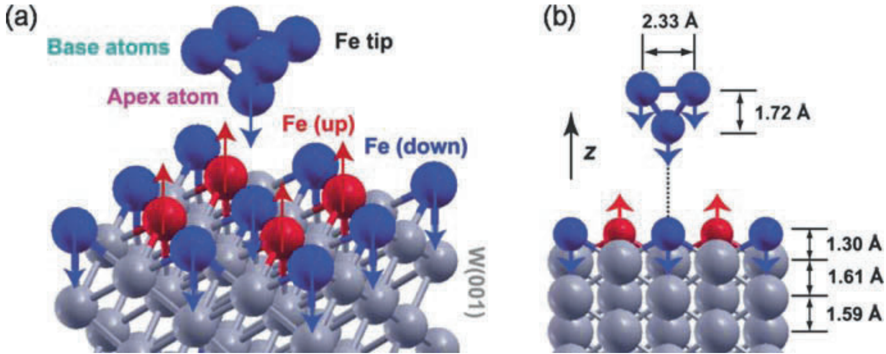

Fig. 14.2. (a) 3D view of the c(4 × 4) unit cell used to calculate the forces between the five Fe atoms pyramid and the Fe monolayer on W(001) which exhibits an antiferromagnetic checkerboard structure. Sites with parallel (p-site) and antiparallel (ap-site) alignment between tip and surface Fe magnetic moments (indicated by *arrows*) are marked. **(b)** Distances given in this side view are obtained after relaxing tip and sample independently. The distance z is defined as tip–sample distance along the approach trajectory (*dotted line*) before considering relaxations due to tip–sample interactions

correlation potential. We apply the full-potential linearized augmented plane wave method as implemented in the WIEN2K [34] code.

We used a ferromagnetic Fe pyramid in bcc-(001) orientation consisting of five Fe atoms as shown in Fig. 14.2. The tip has been fully relaxed, i.e., also the in-plane separation between the base atoms. The coupled system of tip and sample was calculated in a supercell geometry, as shown in Fig. 14.2. The monolayer of Fe on W(001) was modelled by a symmetric slab with five layers of W atoms and one layer of Fe atoms on each side. We used the GGA lattice constant of W (3.181 Å) which is only 0.5% larger than the experimental value (3.165 Å). Tip and surface were initially relaxed independently before considering the coupled system, i.e., the tip–sample interaction.

In two dimensions (2D) our supercell corresponds to a c(4 × 4) unit cell with respect to the Fe/W(001) surface. This choice guarantees that the tip interaction with its lateral image is negligible. The lateral distances between adjacent tips are 9.0 Å for the apex atom and 6.7 Å for the base atoms of the tip. Our supercell is periodic also in z-direction. Choosing a very large vacuum separation of 21 Å between adjacent surfaces, however, allows the tip to approach the surface without interacting with its periodic image. The energy cut-off for the plane wave representation in the interstitial region is $E_{\mathrm{max}}^{\mathrm{wf}} = 11$ Ry and a (3 × 3 × 1) Monkhorst–Pack grid was used for the Brillouin zone integration.

For the relaxed system the separation z is defined as the distance between the center of the tip-apex atom and the probed Fe surface atom before relaxation. It turns out that the relaxation of these atoms is on the order of a few picometers. The force–distance curves discussed in Sect. 14.3 are calculated on two high symmetry points of the surface, which are magnetically different with respect to the magnetization direction of the iron tip pyramid: on-top of an Fe atom with parallel magnetic moment, $F_{\mathrm{p}}(z)$ (p-site), and on top of an Fe atom with antiparallel magnetic moment, $F_{\mathrm{ap}}(z)$ (ap-site). For the simulation of MExFM images, we have calculated an additional force curve on the hollow site, i.e., at the center between the surface atoms.

14.3 Analysis of the Magnetic Exchange Forces

14.3.1 Unrelaxed Tip and Sample

First, we performed separate structural relaxations of tip and sample. Then the tip was approached vertically to the surface of the sample on the p- and ap-site (cf. Fig. 14.2) keeping the internal geometry of the tip and sample fixed, i.e., neglecting structural relaxations due to the tip–sample interaction. The calculated forces acting on the tip are shown in Fig. 14.3a. They display an attractive interaction for the ap- and p-site up to a maximum force of approximately −2.1 and −1.8 nN, respectively, at about 2.7 Å. The difference between the force on the p- and ap-site is the magnetic exchange force (MExF), $F_{\mathrm{ex}}(z)$, defined as

$$F_{\mathrm{ex}}(z) = F_{\mathrm{ap}}(z) - F_{\mathrm{p}}(z) \tag{14.1}$$

which is depicted in Fig. 14.3b by black solid symbols. Interestingly, the magnetic exchange force changes its sign from positive to negative upon

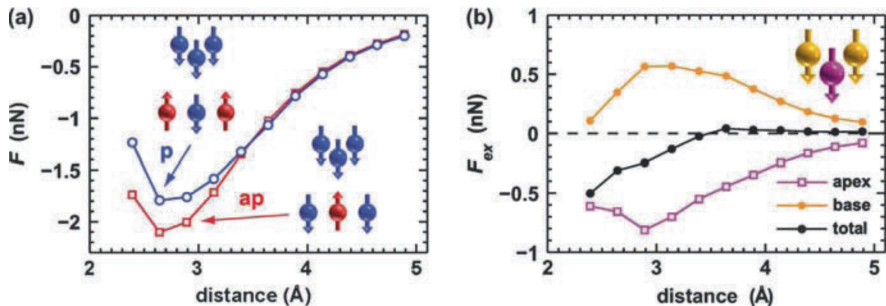

Fig. 14.3. (a) Calculated force–distance curves on the ap-site, $F_{\mathrm{ap}}(z)$, and on the p-site, $F_{\mathrm{p}}(z)$, of the surface (cf. Fig. 14.2), for the tip–sample system neglecting relaxations due to the interaction. **(b)** Total magnetic exchange force and decomposition of the magnetic exchange force into the contributions from different tip atoms

approaching the surface and reaches significant values on the order of 0.2 nN at about 3 Å. The negative sign of the magnetic exchange force indicates a more attractive interaction for an antiparallel alignment of the magnetization of the Fe tip and the Fe surface atom which is being approached (ap-site).

The negative sign of the magnetic exchange force and magnetic exchange energy (see inset of Fig. 14.4b) reveals that antiparallel alignment of tip and sample magnetization, i.e., antiferromagnetic coupling, is favorable. This result may seem rather surprising at first glance as one would intuitively expect ferromagnetic coupling between the interacting Fe atoms of tip and sample. However, the Fe apex atom interacts not only with the Fe surface atom beneath it but also with the four nearest Fe neighbors of this surface atom as will be shown in Sect. 14.3.3. Since the magnetic moments of the Fe atoms on the W(001) surface form an antiferromagnetic checkerboard structure, on the ap-site the magnetization of the tip-apex atom is aligned antiparallel to the moment of the Fe surface atom beneath it and parallel to the moments of the four nearest neighbor Fe surface atoms and vice versa on the p-site. Therefore, if we assume ferromagnetic coupling between individual Fe atoms there is a competition of magnetic exchange interactions with the surface Fe atom and its nearest neighbors.

Further insight into the tip–sample interaction and the forces acting in the system can be obtained by decomposing the total force on the tip (see Fig. 14.3b). The total magnetic exchange force acting on the cluster tip is the sum of the z-components of the magnetic exchange forces acting on the tip-apex atom and the four tip base atoms. As seen in Fig. 14.3b, the magnetic exchange force on the base atoms has an opposite sign to that on the apex atom which leads to a significant reduction of the total magnetic exchange force. As the magnetic exchange force on the apex atom sets in already at much larger tip–sample distances, increasing its contribution to the total magnetic

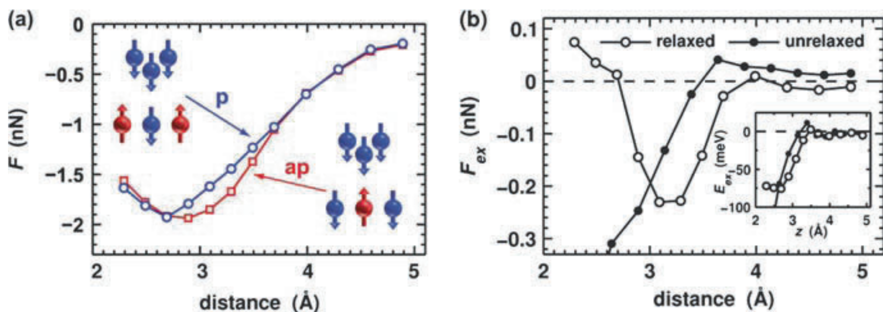

Fig. 14.4. **(a)** Calculated force curves on the ap-site, $F_{\mathrm{ap}}(z)$, and on the p-site, $F_{\mathrm{p}}(z)$, including relaxations of tip and sample due to their interaction. **(b)** Comparison of the magnetic exchange forces between the calculations with and without relaxations as a function of the separation between the unrelaxed tip-apex and probed Fe surface atom. The inset shows the magnetic exchange energies, $E_{\mathrm{ex}}(z) = E_{\mathrm{ap}}(z) - E_{\mathrm{p}}(z)$, for the calculations with and without relaxations

exchange force would greatly enhance the measurable magnetic signal. This result reveals the influence of the interaction of the sample with the tip base atoms. A realistic model of the tip should therefore include not only a single tip-apex atom but at least some tip base atoms. In Sect. 14.3.4, we will explore the influence of the tip size on the obtained magnetic exchange forces in more detail.

14.3.2 Influence of Structural Relaxations

The calculations without structural relaxations presented in Sect. 14.3.1 showed that significant forces act on the tip-apex atom depending on the magnetic configuration between tip and sample. From these results, we conclude that relaxations of tip and sample due to the magnetic interactions should play an important role for the total detectable magnetic exchange force. Therefore, we carried out the same set of calculations as earlier but this time we performed a structural relaxation of the tip-apex atom and the first two layers of the sample at every tip–sample separation.

The force–distance curves shown in Fig. 14.4a explicitly include relaxations due to tip–sample interactions. They look qualitatively similar to the forces for the unrelaxed structure (cf. Fig. 14.3a); however, significant differences arise in the respective magnetic exchange forces which can easily be observed in the splitting between the force curves on the p- and ap-site. On including relaxations, the onset of large magnetic exchange forces shifts towards larger tip–sample distances as seen in Fig. 14.4b. This effect facilitates their experimental detection as the atomic force microscope can be operated at larger distances, i.e., farther from the snap-to-contact point. In addition, $F_{\mathrm{ex}}(z)$ for the relaxed case does not display a marked change of sign at large tip–sample distances. Similar differences are also observed in the magnetic exchange energy for the relaxed and unrelaxed cases (see inset of Fig. 14.4b). Still, antiferromagnetic alignment ($E_{\mathrm{ex}} < 0$) of the Fe tip with respect to the probed Fe surface atom is energetically much more favorable at small separations. As explained in Sect. 14.2, the tip-apex atom interacts not only with the probed Fe surface atom but also with the four neighboring Fe atoms in the surface with antiparallel magnetic moments. Therefore, the negative magnetic exchange energy does not exclude ferromagnetic exchange coupling between the magnetic moments of individual Fe atoms.

These differences in the magnetic exchange forces and energies for the relaxed and unrelaxed case are obviously a result of the relaxation of the tip-apex atom which depends sensitively on its local magnetic configuration with respect to the approached Fe surface atom (see Fig. 14.5a). The tip-apex atom relaxes toward the surface due to the attractive forces and the shape of the relaxation curve. A similar effect is observed for the relaxation of the surface atom being probed which is attracted toward the tip at large distances and repelled at very close separations (see Fig. 14.5b). On the ap-site, the tip-apex atom relaxes about 0.05 Å closer toward the surfaces atom than on the p-site

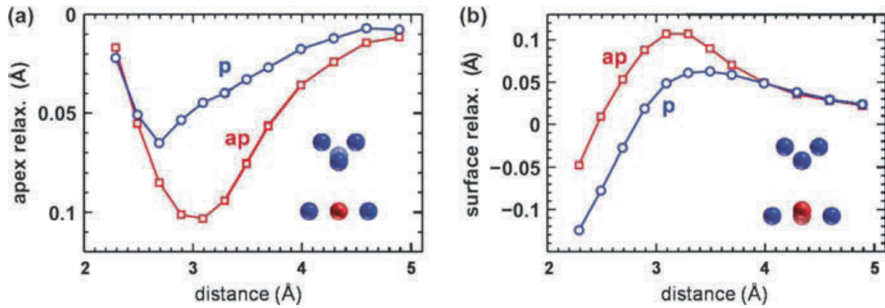

Fig. 14.5. Distance dependence of **(a)** the vertical tip-apex atom relaxation and **(b)** the vertical relaxation of the probed surface Fe atom for the p- and ap-alignment, respectively

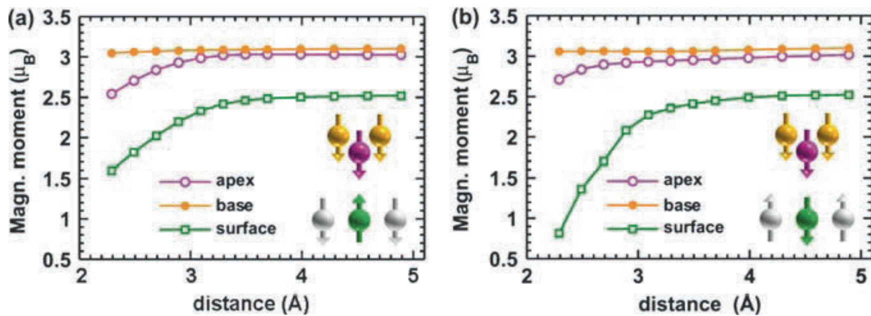

Fig. 14.6. Distance dependence of the absolute magnetic moments of the base (*filled circles*), apex (*circles*), and surface Fe (*squares*) atoms in the case of the five-atoms Fe tip for **(a)** ap-alignment and **(b)** p-alignment between the magnetization of tip and probed Fe surface atom as shown in the insets. These results include structural relaxations of tip and sample

which enhances the magnetic exchange interaction as can be inferred from the force curves of Fig. 14.4.

14.3.3 Electronic and Magnetic Structure Changes due to Tip–Sample Interaction

After analyzing the interaction between tip and sample based on force–distance curves and the resulting relaxations in the earlier sections, we now turn to the modifications of the electronic and magnetic structure due to their interaction. One way to monitor the magnetic interaction is to plot the distance dependence of the magnetic moments of tip-apex atom and surface atom as shown in Fig. 14.6 including structural relaxations.

We find that the magnetic moment of the base atoms remains nearly constant at $m_{\text{base}} \approx 3\,\mu_B$, whereas the moments of the Fe apex and surface atom

decrease as the tip approaches the surface. This decrease becomes significant only at separations below 3 Å, and is due to an increased hybridization between the states of tip apex atom and surface atom. The magnetic moment drop is more pronounced on the p-site than on the ap-site. This result is consistent with the ap-configuration (antiferromagnetic coupling) being energetically more favorable than the p-configuration (inset of Fig. 14.4b), as there is a large energy cost to reduce the magnetic moments from their equilibrium values (obtained at large tip–sample separations).

The origin of the magnetic exchange interaction can be traced to the different electronic interactions in the ap- and p-alignment. In order to study these interactions in detail it is helpful to analyze charge density difference (CDD) plots for the two configurations. This quantity is obtained by subtracting from the charge density of the interacting system consisting of Fe cluster tip and Fe monolayer on W(001) both the charge density of the isolated Fe/W(001) system and that of the isolated Fe cluster tip, using the same atom positions in both cases. The CDD plots visualize the charge transfer associated with the electronic interaction between tip and sample.

Figure 14.7 shows the CDD plots for the ap- and p-alignment at tip–sample distances of $z = 4.9$ and 2.9 Å. At a large separation, there is a small net charge accumulation between the tip-apex atom and the Fe surface atom. Already at this height the interaction depends on the type of spin alignment. The charge accumulation due to tip–sample interaction in the ap-configuration is bound to the Fe surface atom and has a node with the Fe apex atom, while in the p-configuration, it has nodes on both the Fe surface and the tip-apex atom. At a very close distance of $z = 2.9$ Å electronic charge strongly accumulates between the tip-apex atom and the surface Fe atoms, implying a strong electronic interaction between the tip and the surface. The charge accumulation in the ap-alignment is larger than in the p-alignment in agreement with the ap-configuration being energetically more favorable (inset of Fig. 14.4b).

The CDD plots also show that the charge density of the nearest-neighbor Fe atoms (with respect to the probed Fe surface atom) is considerably redistributed on approaching the tip. Therefore, the magnetic exchange coupling of these nearest neighbor Fe atoms with the apex atom of the tip plays an important role to determine whether p- or ap-alignment is more favorable. Similarly, the redistribution of the base atom's charge density indicates a significant contribution to the magnetic exchange interaction between tip and sample.

14.3.4 Influence of Tip Size

One of the more delicate aspects in modeling atomic force microscopy experiments is the geometry used for the tip. Ideally, the tip should consist of thousands of atoms to mimic the tips used in real experiments. However, in practice one is limited by the computational resources required for the calculation. Fortunately, the chemical and magnetic interaction between tip and

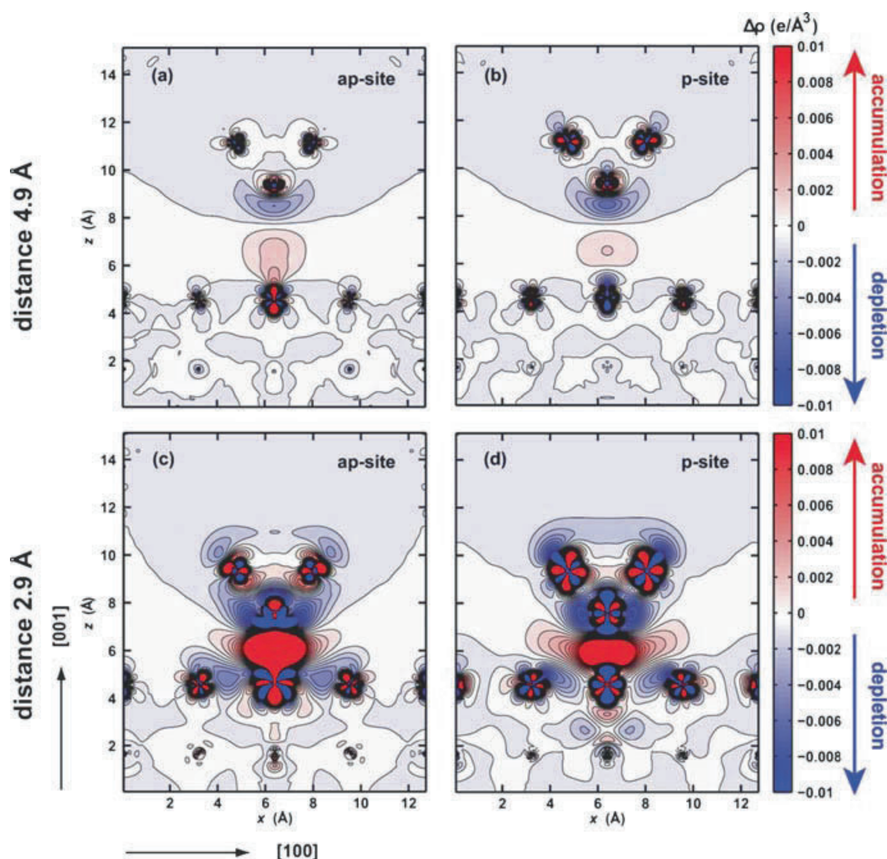

Fig. 14.7. Cross-sectional charge density difference plots along the [011]-direction for the interaction of the five-atoms Fe tip (*top* of each panel) with the Fe monolayer on W(001) (*bottom* of each panel) at tip–sample separations of $z = 4.9\,\text{Å}$ for **(a)** the ap- and **(b)** the p-coupling and at $z = 2.9\,\text{Å}$ for **(c)** the ap- and **(d)** the p-coupling. Zones in *red* and *blue* denote charge accumulation and depletion, respectively. The results presented here correspond to geometries including relaxations due to tip–sample interaction

sample is dominated by the foremost atoms due to the exponential decay of the wave functions while long-range forces can be added based on continuum models [35]. However, the electronic and magnetic properties at the tip-apex are still influenced by the base of the tip used in the model and need to be investigated.

In the past, theoretical calculations have often been carried out using a single Fe atom as an idealized model of the tip to study the magnetic exchange force, e.g., on the NiO(001) surface [20–22]. Here, we assess the validity of such a model using the Fe monolayer on W(001) as a test sample by comparing

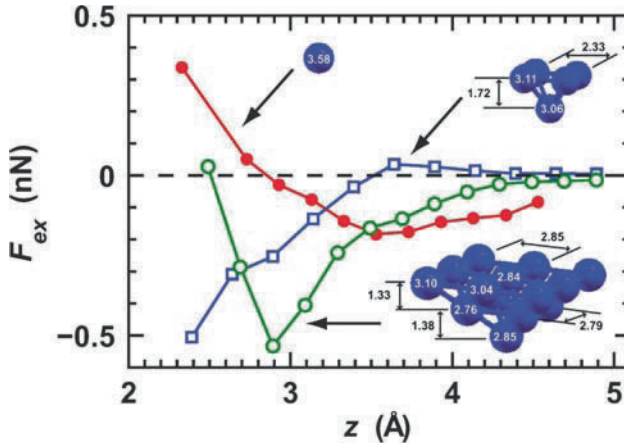

Fig. 14.8. Comparison of the magnetic exchange force $F_{\mathrm{ex}}(z)$ as a function of tip–sample separation z on the Fe monolayer on W(001) using a single Fe atom tip, a five Fe atoms tip, and an Fe tip consisting of 14 atoms. All presented calculations have been performed without structural relaxations of tip and sample due to their interaction. The magnetic moments of the different atoms of the clusters are indicated in *white* in units of the Bohr magneton, μ_B. Additionally, the interlayer distances are indicated in *black* in units of Å (the magnetic moments and geometry values correspond to relaxed geometries of the isolated tip, i.e., without any tip–sample interaction)

calculations using a single Fe atom and the five Fe atoms pyramid tip (discussed in the previous sections) and an even larger 14 Fe atoms tip.

A direct comparison of the magnetic exchange forces for different tip models is given in Fig. 14.8. Obviously, the magnetic exchange force obtained for a single Fe atom tip is even qualitatively different from both pyramid-type tips. At large separations, the magnetic exchange forces are much larger than for the pyramid tips, while they have the opposite sign at close distance. From these calculations, it is quite clear that a single Fe atom cannot mimic the magnetic exchange forces between a magnetic tip and sample. If we compare the two pyramid-type Fe tips, on the other hand, the general shape of the curve is very similar and the smaller tip gives qualitatively the same result. However, the magnetic exchange forces for the bigger Fe tip are significantly enhanced and set in at much larger tip–sample distances which is of crucial importance in experiments.

14.4 Simulation of MExFM Images

Since it is not possible to compare directly the earlier calculated tip–sample forces with the available experimental images [32], a simulation of MExFM images is required. For this procedure, it is essential to consider the long-range

tip–sample interaction caused by the van der Waals forces acting between the macroscopic tip and the sample. As in other studies (see, e.g., [16]), we model the macroscopic part of the tip by a sphere with radius R. The corresponding long-range force is given by $F_{\mathrm{vdW}}(z) = -(A_{\mathrm{H}}R)/(6z^2)$, where A_{H} is the Hamaker constant. For symmetry reasons, we have obtained the total tip–sample force as sum of the long- and short-range forces at three distinct lattice sites: the p-site, ap-site, and the hollow site (h-site). The experimentally measured frequency shift Δf can then be calculated from the numerical solution of the integral [36]

$$\Delta f(D) = \frac{1}{\sqrt{2}\pi}\frac{f_0}{c_z A^{3/2}}\int_D^{\infty}\frac{F_{\mathrm{ts}}(z)}{\sqrt{z-D}}\mathrm{d}z. \tag{14.2}$$

For simplicity we use here reduced units, i.e., the normalized frequency shift $\gamma = c_z A^{3/2}\Delta f/f_0$. This quantity is independent of the actual experimental parameters A, c_z and f_0 [35] and is plotted in Fig. 14.9(a). To simulate constant γ images, we choose a suitable value γ_{c} and determine the corresponding nearest tip–sample distance at the lower turnaround point of the cantilever oscillation, D, numerically by solving $\gamma(D) = \gamma_{\mathrm{c}}$. As a result, we obtain the corrugation amplitudes at the three distinctive lattice sites as a function of γ, and hence, D (see the arrows in Fig. 14.9a). Based on these curves we have simulated complete MExFM images, Fig. 14.9b–d, using the first two non-constant terms of a two-dimensional Fourier expansion [16, 37].

The analysis reveals that the magnetic contrast depends sensitively on the actual normalized frequency shift, i.e., the nearest tip–sample distance D.

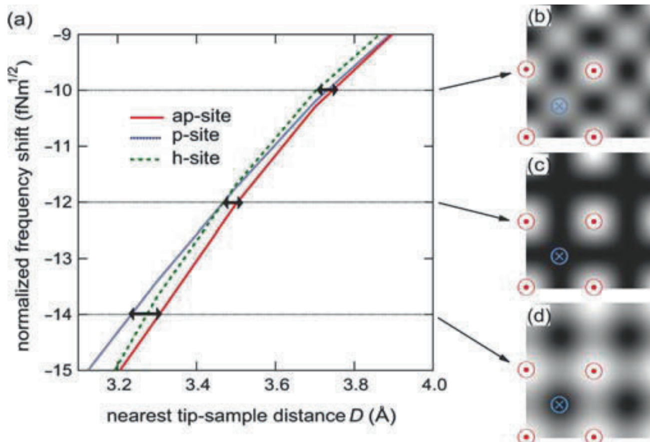

Fig. 14.9. (**a**) Calculated height difference between p-, ap- and h-site, respectively, depending on γ_{c} and hence D. Long-range van der Waals forces were added assuming $R = 8$ nm and $A_{\mathrm{H}} = 0.1$ aJ. The p-site defines the zero line. (**b–d**) Simulated MExFM images at γ_c of $-14, -12$, and -10 fNm$^{1/2}$ corresponding to $D = 3.2, 3.5$, and 3.7 Å, respectively

At large D, Fig. 14.9d, the chemical contrast dominates and the ap- and p-site appear as local maxima of only slightly different height due to a small magnetic exchange force of about 0.06 nN. At very small D, Fig. 14.9b, the magnetic forces dominate and Fe atoms with opposite magnetic moments appear as minima and maxima. At intermediate D, p- and h-site exhibit nearly the same height level and become indistinguishable. At the crossing point in Fig. 14.9a, they are exactly equal and only the ap-sites appear as maxima, (cf. Fig. 14.9c). Note that chemical and magnetic forces are both present and are of considerable magnitude, but the total forces at p- and h-site are equal. The contrast in Fig. 14.9c fits best to the experimental image presented in Chap. 13 of this book [32]. In a different experiment Schmidt et al. [31] also observed a contrast pattern similar to Fig. 14.9d, which is expected to appear at relatively large separations with smaller magnetic contrast. However, up to now, experimental data never exhibited a contrast pattern as shown in the simulated image Fig. 14.9b, probably because stable imaging is difficult at such close distances.

14.5 Summary

Utilizing density functional theory we have analyzed the magnetic exchange forces present in MExFM of an Fe monolayer on W(001), a two-dimensional itinerant antiferromagnet, using an Fe tip. Our study revealed that a single Fe atom is not an adequate tip model as the obtained magnetic exchange forces are even qualitatively different from those calculated with pyramid tips of five and 14 atoms. Surprisingly, the magnetic exchange forces on the tip atoms in the nearest layer from the apex atom are non-negligible and can be opposite to that on the apex atom. We demonstrate that the apex atom interacts not only with the surface atom directly underneath but also with nearest-neighbor atoms in the surface. Interestingly, structural relaxations of tip and sample due to their interaction depend sensitively on the magnetic alignment of the two systems. As a result the onset of significant magnetic exchange forces is shifted toward larger tip–sample separations which facilitates their detection in MExFM. Based on the first-principles calculation of the tip–sample forces we simulated MExFM images of the Fe monolayer on W(001) which showed contrast patterns in excellent agreement with available experimental data [32].

The computations shown here were performed at the Hamburg University of Technology, the Norddeutscher Verbund für Hoch- und Höchstleistungsrechnen (HLRN), and the Forschungszentrum Jülich (JUMP). We acknowledge financial support from the DFG (Grants No. HO 2237/3-1 and HE 3292/4-1). S.H. thanks the Stifterverband für die Deutsche Wissenschaft and the Interdisciplinary Nanoscience Center Hamburg for financial support.

References

1. I.S. Osborne, Science **294**, 1483 (2001)
2. M.R. Freeman, B.C. Choi, Science **294**, 1484 (2001)
3. S. Heinze, M. Bode, A. Kubetzka, O. Pietzsch, X. Nie, S. Blügel, R. Wiesendanger, Science **288**, 1805 (2000)
4. D. Wortmann, S. Heinze, P. Kurz, G. Bihlmayer, S. Blügel, Phys. Rev. Lett. **86**(18), 4132 (2001)
5. H. Yang, A.R.Smith, M. Prikhodko, W.R.L. Lambrecht, Phys. Rev. Lett. **89**, 226101 (2002)
6. A. Kubetzka, P. Ferriani, M. Bode, S. Heinze, G. Bihlmayer, K. von Bergmann, O. Pietzsch, S. Blügel, R. Wiesendanger, Phys. Rev. Lett. **94**, 087204 (2005)
7. M. Bode, Rep. Prog. Phys. **66**, 523 (2003)
8. C.L. Gao, U. Schlickum, W. Wulfhekel, J. Kirschner, Phys. Rev. Lett. **98**, 107203 (2007)
9. C.L. Gao, A. Ernst, A. Winkelmann, J. Henk, W. Wulfhekel, P. Bruno, J. Kirschner, Phys. Rev. Lett. **100**, 237203 (2008)
10. R. Wiesendanger, D. Bürgler, G. Tarrach, A. Wadas, D. Brodbeck, G.G. Güntherodt, H.-J. Güntherodt, R.J. Gambino, R. Ruf, J. Vac. Sci. Technol. B **9**, 519 (1990)
11. R. Pérez, M.C. Payne, I. Stich, K. Terakura, Phys. Rev. Lett. **78**, 678 (1997)
12. R. Pérez, I. Štich, M.C. Payne, K. Terakura, Phys. Rev. B **58**, 10835 (1998)
13. V. Caciuc, H. Hölscher, S. Blügel, H. Fuchs, Phys. Rev. Lett. **96**, 016101 (2006)
14. Y. Sugimoto, P. Pou, M. Abe, P. Jelinek, R. Perez, S. Morita, O. Custance, Nature **446**, 64 (2007)
15. N. Atodiresei, V. Caciuc, S. Blügel, H. Hölscher, Phys. Rev. B **77**, 153408 (2008)
16. V. Caciuc, H. Hölscher, D. Weiner, H. Fuchs, A. Schirmeisen, Phys. Rev. B. **77**, 045411 (2008)
17. H. Ness, F. Gautier, Phys. Rev. B **52**, 7352 (1995)
18. K. Nakamura, H. Hasegawa, T. Oguchi, K. Sueoka, K. Hayakawa, K. Mukasa, Phys. Rev. B **56**, 3218 (1997)
19. K. Nakamura, T. Oguchi, H. Hasegawa, K. Sueoka, K. Hayakawa, K. Mukasa, Appl. Surf. Sci. **142**, 433 (1999)
20. A.S. Foster, A.L. Shluger, Surf. Sci. **490**, 211 (2001)
21. H. Momida, T. Oguchi, J. Phys. Soc. Jpn. **72**, 588 (2003)
22. H. Momida, T. Oguchi, Surf. Sci. **590**, 42 (2005)
23. H. Hosoi, K. Sueoka, K. Hayakawa, K. Mukasa, Appl. Surf. Sci. **157**, 218 (2000)
24. H. Hosoi, K. Sueoka, K. Mukasa, Nanotechnology **15**, 505 (2004)
25. H. Hölscher, S.M. Langkat, A. Schwarz, R. Wiesendanger, Appl. Phys. Lett. **81**, 4428 (2002)
26. S.M. Langkat, H. Hölscher, A. Schwarz, R. Wiesendanger, Surf. Sci. **527**, 12 (2003)
27. R. Hoffmann, M.A. Lantz, H.J. Hug, P.J.A. van Schendel, P. Kappenberger, S. Martin, A. Baratoff, H.J. Güntherodt, Phys. Rev. B **67**, 085402 (2003)
28. M. Schmid, J. Mannhart, F.J. Giessibl, Phys. Rev. B **77**, 045402 (2008)
29. U. Kaiser, A. Schwarz, R. Wiesendanger, Nature **446**, 522 (2007)
30. U. Kaiser, A. Schwarz, R. Wiesendanger, Phys. Rev. B **77**, 153408 (2008)
31. R. Schmidt, C. Lazo, H. Hölscher, U.H. Pi, V. Caciuc, A. Schwarz, R. Wiesendanger, S. Heinze, Nano Lett. **9**, 200 (2009)

32. A. Schwarz, U. Kaiser, R. Schmidt, R. Wiesendanger, in *Magnetic Exchange Force Microscopy: Experiment*, eds. by S. Morita, F.-J. Giessibl, R. Wiesendanger. NC-AFM, vol II (Springer-Verlag Berlin-Heidelberg, 2009)
33. J.P. Perdew, K. Burke, M. Ernzerhof, Phys. Rev. Lett. **77**(18), 3865 (1996)
34. G.K.H. Madsen, P. Blaha, K. Schwarz, E. Sjöstedt, L. Nordström, Phys. Rev. B **64**(19), 195134 (2001)
35. F.J. Giessibl, Phys. Rev. B **1997**, 16010 (1997)
36. U. Dürig, Appl. Phys. Lett. **75**, 433 (1999)
37. N. Sasaki, H. Aizawa, M. Tsukada, Appl. Surf. Sci. **157**, 367 (2000)

15

Frequency Modulation Atomic Force Microscopy in Liquids

Kei Kobayashi and Hirofumi Yamada

Abstract. Atomic force microscopy (AFM) using frequency modulation (FM) detection has been widely used for the atomic-scale investigations of various materials. However, high-resolution imaging in liquids by FM-AFM is severely deteriorated by the extreme reduction of the Q-factor due to the hydrodynamic interaction between the cantilever and the liquid. Recently, the use of the small amplitude mode and the large noise reduction in the cantilever deflection sensor brought great progress in FM-AFM imaging in liquids. In this chapter viscous damping of the cantilever and the electric double layer force are discussed in detail. Following the detailed analysis of the frequency noise in FM-AFM, instrumentation of the optical beam deflection sensor for FM-AFM in liquid environments is described. Finally high-resolution FM-AFM images of muscovite mica, purple membranes, and isolated protein molecules in liquids are presented.

15.1 Brief Overview

Tremendous progress has been made in atomic force microscopy (AFM) using frequency modulation (FM) detection for the past decade [1]. High-resolution imaging of atomically flat surfaces in ultra-high vacuum environment has been completely established. In addition, several analysis methods based on the FM-AFM technique have been developed such as Kelvin-probe force microscopy (KFM) [2, 3], with which we can map local surface potentials or charge, and force mapping method [4], which allows us to differentiate surface atom species as well as to investigate atom–atom interactions.

On the other hand, one of the remarkable features in AFM is that it does not require any special imaging environment. In addition, no special treatment is required for imaging samples such as staining or metal coating, which are common techniques in electron microscopy imaging. Because of these remarkable advantages over other high-resolution imaging methods, AFM applications to atomic/molecular-scale in vivo imaging of biological samples in physiological, aqueous environments are greatly expected.

S. Morita et al. (eds.), *Noncontact Atomic Force Microscopy*,
NanoScience and Technology,
DOI: 10.1007/978-3-642-01495-6_15, © Springer-Verlag Berlin Heidelberg 2009

However, high-resolution imaging in liquids by FM-AFM is severely hindered by the extreme reduction of the Q-factor due to the hydrodynamic interaction between the cantilever and the liquid. Recently, the use of the small amplitude mode and the large noise reduction in the cantilever deflection sensor brought great progress in FM-AFM imaging in liquids [5,6]. In this chapter, the details of the problems in FM-AFM imaging in liquids, the frequency noise analysis of the cantilever oscillation in low-Q environments and the improvements of FM-AFM in liquids are described. The present status of the high-resolution FM-AFM imaging is also presented.

15.2 Problems of Frequency Modulation AFM in Liquids

15.2.1 Viscous Damping of Cantilever in Fluid

The oscillation of the AFM cantilever in liquid is heavily damped by the fluid resistance so that the quality factor (Q-factor) of the cantilever is extremely reduced. This large reduction in Q-factor causes a large increase in frequency noise and hence, deteriorates FM-AFM imaging (see Sect. 15.3.3). Here, the viscous damping of the cantilever oscillation in liquid at a resonance frequency is described.

The cantilever is treated as rectangular, uniform beam fixed at one end for simplicity, as shown in Fig. 15.1 (length: L, width: b, thickness: h). The displacement $\zeta(x,t)$ of the beam at a distance x from the fixed end at a time t is described by the following equation of motion:

$$\rho S \frac{\partial^2 \zeta(x,t)}{\partial t^2} + EI \frac{\partial^4 \zeta(x,t)}{\partial x^4} = f_{\mathrm{h}}(x,t) + f_{\mathrm{d}}(x,t), \tag{15.1}$$

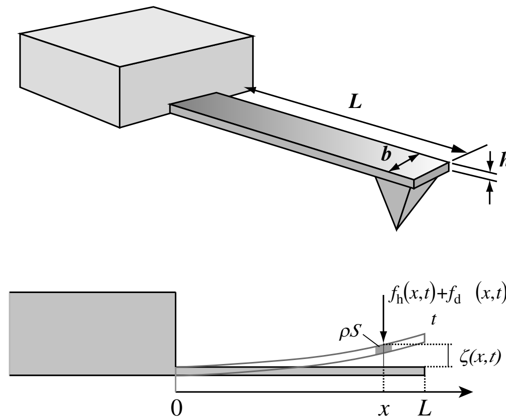

Fig. 15.1. *Top*: Structures of AFM cantilever. *Bottom*: Oscillation motion of cantilever in liquids. The notations are explained in the text

where ρ, S, E, and I are the density, the cross section, Young's modulus and the area moment of inertia of the beam, respectively, which are constant because of the beam uniformity. Two terms, $f_{\mathrm{h}}(x,t)$ and $f_{\mathrm{d}}(x,t)$, in the right-hand side of the equation denote the resistance of the liquid and the driving force to the cantilever (acting on a line element dx of the beam). When the right-hand side is zero, $\zeta(x,t)$ is expanded by the normal-mode functions (eigenfunctions) $\phi_n(x)$ as

$$\begin{aligned} \zeta(x,t) &= \sum_{n\geq 1} \phi_n(x)\,\zeta_n(t) \\ \phi_n(x) &= A\cosh\kappa_n x + B\sinh\kappa_n x + C\cos\kappa_n x + D\sin\kappa_n x. \end{aligned} \tag{15.2}$$

The coefficients A, B, C, D, and eigenfrequency are determined by a boundary condition of the beam. In the case of free oscillation, the condition is that the beam is fixed at $x=0$ and free at $x=L$. The resultant eigenfrequency ω_n is given by

$$\omega_n = \sqrt{\frac{EI}{\rho S}}{\kappa_n}^2, \tag{15.3}$$

where $\kappa_1 L = 1.875104$, $\kappa_2 L = 4.694091$, $\kappa_3 L = 7.854757, \ldots$ The terms in the right-hand side can be also expanded by the normal-mode functions as

$$f_{\mathrm{h}}(x,t) = \sum_n \phi_n(x) f_{\mathrm{h}(n)}(t) \quad \text{and} \quad f_{\mathrm{d}}(x,t) = \sum_n \phi_n(x) f_{\mathrm{d}(n)}(t)\,. \tag{15.4}$$

The equation of motion for the elastic continuum is reduced to that for one-degree-of-freedom motion for each normal mode (n), which is expressed by

$$\rho S\ddot{\zeta}_n + EI{\kappa_n}^4\zeta_n = f_{\mathrm{h}(n)} + f_{\mathrm{d}(n)}. \tag{15.5}$$

This equation can be modified into the following equation by Fourier transform, taking the relationship of $\kappa^2 = \sqrt{\rho S/EI}\omega_0$ into account:

$$-\rho S\omega^2\hat{\zeta} + \rho S{\omega_0}^2\hat{\zeta} = \hat{f}_{\mathrm{hydro}} + \hat{f}_{\mathrm{drive}}, \tag{15.6}$$

where $\hat{\zeta}$, $\hat{f}_{\mathrm{hydro}}$, and $\hat{f}_{\mathrm{drive}}$ are the Fourier transforms of ζ_0, $f_{\mathrm{h}(0)}$, and $f_{\mathrm{d}(0)}$, respectively. Sader and co-workers assumed that the magnitude of $\hat{f}_{\mathrm{hydro}}$ was proportional to the cantilever displacement and introduced dimensionless "hydrodynamic function" Γ [7, 8], representing the real and imaginary parts ($\Gamma = \Gamma_{\mathrm{re}} + j\Gamma_{\mathrm{im}}$) of the pressure of the surrounding on an oscillating rectangles in two dimensions,

$$\hat{f}_{\mathrm{hydro}} = \frac{\pi}{4}\rho_{\mathrm{liq}}\omega^2 b^2\Gamma\hat{\zeta}, \tag{15.7}$$

where ρ_{liq} is density of the liquid. By substituting (15.7) into (15.6), we can readily obtain the following equations:

$$\hat{\zeta} = \frac{{\omega_{0(\mathrm{liq})}}^2}{-\omega^2 + {\omega_{0(\mathrm{liq})}}^2 + j\omega\omega_{0(liq)}/Q_{\mathrm{liq}}} \frac{\hat{F}_{\mathrm{drive}}}{m{\omega_0}^2}, \tag{15.8}$$

$${\omega_{0(\mathrm{liq})}}^2 = \frac{1}{1 + (\pi\rho_{\mathrm{liq}}b/4\rho h)\,\Gamma_{\mathrm{re}}}{\omega_0}^2, \text{ and} \tag{15.9}$$

$$Q_{\mathrm{liq}} = \frac{(4\rho h/\pi\rho_{\mathrm{liq}}b) + \Gamma_{\mathrm{re}}}{\Gamma_{\mathrm{im}}}, \tag{15.10}$$

where m is mass of the cantilever $(= \rho SL)$ and $\hat{F}_{\mathrm{drive}} = \hat{f}_{\mathrm{drive}}L$. Equation (15.8) shows a resonance spectrum of the cantilever displacement, describing the reduction in Q-factor caused by the viscous resistance as well as the decrease of the resonance frequency due to the increase of the effective mass. Using the modified Reynolds number Re,

$$\mathrm{Re} = \frac{\rho_{\mathrm{liq}}\omega b^2}{4\mu}, \tag{15.11}$$

Γ can be approximated as [9,10]

$$\Gamma_{\mathrm{re}} = a_1 + \frac{a_2}{\sqrt{\mathrm{Re}}} \text{ and } \Gamma_{\mathrm{im}} = \frac{b_1}{\sqrt{\mathrm{Re}}} + \frac{b_2}{\mathrm{Re}}, \tag{15.12}$$

where μ is the coefficient of the liquid viscosity and $a_1 = 1.0553$, $a_2 = 3.7997$, $b_1 = 3.8018$, and $b_2 = 2.7364$. For a rectangular Si cantilever with $b = 35$, $L = 125$, and $h = 3.8$ μm ($k = 42$ N/m, $f_0 = 330$ kHz), the approximation gives $Q_{\mathrm{liq}} = 9.3$ and $f_{0(\mathrm{liq})} = 155$ kHz. These numbers are close to the measured values, $Q_{\mathrm{liq}} = 7 \sim 8$ and $f_{0(\mathrm{liq})} = 150$ kHz. Figure 15.2 shows thermal noise (Brownian motion) frequency spectra of a cantilever obtained in liquid and air. The measured Q-value was smaller than the calculated value. This is probably because the actual cross-section of the cantilever was slightly different from a rectangular shape.

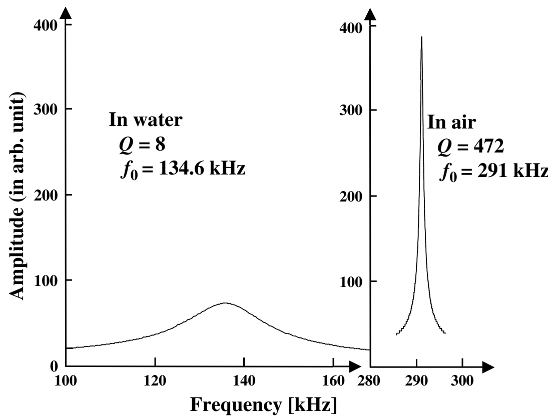

Fig. 15.2. Typical frequency spectra of the Brownian motion of a cantilever ($f_0 = 294$ kHz and $k = 30$ N/m) in water (*left*) and in air (*right*). The vertical scales in both spectra as well as the horizontal scales are equal to each other for comparison

15.2.2 Electric Double Layer Force [11]

The interaction force between an AFM tip and a sample surface in ultra-high vacuum is reasonably assumed to be the simple addition of the long-range van der Waals force and the short-range chemical force, which makes the analysis of the interaction force quite simple. On the other hand, sample surface is often charged in liquid due to the ionization of surface groups and/or ion absorption and the resultant local electrostatic force complicates the interpretation extremely. Surface charge is electrically balanced by the counter ions existing in the proximity of the surface so that an electric double layer is formed on the surface (diffused double layer). An electric double layer also exists on the tip–surface. When the tip is brought into close proximity of the sample surface, an electrostatic interaction is caused between both electric double layers (electric double layer force). If the surfaces of both tip and sample are made of the same material, the polarity of each overlapping layer is the same as each other, which means that the interaction force is repulsive in this case. Since the electric double layer force is relatively large, long-range interaction, it acts on the tip as a large background force, preventing us from imaging the surface with high resolution. Thus, the electric double layer force has to be reduced.

To estimate the electric double layer force we assume for simplicity that the surfaces of both tip and sample are made of the same material. In that case, the electric double layer force $F(d)$ at temperature T in a solution with an ion concentration of c_{ion} is approximately expressed by

$$F(d) = \frac{128\pi R k_{\mathrm{B}} T c_{\mathrm{ion}} {\gamma_0}^2}{\kappa} \exp\left[-\kappa d\right], \tag{15.13}$$

where R, k_{B} and d are tip radius, Boltzmann constant and tip–to–sample distance, respectively. Also γ_0 and κ^{-1} are expressed in the following equations when the sample surface potential ψ_0 is comparable with $k_{\mathrm{B}}T/e$ (25 meV) or smaller:

$$\gamma_0 = \tanh\left(\frac{Ze\psi_0}{4k_{\mathrm{B}}T}\right) \text{ and } \qquad \kappa^{-1} = \sqrt{\frac{\varepsilon_{\mathrm{r}}\varepsilon_0 k_{\mathrm{B}} T}{2\left(Ze\right)^2 c_{\mathrm{ion}}}} \tag{15.14}$$

where Z, e, ϵ_{r}, and ϵ_0 are ion valency, elementary charge, relative dielectric constant of the solution, and the vacuum dielectric constant, respectively. Solution is assumed to be $Z:Z$ electrolyte. κ^{-1} corresponds to the thickness of the electric double layer, so-called the Debye length. The surface charge density is proportional to the product of ψ_0 and κ^{-1}. Figure 15.3 shows three curves in different ion concentration solutions. Distance dependence of the force is drastically changed as the concentration is increased. Solution with high-ion concentration helps the suppression of the long- range force. Furthermore, κ^{-1} can be more reduced by the addition of divalent cation such as Mg^{2+}

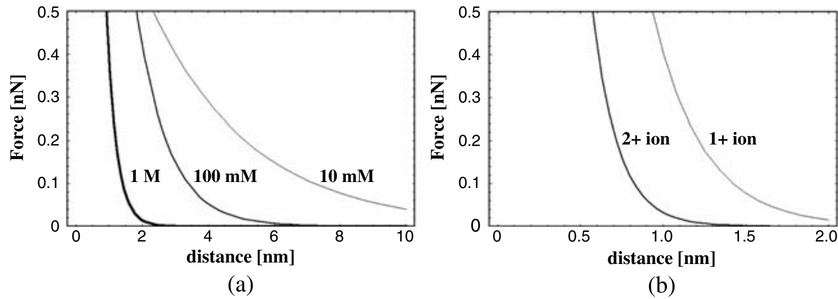

Fig. 15.3. Electric double layer force between a sphere with a radius R and a flat solid surface is plotted as a function of the distance for the solutions with different ion concentrations (a) and for the solutions of the electrolytes with different ionic valences (b)

because it effectively increases the charge density for electrical screening, as shown in Fig. 15.3b.

15.3 Frequency Noise in Frequency Modulation Atomic Force Microscopy [12]

Since FM-AFM detects the interaction forces as a frequency shift of the force sensor (cantilever) and regulate the tip–sample distance at a constant frequency shift, it is important to reduce the frequency noise for obtaining high-resolution FM-AFM images. In this section, the frequency noise in FM-AFM is analyzed in detail especially in terms of how the two major noise souces, which are the Brownian motion of the cantilever and the displacement sensor noise, contribute to the frequency noise.

15.3.1 Basics of Frequency Modulation

In FM-AFM, a cantilever as the force transducer is oscillated at its resonance frequency by the self-oscillation electronics. When the resonance frequency is modulated by the inteaction forces, the oscillation frequency follows the resonance frequency. Suppose that a cantilever with the tip at its end is oscillated with an oscillation amplitude A_0, the displacement of the tip, $s(t)$, is written as

$$s(t) = A_0 \sin \varphi(t). \tag{15.15}$$

Since a frequency is an instantaneous phase change per time, this equation is expressed as

$$s(t) = A_0 \sin \int \omega(t) \mathrm{d}t = A_0 \sin 2\pi \int f(t) \mathrm{d}t. \tag{15.16}$$

If the resonance frequency is modulated by the interaction force with a deviation of Δf at a modulation frequency of f_{m}, the instantaneous frequency can be written as

$$f(t) = f_0 + \Delta f \cos 2\pi f_{\mathrm{m}} t, \tag{15.17}$$

where f_0 is the time-averaged resonance frequency. From (15.16) and (15.17), $s(t)$ becomes

$$s(t) = A_0 \sin\left(2\pi f_0 t + \frac{\Delta f}{f_{\mathrm{m}}} \sin 2\pi f_{\mathrm{m}} t\right). \tag{15.18}$$

As a result, we can understand the FM is essentially the same as the phase modulation (PM) with a phase deviation ($\Delta\varphi$) of $\Delta f / f_{\mathrm{m}}$. Equation (15.18) can be expressed as a series of Bessel functions,

$$s(t) = A_0 \sum_{\mathrm{n}=-\infty}^{\infty} J_{\mathrm{n}}(\Delta\varphi) \sin 2\pi (f_0 + n f_{\mathrm{m}}) t. \tag{15.19}$$

When the phase deviation is sufficiently small ($\Delta f \ll f_{\mathrm{m}}$), (15.19) can be approximated as

$$s(t) \simeq A_0 \sin 2\pi f_0 t + \frac{A_0}{2} \Delta\varphi \sin 2\pi (f_0 + f_{\mathrm{m}}) t - \frac{A_0}{2} \Delta\varphi \sin 2\pi (f_0 - f_{\mathrm{m}}) t. \tag{15.20}$$

In the frequency spectrum of $s(t)$, two side bands with the root-mean-squared (rms) amplitude of $\left(A_0 / 2\sqrt{2}\right) \Delta\varphi$ appear at the frequencies $f_0 \pm f_{\mathrm{m}}$ as shown in Fig. 15.4(a). Therefore, to detect the FM of the resonance frequency at

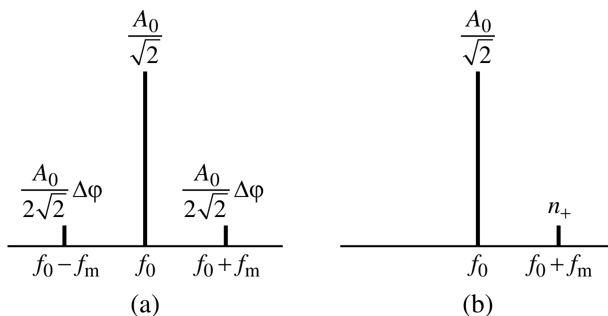

Fig. 15.4. (a) Frequency spectrum of the tip displacement when the interaction force modulates the resonance frequency of the cantilever (f_0) at a modulation frequency of f_{m}. (b) Frequency spectrum of the tip displacement when there is a sinusoidal noise with a frequency and root-mean-squared amplitude of $f_0 + f_{\mathrm{m}}$ and n_+, respectively

the modulation frequency of f_m, it is important to reduce the noise in the cantilever displacement signal at the frequency around $f_0 \pm f_\mathrm{m}$.

In the following, we consider how the displacement noise at the frequency $f_0 + f_\mathrm{m}$ affect the resonance frequency [13]. Suppose there is a sinusoidal noise with the rms amplitude of n_+ at $f_0 + f_\mathrm{m}$ as shown in Fig. 15.4(b), the tip displacement becomes

$$s(t) = A_0 \sin 2\pi f_0 t + \sqrt{2} n_+ \sin\left(2\pi(f_0 + f_\mathrm{m})t + \phi_0\right). \tag{15.21}$$

This equation can be written in the form as

$$\begin{aligned} s(t) = {} & \sin 2\pi f_0 t \left(A_0 + \sqrt{2} n_+ \cos(2\pi f_\mathrm{m} t + \phi_0) \right) \\ & + \cos 2\pi f_0 t \left(\sqrt{2} n_+ \sin(2\pi f_\mathrm{m} t + \phi_0) \right). \end{aligned} \tag{15.22}$$

If the noise amplitude is sufficiently small compared to the oscillation amplitude ($n_+ \ll A_0$), (15.22) can be approximated as

$$s(t) \simeq A_0 \sin(2\pi f_0 t + \delta\varphi_+) \tag{15.23}$$

with

$$\delta\varphi_+ = \sqrt{2} \frac{n_+}{A_0} \sin(2\pi f_\mathrm{m} t + \phi_0). \tag{15.24}$$

Therefore, the displacement noise at $f_0 + f_\mathrm{m}$ with the rms amplifude of n_+ becomes the phase noise with the rms amplitude of n_+/A_0 at the modulation frequency f_m.

Since the instantaneous frequency is the time derivative of the phase, the rms amplitude of the frequency noise δf caused by the phase noise with the rms amplitude of $\delta\varphi$ is

$$\delta f = \delta\varphi f_\mathrm{m}. \tag{15.25}$$

Therefore, the rms amplitude of the frequency noise caused by the displacement noise n_+ at $f_0 + f_\mathrm{m}$ becomes

$$\delta f_+ = \frac{n_+}{A_0} f_\mathrm{m}. \tag{15.26}$$

15.3.2 Frequency Noise Analysis in High-Q Environment

In FM-AFM, the Brownian motion (thermal noise) of the cantilever and the displacement sensor noise are two major noise sources for the phase noise and hence, for the frequency noise. It is intuitive to devide the phase/frequency noise into two parts as that with the modulation frequency within the linewidth of the oscillator ($f_\mathrm{m} \leq f_0/2Q$), which is treated as the frequency

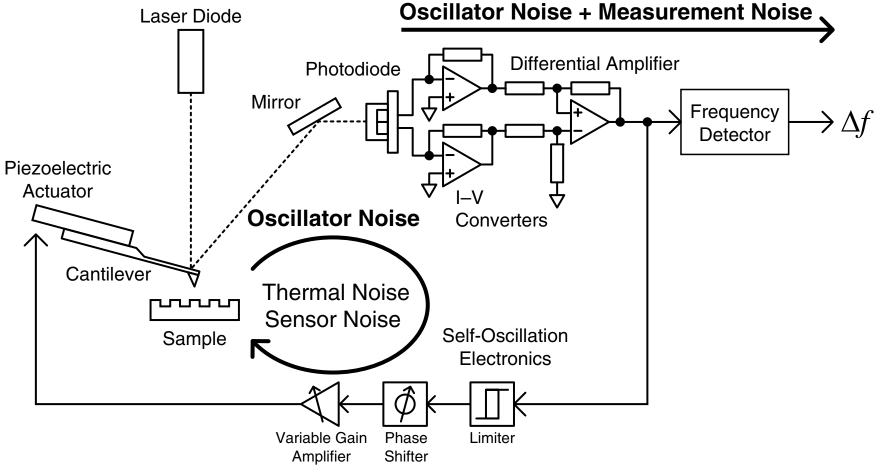

Fig. 15.5. Schematic of the FM-AFM instrument showing possible sources of the frequency noise. The Brownian motion (thermal noise) of the cantilever and the displacement sensor noise within the linewidth of the oscillator ($f_0/2Q$) determine the frequency noise of the oscillator. The noise outside of the linewidth brings additional frequency noise on the frequency measurement

noise of the oscillator, and that outside of it ($f_\mathrm{m} \geq f_0/2Q$), which is treated as the measurement noise in the frequency measurement of the oscillator (see Fig. 15.5).

As discussed in the first paper on FM-AFM by Albrecht et al. [14], in a high-Q enviroment such as in vacuum, the linewidth of the oscilltor becomes very narrow, and thus the modulation frequency of interest is typically outside of it. In such a case, the oscillator noise can be neglected and only the measurement noise is taken into account. This would also hold true for the typical operating parameters for FM-AFM in the ambient condition.

At first, we consider the contribution of the Brownian motion of the cantilever in the measurement noise [14, 15]. The transfer function of the cantilever with the angular resonance frequency of ω_0 and the spring constant of k_z can be written as

$$G(\omega) = \frac{1}{\left(1-(\omega/\omega_0)^2\right) + j\omega/\omega_0 Q}\frac{1}{k_z} = |G(\omega)| \exp\left[j\theta(\omega)\right], \quad (15.27)$$

with

$$|G(\omega)| = \frac{1}{\sqrt{\left(1-(\omega/\omega_0)^2\right)^2 + (\omega/\omega_0 Q)^2}}\frac{1}{k_z} \quad (15.28)$$

and

$$\theta(\omega) = \tan^{-1}\left(\frac{-\omega/\omega_0}{Q\left(1-(\omega/\omega_0)^2\right)}\right). \quad (15.29)$$

An example of $|G(\omega)|$ for a typical cantilever for FM-AFM in air (f_0 = 300 kHz, $k_z = 40$ N/m, and $Q = 500$) is shown in Fig. 15.6a.

From the equipartition theorem, the mean-square displacement of the cantilever end by the thermal energy k_BT is given by

$$\langle {z_{th}}^2 \rangle = \frac{1}{2\pi}\int_0^\infty |G(\omega)|^2 {F_{th}}^2 d\omega = \frac{k_BT}{k_z}, \quad (15.30)$$

where F_{th} is the magnitude of the random driving force with a white spectral density. Therefore the magnitude of F_{th} becomes

$$F_{th} = \sqrt{\frac{4k_zk_BT}{Q\omega_0}}. \quad (15.31)$$

Then, we obtain the thermal noise density $N_{th}(\omega)$ as

$$N_{th}(\omega) = |G(\omega)|F_{th} = \sqrt{\frac{4k_BT}{k_zQ\omega_0\left(\left(1-(\omega/\omega_0)^2\right)^2 + (\omega/\omega_0Q)^2\right)}} \quad (15.32)$$

from (15.28) and (15.31).

The thermal noise spectrum $N_{th}(\omega)$ is proportional to the magnitude of the transfer function $|G(\omega)|$ as shown in Fig. 15.6(a). For high-Q cantilevers, the magnitude of the thermal noise density is significant at f_0 but it is greatly

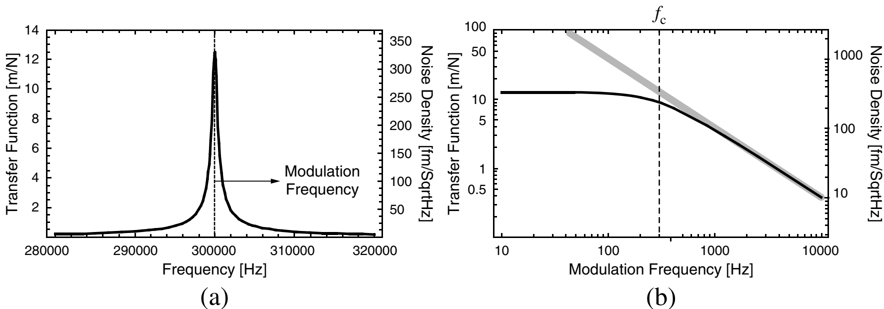

Fig. 15.6. (a) Magnitude of the cantilever transfer function $|G(\omega)|$ and the thermal noise density $N_{th}(\omega)$ for a typical cantilever for FM-AFM in air (f_0 = 300 kHz, $k_z = 40$ N/m, and $Q = 500$). (b) Same as (a) but as a function of the modulation frequency f_m, which is equal to the frequency deviation from f_0

reduced at the frequency apart from f_0. Since the magnitude of the noise at the frequency $f_0 \pm f_\mathrm{m}$ is important for calculating the phase/frequency noise with the modulation frequency f_m, it would be more convenient to plot these curve as a function of f_m. By inserting $\omega_0 \pm \omega_\mathrm{m}$ to $|G(\omega)|$, we obtain $|G(\omega_0 \pm \omega_\mathrm{m})|$ as

$$G(\omega_0 \pm \omega_\mathrm{m}) \simeq \frac{1}{k_z} \frac{-jQ}{1 \pm j\,(f_\mathrm{m}/f_\mathrm{c})}, \tag{15.33}$$

where f_c is the corner frequency given by $f_0/2Q$. The magnitude of the transfer function starts to decrease at f_c as shown in Fig. 15.6b. The thermal noise is proportional to the magnitude of the transfer function, and it can be approximated as

$$N_\mathrm{th}(f_\mathrm{m}) \simeq \sqrt{\frac{k_\mathrm{B} T f_0}{2\pi k_z Q}} \frac{1}{f_\mathrm{m}}, \tag{15.34}$$

as indicated by a thick grey line in Fig. 15.6b.

If the displacement sensor noise is not negligible, the magnitude of the total displacement noise appearing at the frequency around f_0 becomes

$$N_\mathrm{total} = \sqrt{{N_\mathrm{th}}^2 + {N_\mathrm{ds}}^2}. \tag{15.35}$$

as shown in Fig. 15.7(a). Since the total displacement noise at both sidebands $f_0 \pm f_\mathrm{m}$ contribute to the phase/frequency noise, the frequency noise density for high-Q cantilevers becomes

$$N_{\mathrm{FM(high\text{-}}Q)} = \frac{\sqrt{2{N_\mathrm{total}}^2}}{A_0} f_\mathrm{m} = \sqrt{2}\frac{N_\mathrm{total}}{A_0} f_\mathrm{m} = \sqrt{2}\frac{\sqrt{{N_\mathrm{th}}^2 + {N_\mathrm{ds}}^2}}{A_0} f_\mathrm{m}. \tag{15.36}$$

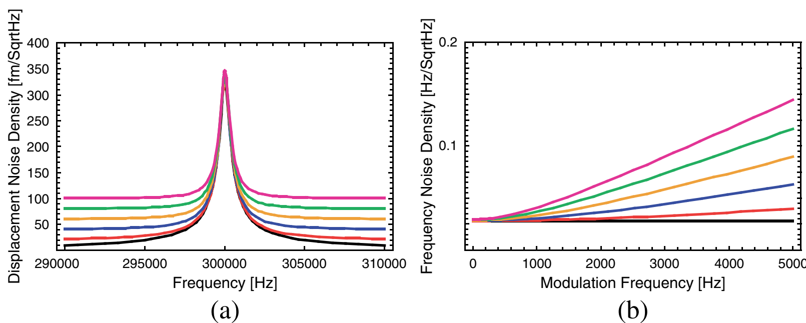

Fig. 15.7. (a) Total displacement noise density N_total for a typical cantilever for FM-AFM in air (f_0 = 300 kHz, k_z = 40 N/m, and Q = 500) measured by the displacement sensor with the sensor noise of 0, 20, 40, 60, 80, and 100 fm/$\sqrt{\mathrm{Hz}}$. (b) Correspondng frequency noise noise density $N_{\mathrm{FM(high\text{-}}Q)}$ at the modulation frequency f_m from 0 to 5 kHz

Therefore, we obtain

$$N_{\mathrm{FM(high-}Q)} = \sqrt{\frac{f_0 k_\mathrm{B} T}{\pi k_z Q {A_0}^2} + \frac{2{N_\mathrm{ds}}^2}{{A_0}^2} {f_\mathrm{m}}^2}. \tag{15.37}$$

The frequency noise density at a typical oscillation amplitude in FM-AFM in air ($A_0 = 5$ nm) is shown in Fig. 15.7(b). The total frequency noise for a given measurement bandwidth B can be obtained by integrating (15.37) as

$$\delta f_{(\mathrm{high-}Q)} = \sqrt{\int_0^B (N_{\mathrm{FM(high-}Q)})^2 df} = \sqrt{\frac{f_0 k_\mathrm{B} T}{\pi k_z Q {A_0}^2} B + \frac{2{N_\mathrm{ds}}^2}{3{A_0}^2} B^3}. \tag{15.38}$$

In the case when the displacement sensor noise is significant, (15.37) and (15.38) become

$$N_{\mathrm{FM(high-}Q)} \simeq \sqrt{2}\frac{n_\mathrm{ds}}{A_0} f_\mathrm{m} \tag{15.39}$$

and

$$\delta f_{(\mathrm{high-}Q)} \simeq \sqrt{\frac{2}{3}} \frac{n_\mathrm{ds}}{A_0} B^{3/2}. \tag{15.40}$$

Note that the total frqeuency noise is proportional to $B^{3/2}$ for high-Q cantilevers.

15.3.3 Frequency Noise Analysis in Low-Q Environment

In the analysis of the frequency noise for high-Q cantilevers, the displacement noise within the linewidth of the oscillator was neglected. However, in a low-Q environment, the linewidth ($f_0/2Q$) becomes very large and hence, cannot be negligible. In other words, since the Q-factor is so small, the frequency fluctiation of the oscillator is very large. Therefore, the oscillator noise has to be considered in addition to the measurement noise considered for high-Q cantilevers. The magnitude of the total displacement noise N_total for a typical low-Q cantilever in liquid ($f_0 = 130$ kHz, $k_z = 40$ N/m, and $Q = 8$) is shown in Fig. 15.8(a).

The oscillation frequency of the cantilever is the frequency at which the phase criterion

$$\theta(f) + \theta_\mathrm{circuit}(f) = 2n\pi \tag{15.41}$$

is met, where $\theta(f)$ is the transfer function of the cantilever given in (15.29) and $\theta_\mathrm{circuit}(f)$ is the phase shift for the input frequency f added by the self-oscillation circuit. The oscillation frequency is determined by the phase response of the cantilever as such, the phase noise of the cantilever turns

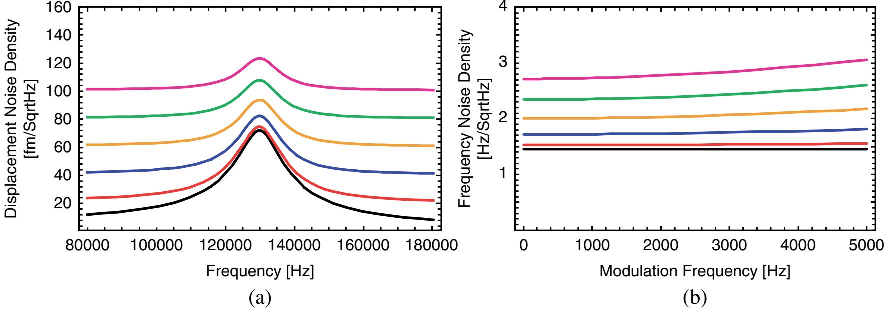

Fig. 15.8. (a) Total displacement noise density N_{total} for a typical cantilever in liquid ($f_0 = 130$ kHz, $k_z = 40$ N/m, and $Q = 8$) measured by the displacement sensor with the sensor noise of 0, 20, 40, 60, 80, and 100 fm/$\sqrt{\text{Hz}}$ (b) Correspondng frequency noise noise density $N_{\text{FM(low-}Q)}$ at the modulation frequency f_{m} from 0 to 5 kHz

into the frequency noise with the factor of the slope of the phase versus frequency curve at the oscillating frequency. From (15.29), the phase shift of the cantilever at f_0 is

$$\theta(f_0) = -\frac{\pi}{2}, \tag{15.42}$$

and the frequency derivative of the phase at f_0 becomes

$$\left.\frac{\mathrm{d}\theta}{\mathrm{d}f}\right|_{f=f_0} = -\frac{2Q}{f_0}. \tag{15.43}$$

Considering that the displacement noise at both sidebands $f_0 \pm f_{\text{m}}$ contribute to the phase noise, the oscillator noise caused by the phase noise becomes

$$N_{\text{osc}} = \left|\frac{\mathrm{d}f}{\mathrm{d}\theta}\right| \frac{\sqrt{2N_{\text{total}}{}^2}}{A_0} = \frac{f_0}{2Q}\frac{\sqrt{2}N_{\text{ds}}}{A_0}. \tag{15.44}$$

Thus, the general equation for the frequency noise density of the oscillator becomes

$$N_{\text{FM}} = \sqrt{N_{\text{high-}Q}{}^2 + N_{\text{osc}}{}^2}. \tag{15.45}$$

The contribution of the Brownian motion of the cantilever to the oscillator noise was not discussed but it was already included in (15.37) for high-Q cantilevers. From (15.37) and (15.45), we finally obtain

$$N_{\text{FM}} = \sqrt{\frac{f_0 k_{\text{B}} T}{\pi k_z Q A_0{}^2} + \frac{2N_{\text{ds}}{}^2}{A_0{}^2} f_{\text{m}}{}^2 + \frac{f_0{}^2}{2Q^2 A_0{}^2} N_{\text{ds}}{}^2}. \tag{15.46}$$

Typical frequency noise density at a typical oscillation amplitude in FM-AFM in liquid ($A_0 = 0.5$ nm) is shown in Fig. 15.8(b). Since the modulation frequency f_m of interest is usually within the linewidth of the oscillator ($f_0/2Q$), the displacement sensor noise contribution outside of the linewidth can be neglected and (15.46) can be approximated as

$$N_{\mathrm{FM(low\text{-}}Q)} \simeq \sqrt{\frac{f_0 k_B T}{\pi k_z Q {A_0}^2} + \frac{{f_0}^2}{2Q^2 {A_0}^2} {N_{ds}}^2}. \tag{15.47}$$

The total frequency noise for a given measurement bandwidth B can be obtained by integrating (15.47) as

$$\delta f_{(\mathrm{low\text{-}}Q)} = \sqrt{\int_0^B (N_{\mathrm{FM(low\text{-}}Q)})^2 df} \simeq \sqrt{\frac{f_0 k_B T}{\pi k_z Q {A_0}^2} B + \frac{{f_0}^2}{2Q^2 {A_0}^2} {N_{ds}}^2 B}. \tag{15.48}$$

In the case when the displacement sensor noise is significant, (15.47) and (15.48) become

$$N_{\mathrm{FM(low\text{-}}Q)} \simeq \frac{f_0}{\sqrt{2} Q A_0} N_{ds} \tag{15.49}$$

and

$$\delta f_{(\mathrm{low\text{-}}Q)} \simeq \frac{f_0}{\sqrt{2} Q A_0} N_{ds} \sqrt{B}. \tag{15.50}$$

Note that the total frqeuency noise is proportional to $B^{1/2}$ in this case. It is also proportional to Q^{-1}, indicating the reduction of the displacement sensor noise is essential in low-Q environments.

15.4 Improvement of FM-AFM for Liquid Environment

As described in Sect. 15.3, the frequency noise is proportional to the displacement sensor noise, it is very important to reduce the displacement sensor noise for reducing the frequency noise. In this section, instrumentation of the low-noise optical beam deflection sensor, which we utilized for high-resolution FM-AFM imaging described in later sections, is described.

15.4.1 Optimization of Optical Beam Deflection Sensor

The optical beam deflection sensor, first introduced by Meyer and Amer [16], is a simple but highly sensitive displacement sensor for AFM. Here, we describe the displacement noise determined by the shot noise for considering the optimized setup [17].

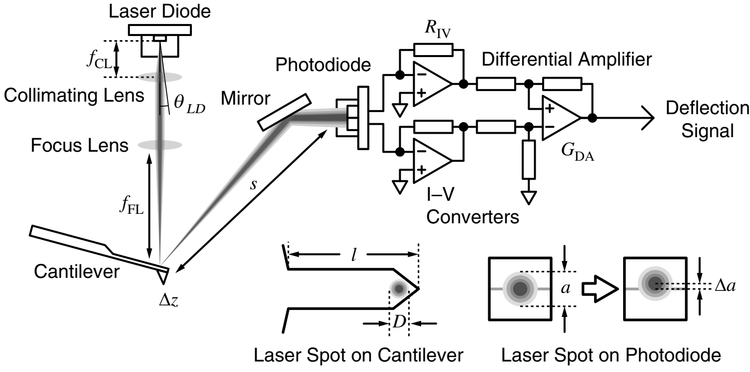

Fig. 15.9. Schematic of the optical beam deflection sensor used in AFM. The Gaussian laser beam is focused on the backside of the cantilever for achieving maximum sensitivity for a given laser power

Typical setup of the optical beam deflection sensor is shown in Fig. 15.9. The laser light is usually focused at the backside of the cantilever for achieving maximum sensitivity for a given laser power, and reflected to the segmented photodiode (PD). Suppose that the laser is the circular, Gaussian beam and its spot is on the center of the PD, the intensity distribution of the laser spot on the PD along its vertical axis y is given by

$$I(y) = \sqrt{\frac{2}{\pi}}\frac{1}{r} P_{\mathrm{PD}} \exp\left[-\frac{2y^2}{r^2}\right], \tag{15.51}$$

where P_{PD} is the laser power on the PD and r is the radius of the beam spot on the cantilever. Since the intensity at the center is

$$I(0) = \sqrt{\frac{2}{\pi}}\frac{1}{r} P_{\mathrm{PD}}, \tag{15.52}$$

the power difference caused by the displacement of the spot by Δs is given by

$$\Delta P = \sqrt{\frac{8}{\pi}}\frac{1}{r} P_{\mathrm{PD}} \exp\left[-\frac{g^2}{2r^2}\right] \Delta s, \tag{15.53}$$

where g is the width of the gap between the segments of the PD.

When the cantilever with the length of l_{CL} is displaced by Δz, the change in the reflection angle according to the displacement is

$$\Delta\theta = \frac{3}{2}\frac{\Delta z}{l_{\mathrm{CL}}}. \tag{15.54}$$

Then, the displacement of the spot on the PD which is located at a distance of l_{PD} from the cantilever becomes $\Delta s = 2 l_{\mathrm{PD}} \Delta\theta$. Therefore ΔP becomes

$$\Delta P = 6\sqrt{\frac{2}{\pi}}\frac{1}{r}P_{\mathrm{PD}}\exp\left[-\frac{g^2}{2r^2}\right]l_{\mathrm{PD}}\frac{\Delta z}{l_{\mathrm{CL}}}. \quad (15.55)$$

Since the laser beam is focused by the focus lens with the focal length of f_{FL}, the radius of the laser spot on the PD r is given by

$$r = \frac{l_{\mathrm{PD}}}{f_{\mathrm{FL}}}R, \quad (15.56)$$

where R is the radius of the collimated beam before focusing. R is determined by the focal length of the collimating lens f_{CL} and the half-cone angle of the beam divergence for the laser diode as $f_{\mathrm{CL}}\tan\theta_{\mathrm{LD}}$. Then, (15.55) becomes

$$\Delta P = 6\sqrt{\frac{2}{\pi}}\frac{f_{\mathrm{FL}}}{l_{\mathrm{PD}}f_{\mathrm{CL}}\tan\theta_{\mathrm{LD}}}P_{\mathrm{PD}}\exp\left[-\frac{(gf_{\mathrm{FL}})^2}{2\left(l_{\mathrm{PD}}f_{\mathrm{CL}}\tan\theta_{\mathrm{LD}}\right)^2}\right]l_{\mathrm{PD}}\frac{\Delta z}{l_{\mathrm{CL}}}. \quad (15.57)$$

If the responsivity of the PD is η, and the gains of the transimpedance amplifier and the differential amplifier are R_{IV} and G_{DA}, respectively, the output signal becomes

$$\Delta V = 6\sqrt{\frac{2}{\pi}}\frac{f_{\mathrm{FL}}}{f_{\mathrm{CL}}\tan\theta_{\mathrm{LD}}}P_{\mathrm{PD}}\exp\left[-\frac{(gf_{\mathrm{FL}})^2}{2\left(l_{\mathrm{PD}}f_{\mathrm{CL}}\tan\theta_{\mathrm{LD}}\right)^2}\right]\frac{\Delta z}{l_{\mathrm{CL}}}\eta R_{\mathrm{IV}}G_{\mathrm{DA}}. \quad (15.58)$$

The dominant noise source in the typical optical beam deflection sensor is the shot noise. The shot noise energy is proportional to the magnitude of the photocurrent of the PD, and the shot noise voltage density at the output of the sensor becomes

$$\delta v_{\mathrm{shot}} = R_{\mathrm{IV}}G_{\mathrm{DA}}\sqrt{2e\eta P_{\mathrm{PD}}}. \quad (15.59)$$

Finally we obtain the displacement sensor noise density, or the minimum detectable displacement per measurement bandwidth, as

$$N_{\mathrm{ds}} = \frac{\delta v_{\mathrm{shot}}}{\Delta V/\Delta z} = \frac{\sqrt{\pi e}\,l_{\mathrm{CL}}f_{\mathrm{CL}}\tan\theta_{\mathrm{LD}}}{6f_{\mathrm{FL}}\sqrt{P_{\mathrm{PD}}\eta}}\exp\left[\frac{(gf_{\mathrm{FL}})^2}{2\left(l_{\mathrm{PD}}f_{\mathrm{CL}}\tan\theta_{\mathrm{LD}}\right)^2}\right]. \quad (15.60)$$

If the optics and electronics are properly designed, the displacement sensor noise density falls in the range of a few tens of fm $\sqrt{\mathrm{Hz}}^{-1}$ with the laser power of 1 mW.

15.4.2 Reduction of Coherence Length of Laser

One of the problems in the optical beam deflection sensor for AFM in liquids, is that the output of the sensor fluctuates because of the interference noise,

the optical feedback noise or the mode-hop noise of the laser. This often happens when the single-mode semiconductor laser is used in the optical beam deflection sensor in which the laser light goes through many optical interfaces. It has been demonstrated that the modulation of the laser current at the radio frequency (RF), as shown in Fig. 15.10(a), can suppress such fluctuations [18, 19]. This is due to the fact that the single-mode laser initially oscillates in multiple modes for several nanoseconds, thus the RF typically ranges from 300 to 600 MHz.

If the laser keep oscillates at multiple modes, the laser becomes immune to the mode-hop noise and tolerant to the optical feedback. Moreoever, the effective coherence length becomes greatly reduced thereby the optical interference of the laser becomes less probable. The probability of the optical interference is closely related to the visibility of the laser light, which can be calculated from the optical spectrum [20]. The visibility of the light source is $\sqrt{C^2 + S^2}/P$, where P, C, and S are defined as

$$\begin{aligned} P &= 2 \int j(x) \mathrm{d}x, \\ C(\Delta L) &= 2 \int j(x) \cos(x \Delta L) \mathrm{d}x, \text{ and} \\ S(\Delta L) &= 2 \int j(x) \sin(x \Delta L) \mathrm{d}x. \end{aligned} \tag{15.61}$$

ΔL is the optical path difference and $j(x)$ is the spectral distribution of laser intensity as a function of wavenumber difference from the mean wavenumber $\overline{k_0}$ for the mean wavelength $\overline{\lambda_0}$.

For the multi-mode laser, the visibility immdiately starts to decrease as ΔL increases as shown in Fig. 15.10(b). The coherency of the laser is greatly reduced expect when the ΔL matches to multiples of nL, where L is the the

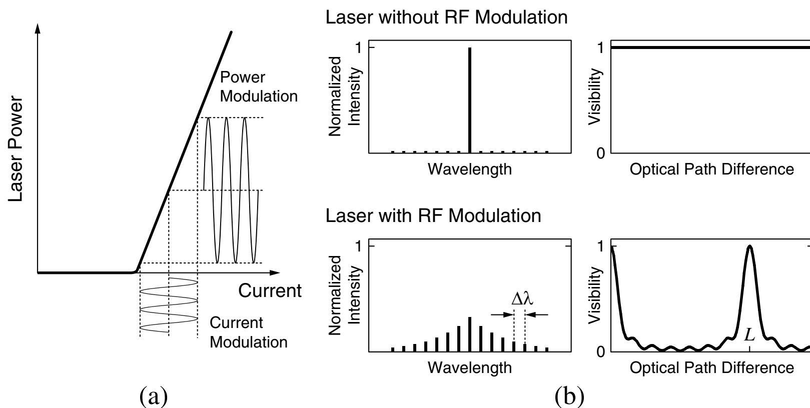

Fig. 15.10. (a) Schematic of the RF modulation of the laser current. (b) Schematic of the optical spectra of the laser light with and without the RF modulation and the visibility as a function of the optical path difference

effective length of the optical cavity in the laser, given by $L = \overline{\lambda_0}^2/2\Delta\lambda$. The typical effective coherence length of the sigle-mode red laser decreases down to a few hundred micrometers by the RF modulation.

Note that the usage of an incoherent light source such as a superluminescent light-emitting diode can also solve these problems.

15.4.3 Reduction of Oscillation Amplitude

As mentioned earlier, reducing the displacement sensor noise is critical in the low-Q enviroment. However, another important factor in FM-AFM is to reduce the oscillation amplitude so that the short-range interaction force is effectively detected as the frequency shift. If the oscillation amplitude is large compared to the interaction range λ, the tip stays in the interaction range only for a short time. However, if the oscillation amplitude is smaller than λ, the tip stays in the interaction range during a whole period of the oscillation, as shown in Fig. 15.11(a).

The frequency shift caused by the interaction force F_{ts} in FM-AFM is given by the following equation [21]:

$$\Delta f = \frac{f_0}{k_z {A_0}^2} \langle F_{\mathrm{ts}} \cdot z \rangle = -\frac{f_0}{\pi k_z A_0} \int_{-1}^{1} F_{\mathrm{ts}} \left(d_0 + A_0 + u \right) \frac{u}{\sqrt{1-u^2}} du, \quad (15.62)$$

where d_0 is the closest distance of the tip from the surface, and u is the tip position relative to the mean position ($= A_0 \cos \omega t$). This is proportinal to the integral of the interaction forces with a weight function $u/\sqrt{1-u^2}$, which is depicted in Fig. 15.11b. Therefore, the frequency shift caused by the interaction forces becomes larger with the smaller amplitude.

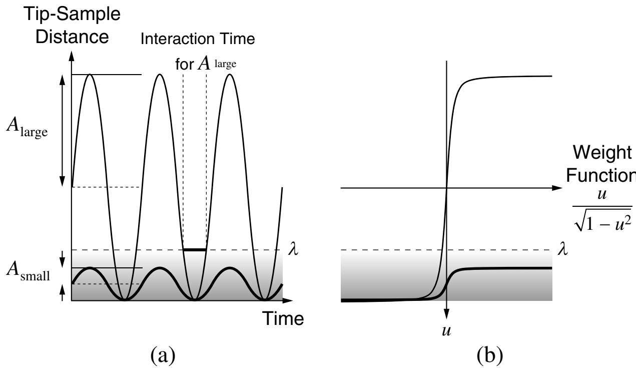

Fig. 15.11. (a) Comparison of the tip–sample interaction time during the cantilever oscillation with a larger amplitude (A_{large}) and that with a smaller amplitude (A_{small}) than the interaction range λ. (b) Schematic of the weight function $u/\sqrt{1-u^2}$ as a function of the tip position $u(= A_0 \cos \omega t)$, with which the frequency shift is calculated by the integration of the interaction force

15.5 High-Resolution Imaging by FM-AFM in Liquid

15.5.1 Muscovite Mica [22]

Muscovite mica ($KAl_2(Si_3Al)O_{10}(OH)_2$) is often used as a substrate for high-resolution imaging of biological samples because it has a hydrophilic surface, which is suitable for the adsorption of biological molecules, and because one can easily obtain an atomically flat surface by cleavage. Mica is a silicate mineral, having layered crystal structures containing SiO_4 tetrahedrons. As shown in Fig. 15.12, the fundamental structure along the *c*-axis contains two layers of SiO_4 tetrahedrons, shifted with each other along the *a*-axis by 1/3 of the pseudo-hexagonal lattice, a layer of octahedron composed of Al^{3+} and OH^- ions, sandwiched between the two SiO_4 layers, and a K^+ ion layer. The SiO_4 layer makes a honeycomb network with a period of 0.52 nm, where each honeycomb hole is a relatively large diameter (0.32 nm).

Since Si^{4+} ions in this layer are partly replaced with Al^{3+} ions with a ratio of 1/4, the layer is negatively charged. Although the K^+ ion layer connects the two SiO_4 layers, compensating for their negative charge. However, since this electrostatic bonding between the K^+ and the SiO_4 layers is weak, mica can be easily cleaved at the K^+ layer. In water, K^+ ions on the cleavage plane (SiO_4 layer) are detached and the surface is hydrated.

Figure 15.13 shows an FM-AFM image obtained in pure water. A hexagonal lattice structure with a period of 0.52 nm is clearly observed. Although lattice structure can be seen over the entire area of the image, there is some height variation. This gradual variation in height has been always appeared in AFM imaging of mica in water. Possible origins of this variation are electrostatic force variation caused by non-uniform Al^{3+} ion distribution or statistical fluctuation of the hydration structures on the mica surface.

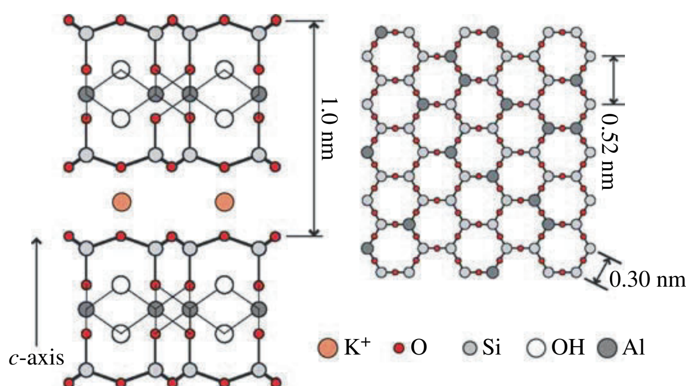

Fig. 15.12. Crysral structure of muscovite mica. *Left*: Structure viewed along the a-axis. *Right*: Structure of the cleaved surface (K^+ ions are not shown)

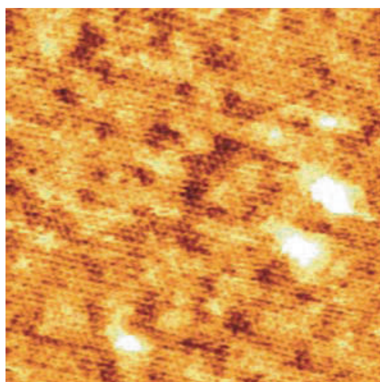

Fig. 15.13. FM-AFM image of a mica surface obtained in pure water. (Scan range: $30 \times 30\,\text{nm}$, $\Delta f = +360$ Hz, $A_0 = 0.33$ nm)

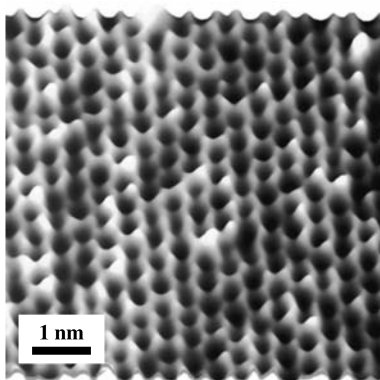

Fig. 15.14. FM-AFM image of a mica surface obtained in pure water. (Scan range: $8 \times 8\,\text{nm}$, $\Delta f = +54$ Hz, $A_0 = 0.24$ nm)

Figure 15.14 shows an FM-AFM image of a small area of the mica surface taken in pure water. The image presents a honeycomb-like pattern consisting of connected rings, which is a distinct contrast to a dot-like pattern or a triangle pattern obtained by contact mode AFM. In contact mode AFM, only periodic structures are imaged through the frictional interaction averaged over a relatively large tip–sample contact area. In addition, the obtained FM-AFM image shows a subnanometer-scale structural variation while only simple periodic patterns with no topographic variation are observed in contact mode AFM. This subnanometer-scale structural variation is possibly related to ion adsorption.

15.5.2 Purple Membrane Proteins [23]

The purple membrane (PM) is a highly ordered, native two-dimensional crystal composed of *bacteriorhodopsin* (bR) proteins and lipids, present as part of the plasmic membrane of *Halobacterium salinarum.* The bR molecule acts as a light-driven proton pump, which transfers protons from the cytoplasmic side to the extracellular side of the membrane by converting light energy into a proton gradient. High-resolution structural studies by electron microscopy and X-ray analysis have been intensively made because of the high degree of crystallinity. However, there have been few investigations on high-resolution imaging of the bR molecules in liquid as well as the relationship between the structure and the function. Thus, high-resolution analysis by AFM in liquid has been greatly expected.

The following describes a typical preparation method for PMs. A droplet of phosphate buffer solution containing PMs (10 mM PBS, 300 mM KCl, pH = 7.4) is deposited onto a freshly cleaved mica surface. We should wait for some time (typically 1 h) for the purple membranes to be sufficiently adsorbed onto the substrate and then the sample is rinsed in PBS for removing weakly bound membranes and contaminants. Finally the sample is imaged by FM-AFM in an imaging PBS (10 mM PBS, 200 mM KCl, pH = 7.4).

Strength of the membrane adsorption onto a mica surface is closely related to the interaction force between the electric double layers formed on top of the membrane and the mica surface. The electric double layer force can be repulsive or attractive depending on surface charge and on pH value of the buffer solution, as mentioned in Sect. 15.2.2. Since it also depends on ion concentration of an electrolyte, the strength of adsorption is strongly affected by the concentration of KCl. In fact PMs are not well-adsorbed to mica in a KCl solution of 0.1 mM. Use of KCl solution of high concentration (e.g. 300 mM) helps the improvement of the membrane adsorption. Besides, addition of divalent cation salt such as $MgCl_2$ to the solution is effective for the reduction of the electric double layer force, which is important for high-resolution AFM imaging.

Figure 15.15(a) shows an FM-AFM image of PMs in PBS. The bR molecules, each of which consists of seven transmembrane alpha helices (A-G), are known to form into a trimer. These trimers make a two-dimensional hexagonal array with a period of 6.2 nm. Figure 15.15(b) shows a structural model of the hexagonal array of the bR trimers (cytoplasmic side). We can clearly see a hexagonal array of three bright dots with a periodic unit spacing of about 6 nm accompanied by some defects, which agrees well with the structural model. Close comparison between the model and the image also clarified that the bright dot corresponded to the loop connecting E- and F-helices.

15.5.3 Isolated Protein Molecules [23]

A GroEL is a tetradecamer protein molecule, where seven identical subunits form a donut-like heptamer and the two heptamers are facing each other. The

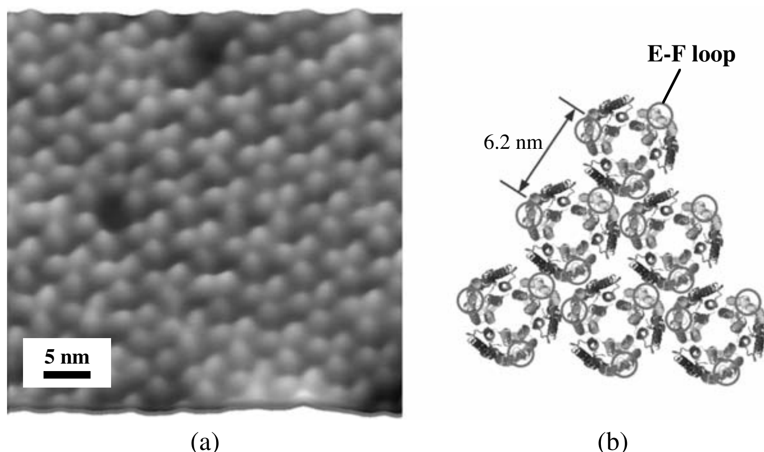

Fig. 15.15. (a) FM-AFM image of a purple membrane consistng of a hexagonal array of bacteriorhodopsin (bR) molecule trimers (Δf = +54 Hz, A_0 = 1.6 nm). The image was taken in a phosphate buffer solution (10 mM PBS, 50 mM KCl). (b) Structural model of the hexagonal array of the bR trimers

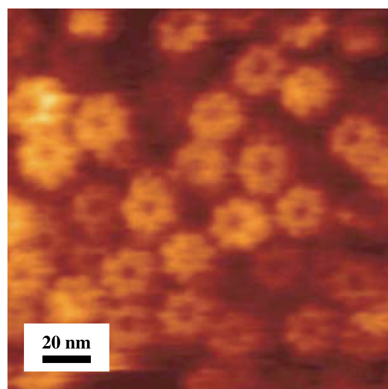

Fig. 15.16. FM-AFM image of chaperonin protein molecules attached on muscovite mica in phosphate buffer solution (Δf = +50 Hz, A_0 = 0.5 nm)

apparent size of the individual GroEL molecules is about 14 nm in diameter and 14 nm in height.

Figure 16 shows an FM-AFM image of GroEL protein molecules adsorbed on a mica surface in buffer solution. The outer surface (apical domain) of the tetradodecamer unit is clearly observed. The apical domain of the molecule appears like a flower with seven petals. Note that the individual subunits are nearly resolved in the AFM image. We sometimes found bottom heptamer molecules exposing equatorial domains, whose top heptamers were accidentally removed.

15.5.4 Measurement of Local Hydration Strcutres

Although liquid is treated as uniform continuum in fluid dynamics, the size effect of the liquid molecule has to be considered at a molecular scale. For instance, liquid density around an arbitrarily chosen single molecule cannot be uniform because of preferential coordination of neighboring molecules, which is described as density distribution function. This is also the case with the density distribution at a liquid-solid interface, which is known as solvation (hydration) structure (Fig. 15.17). In fact, there have been a large number of studies on liquid density distribution on a solid surface by X-ray structural analysis and surface force apparatus. Typical molecule density distribution shows a diminishing oscillation structure with an approximate periodicity of the molecule size. However, measured density distribution by these methods is not three-dimensional density distribution but one-dimensional distribution along the normal axis to the solid surface, which is averaged density distribution over a plane parallel to the surface. Since hydration structures play essential roles in the stabilization of protein structures as well as in various biological functions, investigation of molecular-scale hydration structures are required.

We recently found that frequency shift vs distance curve measured in water by FM-AFM reflects local hydration structure [5]. Figure 15.18 shows two frequency shift vs distance curves (approach and retract curves) taken in pure water on a polydiacetylene crystal surface. The oscillation structures with a period of about 0.2 nm reproducibly appeared in both curves. At present, this new method for the investigations of local hydration structures is being combined with the force mapping method, where forces (frequency

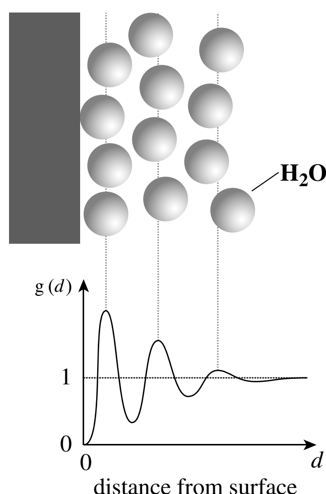

Fig. 15.17. *Top*: Schematic of hydration structure formed on a solid surface. *Bottom*: Normalized density distribution function $g(d)$ (d: distance from the surface)

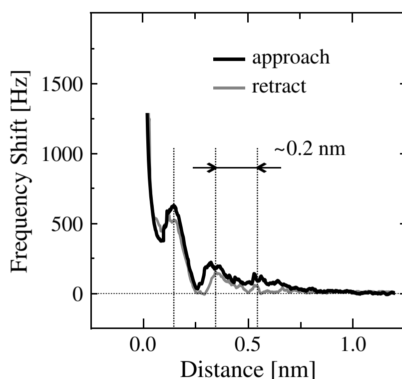

Fig. 15.18. Frequency shift versus distance curve measured on a polydiacetylene surface in pure water

shifts) are three-dimensionally mapped by measuring the force (frequency shift) curves over the sample surface. Although theoretical calculations are required for the interpretation of the relationship between the force data and the molecular density, the method is strongly expected to allow us to directly study molecular-scale hydration structures around biological molecules.

15.6 Summary and Outlook

This chapter has focused on recent progress in FM-AFM in liquids. The frequency noise analysis in low-Q and high-Q environments, the improvement of FM-AFM for liquid environments and the applications to high-resolution imaging as well as to the measurement of hydration structures have been described.

Achievements of true atomic resolution imaging in liquid by dynamic mode AFM open a new gate to a wide variety of application fields. In particular, it is a remarkably powerful tool for the study of molecular scale biology. Furthermore, the applications of various analytical methods based on FM-AFM such as KFM to biology is also greatly expected. On the other hand, there are still several problems to be solved for practical imaging applications.

When the cantilever in liquid is mechanically vibrated, the whole liquid container is also vibrated through liquid. This causes unwanted, various vibrations of the mechanical parts in the proximity of the container, which heavily distorts the cantilever vibration [24]. As a result, the oscillation spectrum of the cantilever contains many spurious peaks, which makes not only the identification of resonance of the cantilever more difficult but also the force sensitivity drastically decreased. In this case dynamic mode AFM does not work properly. Thus to avoid such problems, "development of a liquid container without generating spurious peaks" or "development of direct excitation

method for cantilever vibration" is required. The vibration excitation methods using external magnetic force, photothermal effect or a piezoelectric cantilever are appropriate as excitation techniques producing relatively less spurious peaks.

In FM-AFM imaging of a sample having large height difference in topography, the cantilever oscillation tends to be unstable or stops in the worst case. When the oscillation stops, the AFM imaging signal is inevitably lost; besides the tip can crash anytime into the sample. By setting the frequency shift at a small value (the tip is positioned far from the sample surface), the risk of the oscillation stop can be eliminated at the severe sacrifice of the imaging resolution. A new intelligent control method of the frequency shift, flexibly changing according to sample topography, is required.

References

1. *Noncontact Atomic Force Microscopy*, ed. by S.Morita, R. Wiesendanger, E. Meyer (Springer, Berlin, 2002)
2. T. Eguchi, Y. Fujikawa, K. Akiyama, T. An, M. Ono, T. Hashimoto, Y. Morikawa, K. Terakura, T. Sakurai, M.G. Lagally, Y. Hasegawa, Phys. Rev. Lett. **93**, 266102 (2004)
3. T. Ichii, T. Fukuma, K. Kobayashi, H. Yamada, K. Matsushige, Nanotechnology **15**, S30 (2004)
4. Y. Sugimoto, M. Abe, S. Hirayama, N. Oyabu, O. Custance, S. Morita, Nature Materials **4**, 156 (2005)
5. T. Fukuma, K. Kobayashi, K. Matsushige, H. Yamada, Appl. Phys. Lett. **86**, 193108 (2005)
6. T. Fukuma, M. Kimura, K. Kobayashi, K. Matsushige, H. Yamada, Rev. Sci. Instrum. **76**, 053704 (2005)
7. C.P. Green, John E. Sader, J. Appl. Phys. **98**, 114913 (2005)
8. J.E. Sader, J. Appl. Phys. **84**, 64 (1998)
9. S. Basak, A. Raman, J. Appl. Phys. **99**, 114906 (2006)
10. A. Maali, C. Hurth, R. Boisgard, C. Jai, T. Cohen-Bouhacina, J.P. Aime, J. Appl. Phys. **97**, 074907 (2005)
11. J.N. Israelachvili, *Intermolecular and Surface Forces*, 2nd edn. (Academic Press, 1992)
12. K. Kobayashi, H. Yamada, and K. Matsushige, Rev. Sci. Instrum. **80**, 043708 (2009)
13. W.P. Robins, *Phase Noise in Signal Sources* (Peregrinus, London, 1988), Chap. 3
14. T.R. Albrecht, P. Grütter, P. Horne, D. Rugar, J. Appl. Phys. **69**, 668 (1991)
15. P.R. Saulson, Phys. Rev. D **42**, 2437 (1990)
16. G. Meyer, N.M. Amer, Appl. Phys. Lett. **53**, 1045 (1988)
17. G. Meyer, N.M. Amer, Appl. Phys. Lett. **56**, 2100 (1990)
18. M. Ojima, A. Arimoto, N. Chinone, T. Gotoh, K. Aiki, Applied Optics **25**, 1404 (1986)
19. R. Kassies, K.O. van der Werf, M.L. Bennink, C. Otto, Rev. Sci. Instrum. **75**, 689 (2005)

20. M. Born, E. Wolf, *Principles of Optics*, 7th edn. (Cambridge University Press, Cambridge, 1999), Chap. 7
21. F. Giessibl, Phys. Rev. B **56**, 16010 (1997)
22. T. Fukuma, T. Ichii, K. Kobayashi, H. Yamada, K. Matsushige, Appl. Phys. Lett. **86**, 034103 (2005)
23. H. Yamada, T. Fukuma, K. Kobayashi, Y. Hirata, T. Kajita, T. Horiuchi, K. Matsushige, in preparation
24. M. Lantz, Y.Z. Liu, X.D. Cui, H. Tokumoto, S.M. Lindsay, Surf. and Interface Anal. **27**, 354 (1999)

16

Biological Applications of FM-AFM in Liquid Environment

Takeshi Fukuma and Suzanne P. Jarvis

Abstract. Atomic force microscopy (AFM) was noted for its potential to study biological materials shortly after its first development in 1986 due to its ability to image insulators in liquid environments. The subsequent application of AFM to biology has included lateral characterization via imaging, unraveling of molecules under a tensile load and application of a force either to measure mechanical properties under the tip or to instigate a biochemical response in living cells. To date, the application of frequency modulation AFM (FM-AFM) specifically to biological materials has been limited to relatively few research groups when compared to the extensive application of AFM to biological materials. This is probably due to the perceived complexity of the technique both by researchers in the life sciences and those manufacturing liquid AFMs for biological research. In this chapter, we aim to highlight the advantages of applying the technique to biological materials.

16.1 Quantitative Force Measurements

One of the advantages of the FM-AFM technique in any environment is that when operated in constant-amplitude mode it implicitly decouples the influence of conservative and dissipative forces. To fully take advantage of this fact it is necessary to be able to both implement the technique correctly and convert the resulting frequency shifts and driving signals into quantitative measures of conservative and dissipative interaction forces. In this section we discuss the quantification of FM-AFM and issues arising from the method of implementation.

16.1.1 Calculating Force from Frequency Shift

In contrast to the simple Hooke's law relation connecting the static deflection of a cantilever to the interaction force, the corresponding relation for FM-AFM is significantly more complex and depends on both the spring constant and amplitude of oscillation of the cantilever. This relation was first derived by Giessibl [1], and is valid for any amplitude of oscillation:

S. Morita et al. (eds.), *Noncontact Atomic Force Microscopy*,
NanoScience and Technology,
DOI: 10.1007/978-3-642-01495-6_16, © Springer-Verlag Berlin Heidelberg 2009

$$\frac{\Delta\omega}{\omega_0} = -\frac{1}{\pi A k}\int_{-1}^{1} F(z + A(1+u))\frac{u}{\sqrt{1-u^2}}\mathrm{d}u, \tag{16.1}$$

where k is the spring constant of the cantilever, F the interaction force between tip and sample, ω_0 its unperturbed resonant frequency, $\Delta\omega$ the change in resonant frequency, A the amplitude of oscillation, and z is the distance of closest approach between tip and sample.

To determine the interaction force from the observed frequency shift, (16.1) must be inverted. For many years this has been performed analytically for cases where the amplitude of oscillation was far smaller or greater than all characteristic length scales of the interaction force [2,3]. However, use of these limiting formulas in practice can potentially lead to significant errors, unless the precise nature of the force is known. This is particularly problematic if the interaction force contains a spectrum of length scales, encompassing short- to long-range components, as is often the case. In such situations, it is possible that the oscillation amplitude may be considered small with respect to long-range components, but large for short-range components. Accurate determination of the interaction force may therefore not be possible using these limiting formulas.

A simple yet accurate analytical formula that enables the direct determination of the interaction force from the measured frequency shift was proposed by Sader and Jarvis in 2004:

$$F(z) = 2k\int_{z}^{\infty}\left(1+\frac{A^{1/2}}{8\sqrt{\pi(1-z)}}\right)\Omega(t) - \frac{A^{3/2}}{\sqrt{2(t-z)}}\frac{\mathrm{d}\Omega(t)}{\mathrm{d}t}\mathrm{d}t, \tag{16.2}$$

where $\Omega(z) = \Delta\omega(z)/\omega_0$. This formula has been shown to be both mathematically and experimentally robust [4,5], is valid for any amplitude of oscillation and is applicable to any force law. However, it is only valid when the amplitude of oscillation is kept constant (i.e., it is not applicable to constant excitation FM-AFM). Further, an inherent assumption in deriving this formula is that the interaction force is continuous. This is not the case when discontinuities occur due to bond breaking as is the case in single molecule spectroscopy measurements. Thus, care must be taken in these experiments to only apply the formula in the region where this assumption is valid. It should also be noted that this formula assumes that the resonance condition is met. If the measurements are made off resonance (this can easily be done in error in low Q environments such as liquid) then the correct force is only retrieved if the phase error is known and accounted for in the calculation [6,7].

16.1.2 Cantilever Excitation in Liquid

For operation, FM-AFM requires mechanical excitation of the cantilever at the resonance frequency. When investigating biological samples either piezo activation or magnetic activation [8] has been chosen. The piezo activation

method is usually considered the easiest activation method to implement because it does not require any modification to standard commercial cantilevers. In this case, a small piece of piezoelectric actuator is placed adjacent to the cantilever holder. An alternating voltage signal, which is referred to as the cantilever excitation signal, is applied across the actuator to induce a vibration. This vibration is transmitted through the cantilever holder and cantilever base to the cantilever itself. Since the actuator does not directly drive the cantilever end but instead drives it via other mechanical elements, the vibration of the actuator excites the resonances of all the elements mechanically coupled with the actuator. Consequently, the phase and amplitude of the deflection signal can be influenced by the spurious resonances that do not represent the true cantilever vibration characteristics. Such influence can lead to an error in the quantification of force from frequency shift and dissipation measurements. It can also prevent stable cantilever vibration especially in FM-AFM, where the phase information of the deflection signal is used in the self-excitation circuit. Such influence is often a serious problem in liquid. The Q-factor in liquid (typically $Q < 10$) is much lower than that in air and vacuum so that the phase delay and amplitude distortion induced by the spurious resonances are not negligible. In addition, the actuator is mechanically coupled with additional elements (e.g., the liquid cell) through the liquid. This forms a complicated mechanical transmission path through which the vibration energy of the actuator can excite a number of spurious resonances.

To avoid any influence from spurious resonances, it is desirable to apply an excitation force directly to the end of the cantilever. Magnetic activation [8] fulfills this requirement. With this method, the cantilever is usually modified to have magnetic sensitivity either by coating it with a thin magnetic film or attaching a magnetic particle on the backside of the cantilever. The film, or the particle, is magnetized by applying a strong magnetic field. With this configuration an excitation signal is fed into a $V - I$ converter, which drives a coil placed close to the cantilever (usually underneath the sample), to produce an alternating magnetic field at the frequency of the cantilever resonance. The coil is usually aligned such that the interaction between the alternating magnetic field and the magnetic moment of the modified cantilever gives rise to a magnetic force perpendicular to the cantilever in order to excite the cantilever vibration normal to the surface. In an alternative arrangement of magnetic activation, cantilever actuation is achieved by passing an alternating electric current through a triangular cantilever. Thus, forming a current loop with a magnetic moment perpendicular to the plane of the cantilever. When placed at an angle in a static magnetic field, a force proportional to the current through the cantilever is generated [9].

The difference in measured amplitude and phase vs. frequency response obtained for the two different activation techniques with the same cantilever can be seen in Fig. 16.1a for piezo activation and Fig. 16.1b for magnetic excitation. The curves obtained with magnetic excitation show the typical amplitude and phase response of a simple harmonic oscillator while those

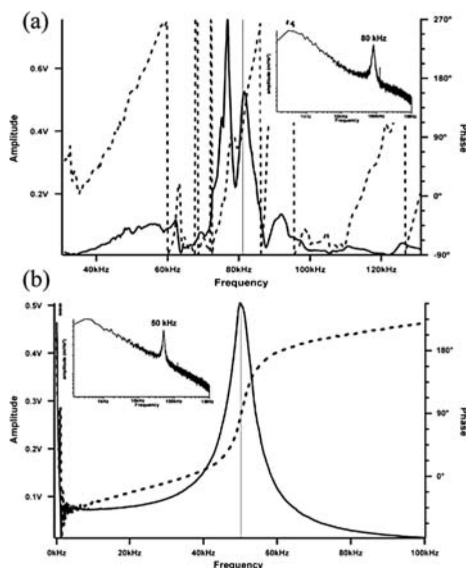

Fig. 16.1. Amplitude and phase vs. frequency characteristics of (**a**) cantilever oscillated in a liquid with a piezo excitation and (**b**) magnetic excitation. The insets show fast fourier transform spectra of the cantilever deflection signals showing thermal brownian vibration peaks (Reused with permission from Higgins et al. [10]. Copyright 2005, Institute of Physics)

obtained with piezo excitation show a number of spurious peaks. Simple phase vs. frequency characteristic are desirable for stable operation and quantitative measurements by FM-AFM, where the phase information is used for driving the cantilever.

16.1.3 Single Molecule Spectroscopy

FM-AFM being a relatively new technique, many applications of FM-AFM to biology have involved model samples that have already been studied extensively by other AFM techniques. In such cases, the primary motivation has been to characterize the FM technique itself rather than to elucidate new information about the chosen sample. In some cases new information has been obtained by utilizing the unique capability of FM-AFM to separate out conservative and dissipative components of the interaction, while in other cases it has been the enhanced sensitivity of the technique in comparison to alternative dynamic techniques which has revealed previously unobservable phenomena.

The first application of FM-AFM (actually FM-AFM combined with Q control) to a biological sample utilized the capacity of FM-AFM to separate out conservative and dissipative components of the interaction to estimate

the effective viscosity of a single dextran molecule [11]. In this measurement, FM-AFM was not applied in imaging mode but instead the technique was applied to single molecule force spectroscopy and found to provide significant improvement over conventional dynamic and static measurements. Specifically, they were able to measure a phase transition during the elongation of the dextran molecule and its effective viscosity to be 6,000 Pa·s, information not accessible with conventional static force spectroscopy. Although this experiment used oscillation amplitudes of approximately 10 nm this was still at least 1 order-of-magnitude smaller than the length of the dextran molecules and as such the magnitude of the oscillation was not found to be detrimental to the measurement. Similar measurements of dextran were subsequently made by the same group using transverse oscillations of a vertically mounted probe, the stiffness of which negated the addition of active Q control to achieve the same results [12].

The impact of oscillation amplitude in FM-AFM single molecule force spectroscopy was investigated in more detail with the mechanical unfolding of tandem repeats of titin I27 domains [13]. Unfolding intermediates were observed in each unfolded domain, which had not been observed previously with conventional force spectroscopy. The sensitivity of the FM technique to these intermediates was found to be related to the oscillation amplitude of the cantilever with smaller oscillation amplitudes providing higher sensitivity, as expected. In these measurements the smallest stable oscillation amplitude was 4.5 nm.

FM-AFM has also been applied to the measurement of ligand-receptor interactions, where the well-studied biotin–avidin system was chosen [10]. In this case, the mean unbinding force of a single unbinding event was found to be significantly higher than any measurements made with static force microscopy at different retraction rates. This was attributed to the significantly higher velocities achieved with FM-AFM, where the tip velocity is dependent on the resonant frequency and the oscillation amplitude of the cantilever (in this case 16.8 kHz and 6.3 nm, respectively). In the case of static-mode AFM, tip velocities are governed by z-piezo velocity and are typically limited to around 103 nm/s or less due to hydrodynamic drag forces.

16.2 Subnanometer-Resolution Imaging

16.2.1 Overview

Many examples of FM-AFM imaging of biological materials performed in the early stage have focused on comparing variations in experimental technique either by comparing the FM-AFM technique to other dynamic methods, comparing different feedback parameters within the FM-AFM technique or variations of the FM-AFM technique such as constant excitation FM-AFM

or FM-AFM plus Q control. Most of these comparisons were made with relatively large oscillation of the cantilever typically around 10 nm in amplitude which as we will see in Sect. 16.2.2 would have substantially decreased the overall sensitivity of the technique.

The first application of FM-AFM to imaging a biological sample was performed in 2001 by Tamayo et al. FM-AFM was again combined with Q control. In this case, living rat kidney cells were imaged with cantilever oscillation amplitudes typically in the region of 10 nm and imaging forces of less than 100 pN. Although the image was obtained as a frequency shift variation, the tip–sample distance regulation was made by keeping the oscillation amplitude constant. Thus, one may call it amplitude-modulation AFM rather than FM-AFM, depending on the definition. Although scan sizes were of the order of microns and the limits to resolution were consequently not explored, the authors note higher resolution than with the conventional tapping mode technique (see Fig. 11 in [14]) and predict that the technique may one day have comparable sensitivity to the optical tweezers technique. The authors highlight that at this level of sensitivity new interactions must be considered, in particular the role of confined liquid between tip and sample (Fig. 16.2) [15].

The low level of applied force during FM-AFM imaging was also observed by Sekiguchi et al. who used fragile protein aggregates known as amyloid fibrils in phosphate buffered saline to compare frequency feedback with amplitude feedback for a self-oscillating cantilever with a fixed driving amplitude

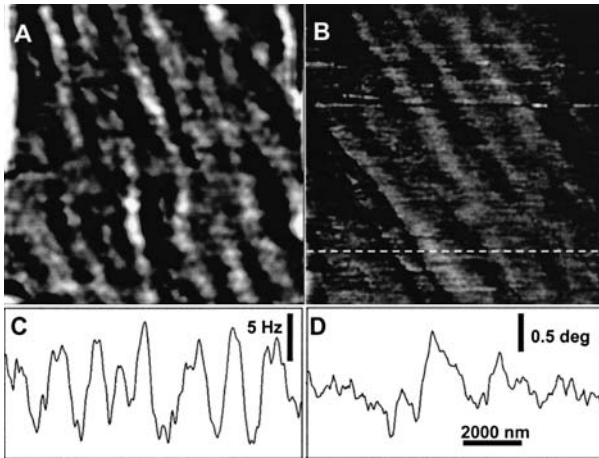

Fig. 16.2. (**a**) Resonant frequency image of a living rat kidney cell produced by combining FM-AFM and Q control. (**b**) Phase shift image of the same region with conventional tapping mode AFM in liquid. (**c**) and (**d**) are the profiles along the same scan line in (**a**) and (**b**). The scan line is marked in (**b**) with a *dashed line*. Scan size is $10 \times 10\,\mu$m. (Reused with permission from Tamayo et al. [14] Copyright 2001, Biophysical Society)

(constant excitation FM-AFM) [16]. They found a positive shift of the frequency to be more sensitive than a decrease in the amplitude (free lever amplitude 10 nm) and therefore used the frequency signal as the feedback signal for nondestructive imaging of the amyloid fibrils . They found that nondestructive imaging could only be achieved with an imaging force of 100 pN or less for these soft protein aggregates.

A similar comparison, this time between amplitude modulation AFM (AM-AFM) and FM-AFM imaging of DNA was made in pure water [17]. The cantilever amplitude during imaging was the same in both cases (4.8 nm), although the distance over which a frequency shift could be detected prior to hard contact with the sample, was approximately four times longer in the case of FM-AFM than the distance over which a decrease in cantilever amplitude could be detected in the case of AM-AFM. Thus the intermittent force applied could be more accurately controlled resulting in higher resolution and less sample deformation using FM-AFM.

Ebling et al. combined Q control with constant-excitation FM-AFM and directly compared the effect of enhanced Q when imaging DNA and a DPPC lipid bilayer lipid bilayers deposited onto a mica surface [18]. Feedback operated on change in amplitude of the cantilever and was set as close as possible to the free lever amplitude (typically 7 nm or greater) while still maintaining a stable image. In both cases increased corrugation of the topography was observed and attributed to a reduction of tip–sample indentation force.

While most comparisons have been made between different implementations of various dynamic techniques, in 2006 Hoogenboom et al. [19] made a direct comparison of constant-force contact mode images with FM-AFM images of bacteriorhodopsin formed with oscillation amplitudes in the range 0.64–1.00 nm. In their case, they note that higher normal forces were actually applied using the FM-AFM technique ($\sim$300 pN) although lateral forces were clearly minimized. In this case, the resolution appeared to be worse than that obtained using constant-force contact mode. Again using oscillation amplitudes of $\sim$1 nm but lower applied forces of $<$100 pN Hoogenboom et al. subsequently used FM-AFM to image various oligomeric states of voltage-dependent anion channels [20]. Although, in this case, FM-AFM allowed them to image with higher resolution they attributed this to a lack of lateral forces and still noted height inaccuracies in their FM-AFM images that they attributed to larger indentation forces than those observed in contact mode.

In 2006, Higgins et al. combined both imaging and force spectroscopy FM-AFM to investigate hydration at the membrane-fluid interfaces of two different supported lipid bilayers as a function of bilayer fluidity [21]. In this case the FM technique was utilized for its sensitivity and stability especially in regions of high attractive force gradients which result from the oscillatory nature of the force profile caused by the removal of successive hydration layers in the near surface region. The technique was found to be sensitive to individual hydration layers when operated with cantilever oscillation amplitudes between 0.8 and

3.2 nm. The authors established that structured water layers were present in the case of lipid bilayers in the gel phase but not in the fluid phase and thus hydration effects should be considered as an integral component in cell membrane theory.

16.2.2 Technical Progresses

FM-AFM was originally introduced by Albrecht et al. in 1991 to operate dynamic-mode AFM in ultrahigh vacuum (UHV) environment [2]. Since the first demonstration of true atomic resolution in 1995 [22, 23], FM-AFM has been used for imaging various surfaces at subnanometer resolution. Until recently, however, the subnanometer-resolution imaging capability of FM-AFM had been limited to UHV environments.

In 2005, Fukuma et al. presented a way to overcome this limitation. True molecular-resolution imaging of a polydiacetylene single crystal was demonstrated in vacuum, air and liquid with a specially developed multi-environment FM-AFM [24]. True atomic-resolution imaging in liquid by FM-AFM was also demonstrated by imaging mica in water [25]. This technical innovation was brought about by major improvements in instrumentation and operating conditions, namely; deflection sensor, oscillation amplitude, and stiffness of the cantilever.

First of all, a stiff cantilever is necessary to reduce the cantilever thermal vibration as well as to avoid instabilities known as "jump-to-contact." True atomic- or molecular-resolution imaging requires a vertical resolution better than 10 pm. The root-mean-square (RMS) amplitude of the cantilever thermal vibration $\langle z_{\mathrm{th}} \rangle$ is given by

$$\langle z_{\mathrm{th}} \rangle = \sqrt{\frac{k_{\mathrm{B}} T}{k}}, \tag{16.3}$$

where k_{B}, T and k shows Boltzmann's constant, absolute temperature and the cantilever spring constant, respectively. This equation shows that thermal vibration of less than 10 pm requires a cantilever stiffness higher than 40 N/m. Fukuma et al. employed a cantilever with a nominal spring constant of 42 N/m instead of soft cantilevers (<1 N/m) typically used for in-liquid applications [26]. Note that it is possible to reduce the thermal vibration amplitude via the gentle contact of the tip with the surface, such as in contact-mode AFM. However, this method can often prohibit the precise control of the vertical tip position at the atomic-scale transient regime between "contact" and "non-contact", a capability essential for "true" atomic- and molecular-resolution imaging as well as for atomic-scale manipulation.

Secondly, small amplitude oscillation is essential to enhance the sensitivity to the short-range interaction forces and thereby obtaining high spatial resolution. The RMS amplitude of the noise in z (δz) caused by the frequency noise (δf) is given by [27],

$$\delta z = \frac{\delta f}{\partial \Delta f / \partial z}. \tag{16.4}$$

Giessibl et al. described that frequency noise is proportional to A^{-1} whereas $\partial \Delta f / \partial z$ is constant for small amplitudes and proportional to $A^{-3/2}$ for large amplitudes, hence the existence of an optimal amplitude [28]. This calculation showed that the optimal amplitude is of the order of the decay length of the force components. As for the short-range interaction force, this typically corresponds to the values less than 0.5 nm. Fukuma et al. used an oscillation amplitude of 0.2–0.3 nm [26] while the amplitude typically used for in-liquid application is larger than 2–3 nm.

Finally, the use of a low noise cantilever deflection sensor is necessary for the stable oscillation of a stiff cantilever with small amplitude as well as for ensuring thermal-noise-limited performance [24]. In FM-AFM, the deflection signal is used for generating the excitation signal as well as for detecting the frequency shift. Thus, stable self-oscillation with a small amplitude requires a low noise deflection signal. In addition, stiffer cantilevers make it more difficult to achieve thermal-noise-limited performance in FM-AFM [29]. The peak value of the power spectrum density (PSD) of the cantilever thermal vibration $(z_{\mathrm{th}})_{\mathrm{peak}}$ is given by,

$$(z_{\mathrm{th}})_{\mathrm{peak}} = \sqrt{\frac{2k_{\mathrm{B}}TQ}{\pi f_0 k}}, \tag{16.5}$$

where f_0 and Q are resonance frequency and the Q factor of the cantilever. Assume that $k = 40\,\mathrm{N/m}$, $Q = 10$, $f_0 = 130\,\mathrm{kHz}$, $(z_{\mathrm{th}})_{\mathrm{peak}}$ is 71 fm/$\sqrt{\mathrm{Hz}}$. To reduce the influence of the deflection sensor to less than 10% of this value, the deflection noise from the sensor should be less than $71 \times 1/3 = 24$ fm/$\sqrt{\mathrm{Hz}}$. Whilst the deflection PSD from the sensor is 100–1,000 fm/$\sqrt{\mathrm{Hz}}$, the PSD of the deflection sensor developed by Fukuma et al. in 2005, was 17 fm/$\sqrt{\mathrm{Hz}}$ [24]. Details of the instrumentation required to achieve this noise performance are described in the previous chapter.

The impact of the technical innovation on the field of AFM research stimulated subsequent instrumentation development and additional exploration of these technologies for use in biological applications. Fukuma et al. further reduced the deflection noise density of the optical beam deflection sensor to 5.7 fm/Hz [29] and utilized these techniques in the investigations of biological materials [30–32] They also showed that true atomic resolution can be obtained not only by FM-AFM but also by phase-modulation AFM (PM-AFM) [33] when operated with a low noise deflection sensor, a stiff cantilever and small amplitude. Hoogenboom et al. obtained atomic-scale images of mica in liquid with a low-noise Fabry-Perot interferometer [19]. These technical advancements opened up the possibility of subnanometer-scale investigations on biological systems directly under physiological environment.

16.2.3 Biological Applications

In 1993, Ohnesorge et al. presented the first atomic-resolution image obtained in liquid by contact-mode AFM [34]. Compared to contact-mode AFM, FM-AFM has three major advantages: (1) precise control of the vertical tip position, (2) high spatial resolution, and (3) capability of imaging isolated molecules. Here, we show FM-AFM applications for biological systems, highlighting these three advantages.

Hydration Layers

In contact-mode AFM, a soft (<1 N/m) cantilever is generally used to obtain sufficient force sensitivity. However, the short-range attractive force at the atomic-scale non-contact regime, often presents a large force gradient exceeding the cantilever spring constant thus causing a cantilever instability known as "jump-to-contact". In addition, soft cantilevers can suffer from large thermal fluctuations, which can reduce control of the vertical tip position. In FM-AFM, the high stiffness of the cantilever, together with the restoring force of the vibrating cantilever, helps to avoid such instabilities, giving precise control over the tip vertical position at the atomic-scale contact/noncontact regime. Here, we present a biological application making the best use of this advantage [30].

Water molecules adjacent to biological membranes can potentially play a key role in the biological processes, particularly when they form hydration layers in which the water molecules are partially ordered due to interactions with the membrane, through dipole potentials or hydrogen bonding. If such hydration layers exist, they should alter the local interaction potential at the water/lipid interface, which can significantly influence the function of membrane proteins and molecular transport across the membranes. FM-AFM has a unique capability of measuring local interaction potentials with a nanometer-scale cross-section, using a sharp tip as a force probe. This capability is ideal to directly probe the interaction forces that nanoscale objects (e.g., proteins and solvated ions) would experience when they approach a membrane surface.

Figure 16.3 shows an example of such applications: a Δf vs. distance curve measured on a mica supported dipalmitoylphosphatidylcholine (DPPC) bilayer in phosphate buffer saline (PBS) solution. The Δf vs. distance curves obtained on the DPPC bilayer typically show an oscillatory force profile with one or two peaks. The averaged separation of the two peaks is 0.28 ± 0.05 nm. This distance is in agreement with the size of a water molecule and hence suggests that the oscillatory force profile corresponds to the sequential removal of ordered water molecules.

Tip–sample distance feedback regulation in liquid-environment FM-AFM operates based on the assumption that Δf increases with decreasing tip–sample separation, such as in the force branches indicated by arrows (1)–(3) in Fig. 16.3b. Therefore, if the Δf vs. distance curve shows an oscillatory profile,

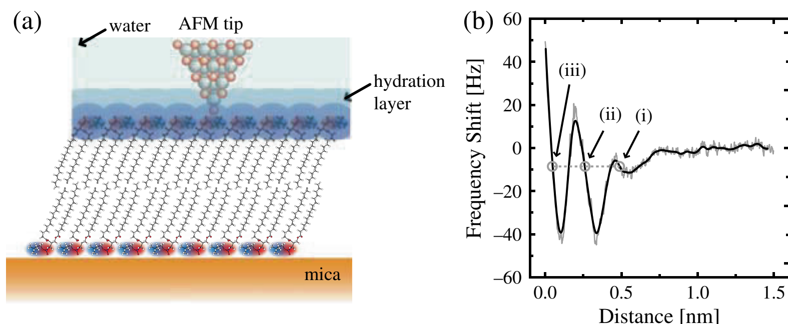

Fig. 16.3. (**a**) A DPPC bilayer formed on mica investigated by AFM in liquid. (**b**) Δf vs. distance curve measured on the DPPC bilayer in the PBS solution, showing oscillatory profile with two peaks. The smoothed line (*solid*) is obtained by averaging the raw data (*shaded*) over the distance range of 0.02 nm from each data point. (Reused with permission from Fukuma et al. [30] Copyright 2007, Biophysical Society)

the feedback can operate at multiple tip positions corresponding to one setpoint as indicated by the circles in Fig. 16.3b. Thus, the tip can spontaneously jump between those positions even if the setpoint is left unchanged.

Figure 16.4 shows an example of such spontaneous jumps during FM-AFM imaging of the DPPC bilayer in PBS solution. In the image shown in Fig. 16.4a, the tip is scanned from the lowest terrace (Terrace 1) and as the imaging progresses the tip jumps spontaneously twice. Terrace 1 shows a highly ordered arrangement of bright spots separated by 0.50 ± 0.05 nm along the stripes. The first jump of 0.26 nm (Terrace 1–2) results in subtle changes to the image although discrete corrugations are still observed. The second jump of 0.23 nm (Terrace 2–3) results in a less-ordered contrast although imaging resolution is still high. The heights of the spontaneous jumps (0.29 ± 0.06 nm) agree well with the size of a water molecule and the peak distance of the oscillatory force profile (0.28 ± 0.05 nm). This confirms that the tip is jumping between water layers and the individual layers are imaged with molecular-scale corrugations of the lipid headgroups. The result shows that the small loading force during FM-AFM imaging makes it possible to visualize weak interaction potentials presented by the water molecules adjacent to the biological membrane.

Lipid-Ion Network

In contact-mode AFM, long-range and short-range interaction forces are detected with equal sensitivity. In FM-AFM, the reduction of cantilever oscillation amplitude enhances the sensitivity to the short-range interaction force, and, at the same time, reduces the sensitivity to the long-range interaction force, thus giving higher spatial resolution than contact-mode AFM [28, 35].

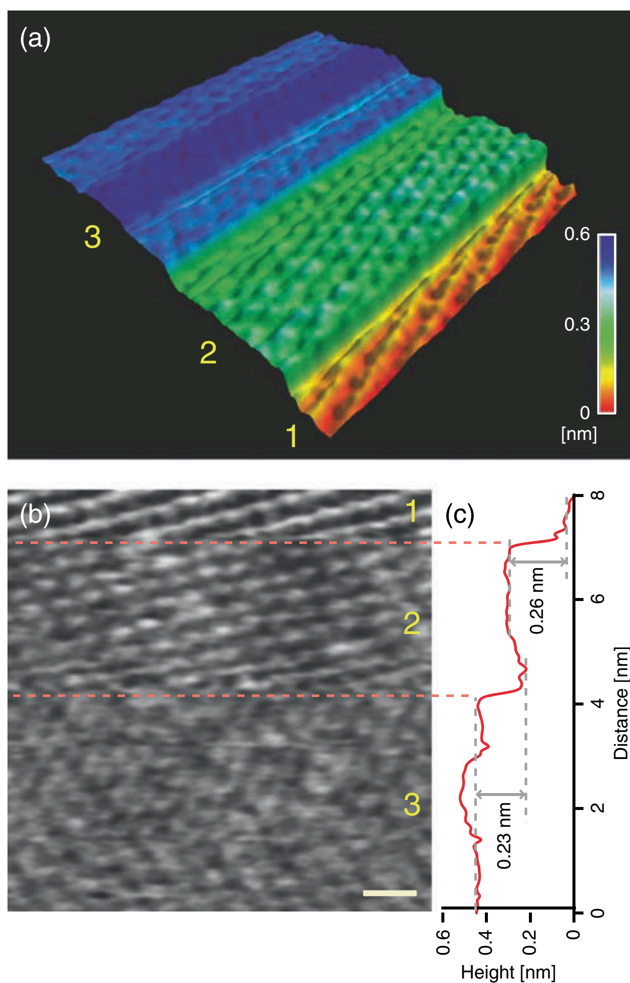

Fig. 16.4. (**a**) FM-AFM image of the DPPC bilayer in phosphate buffer solution showing spontaneous jumps during imaging. $8 \times 8\,\mathrm{nm}^2$, Tip velocity: 120 nm/s. Imaging speed: 85 s/frame. (**b**) Line-by-line flattened image of (**a**). Scale bar: 1 nm, Height range: 0.1 nm (*black to white*). Fast and slow scan directions: *left to right* and *top to bottom*. The regions indicated by the numbers 1, 2, and 3 correspond to the Terraces 1, 2, and 3 in (**a**). (**c**) Line-averaged height profile of (**b**) plotted along the slow scan direction. (Reused with permission from Fukuma et al. [30] Copyright 2007, Biophysical Society)

The following example of the use of FM-AFM in a biological application highlights this advantage, showing the unprecedented spatial resolution of 90 pm in liquid [31].

Under physiological conditions, biological membranes are surrounded by an electrolytic solution containing various metal cations. The influence of

these cations on membrane structure and stability has been studied intensively using model lipid bilayers. The addition of salts can trigger lipid bilayer phase separation [36–38], and vesicle aggregation and fusion processes [39,40]. The striking influence of the ions on membrane structure has highlighted the importance of lipid-ion interactions in biological processes. So far, a number of spectroscopy experiments have revealed that metal cations specifically interact with negatively charged moieties of the lipid headgroups [41–44]. These experiments, together with theoretical simulations [45], support the theory that individual ions may be interacting with multiple headgroups to form complex "lipid-ion networks" (Fig. 16.5a). This concept has been used to explain the observed influence of such ions in the enhanced mechanical strength of membranes [46] and the reduced mobility of the lipid molecules therein [47]. However, it has been a great challenge to experimentally access such lipid-ion networks due to the lack of a viable method for investigation of local lipid-ion interactions with Angstrom resolution. FM-AFM is an ideal tool for this, allowing direct investigation of the local lipid-ion networks formed at water/lipid interface.

Sequential FM-AFM images taken on the DPPC bilayer in PBS solution (Fig. 16.5) reveal that some of the surface groups change their configurations upon formation or disappearance of lipid-ion networks. For example, Subunit 1 is not pairing with another subunit in Fig. 16.5b while a pair of Subunits 3 and 4 appears in the next image (Fig. 16.5c) but with a darker contrast than other subunits, suggesting the lower height of this headgroup. It is likely that this particular headgroup was temporarily at an irregular tilt angle due to the interaction between Subunit 1 and 2 against the slight height difference when the first image was taken.

The observed structural changes due to the formation and disappearance of the lipid-ion networks indicates that the negatively charged phosphate groups are sharing the positive charge of cations, by which an attractive electrostatic force is exerted on all the headgroups involved in the network. The attractive

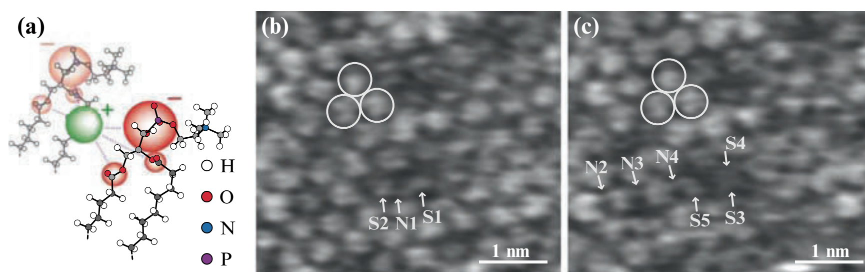

Fig. 16.5. (**a**) The lipid-ion complex formed the lipid/water interface. (**b**) and (**c**) Sequential FM-AFM images of the same area of the DPPC bilayer in PBS solution. Height range: 0.1 nm. Tip velocity: 120 nm/s. Imaging speed: 85 s/image (Reused with permission from Fukuma et al. [31] Copyright 2007, American Physical Society)

interaction force mediated through such complex lipid-ion networks should bind the headgroups together and increase the global mechanical strength of the membrane. In fact, it has been shown that the addition of metal cations increases the mechanical strength of the DPPC bilayer [46]. The FM-AFM images presented here reveal the submolecular-scale origin of such an influence of ions on the mechanical properties of the biological membrane.

Amyloid Fibrils

In contact-mode AFM, scanning the tip in contact with the surface inevitably causes a large friction force. This has hindered nondestructive imaging of isolated molecules or assemblies weakly bound to the substrate. As the vertical motion of the cantilever in dynamic-mode AFM dramatically reduces the lateral friction force, FM-AFM should be capable of imaging molecular-scale surface structures of such isolated systems. This capability has been demonstrated by imaging amyloid fibrils in PBS solution as described in the following section [32].

Amyloid fibrils are formed from a variety of proteins which are normally soluble in physiological solution [48, 49]. Under certain conditions, the precursor proteins misfold to form amyloid fibrils which are typically 10–30 nm in diameter and up to several micrometers in length as shown in Fig. 16.6a. The fibrils are insoluble β-sheet structures that can form aggregates in tissues and organs known as amyloid deposits. These deposits are found in a range of

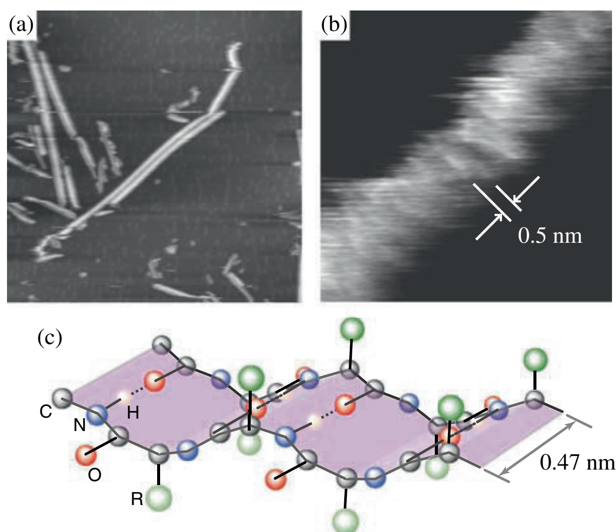

Fig. 16.6. FM-AFM images of IAPP fibrils on mica in PBS solution (**a**) 800×800 nm, $\Delta f = -55$ Hz, tip velocity: 1 μm/s. (**b**) 10×10 nm, $\Delta f = +50$ Hz, tip velocity: 195 nm/s. (**c**) Schematic model of the β-strands. (Reused with permission from Fukuma et al. [32] Copyright 2008, Institute of Physics)

neurodegenerative diseases such as Alzheimer's, Parkinson's and Huntington's disease [48]. Understanding the structure of amyloid fibrils is essential for elucidating the nucleation and kinetics of fibrillation in relation to the pathogenic pathway of amyloidoses.

Figure 16.6a, b show FM-AFM images of amyloid fibrils formed from the islet amyloid polypeptide (IAPP) deposited on mica in PBS solution. IAPP fibrils are associated with type 2 diabetes when deposited in pancreatic islets [50], The image shows finely striped features perpendicular to the fibril axis. The distance between adjacent stripes is approximately 0.5 nm. A previous X-ray diffraction study suggested the existence of periodic structure along IAPP fibril axes with a characteristic spacing of 0.47 nm [51]. Since this periodicity corresponds to hydrogen bond spacing between the β-strands (Fig. 16.6c), the periodic structure was attributed to the alignment of the β-strands perpendicular to the fibril axis [51]. The fine stripes observed in the FM-AFM image have comparable spacing aligned perpendicular to the fibril axis. Therefore, the striped features are attributed to the β-strands of IAPP fibrils. This demonstrates the possibility of FM-AFM to visualize individual β-strands in real space in a physiologically-relevant liquid environment.

16.3 Future Prospects

The theory and instrumentation of liquid-environment FM-AFM has dramatically progressed in the last 10 years. This has enabled quantitative measurements of conservative and dissipative forces and subnanometer-resolution imaging with piconewton-order loading forces at the solid/liquid interface. The biological applications presented here demonstrate that FM-AFM is capable of probing and visualizing the local interactions between the bio-molecules and surrounding physiological environment (i.e., water molecules and ions) as well as the structures of bio-molecules themselves.

There are still a number of technical issues and challenges to be overcome in order to make the technique more useful in practical studies. Among the most urgent of these are improvements in operation speed. This is important not only for visualizing dynamic processes but also for high-resolution imaging of large areas containing inhomogeneous complexes and also non-destructive high-resolution imaging of large isolated bio-molecules. These applications may not require high frame rate but do require a high feedback bandwidth. As up to now, imaging speed was not a major priority for applications performed in vacuum, there is considerable room for improvement.

Another important issue is the stability. As seen in Fig. 16.4, multiple feedback points can exist at the solid/liquid interface. Although this could be a useful tool for visualization of individual hydration layers, it can also make it difficult to control vertical tip position. This is not a simple technical issue as the solid/liquid interface inherently has a three-dimensional extension. This issue may be solved by employing the three-dimensional imaging technique developed for applications in UHV at low temperature [52], together with the

feedforward drift compensation technique developed for atom manipulation at room temperature [53].

There are also many application areas that have not been explored fully, including biology and electrochemistry. So far, the latter has not been explored at all by FM-AFM. This is partly because of the existence of electrochemical STM. However, there are emerging interests in the electrochemical processes of organic and biological molecules in relation to their applications to organic- and bio-electronics. Since these non-conductive molecules cannot be imaged by STM, we expect that the application of FM-AFM to this area will also grow in the near future.

References

1. F.J. Giessibl, Phys. Rev. B **56**, 16010 (1997)
2. T.R. Albrecht, P. Grütter, D. Horne, D. Ruger, J. Appl. Phys. **69**, 668 (1991)
3. U. Dürig, Appl. Phys. Lett. **75**, 433 (1999)
4. J.. Sader, S.P. Jarvis, Appl. Phys. Lett. **84**, 1801 (2004)
5. T. Uchihashi et al., Appl. Phys. Lett. **85**, 3575 (2004)
6. J.E. Sader, S.P. Jarvis, Phys. Rev. B **74**, 195424 (2006)
7. G.B. Kaggwa, J.I. Kilpatrick, J.E. Sader, S.P. Jarvis, Appl. Phys. Lett. **93**, 011909 (2008)
8. S.P. Jarvis, A. Oral, T.P. Weihs, J.B. Pethica, Rev. Sci. Instrum. **64**, 3515 (1993)
9. A. Buguin, O.D. Roure, P. Silberzan, Appl. Phys. Lett. **78**, 2982 (2001)
10. M.J. Higgins, C.K. Riener, T. Uchihashi, J.E. Sader, Nanotechnology **16**, S85 (2005)
11. A.D.L. Humphris, J. Tamayo, M.J. Miles, Langmuir **16**, 7891 (2000)
12. A.D.L. Humphris, M. Antognozzi, T.J. McMaster, M.J. Miles, Langmuir **18**, 1729 (2002)
13. M. Higgins, J.E. Sader, S.P. Jarvis, Biophys. J. **90**, 640 (2006)
14. J. Tamayo, A.D.L. Humphris, R.J. Owen, M.J. Miles, Biophys. J. **81**, 526 (2001)
15. S.P. Jarvis et al., J. Phys. Chem. B **104**, 6091 (2000)
16. H. Sekiguchi et al., Appl. Surf. Sci. **210**, 61 (2003)
17. C.-W. Yang et al., Nanotechnology **18**, 084009 (2007)
18. D. Ebling, H. Hölscher, B. Anczykowski, Appl. Phys. Lett. **89**, 203511 (2006)
19. B.W. Hoogenboom et al., Appl. Phys. Lett. **88**, 193109 (2006)
20. B.W. Hoogenboom, K. Suda, A. Engel, D. Fotiadis, **370**, 246 (2007)
21. M. Higgins et al., Biophys. J. **91**, 2532 (2006)
22. F.J. Giessibl, Science **267**, 68 (1995)
23. S. Kitamura M. Iwatsuki, Jpn. J. Appl. Phys. Part II **34**, L145 (1995)
24. T. Fukuma et al., Rev. Sci. Instrum. **76**, 053704 (2005)
25. T. Fukuma, K. Kobayashi, K. Matsushige, H. Yamada, Appl. Phys. Lett. **87**, 034101 (2005)
26. T. Fukuma et al., Appl. Phys. Lett. **86**, 034103 (2005)
27. edited by S. Morita, R. Wiesendanger, E. Meyer (Eds.), *Noncontact Atomic Force Microscopy (Nanoscience and Technology)* (Springer, Berlin, 2002)
28. F.J. Giessibl, H. Bielefeldt, S. Hembacher, J. Mannhart, Appl. Surf. Sci. **140**, 352 (1999)

29. T. Fukuma, S.P. Jarvis, Rev. Sci. Instrum. **77**, 043701 (2006)
30. T. Fukuma, M.J. Higgins, S.P. Jarvis, Biophys. J. **92**, 3603 (2007)
31. T. Fukuma, M.J. Higgins, S.P. Jarvis, Phys. Rev. Lett. **98**, 106101 (2007)
32. T. Fukuma, A.S. Mostaert, S.P. Jarvis, Nanotechnology **19**, 384010 (2008)
33. T. Fukuma, J.I. Kilpatrick, S.P. Jarvis, Rev. Sci. Instrum. **77**, 123703 (2006)
34. F. Ohnesorge, G. Binnig, Science **260**, 1451 (1993)
35. F.J. Giessibl, S. Hembacher, H. Bielefeldt, J. Mannhart, Science **289**, 422 (2000)
36. M. Rappolt, G. Pabst, H. Amenitsch, P. Laggner, Coll. Surf. A **183–185**, 171 (2001)
37. M. Ross, C. Steinen, H.-J. Galla, A. Janshoff, Langmuir **17**, 2437 (2001)
38. J.T. Groves, S.G. Boxer, H.M. McConnell, J. Phys. Chem. B **104**, 11409 (2000)
39. S. Ohki, N. Düzgüneş, K. Leonards, Biochemistry **21**, 2127 (1982)
40. S. Ohki, K. Arnold, Coll. Surf. B **18**, 83 (2000)
41. L. Herbette, C.A. Napolitano, R.V. McDaniel, Biophys. J. **46**, 677 (1984)
42. C. Altenbach, J. Seelig, Biochemistry **23**, 3913 (1984)
43. T.R. Hermann, A.R. Jayaweera, A.E. Shamoo, Biochemistry **25**, 5834 (1986)
44. H. Binder, O. Zschörnig, Chem. Phys. Lipids **115**, 39 (2002)
45. M.L. Berkowitz, D.L. Bostick, S. Pandit, Chem. Rev. **106**, 1527 (2006)
46. S. Garcia-Manyes, G. Oncins, F. Sanz, Biophys. J. **89**, 1812 (2005)
47. R.A. Böckmann, A. Hac, T. Heimburg, H. Grubmüller, Biophys. J. **85**, 1647 (2003)
48. P. Westermark et al., Amyloid **12**, 1 (2005)
49. P. Westermark, FEBS J. **272**, 5942 (2005)
50. P. Westermark, C. Wernstedt, E. Wilander, D.W. Hayden, Proc. Natl. Acad. Sci. USA **84**, 3881 (1987)
51. O.S. Makin, L.C. Serpell, J. Mol. Biol. **335**, 1279 (2004)
52. H. Hölscher, S.M. Langkat, A. Schwarz, R. Wiesendanger, Appl. Phys. Lett. **81**, 4428 (2002)
53. M. Abe et al., Appl. Phys. Lett. **90**, 203103 (2007)

17

High-Frequency Low Amplitude Atomic Force Microscopy

Hideki Kawakatsu,[1] Shuhei Nishida, Dai Kobayashi,
Kazuhisa Nakagawa, and Shigeki Kawai[2]

[1] Institute of Industrial Science, the University of Tokyo, 4-6-1 Komaba, Meguro-ku, Tokyo 153-8505, Japan kawakatu@iis.u-tokyo.ac.jp
[2] Institute for Physics, University of Basel, 82 Klingelbergstrasse, Basel, Switzerland shigeki.kawai@unibas.ch

Abstract. This chapter explains a series of work carried out to implement atomic force microscopy (AFM) capable of operating at frequencies above 1–200 MHz with an amplitude of drive of a few 10–100 pm, both in the deflection and torsional modes. To implement such a microscope, various elements that constitute the AFM were reconsidered from scratch. The issues are; (i) Cantilever, (ii) Cantilever vibration excitation, (iii) Cantilever vibration detection, (iv) AFM head, and (v) Control scheme. The instrumental aspect of the microscope will be discussed in the former half, and the results obtained will be discussed in the latter.

17.1 Cantilever

Miniaturization of the cantilever enables increase of natural frequency f_o while maintaining a set value for the spring constant. Mass sensitivity of a cantilever improves with increasing frequency. For example, a cantilever with a natural frequency of 100 MHz, Q factor 10,000, spring constant 1 N/m, temperature 10 K, driven with an amplitude of drive of 10 nm has in principle, frequency noise comparable to change in mass by one hydrogen atom [1]. The use of small cantilevers is expected to introduce the function of mass detection at the molecular or atomic level to cantilever based microscopy. It should, however, be noted that exploiting the intrinsically high sensitivity of a nanocantilever, or coupling to a nano device is in itself a challenging topic, and has a lot of technical issues such as measurement related frequency noise to be cleared. Various attempts to fabricate small cantilevers or high-frequency cantilevers and beams have been made over the past 20 years. The term "nanocantilever" first appeared for a metallic ball held by a filiform neck. Formation of such a structure was predicted by Mullins in 1965, and confirmed experimentally in 1969 in the process of sharpening metal tips for field emission [2]. In the

S. Morita et al. (eds.), *Noncontact Atomic Force Microscopy*, NanoScience and Technology,
DOI: 10.1007/978-3-642-01495-6_17, © Springer-Verlag Berlin Heidelberg 2009

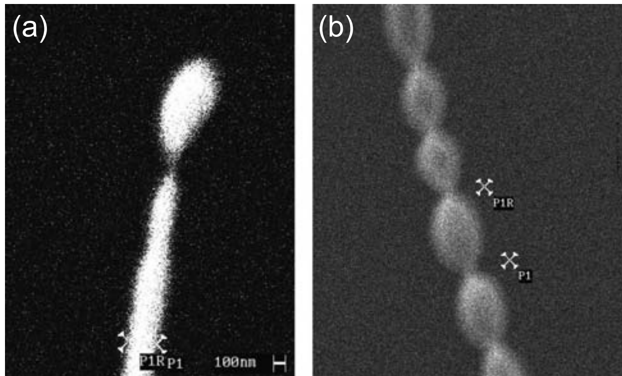

Fig. 17.1. Examples of metal nanocantilevers fabricated by heating a low tapered metal tip. (a) a 200 nm diameter metal ball ripening, (b) multiple ripening connected by filiform necks

early 1990s, N. Garcia and Vu Thien Binh published a paper on using such structures, which may attain a natural frequency of 1 GHz, as a force and mass sensor in AFM [3]. From 1995, the authors carried out a series of experiments on the method introduced earlier. Examples are shown in Fig. 17.1. In many cases, the tip-apex formed a sphere and a filiform neck due to Oswald ripening, but the morphological evolution was difficult to predict or control as shown in Fig. 17.1(b), not to mention batch fabricating a large number of cantilevers as a stock for AFM use [4]. Fabrication of AFM tips on the spherical mass was also an unsolved problem.

nanocantilever fabrication shifted to the use of MEMS fabrication techniques, where the cantilever could be tailor made with large numbers of hundreds or millions [5]. Due to the small size of the cantilever, the use of anisotropic etching of silicon was employed to ensure repeatability of fabrication that is not so much affected by the accuracy of the photolithography process [1]. Figure 17.2 shows some examples of the fabricated cantilevers. Some measure a few microns, and their natural frequency can be as high as 100 MHz. Attaining an amplitude of drive of around 100 pm, became the key issue in actually utilizing these cantilevers for AFM imaging. Fabrication of small cantilevers can be found in the literature [6–9].

17.2 Cantilever Vibration Excitation

The stable fabrication of small- and high-frequency cantilevers necessitated the selection of a reliable vibration excitation method. Massive piezo elements, a widely used device, attached to the base of the cantilever did not show a flat frequency response, and were not suitable for frequencies above

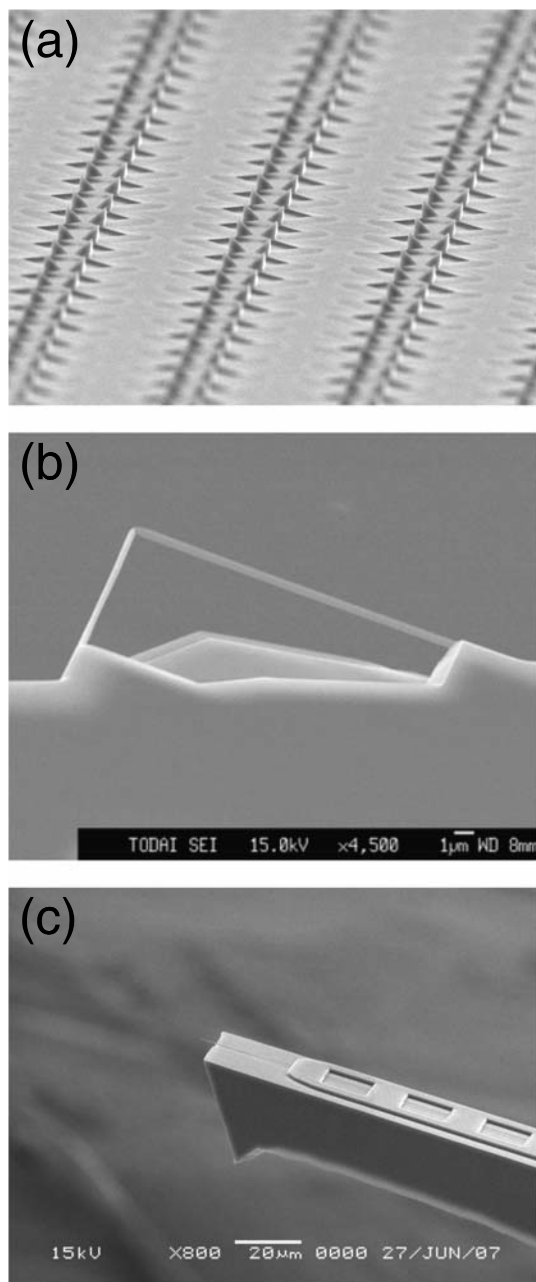

Fig. 17.2. Small cantilevers and oscillators fabricated from bulk silicon. (a) millions of cantilevers made by anisotropic etching of silicon, (b) triangular cantilevers composed of silicon nanowires, and (c) silicon nanowire cantilever with tip

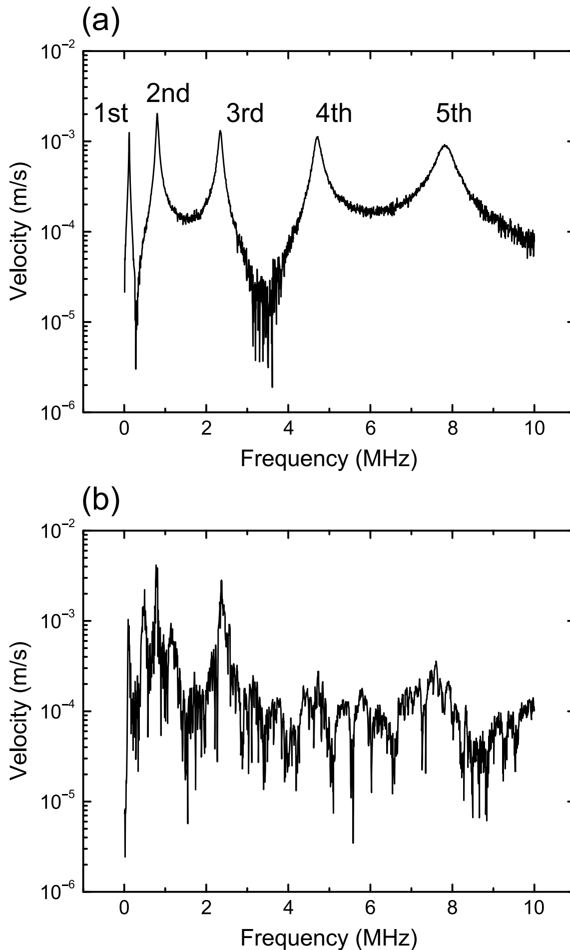

Fig. 17.3. Comparison of photothermal excitation and piezo excitation

ca. 5 MHz. Photothermal excitation proved to be effective in a wide range of frequency from DC to above 100 MHz [10–12]. In this method, a focalized beam from an intensity modulated laser diode was guided to the surface of the cantilever through an objective lens. For commercially available cantilevers, an intensity of 1 mW was sufficient in vacuum, and 2 mW in water. Figure 17.3 shows a comparison of photothermal excitation and piezo excitation made with the same liquid AFM. Since the actuation acts on the oscillator directly, various vibration modes of the oscillator could be excited with clarity. Phase rotation around resonance was also clear, facilitating phase based controls. Positioning of the excitation laser spot enabled the selection of modes to be excited, while surpressing unexpected mode-hopping. Other possible excitation methods have been employed in the field of mass sensing

with mechanical oscillators, such as, electrostatic excitation, joule heating excitation [13], surface acoustic wave excitation, magnetic excitation [14], and piezoelectric actuation [15, 16]. In terms of simplicity, photothermal excitation is favorable, but for cantilevers measuring below 1 μm in width or length, the other methods listed earlier may prove to be more feasible.

17.3 Cantilever Vibration Detection

Stable fabrication of micron sized cantilevers also facilitated the comparison and development of various cantilever vibration detection schemes. Issues put to question were (i) focalization down to the diffraction limit to accommodate micron sized cantilevers, (ii) capacity to measure the vibration of cantilevers up to the 100 MHz regime, (iii) ease of use in UHV and cryostats, (iv) compatibility with the photothermal excitation method, and (v) stability. Optical methods were considered first to lessen the requirements on the cantilever. Two methods were considered; (i) Homodyne detection using a focusing mirror and a reference arm incorporated with in the millimeter sized optical probe, with two optical fibres supplying and retrieving light to and from the optical probe and (ii) heterodyne laser Doppler detection with various carrier generating schemes. Among the two, the latter was superior in performance due to the high signal-to-noise ratio and stable operating point, typical of heterodyning techniques. The fact that velocity was directly measured acted favourably for small- and high- frequency cantilevers because the velocity signal increased in proportion to frequency for a given amplitude of drive. As the result, the noise floor of the measurement scheme gave a $1/f$ decrease in

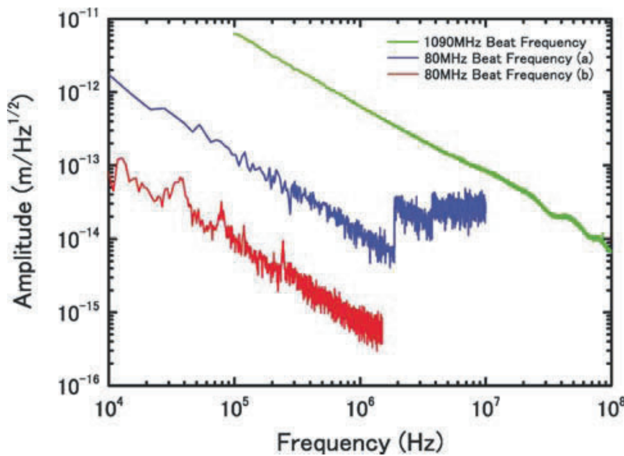

Fig. 17.4. Typical noise floors of the heterodyne laser Doppler interferometer with 80 MHz or 1.1 GHz carrier

terms of displacement [17]. Figure 17.4 shows typical noise floors for various sensitivity and frequency ranges of the Doppler interferometer. Noise level below 1 fm/$\sqrt{}$Hz was attained around 2 MHz. For high-frequency measurement above 20–200 MHz, the beat between two longitudinal modes of a He–Ne laser at 880 MHz plus a 200 MHz AOM, or a cascade of two AOMs operating at 540 MHz were used to generate a carrier above 1 GHz. For frequency range below 20 MHz, the use of a 80 MHz AOM proved to give the best performance in terms of signal-to-noise ratio, and are used our liquid AFMs and UHV AFMs operating below 20 MHz. The method could detect the vibration of a tungsten suboxide whisker measuring 70 nm in diameter, but requiring a narrow bandwidth in such a case, and not suitable as yet to accommodate such cantilevers for AFM and image with a reasonable scan rate. On the other hand, cantilevers measuring a few microns, and larger than the focal diameter could be measured with a good signal level up to 200 MHz. Heterodyne detection was effective in avoiding cross-talk between optical vibration excitation and measurement down to the fm level, since measurement was carried out around 80 MHz or 1.1 GHz, and not in the vicinity of the cantilever vibration modes.

17.4 AFM Head

Since detection and excitation of the cantilever vibration can be implemented by optical means, the design of the AFM is a relatively simple matter of positioning a focusing lens with respect to the cantilever. Figure 17.5 depicts the schematic of the laser Doppler optics with a 80 MHz AOM, and Figure 17.6 depicts a liquid AFM composed of an inverted optical microscope objective, two photothermal excitation lasers operating at 405 and 780 nm, illumination laserdiode, a CCD and the laser Doppler optics. The returning beam of the laser Doppler measurement is collected through the same optical path, so steering of the laser beam with a mirror was enough to position the laser spot on the designated location of the cantilever. Figure 17.7 shows the optical probe of an UHV AFM. Four beams guided to the optical probe are, the measurement beam, the reference beam, the photothermal laser beam, and the illumination beam. Guiding the reference arm to the optical probe was effective in decreasing the effect of axial and orthogonal vibration of the optical probe with respect to the laser source and the axis of the laser beam. The same optics was also applied to an UHV TEMAFM, with the exception of the focusing lens, which was replaced by a grin lens measuring 2 mm in diameter. The lens was inserted between the yokes of the TEM. Equivalent signal-to-noise ratio was confirmed, but the excitation efficiency was lower due to achromatic error of the lens. An optical probe with the function of Doppler measurement only was also implemented, and in such a case, the optical probe was connected to a polarization maintaining optical fibre [17].

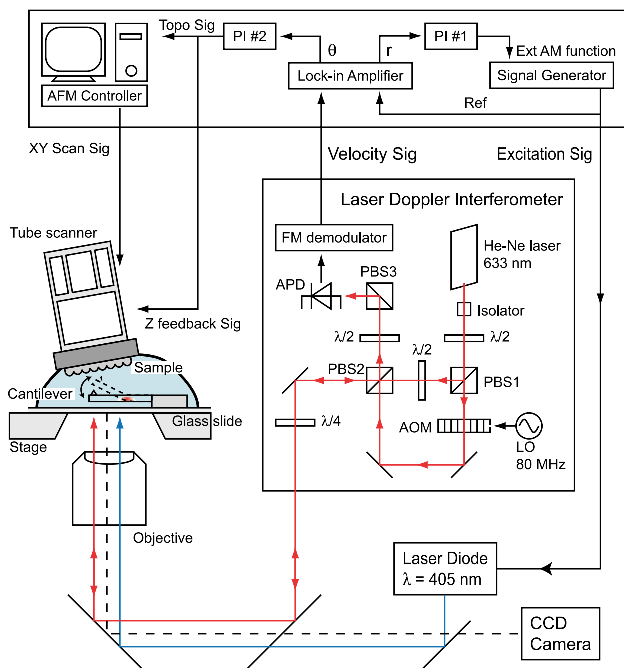

Fig. 17.5. Schematic of the liquid AFM with heterodyne laser doppler interferometry and photothermal vibration excitation. Self-excitation is not utilised in imaging

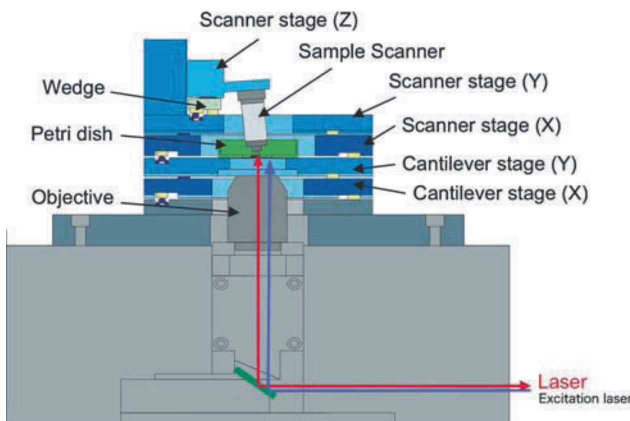

Fig. 17.6. Head of the liquid AFM

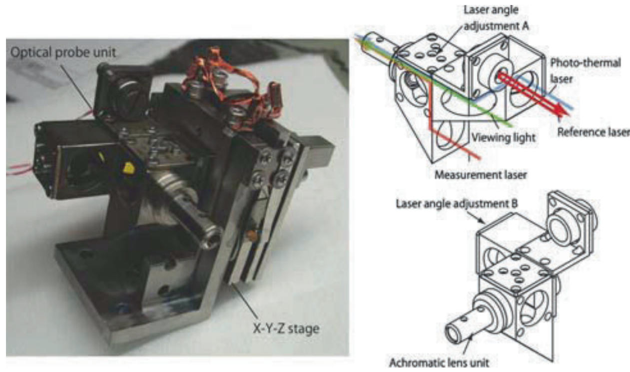

Fig. 17.7. Optical probes of UHV AFM. (a) for a Low temperature UHV AFM. For an UHV TEMAFM, a longer objective with a grin lens at the apex is inserted in the pole gap of the TEM

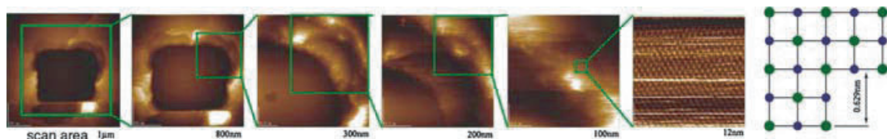

Fig. 17.8. KCl imaged from low resolution to high resolution. The imaged area is zoomed to a terrace at the top right corner

17.5 Control Scheme

For UHV AFM applications, the Doppler interferometer was inserted within the self-excitation loop of the cantilever, together with a phase shifter and auto gain control. The configuration is not so different from other UHV AFM, expect for the fact that the velocity signal is used for the self excitation. In the case of the liquid AFM, we have adopted a different scheme, as depicted in Fig. 17.5. The tip approach is accomplished by monitoring the self-excitation frequency of the cantilever, where an FM controlled signal generator is used within the self-excitation loop. After the cantilever has reached its operating point, in other words, the designated frequency shift has been met, the FM function of the signal generator is turned off, and the cantilever is driven at a fixed frequency. At the same time, tip to sample distance regulation is activated, in such a manner that the phase shift between the signal generator and the Doppler output is kept to a constant value by proportional-integral control. As the result, an equi-frequency shift surface can be mapped at the chosen value of the frequency shift. The advantage of this method over the conventional FM, AM, or PM methods is that: (i) the vibration amplitude is maintained in a damped environment, and imaging of stepped or corrugated surfaces is possible, (ii) the operating point can be reached in a gentle, quasi-static fashion, since approach is done in the slow self-excitation mode. Figure 17.8 shows KCl imaged in saturated butanol. Scanning with a relatively

high-positive frequency shift leads to dessorption of the KCl ions, leaving a square hole corresponding to the scanned area. Then imaging the same area can be carried out by lowering the amount of frequency shift. In the figure, the image area is zoomed to a small terrace on the top right corner of the hole, eventually attaining atomic resolution [18]. The result demonstrates the potential of the control method to image rough surfaces in liquid, and attain atomic resolution.

17.6 Imaging with Small Amplitude of Drive

As depicted in Fig. 17.4, the noise floor of the Doppler interferometer reaches the 1 fm/$\sqrt{\text{Hz}}$ level around 1 MHz. This allows for a relatively large signal-to-noise margin, giving the possibility to either (i) scan very fast by using a wide bandwidth, or (ii) image with a very small amplitude of drive. We have demonstrated the latter, since imaging with small amplitude has such physical significance as (i) local three-dimensional probing of the field that allow linear modelling of the system, (ii) possibility to map sub Å feature, and (iii) less disturbing to the sample and the structured liquid molecules in liquid. Figure 17.9 shows a series of Si(111) 7 × 7 surfaces imaged with an amplitude of drive of less than 1 Å [19]. The image with the smallest amplitude of drive reaches a value below 0.3 Å, which is a factor of 1/1,000 smaller than the value used when true atomic resolution was first achieved ten years earlier. The cantilever used for the imaging was a commercially available cantilever with a natural frequency of about 300 kHz, and a spring constant of 40 N/m, but driven at the second mode of deflection at around 1 MHz.

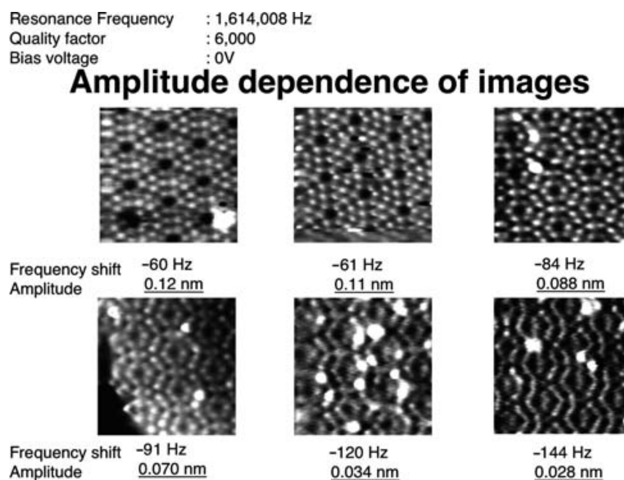

Fig. 17.9. Images of Si(111) 7 × 7 imaged with different amplitude of drive. The smallest amplitude can be as small as 10 pm

The higher spring constant of the higher mode is in part responsible for the success of imaging with the small amplitude of drive. Imaging of metastable surfaces of quenched Si(111), as well as single atom manipulation at room temperature were confirmed with the AFM operating with an amplitude of drive of around 100 pm or less [20, 21]. The same cantilever was driven at around 5 MHz, the third mode of deflection. Despite the increased level of spring constant, in the kN/m range, cleaved graphite, commonly known to be difficult to be observed by AFM due to its low level of force corrugation, was imaged readily [22]. Simultaneous imaging of STM and AFM gave new understanding of the contrast mechanism, the origin of giant corrugations, and contrast mechanism of AFM on graphite [23]. In liquid, true atomic resolution of such samples as NaCl, KCl, and mica were confirmed, also with sub Å amplitudes [24]. When imaging mica in pure water, lattice structures were seen to exist for a vertical approach of the tip to the sample for a range of over 10 Å, with a marked shift in vertical stiffness of the sample between the lattice layers. The fact that atomic resolution was obtained for a wide range of z position, is a strong indication that the AFM is mapping structured liquid molecules with unprecedented resolution. Fig.17.10 shows features obtained on mica immersed in pure water, which could be acquired with subangstrom amplitude of drive. High contrast features with a 60 pm height difference could be resolved [25].

17.7 Lateral Dynamic Force Microscopy

Various vibrational modes could be excited with a piezo element, or by the earlier mentioned photothermal excitation, with the latter capable of driving from DC to frequencies above 100 MHz. As depicted in Fig. 17.3, imaging with the torsion of the cantilever was just a matter of selecting the operating frequency to match the torsional mode of the AFM cantilever. In the case of photothermal excitation, the obtained vibration signal was even more clearer due to the low suprious vibrations. Figure 17.11 shows Si(111) 7×7 imaged with the first torsional mode of a commercially available cantilever. Although not the entire field of view, features corresponding to the 7×7 structure could be resolved. This was imaged with the FM mode, and no tunneling current was used for the control. A more detailed study was carried out using tunneling for gap control, and with an amplitude of drive of a few 10 to around 100 pm. Due to the drastically reduced level of lateral amplitude, lateral force gradient could clearly be resolved at the atomic level. Simulation based on first-principle calculation matched very well the experimental results, and also could explain the artefacts observed to be due to cross talk of vertical and lateral vibrations [26].

In the case of the liquid AFM operated in the torsional mode, clear true atomic resolution images could be resolved readily using the control scheme introduced in the former chapter. Fig. 17.12 shows mica imaged with the torsional mode at 1.16 MHz, amplitude to drive 130 pm. The image contrast

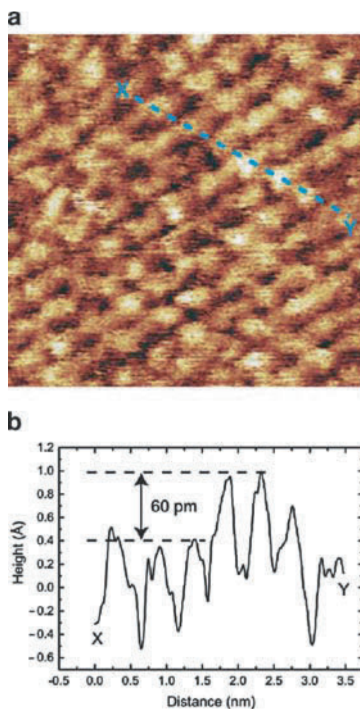

Fig. 17.10. Mica imaged in pure water. frequency: 964.750 kHz, amplitude: 99 pm

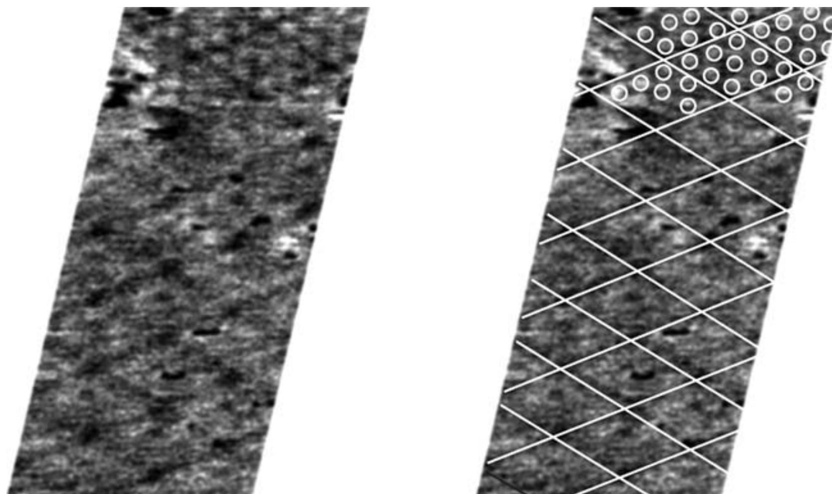

Fig. 17.11. Si(111) 7 × 7 imaged by dynamic mode lateral force microscopy. The tip height was regulated by the frequency shift of the torsional self excitation

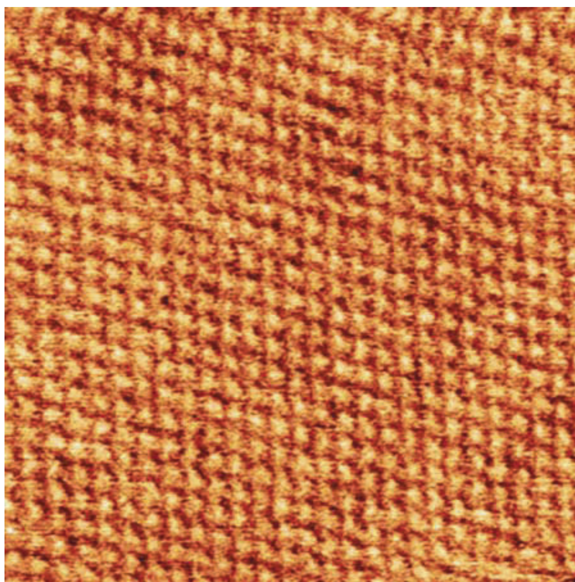

Fig. 17.12. Image of mica acquired with dynamic mode lateral force microscopy. Frequency 1.1 MHz, amplitude of drive 100 pm

was exceedingly better than lateral force imaging in vacuum [27]. In liquid AFM, the effect of amplitude and frequency of drive on the structured liquid molecules needs to be taken into account, since the choice these conditions may drastically change the physics of the confined region. At the expense of losing signal-to-noise ratio, it is meaningful in liquid AFM to decrease the amplitude of drive to the 10 pm order. It should also be pointed out that the surface mapped in liquid AFM may not be the true surface. The existence of a single molecule resting in registry with the lower layer is an indication that there are other similar molecules with a shorter lifetime equally resting on the surface. Due to the bandwidth of the detection or the electronic circuitry, the existence of the upper layer may have been overlooked and not mapped. Change of bandwidth at the cost of signal-to-noise ratio may reveal and possibly allow mapping of the upper layers. Temperature control in liquid AFM is underway to measure change in surface structure and to carry out time resolved measurements.

17.8 Summary

Small amplitude high-frequency AFM was discussed, with one eventual goal as the use of nanocantilevers as the force detector. Further miniaturization of the cantilever is faced with the issue of how to maintain a suitable level of

signal-to-noise ratio and bandwidth for their measurement. In other words, the issue comes down to how to couple to nanodevices with a reasonable bandwidth to exploit their intrinsically high sensitivity. This can be put in a perspective of how to concentrate energy used for measurement in a small volume. Exploring techniques both old and new, such as electron emission [28, 29] and near field optics is needed for a significant breakthrough.

References

1. H. Kawakatsu, S. Kawai, D. Saya, M. Nagashio, D. Kobayashi, H. Toshiyoshi, and H. Fujita, Rev. Sci. Instrum. **73**, 2317 (2002)
2. M. Drechsler, A. Piquet, R. Uzan, and Vu Thien Bihn, Surf. Sci. **14**, 457 (1969)
3. Vu. Thien Binh, N. Garcia, and A.L. Levanuyk, Surf. Sci. Lett. **301**, L224 (1994)
4. H. Kawakatsu, D. Saya, M. de Labachelerie, H.-J. Hug, and H.-J. Guentherodt, Jpn. J. Appl. Phys., Part 1 **38**, 3954 (1999)
5. H. Kawakatsu, H. Toshiyoshi, D. Saya, and H. Fujita, Jpn. J. Appl. Phys., Part 1 **38**, 3962 (1999)
6. J.L. Yang, M. Despont, U. Drechsler, B.W. Hoogenboom, M.E. Muller, P.L.T. M. Frederix, M.E. Muller, S. Martin, A. Engel, P. Vettiger, and H.J. Hug,. Appl. Phys. Lett. **86**, 134101 (2005)
7. S. Hosaka, K. Etoh, A. Kikukawa, and H. Koyanagi, J. Vac. Sci. Technol. B, **94**, 94 (2000)
8. J.L. Yang, T. Ono, and M. Esashi, Appl. Phys. Lett., **77**, 3860 (2000)
9. M.B. Viani, T.E. Schaffer, A. Chand, M. Rief, H.E. Gaub, and P.K. Hansma, J. Appl. Phys., **86**, 2258 (1999)
10. N. Umeda, S. Ishizaki, and H. Uwai, J. Vac. Sci. Technol. B **9**, 1318 (1991)
11. G.M. Kim, S. Kawai, M. Nagashio, H. Kawakatsu and J. Brugger, J. Vac. Sci. Technol. B **22**, 1658 (2004)
12. S. Nishida, D. Kobayashi, H. Kawakatsu, and Y. Nishimori, J. Vac. Sci. Technol. B 27, 964 (2009)
13. I. Bargatin, I. Kozinsky, and M.L. Roukes, Appl. Phys. Lett. **90**, 093116 (2007)
14. X.L. Feng, Rongrui He, Peidong Yang, and M.L. Roukes, Nano lett, **7**, 1953 (2007)
15. Sotiris C. Masmanidis, Rassul B. Karabalin, Iwijn De Vlaminck, Gustaaf Borghs, Mark R. Freeman, Michael L. Roukes, Science **317** no. 5839, 780 (2007)
16. J.L. Arlett, J.R. Maloney, B. Gudlewski, M. Muluneh, and M.L. Roukes, Nano Lett. **6**, 1000 (2006)
17. S. Kawai, D. kobayashi, S. Kitamura, S. Meguro, and H. Kawakatsu, Rev. Sci. Instrum. **76**, 083703 (2005)
18. S. Nishida, D. Kobayashi, T. Sakurada, T. Nakazawa, Y. Hoshi, and H. Kawakatsu, Rev. Sci. Instrum. 79, 123703 (2008)
19. S. Kawai, S. Kitamura, D. Kobayashi, S. Meguro, and H. Kawakatsu, Appl. Phys. Lett. **86**, 193107 (2005)
20. S. Kawai, F. Rose, T. Ishii, H. Kawakatsu, J. Appl. Phys. **99**, 104312 (2006)
21. S. Kawai, and H. Kawakatsu, Appl. Phys. Lett. **89**, 023113 (2006)

22. S. Kawai and H. Kawakatsu, App. Phys. Lett. **88**, 133103 (2006)
23. S. Kawai and H. Kawakatsu, Phys. Rev. B 79, 115440 (2009)
24. S. Nishida, D. Kobayashi, T. Sakurada and H. Kawakatsu unpublished
25. S. Nishida, D. Kobayashi, T. Sakurada, T. Nakawasa, Y. Hoshi, and H. Kawakatsu, Rev. Sci. Instrum. 79, 123703 (2008)
26. S. Kawai, N. Sasaki, and H. Kawakatsu, Phys. Rev. B 79, 195412 (2009)
27. S. Nishida, D. Kobayashi and H. Kawakatsu, unpublished
28. E. Mueller. Z. Phys. **102**, 734 (1936)
29. K. Jensen, Kwanpyo Kim and A. Zettl, Nature Nanotechnology **3**, 533 (2008)

18

Cantilever Dynamics and Nonlinear Effects in Atomic Force Microscopy

A. Raman, R. Reifenberger, J. Melcher, and R. Tung

Abstract. With increasing efforts to improve resolution and material contrast in dynamic atomic force microscopy (dAFM), it has become important to precisely understand and exploit the mechanical dynamics of the AFM probe as it interacts with samples. Here we provide a broad overview of several topics in this area relevant to both amplitude and frequency modulated (AM and FM) AFM. We discuss three-dimensional eigenmodes of cantilever probes and tuning forks, and summarize their nonlinear dynamical interactions with the sample and their operation in liquids. An emphasis is placed on experimental implications of these physical phenomena. We conclude with an outlook of the relevance of these new developments for atomic resolution dAFM and for low-force biological applications.

18.1 Introduction

As described in many chapters of this book, dynamic atomic force microscopy (dAFM) [1] has become a major scientific instrument for nanoscale and atomic resolution imaging, manipulation, and force spectroscopy. The past two decades have witnessed many spectacular successes of dAFM from subatomic resolution imaging [2], atomic resolution force spectroscopy, and atomic recognition [3], to angstrom resolution imaging of soft biological membranes under liquids [4] and submicron imaging on the Martian surface [5]. As with any other enabling technology, this success has bred new research directions in surface physics, nanoscience, materials science, and biophysics, which in turn have created many new demands for next generation dAFM instrumentation. Of the many driving forces guiding the development of the next generation of dAFM, probably the two most important ones are (a) the need for greatly improved resolution so that imaging and manipulation with molecular and atomic resolution are made routinely possible, and (b) the need to significantly enhance material contrast while applying extremely gentle imaging forces especially for soft, heterogeneous biological samples under quasi-physiological conditions.

S. Morita et al. (eds.), *Noncontact Atomic Force Microscopy*, NanoScience and Technology,
DOI: 10.1007/978-3-642-01495-6_18, © Springer-Verlag Berlin Heidelberg 2009

The development of next generation dAFM will likely involve major efforts in (a) the fabrication of highly optimized, possibly nanoscale, calibrated suspended probes with ultra-high bandwidths, sensitivity, low-noise, self-sensing capability and with specially engineered nanoscale tips for improved spatial resolution, (b) the development of ultra-low noise, high bandwidth instrumentation for sensing the motion of the cantilever probe, including both self-sensing cantilevers or new optical detection methods, (c) the development of novel low-force modes that open up new channels for interrogating material properties with very high sensitivity, and (d) improving significantly the dynamics and control of the imaging or force spectroscopy process, possibly with the use of better control hardware, improved control algorithms, or new and better nano-positioning devices. The implementation of these efforts for the imaging and force spectroscopy of biological materials under liquid environments will be especially challenging.

Central to these efforts is an improved understanding of the mechanical motion and dynamics of the cantilever probe as it interacts with the sample. Early theory described these dynamics in terms of a simple point mass oscillator whose linear resonance frequency changes in response to local force gradients [1]. Since then, major theoretical and experimental advances have been made in understanding the cantilever mechanics and nonlinear dynamics of the interactions between the cantilever and short- and long-range tip–sample interactions in ambient, vacuum, and liquid environments.

As a consequence of these efforts to understand probe dynamics, we are at present witnessing the cusp of a wave of new innovations in dAFM that are beginning to shape the development of the next generation dAFM. The purpose of this chapter is to provide an overview and historical context for the main results that have been achieved in understanding and exploiting cantilever dynamics in atomic force microscopy in both the so-called amplitude-modulated AFM (AM-AFM) or tapping mode, and the frequency-modulation AFM (FM-AFM) or noncontact modes of operation. Nonlinear dynamic effects in AM-AFM are also covered in detail, and to a lesser extent in FM-AFM applications.

In Sect. 18.2, we discuss the vibration spectra of AFM microcantilevers and their eigenmodes and discuss the potential advantages offered to dAFM through the use of these higher eigenmodes. In Sect. 18.3, we focus on applications to AM-AFM and discuss efforts at mathematical modeling and simulation of AFM probe tips interacting with samples. With this in place, we move to reviewing different nonlinear dynamic phenomena that underpin dAFM operation including bifurcations, multiple oscillation states, grazing oscillations, chaotic dynamics, nonlinear interactions in multifrequency or bimodal AFM, and finally we discuss cantilever dynamics in liquid environments. In Sect. 18.4, we review the basic principle of FM-AFM and frequency shift measurements, discuss the dynamics of ultra-high frequency oscillators and ultra stiff oscillators such as tuning forks, and the use of nonlinear effects

in FM-AFM. Finally, we conclude with an outlook of ongoing and future developments in cantilever dynamics in Sect. 18.5.

To keep the scope of the chapter manageable, we omit the literature on dynamics of cantilevers modified by active feedback (including Q-control, self-excited, or parametrically excited) or cantilever dynamics in contact resonance/ultrasonic force microscopy, and only minimally touch upon lateral force measurements using dAFM.

18.2 Eigenmodes of AFM Cantilevers

Conventional AFM probes consist of a single crystal silicon or silicon nitride microcantilever, and possess a sharp conical or pyramidal tip near their free end to probe the sample surface. Like any vibrating structure, AFM microcantilevers possess an infinite number of eigenmodes, each with its own natural frequency, Q-factor and stiffness. Each eigenmode represents a harmonic motion at its natural frequency of the microcantilever with bending, or torsional, or lateral deformations with a specific number of nodes and anti-nodes. The intent in dAFM is to excite these eigenmodes using either (a) inertial excitation, say from a dither piezoelectric actuator, or (b) direct excitation such as from magnetic excitation [6] or Lorenz forces [7], or magnetostrictive excitation [8], or electrostrictive effects of a Schottky barrier [9], or using a band of excitation frequencies near the natural resonance frequency [10]. When the external excitation frequency is tuned to lie near the natural frequency of a specific eigenmode, the microcantilever oscillates at the excitation frequency in the shape of that eigenmode, even if the excitation frequency is not identical to the natural frequency of the eigenmode. Thus, it is instructive to understand what the eigenmodes of AFM microcantilevers are and how they are used in dAFM.

To understand the mechanical resonances and eigenmodes of AFM microcantilevers, we provide in Fig. 1 vibration spectra of (a) a tipless silicon cantilever (∼200 μm long), and (b) a tapping mode AFM silicon cantilever (∼100 μm long) with a large pyramidal tip. These measurements are made using a Polytec MSA-400 Scanning Laser Doppler Vibrometer (www.polytec.com). The cantilever bearing chip is attached to a dither piezo and deterministic excitation is applied over a wide range of excitation frequencies. The shape assumed by the cantilever when it is excited at a particular frequency is referred to as the operating deflection shape (ODS) and is shown in Fig. 18.1. For structures with well-spaced resonances, the ODS is essentially the same as the eigenmode.

18.2.1 Eigenmodes of Tipless Microcantilevers

First consider Fig. 18.1a where results from the tipless microcantilever are shown. By examining the ODS or eigenmode corresponding to each peak in the

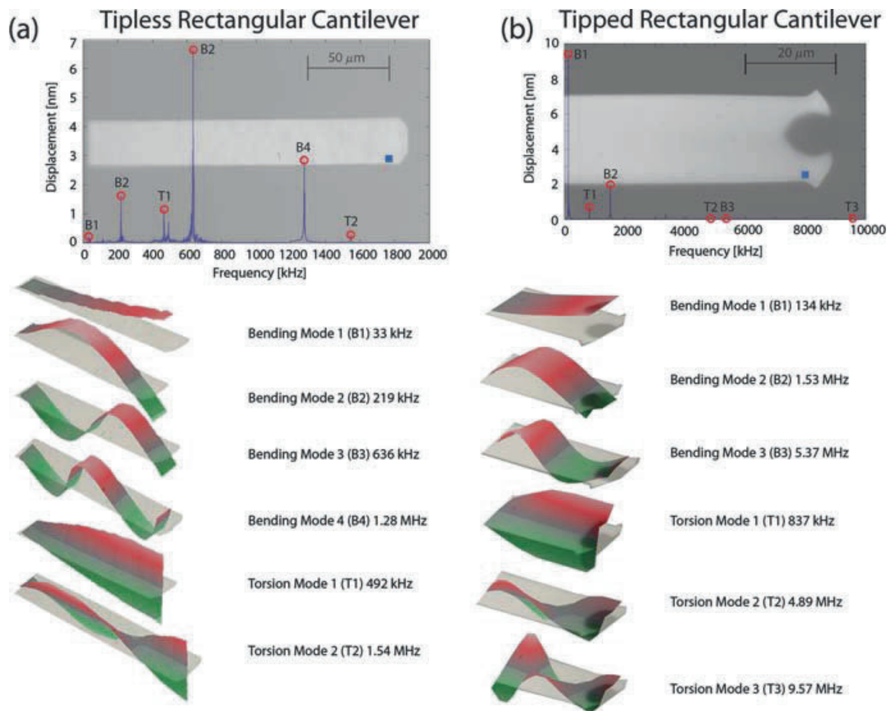

Fig. 18.1. Optical images and experimentally measured vibration spectra and three-dimensional eigenmodes of (**a**) a tipless Si microcantilever where the frequency spacings and eigenmodes follow theoretical predictions of a uniform elastic beam, and (**b**) of a short Si microcantilever with a large tip where the influence of tip mass significantly distorts eigenmodes and frequency spacings away from those of a uniform elastic beam. These data were acquired by mounting the AFM chip on a dither piezo exciter and measuring the vibration response in a Polytec MSA-400 Scanning Laser Doppler Vibrometer system. The vibration spectra plotted correspond to data collected near the free end of the cantilever as indicated by the blue square in the optical images

vibration spectrum, it becomes possible to identify the cantilever transverse bending eigenmodes, denoted as B_n, $n = 1, 2, \ldots$, the torsional eigenmodes, denoted T_n, $n = 1, 2, \ldots$, where the T_n or B_n eigenmode contains $n-1$ vibration nodes along the axis of the cantilever. However, sometimes the lateral bending eigenmodes L_1, L_2, etc. can also be observed where the cantilever bends in its plane laterally. The greater the eigenmode number, the larger its resonance frequency and Q-factor and the greater its spatial modulation. The *fundamental* transverse bending, lateral bending, and torsional eigenmodes are B_1, L_1, and T_1, respectively, while B_n, L_n, and T_n, $n > 1$ are referred to as the *higher-order* eigenmodes.

In the absence of tip mass, the resonance frequencies of these eigenmodes are spaced apart as predicted by simple classical elastic beam theory [11] for a uniform rectangular beam. For instance, the measured ratios of resonance frequencies of the B_1, B_2, and B_3 eigenmodes in Fig. 18.1a are close to the theoretically predicted ratio [11] of 1:6.3:17.5. Likewise, the ratios of resonance frequencies of the T_1, T_2, and T_3 eigenmodes in Fig. 18.1a are close to the theoretical ratio of 1:3:5. Thus, the eigenmodes of tipless microcantilevers for the most part behave as anticipated by the vibration theory of a uniform rectangular beam.

When a microcantilever eigenmode is excited, the tip should oscillate harmonically with a well-defined motion. If a transverse bending eigenmode B_n, $n = 1, 2, \ldots$, is excited, the sharp tip should oscillate perpendicular to the surface experiencing normal force gradients, while if one of the torsion eigenmodes is excited, T_n, $n = 1, 2, \ldots$, then the tip should oscillate tangentially to the sample surface sensing the lateral (friction) force gradients. Of course, small misalignments of the AFM probe relative to the sample surface can cause the B_n eigenmodes to sense some frictional forces [12] when they ought to sense only normal forces; conversely, the B_n or L_n eigenmodes can detect some normal forces due to misalignment with the surface [13].

One important observation on the vibrations of the tipless rectangular cantilevers (Fig. 18.1a) is that the cantilever oscillation near the free end (the tip motion) is comparable in magnitude to the cantilever oscillation at any other antinode of vibration. As we will see soon, the influence of a tip mass significantly alters this result and has important ramifications for small amplitude dAFM using higher-order eigenmodes.

18.2.2 Influence of Tip Mass on AFM Cantilever Eigenmodes

From the results provided in Fig. 18.1b the major differences between the eigenmodes of a *tipless* and *tipped* microcantilever become abundantly clear:

1. First of all, the experimental frequency ratios of the B_1, B_2, and B_3 eigenmodes or the T_1, T_2, and T_3 eigenmodes are quite different from those predicted by the theory of a tipless, uniform rectangular beam. For example, the experimental frequency ratios of the B_1, B_2, and B_3 eigenmodes in Fig. 18.1b are 1:11.4:40.1 as compared to the theoretical ratios of 1:6.3:17.5 for a uniform tipless rectangular beam. Similarly, the measured frequencies of the T_1, T_2, and T_3 eigenmodes in Fig. 18.1b are in the ratio 1:5.8:11.4 instead of 1:3:5 as predicted by the theory of a tipless, uniform rectangular cantilever. However, when an appropriate tip mass is incorporated into the theoretical model [14, 15], this discrepancy between theory and experiment can be resolved. Typically, the tip mass is 5–20% of the cantilever mass, and sometimes, as for the cantilever in Fig. 18.1b, the tip mass may be 40–50% of the cantilever mass.
2. Second, while the shape of the fundamental eigenmodes B_1, T_1 of the tipped microcantilever are identical to that of a tipless microcantilever, the

shape of the higher-order eigenmodes of tipped microcantilevers B_2, B_3, T_2, T_3, are quite different from those of the tipless cantilevers. A salient feature of the higher eigenmodes of tipped microcantilevers is that the motion at the free end of the cantilever (tip motion) is much smaller than at any other antinode of vibration. This is directly due to the large inertia of the tip mass. The greater the order of the eigenmode, the lesser the tip vibration amplitude is compared to the vibration at any other antinode. This means that the equivalent stiffness of the higher eigenmodes of tipped cantilevers are much greater than that for tipless cantilevers [15]. This allows for extremely small tip motion in higher eigenmodes. For example, in Fig. 18.1b, the vibration amplitude near the free end of the microcantilever in eigenmode B_1 is $\sim$9.5 nm, while that of B_2 is $\sim$2 nm, and that of B_3 is $\sim$0.1 nm.

3. A third important effect, not described in Fig. 18.1 but known in the literature [16–20] is due to the unavoidable asymmetry of the sharp tip with respect to the longitudinal axis of the cantilever. Under these conditions, torsional and bending motions or torsional and lateral motions may couple in an eigenmode. Such coupled motion eigenmodes are denoted as bending-torsion (BT) eigenmodes or lateral-torsional (LT) eigenmodes. If such eigenmodes are excited, the tip moves both tangentially and normally to the sample surface.

A majority of research in dAFM has used the fundamental bending eigenmode B_1 for topography imaging and normal force spectroscopy, and the fundamental torsion eigenmode or lateral bending eigenmodes T_1 or L_1 have been used [21–26] to measure lateral force gradients, frictional contrasts at the nanoscale, and for topography imaging.

However, there has been a surge of interest in using dAFM with higher-order bending eigenmodes as their Q-factors are very high under ambient conditions (Fig. 18.1b) and their dynamic stiffness is also very high [14,24,27–36]. Consequently, it becomes possible to drive the tip with very small amplitudes (less than 1 nm) comparable to the decay length of short-range forces, which in turn enables atomic scale resolution. Another possible advantage of using higher-order bending eigenmodes for dAFM is that the settling time of the driven cantilever is significantly reduced, allowing for faster scan speeds [29, 37]. Likewise, higher-order torsional eigenmodes are promising as the lateral tip motion can be much smaller than 1 nm, possibly enabling atomic resolution lateral force measurements in dAFM.

18.2.3 Eigenmodes of Triangular AFM Microcantilevers

Triangular or V-shaped microcantilevers fabricated from silicon nitride are usually soft probes that are often used for imaging soft materials and samples both in the contact mode as well as in the dAFM applications. The eigenmodes of triangular or V-shaped microcantilevers are not as well known as those

of rectangular cantilevers, and only a few authors have investigated these eigenmodes [38–41].

In Fig. 18.2, we show the frequency spectrum and eigenmodes of a commercial V-shaped silicon nitride microcantilever, which can be considered as two separate beams (the arms) joined together at their free ends. As a result of this coupling between the two arms, the eigenmodes of V-shaped cantilevers are quite different from those of rectangular cantilevers. As shown in Fig. 18.2, the eigenmodes appear in pairs, each pair consisting of the *symmetric* eigenmode (labeled without asterisks) where the two arms vibrate in-phase with a specific number of nodal points and the *antisymmetric* eigenmode (labeled with asterisks) where the two arms vibrate out-of-phase with the same, identical number of nodal points along each arm [38].

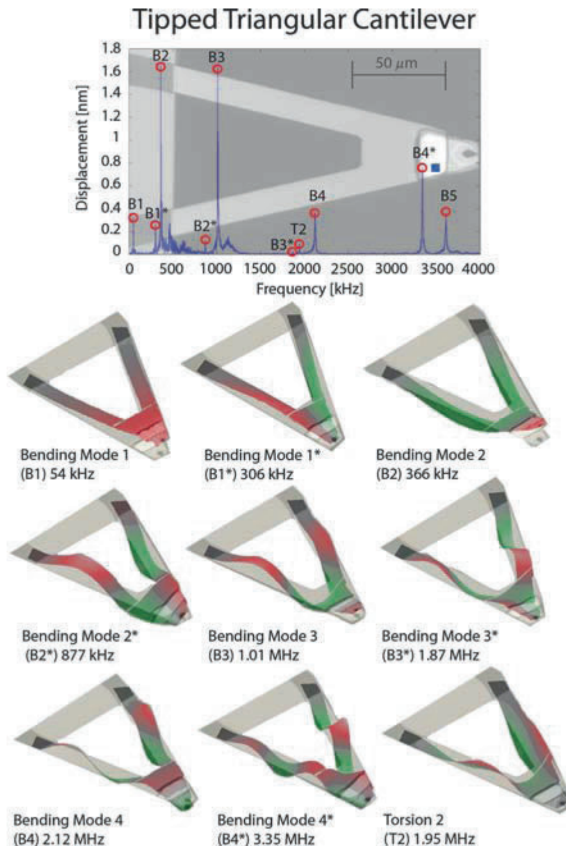

Fig. 18.2. Optical image, experimental vibration spectra, and eigenmodes of a commercial Si_3N_4 triangular cantilever. The vibration spectrum clearly shows that eigenmodes occur in pairs of symmetric modes where both beams vibrate in phase and anti-symmetric eigenmodes (eigenmode names with asterisks), each such pair consisting of a specific number of nodal points in the eigenmode

The natural frequencies of the fundamental and higher-order eigenmodes of V-shaped microcantilevers are quite different from those of single rectangular cantilevers. For instance, the natural frequency of the fundamental antisymmetric bending eigenmode B_1^* is only a little higher than that of the fundamental symmetric eigenmode B_1.

When the symmetric eigenmode is excited, the probe tip oscillates normal to the surface, while in an antisymmetric eigenmode, the tip oscillates lateral to the surface. Thus in applications of V-shaped cantilevers to lateral force microscopy, one can oscillate the tip lateral to the surface at excitation frequencies that are not much higher than that of the fundamental symmetric eigenmode.

By selecting specific eigenmodes of AFM microcantilevers, innovative dAFM experiments can be performed. We now describe the dynamics that ensue when the oscillating tip is brought close to the sample surface in AM-AFM or tapping mode AFM.

18.3 Cantilever Dynamics in AM-AFM

18.3.1 Mathematical Simulations of Cantilever Dynamics

Once an AFM cantilever is excited near the mechanical resonance of one of its eigenmodes and brought in close proximity of a sample, the cantilever dynamics are affected in many ways that are best understood with the aid of mathematical models. In the most general case, the continuous microcantilever possesses infinite degrees-of-freedom (DOF), each one corresponding to a single eigenmode. Therefore, in the quest to understand the precise nature by which the AFM probe interacts with a sample, a reduced order model where only the dominant eigenmodes are retained is essential.

Constructing a reduced order model of the microcantilever has generally been accomplished by one of the two ways: (a) assuming that the cantilever bends as if a static point load was applied at the cantilever's free-end and using the corresponding static stiffness to derive a single DOF (point-mass) model [42–46], or (b) discretizing the classical beam equation using the normal eigenmodes as a basis, which results in either single or multiple DOF models [47–54]. While the former approach cannot be used to model higher eigenmodes, the latter approach has reported nonunique modal masses and stiffnesses [42, 55–57], which is a cause for concern in many dAFM formulae [50, 51, 58]. It is important to note that the source of nonunique modal parameters is from the classical solution process that allows the generalized coordinates for beam deflection to refer to any point on the beam. In AFM applications, however, the only logical choice for the generalized coordinates is the deflection of the cantilever at the tip location. Taking this into account allows unique modal parameters, or equivalent parameters [14] to be defined.

Throughout this chapter we have shown experimentally measured eigenmodes for various AFM probes. Regardless of whether a given eigenmode is a transverse bending eigenmode, torsion eigenmode, symmetric or asymmetric eigenmode of a triangular cantilever, it represents a single DOF oscillator that can be characterized by a natural frequency ω_i, quality factor Q_i, and equivalent stiffness k_i, $i = 1, 2, 3 \ldots$ [14]. Accordingly, a multiple DOF model for the AFM probe interacting with a sample is expressed as

$$\frac{\ddot{q}_i}{\omega_i^2} + \frac{\dot{q}_i}{Q_i \omega_i} + q_i = \frac{1}{k_i} \left(F_i + F_{\mathrm{ts}} \right), \tag{18.1}$$

where $i = 1 \ldots N$ refers to the motion of the ith eigenmode of the N eigenmodes retained in the model, q_i is the generalized coordinate for the tip deflection for each eigenmode, $F_i(t)$ is the equivalent modal harmonic excitation at the drive frequency ω and F_{ts} is the tip–sample interaction force. q_i can be regarded as the contribution of the ith eigenmode to the displacement of the AFM probe tip.

There are many models for F_{ts} depending on the relevant physical forces acting between the tip and the sample [59]; however, for *conservative interactions*, $F_{\mathrm{ts}} = F_{\mathrm{ts}}(d)$ is a nonlinear function of the instantaneous gap, d, between the tip and the sample:

$$d = Z + \sum_{i=1}^{N} q_i, \tag{18.2}$$

where Z is the equilibrium or average separation between the tip and the sample. Furthermore, during an oscillation cycle, the closest approach distance of the tip to the sample D is given by

$$D = \min(d), \tag{18.3}$$

and is an important quantity particularly in FM-AFM. *Nonconservative interactions*, on the other hand, also depend on tip velocity and take the form of $F_{\mathrm{ts}} = F_{\mathrm{ts}}(d, \dot{d})$. Regardless of its conservative or nonconservative nature, F_{ts} is a nonlinear function, either of d alone or of d and $\dot{d}$ together, which has a dependence on the response of all eigenmodes through (18.2). Mathematically, this couples each DOF in the system of differential equations in (18.1).

The question now becomes which eigenmodes should be retained in the reduced order model given in (18.1). Through interaction with the sample, the response of all eigenmodes of the microcantilever couple nonlinearly. Whether or not the magnitude of the response of a given eigenmode is significant will depend on the operating conditions and specific properties of the cantilever. For standard operation in air or vacuum when the excitation frequency is tuned to the lowest natural frequency of the cantilever, the overall response is typically dominated by the fundamental eigenmode [45]. In this case, (18.1) can be reduced to a single DOF model ($i = 1$). In other cases, as we will see soon, multiple DOF models become necessary.

In contrast to operation in air or vacuum, it has been demonstrated that operation in liquid environments typically requires at least two DOF model ($i = 1, 2$ in (18.1)) to accurately predict the dynamics of soft microcantilevers tapping on samples [60]. Emerging operating modes that focus on material property measurements also require two DOF models. For example, *internally resonant* or so-called "harmonic" cantilevers [61–66], are specially fabricated to tune the frequency ratios of two eigenmodes to lie near integer ratios, intentionally enhancing the coupling between eigenmodes resulting from interaction with the sample. In addition, bimodal schemes [67, 68] where two eigenmodes are simultaneously excited naturally require a two or greater DOF model.

Once the appropriate form of (18.1) is chosen, simulations of tip motion during approach to the sample can be performed by numerically integrating (18.1). To simulate an AM-AFM scan over a sample, an additional model for the controller is required. While scanning, the separation Z is adjusted by the controller in an effort to maintain the amplitude A of the first harmonic of the tip deflection as close as possible to the desired setpoint amplitude A_{sp} [69]. A_{sp} is usually required to be less than the unconstrained amplitude A_0, which refers to the steady state tip amplitude before it begins to interact with the sample. This is commonly achieved by a proportional integral (PI) controller, which is modeled by

$$\Delta Z_n = -K_{\mathrm{P}} e_n - K_{\mathrm{I}} \sum_{i=0}^{n} e_i \cdot \Delta t, \tag{18.4}$$

where Δt is the time interval over which the AFM system lock-in amplifier measures the tip amplitude, K_{p} and K_{I} are the proportional and integral gains, respectively, and $e_n = A(n\Delta t) - A_{\mathrm{sp}}$ is the amplitude error for the nth time interval. With the addition of (18.4), simulations can explain how transient cantilever dynamics contribute to imaging artifacts, imaging forces, and more [69–76].

While simulations have played a critical role in the development and understanding of dAFM [53, 54, 60, 70–78], accurate simulations of cantilever dynamics in dAFM are inaccessible to most experimentalists as well as many students attempting to learn dAFM. Through the aid of cyber-infrastructure, advanced simulation tools for dAFM [69, 79, 80] are now openly available at nanoHUB.org.

18.3.2 Single Mode Nonlinear Phenomena in dAFM: Bifurcations, Higher Harmonics, and Chaos

Mathematical models such as those described in the previous section and experiments have revealed that upon approach to the sample, the cantilever dynamics become quite nonlinear due to the tip–sample interactions. Fundamentally speaking, the nonlinearity arises because typical tip oscillation amplitudes ($A_0 > 5\,\mathrm{nm}$) are larger than the decay lengths associated with the

short range interaction forces (<1 nm). For linear vibration theory to hold, the tip vibration amplitude would need to be much smaller (tens of picometers) than the decay length of short-range interaction forces, a situation rarely encountered in practice. Thus the cantilever dynamics cannot be predicted by simply linearizing the interaction forces about an equilibrium position. In this subsection, we focus on nonlinear phenomena that can be explained by examining the nonlinear dynamics of the single DOF oscillator model, also known as the point-mass oscillator model.

Early studies [81] on the dynamic response of AFM cantilevers oscillating near a sample surface demonstrated surprising hystereses in both the amplitude and phase as the drive frequency was increased and then decreased across the cantilever's resonance. Later, the hystereses were experimentally observed [77] when the cantilever approached and then retracted from the surface at a constant drive frequency. It was proposed [77] that this behavior is due to a transition between two stable oscillation regimes of the microcantilever, one dominated by attractive forces and another by repulsive interactions [82–84]. Subsequent studies have explained this phenomenon in terms of attractive and repulsive forces and correlated it to imaging stability. Wang [85,86] applied the Krylov–Bogoliubov–Mitropolsky asymptotic method to predict the multivalued amplitude response and made comparisons with experiments (Fig. 18.3a). Boisgard et al. [87–89] used a variational principle of least action to explain the hysteresis in amplitude–distance curves. San Paulo and Garcia [53, 90–92] demonstrated by numerical simulation the coexistence of two stable oscillation states in AM-AFM: the large amplitude state was termed as the net repulsive regime while the lower amplitude state was called the attractive regime. The describing function method was used to understand the nonlinear response of the cantilever and its imaging bandwidth [93]. The influence of sample viscoelasticity on the transition between attractive and repulsive regimes was studied by Wang [86]. The influence of different tip–sample interaction models on the nonlinear response was performed by Lee et al [94]. A systematic analysis of the competing effects of nonlinearity of the piezo layer and tip–sample forces were performed by Wolf and Gottlieb [95].

An investigation of the bifurcations and stability of the oscillations in AM-AFM were performed by Reutzel et al. [46] and Lee et al. [48, 96], and later by Yagasaki [97]. The influence of random disturbances on these oscillatory states has also been studied [98]. The connection between the nonlinear response when (a) the cantilever is brought close to the sample at a constant frequency and (b) when the drive frequency is swept across resonance while the cantilever is kept at a fixed distance from the sample has also been examined in [96, 99]. This bistable oscillatory behavior is of great interest as it is directly correlated to imaging instabilities. Specifically, this creates the possibility that the setpoint tip oscillation amplitude, A_{sp}, is identical at two different separations, Z, from the sample, causing the feedback controller to switch intermittently between these two separation distances to maintain constant amplitude, thus creating serious imaging artifacts [90, 91, 100–102].

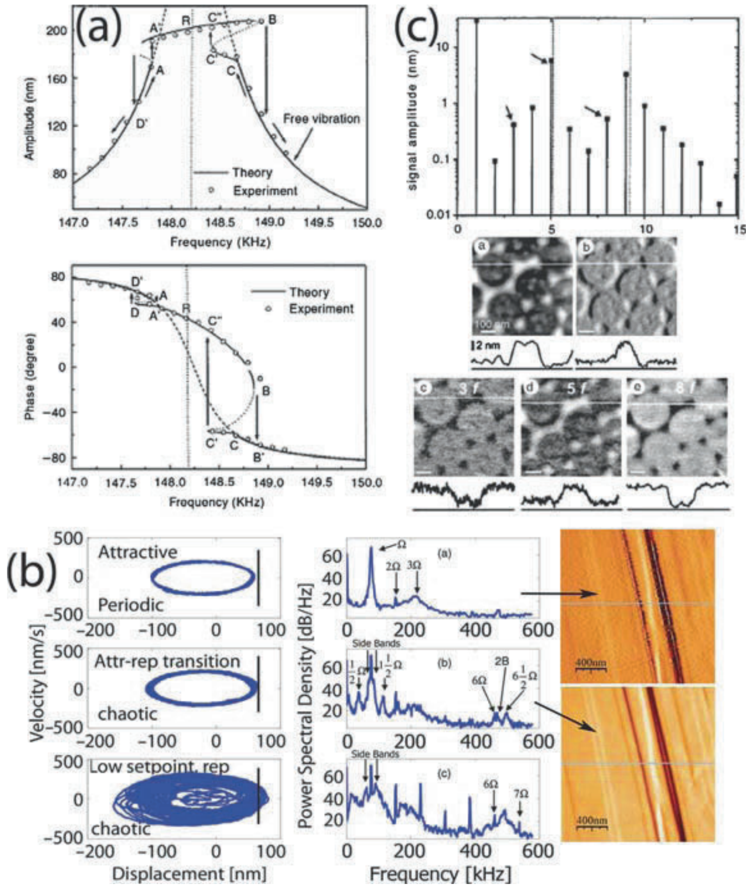

Fig. 18.3. Nonlinear dynamic phenomena in dAFM that can be explained by one DOF or point mass models. (**a**) The co-existence of two stable oscillating states (one in the net repulsive another in the attractive regime) can be seen while keeping an AFM probe close to a surface and sweeping the drive frequency up and down across resonance and plotting the tip amplitude and phase [85]. *Solid black curves* are theoretically predicted stable response; *dashed lines* are unstable solutions; *open circles* are experimentally measured data using a stiff 40 N m^{-1} silicon cantilever on a polyethylene sample. (**b**) Experimental phase portraits of a soft silicon cantilever tapping on a graphite substrate in the attractive regime, transition from attractive to repulsive and then again in the deep repulsive regime at small setpoint amplitudes. The corresponding vibration spectra are also shown. Chaotic spectra are characterized by subharmonic peaks and broadband "noise" below 150 kHz. Insets show error maps taken of a graphite substrate when the tip is oscillating periodically and chaotically, indicating that chaotic dynamics can introduce small but measurable uncertainty in nanometrology [116]. (**c**) Theoretical simulations from the work of Stark and Heckl [126] showing the higher harmonics expected in the vibration frequency spectrum when a 52 kHz rectangular silicon cantilever taps on a fused silica sample. Also shown below are experimental images taken using multiple higher harmonics in air of a Pt-C layer on a fused silica cover slip silicon oxide grating. (Reproduced with permission from [72, 113, 127])

The study of dynamics of AM-AFM microcantilevers has also benefited from the theory of impact oscillators and of grazing bifurcations in nonsmooth systems [103]. Because the tip–sample interaction forces change rapidly near contact, it is reasonable to expect that tip–sample interaction forces can be represented as nonsmooth or even discontinuous forces, in which case the many tools from nonsmooth dynamical systems theory can be utilized to understand the dynamics. In the limiting case of zero contact time, impact oscillator models have been used to understand AM-AFM dynamics [104,105]. For nonsmooth interaction models with finite contact time, the theory of grazing bifurcations can be applied to understand the stability of periodic solutions in the vicinity of the grazing trajectory [106, 107]. Such approaches are especially useful for understanding the effects of capillary forces on AM-AFM under ambient conditions because the capillary force models are discontinuous, representing an extreme case of nonsmoothness [56, 106, 108].

In addition to the existence of multiple oscillation states, their stability, and bifurcation discussed earlier, it is also possible for the cantilever to undergo chaotic oscillations in AM-AFM. Ashhab et al. and Basso et al. [109–111] used Melnikov theory to predict homoclinic chaos in a point-mass model of the AFM cantilever. Homoclinic chaos refers to a mechanism of chaos that can occur in a lightly damped, harmonically excited single-degree-of-freedom oscillator possessing one unstable equilibrium and two stable equilibria [112]. In dAFM, this situation can arise when a soft cantilever is brought very close to the sample so that the tip has two coexisting stable positions: one where the cantilever is slightly bent towards the sample, and the second where the tip is snapped into the sample. Physically this chaotic motion is manifest in the chaotic switching of the tip between oscillating around two stable positions, one where the tip equilibrates under a small attractive force and another where it is "stuck" to the sample. A more typical situation for AM-AFM is when the cantilever tip lies in a single-well potential and intermittently dynamically interacts with the sample.

In contrast, Molenaar et al. [106], Hunt and Sarid [104], Berg and Briggs [105], and Dankowicz [107] have all predicted the onset of subharmonic motions and chaos in AM-AFM based on impact oscillator models of AM-AFM or using the theory of grazing bifurcations in nonsmooth systems. Sasaki et al. [113] also theoretically predicted the existence of quasiperiodic oscillations as well as fractional resonances.

Experimentally, both Burnham et al. [114] and Salapaka et al. [115] reported the observation of subharmonics- and chaos-like motions in experiments where vibrating samples were made to impact a stationary cantilever (not necessarily an AFM microcantilever). However, it was not until recently [117, 137] that the onset of chaotic motion in AM-AFM was systematically studied experimentally. In [116], it was shown that chaotic oscillations set in for soft cantilevers when the tip initially transitions from the attractive to the repulsive regime of oscillation and then again when they are driven hard at low setpoint amplitudes (Fig. 18.3b). The onset of chaos in AM-AFM under

realistic operating conditions leads to small but measurable "deterministic" uncertainty in nanoscale measurements.

Recently, it has even been proposed to use methods from nonlinear time series analysis to utilize the chaotic dynamics to create new sensitive imaging modes [118]. Conversely, Yamasue and Hikihara [119] proposed the use of time-delayed feedback control to quench the chaotic motions in dAFM.

The generation of higher harmonics is yet another nonlinear dynamic phenomenon in dAFM that has provided many opportunities for improving sensitivity and material contrast. For example, it was observed early on [120] that when a harmonically excited cantilever is brought in close proximity of a surface, then its harmonic motion is mixed with higher harmonic distortions due to the nonlinear tip–sample interactions. It is important to understand that physically the cantilever continues to oscillate in its driven eigenmode, but its oscillations in time are distorted by higher harmonics resulting from the nonlinear tip–sample interaction forces. Thus the higher harmonics contain detailed information about the tip–sample interaction forces [121] and can be used to extract this information.

This idea has been taken up by several research groups and its physical basis is reasonably well understood at least under ambient and vacuum conditions and for cantilevers for which the single DOF or point-mass oscillator model is valid [121–130]. If the probe is operated in the attractive regime, then the higher harmonics provide information about the local van der Waals and electrostatic forces [131]. On the other hand, the higher harmonics generated when the tips taps on the sample in the repulsive regime provide information on the local sample elasticity as well as the attractive van der Waals and electrostatic forces [122,132]. In principle, it is possible to reconstruct the entire tip–sample interaction potential well by measuring the amplitudes of all the higher harmonics of tip oscillation, while the cantilever remains fixed at some distance Z from the sample [121]. However, in reality, because of the different noise sources and the finite frequency bandwidth of the photodiode detector, it is difficult to measure higher harmonics beyond the first 20 or so under ambient or ultra high vacuum (UHV) conditions. This poses one practical limitation to the reconstruction of tip–sample forces using higher harmonics data alone. Another practical issue that needs to be taken into account is that experimental tip deflection data often contain higher harmonics that arise due to factors other than tip–sample interactions such as nonlinearity of the measuring photodiode, air damping, and anharmonics in the piezo drive signal [131]. These "instrumental" higher harmonics need to be systematically accounted for while using higher harmonics for the quantitative measurement of tip–sample interaction properties. The magnitudes of higher harmonics depend on a number of parameters, including the quality factor of the driven eigenmode, the relative strength of tip–sample interaction forces, A_0 and A_{sp}, the unconstrained and setpoint vibration amplitudes [131]. More recently, the influence of tip mass on higher harmonic generation has also been studied [133]. Beyond the use for interaction force reconstruction, it

was quickly recognized that higher harmonics could also be used to enhance material contrast during topographical imaging – an insight that portends the simultaneous acquisition of topography and material properties. By mapping the magnitudes of higher harmonics over a sample, it then becomes possible to obtain material property contrasts when imaging in liquids [120, 134] and in air [131, 135] (Fig. 18.3c). Higher harmonics have also been used to achieve subatomic contrast in low temperature FM-AFM under UHV conditions [2] and are discussed further in Sect. 18.4.

While all these works above deal with cantilevers excited at the resonance frequency of an eigenmode and consider higher harmonics in the motion of that eigenmode, there also exists the possibility of exciting the cantilever away from its natural resonance and utilizing nonlinear effects. For instance, Balentekin and Atalar [136] show that if the cantilever is excited at a submultiple of its natural resonance frequency ($\omega = \frac{\omega_1}{N}$ where N is an integer), then the Nth higher harmonic of the response lies near the natural frequency (say ω_1) of an eigenmode and is thus enhanced by the resonance peak of the eigenmode. This enhanced higher harmonic then shows increased sensitivity to local elasticity; however, off-resonance operation usually comes at the cost of increased imaging forces. Recently, the concept of *intermodulation* dAFM has also been introduced, where the cantilever is excited by two drive frequencies one on either side and close to a natural frequency of an eigenmode, and the sum and difference frequency responses (intermodulation frequencies) are measured and mapped on the sample [137]. The theoretical advantage of this technique is that by measuring the cantilever response at all intermodulation frequencies, it may be possible to reconstruct the tip–sample interaction forces without requiring a high bandwidth system to measure all higher harmonic data as in the case of higher harmonic force spectroscopy.

18.3.3 Multimode Nonlinear Dynamics in dAFM

Thus far, we have discussed nonlinear phenomena that can be explained by assuming that only one eigenmode dominates the driven cantilever dynamics as it interacts with the sample. This assumption fails under one of the three conditions:

1. In ambient or UHV environments when the natural frequencies of two different eigenmodes are close to a specific rational ratio of each other [138], it then becomes possible for two eigenmodes to couple in the microcantilever response. This interesting nonlinear modal interaction phenomenon is usually referred to as *internal resonance* [138] in the nonlinear dynamics community and requires that all the interacting eigenmodes be included in the model.
2. When multiple eigenmodes are simultaneously excited, then multiple DOF models must be used to explain the cantilever motion.

3. In liquids, while using soft cantilevers it becomes possible for higher eigenmodes to become momentarily excited [60] even without conditions of internal resonance; this interesting issue is discussed in the next section.

Sahin and Atalar et al. [61–66] first demonstrated the use of internal resonance in dAFM theoretically and experimentally by fabricating cantilevers for which the B_2 or T_1 eigenmode frequencies are very close to an integer multiple of the B_1 natural frequency. When such a cantilever is driven at resonance of the B_1 eigenmode and brought close to the sample, some higher harmonics of the drive frequency are able to excite the B_2 or T_1 eigenmodes in a sensitive fashion. This then allows the sensitive measurement of nanomechanical properties using a specially designed cantilever.

Another approach has been to simultaneously excite multiple eigenmodes of the microcantilever [10, 139–145]. This approach arose out of the need to create interaction channels between multiple cantilever eigenmodes in commercially available cantilevers without requiring the specialized fabrication of specially tuned "harmonic" cantilevers, where the two eigenmodes are designed to be at internal resonance. The basic principle of operation is that the amplitude of the first eigenmode is kept constant via feedback control while the phase of the first and second eigenmode is monitored. The physical basis of this so-called"bimodal" dAFM under ambient conditions is as follows [67, 68, 145]. When both the first and second eigenmodes are excited simultaneously, their dynamics are independent and there can be no interaction between these two eigenmodes until the cantilever is brought in close proximity to the sample. Under these conditions, if the tip motion in the second eigenmode is small compared to that of the fundamental, then it can be shown [68] that the phase of the second eigenmode contains information about the conservative as well as the dissipative interactions. This method is especially advantageous in imaging material property contrast when the fundamental eigenmode phase contrast is negligible, for instance, when the tip is oscillating in the attractive regime. From a broader perspective, the simultaneous excitation of two eigenmodes opens up new channels for interrogating the material properties of the sample. Recently, evidence has been provided that the attractive–repulsive bistability described earlier in this chapter is reduced significantly when B_1 and B_2 are simultaneously excited [146]. Given the significant improvements in image contrast that have been observed using multiple eigenmode excitations, it is one of the promising techniques for improving material contrast without significantly affecting the imaging forces.

18.3.4 Cantilever Dynamics in Liquids

There are special hydrodynamic considerations that must be taken into account if (18.1) is to be used to describe a cantilever oscillating in a viscous medium like a liquid. Because of the high viscosity and the tight coupling of the cantilever motion to the viscous medium, the Q-factors of different

eigenmodes are drastically decreased, allowing new nonlinear phenomena to appear.

The potential of using dAFM in liquids was recognized in the early nineties and two important driving modes – the acoustic excitation mode [147, 148] and the magnetic mode [6] – were established. In the acoustic mode excitation, some of the dither piezo vibrations are transferred to the cantilever mechanically (structure-borne vibration) but most are transferred indirectly through the fluid (fluid-borne vibration) [149, 150], whereas in the magnetic mode, a cantilever coated with a sputtered magnetic film is excited magnetically by a solenoid. Alternatively, magnetic beads can be attached to the microcantilever. The differences in cantilever response in these two excitation modes are insignificant in air but become amplified in liquids due to the low Q-factors of the cantilever eigenmodes [150, 151]. However, it is generally believed [152] that while neither excitation mode offers improved imaging capability compared to the other, direct excitation methods (such as magnetic excitation) are more amenable for quantitative spectroscopy applications, at least for soft microcantilevers.

The primary effect of the surrounding liquid is to modify the "wet" resonance frequencies (natural frequencies in liquid) and Q-factors of different cantilever eigenmodes; this effect depends sensitively on the distance of the microcantilever from the sample because of the fluid squeeze film that develops between the microcantilever and the rigid substrate. In principle, the increased damping of eigenmodes in the close proximity of a wall is due to both the damping of the sharp tip and that of the microcantilever, but it is generally assumed that the hydrodynamic damping of the microcantilever dominates the damping of the eigenmode. Predicting the hydrodynamics of cantilevers near a substrate has been a focus of many research groups and has been based broadly speaking on (a) *ad hoc*, but intuitive models [153, 154], (b) computational solutions using the boundary element method of the unsteady Stokes equations in two and three dimensions [155–159], and (c) transient, fully coupled fluid–structure interaction calculations using the Navier–Stokes equations [160–162] (Fig. 18.4a). Many experimental results have also been performed to study this phenomenon [163–165].

Both theory and experiment clearly indicate that when a cantilever is brought close to a surface in a liquid medium, the Q-factors and wet resonance frequencies of the different eigenmodes decrease significantly (Fig. 18.4b). The rate of decrease with gap depends strongly on the eigenmode of interest and also on the orientation of the cantilever relative to the surface (Fig. 18.4 b). This phenomenon is especially important for soft cantilevers in liquids, because it is often observed that the cantilever eigenmodes become overdamped and no resonance peak is observed when the cantilever is brought within imaging distance of the sample [161, 166, 167].

While the dynamics of a microcantilever tapping on a sample are well-understood under ambient or UHV conditions, they have been studied to a lesser extent under liquid environments. Tapping dynamics in liquids are

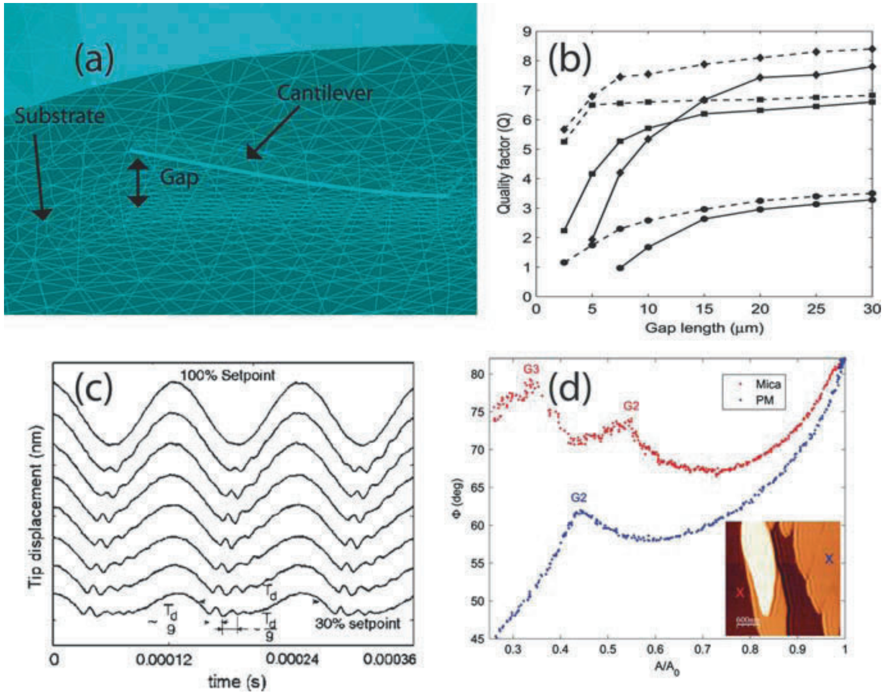

Fig. 18.4. Some key results on cantilever dynamics in liquids, (**a**) Computational three-dimensional flow-structure model of a rectangular Si cantilever ($197 \times 20 \times 2\,\mathrm{m}^3$) close to a surface in water using the finite element code ADINA, (**b**) ADINA computed Q-factors of the B_1 (*circles*), B_2 (*diamonds*), and T_1 (*squares*) eigenmodes computed [160] show that their Q-factors (and wet resonance frequencies – not shown) decrease rapidly upon decrease of gap. The rate of decrease depends on the eigenmode number and on the orientation of the cantilever (*dashed lines* are for a cantilever oriented at 11° to the sample surface), (**c**) the tip oscillation waveform distorts significantly and often shows that the B_2 eigenmode is momentarily excited near tip–sample impact events. The waveform distortion in liquids while tapping samples is observed for both hard and soft samples and is characteristic of soft cantilever dynamics in liquid environments [60]. (**d**) Experimentally acquired phase vs. amplitude ratio curves extracted on a mica and single layer purple membrane [15]. The abrupt behavior in the phase occurring at points $G2$ and $G3$ marks grazing trajectories that indicate onset of oscillations with two and three impacts per period, respectively [15] (Reproduced with permission from [15, 60, 160])

strongly influenced by the low Q-factors and the tip–sample interaction forces that prevail under liquids. In contrast to ambient or UHV conditions, in liquids, the tip–sample interaction forces are usually repulsive due to the electric double layer effect [59] with slightly attractive force gradient due to van der Waals forces. Previous attempts at mathematical modeling of tip dynamics in liquids have used a Lennard–Jones type interaction potential [120, 168], an

exponentially growing force [169], or a discontinuous interaction force [170]. Recently, Basak and Raman [60] combined the Derjaguin–Landau–Verwey–Overbeek (DLVO) theory in the noncontact regime with a Hertzian model so that the resulting interaction force was continuous. This model led to accurate predictions of tip dynamics in comparison to experimental data.

In all cases it has been observed that, unlike in air, when a tip taps on a sample in liquids, significant higher harmonics are generated and the tip motion distorts noticeably from a sine wave. More recently [60], it has been shown that the second lateral bending eigenmode, B_2, plays a significant role in the tip motion in liquids. Specifically, it was shown that when the tip is excited in the B_1 eigenmode and taps on a sample in a liquid medium, then the B_2 eigenmode is also *momentarily excited* near the time interval of tip–sample impact (Fig. 18.4). This implies that while point-mass oscillator models are, for the most part, sufficient to explain AM-AFM dynamics under ambient or UHV conditions, models that include multiple cantilever eigenmodes are required to predict the motion of soft cantilevers tapping on samples in liquids. The participation of the B_2 eigenmode in the overall response has many implications for liquid operation. Perhaps the most profound implication is the existence of multiple impact regimes where the tip interacts with the sample more than once per oscillation period (see Fig. 18.4) [15]. This in turn can have important implications for interpretation of phase data from dAFM images in liquids.

The dynamics of AM-AFM in liquid environments using soft cantilevers with low Q-factors are quite distinct from operation in ambient or UHV conditions. Much of the core AFM theory and understanding, which has derived from considering a point-mass model, is in question for liquid applications with soft cantilevers. All these studies are beginning to answer important questions regarding cantilever dynamics in liquid environments for AM-AFM applications.

18.4 Cantilever Dynamics in FM-AFM

In contrast to the AM-AFM scheme discussed thus far in which only the tip amplitude is controlled, in frequency modulated AFM (FM-AFM) the cantilever's natural frequency, phase, and amplitude are all monitored to provide information on nanoscale surface topography, tip–sample interaction forces, and energy dissipation. Not surprisingly, optimization of this dAFM mode also requires a deep appreciation of cantilever dynamics and the nonlinear interactions of the tip with the sample. However, in comparison to AM-AFM, the influence of nonlinear dynamics in FM-AFM is relatively minor.

The results of using FM-AFM in experiments have been quite spectacular. By measuring the shift in natural frequency of an eigenmode as a function of tip–sample separation, Z, a mathematical formalism to recover the interaction force has been devised [171]. Atomic scale images can be obtained by

keeping the frequency shift constant using a feedback circuit as the tip is rastered across a sample [47, 172–174]. With care, even the chemical nature of individual atoms can now be identified using FM-AFM techniques [3]. In 1995, atomic resolution of reconstructed Si(111) was achieved using a constant frequency feedback with a tip amplitude of 34 nm [172]. By 2005, high resolution, atomically resolved images of reconstructed Si(111) were obtained with a tip amplitude of only 70 pm [24].

Because the amplitudes deployed in FM-AFM are typically smaller than in AM-AFM and k's are large, the effects of the tip–sample interaction force nonlinearities are greatly reduced from AM-AFM. In the limit of small tip amplitude, one can simply linearize (18.1) by replacing the full form of F_{ts} by its gradient at equilibrium. Under these conditions, a fixed separation from the sample Z, the dynamics of the cantilever become linear; however, as Z is varied, a new equilibrium is established where the gradient of the interaction force has changed. The dependence of the gradient of the interaction force on the Z separation becomes the basis of FM-AFM.

Although small tip amplitudes may make the reconstruction of interaction forces more straightforward in FM-AFM when compared to AM-AFM, when the amplitude of the tip motion approaches tens of picometers, high confidence is required so that the motion of the tip is well-understood to a high level of precision. Thus the presence of higher harmonics, the excitation of higher transverse bending eigenmodes, or even the inadvertent excitation of a torsional cantilever eigenmode, although small, can alter the tip motion from a purely sinusoidal (harmonic) motion perpendicular to the surface and can be particularly problematic when picometer accuracy is assumed. Without knowledge of these possible complications in the tip motion, the interpretation of FM-AFM data acquired with subnanometer precision can become difficult.

18.4.1 Origins of Frequency Shift and Its Measurement

The FM-AFM operation focuses on an accurate measurement of the natural frequency of a chosen cantilever eigenmode and was introduced in 1991. This scheme of AFM operation is referred to as frequency modulation AFM simply because a frequency demodulation scheme was initially employed to implement the technique. The FM-AFM technique is most often used under UHV conditions in part because the cantilever resonance peak sharpens dramatically as the pressure is reduced, allowing higher sensitivity to the small shifts in eigenmode natural frequency that occur as the tip interacts with a sample. Not surprisingly, as frequency shifts are of prime importance, FM-AFM utilizes a phase-locked-loop (PLL) to accurately measure the small shifts (typically 1 part in 10^5) in the natural frequency of the cantilever as it approaches the sample. As will be discussed later, FM-AFM offers unique advantages and provides a valuable tool in the suite of scanning probe techniques.

It is well established that the origin of the frequency shift as the cantilever approaches the sample is the nonlinearity introduced by the asymmetric

potential well describing the forces between the tip and the sample [175]. The theoretical basis of FM-AFM rests on the theory of undamped, free oscillations of point-mass oscillators in potential wells so that Hamiltonian perturbation theory can be applied to this situation. When the cantilever is far from the sample, the tip naturally oscillates in a parabolic and symmetric potential and the tip motion is well-characterized by a purely sinusoidal motion at the linear natural frequency f_0 *regardless of oscillation amplitude.* As the cantilever approaches the sample, the tip–sample interaction modifies the symmetric potential, producing a small deviation in the parabolic potential related to the strength of the tip–sample interaction.

As a result of the perturbed potential, the natural resonance frequency f_0 of the cantilever shifts from f_0 to a new frequency f_0', which now *depends on the amplitude of natural oscillation.* In the limit of infinitesimally small oscillation amplitude, for a single cantilever eigenmode with equivalent stiffness k, the force gradient acting on the tip can be shown to be constant over one cycle of oscillation, and the corresponding frequency shift can be written as

$$f_0' = f_0\sqrt{1 - \frac{1}{k}\frac{\partial F_{\mathrm{ts}}}{\partial z}}, \tag{18.5}$$

where $\partial F_{\mathrm{ts}}/\partial z$ is the tip–sample interaction force gradient. As the oscillation amplitude increases, the equation for the frequency shift becomes more complicated and the small amplitude approximation is no longer valid. A general expression applicable for conservative tip–sample forces and arbitrary tip oscillation amplitude has been derived [176]. The frequency shift for a given unconstrained tip amplitude A_0 and set point amplitude A_{sp} is given by

$$\Delta f_0 = -\frac{f_0}{\pi A_0 k}\int_{-1}^{1} F_{\mathrm{ts}}[D + A_{\mathrm{sp}}(1+u)]\frac{u}{\sqrt{1-u^2}}\,\mathrm{d}u, \tag{18.6}$$

where D is the distance of closest approach between the tip and sample defined in (18.3). Equation 18.6 is valid when the frequency shift is much smaller than the natural, unperturbed resonant frequency f_0. This restriction is very well satisfied for virtually all FM-AFM applications.

To exert small forces on the sample and to achieve a stable tip with little wear, the amplitude of the tip's oscillation should be comparable to the decay length of the interaction force, which is typically less than a nanometer. This qualitative picture offers the possibility that by measuring the frequency shift, information about the tip–sample interaction forces can be recovered with high fidelity.

In (18.5) and (18.6) above, f_0 and f_0' refer to the undamped natural frequency of the probe, that is, its natural frequency if the probe were allowed to ring in an ideal situation without excitation or damping. However, the frequency shift $f_0 - {f_0}'$ is measured experimentally in the presence of damping and external forcing by exciting the probe near resonance and using a lock-in amplifier. Thus, it is useful to contrast the effects of F_{ts} on the

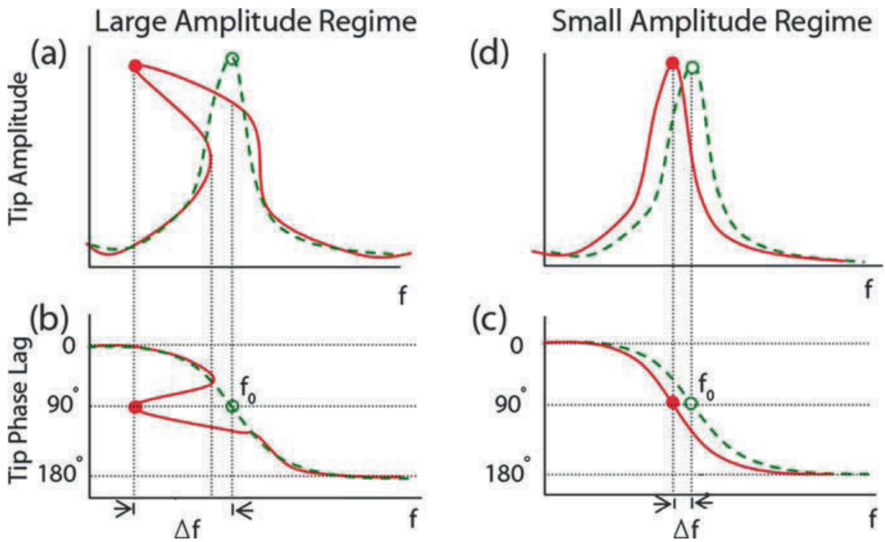

Fig. 18.5. Two different mechanisms by which frequency shifts Δf are measured from the driven response of the AFM probe with the help of a phase-locked loop in FM-AFM. The steady state amplitude and phase response of a tip oscillating under the influence of attractive tip–sample forces are sketched as the driving frequency f is swept across the natural frequency f_0. The figure illustrates the response for both large amplitude (**a**, **b**) and small amplitude oscillation regimes (**c**, **d**). The *dashed* (*solid*) line indicates the response of the cantilever when the tip is far (close) to the sample surface

cantilever resonance response for both large and small amplitude of oscillation as schematically illustrated in Fig. 18.5. The resonant response curve (both amplitude and phase) as a function of the excitation frequency are sketched, and clearly indicate why the limit of small tip oscillation amplitude is desirable when frequency shifts in FM-AFM are to be measured.

The response as a function of drive frequency for large amplitude oscillation is illustrated in Fig. 18.5a. In this case, when the tip is in close proximity to the surface (solid line), a "bistable" behavior arises in which both the tip amplitude and the phase show reproducible hysteresis as the driving frequency is swept up and down across the natural frequency. This phenomenon is fundamentally the combined result of the interaction of a harmonic oscillator with the attractive and the repulsive regions of the nonlinear interaction potential [48]. If the tip amplitude is large enough that this behavior is encountered in FM-AFM operation, the resulting frequency shift in the resonance response curve will be determined by a PLL controller locking into the 90° phase condition as shown Fig. 18.5b. As indicated schematically, the high nonlinearity of the phase with excitation frequency will present inherent measurement

difficulties, resulting in bistable behavior due to the double valued nature of the phase with excitation frequency.

In contrast, the resonance response of both amplitude and phase as a function of drive frequency for small amplitude oscillation are illustrated in Fig. 18.5c, d. Because the amplitude of the tip oscillation is small, the resulting shift in both frequency and phase is linear, leading to an inherently more stable measurement of the 90° phase condition using PLL techniques.

The physical models employed to understand each limit are significantly different and the preferred implementations address vastly different questions. For small amplitude tip oscillation (commonly employed in FM-AFM), the phase shift is the control variable of choice as it varies linearly for a small shift in resonance frequency. For large amplitude tip oscillation (commonly employed in AM-AFM), both the amplitude and the phase response can exhibit hysteretic behavior and the amplitude becomes the control variable of choice. A consequence of these differences is that FM-AFM is an excellent technique for the investigation of clean surfaces with atomic resolution, while AM-AFM is more useful for the investigation of material properties of surfaces under ambient conditions with a resolution better than the nanometer length scale.

18.4.2 Selecting Probes for FM-AFM

In FM-AFM, it becomes necessary to accurately measure the frequency f_0' given by (18.5) as a function of the tip–sample separation. In this regard, there is a fundamental tradeoff between two important quantities, the minimum detectable force gradient that can be measured with a given cantilever compared to the frequency noise resulting from the thermal motion of that cantilever.

The minimum detectable tip–sample interaction force gradient is given by [177]

$$\left.\frac{\partial F_{\mathrm{ts}}}{\partial z}\right|_{\mathrm{min}} = \frac{1}{A_0}\sqrt{\frac{4k_{\mathrm{B}}TBk}{2\pi f_0 Q}}, \tag{18.7}$$

where k_{B} is Boltzmann's constant, T is the temperature in Kelvins, B is the detection bandwidth, and Q is quality factor of the cantilever's resonance.

Equation 18.7 is expressed in terms of the probe's properties k, f_0, and Q, which are easily measured; however, one must recognize that the parameters are not independent of each other as $f_0 = 2\pi\sqrt{k/m}$ and $Q = \sqrt{mk}/c$, where m is the equivalent mass and c is the effective linear damping coefficient. It is important to recognize that a number of physical effects contribute to c, such as air damping, intrinsic cantilever defects, and clamping losses due to attachment of the cantilever to an appropriate support. All these contributing factors are difficult to measure individually, and so it is convenient to lump their collective effects into one parameter, c. It is evident that the dependence

on both k and m cancel in (18.7) and we are left with a $c^{1/4}$ dependence that accounts for the probe's mechanical properties.

To decrease the damping coefficient, it is advantageous to conduct experiments under vacuum conditions to eliminate hydrodynamic damping. Without air damping, seemingly identical cantilevers in vacuum can exhibit different Q's, reflecting small differences related to intrinsic defects or clamping losses. However, cantilevers with high k are also useful because they obviate any jump-to-contact complications, which can be especially bothersome for small amplitude cantilever oscillations.

A second important consideration is related to the amplitude of the thermal fluctuations that cause the cantilever to vibrate randomly. If these fluctuations are comparable to the cantilever's driven oscillatory amplitude, then thermal noise can obscure the tip's driven motion. For precise FM-AFM applications, conditions that minimize the frequency fluctuations are desirable. The equipartition theorem can be used to estimate thermal fluctuations at a fixed temperature. Following Giessibl [177], these amplitude fluctuations give rise to a frequency fluctuation δf_0 given by

$$\frac{\delta f}{f_0} = \sqrt{\frac{2k_\mathrm{B}TB}{\pi^3 f_0 kQ}}. \tag{18.8}$$

Giessibl et al. have analyzed the conditions required to minimize noise at a fixed temperature and bandwidth in detecting the force gradient for different tip–sample interaction force laws [178]. They find that the noise in the z-position of the tip is minimized when (a) the cantilever oscillation is less than or comparable to the minimum distance between the cantilever tip and the sample, and (b) k lies in the range between 500 and 3,000 $\mathrm{N\,m^{-1}}$.

Evidently, when using force gradients to image samples at the atomic length scale, a small tip oscillation amplitude that is noisy is better than a large and well defined amplitude of oscillation. In other words, immersing the tip in the interaction force is better than allowing the tip to interact with the sample for only a short time interval during each period of oscillation.

Three experimental approaches have evolved to faithfully monitor tip motion in FM-AFM experiments. One approach is based on the use of optical beam bounce techniques to monitor the motion of ultra-small cantilevers with a size designed to increase k by orders of magnitude when compared to conventional cantilevers. The second approach is to utilize stiff vibrating bars (tuning forks) that have inherently high k. The third approach is to use optical heterodyne circuits to measure the Doppler shift of a laser beam reflected from the cantilever. All three approaches have been successfully explored by the FM-AFM community.

Cantilevers suitable for FM-AFM tend to have a higher resonance frequency than cantilevers used in AM-AFM, and advanced fabrication techniques are pushing cantilever dynamics well into the mega hertz regime [179, 180]. The advantage that high frequency cantilevers offer is primarily

speed. There are two primary considerations. First, a higher natural frequency implies an intrinsic ability to image dynamic processes. Second, as a PLL or lock-in amplifier requires a set number of oscillation cycles to measure phase accurately, a higher frequency enables a more rapid response time of the controlling electronics simply because the resonance frequency is high, the settling time for phase detection is shortened because the period of oscillation is reduced. As a consequence, the required time for the tip to settle to a fixed height above the sample is reduced, thus enabling faster scanning.

Unfortunately, for high Q cantilevers, there are other trade-offs that limit faster scanning. It is well established that any sudden perturbation during AFM image acquisition will cause the tip to oscillate in a damped motion [181]. If the tip is modeled as a simple damped oscillator, the time constant for ring down is given by

$$\tau = \frac{Q}{\pi f_0}. \tag{18.9}$$

Clearly, for high Q, this decay time becomes excessive, resulting in a much slower scanning speed. However, by increasing the cantilever frequency while maintaining a high Q, the ring down time in (18.9) can be reduced with a resulting increase in the scanning speed.

18.4.3 Dynamic Characteristics of High Frequency Cantilevers and Tuning Forks

The need for producing very high frequency cantilevers should be clear. High frequency cantilevers can be fabricated by stiffening the cantilever significantly, usually by increasing the thickness and decreasing the length. Alternatively, if the mass of the cantilever is reduced, the natural frequency will also increase. This implies that very thin, very short cantilevers are required. Again there are trade-offs because very high stiffness is not necessarily desirable as the intermittent contact force between the tip and sample also increases with k. A solution is to fabricate cantilevers with moderately high stiffness but ultra-small mass. The free vibration spectra of such a typical ultra-small cantilever, with a first transverse bending eigenmode frequency near 1.6 MHz, has been measured using a Doppler laser interferometer and is plotted in Fig. 18.6. The interferometer provides a direct measure of cantilever's oscillation, which in this case was only ~2.7 nm at resonance.

An innovative development in the implementation of FM-AFM techniques was the realization that quartz tuning forks could be used to replace the traditional cantilever [182, 183]. Commercially available tuning forks are used as high accuracy oscillators, and take full advantage of the piezoelectric properties of quartz. Tuning forks have a number of advantages over conventional cantilevers (a) because quartz is piezoelectric, the detection of the motion of a tuning fork tine is electrical and does not require a laser beam and a quadrant photodiode, (b) k of the tuning fork is high ($\sim 10^4\,\mathrm{N\,m^{-1}}$), obviating any jump-to-contact complications, (c) Q of the quartz tuning fork is ~9,000 in

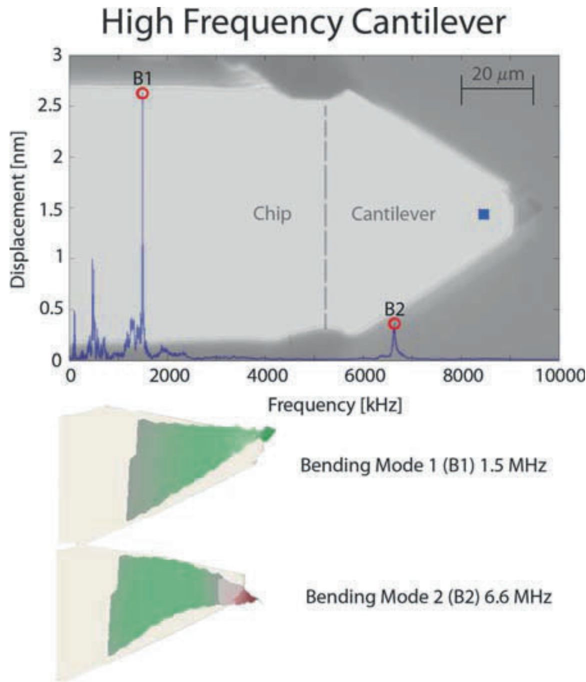

Fig. 18.6. Optical images and experimentally measured vibration spectra and three-dimensional eigenmodes of a high frequency microcantilever. These data were acquired by mounting the microcantilever chip on a dither piezo exciter and measuring the vibration response in a Polytec MSA-400 Scanning Laser Doppler Vibrometer system. The vibration spectra plotted correspond to data collected near the free end of the cantilever. The first and second bending eigenmodes are designated as B_1 and B_2. The sharp resonance near 500 kHz and the smaller broadband resonance near 1.4 MHz are associated with the cantilever mount

air, reaching values of ~40,000 in high vacuum, (d) the thermal expansion coefficient of quartz along certain crystallographic directions is many times smaller than for Si[110] cantilevers, leading to a resonator frequency that is inherently more stable than a conventional Si AFM cantilever [177], and (e) because quartz tuning forks are mass produced for widespread use in the electronics industry, they have highly reproducible mechanical properties and their per unit cost is ~100 times less than for a typical microfabricated AFM cantilever.

Two different techniques to implement tuning fork FM-AFM have been proposed. Both techniques require the attachment of a sharp tip to one end of a tuning fork tine. The tip can be or insulating, depending on the experiment performed. One implementation requires the immobilization of the tine that does not include the tip. This tactic obviates the need to use tips that have a small mass, but requires care in immobilizing the tine, least the Q of the

tuning fork is markedly degraded. A second implementation uses the tuning fork as is, allowing both tines to oscillate freely. Attaching a small tip to one tine produces a sensitive force sensor for FM-AFM experiments. A drawback of the second implementation is the requirement that the tip mass be small compared to the mass of the tine, otherwise, the resonance frequencies of the two tines will deviate. If this condition is not satisfied, the resulting oscillation becomes asymmetric and the amplitude of the tip oscillation can no longer be accurately inferred from the current that develops when a voltage is applied to the tuning fork.

The vibration spectrum from a typical, commercially available 100 kHz tuning fork operating under ambient conditions is plotted in Fig. 18.7. The oscillation spectrum was measured fork using a laser Doppler vibrometer. To obtain this spectrum, the base of the tuning fork (no tip attached) was rigidly mounted and an applied voltage of 100 mV at a variable frequency was applied to the tuning fork electrodes. By scanning the laser beam over one tine of the tuning fork, the Doppler vibrometer measures the velocity of the tine at a grid of different positions, allowing a convincing determination of the tine motion when a dominant eigenmode of oscillation is excited. This eigenmode identification is not possible by simply measuring the voltage that develops across the tuning fork as a function of the drive frequency.

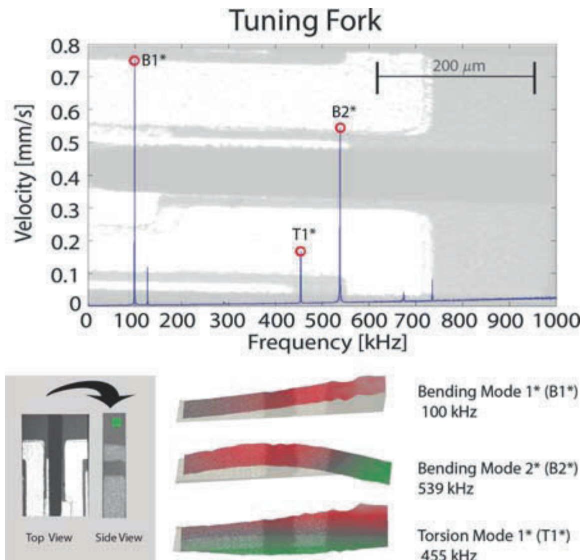

Fig. 18.7. Optical images and experimentally measured vibration spectra and three-dimensional eigenmodes of a quartz tuning fork. These data were acquired by mounting the microcantilever chip on a dither piezo exciter and measuring the vibration response in a Polytec MSA-400 Scanning Laser Doppler Vibrometer system. The vibration spectra plotted correspond to data collected near the free end of one tine of the tuning fork

The dominant eigenfrequencies are labeled in Fig. 18.7 as B_1, T_1, and B_2. The vibration B_1 (at 100 kHz) is the fundamental eigenmode of the tuning fork and corresponds to the out of phase motion of each tine beating against one another. B_2 (at 540 kHz) is identified as the second eigenmode of oscillation. T_1 (at 460 kHz) is unambiguously identified as a torsional eigenmode of oscillation. From the velocity data at the first resonance (B_1), a ∼1.2 nm amplitude of oscillation of the tine is inferred.

To date, little use of the higher-order eigenmodes has been made in FM-AFM, but this situation is rapidly changing since recent force spectroscopy measurements have utilized the B_2[24, 27, 184] and B_3[32] transverse bending eigenmodes of a cantilever using FM-AFM techniques. The advantage of this approach is twofold: (a) the effective stiffness of B_2 is ∼40–80 times the first bending eigenmode [14], and (b) the intrinsic shape of B_2 dictates a small amplitude for the tip oscillation.

The large effective stiffness enabled force spectroscopy experiments with a cantilever oscillation amplitude thought to be as small as 28 pm [184]. We anticipate more work in this area in the next few years, with a natural extension to tuning forks as the increased frequency of the higher-order bending eigenmodes implies a proportionately larger current [185].

18.4.4 Higher Harmonics in FM-AFM

Higher harmonics in FM-AFM arise from the nonlinear force acting on the tip. The response of the tip oscillating in a nonquadratic potential well can be described by the Fourier series [121]

$$q(t) = \sum_{n=0}^{\infty} A_n \cos(2\pi n f t). \tag{18.10}$$

If the primary amplitude is sufficiently small, it can be shown that the amplitude A_n of the nth harmonic can be related to the nth derivative of the tip–sample force [130]. Thus, in principle, information about the tip–sample force can be recovered by monitoring the emergence of higher harmonics.

As previously mentioned, in the limit of small amplitude, the tip–sample interaction force can be replaced by its gradient at the equilibrium point. This results in a quadratic potential well that eliminates higher harmonics. In FM-AFM, where amplitudes are small, but not too small, a small higher harmonic content should emerge [121]. Giessibl has discussed higher harmonics within the context of FM-AFM [130], predicting sub-picometer amplitudes that would be difficult to detect via optical beam bounce detection schemes. The tuning fork, however, is ideally suited for this application because of the proportional dependence of the current generated with frequency, resulting in a built-in amplification of higher harmonic content [130, 185]. Indeed, using higher harmonic imaging and a tuning fork force sensor, subatomic structure

has been reported in FM-AFM images of a graphite surface imaged by a tungsten tip [2]. Finally, the use internal resonance of harmonic cantilevers [61–66] to enhance higher harmonic content is unlikely in FM-AFM at least under ambient or vacuum conditions. Since quality factors are so large, any slight deviation of the frequency ratio of two eigenmodes will doom this approach.

18.4.5 FM-AFM Under Liquids

Traditionally, FM-AFM requires high Q for implementation, but recent developments have shown that it is possible to implement FM-AFM techniques under liquids. Operation under liquids highlights two important differences from FM-AFM operation in vacuum. First, the Q of the cantilever resonance is greatly reduced by orders of magnitude from ambient conditions. Second, the double layer that forms at the sample's surface under liquid effectively eliminates the short-range attractive force influencing the tip's motion in vacuum. Based on (18.8), a low Q implies an increase in frequency noise, suggesting that any implementation of FM-AFM will be less than optimal. However, by reducing the oscillation amplitude to the scale of a chemical bond, the sensitivity of the frequency signal to the short-range interaction forces is evidently enhanced, allowing the resolution of molecular scale features under liquids [186].

Progress in the development of new FM-AFM techniques resulting in higher resolution images under liquids continues at a rapid pace. Recently, a heterodyne optical beam detection method has been developed that extends the ability of FM-AFM into the mega hertz regime [187]. Atomic resolution under water of both mica [186,188] and calcite [189] surfaces has been achieved (see Fig. 18.8). Under-water images of the major and minor grooves of plasmid DNA has been reported [190]. Evidence for solvation shells near an HOPG surface using a MWCNT tip has appeared [191,192]. To further optimize scanning under liquids, a number of technical improvements to increase the bandwidth of all components are under development [193]. These include a faster response of the position sensitive photodiode, the development of a fast phase detection scheme, the photo-thermal excitation of the cantilever's motion, and the development of high speed z-positioning stages. Further improvements in under-water simulations taking into account realistic damping and dissipation are also required [69, 194]. Clearly, FM-AFM is ready to address interesting new biological problems in the near future.

18.5 Outlook

In this chapter we have provided an overview of some of the key advances in cantilever dynamics and nonlinear effects in dAFM over the past two decades. Specifically we have dealt with multiple eigenmodes of cantilevers and tuning forks, the trade-offs in optimizing the dynamic response of cantilevers for

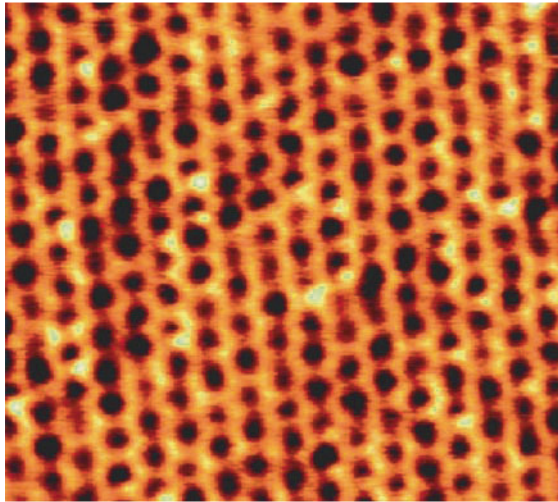

Fig. 18.8. Atomically resolved FM-AFM image of mica under water. (Reproduced with permission from [186])

dAFM, and the nonlinear probe dynamics of tip sample interaction that are central to dAFM operation.

Research efforts in the first decade since birth of dAFM [1] focused on a number of interesting applications of the technique. In the second decade, many advances were made to experimental techniques and the theoretical basis of dAFM towards the goal of making it more quantitative and easy to use. The coming third decade will likely see a strong emphasis on greatly improved performance or functionality. This new phase of dAFM development will necessarily require a deep understanding of cantilever dynamics towards (a) the development of new optimized high-bandwidth probes, (b) new material contrast imaging modes or methods to achieve atomic resolution, (c) new imaging control hardware or algorithms for reduced error, fast scanning, and (d) for new cantilever motion detection techniques.

As this chapter has shown, a large body of literature is testament to the efforts that have taken place to understand cantilever dynamics and nonlinear effects in dAFM. However, many venues of research remain open in this area, specifically, (a) nonlinear dynamics of soft microcantilevers in liquids, (b) nonlinear dynamics of multifrequency AFM, and (c) the optimal design of microcantilevers for tuning the properties of specific eigenmodes. We expect to see significant progress on these issues in the coming years.

This material is based in part upon work supported by the National Science Foundation under Grant Numbers CMMI-0700289, and CMMI-0927648. Any opinions, findings, and conclusions or recommendations expressed in this material are those of the authors and do not necessarily reflect the views of the National Science Foundation.

References

1. Y. Martin, C.C. Williams, H.K. Wickramasinghe, J. Appl. Phys. **61**, 4723 (1987)
2. S. Hembacher, F.J. Giessibl, J. Mannhart, Science **305**, 380 (2004)
3. Y. Sugimoto et al., Nature **446**, 64 (2007)
4. T. Fukuma, M.J. Higgins, S.P. Jarvis, Phys. Rev. Lett. **98**, 106101 (2007)
5. T. Akiyama et al., Sens. Actuat. A Phys. **91**, 321 (2001)
6. W.H. Han, S.M. Lindsay, T.W. Jing, Appl. Phys. Lett. **69**, 4111 (1996)
7. O. Enders, F. Korte, H.A. Kolb, Surf. Int. Anal. **36**, 119 (2004)
8. N. Mullin, J. Hobbs, Appl. Phys. Lett. **92**, 053103 (2008)
9. K. Schwarz, U. Rabe, S. Hirsekorn, W. Arnold, Appl. Phys. Lett. **92**, 183105 (2008)
10. S. Jesse et al., Nanotechnology **18**, 435503 (2007)
11. L. Merirovitch, *Principals and Techniques of Vibrations* (Prentice Hall, New Jersey, 1997)
12. M. D'Amato, M. Marcus, M. Eriksson, R. Carpick, Appl. Phys. Lett. **85**, 4738 (2004)
13. A. Yurtsever, A.M. Gigler, E. Macias, R.W. Stark, Appl. Phys. Lett. **91**, 253120 (2007)
14. J. Melcher, S. Hu, A. Raman, Appl. Phys. Lett. **91**, 053101 (2007)
15. J. Melcher, X. Xu, A. Raman, Appl. Phys. Lett. **93**, 093111 (2008)
16. L. Sharos, A. Raman, S. Crittenden, R. Reifenberger, Appl. Phys. Lett. **84**, 4638 (2004)
17. M. Reinstaedtler et al., Surf. Sci. **532**, 1152 (2003)
18. Y.X. Song, B. Bhushan, Ultramicroscopy **106**, 847 (2006)
19. Y. Song, B. Bhushan, J. Appl. Phys. **99**, 094911 (2006)
20. U. Rabe, K. Janser, W. Arnold, Rev. Sci. Instrum. **67**, 3281 (1996)
21. M. Reinstadtler et al., J. Phys. D Appl. Phys. **38**, 269 (2005)
22. M. Reinstadtler et al., Appl. Phys. Lett. **82**, 2604 (2003)
23. A. Caron et al., Appl. Phys. Lett. **85**, 6398 (2004)
24. S. Kawai et al., Appl. Phys. Lett. **86**, 193107 (2005)
25. T. Kawagishi, A. Kato, Y. Hoshi, H. Kawakatsu, Ultramicroscopy **91**, 37 (2002)
26. L. Huang, C.M. Su, Ultramicroscopy **100**, 277 (2004)
27. Y. Sugimoto et al., Appl. Phys. Lett. **91**, 093120 (2007)
28. M. Hoummady, E. Farnault, Appl. Phys. A **66**, 361 (1998)
29. R.W. Stark, T. Drobek, W.M. Heckl, Appl. Phys. Lett. **74**, 3296 (1999)
30. A. Ulcinas, V. Snitka, Ultramicroscopy **86**, 217 (2001)
31. S. Kawai et al., Rev. Sci. Instrum. **76**, 083703 (2005)
32. S. Kawai, H. Kawakatsu, Appl. Phys. Lett. **88**, 133103 (2006)
33. R.W. Stark, Rev. Sci. Instrum. **75**, 5053 (2004)
34. S. Sadewasser, G. Villanueva, J.A. Plaza, Appl. Phys. Lett. **89**, 033106 (2006)
35. T. Schaffer, H. Fuchs, J. Appl. Phys. **97**, 83524 (2005)
36. O. Pfeiffer et al., Appl. Surf. Sci. **157**, 337 (2000)
37. P. Girard, M. Ramonda, R. Arinero, Rev. Sci. Instrum. **77**, 096105 (2006)
38. R. Stark, T. Drobek, W. Heckl, Ultramicroscopy **86**, 207 (2001)
39. N. Pedersen, Eng. Optimiz. **32**, 373 (2000)
40. H.-L. Lee, Y.-C. Yang, W.-J. Chang, S.-S. Chu, Jpn. J. Appl. Phys. 1 **45**, 6017 (2006)

41. K.-N. Chen, Eng. Optimiz. **38**, 755 (2006)
42. J. Sader, I. Larson, P. Mulvaney, L. White, Rev. Sci. Instrum. **66**, 3789 (1995)
43. H.J. Butt, M. Jaschke, Nanotechnology **6**, 1 (1995)
44. M.V. Salapaka et al., J. Appl. Phys. **81**, 2480 (1997)
45. T.R. Rodriguez, R. Garcia, Appl. Phys. Lett. **80**, 1646 (2002)
46. S. Rutzel, S.I. Lee, A. Raman, Proc. Roy. Soc. A **459**, 1925 (2003)
47. F.J. Giessibl, Rev. Mod. Phys. **75**, 949 (2003)
48. S.I. Lee, S.W. Howell, A. Raman, R. Reifenberger, Phys. Rev. B **66**, 115409 (2002)
49. S. Rast, C. Wattinger, U. Gysin, E. Meyer, Rev. Sci. Instrum. **71**, 2772 (2000)
50. B. Anczykowski et al., Appl. Surf. Sci. **140**, 376 (1999)
51. F.J. Giessibl, Appl. Phys. Lett. **78**, 123 (2001)
52. S. Hu, A. Raman, Appl. Phys. Lett. **91**, 123106 (2007)
53. R. Garcia, A. San Paulo, Phys. Rev. B **60**, 4961 (1999)
54. R. Garcia et al., Phys. Rev. Lett. **97**, 016103 (2006)
55. N. Oyabu et al., Phys. Rev. Lett. **96**, 106101 (2006)
56. L. Zitzler, S. Herminghaus, F. Mugele, Phys. Rev. B **66**, 155436 (2002)
57. E. Sahagun, P. Garcia-Mochales, G.M. Sacha, J.J. Saenz, Phys. Rev. Lett. **98**, 176106 (2007)
58. A. San Paulo, R. Garcia, Phys. Rev. B **64**, 193411 (2001)
59. H.J. Butt, B. Cappella, M. Kappl, Surf. Sci. Rep. **59**, 1 (2005)
60. S. Basak, A. Raman, Appl. Phys. Lett. **91**, 064107 (2007)
61. O. Sahin, C.F. Quate, O. Solgaard, A. Atalar, Phys. Rev. B **69**, 165416 (2004)
62. O. Sahin et al., Sens. Actuat. A Phys. **114**, 183 (2004)
63. M. Balantekin, A. Atalar, Appl. Phys. Lett. **87**, 243513 (2005)
64. O. Sahin et al., Nat. Nanotechnol. **2**, 507 (2007)
65. O. Sahin, Rev. Sci. Instrum. **78**, 103707 (2007)
66. O. Sahin, Phys. Rev. B **77**, 115405 (2008)
67. R. Proksch, Appl. Phys. Lett. **89**, 113121 (2006)
68. J.R. Lozano, R. Garcia, Phys. Rev. Lett. **1**, 076102 (2008)
69. J. Melcher, S. Hu, A. Raman, Rev. Sci. Instrum. **79**, 061301 (2008)
70. G. Couturier, J.P. Aime, J. Salardenne, R. Boisgard, Euro. Phys. J. Appl. Phys. **15**, 141 (2001)
71. L. Nony, A. Baratoff, Phys. Rev. B **74**, 235439 (2006)
72. J. Polesel-Maris, S. Gauthier, J. Appl. Phys. **97**, 044902 (2005)
73. A. Abdurixit, A. Baratoff, E. Meyer, Appl. Surf. Sci. **157**, 355 (2000)
74. M. Watkins, T. Trevethan, A.L. Shluger, L.N. Kantorovich, Phys. Rev. B **76**, 245421 (2007)
75. T. Trevethan, M. Watkins, L.N. Kantorovich, A.L. Shluger, Phys. Rev. Lett. **98**, 028101 (2007)
76. P.D. Ashby, Appl. Phys. Lett. **91**, 254102 (2007)
77. B. Anczykowski, D. Kruger, H. Fuchs, Phys. Rev. B **53**, 15485 (1996)
78. H. Holscher, U.D. Schwarz, Int. J. Non-Linear Mech. **42**, 608 (2007)
79. J. Melcher, S. Hu, A. Raman, VEDA: Dynamic Approach Curves, 2007
80. J. Melcher, S. Hu, A. Raman, VEDA: Amplitude Modulated Scanning, 2007
81. P. Gleyzes, P.K. Kuo, A.C. Boccara, Appl. Phys. Lett. **58**, 2989 (1991)
82. N. Sasaki, M. Tsukada, Sci. Rep. Res. Tohoku A **44**, 1 (1997)
83. A. Kuhle, A. Sorensen, J. Bohr, J. Appl. Phys. **81**, 6562 (1997)
84. D. Sarid, T.G. Ruskell, R.K. Workman, D. Chen, J. Vac. Sci. Technol. B **14**, 864 (1996)

85. L. Wang, Appl. Phys. Lett. **73**, 3781 (1998)
86. L.G. Wang, Surf. Sci. **429**, 178 (1999)
87. L. Nony, R. Boisgard, J.P. Aime, J. Chem. Phys. **111**, 1615 (1999)
88. R. Boisgard, D. Michel, J.P. Aime, Surf. Sci. **401**, 199 (1998)
89. R. Boisgard, J.P. Aime, G. Couturier, Int. J. Non-Linear Mech. **42**, 673 (2007)
90. R. Garcia, A. San Paulo, Phys. Rev. B **61**, 13381 (2000)
91. A. San Paulo, R. Garcia, Biophys. J. **78**, 1599 (2000)
92. A. San Paulo, R. Garcia, Phys. Rev. B **66**, 041406 (2002)
93. J. Kokavecz, O. Marti, P. Heszler, A. Mechler, Phys. Rev. B **73**, (2006)
94. S.I. Lee, J.M. Lee, S.H. Hong, CIRP Ann. Manuf. Techn. **54**, 527 (2005)
95. K. Wolf, O. Gottlieb, J. Appl. Phys. **91**, 4701 (2002)
96. S.I. Lee, S.W. Howell, A. Raman, R. Reifenberger, Ultramicroscopy **97**, 185 (2003)
97. K. Yagasaki, Int. J. Non-Linear Mech. **42**, 658 (2007)
98. H.N. Pishkenari, M. Behzad, A. Meghdari, Chaos Soliton Fract. **37**, 748 (2008)
99. S. Das, P.A. Sreeram, A.K. Raychaudhuri, Nanotechnology **18**, 035501 (2007)
100. M. Balantekin, A. Atalar, Appl. Surf. Sci. **205**, 86 (2003)
101. X. Chen et al., Surf. Sci. **460**, 292 (2000)
102. A.N. Round, M.J. Miles, Nanotechnology **15**, 176 (2004)
103. H. Dankowicz, Philos. Trans. R. Soc. London, Ser. A **364**, 3505 (2006)
104. J.P. Hunt, D. Sarid, Appl. Phys. Lett. **72**, 2969 (1998)
105. J. Berg, G. Briggs, Phys. Rev. B **55**, 14899 (1997)
106. W. van de Water, J. Molenaar, Nanotechnology **11**, 192 (2000)
107. H. Dankowicz, X. Zhao, S. Misra, Int. J. Non-Linear Mech. **42**, 697 (2007)
108. N. Hashemi, H. Dankowicz, M.R. Paul, J. Appl. Phys. **103**, 093512 (2008)
109. M. Ashhab, M.V. Salapaka, M. Dahleh, I. Mezic, Nonlinear Dyn. **20**, 197 (1999)
110. M. Ashhab, M.V. Salapaka, M. Dahleh, I. Mezic, Automatica **35**, 1663 (1999)
111. M. Basso, L. Giarre, M. Dahleh, I. Mezic, J. Dyn. Syst. Meas. Control **122**, 240 (2000)
112. J. Guckenheimer, P. Holmes, *Nonlinear Oscillations, Dynamical Systems, and Bifurcations of Vector Fields* (Springer-Verlag, New York, 1983)
113. N. Sasaki et al., Appl. Phys. A **66**, 287 (1998)
114. N.A. Burnham, A.J. Kulik, G. Gremaud, G.A.D. Briggs, Phys. Rev. Lett. **74**, 5092 (1995)
115. S. Salapaka, M. Dahleh, I. Mezic, Nonlinear Dyn. **24**, 333 (2001)
116. S.Q. Hu, A. Raman, Phys. Rev. Lett. **96**, 036107 (2006)
117. F. Jamitzky et al., Nanotechnology **17**, 213 (2006)
118. M. Liu, D. Chelidze, Int. J. Non-Linear Mech. **43**, 521 (2008)
119. K. Yamasue, T. Hikihara, Rev. Sci. Instrum. **77**, (2006)
120. S.J.T. van Noort et al., Langmuir **15**, 7101 (1999)
121. U. Durig, New J. Phys. **2**, 1 (2000)
122. M. Stark, R.W. Stark, W.M. Heckl, R. Guckenberger, PNAS **99**, 8473 (2002)
123. U. Durig, Appl. Phys. Lett. **76**, 1203 (2000)
124. R. Hillenbrand, M. Stark, R. Guckenberger, Appl. Phys. Lett. **76**, 3478 (2000)
125. M. Stark, R.W. Stark, W.M. Heckl, R. Guckenberger, Appl. Phys. Lett. **77**, 3293 (2000)
126. R.W. Stark, W.M. Heckl, Surf. Sci. **457**, 219 (2000)
127. R.W. Stark, Nanotechnology **15**, 347 (2004)
128. A. Sebastian, A. Gannepalli, M.V. Salapaka, IEEE Trans. Control. Syst. Technol. **15**, 952 (2007)

129. A. Sebastian, M.V. Salapaka, D.J. Chen, J.P. Cleveland, J. Appl. Phys. **89**, 6473 (2001)
130. F.J. Giessibl, Surf. Int. Anal. **38**, 1696 (2006)
131. S. Crittenden, A. Raman, R. Reifenberger, Phys. Rev. B **72**, 235422 (2005)
132. S. Hu et al., J. Vibrat. Acous. Trans. ASME **126**, 343 (2004)
133. H. Li, Y. Chen, L. Dai, Appl. Phys. Lett. **92**, 151903 (2008)
134. J. Preiner, J.L. Tang, V. Pastushenko, P. Hinterdorfer, Phys. Rev. Lett. **99**, 046102 (2007)
135. R.W. Stark, W.M. Heckl, Rev. Sci. Instrum. **74**, 5111 (2003)
136. M. Balantekin, A. Atalar, Phys. Rev. B **71**, 125416 (2005)
137. D. Platz, E.A. Tholen, D. Pesen, D.B. Haviland, Appl. Phys. Lett. **92**, 153106 (2008)
138. A.H. Nayfeh, B. Balachandran, *Applied Nonlinear dynamics: Analytical, Computational, and Experimental Methods* (Wiley, New York, 1995)
139. R.W. Stark, N. Naujoks, A. Stemmer, Nanotechnology **18**, 065502 (2007)
140. B.J. Rodriguez, C. Callahan, S.V. Kalinin, R. Proksch, Nanotechnology **18**, 475504 (2007)
141. N.F. Martinez, S. Patil, J.R. Lozano, R. Garcia, Appl. Phys. Lett. **89**, 153115 (2006)
142. S. Patil, N.F. Martinez, J.R. Lozano, R. Garcia, J. Mol. Recognit. **20**, 516 (2007)
143. T.R. Rodriguez, R. Garcia, Appl. Phys. Lett. **84**, 449 (2004)
144. C. Dietz et al., Appl. Phys. Lett. **92**, 143107 (2008)
145. N.F. Martinez et al., Nanotechnology **19**, 153115 (2008)
146. P. Thota, S. MacLaren, H. Dankowicz, Appl. Phys. Lett. **91**, 093108 (2007)
147. C.A.J. Putman et al., Appl. Phys. Lett. **64**, 2454 (1994)
148. T.E. Schaffer et al., J. Appl. Phys. **80**, 3622 (1996)
149. A.O. Volkov, J.S. Burnell-Gray, P.K. Datta, Appl. Phys. Lett. **85**, 5397 (2004)
150. X. Xu, A. Raman, J. Appl. Phys. **102**, 034303 (2007)
151. J. Kokavecz, A. Mechler, Appl. Phys. Lett. **91**, 023113 (2007)
152. I. Revenko, R. Proksch, J. Appl. Phys. **87**, 526 (2000)
153. C. Rankl et al., Ultramicroscopy **100**, 301 (2004)
154. I. Nnebe, J.W. Schneider, Langmuir **20**, 3195 (2004)
155. C.P. Green, J.E. Sader, Phys. Fluids **17**, 073102 (2005)
156. C.P. Green, J.E. Sader, J. Appl. Phys. **98**, 114913 (2005)
157. R.J. Clarke, S.M. Cox, P.M. Williams, O.E. Jensen, J. Fluid Mech. **545**, 397 (2005)
158. R.J. Clarke, O.E. Jensen, J. Billingham, P.M. Williams, Proc. Roy. Soc. A **462**, 913 (2006)
159. R.J. Clarke et al., Phys. Rev. Lett. **96**, 050801 (2006)
160. S. Basak, A. Raman, S.V. Garimella, J. Appl. Phys. **99**, 114906 (2006)
161. S. Basak et al., J. Appl. Phys. **102**, 064107 (2007)
162. M.T. Clark, M.R. Paul, J. Appl. Phys. **103**, 094910 (2008)
163. C. Harrison et al., Sensor Actuat. A Phys. **134**, 414 (2007)
164. A. Roters, D. Johannsmann, J. Phys. Condes. Mat. **8**, 7561 (1996)
165. T. Naik, E. Longmire, S. Mantell, Sensor Actuat. A Phys. **102**, 240 (2003)
166. P. Decuzzi, A. Granaldi, G. Pascazio, J. Appl. Phys. **101**, 024303 (2007)
167. X. Xin et al., Biophys. J. **95**, 2520 (2008)
168. D. Sarid, J. Chen, R.K. Workman, Comput. Mater. Sci. **3**, 475 (1995)

169. G.Y. Chen, R.J. Warmack, P.I. Oden, T. Thundat, J. Vac. Sci. Technol. B **14**, 1313 (1996)
170. J. Legleiter, T. Kowalewski, Appl. Phys. Lett. **87**, 163120 (2005)
171. J.E. Sader, S.P. Jarvis, Appl. Phys. Lett. **84**, 1801 (2004)
172. F.J. Giessibl, Science **267**, 68 (1995)
173. F.J. Giessibl, S. Hembacher, H. Bielefeldt, J. Mannhart, Science **289**, 422 (2000)
174. F.J. Giessibl, Appl. Phys. Lett. **76**, 1470 (2000)
175. H. Hölscher, in *Noncontact Atomic Force Microscopy*, ed. by S. Morita, R. Wiesendanger, E. Meyers (Springer, Berlin, 2002)
176. F.J. Giessibl, Phys. Rev. B **56**, 16010 (1997)
177. F.J. Giessibl, in *Noncontact Atomic Force Microscopy*, ed. by S. Morita, R. Wiesendanger, E. Meyers (Springer, Berlin, 2002)
178. F.J. Giessibl, H. Bielefeldt, S. Hembacher, J. Mannhart, Appl. Surf. Sci. **140**, 352 (1999)
179. S. Hosaka, K. Etoh, A. Kikukawa, H. Koyanagi, J. Vac. Sci. Technol. B **18**, 94 (2000)
180. H. Kawakatsu et al., Rev. Sci. Instrum. **73**, 2317 (2002)
181. T.R. Albrecht, P. Grutter, D. Horne, D. Rugar, J. Appl. Phys. **69**, 668 (1991)
182. H. Edwards, L. Taylor, W. Duncan, A.J. Melmed, J. Appl. Phys. **82**, 980 (1997)
183. F.J. Giessibl, Appl. Phys. Lett. **73**, 3956 (1998)
184. H. Kawakatsu et al., e-J. Surf. Sci. Nanotechnol. **4**, 110 (2006)
185. Y. Qin, R. Reifenberger, Rev. Sci. Instrum. **78**, 063704 (2007)
186. T. Fukuma, K. Kobayashi, K. Matsushige, H. Yamada, Appl. Phys. Lett. **87**, 034101 (2005)
187. T. Fukuma et al., Rev. Sci. Instrum. **76**, 126110 (2005)
188. T. Fukuma, S. Jarvis, Rev. Sci. Instrum. **77**, 043701 (2006)
189. S. Rode et al., Langmuir 25, 2850 (2009)
190. S. Ido et al., 11th International Conference on Non-Contact Atomic Force Microscopy (Madrid, Spain, 2008)
191. M.J. Higgins et al., Nanotechnology **16**, S85 (2005)
192. T. Uchihashi et al., Nanotechnology **16**, S49 (2005)
193. T. Fukuma, 11th International Conference on Non-Contact Atomic Force Microscopy (Madrid, Spain, 2008)
194. M. Tsukada, K. Tagami, Q. Gao, N. Watanabe, Curr. Nanosci. **3**, 57 (2007)

Index

adhesion maps, 46
adsorbed metal particle, 145
AFM
  frequency modulation, 195
AFM in Liquids, 304
AFM/STM, 11, 195
air, 74, 80, 81
Alumina/NiAl(110), 143, 144, 150–152, 165
amplifier, 146, 151
amplitude, 143, 144, 147–150, 152, 156, 159
amyloid fibrils, 334, 335, 342, 343
apparent barrier height, 161, 164
artifact, 38, 40
artificial nanostructure, 169, 177, 178
atom inlay, 4, 7, 8, 12, 177
atom letter, 4, 7, 8, 188
atom manipulatio, 169
atom manipulation, 4, 7, 12, 169
  interchange, 7
  interchange lateral, 179
  lateral, 194, 228, 229, 231–234, 236, 237, 245
  mechanical, 1, 3
  vertical, 193
atom-by-atom assembly, 12
atom-tracking, 17, 34, 51
atomic height differences, 53
atomic pattern, 187, 188
atomic recognition, 45
atomic relaxations, 32, 48, 51
atomic resolution, 31, 33, 57, 143–145, 150–152, 158, 159
atomic-resolution imaging, 95, 103, 113
atomically reactive tips, 33

bacteriorhodopsin, 323, 324
barrier field, 255
Bessel functions, 309
bias voltage, 33, 147, 162, 163
bifurcation, 362, 370, 371, 373
biological membrane, 338–340, 342
bridge site, 82–84, 91
Brownian motion, 308, 310, 311

C_{60} molecule, 265
CaF_2, 69, 74, 80, 81, 221
calibration, 149, 150
calibration of the cantilever oscillation amplitude, 37
cantilever dynamics in liquids, 376, 378
cantilever higher flexural modes, 62, 64
cantilever static stiffness, 61
cantilever stiffness, 34, 36, 40, 54
CeO_2, 263
chaos, 373
charge density, 279
  difference, 296
charge transfer, 145, 157, 160, 161, 165, 296
chemical bonding force, 178, 180, 183, 185
chemical coordination, 4, 6
chemical identification, 32, 53, 58

Co
  on Cu(111), 205
  on Pt(111), 199
CO on Cu(111), 200, 206
coherence length, 318–320
color centers, 157, 160
complex nanostructure, 12
contact potential
  tip-surface, 33, 36
contact potential difference (CPD), 144, 161, 163–165
contrast
  chemical, 299
  magnetic, 299
contrast inversion, 222, 223
contrast reversal, 281
corrugation amplitude, 277, 298
  chemical, 279
  magnetic, 280
cryogenic environment, 143
cryogenic temperature, 145

dangling bonds, 230, 231, 236
Debye length, 307
defect, 75, 83, 87, 88, 143, 157, 160
density distribution function, 325
Density Functional Theory, 255, 266
density functional theory, 155, 157, 160, 164, 229
density functional theory (DFT), 277, 283, 287
  energy cut-off, 290
  full-potential linearized augmented plane wave method, 290
  generalized gradient approximation, 289
  Monkhorst-Pack grid, 290
  supercell geometry, 290
  wien2k, 290
DFT, 144, 151, 153, 154, 156, 160, 164, 165
differentiation of atomic force, 11
diffusion, 252, 253, 257
diffusion barrier, 210
diffusion barrier measurement, 96, 107
diffusion barriers, 235, 236
displacement sensor noise, 311
dissipation, 69, 70, 86–92, 238, 246, 247, 262, 263
  detection, 198
  during atom manipulation, 210
dissipation image, 39, 45
dither piezo, 146, 147
domain, 150–155
domain wall, 285
drift, 152, 156, 158
dynamic characteristic, 385

eigenmodes of AFM cantilevers, 363
electric double layer force, 307, 308
electrostatic force, 161–163
energy
  magnetic exchange, 276, 277, 292
  magneto-crystalline anisotropy, 277, 281
  shape anisotropy, 277
  Zeeman, 277, 282
energy barriers, 227, 228, 233–236, 239, 243–248
energy dissipation, 42, 44, 45, 61
energy dissipation maps, 105, 106, 114
energy map, 209
excitation signal, 33

Fe/W(001), 275, 282, 287
feedforward, 23
field emission, 145, 152
field emission resonance (FER), 161, 162, 164, 165
film thickness, 143, 157, 160, 161
FIREBALL code, 229
first principles, 277, 283, 287
first-principles simulations, 227–229, 242, 247
FM-DFM, 145
force
  attractive, 71, 73, 78, 82, 84, 85
  chemical, 276, 284, 299
  chemical bonding, 76, 78
  electron mediated, 284
  lateral, 69, 70, 108, 109, 112, 113, 203
  long-range, 74, 75, 79, 82, 275, 296, 298
  magnetic exchange, 8, 276, 280, 284, 287, 291, 299
  magnetostatic, 275
  repulsive, 76, 78, 81, 84

short-range, 70, 75, 76, 78, 233, 235, 238, 245–247, 284
site-specific, 69
van der Waals, 74–76, 259, 264, 284, 298
Hamaker constant, 298
force distance curves, 159
force distance measurements, 143
force field
three dimensional, 83
force field (1D,2D,3D), 143, 144, 158
force mapping, 23, 24, 26, 29
force microscopy
lateral dynamic, 356
force spectroscopy, 1–3, 23, 95, 171, 183, 228, 229, 241, 246
acquisition, 32
dynamic, 96
site-specific, 16, 20
three-dimensional, 95, 102, 103, 113
force vector fields, 110
force-distance curve, 284, 291
force-field, 254
Fourier transform, 279
free oscillation region, 34, 36
frequency modulation, 145, 147, 149
frequency modulation detection method, 32
frequency shift, 33, 34, 70, 72, 73, 76, 79, 82, 85, 90
normalized, 72
frequency shift curves, 144, 158

Ge(111)-c(2×8), 172, 174, 176, 178
Ge(111)-c(2×8), 175, 176
Graphite, 113, 115
GroEL, 323
growth
pseudomorphic, 283
step flow, 283
wetting layer, 283

height determination, 198
Heisenberg model, 276
exchange coupling constant, 276
helium, 146
heterodyne laser Doppler detection, 351
higher harmonics, 370, 372, 374–376, 379, 380, 388, 389
higher mode, 355
hopping motion, 225
hybridization, 282, 285, 295
hydration layers, 335, 338, 343
hydration structure, 325

image potential, 163
imaging in liquid, 8
In/Si(111)-($\sqrt{3} \times \sqrt{3}$), 179
In/Si(111)-($\sqrt{3} \times \sqrt{3}$), 178, 179, 188
In/Si(111)-($\sqrt{3} \times \sqrt{3}$), 171
insulator, 218
interaction
chemical, 284
electron mediated, 277, 284
electrostatic, 33
long-range, 275
magnetic exchange, 284
short-range, 32, 34, 36, 38, 46, 50, 53, 56, 58, 59, 277, 284
van der Waals, 33, 36
interaction potential, 203
interatomic forces, 31
interchange lateral atom manipulation, 175
interchange vertical atom manipulation, 184
interference noise, 318
inversion procedures, 35
ionic surface, 159

KBr, 78, 79, 82, 83, 85, 88, 91, 110
Kelvin probe force microscopy, 61
kinetic Monte Carlo, 256

large-amplitude limit, 72
lateral force microscopy, 138
lateral manipulation, 175, 180, 181
line scan, 174, 181
lipid bilayers, 335, 336, 341
lipid-ion interaction, 341
liquid AFM, 350, 352–354, 356, 358
liquid-environment FM-AFM, 338, 343
local density of states (LDOS), 285
lock-in amplifier, 18
low-temperature preamplifier, 195

magnetic exchange
  double exchange, 285
  RKKY, 285
  superexchange, 281, 285
magnetic exchange force microscopy (MExFM), 275, 287
magnetic force microscopy (MFM), 275, 287
magnetic moment, 276, 294
magnetic polarization
  easy axis, 277
  saturation, 277
manipulation, 218
manipulation protocols, 262, 271
manipulation threshold, 200
measurement noise, 311
metal-oxide, 143, 144
MgO, 80, 82, 143, 145, 157, 158, 160, 161, 163, 164, 258
MgO/Ag(001), 143, 144, 158, 159, 161, 163
MgO/Mo(001), 161
microscopic tip, 144, 145, 147, 149, 152, 153
mode-hop noise, 319
Muscovite Mica, 321

NaCl, 69, 77, 79, 80, 82, 83, 104
nano cantilever, 347, 348
nanoindentation, 172, 185
NC-AFM/STM, 145, 146
  combined, 165
  dual mode, 143, 145, 156
nearcontact region, 3, 7
negatively terminated tip, 81, 85, 86
nickel oxide, 102
NiO, 80, 89
NiO(001), 275
non-contact, 145
noncontact, 143
nonlinear dynamics, 362, 371, 375, 379, 390
  multi-mode, 375
normalized frequency shif, 149
normalized frequency shift, 298
normalized frequency shift scaling, 64
Nudge Elastic Band Method, 245

oscillation amplitude, 33, 34, 38, 54
  calibartion, 198
  cantilever, 32, 34, 36, 38, 46, 61, 64
  small, 196
oscillator noise, 311
oxide, 143, 144, 146, 150–152, 154, 155, 161
oxide film, 145, 155, 157, 160
oxygen, 151, 153–156, 160, 165

Pauli exclusion principle, 76
phase modulation, 309
photothermal excitation, 350, 351, 356
piezo actuator, 33
piezo creep, 37, 145
piezo hysteresis, 145
piezoelectric detection, 121
point-mass model, 34, 63
positively terminated tip, 81, 85, 86
potential energy landscape measurement, 96, 107
potential trough, 225
PtIr, 145
pulling mode, 174, 182
purple membrane, 323, 324

Q-value, 40, 54, 63
qPlus sensor, 11, 121, 122, 131–135, 137, 139, 140
quality factor, 36, 304
quality factor Q, 147
quartz tuning fork, 195

reflection domain, 143, 144, 150–153, 165
relative interaction ratio, 54, 56, 58
relaxation, 70, 76, 78, 80, 83, 84, 293
  sample, 287, 291, 293
  surface, 293
  tip, 287, 291, 293, 294
repulsive interaction force, 186
resolution
  MExFM, 276
  MFM, 275
  SP-STM, 275
rolling, 265, 266

s-wave model, 207
Sb/Si(111)-(7×7), 172, 178, 179

Sb/Si(111)-(7×7), 179
scanning tunneling microscopy (STM), 275
  spin-polarized (SP-STM), 287
  spin-polarized (SP-STM), 275
sensor, 143, 145–150, 156
short-range chemical interaction, 237, 241, 246
shot noise, 316, 318
Si, 75, 80, 90, 92
Si(111)-(7×7), 171
Si(111)-(7×7), 171–173, 179, 180, 183
Si(111)-(7×7), 180, 182
signal-to-noise ratio, 127, 136
silicon, 254
simulation, 277, 283, 287, 297
SiO_x, 80
site-specific, 145, 156, 159, 165
small amplitude, 355, 356
small cantilever, 347, 358
small cantilever oscillation, 32, 61
small cantilevers, 61
Sn/Ge(111)-c(2×8), 172, 175, 176, 178, 179
Sn/Si(111)-($\sqrt{3} \times \sqrt{3}$), 179
Sn/Si(111)-($\sqrt{3} \times \sqrt{3}$), 172, 178, 179, 184, 188
Sn/Si(111)-($\sqrt{3} \times \sqrt{3}$), 171
snap to contact, 196
solvation (hydration) structure, 325
spatial resolution, 4
spin, 276
spin spiral, 285
spin-orbit coupling, 281
spring constant, 146–149
stable adsorption sites, 210
stable cantilever oscillation, 61
stiffness
  lateral, 206
  vertical, 197
STM, 143–147, 149–151, 157, 160, 165
STM/AFM, 195
structured liquid molecules, 355
STS, 156, 157
sub-lattice, 220
subatomic resolution, 4, 11, 137

thermal drift, 145
thermal noise, 310–313
thermally activated hopping, 183
thickness of electric double layer, 307
thin oxide film, 160
tight binding, 266
tip
  apex, 277, 293
  asymmetric, 281
  change, 277, 283
  configuration, 277, 293
  ferromagnetic, 277
  Ir, 196
  iron, 277, 287
    five atom, 287, 289, 290, 297
    fourteen atom, 287, 297
    in-plane sensitive, 276
    out-of-plane sensitive, 276
    single atom, 287, 288, 296
  magnetic double, 280
  wedge-shaped, 281
tip asymmetry, 181
tip characterization, 40
tip models, 40, 52, 56
tip preparation, 145, 153
tip–sample, 143, 148, 149, 156, 158, 159
tip-sample, 147
tip-sample interaction, 228, 232–235
topographic height, 143, 155
topographic maps, 33
topographic measurements, 53
topography effect compensation, 50
torsional mode, 356
tuning fork, 11, 143, 145–149
tunneling current, 143, 145–147, 149, 156, 161, 163
two-dimensional antiferromagnet, 287

UHV, 143, 145–148, 150, 151
unit cell, 143, 144, 150–155, 165, 283
  averaging, 279, 281

van der Waals, 269
vertical interchange, 227, 228, 240–243, 245, 248
vertical manipulation, 172
virtual AFM, 254
viscous damping, 304
visibility, 319

water, 74, 75, 80, 87
water exposure, 221
water molecule, 263–265
work function, 143, 145, 157, 160–165